

申 报	系列：研究系列普通型
	专业：木材加工
	职称：副研究员

业绩成果材料

（申报人的业绩成果材料包括论文、科研项目、获奖以及其他成果等）

单 位（二级单位） 材料与能源学院

姓 名 樊奇

材料核对人：

单位盖章：

核对时间：

华南农业大学制

目 录

一、教学研究业绩

1. 广东省教学质量工程项目：生物质先进材料课程教研室. 5
2. 教学比赛证书 7

二、科研项目

1. 主持：国自然项目-《烷基酚-马来酸酐络合物对木质素高效溶解与抗氧化增效机理》项目的立项通知（合同）及有关佐证材料..... 8
2. 主持：中国博后面上项目-《3D 超强矿化木质素气凝胶的仿生构建及其对蛋白质的分离与传质机制》项目的立项通知（合同）及有关佐证材料 10
3. 主持：企业委托项目-《木质素基新材料开发及性能测试》项目的立项通知（合同）及有关佐证材料 11
4. 主参：广州市重点研发计划项目-《农林废弃物联产轻质高强复合材料与功能助剂技术开发与应用》项目的立项通知（合同）及有关佐证材料 21
5. 主参：企业委托项目-《家居材料研发合作》项目的立项通知（合同）及有关佐证材料 47

三、论文、著作等

1. 检索证明..... 57
2. 以第一作者发表本专业论文情况
 - 2.1. <ACS nano> (T2, IF=18.03) -Water-Induced Self-Assembly and In Situ Mineralization within Plant Phenolic Glycol-Gel toward Ultrastrong and Multifunctional Thermal Insulating Aerogels 62
 - 2.2. <Composites Part B> (T2, IF=13.1) -Biomimetic versatile wood hybrids with gradient structure towards lightweight, high

strength, fire-retardant, and deterioration-resistant materials	79
2.3. <Construction and Building Materials> (T2, IF=7.4)	
-Fast realization of high-strength, repeatable, damp-heat resistant bamboo-strip scarf bonding joints via hot-melt adhesives	94
2.4. <Construction and Building Materials> (T2, IF=7.4)	
-Modification of poplar wood cells using 1,3-dihydroxymethyl-4,5-dihydroxyethylideneurea-alkaline lignin for enhanced mechanical properties and decay resistance	104
3.以通讯作者发表本专业论文情况	
3.1. <Advanced Functional Materials> (T2, IF=19.0)	
-Ultrastrong and Thermo-Remoldable Lignin-Based Polyurethane Foam Insulation with Active-Passive Fire Resistance.....	118
3.2. <Industrial Crops & Products> (T2, IF=5.9)	
-Handling-friendly, waterproof, and mildew-resistant all-bio-based soybean protein adhesives with high-bonding performance via bio-inspired hydrophobic-enhanced crosslinking network.....	134
3.3. <Construction and Building Materials> (T2, IF=7.4)	
-Enhanced mechanical performance and fire resistance of poplar wood-Unilateral surface densification assisted with N-P doped acrylic resin impregnation	148
3.4. <复合材料学报> (A) -多层夹芯结构木塑复合材料阻燃与力学性能.....	163
4.理论文章、学术专著等	
4.1. Chapter-Lignin-based polymers	174

四、科研成果

1. 知识产权

1.1.专利授权证书：块状木质素—二氧化硅复合气凝胶 217

1.2.专利授权证书：一种含有三维网络结构天然纤维复合材料的制造方法..... 219

五、其他业绩

1. 指导学生学科竞赛

1.1. 中国国际大学生创新大赛（2024）广东省分赛银奖... 221

1.2. 华南农业大学“创客杯”大学生创新大赛 222

关于公示2024年度省级教改项目和质量工程项目拟推荐名单的通知 2

本科生院（招生办公室）直通车 2024-10-24

各学院、部处、各单位:

根据《关于开展2024年度广东省本科高校教学质量与教学改革工程项目申报推荐工作的通知》精神,经项目负责人申报、所在单位推荐和学校组织专家评审,拟推荐“新工科背景下一流农林院校《材料物理》课程教学改革与实践”等32个项目为2024年度省级高等教育教学改革项目;拟推荐“公共管理新文科和领导力专项人才培养计划”等18个项目为2024年度省级教学质量工程项目。现予以公示,具体名单见附件。

公示期自2024年10月24日至10月30日。如有异议,请在公示期内以书面方式提交(附必要的证据材料,并署真实姓名),未署真实姓名或逾期者不予受理。

联系人: 孙齐胜

电 话: 85288020

地 址: 行政楼329

邮 箱: gjyj@scau.edu.cn

本科生院（招生办

公

2024年10月24日

附件: 1.2024年度省级高等教育教学改革项目拟推荐名单.pdf

2.2024年度省级教学质量工程项目拟推荐名单.pdf

附件(2)



2024年度省级高等教育教学改革项目拟推...
365KB



2024年度省级教学质量工程项目拟推荐名...
299KB

阅读 818  0

附件2
2024年度省级教学质量工程项目拟推荐名单

序号	项目类别	项目名称	单位	负责人	成员
1	专项人才培养计划	公共管理新文科和领导力专项人才培养计划	公共管理学院	史传林	蔡茂华、唐斌、王希、贾海薇、袁中友、古佳妍、余祥
2	校企联合实验室	环境友好高分子材料联合实验室	材料与能源学院	张超群	罗颖、刘威、张淑婷、王洋、董先明、李宗翰
3	校企联合实验室	熟成肉制品微生物精准调控实验室	食品学院	方梓	董飒爽、吴健锋、钟青萍、廖振林、王刚、王洁、艾民珉
4	现代产业学院	低碳农业现代产业学院	资源环境学院	余光伟	余光伟、仇荣亮、舒迎花、邓兰生、张池、姚朝龙、钟晓兰、梁瑜海、郭勇军、周坚兵、李择佳、蔺俊鹏、王泽钊、郑边麟
5	课程教研室	普通生态学课程教研室	资源环境学院	舒迎花	王建武、陈桂葵、危晖、谈凤笑、李荣华、陈永健
6	课程教研室	遗传学实验课程教研室	农学院	刘自强	王少奎、胡斌、谢庆军、王兰、李楠
7	课程教研室	建设工程造价课程教研室	水利与土木工程学院	李高扬	黄俐、李东南、陆金驰、李庚英、陈幸斌
8	课程教研室	智慧农业课程教研室	数学与信息学院软件学院	黄栋	黄琼、胡炼、王燕、陈湘骥、崔金荣、高月芳、肖媚燕、涂淑琴
9	课程教研室	农科数学课程教研室	数学与信息学院软件学院	杨德贵	肖莉、李风、岑冠军、杨志程、周燕、陆琪、丁仕虹、刘曼莉、姚焕城
10	课程教研室	生物质先进材料课程教研室	材料与能源学院	孙理超	樊奇、郝笑龙、欧荣贤、周海洋、易欣、李丽萍、郭垂根、王清文
11	课程教研室	农业历史教研室	人文与法学院	赵艳萍	王福昌、赵飞、陈志国、龚金红、余格格、袁海燕、刘玲娣
12	科产教融合实践教学基地	华南农业大学-广东爱健康清远麻鸡全产业链科产教融合实践教学基地	动物科学学院	陈伟国	谢青梅、孙宝丽、张新珩、李鸿鑫
13	科产教融合实践教学基地	华南农业大学广州维德科技有限公司科产教融合实践教学基地	数学与信息学院软件学院	张昕	周裕中、方平、陈羽、袁利国、邱华、陈银辉
14	科产教融合实践教学基地	华南农业大学-盛方达本科生产学研培养基地	水利与土木工程学院	王海洋	张敏、陈幸斌、李庚英、毕敏娜、韦未、曾皓鹏
15	大学生实践教学基地	华南农业大学广东华农大新龙畜牧股份有限公司大学生社会实践教学基地	动物科学学院	邓铭	陈飞洋、李耀坤、徐智城、贾坤、刘天增、何杰、孙宝丽
16	大学生实践教学基地	华南农业大学广州市威控机器人有限公司实践教学基地	工程学院	孙振刚	莫嘉嗣、周锡恩、漆海霞、孔莲芳、梅慧兰、赵祚喜、周学成

奖状

樊奇 老师：

荣获华南农业大学材料与能源学院 2024 年青年教师

教学观摩竞赛 一 等奖。

特发此状，以资鼓励！

华南农业大学材料与能源学院

2024 年 12 月 19 日

国家自然科学基金资助项目批准通知

(包干制项目)



樊奇 先生/女士:

根据《国家自然科学基金条例》、相关项目管理办法规定和专家评审意见,国家自然科学基金委员会(以下简称自然科学基金委)决定资助您申请的项目。项目批准号: 52103110, 项目名称: 烷基酚-马来酸酐络合物对木质素高效溶解与抗氧化增效机理, 资助经费: 30.00万元, 项目起止年月: 2022年01月至 2024年12月, 有关项目的评审意见及修改意见附后。

请您尽快登录科学基金网络信息系统(<https://isisn.nsfc.gov.cn>), 认真阅读《国家自然科学基金资助项目计划书填报说明》并按要求填写《国家自然科学基金资助项目计划书》(以下简称计划书)。对于有修改意见的项目, 请您按修改意见及时调整计划书相关内容; 如您对修改意见有异议, 须在电子版计划书报送截止日期前向相关科学处提出。

请您将电子版计划书通过科学基金网络信息系统(<https://isisn.nsfc.gov.cn>)提交, 由依托单位审核后提交至自然科学基金委。自然科学基金委审核未通过者, 将退回的电子版计划书修改后再行提交; 审核通过者, 打印纸质版计划书(一式两份, 双面打印)并在项目负责人承诺栏签字, 由依托单位在承诺栏加盖依托单位公章, 且将申请书纸质签字盖章页订在其中一份计划书之后, 一并报送至自然科学基金委项目材料接收工作组。纸质版计划书应当保证与审核通过的电子版计划书内容一致。自然科学基金委将对申请书纸质签字盖章页进行审核, 对存在问题的, 允许依托单位进行一次修改或补齐。

向自然科学基金委提交电子版计划书、报送纸质版计划书并补交申请书纸质签字盖章页截止时间节点如下:

1. 2021年10月22日16点: 提交电子版计划书的截止时间(视为计划书正式提交时间);
2. 2021年10月29日16点: 提交修改后电子版计划书的截止时间;
3. 2021年11月5日16点: 报送纸质版计划书(其中一份包含申请书纸质签字盖章页)的截止时间

4. 2021年11月25日16点：报送修改后的申请书纸质签字盖章页的截止时间。

请按照以上规定及时提交电子版计划书，并报送纸质版计划书和申请书纸质签字盖章页，未说明理由且逾期不报计划书或申请书纸质签字盖章页者，视为自动放弃接受资助；未按要求修改或逾期提交申请书纸质签字盖章页者，将视情况给予暂缓拨付经费等处理。

附件：项目评审意见及修改意见表

国家自然科学基金委员会
2021年10月12日



资助证书

华南农业大学 樊奇 (全国博管会编号:279341) 获得中国博士后科学基金
第70批面上资助二等。 资助编号: 2021M701258。

特颁此证。

The certificate certifies its holder is awarded the fellowship of China Postdoctoral
Science Foundation .

中国博士后科学基金会

2021 年 11 月 15 日



mx/cm/20242706

合同编号：

技术服务合同

项 目 名 称：木质素基新材料开发及性能测试

委托方（甲方）：广州埃登达化工有限公司

受托方（乙方）：华南农业大学

签 订 时 间：2024 年 12 月 15 日

签 订 地 点：华南农业大学

有 效 期 限：2024.12—2026.12



中华人民共和国科学技术部印制

填写说明

一、本合同为中华人民共和国科学技术部印制的技术服务合同示范文本，各技术合同认定登记机构可推介技术合同当事人参照使用。

二、本合同书适用于一方当事人（受托方）以技术知识为另一方（委托方）解决特定技术问题所订立的合同。

三、签约一方为多个当事人的，可按各自在合同关系中的作用等，在“委托方”、“受托方”项下（增页）分别排列为共同委托人或共同受托人。

四、本合同书未尽事项，可由当事人附页另行约定，并作为本合同的组成部分。

五、当事人使用本合同书时约定无需填写的条款，应在该条款处注明“无”等字样。

技术服务合同

委托方（甲方）：_____广州埃登达化工有限公司

住 所 地: 广州市黄埔区科丰路 31 号华南新材料创新园 G2 栋 518

法定代表人： 李志斌

项目联系人：_____ 罗辉

联系方式：15889964188

通讯地址: 广州市黄埔区科丰路 31 号华南新材料创新园 G1 栋 304

电 话: _____ 传真: _____

电子信箱: _____

受托方（乙方）：_____华南农业大学_____

住 所 地: 广州市天河区五山路 483 号

法定代表人：薛红卫

项目联系人: 樊 奇

联系方式：15813378300

通讯地址: 广州市天河区五山路 483 号华南农业大学 18 号楼

电 话: 02085280319 传真: 02085280319

电子信箱: fanqi2021@scau.edu.cn

本合同甲方委托乙方就 木质素基新材料开发及性能测试 项目进行的专项技术服务，并支付相应的技术服务报酬。双方经过平等协商，在真实、充分地表达各自意愿的基础上，根据《中华人民共和国民法典》的规定，达成如下协议，并由双方共同恪守。

第一条：甲方委托乙方进行技术服务的内容如下：

1. 技术服务的目标：通过甲乙双方优势互补、深度合作，乙方为甲方有关于木质素基新材料开发方面提供必要的性质表征、图谱解析以及技术升级攻关等技术服务。

2. 技术服务的内容：乙方为甲方在木质素基新材料研发中遇到的关于木质素结构特征难以表征、基本性质难以明确以及改性技术瓶颈等方面进行预研和相关的技术服务。

3. 技术服务的方式：甲乙双方基于技术服务内容进行友好协商确定。

第二条：乙方应按下列要求完成技术服务工作：

1. 技术服务地点：华南农业大学、广州埃登达化工有限公司

2. 技术服务期限：2024.12—2026.12

3. 技术服务进度：甲乙双方依据实际情况进行。

4. 技术服务质量要求：无

5. 技术服务质量期限要求：协议期内。

第三条：为保证乙方有效进行技术服务工作，甲方应当向乙方提供下列工作条件和协作事项：

1. 提供技术资料：项目过程中所需的原始物料与技术资料。

2. 提供工作条件：项目技术服务内容进行过程中所需的相关费用。

3. 其他：无。

4. 甲方提供上述工作条件和协作事项的时间及方式：甲方根据

实际情况在提前 7 个工作日通过电子文档或纸质传输的方式提供给
乙方。

第四条：甲方向乙方支付技术服务报酬及支付方式为：

1. 技术服务费总额为： 3 万元整（叁万元整）
2. 技术服务费由甲方 一次 （一次或分期）支付乙方。

具体支付方式和时间如下：

（1）合同签订后 10 个工作日内甲方向乙方一次支付技术服务费 3 万元整（叁万元整）。

（2）乙方在收到金额后 10 个工作日内向甲方开具发票，发票为税点 3.29%的增值税专用发票。

乙方开户银行名称、地址和账号为：

开户银行： 广州工行五山支行

地址： 广州市天河区五山路 483 号

账号： 3602002609000310520

第五条：双方确定因履行本合同应遵守的保密义务如下：

甲方：

1. 保密内容（包括技术信息和经营信息）：由双方合作共同研发产生的科研成果，可共同申请专利，未经双方同意不得转让第三方或者一方单独申请专利，经双方友好协商，甲方可有偿并优先优惠地取得该知识产权。

2. 涉密人员范围： 甲方项目参与人员。

3. 保密期限： 协议期内。

4. 泄密责任：甲方有义务保守知识产权、技术资料、工艺、产品、企业经营状况以及双方约定的其技术和商业秘密。

乙方：

1. 保密内容（包括技术信息和经营信息）：由双方合作共同研发产生的科研成果，可共同申请专利，未经双方同意不得转让第三方或者一方单独申请专利，经双方友好协商，甲方可有偿并优先优惠地取得该知识产权。

2. 涉密人员范围：乙方项目参与人员。

3. 保密期限：协议期内。

4. 泄密责任：乙方有义务保守知识产权、技术资料、工艺、产品、企业经营状况以及双方约定的其技术和商业秘密。

第六条：本合同的变更必须由双方协商一致，并以书面形式确定。但有下列情形之一的，一方可以向另一方提出变更合同权利与义务的请求，另一方应当在30日内予以答复；逾期未予答复的，视为同意：

1. 技术服务内容。

2. 技术服务费用。

第七条：双方确定以下列标准和方式对乙方的技术服务工作成果进行验收：

1. 乙方完成技术服务工作的形式：通过电子文件或纸质文件为甲方提供相关的技术服务。

2. 技术服务工作成果的验收标准：无。

3. 技术服务工作成果的验收方法：甲乙双方根据具体情况确定。

4. 验收的时间和地点：甲乙双方根据具体情况确定。

第八条：双方确定：

1. 在本合同有效期内，甲方利用乙方提交的技术服务工作成果所完成的新的技术成果，归甲（甲、双）方所有。

2. 在本合同有效期内，乙方利用甲方提供的技术资料和工作条件所完成的新的技术成果，归甲（乙、双）方所有。

第九条：双方确定，按以下约定承担各自的违约责任：

1. 甲方违反本合同第四条约定，应当双方友好协商确定支付违约金（支付违约金或损失赔偿额的计算方法）。

2. 除上述约定外，由于甲乙双方任何一方违约，造成本协议不能履行或不能完全履行时，守约方有权要求终止协议，并要求违约方赔偿损失，具体由生效的法律文书认定，该损失包括为主张权利而支付的费用，如诉讼费、律师费、公证费、评估费、鉴定费等。

第十条：双方确定，在本合同有效期内，甲方指定罗辉为甲方项目联系人，乙方指定樊奇为乙方项目联系人。项目联系人承担以下责任：

1. 负责及时处理相关合作事宜，甲方联系人负责为合作团队提供必要的在甲方的工作和生活条件，双方联系人落实本方科技资源向产学研团队开放，确保按计划完成工作任务。

一方变更项目联系人的，应当及时以书面形式通知另一方，未及

时通知并影响本合同履行或造成损失的，应承担相应的责任。

第十一条：双方确定，出现下列情形，致使本合同的履行成为不必要或不可能的，可以解除本合同：

1. 发生不可抗力；不可抗力是指不能预见、不能避免且不能克服的客观情况，如自然灾害和社会异常事件等。

2. 在履行期限届满之前，一方当事人明确表示不需要继续履行合同主要义务。

3. 合同期满或双方的义务履行完毕。

第十二条：双方因履行本合同而发生的争议，应协商、调解解决。协商、调解不成的，确定按以下第 2 种方式处理：

1. 提交_____仲裁委员会仲裁；

2. 依法向人民法院起诉。

第十三条：双方确定：本合同及相关附件中所涉及的有关名词和技术术语，其定义和解释如下：

1. _____无_____

第十四条：与履行本合同有关的下列技术文件，经双方确认后，无_____为本合同的组成部分：

1. 技术背景资料：_____无_____；

2. 可行性论证报告：_____无_____；

3. 技术评价报告：_____无_____；

4. 技术标准和规范：_____无_____；

5. 原始设计和工艺文件：_____无_____；

6. 其他：_____无_____；

第十五条：双方约定本合同其他相关事项为：_____无_____。

第十六条：本合同一式_____4_____份，具有同等法律效力。

第十七条：本合同经双方签字盖章后生效。

甲方：_____（盖章）

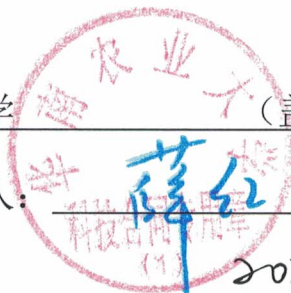
法定代表人 / 委托代理人：_____（签名）



2024年 12 月 15 日

乙方：_____华南农业大学_____（盖章）

法定代表人 / 委托代理人：_____（签名）



2024年 12 月 15 日

印花税票粘贴处：

(以下由技术合同登记机构填写)

合同登记编号：

--	--	--	--	--	--	--	--	--	--	--	--	--	--	--	--	--	--

1. 申请登记人：_____

2. 登记材料：(1) _____

(2) _____

(3) _____

3. 合同类型：_____

4. 合同交易额：_____

5. 技术交易额：_____

技术合同登记机构（印章）

经办人：

年 月 日

任务书编号：2024B03J1380

广州市科技计划项目 任务书

项目名称：	农林废弃物联产轻质高强复合材料与功能助剂 技术开发与应用
承担单位：	华南农业大学
项目负责人：	欧荣贤
计划类别：	重点研发计划
专题名称：	2024年度农业和社会发展科技专题
支持方向：	绿色低碳循环技术方向
组织单位：	华南农业大学
起止时间：	2024-01-01 至 2026-12-31
主管处室：	农村和社会发展科技处

广州市科学技术局制

二〇二四年

填写说明

1. 任务书甲方为广州市科学技术局；乙方为项目承担单位；丙方为项目组织单位。

2. 任务书基于项目申报书转换而成，请按照“广州科技大脑”提示在线填写核实，若存在不填写内容的栏目，请用“无”表示；任务书中的单位名称应为规范全称，并与单位公章一致。

3. 乙方与合作单位的合作协议自动从项目申报书中读取，如需变化调整，须待任务书签订后，按要求及时办理重大变更。

4. 乙方完成项目任务书在线填写，依次提交丙方和甲方审核确认后，按要求登录“穗好办”APP完成电子签章。不具备电子签章条件的单位，经与业务主管处室沟通对接后，可下载电子版项目任务书用A4纸双面打印装订签章；一式六份报甲方和丙方签章，其中甲方两份丙方两份，项目承担单位和项目负责人各一份。

5. 涉密项目请在“广州科技大脑”下载项目任务书模板，按保密要求离线填写报送。

6. 项目申报书是项目任务书填报的重要依据，未经甲方许可，乙方不得修改考核指标，调整主要研究内容。项目任务书将作为项目实施管理、验收结题和监督评估的重要依据。

7. 项目任务书中的“备注”，包括重要的必须补充的内容。

8. “广州科技大脑”是项目管理过程中重要通知和文书的电子送达平台。为确保电子送达渠道畅通，乙方和项目负责人应及时更新维护“广州科技大脑”的单位和个人信息。

9. 根据相关要求，项目涉及人体临床研究的，项目需经医学伦理委员会审查通过并在任务书附件栏上传相关佐证材料。

一、项目基本信息

项目名称	农林废弃物联产轻质高强复合材料与功能助剂技术开发与应用			
计划类别	重点研发计划		专题名称	2024年度农业和社会发展科技专题
支持方向	绿色低碳循环技术方向			
支持内容	5. 农林废弃物制备生物质基材料（工业用途原料）和联产高附加值化学品技术研究及应用			
指南发布日	2023-04-15			
项目开始时间	2024-01-01		项目结束时间	2026-12-31
资助方式	竞争性前资助		申请市财政科技经费(万元)	100
广东省技术领域	节能环保资源综合利用及生态环境保护；			
承担单位	华南农业大学			
合作单位	华南理工大学；中国科学院广州能源研究所；广州华坊洲木业有限公司；			
组织单位	华南农业大学			
	姓名	办公电话	手机号码	电子邮箱
项目负责人	欧荣贤	020-85280319	13926498006	ourongxianvx@163.com
项目联系人	欧荣贤	020-85280319	13926498006	ourongxianvx@163.com
科研财务助理	樊奇	020-85280319	15813378300	fanqiscience@126.com
项目摘要	针对传统木质人造板强度低、易变形、保温隔声性能差、依赖木材资源等问题，项目以竹材、甘蔗渣、木质素等农林废弃物为原料，利用竹材的高机械强度、甘蔗渣的多孔蓬松结构、木质素的抗老化和抗菌防霉等特性，通过材料结构创新设计和力学仿真模拟、生物质大分子定向解聚、生物基无甲醛胶黏剂合成，联产制备高性能竹材/甘蔗渣复合材料和糠醛类与酚类高值化学品，构建绿色低碳联产和综合利用体系。开发竹材绿色干燥技术、竹篾形态精准可控制备与连续接长技术、甘蔗渣预处理技术、木质素基无甲醛胶黏剂制备技术、竹材/甘蔗渣复合材料连续自动化制造技术。研究预处理方法对甘蔗渣孔隙结构、化学性质和纤维形态的调控作用，联产糠醛类和酚类化学品对木质素基胶黏剂粘接强度、抗菌防霉性能的影响，以及竹材增强形式、分层铺装结构、多级分段施胶工艺对竹材/甘蔗渣复合材料力学强度、尺寸稳定性、保温隔声等性能的影响。			

最终研发轻质高强、结构稳定、保温隔声、抗菌防霉、绿色无甲醛的竹材/甘蔗渣复合板材，并在定制家居、建筑装饰装修领域进行推广应用。项目的实施对于持续深入推进我国“双碳”战略实现、助力乡村振兴、推动我市家居与建材产业高质量绿色低碳发展具有重要意义。

二、承担单位基本情况

单位名称	华南农业大学	统一社会信用代码	124400004554165634
注册时间	1952-01-01	单位类型	高等院校
注册地址	广东省广州市天河区五山路483号		
办公地址	广东省广州市天河区五山路483号		
联系人	姓名	倪慧群	
	手机号码	13711345768	
	电子邮箱	kjcgxk@scau.edu.cn	
开户银行	广东广州工行五山支行		
开户户名	华南农业大学		
银行账号	3602002609000310520		
任务分工	项目总体规划和实施协调；新鲜竹材高效节能绿色干燥技术开发；高精度高强度竹篾撕篾技术开发、竹篾连续接长技术开发、竹篾连续增强片材制备；轻质高强竹材/甘蔗渣复合板材研发。		
知识产权分配	申请与研究内容相关的发明专利2件/授权发明专利1件，发表与研究内容相关的学术论文2篇，开发新技术1项，培养博士研究生1名，硕士研究生2名。		

三、合作单位基本情况

单位名称1	华南理工大学	单位类型	高等院校
所属国别或地区	中国	统一社会信用代码	12100000455414429R
联系人	姓名	谭锦才	
	办公电话	020-87110625	
	手机号码	13378687813	
任务分工	木质素基无甲醛胶黏剂一锅法制备技术开发。		
知识产权分配	申请与研究内容相关的发明专利1件，发表与研究内容相关的学术论文2篇，培养博士研究生1名，硕士研究生1名。		
单位名称2	中国科学院广州能源研究所	单位类型	科研院所
所属国别或地区	中国	统一社会信用代码	12100000455860816A
联系人	姓名	马玲玲	
	办公电话	020-37029825	
	手机号码	15804209200	
任务分工	甘蔗渣预处理联产高附加值化学品。		
知识产权分配	申请与研究内容相关的发明专利1件，发表与研究内容相关的学术论文3篇。		
单位名称3	广州华坊洲木业有限公司	单位类型	有限责任公司
所属国别或地区	中国	统一社会信用代码	91440113781234298U
联系人	姓名	陈瑞建	
	办公电话	020-34826813	
	手机号码	13570759035	
任务分工	农林废弃物绿色低碳联产技术体系熟化及产业化应用。		
知识产权分配	完成新产品鉴定1项。		

四、项目组成员信息

项目负责人	姓名	欧荣贤		证件类型	身份证	证件号码	4304191984070011	
	出生日期	1984-07-04		民族	汉族	国籍	中国	
	学位	博士		学位授予国家（或地区）	中国	职务	院长助理	
	所学专业	木材科学与技术		手机号码	13926498006	办公电话	020-85280319	
项目组成员（含项目负责人）								
序号	姓名	证件类型	证件号码	年龄	职务	职称	学位	项目分工
1	欧荣贤	身份证	430419198407040011	38	院长助理	副高级	博士	项目负责人
2	樊奇	身份证	342401199309296110	29	无	无	博士	竹篾连续高强度接长研究
3	刘伟峰	身份证	362325198706292919	35	无	正高级	博士	木质素基无甲醛胶黏剂一锅法制备
4	王闻	身份证	360426198510043013	37	无	副高级	博士	甘蔗渣预处理生产高附加值化学品
5	陈瑞建	身份证	510122198607026216	36	董事长助理	中级	硕士	技术体系熟化产业化应用

6	王清文	身份证	230107196107010410	61	无	正高级	博士	项目指导
7	涂登云	身份证	440106197601085618	47	无	正高级	博士	新鲜竹材干燥技术研究
8	郝笑龙	身份证	130431199004190312	33	无	副高级	博士	高精度高强度竹篾全自动撕篾技术研究
9	刘涛	身份证	510722198602150130	37	无	副高级	博士	轻质高强竹材/蔗渣复合板材性能研究
10	唐伟	身份证	430703198902215072	34	无	无	博士	轻质高强竹材/蔗渣复合板材性能制造工艺研究
11	张凤岚	身份证	362101196610291312	56	董事长	副高级	学士	资源调配
12	邹名星	身份证	320102196502053218	58	集团副总经理	中级	学士	资源调配
13	林卫东	身份证	441224196812040035	54	集团总工程师	副高级	学士	技术体系熟化产业化应用指导
14	陈川富	身份证	460005199411234134	28	无	无	硕士	干燥竹材性能评价
15	张成林	身份证	371421199501276777	28	无	无	硕士	竹篾性能评价

第8页 共25页

16	陈园	身份证	411521198701160043	36	无	无	硕士	竹席/竹帘编织结构设计性能研究
17	王耀程	身份证	152104199611261215	26	无	无	硕士	连续竹篾增强薄片材制备与性能研究
18	王海旭	身份证	410782199412200931	28	无	无	硕士	木质素胶黏剂配方研究
19	陈磊	身份证	341202199908131718	23	无	无	学士	轻质高强竹材/蔗渣复合板材抗菌防霉性能研究
20	雷春光	身份证	440881200108264156	21	无	无	学士	轻质高强竹材/蔗渣复合板材保温隔声性能研究
21	许露瑶	身份证	412825199901302103	24	无	无	学士	甘蔗渣预处理
22	麦颖桉	身份证	440783200104162141	22	无	无	学士	木质素无甲醛黏剂性能评价

第9页 共25页

五、项目经费信息

本项目总投入：¥（200）万元，其中，市财政科技经费：¥（100）万元，自筹经费：¥（100）万元。

项目经费			
资金来源	小计	市财政科技经费	自筹经费
2024	120	60	60
2025	0	0	0
2026	80	40	40
2027	0	0	0
总计	200	100	100
支出预算明细			
支出科目	小计	市财政科技经费	自筹经费
一、直接费用	185	85	100
（一）设备费	10	10	0
（二）业务费	135	55	80
（三）直接人力资源成本费	40	20	20
二、间接费用	15	15	0
合 计	200	100	100

（单位：万元）

注：自筹经费由项目承担单位自身筹措，不包含来自各级政府部门的财政资金。

单位名称	市财政科技经费分配	自筹经费分配	总经费分配
华南农业大学	50	0	50
合作单位1： 华南理工大学	20	0	20
合作单位2： 中国科学院广州能源研究所	20	0	20

合作单位3: 广州华坊洲木 业有限公司	10	100	110
合计	100	100	200

(单位: 万元)

六、设备仪器购置明细

序号	名称	数量	预计费用		其中： 市财政科技 经费	其中： 自筹经费	
		台/套	单价	总价			
	合计	0		0			

注明：单台套价值在50万元及以上的科学仪器设备必须纳入粤科汇（广东省科技资源共享服务平台）。

七、项目概述

研究目标

项目通过开展农林废弃物资源大宗利用研究，解决传统木质人造板强度低、易变形、严重依赖木材资源的技术难题，构建绿色低碳联产和综合利用体系，研究目标如下。

1. 建立湿竹低温绿色干燥技术，联产竹醋液用于种植养殖，实现竹材干湿全组分利用，解决利用竹材制造人造板成本高、易霉变的技术难题。
2. 突破高精度高强度竹篾撕篾技术和连续接长技术，制备连续增强片材。
3. 建立甘蔗渣高效预处理技术，定向调控甘蔗渣孔隙结构和表面性质，提升原料品质，解决其易霉变问题，同时联产糠醛类与酚类化学品，用于制备高性能木质素基无甲醛胶黏剂。
4. 以工业木质素和甘蔗渣衍生糠醛与酚类为主要原料，建立木质素基无甲醛胶黏剂一锅法制备技术，解决甲醛类胶黏剂污染问题，以及粘接强度低，抗菌防霉性能差的技术难题。
5. 以竹篾连续增强片材为表层、竹纤维为过渡层、甘蔗渣为芯层，利用木质素基胶黏剂制备轻质高强、结构稳定、保温隔声、抗菌防霉的竹材/甘蔗渣复合板材，突破板材连续自动化制造技术。
6. 集成农林废弃物制备竹材/甘蔗渣复合板和联产无甲醛胶黏剂用功能助剂关键技术体系，建成产业化应用示范线，实现轻质高强竹材/甘蔗渣复合无甲醛板的规模示范应用。

研究内容

（1）新鲜竹材低温绿色干燥联产竹醋液技术开发

新鲜竹材中含有约50%质量份数的水分，竹材利用率低于50%，且未处理竹材极易发生霉变，传统高温碳化处理易造成竹材碳化降解且产生大量棕褐色废液，增加废液处理成本，最终导致生产成本过高。项目通过干燥原理创新，在低温厌氧环境中对新鲜竹材进行干燥处理，采用气、液分离技术从循环热风中分离液体，联产制得高附加值的澄清竹醋液，解决竹材利用率低、易霉变的技术难题，新鲜竹材全组分利用率接近100%，实现了对新鲜竹材“吃干榨净”，“干湿”全组分高附加值利用。研究热处理工艺对竹材物理力学性能和防霉性能、竹醋液品质和产量的影响，突破新鲜竹材高效节能绿色干燥关键技术，研发专用于干燥装备。

（2）连续竹篾增强超薄片材制备技术开发

开展高精度高强度竹篾全自动撕篾技术研究。基于仿生篾匠手工精细撕篾原理，充分利用了竹材横向强度远低于纵向的特点，结合现代工业自动化技术，开发以竹条专用上料机构、进料器、可调速压轮、竹节视觉识别器、篾刀口形态变化、刀座行进变换、出料夹持轮拉篾、窄刀精修定宽、多重刮刀表面抛光等为技术要点的成套自动化撕篾装备和技术方法，以实现高厚度精度高强度竹篾的高效、自动化连续制备。研究撕篾工艺对竹篾抗拉强度和厚度精度的影响。开展竹篾连续快速高强度接长技术研究。研发竹篾连续快速接长装备，以斜接方式制备加长竹篾，分别探究不同斜接角度、胶黏剂种类和粘接工艺对胶接强度的影响，并进一步评价斜接竹篾的湿热老化强度与二次重复胶接性能，开发出能够满足机械化连续编织性能要求的竹篾高强度快速接长技术。

以连续接长竹篾为基本单元，机械编织成连续竹席或竹帘，研究竹篾厚度、编

织结构和疏密程度对竹篾编织材料力学性能的影响；进一步以速生杨木单板为表层、连续竹席或竹帘为芯层，制备高强度的连续竹篾增强超薄片材，研究单板厚度和含水率、胶黏剂种类和用量、热压工艺对连续竹篾增强超薄片材密度、板内密度偏差、含水率、静曲强度和弹性模量、内结合强度、表面结合强度、吸水厚度膨胀率的影响，为大幅面竹材/甘蔗渣复合材料的连续自动化制造提供技术支撑。

（3）甘蔗渣预处理联产高附加值化学品

开展甘蔗渣木质素定量脱除偶联表面结构定向调控技术，获得木质素溶液和改性甘蔗渣；基于木质素物理化学特性分析，设计并制备固体酸催化剂，定向解聚木质素C-O键和C-C键，经过催化剂结构、功能基团表征联合催化效率评价，优化固体酸催化剂的制备，通过催化反应条件控制，获得小分子酚类化合物，用作木质素基无甲醛胶黏剂的原料，赋予复合板抗腐败功能；基于改性甘蔗渣的微观结构和表面特性分析，采用酶法选择性部分降解半纤维素，获得木糖溶液和用作复合板原料的孔径均一度分布较好的甘蔗渣纤维，该纤维赋予复合板降噪功能；考察木糖在上述固体酸催化剂作用下的糠醛得率，经优化催化剂设计和反应条件，实现木质素和木糖一锅法高效制备酚类和糠醛类化合物，用作木质素基无甲醛胶黏剂的原料。

（4）木质素基无醛胶黏剂一锅法制备技术开发

以工业木质素为原料，将木质素在碱性条件下部分解聚，对木质素分子醚键断裂，再将部分解聚后富含酚羟基的木质素进行原位脱甲基改性制备高反应活性的酚化木质素，解决木质素反应活性不匹配的问题。

以酚化木质素和甘蔗渣联产的糠醛、羟甲基糠醛等为原料，辅助聚醚类、聚醚胺、异氰酸酯等辅料，一锅法制备木质素基无甲醛胶黏剂，并提高木质素在胶黏剂中的相容性。在合成过程中还可以引入通过木质素对银离子的吸附还原功能，原位负载纳米银抗菌剂，以提升木质素基无甲醛胶黏剂抗菌防霉性能。探究优化合成工艺条件，包括木质素/糠醛/辅料的比、反应温度和时间、动态键种类等因素对产品结构与性能的影响。

考查酚化改性木质素的结构和用量、原料配比、化学交联程度、银离子的用量等因素对木质素基无甲醛胶黏剂的初始粘度、固化温度、固化速率，对竹材/甘蔗渣复合材料粘接强度、耐水性、循环加工性能、耐低温性能、热稳定性、抗老化等性能的影响，重点从分子结构探究酚化改性木质素对银离子还原制备纳米银的能力，以及酚化改性木质素结构对木质素基无甲醛胶黏剂的粘接性能和抗菌防霉性能调控机理，揭示木质素的结构调控作用机制。

（5）轻质高强竹材/甘蔗渣复合板材研发及功能化研究

开展轻质高强竹材/甘蔗渣复合板材制备与功能化研究。针对连续竹篾增强超薄片材、竹纤维和甘蔗渣的不同特点，通过材料结构创新设计和力学仿真模拟，扬长避短、优势互补，以高强韧的超薄片材为上下表层、高刚性的竹纤维为过渡层、柔性多孔结构的甘蔗渣为芯层，采用连续自动化热压胶合成型工艺，制备轻质高强竹材/甘蔗渣复合板材。研究竹纤维和甘蔗渣比例、胶黏剂配方、施胶工艺和热压工艺等对板材物理力学性能、尺寸稳定性、保温隔热、吸音隔声、甲醛释放、抗菌防霉等性能的影响，形成轻质高强、结构稳定、保温隔声、抗菌防霉的竹材/甘蔗渣复合板材制造技术。

（6）农林废弃物联产技术体系熟化及产业化应用

集成农林废弃物制备轻质高强竹材/甘蔗渣复合板材和联产无甲醛胶黏剂用功能

助剂关键技术体系，建成产业化应用示范线，实现轻质高强竹材/甘蔗渣复合无甲醛板材示范应用10万平方。

拟解决的关键技术问题

（1）新鲜竹材高效节能绿色干燥关键技术

针对竹材易霉变，而传统高温碳化处理成本高、竹材碳化降解且产生大量棕褐色废液造成环境污染等问题，研发新鲜竹材高效节能绿色干燥装备与工艺，通过在低温（ $<170^{\circ}\text{C}$ ）厌氧环境中，采用气、液分离技术从循环热风中分离液体，联产高附加值澄清竹醋液，延伸产业链，降低竹材干燥成本，解决竹材干燥易降解劣化、成本高，竹制品易霉变的关键技术问题。

（2）高精度高强度薄竹篾全自动撕篾与连续快速高强度接长关键技术

本项目以竹篾为增强单元，其厚度精度、高强度和连续性是实现轻质高强复合板材连续化稳定制备的关键，针对传统手工剖篾效率低，机械切削制篾加工精度差、竹篾强度损伤严重，因竹材长度受限而无法生产高强度连续竹篾等技术瓶颈，利用竹材横向强度远低于纵向的特点，基于仿生篾匠手工精细撕篾原理，结合现代工业自动化装备，解决高精度高强度薄竹篾全自动撕篾与连续快速高强度接长关键技术问题。

（3）甘蔗渣木质素定向解聚制备酚类化合物技术

甘蔗渣木质素定量脱除后获得的木质素产品分子量分布广泛，产物种类多样，采用固体酸催化木质素溶液制备酚类化合物，对催化剂的底物适应性和反应选择性要求较高，直接关系到木质素基无甲醛胶黏剂的性能与品质，因此，设计并制备反应效率高、选择性好的固体酸催化剂是本项目需要解决的一个关键技术问题。

（4）木质素基无甲醛胶黏剂制备关键技术

如何提高木质素与糠醛类单体的反应活性，提高木质素与胶黏剂基体的相容性，是本项目着重需要解决的关键技术问题。木质素分子结构复杂，反应位点的空间位阻较大，反应活性较低；此外，木质素与胶黏剂基体相容性差，引入木质素易破坏材料规整结构，从而造成性能下降。部分解聚和酚化改性可减少木质素的空间位阻，提高其与糠醛类单体的反应活性。引入聚醚类、聚醚胺和异氰酸酯等辅料，可进一步提高体系的交联度，也可提高木质素与胶黏剂基体的相容性，并强化共聚产物的整体柔韧性和粘结性。

（5）轻质高强竹材/甘蔗渣复合板材连续自动化制造关键技术

针对竹篾增强超薄片材、竹纤维和甘蔗渣的形态和结构差异，通过材料结构创新设计、连续分层铺装和多级分段施胶，采用连续自动化热压胶合成型工艺，解决具有轻质高强、结构稳定、保温隔热、吸音隔声功能的竹材/甘蔗渣复合板材连续自动化制造关键技术问题。

主要创新点

(1) 采用木质素定量脱除预处理联合酶法选择性部分降解半纤维素，可较易实现甘蔗渣孔隙结构的精准调控，同时将脱除木质素和半纤维素降解的木糖经一锅法催化制备酚类化合物和糠醛，具有方法上的创新；此外，甘蔗渣三组分通过不同的方式成为复合板材的组成部分并发挥不同的作用，是生物质高值化利用思路上的创新。

(2) 通过部分解聚和酚化改性减少木质素的空间位阻，提高其与糠醛类单体的反应活性；引入聚醚类、聚醚胺和异氰酸酯等辅料，不仅可以提高体系的交联度，还可以提高木质素与胶黏剂基体的相容性，并强化共聚产物的整体柔韧性和粘结性。同时利用木质素对银离子的吸附还原功能，原位负载纳米银抗菌剂，提升木质素基无甲醛胶黏剂抗菌防霉性能。

(3) 通过在低温厌氧环境中，采用气、液分离技术从新鲜竹材中直接提取澄清竹醋液，来提高竹材强度和防霉性能，并大幅降低生产成本；以连续接长高强度高厚度精度竹篾为基本单元，开发高强度超薄增强片材，进一步制备轻质高强竹材/甘蔗渣复合板材。所开发的新鲜竹材低温绿色干燥技术、高精度高强度薄竹篾全自动撕篾技术、竹篾连续快速高强度接长技术、超薄片材制造技术、复合板材连续自动化生产技术均属原始创新。

采用的方法、技术路线及工艺流程

项目采用低温绿色干燥技术处理新鲜竹材，提高竹材强度和防霉性能，同时联产高附加值竹醋液，进一步将干燥处理的竹材制备成高厚度精度高强度的竹篾并进行连续接长，加工剩余物制备成竹纤维，再将连续接长竹席制备成高强度超薄片材；同时对甘蔗渣进行预处理以调控其孔隙结构、提高防霉性能，联产高附加值糠醛类和酚类化学品，与经活化的工业木质素为主要原料制备木质素基无醛胶黏剂；以高强度超薄片材、竹纤维、甘蔗渣、木质素基胶黏剂为原料，制备轻质高强、结构稳定、保温隔声、抗菌防霉、绿色无醛的竹材/甘蔗渣复合材料，应用于定制家居、建筑装饰装修领域。采用的研究方法如下：

(1) 采用凝胶色谱仪、核磁共振波谱仪（NMR）、气相色谱-质谱联用仪等解析木质素溶液的分子量大小分布、化学基团特征和产物类别；采用SEM、傅里叶红外光谱仪（FTIR）、X射线荧光光谱仪、NMR等对固体酸催化剂进行物化特性分析，以酚类化合物和糠醛得率为因变量，优化木质素-木糖溶液催化反应条件。

(2) 采用显微（光学显微镜、SEM、透射电镜（TEM）等）、光谱（FTIR、拉曼光谱、共聚焦荧光光谱、紫外光谱等）、高分辨率NMR定性和定量分析甘蔗渣细胞及亚细胞水平原位状态的胞壁表面、内部结构及组分信息，深入理解甘蔗渣预处理过程中微观结构的变化及演变规律。

(3) 通过FTIR、核磁氢谱，GPC表征木质素的官能团转化和分子量变化；通过³¹P-NMR表征改性木质素样品，定量分析改性木质素中酚羟基、醇羟基、羧基的含量；通过二维核磁表征分析木质素结构变化。

(4) 通过FTIR研究胶黏剂聚合反应动力学过程与官能团转化率；通过差式扫描量热仪分析研究胶黏剂固化热行为；通过动态力学分析仪研究动静态粘弹性变化；通过热重分析仪分析耐热性；通过紫外老化、自然老化试验研究胶层的抗老化性能。

(5) 采用X-射线断层扫描技术（X-CT）、SEM、TEM、原子力显微镜（AFM）、激光显微拉曼成像等各种测试分析技术，表征甘蔗渣、复合材料的孔隙结构。

(6) 通过紫外老化、自然环境老化试验研究竹材/甘蔗渣复合板材在人为周期

性变化环境或自然环境下，不同湿度、温度环境中的胶接耐久失效行为。

(7) 通过数字图像相关技术对竹篾接头、复合板材的复合应变场和失效行为进行表征，并对其失效机理进行分析；参照国家标准测试竹材/甘蔗渣复合板材的物理力学性能，尺寸稳定性、保温隔声、抗菌防霉等性能。

技术先进性（与国际领先水平、国内领先水平的对比）

(1) 采用传统碱法定量脱除木质素通常存在预处理废液难以处置的问题，本项目采用碱性尿素溶液处理甘蔗渣分离出木质素后，剩余的废液经调配可直接作为植物生长营养液，实现了废液资源化利用；同时采用酶法对预处理甘蔗渣进行孔隙度调节，相比于化学法具有操作简单、条件温和、绿色环保、选择性高、避免物料结构的深度改变等优点。

(2) 以工业木质素和蔗渣预处理产物糠醛类单体为原料，利用木质素替代石油基酚类化合物、糠醛类单体替代甲醛，合成高生物基含量无甲醛胶黏剂。通过部分解聚和酚化改性提高木质素与糠醛类单体的反应活性，同时利用木质素对银离子的吸附还原功能，原位负载纳米银抗菌剂，提升木质素基无甲醛胶黏剂抗菌防霉性能，目前国内外尚未见报道，技术有望达到国内领先水平。

(3) 通过在低温厌氧环境中，首次采用气、液分离技术从新鲜竹材中直接提取澄清竹醋液，延伸产业链，降低竹材干燥成本，并提高竹材强度和防霉性能，在此基础上开发连续接长高强度高厚度精度竹篾增强超薄片材，对竹纤维/甘蔗渣复合芯材进行增强，采用连续自动化热压胶合成型工艺制备轻质高强、结构稳定、保温隔声、抗菌防霉的竹材/甘蔗渣复合板材，技术有望达到国际领先水平。

项目预期风险及规避措施

技术方面，本项目团队在农林废弃生物质大宗利用、木竹材改性、木质复合板材等产业化方面已有丰富的技术积累，相关成果已获国家科学技术奖3项、省科学技术一等奖4项。因此，技术风险极低。

政策方面，本项目研究符合《中国制造2025》生物基材料、复合材料等材料的重点布局。国家林业和草原局等10部委于2021年11月联合印发了《关于加快推进竹产业创新发展的意见》，随后广东省林业局等10部门于2022年11月联合印发了《关于加快推进广东竹产业创新发展的实施意见》，倡导大力发展竹产业，进一步夯实了本项目的政策基础，没有政策风险。

产业化方面，轻质高强竹材/甘蔗渣复合板材作为新产品，其市场导入期会面临不确定性，存在一定风险。由于竹材和甘蔗渣等原材料资源丰富、价格低廉，项目通过联产高附加值竹醋液和功能助剂，可降低全产业链综合成本，再加上产品的高性能和多功能，具有高性价比。项目参与企业作为人造板研发、生产和销售的国家重点林业龙头企业，拥有稳定的大客户（欧派、索菲亚、金螳螂、碧桂园等行业头部企业）资源，依托这些企业良好口碑和市场影响力，进行本项目所开发产品的家具化制造与品牌推广，打造标杆，进一步提高市场占有率。

八、工作进度安排

序号	起止时间	预计总经费使用进度 (%)	阶段目标、主要内容及成果
1	2024-01-01 -- 2024-12-31	35	研究新鲜竹材干燥工艺，优化改进干燥设备；设计试制高精度高强度竹篾撕篾装置，开发竹篾连续高强接长技术；建立甘蔗渣木质素定量脱除偶联表面结构定向调控技术，解析脱除木质素的物理化学特性，设计并制备固体酸催化剂；木质素的分离提纯、部分解聚、酚化改性；发表学术论文2篇，申请发明专利1件。
2	2025-01-01 -- 2025-12-31	70	研究竹材干燥工艺对竹材力学强度、防霉性能、竹醋液产量和品质的影响；批了量化制备高厚度精度高强度竹篾，研究斜接角度和胶黏剂种类最斜接竹篾拉伸性能、湿热老化强度与二次重复胶接性能；制备高强度的连续竹篾增强超薄片材，研究单板厚度和含水率、胶黏剂种类和用量、热压工艺对连续竹篾增强超薄片材性能的影响；制备出高效固体酸催化剂，定向解聚木质素并高效催化木糖，获得组成较高的小分子酚类化合物和糠醛；木质素与糠醛类单体一锅法制备无甲醛胶黏剂、木质素原位负载纳米银，木质素基无甲醛胶黏剂结构与性能研究；制备轻质高强竹材/甘蔗渣复合板材，研究竹纤维和甘蔗渣比例、胶黏剂配方、施胶工艺和热压工艺等对板材理力学性能、尺寸稳定性、保温隔热、吸音隔声、甲醛释放、抗菌防霉等性能的影响；发表学术论文2篇，申请发明专利1件，博士研究生1名，培养硕士研究生1名。
3	2026-01-01 -- 2026-12-31	100	熟化新鲜竹材高效节能绿色干燥技术、高精度高强度薄竹篾全自动撕篾技术、竹篾连续快速高强度接长关键技术、孔径均一度分布较好的甘蔗渣纤维制备技术、木质素基无甲醛胶黏剂一锅法制备技术、轻质高强竹材/甘蔗渣复合材料连续自动化制造技术；建成产业化应用示范线，实现轻质高强竹材/甘蔗渣复合无甲醛板材示范应用1万立方；发表学术论文3篇，申请发明专利2件，授权发明专利1件，开发新技术1项

			、新产品1个，博士研究生1名，培养硕士研究生2名。
--	--	--	---------------------------

广州市科技项目任务书2024-01-09

九、项目预期成果

(一) 预期代表性成果

预期代表性成果
要求项目形成的技术成果在广州地区转化应用，并明确将获得由在穗单位出具的项目技术成果

(二) 预期一般性成果

技术价值						
序号	成果类型	考核指标				
		指标名称	立项时已有指标值/状态	实施期第一年关键节点指标值/状态	实施期第二年关键节点指标值/状态	项目指标
1	新技术	新鲜竹材高效节能绿色干燥技术	无	完成竹材干燥10吨，联产竹醋液2吨	完成竹材干燥30吨，联产竹醋液6吨	完成干燥50产竹
2	新产品	轻质高强竹材/甘蔗渣复合板材	无	完成实验室样品制备	完成设备调试、试生产	可验次产00立

科学价值						
序号	成果类型	考核指标				
		指标名称	立项时已有指标值/状态	实施期第一年关键节点指标值/状态	实施期第二年关键节点指标值/状态	项目指标值/状态
1	新理论	论文	无	发表论文2篇	发表论文4篇	发表1篇
2	新方法	专利	无	申请发明专利1件	申请发明专利2件	申请发明专利4件
3	培养人才	培养人才	无	无	培养硕士研究生2人、博士研究生1人	培养研究生3人

经济价值
作为全球“定制之都”，广州拥有5家制家居上市企业（全国9家），总市值超1000亿，2022年0亿。按每亿元产值消耗1万m ³ 板材，使用竹材/甘蔗渣复合板材可节约木材用量2500万m ³ /年，按照全国碳市场48元/吨估算，潜在碳汇交易额将达12亿元。

社会价值

农林废弃物资源化大宗利用不仅可解决当前废弃物填埋或焚烧对土壤、水体和空气造成的环境需矛盾，保障国家生态和木材安全。将废弃生物质原料转化为低碳、绿色、可循环的高性能、于推动经济高质量绿色低碳循环发展、助力乡村振兴、建设无废社会、实现“双碳”目标具有

文化价值

十、备注

专题补充约定条款：

甲方对未履行勤勉尽责义务的相关责任主体，自作出处理结论之日起，依照法律法规规定或任务书约定实施惩戒5年，取消相关责任主体申报市科技计划项目、申领市科技计划项目经费的资格。

项目承担单位（乙方）及项目负责人承诺书

承诺书

本单位/本人作为广州市科技计划项目承担单位/项目负责人，将严格遵守广州市科技计划管理相关规定，严格履行自身责任，加强对项目组人员及合作单位的管理，在此郑重承诺：

（一）确保与本项目有关的全部材料真实、合法、有效，未侵犯其他方知识产权等权利，不存在多头申报、重复申报行为；

（二）严格遵守《广州市科技创新条例》《广州市科技计划项目管理办法》《广州市科技计划项目经费管理办法》《广州市科技计划科技报告管理办法》等相关规定，实施项目和经费管理；

（三）严格遵守国家、省、市关于科研诚信和科技伦理的有关法律、法规，相关政策以及各项规定，加强项目实施过程中的科研诚信及科技伦理管理，恪守科研道德准则。

如有违反，本单位/本人愿意接受相关部门做出的各项处理决定，包括但不限于终止项目、停拨经费、核减经费、追回经费，取消一定期限广州市科技计划项目申报资格，记入科研失信行为数据库，将不良行为向社会公开等。

项目承担单位：华南农业大学

日期：年 月 日

项目负责人：欧荣贤

日期：2023年12月15日

任务书签署

甲乙丙三方根据《广州市科技计划项目管理办法》《广州市科技计划项目经费管理办法》《广州市科技计划科技报告管理办法》等有关文件规定，以及有关法律、政策和管理要求，签署本任务书。

签订地点：广州市越秀区

广州市科学技术局（甲方）：广州市科学技术局
局项目经办人：刘晓辉 联系电话：83124045
责任处室负责人：陈洁



2024年01月09日

项目承担单位(乙方): 华南农业大学
二级部门: 华南农业大学生物质工程研究院
项目负责人: 欧荣贤
项目经费汇入账号
账户名: 华南农业大学 账号: 3602002609009210520
开户银行: 广东广州工行五山支行
财务负责人: 肖斐



2023年12月15日

组织单位(丙方): 华南农业大学
项目经办人: 倪慧群



2023年12月16日

华南农业大学签订横向科技合同审批表

项目名称	家居材料研发合作				受理号	HXKHJT20242526	
合同类别	技术开发						
项目负责人	孙理超	职称	单位副职领导	所在单位	材料与能源学院	手机号	18320722418

合作单位信息

合作方单位	联系人	联系方式	国别	省	市	区(县)	合作单位性质
广东煜丰实业(集团)有限公司	唐松波	13829280961	中国	广东	广州	从化区	企业

是否涉外合作	<input type="radio"/> 是 <input checked="" type="radio"/> 否	
--------	--	--

校内项目组成员(包括项目负责人)

序号	姓名	工号/学号	所在单位	职称	年龄
1.00	孙理超	30004215	材料与能源学院	副教授	38
2.00	樊奇	31000474	材料与能源学院	副教授	32
3.00	彭子华	20232149009	材料与能源学院	研究生	21
4.00	贾曼	20243178003	材料与能源学院	研究生	20
5.00	麦泽桐	20242189002	材料与能源学院	研究生	20
6.00	彭若祎	20242189033	材料与能源学院	研究生	20
7.00	张志岩	31002501	总务部	主管	38

注：项目组成成员可以添加多项成员、添加行点击框内会显示三个符号，选择中间框不会复制内容。

			同意。
--	--	--	-----

uxkm/20202526

合同编号：

技术服务（研发）合同

项目名称： 家居材料研发合作

委 托 方： 广东煜丰实业（集团）有限公司
（甲 方）

受 托 方： 华南农业大学
（乙 方）

签订时间： 2024 年 11 月 1 日

签订地点： 华南农业大学

有效期限： 3 年

中华人民共和国科学技术部印制

填 写 说 明

一、本合同为中华人民共和国科学技术部印制的技术服务合同示范文本，各技术合同认定登记机构可推介技术合同当事人参照使用。

二、本合同书适用于一方当事人（受托方）以技术知识为另一方（委托方）解决特定技术问题所订立的合同。

三、签约一方为多个当事人的，可按各自在合同关系中的作用等，在“委托方”、“受托方”项下（增页）分别排列为共同委托人或共同受托人。

四、本合同书未尽事项，可由当事人附页另行约定，并作为本合同的组成部分。

五、当事人使用本合同书时约定无需填写的条款，应在该条款处注明“无”等字样。

技术服务（研发）合同

委托方（甲方）： 广东煜丰实业（集团）有限公司

住 所 地： 广州市从化区鳌头镇龙潭大道 19 号

法定代表人： 李群建

项目联系人： 唐松波

联系方式： 13829280961

通讯地址： 广州市从化区鳌头镇龙潭大道 19 号

电 话： 020-87889811 传真： 020-87889811

电子信箱： songbo.tang@yufengindustrial.com

受托方（乙方）： 华南农业大学

住 所 地： 广州市天河区五山路 483 号

法定代表人： 薛红卫

项目联系人： 孙理超

联系方式： 18320722418

通讯地址： 广州市天河区五山路 483 号华南农业大学 18 号楼

电 话： 02085280319 传真： 02085280319

电子信箱： sunlichao@scau.edu.cn

本合同甲方委托乙方就 家居材料研发合作 项目进行专项的技术服务，并支付相应的技术服务报酬。双方经过平等协商，在真实、充分地表达各自意愿的基础上，根据《民法典》的规定，达成如下协议，并由双方共同恪守。

第一条：甲方委托乙方进行技术服务的内容如下：

1. 技术服务的目标：通过甲乙双方优势互补、深度合作，共同开展科技开发工作，主要开展新产品研发、新材料、新工艺、新技术的推广与应用，共同推进甲方在高端木作、家居家装新材料上的研发和技术方面的储备能力。

2. 技术服务的内容：(1) 乙方协助甲方解决生产过程中存在的技术问题。若乙方有重大的科研项目立项招标，在同等条件下应优先考虑选择与甲方合作。(2) 根据国内外发展趋势和市场需求，双方组织研究团队联合向国家、省部有关部门申请项目和经费，开展科研合作和技术攻关。如联合申报项目获批立项，经费分配另行商议。(3) 针对甲方现有木质家居材料阻燃、防霉等功能化研究需要，乙方利用其科研条件进行理论分析和实验研究，协助甲方优化木质家居产品和技术升级，涉及具体产品和技术开发经协商后需另行签订合作协议。(4) 乙方优先考虑把相关科技成果提供给甲方进行成果转化、产业化生产和市场推广。(5) 根据甲方的需求，乙方不定期对甲方技术人员和管理人员进行技术培训，所需费用由甲方解决。(6) 根据甲方的需求，乙方在符合国家相关规定的前提下，对甲方企业负责人或相关从业人员进行学历提升教育。所需费用由甲方解决。

第二条：乙方应按下列要求完成技术服务（合作）工作：

1. 技术服务地点：华南农业大学、广东煜丰实业（集团）有限公司

2. 技术服务期限：2024年11月1日—2027年10月30日

3. 技术服务进度：依据实际情况具体开展。

4. 技术服务质量要求：无。

5. 技术服务质量期限要求：协议期内。

第三条：为保证乙方有效进行技术服务（合作）工作，甲方应当向乙方提供下列工作条件和协作事项：

1. 提供技术资料：项目中所需要的原始技术资料。

2. 提供工作条件：专利的申报费用和协助项目研发所需要的相关费用等。

3. 其他：无。

4. 甲方提供上述工作条件和协作事项的时间及方式：根据甲方具体需求，提前 7 个工作日通过电子文档或纸质文档提供给乙方。

第四条：甲方向乙方支付技术服务（合作）报酬及支付方式为：

1. 技术服务（合作）费总额为：陆万元整

2. 技术服务（合作）费由甲方一次支付乙方。

具体支付方式和时间如下：

(1) 2024 年，合同签订 10 日内，支付陆万元整

乙方开户银行名称、地址和账号为：

开户银行：华南农业大学

地址：广州工行五山支行

账号：3602002609000310520

第五条：双方确定因履行本合同应遵守的保密义务如下：

甲方：

1. 保密内容（包括技术信息和经营信息）：由双方合作共同研发产生的科研成果，其知识产权为双方共有，可共同申请专利，未经双方同意不得转让第三方或者一方单独申请专利，经双方友好协商，甲方可有偿并优先优惠地取得该知识产权。

2. 涉密人员范围：甲方全体工作人员；

3. 保密期限：协议期内。

4. 泄密责任：甲方有义务保守知识产权、技术资料、工艺、产品、企业经营状况以及双方约定的其技术和商业秘密。

乙方：

1. 保密内容（包括技术信息和经营信息）：由双方合作共同研发产生的科研成果，其知识产权为双方共有，可共同申请专利，未经双方同意不得转让第三方或者一方单独申请专利，经双方友好协商，甲方可有偿并优先地取得该知识产权。

2. 涉密人员范围：乙方项目参与人员；

3. 保密期限：协议期内。

4. 泄密责任：乙方有义务保守知识产权、技术资料、工艺、产品、企业经营状况以及双方约定的其技术和商业秘密。

第六条：本合同的变更必须由双方协商一致，并以书面形式确定。但有下列情形之一的，一方可以向另一提出变更合同权利与义务的请求，另一方应当在15日内予以答复；逾期未予答复的，视为同意：

1、服务内容变更_____；

2、研究经费超出计划_____；

第七条：双方确定：

1. 在本合同有效期内，甲方利用乙方提交的技术服务（合作）工作成果所完成的新的技术成果，归双（甲、双）方所有。

2. 在本合同有效期内，乙方利用甲方提供的技术资料和工作条件所完成的新的技术成果，归双（乙、双）方所有。

第八条：双方确定，按以下约定承担各自的违约责任：

1. 甲方违反本合同第四条约定，应当支付违约金（每逾期一日，甲方应按当年度合作费用总额的 1%向乙方支付违约金。逾期超过三十日，甲方除了应按前述标准向乙方支付违约金之外，乙方还有权立即解除本协议并要求甲方承担由此造成的一切损失（包括但不限于实际损失、既得利益损失、声誉损失及合理的调查费、律师费等相关费用）。

2. 除上述约定外，由于甲乙双方任何一方违约，造成本协议不能履行或不能完全履行时，守约方有权要求终止协议，并要求违约方赔偿损失，具体由生效的法律文书认定，该损失包括为主张权利而支付的费用，如诉讼费、律师费、公证费、评估费、鉴定费等。

第九条：双方确定，在本合同有效期内，甲乙双方分别成立研发合作课题组，甲方由唐松波任组长，指定唐松波为甲方项目联系人，乙方由孙理超任组长，指定孙理超为乙方项目执行组长兼联系人。项目联系人承担以下责任：

甲乙双方联系人负责及时处理相关合作事宜，甲方联系人负责为合作团队提供必要的在甲方的工作和生活条件，双方联系人落实本方科技资源向研发团队开放，确保按计划完成工作任务。

一方变更项目联系人的，应当及时以书面形式通知另一方，未及时通知并影响本合同履行或造成损失的，应承担相应的责任。

第十条：双方确定，出现下列情形，致使本合同的履行成为不必要或不可能的，可以解除本合同，双方均不承担违约责任：

1. 发生不可抗力。不可抗力是指无法预见、无法避免、无法克服的客观情况，包括自然灾害、军事行动、工人罢工、暴乱、法律法规强制规定、政府政策限制。遇到上述不可抗力事件的一方，应立即书面通知协议相对方，并应在不可抗力事件发生后十五天内，向协议相对方提供经不可抗力事件发生地区县级以上政府部门出具的证明协议不能履行或需要延期履行、部分履行的有效证明文件原件，由协议各方按事件对履行协议影响的程度协商决定是否解除协议、或者部分或全部免除履行协议的责任、或者延期履行协议。遭受不可抗力的一方未履行上述义务的，不能免除其违约责任。

第十一条：双方因履行本合同而发生的争议，应协商、调解解决。协商、调解不成的，确定按以下第2种方式处理：

1. 提交_____仲裁委员会仲裁；
2. 依法向人民法院起诉。

第十二条：双方确定：本合同及相关附件中所涉及的有关名词和技术术语，其定义和解释如下：

1. 无

第十三条：与履行本合同有关的下列技术文件，经双方确认后，无为本合同的组成部分：

1. 技术背景资料: _____;
2. 可行性论证报告: _____;
3. 技术评价报告: _____;
4. 技术标准和规范: _____;
5. 原始设计和工艺文件: _____;

第十四条: 双方约定本合同其他相关事项为: 无。

第十五条: 本协议一式四份, 双方各持二份, 具有同等法律效力。

第十六条: 本合同经双方签字盖章后生效。

甲方 (盖章):

法定代表人 / 委托代理人 (签名):

年 月 日

乙方: 华南农业大学 (盖章)

法定代表人 / 委托代理人 (签名):

年 月 日

印花税票粘贴处:

(以下由技术合同登记机构填写)

合同登记编号:

--	--	--	--	--	--	--	--	--	--	--	--	--	--	--	--

1. 申请登记人: _____

2. 登记材料: (1) _____

(2) _____

(3) _____

3. 合同类型: _____

4. 合同交易额: _____

5. 技术交易额: _____

技术合同登记机构 (印章)

经办人:

年 月 日

检索证明

根据委托人提供的论文材料，委托人华南农业大学材料与能源学院 樊奇 14 篇论文收录情况如下表。

序号	论文名称	发表刊物及发表的年月卷期/页码等	作者排名	论文等级	作者文中单位	收录情况	影响因子	中科院大类分区
1	Water-Induced Self-Assembly and In Situ Mineralization within Plant Phenolic Glycol-Gel toward Ultrastrong and Multifunctional Thermal Insulating Aerogels	ACS NANO 出版年：2022 出版日期：JUN 28 卷期：16 6 页码：9062-9076 文献类型：Article	第一作者	T2 类	华南农业大学 材料与能源学院	SCI	IF2-year=17.1 IF5-year=17.1 (2022)	材料科学 1 区 Top 期刊：是 (2022)
2	Ultrastrong and Thermo-Remoldable Lignin-Based Polyurethane Foam Insulation with Active-Passive Fire Resistance	ADVANCED FUNCTIONAL MATERIALS 出版年：2024 出版日期：OCT 卷期：34 40 页码：- 文献类型：Article	通讯作者	T2 类	华南农业大学 材料与能源学院	SCI	IF2-year=19.0 IF5-year=19.4 (2024)	材料科学 1 区 Top 期刊：是 (2025)
3	Enhanced mechanical performance and fire resistance of poplar wood: Unilateral surface densification assisted with N/P doped acrylic resin impregnation	CONSTRUCTION AND BUILDING MATERIALS 出版年：2023 出版日期：SEP 22 卷期：398 页码：- 文献号：132470	共同通讯作者	T2 类	华南农业大学 材料与能源学院	SCI	IF2-year=7.4 IF5-year=8.0 (2023)	工程技术 1 区 Top 期刊：是 (2023)

		文献类型: Article						
4	Fast realization of high-strength, repeatable, damp-heat resistant bamboo-strip scarf bonding joints via hot-melt adhesives	CONSTRUCTION AND BUILDING MATERIALS 出版年: 2023 出版日期: JUN 27 卷期: 384 页码: - 文献号: 131331 文献类型: Article	并列第一作者	T2 类	华南农业大学 材料与能源学院	SCI	IF2-year=7.4 IF5-year=8.0 (2023)	工程技术 1 区 Top 期刊: 是 (2023)
5	Modification of poplar wood cells using 1,3-dihydroxymethyl-4,5-dihydroxyethylideneurea/alkaline lignin for enhanced mechanical properties and decay resistance	CONSTRUCTION AND BUILDING MATERIALS 出版年: 2023 出版日期: MAR 3 卷期: 368 页码: - 文献号: 130354 文献类型: Article	并列第一作者	T2 类	华南农业大学 材料与能源学院	SCI	IF2-year=7.4 IF5-year=8.0 (2023)	工程技术 1 区 Top 期刊: 是 (2023)
6	Biomimetic versatile wood hybrids with gradient structure towards lightweight, high strength, fire-retardant, and deterioration-resistant materials	COMPOSITES PART B-ENGINEERING 出版年: 2024 出版日期: JUL 1 卷期: 280 页码: - 文献号: 111483 文献类型: Article	第一作者	T2 类	华南农业大学 材料与能源学院	SCI	IF2-year=14.2 IF5-year=12.7 (2024)	材料科学 1 区 Top 期刊: 是 (2025)

7	Handling-friendly, waterproof, and mildew-resistant all-bio-based soybean protein adhesives with high-bonding performance via bio-inspired hydrophobic-enhanced crosslinking network	INDUSTRIAL CROPS AND PRODUCTS 出版年: 2024 出版日期: AUG 卷期: 214 页码: - 文献号: 118583 文献类型: Article	通讯作者	T2 类	华南农业大学 材料与能源学院	SCI	IF2-year=6.2 IF5-year=6.2 (2024)	农林科学 1 区 Top 期刊: 是 (2025)
8	Ultra-strong and solvent-resistant lignin-based non-isocyanate polyurethane adhesives: One-pot strategy toward versatile bonding	INTERNATIONAL JOURNAL OF BIOLOGICAL MACROMOLECULES 出版年: 2025 出版日期: JAN 卷期: 287 页码: - 文献号: 138622 文献类型: Article	通讯作者	A 类	华南农业大学 材料与能源学院	SCI	IF2-year=8.5 IF5-year=8.7 (2024)	生物学 2 区 Top 期刊: 是 (2025)
9	多层夹芯结构木塑复合材料阻燃与力学性能	复合材料学报 出版年: 2024 出版日期: 2023-11-06 17:06 卷期: 41 07 页码: 3737-3745 文献号: 文献类型: 期刊论文	共同通讯作者	A 类	华南农业大学 材料与能源学院	北大核心	无	无

10	Fully Biobased Soy Protein Adhesives with Integrated High-Strength, Waterproof, Mildew-Resistant, and Flame-Retardant Properties	ACS SUSTAINABLE CHEMISTRY & ENGINEERING 出版年: 2022 出版日期: MAY 23 卷期: 10 20 页码: 6675-6686 文献类型: Article	第五作者	T2 类	华南农业大学 材料与能源学院	SCI	IF2-year=8.4 IF5-year=8.7 (2022)	化学 1 区 Top 期刊: 是 (2022)
11	Rheological behavior and mechanical properties of ultra-high-filled wood fiber/polypropylene composites using waste wood sawdust and recycled polypropylene as raw materials	CONSTRUCTION AND BUILDING MATERIALS 出版年: 2022 出版日期: OCT 10 卷期: 351 页码: - 文献号: 128977 文献类型: Article	第三作者	T2 类	华南农业大学 材料与能源学院	SCI	IF2-year=7.4 IF5-year=7.9 (2022)	工程技术 1 区 Top 期刊: 是 (2022)
12	Rapid production of high-performance unilaterally surface-densified wood through integrating mechanical compression and thermochemical modification	CONSTRUCTION AND BUILDING MATERIALS 出版年: 2024 出版日期: NOV 29 卷期: 453 页码: - 文献号: 139014 文献类型: Article	第二作者	T2 类	华南农业大学 材料与能源学院	SCI	IF2-year=8.0 IF5-year=8.6 (2024)	工程技术 1 区 Top 期刊: 是 (2025)
13	Sustainable, high-performance, flame-retardant waterborne wood coatings via phytic acid based green	PROGRESS IN ORGANIC COATINGS 出版年: 2022	第三作者	T2 类	华南农业大学 材料与能源学院	SCI	IF2-year=6.6 IF5-year=5.9 (2022)	材料科学 1 区 Top 期刊: 是 (2022)

	curing agent for melamine-urea-formaldehyde resin	出版日期: JAN 卷期: 162 页码: - 文献号: 106597 文献类型: Article						
14	Preparation and properties of spirulina protein graft modified adhesive, used in plywood wood bonding	JOURNAL OF ADHESION SCIENCE AND TECHNOLOGY 出版年: 2024 出版日期: JUL 2 卷期: 38 13 页码: 2350-2366 文献类型: Article	第四作者	B 类	华南农业大学 材料与能源学院	SCI	IF2-year=3.7 IF5-year=3.0 (2024)	材料科学 4 区 Top 期刊: 否 (2025)

说明: 论文等级和中科院大类分区按《华南农业大学学术论文评价方案(试行)》划分。

报告免责声明: 如未盖章, 报告无效



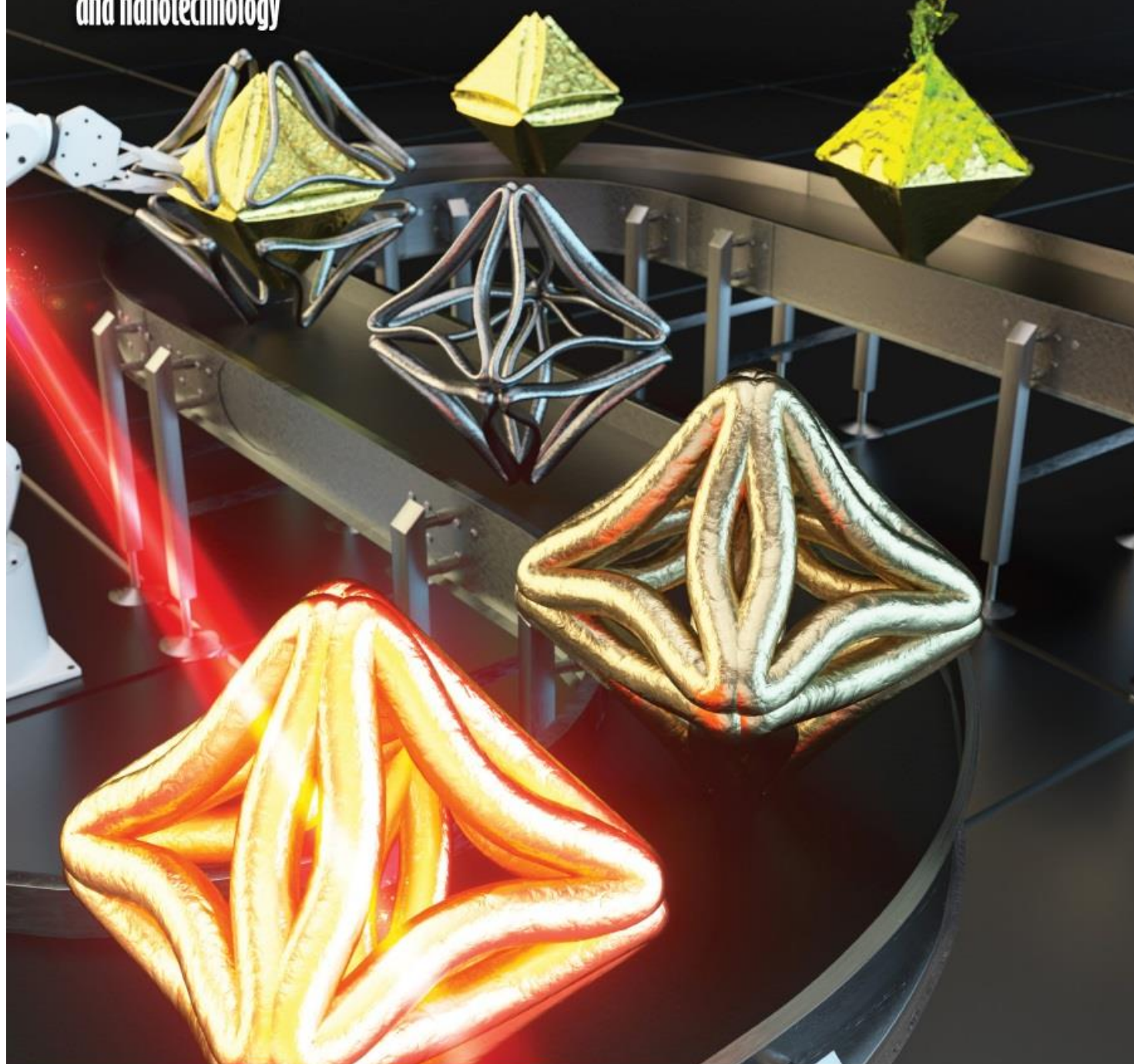
ACS NANO

JUNE 2022

VOLUME 16 NUMBER 6

pubs.acs.org/acsnano

Defining nanoscience
and nanotechnology



ACS Publications
Most Trusted. Most Cited. Most Read.

www.acs.org

Search text, DOI, authors, etc.



My Activity

Publications



Water-Phase Lateral Interconnecting Quantum Dots as Free-Floating 2D Film Assembled by Hydrogen-Bonding Interactions to Acquire Excellent Electrocatalytic Activity

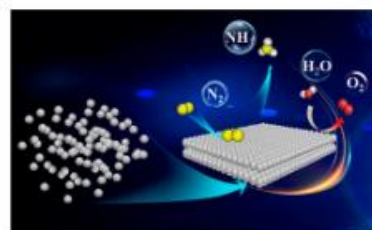
Feifei Wang, Qiguan Wang*, Sumin Wang*, Kai Zhang, Siqin Jia, Jian Chen, and Xinhai Wang

ACS Nano 2022, 16, 6, 9049-9061 (Article) ✓ Subscribed

Publication Date (Web): June 13, 2022

[Abstract](#)[Full text](#)[PDF](#)

ABSTRACT



Water-Induced Self-Assembly and *In Situ* Mineralization within Plant Phenolic Glycol-Gel toward Ultrastrong and Multifunctional Thermal Insulating Aerogels

Qi Fan, Rongxian Ou*, Xiaolong Hao, Qianyun Deng, Zhenzhen Liu, Lichao Sun, Chaoqun Zhang, Chuigen Guo, Xiaojing Bai, and Qingwen Wang*

ACS Nano 2022, 16, 6, 9062-9076 (Article) ✓ Subscribed

Publication Date (Web): June 2, 2022

[Abstract](#)[Full text](#)[PDF](#)

ABSTRACT

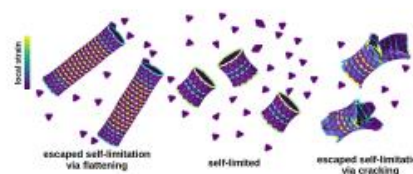


Thermodynamic Size Control in Curvature-Frustrated Tubules: Self-Limitation with Open Boundaries

Botond Tyukodi, Farzaneh Mohajerani, Douglas M. Hall, Gregory M. Grason*, and Michael F. Hagan*

ACS Nano 2022, 16, 6, 9077-9085 (Article) ✓ Subscribed

Publication Date (Web): May 31, 2022

[Abstract](#)[Full text](#)[PDF](#)

Water-Induced Self-Assembly and *In Situ* Mineralization within Plant Phenolic Glycol-Gel toward Ultrastrong and Multifunctional Thermal Insulating Aerogels

Qi Fan, Rongxian Ou,* Xiaolong Hao, Qianyun Deng, Zhenzhen Liu, Lichao Sun, Chaoqun Zhang, Chuigen Guo, Xiaojing Bai, and Qingwen Wang*



Cite This: *ACS Nano* 2022, 16, 9062–9076



Read Online

ACCESS |



Metrics & More



Article Recommendations



Supporting Information

ABSTRACT: Biopolymer/silica nanocomposite aerogels are highly attractive as thermally insulating materials for prevailing energy-saving engineering but are usually plagued by their lack of mechanical strength and environmental stability. Lignin is an appealing plant phenolic biopolymer due to its natural abundance, high stiffness, water repellency, and thermostability. However, integrating lignin and silica into high-performance 3D hybrid aerogels remains a substantial challenge due to the unstable co-sol process. In diatoms, the silicic acid stabilization prior to the condensation reaction is enhanced by the intervention of biomolecules in noncovalent interactions. Inspired by this mechanism, we herein rationally design an ultrastrong silica-mineralized lignin nanocomposite aerogel (LigSi) with an adjustable multilevel micro/nanostructure and arbitrary machinability through an unusual water-induced self-assembly and *in situ* mineralization based on ethylene glycol-stabilized lignin/siloxane colloid. The optimized LigSi exhibits an ultrahigh stiffness (a specific modulus of $\sim 376.3 \text{ kN m kg}^{-1}$) and can support over 5000 times its own weight without obvious deformation. Moreover, the aerogel demonstrates a combination of outstanding properties, including superior and humidity-tolerant thermal insulation (maintained at $\sim 0.04 \text{ W m}^{-1} \text{ K}^{-1}$ under a relative humidity of 33–94%), excellent fire resistance withstanding an $\sim 1200^\circ \text{C}$ flame without disintegration, low near-infrared absorption ($\sim 9\%$), and intrinsic self-cleaning/superhydrophobic performance (158°WCA). These advanced properties make it an ideal thermally insulating material for diversified applications in harsh environments. As a proof of concept, a dual-mode LigSi thermal device was designed to demonstrate the application prospect of combining passive heat-trapping and active heating in the building.

KEYWORDS: plant phenolic polymers, nanocomposite aerogels, self-assembly, mineralization, multifunctionality



Maintaining a pleasant building interior temperature accounts for more than 12% of global energy consumption,^{1,2} which contributes to a significant portion of the negative environmental consequences,³ such as the greenhouse effect. Circumventing these impacts requires the development of ecofriendly and energy-efficient insulated alternatives.^{4,5} In the context of carbon neutrality, the recently thriving renewable thermal insulation materials, including biopolymer (e.g., natural polysaccharide, lignin, and protein) aerogels or foams,^{2,6,7} symbolizes an essential component of the technology change required to create a sustainable energy-saving society.^{8–10} However, the comprehensive performance of these biopolymer thermal insulation materials in terms of thermal insulation, mechanical strength, and environmental stability cannot compete with those of commercial rigid

polymer insulation materials,⁹ such as phenolic foam (PF) and extruded polystyrene foam (EPF).

Biomimetic silicification provides a possible technology platform for creating biopolymers nanocomposite aerogels as high-performance thermal insulators, which usually have intriguing versatility that combines the advantages of biopolymers and inorganic silica.^{11–13} Over the past several years, extensive efforts have mainly focused on the exploitation

Received: January 22, 2022

Accepted: May 31, 2022

Published: June 2, 2022



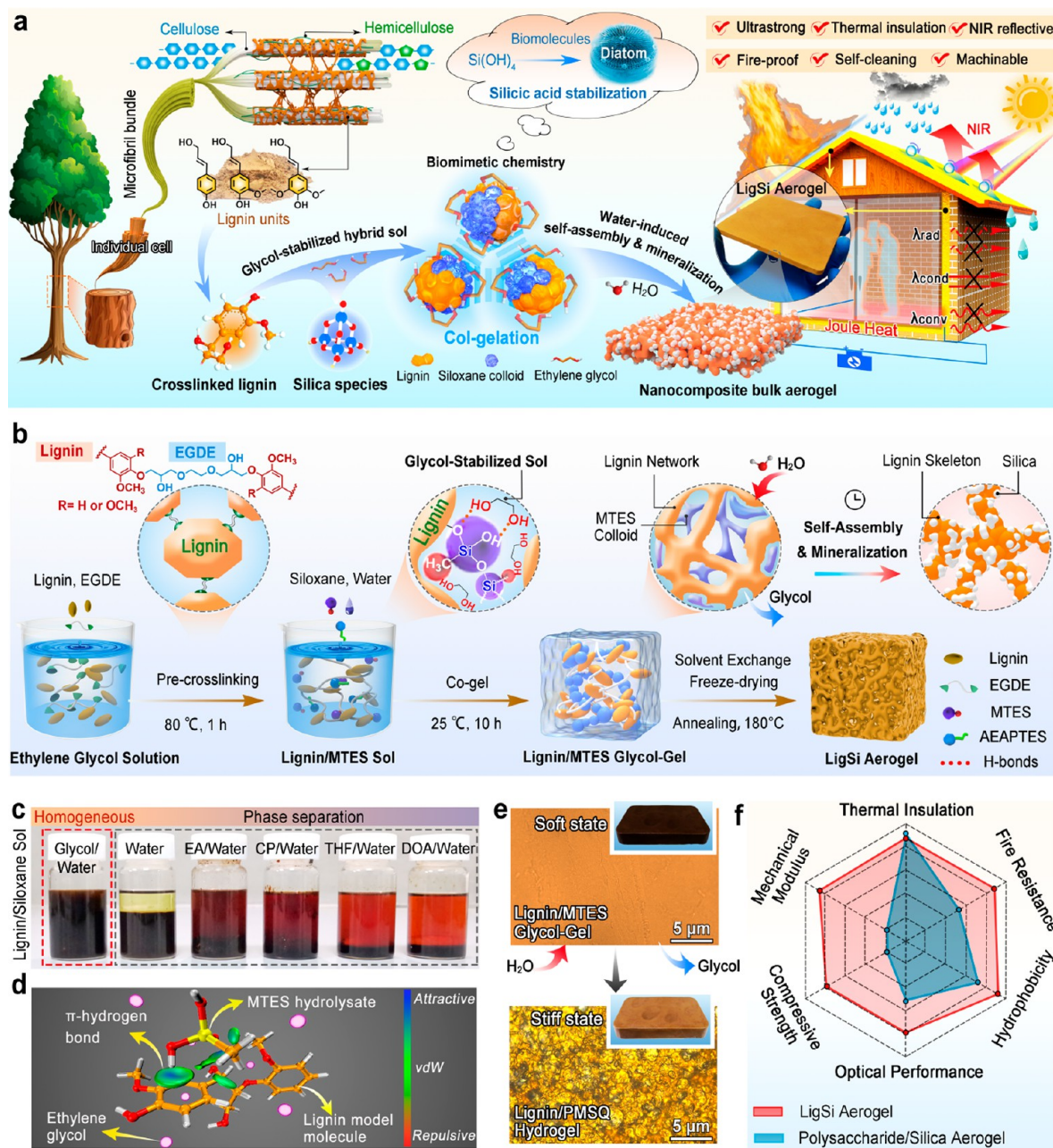


Figure 1. Bioinspired design of the LigSi. (a) Schematic illustration showing the multifunctional LigSi preparation strategy of the water-induced self-assembly and *in situ* mineralization based on the bionic ethylene glycol-stabilized hybrid sol. (b) Schematic description of the LigSi preparation process. (c) Photos of EHL (70 mg mL⁻¹) and MTES (340 mg mL⁻¹) dispersed in the various solvents after stirring for 5 min and standing for 2 h. The ratio of organic solvent to water was 11:1 (w/w). (d) Noncovalent interaction analysis between MTES hydrolysate and lignin model compound (GG, guaiacylglycerol-beta-guaiacyl ether), where ethylene glycol is shown as pink bubbles. (e) Optical images of EHL/MTES glycol-gel before and after solvent exchange. (f) Qualitative comparison of typical properties of LigSi aerogels and polysaccharide/silica composite aerogels by a radar chart.

of advanced silica-mineralized polysaccharides aerogels, such as cellulose/silica aerogels,^{13–16} pectin/silica aerogels,¹⁷ and chitosan/silica aerogels.¹⁸ Underlying these designs lies a common feature, that is, the attainment of low thermal conductivity and the remediation of the intrinsic disadvantages of polysaccharide aerogels including poor elasticity and high hygroscopicity.^{11,19,20} Nevertheless, these nanocomposite aerogels are mechanically weak (dimensional instability) and inferior to rigid plastic foams.^{7,21} Moreover, the mechanical properties and thermal insulation capacity of these materials are susceptible to relative humidity and temperature,^{13,22}

which prevents them from meeting the stringent requirements of direct exposure to the external or harsh environments.^{7,10} In addition, once a fire occurs, the low charring capability of polysaccharides will cause these hybrid aerogels to severely shrink and collapse.^{7,23} This will pose a significant fire threat to life and property when they are used as thermal insulators of buildings.^{2,24}

Lignin, the main component of plant biomass, appears as a plausible candidate to reverse the above unfavorable situation.^{25,26} Due to its stable aromatic structure, lignin demonstrates various attractive properties,^{25,27} including high

stiffness, excellent water repellency, thermostability, and UV-blocking capability, which can present different functionalities and application scenarios as compared with polysaccharide-based materials.^{28,29} Additionally, lignin is removed from lignocellulose in the chemical pulping or biorefining processes,²⁵ making this plant polyphenol abundantly available. However, lignin has to date been underexploited in high-value commercial applications due to its structural complexity and heterogeneity.³⁰ In recent years, the ongoing paradigm shift toward lignin-based advanced materials is largely based on the strong hydrophobic self-assembly behavior of lignin macromolecules,³¹ which can be easily converted into superior micro/nano-structures or domains.^{32–34} Importantly, lignin macromolecules contains abundant phenolic hydroxyl groups,²⁹ which can provide coordination sites for silicic acid and catalyze its polycondensation process.^{35,36} Therefore, it is expected to develop a combined strategy of self-assembly and cogelation to fabricate high-performance three-dimensional (3D) lignin/silica nanocomposite aerogel, which could be an important contribution for broadening structure and function choices of biobased thermal insulation aerogels. Although the few hints of lignin/silica hybrid materials can be found in previous reports,^{37,38} they are all in powder form with uncontrollable morphology and weak mechanical properties, resulting in the failure to meet the stringent requirements of integrated energy-efficient engineering. Currently, the robust and multifunctional lignin/silica nanocomposite bulk aerogel has not yet been reported due to there remaining two intractable challenges: (i) the poor solubility of lignin in most solvents significantly restricts the application of wet chemical methods for preparing porous lignin-based bulk materials,^{39,40} and (ii) the complex intra- and intermolecular noncovalent interactions of lignin,³⁹ especially π -stacking and H-bond, generally results in rapid phase separation and coprecipitation of lignin/siloxane colloid rather than the formation of a homogeneous gel network.^{40,41}

In nature, silica-producing marine microorganisms such as diatoms can efficiently stabilize the high concentrations of silicic acid before silica morphogenesis occurs.⁴² Biopolymers play a profound role in the above process. For example, the silicic acid stabilization prior to the condensation reaction in diatoms is enhanced by the intervention of biomolecules such as polysaccharides and polyamines that are found covalently attached to residues of special proteins, so-called silaffins.^{43,44} Recent research studies have demonstrated that bioinspired/biomimetic certain polymers, as direct analogues of biomolecules, such as polyamines,⁴⁵ zwitterionic polymers,⁴⁶ and polyether polyols,⁴⁷ can also stabilize silicic acid via balancing the noncovalent interactions.⁴⁷ These “Si” metabolism mechanisms and biomimetic chemistry offer inspirations to enable the formation of a homogeneous 3D lignin/silica hybrid network by employing biomimetic molecules to effectively regulate the noncovalent interactions of lignin and silica precursors.

In this work, we successfully fabricate a boardlike structure of monolithic silica-mineralized lignin nanocomposite aerogel (LigSi) through unusual water-induced self-assembly and *in situ* mineralization within the original homogeneous lignin/siloxane glycol-gel (Figure 1a). Inspired by the above intriguing silicic acid stabilization mechanisms in diatoms, we employ ethylene glycol as an efficient molecular machinery to suppress the rapid phase separation of cross-linked lignin/siloxane colloid and ensure the formation of homogeneous

lignin/siloxane bulk glycol-gel precursor. Then, the strong self-assembly behavior of the cross-linked lignin network is activated upon exposing the bulk glycol-gel to water, leading to an enhanced noncovalent interaction, such as π -stacking. The accompanying *in situ* mineralization of ethylene glycol-stabilized siloxane colloid further improves the skeleton strength of the hybrid glycol-gel network and generates a tunable multilevel microstructure. The LigSi obtained after drying and annealing exhibits outstanding mechanical strength/modulus and arbitrary machinability as well as desirable multifunctionality, i.e., excellent thermal insulation, fire resistance, intrinsic superhydrophobic/self-cleaning performance, and low solar thermal energy absorbance ($\sim 9\%$). Moreover, the durable thermal insulation has been demonstrated at a wide range of relative humidity of 33–94%. As a proof of concept, a dual-mode thermal device was designed by integrating Joule heating and thermal insulation functions into a single LigSi material, which can be used in precise supplemental heating systems for the interiors of intelligent buildings. As depicted in Figure 1a, the ultrastrong, environmentally stable, and versatile LigSi reflects great potential for application in energy-efficient building materials, especially in harsh environments.

RESULTS AND DISCUSSION

Fabrication Principles of Hybrid Aerogels. Figure 1b describes the fabrication pathway of LigSi hybrid aerogels (Figure S1). The hydrophobic enzymatic hydrolysis lignin (EHL) was chosen as the raw material to prepare the LigSi because of its high reactivity and chemical structure close to original lignin. First, the EHL was initially cross-linked by ethylene glycol diglycidyl ether (EGDE) in ethylene glycol, which was chosen as both an efficient solvent and biomimetic molecular machinery to stabilize the lignin/siloxane co-sol. Then, the siloxane including methyltriethoxysilane (MTES) and *N*-(β -aminoethyl)- γ -aminopropyl-trimethoxysilane (AEAPTES) with a small amount of water was added at predetermined ratios for hydrolytic polycondensation reactions, resulting in the formation of a homogeneous co-gel (Figure S1). The hydrophobic self-assembly of the lignin network and *in situ* mineralization behavior (the hydrolytic polycondensation of the free siloxane groups and the deposition of MTES colloid) was triggered when the external water molecules diffused into the lignin/siloxane glycol-gel networks in the solvent-exchange process (Figure 1b and Figure S1).

In this pathway, MTES with one nonhydrolyzable hydrophobic group was used because of the resultant polymethylsilsesquioxane (PMSQ) networks endowed with mesopores and a certain extent of intrinsic softness. AEAPTES not only provides a favorable fusion of EHL and PMSQ through the formation of intermolecular hydrogen bonds or even covalent linkages but also serve as an “internal catalyst” based on the amino groups for accelerating the sol–gel process. Importantly, ethylene glycol has outstanding solvation ability for lignin and MTES hydrolysate molecules as illustrated by the molecular dynamic simulation (Figure S2) and can ensure the formation of a homogeneous EHL/siloxane co-gel as opposed to coprecipitation as in other solvents (Figure 1c), including ethyl alcohol (EA)/water, acetone (CP)/water, tetrahydrofuran (THF)/water, and dioxane (DOA)/water, which are common binary solvents for siloxane hydrolysis or lignin processing.^{39,48} The reason for this is 2-fold: on the one hand,

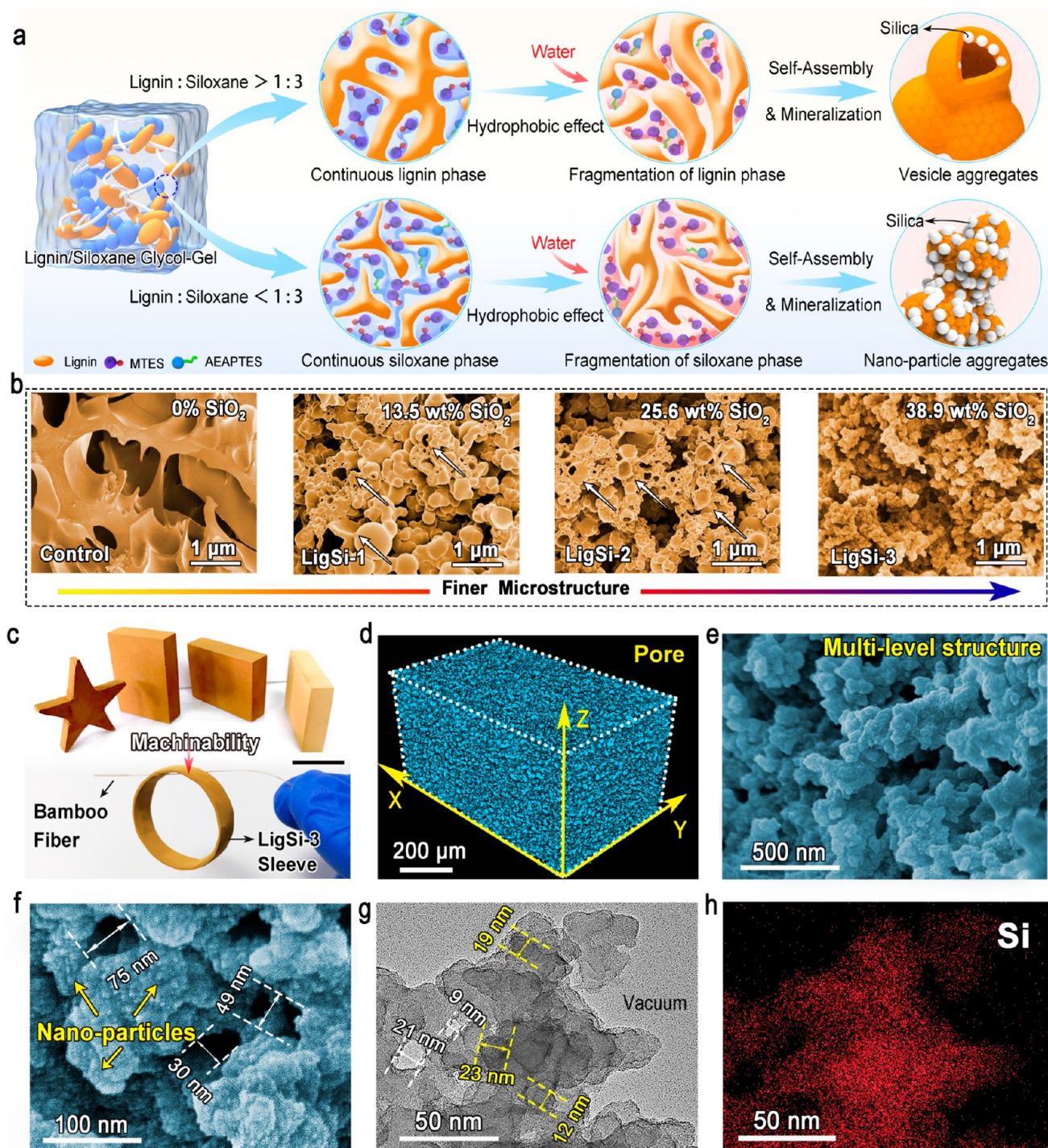


Figure 2. Morphology and structural characteristics of the LigSi aerogels. (a) Schematic diagrams of tunable micromorphology of the LigSi from continuous vesicle structure to nanoparticle aggregates by changing the mass ratio of siloxane. (b) SEM images of the control and LigSi samples with different degrees of mineralization. (c) Photo of the tailored LigSi aerogels with different sizes and shapes (scale bar, 2 cm), and LigSi-3 can be easily machined into a sleeve, which can be supported by a bamboo fiber. (d) Reconstructed 3D micro-CT images of the representative LigSi-3. False colors were applied to highlight the total extracted macropore. (e,f) SEM images of the fracture surface of the LigSi-3. (g,h) HRTEM and elemental mapping images show the nanostructure and the homogeneous distribution of the silica domain (red Si).

ethylene glycol can efficiently dissolve lignin (Figure S3);⁴⁹ on the other hand, ethylene glycol retards the rapid condensation and phase separation of the EHL/siloxane sol by forming a rich network of hydrogen bonds and van der Waals forces, which is elucidated by noncovalent interaction analysis (Figure 1d and Figure S4). Thus, the co-gelation process precedes the

occurrence of coprecipitation. When the EHL/MTES glycol-gel with an original homogeneous phase was soaked in water (Figure 1e), the aromatic hydrophobic region of the EHL network underwent strong self-assembly induced by the hydrophobic interaction, and the PMSQ colloidal grew and *in situ* deposited through the further hydrolytic polycondensa-

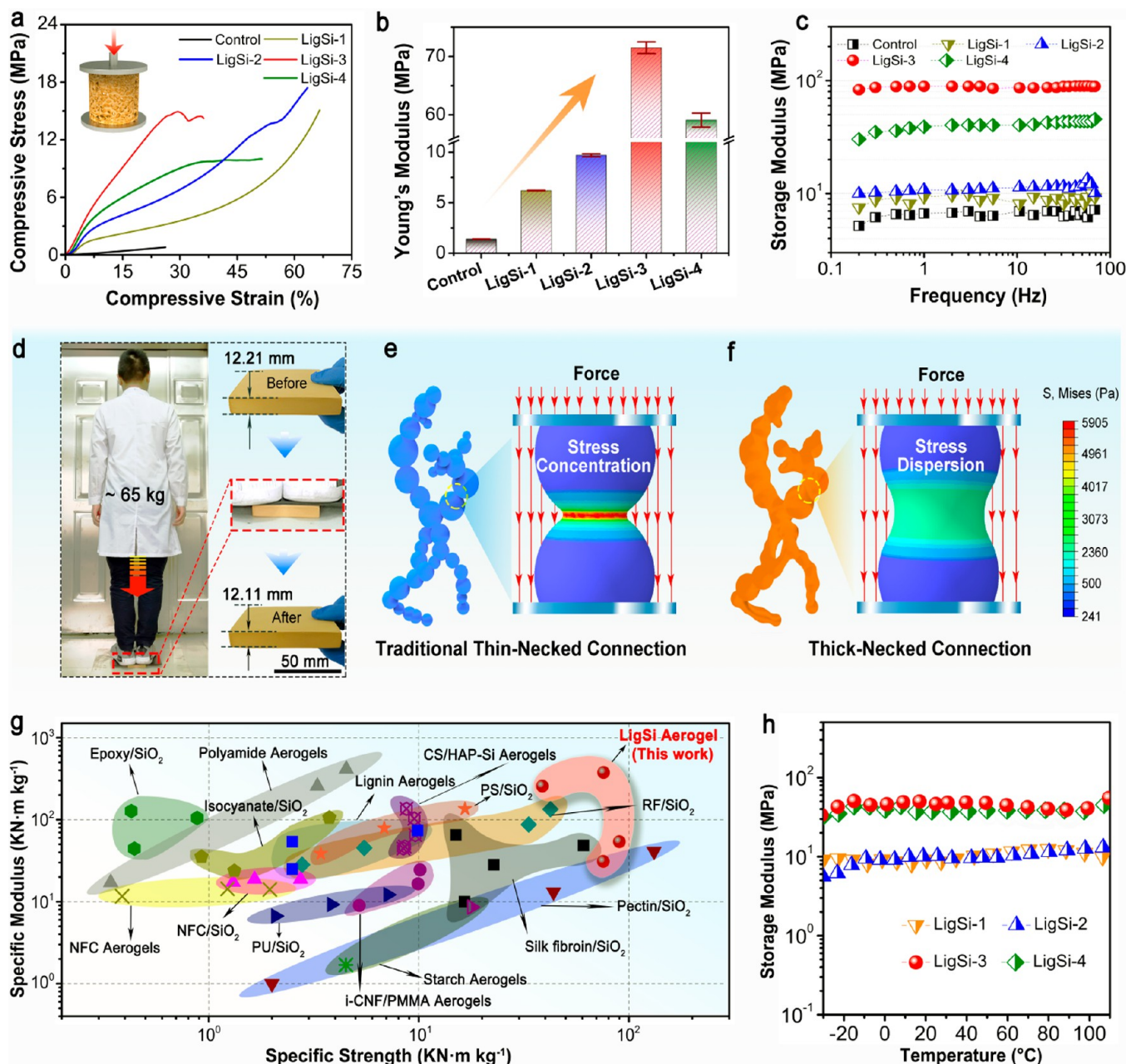


Figure 3. Mechanical properties. (a) Compressive stress–strain curves of typical LigSi materials. (b) Young's moduli of the LigSi aerogels. (c) Dynamic compressive performance at frequency from 0.3 to 100 Hz. (d) Intuitive representation of the mechanical property. Photographs of LigSi-3 aerogel with a density of 0.19 g m^{-3} supporting a 65 kg weight of human, with no obvious deformation. (e,f) Finite-element simulations of thin- and thick-necked connection structures for the particles aggregated aerogels, illustrating stress distribution upon a force of compression. (g) Specific final compression strength versus specific Young's modulus for various aerogel materials. Details of the mechanical properties are included in Table S4. (h) Dynamic thermomechanical performance with a fixed frequency of 1 Hz.

tion. Therefore, the phase separation of EHL/MTES glycol-gel evolved over time until an elaborate hierarchical structure developed and matured (Figure 1e). Upon further freeze-drying and annealing, the final hybrid aerogels were obtained. A series of hybrid aerogels (LigSi- x , $x = 1, 2, 3, 4$, where x represents the amount trend of siloxane used) was developed by tuning the amount of added MTES and AEAPTES, as shown in Table S1. For comparison, a cross-linked lignin aerogel without siloxane was also synthesized as a control sample. Comparing with thriving polysaccharide/silica composite aerogels,^{15,17,21,50} the LigSi displays added and even advanced features of outstanding mechanical robustness, fire

resistance, hydrophobicity, and optical performance (near-infrared reflectance and ultraviolet absorption) (Figure 1f).

Morphology and Structure. The microstructure of the LigSi prepared in this research is highly adjustable. When the mass ratio of added lignin and siloxane exceeds about 1:3, an unusual aggregated vesicle structure formed in self-assembly processing (Figure 2a), which is presumably driven by the hydrophobic interaction of the dominant lignin phase. In contrast, increasing the addition ratio of siloxane/lignin leads to finer microstructures consisting of secondary particle aggregates of tens of nanometers in size (Figure 2a). This morphological transformation is probably due to the large

amounts of siloxane make it difficult to form thermodynamically stable vesicle systems. As shown in Figure 2b, the results of scanning electron microscopy (SEM) of LigSi aerogels with increasing silica content, which was determined by thermal gravimetric (TG) analysis (Figure S5), further confirm the above results. That is, LigSi-1 and LigSi-2 with higher proportion of lignin exhibited a continuous vesicle aggregation structure. When the ratio of lignin and siloxane is less than 1:3, LigSi-3 exhibits a nanoparticle aggregated microstructure.

Benefiting from the one-pot synthesis route, the LigSi can be readily molded in a variety of sizes and shapes (Figure 2c), such as pentagonal prisms and rectangular solids. The obtained LigSi aerogel can also be processed into the required shape via subtractive manufacturing due to its excellent mechanical stability, which making it possible to use them as thermal insulation materials for a variety of different occasions. LigSi-3 sleeves were machined with a wall thickness of 1 mm and an outer diameter of 2 cm (Figure 2c). Further details of the processing steps are presented in Figure S6. The sleeve could be supported by bamboo fiber, demonstrating the good mechanical properties and low density of LigSi-3 (Table S1). Using LigSi-3 as an example, the X-ray microcomputed tomography (micro-CT) image of the total extracted macropores in LigSi-3 is displayed in Figure 2d. The resolved micrometer-sized macropores colored in cyan were found to be homogeneously dispersed in the bulk aerogels. In addition, the tomographic cross-section image and full-scale view of the solid body are shown in Figure S7. LigSi-3 exhibited a coarser microstructure than LigSi-1 and LigSi-2 prepared at a lower siloxane loading amount, and the frameworks were characterized by multilevel micro-nanoblocks composed of organic–inorganic hybrid nanoparticles (Figure 2e,f). As will be demonstrated later, the formation of these multilevel micro-nanoporous structures was expected to endow the materials with low thermal conductivity.^{51,52} In addition, the structure of LigSi is different from the traditional thin-necked “pearl-necklace-type” network structure of inorganic aerogels.¹⁷ Due to the interpenetrating constraint effect of the lignin/silica wet gel network, the LigSi exhibits a thick-necked micro-nanonetwork structure, which may be indirectly indicative of a mechanically strong aerogel. The microstructure of the lignin/silica hybrid domain was further examined by high-resolution transmission electron microscopy (HRTEM) and energy-dispersive X-ray spectroscopy (EDX) elemental mapping measurements. The composite skeleton structure of organic lignin polymer and methylsilsesquioxane-derived silica was found to have a continuous amorphous phase, and no obvious interphase correlation existed within the solid aerogel body (Figure 2g and Figure S8). The elemental mapping images corroborate the uniform distribution of the silica constituent in the aerogel skeleton (Figure 2h and Figure S9), which is attributed to the ethylene glycol-stabilized lignin/silica sol–gel process. The porous structures of the prepared LigSi were further probed using nitrogen sorption (Figure S10) and mercury intrusion porosimetry (Figure S11). The nitrogen adsorption and desorption curves of the LigSi materials displayed Types II and IV isotherm features according to the IUPAC classification (Figure S10),⁵³ indicating the coexistence of meso- and macropores. The average pore diameter of the mesopores was approximately 30–80 nm (Table S2), which is in agreement with the SEM image. Mercury intrusion measurements revealed that the average macropore size ranged from 270 to 1120 nm (Table S2).

Hydroxyl (–OH) groups of the lignin macromolecules can provide reactive and anchoring sites for silicification. According to the solid-state ²⁹Si NMR spectra of LigSi-3 (Figure S12), the Si peaks that completely overlap at –66 and –58 ppm were due to the R–Si(–OSi)₃ and R–Si(–OSi)₂O– formed by the hydrolysis and condensation of the silica precursors.^{13,53} The presence of the signal at –58 ppm indicates that the hydrolyzed MTES within the material did not form a fully condensed siloxane network, likely because some copolycondensation and hydrogen bonding concurrently occurred between polysiloxane and lignin. Therefore, the chelation of the lignin and silica phase was speculated to occur through hydrogen bonding interactions and covalent cross-linking (Figure S1c). As described in Figures S12 and S13 and the Supplementary Discussion, this speculation can be also confirmed by the results of Fourier transform infrared spectrometry (FTIR), ¹³C NMR spectroscopy, and X-ray photoelectron spectroscopy (XPS).

Strong Mechanical Properties. Outstanding mechanical strength is highly desired for aerogel materials applied in stressed situations, such as energy-efficient building envelopes.⁵⁴ The stress–strain curves obtained from the compression testing of the LigSi aerogels are shown in Figure 3a. The linear elastic regions of the LigSi were approximately 5–10% strain, and the yields were approximately 30–60% strain (Figure 3a). The slopes of the stress–strain curves in the elastic region were used to derive the Young’s moduli (Figure 3b). Consequently, LigSi-3 exhibited a superb final strength of 14.4 MPa and an ultrahigh compressive modulus of 71.5 MPa (Table S3). The samples with a relatively low degree of silicidation, such as LigSi-1 and LigSi-2, gradually undergo plastic deformation after reaching the yield point (Figure 3a). However, the LigSi-3 and LigSi-4 with a relatively high degree of silicidation presented a brittle fracture behavior. Moreover, LigSi-4 has a higher degree of silicidation but exhibits a slightly lower modulus and higher deformation, which probably originates from the leaching of excess MTES during solvent exchange and the plasticization of excess AEAPTES. A dynamic compressive analysis was conducted to further characterize the mechanical behaviors of LigSi materials at low strain (Figure 3c). The values of the storage modulus were found to have the same trend and order of magnitude as the Young’s modulus. Moreover, the storage modulus was found to be almost independent of the frequency (0.3–100 Hz) and remained nearly constant, which suggests that a robust microstructure was dominant in the LigSi.

As shown in Figure 3d, the ultrastrong LigSi-3 could even bear being stepped on by an adult with only minimal ~0.8% deformation. The super mechanical behavior was further explored by mechanical simulations. The finite-elements model was built to mimic the architectures of the particle aggregated aerogels (Figure 3e,f). Comparing with the traditional thin-necked connection (Figure 3e), the thick-necked one in our LigSi system was more capable of dispersing stress (Figure 3f), which could prevent the fracture and would be responsible for the outstanding mechanical properties of the hybrid aerogel materials. The above results suggest that the mechanical reinforcement was closely related to the degree of mineralization and thick-necked microstructure.¹⁷ Although the density of LigSi (0.18–0.23 g cm^{–3}) was slightly higher than those of traditional biobased hybrid aerogels, the LigSi materials exhibited superior performance in terms of their specific strength (75.79 kN m kg^{–1}) and specific modulus (376.32 kN

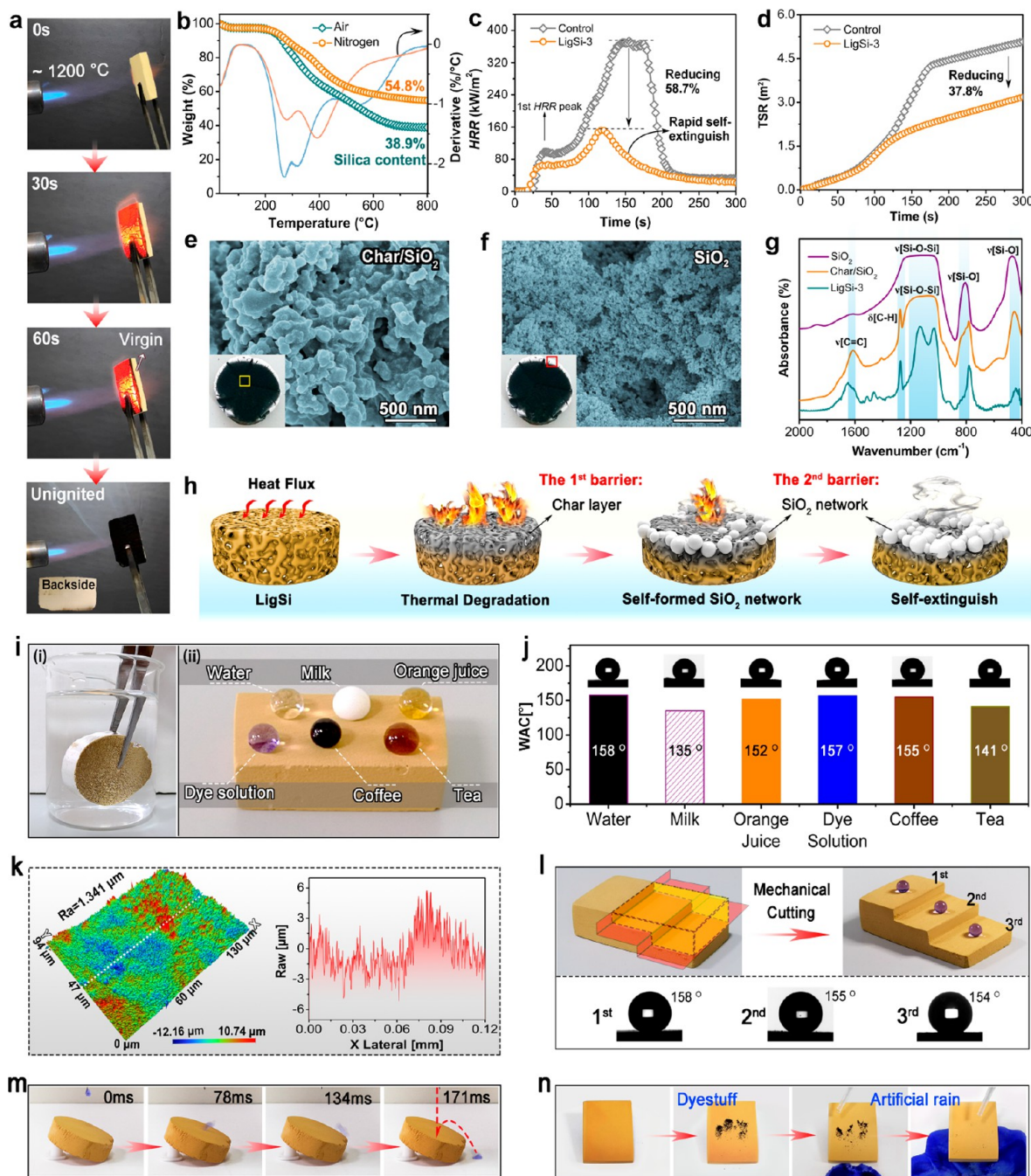


Figure 4. Fire-retardant properties and self-cleaning (superhydrophobic) performance. (a) Photographs of the high-temperature flame resistance behavior. (b) TGA curves and their derivatives of the LigSi-3, respectively, measured in air and nitrogen. (c,d) HRR and TSR plots of the LigSi-3 and control sample. (e,f) SEM images of the char/SiO₂ network and SiO₂ network produced from burnt LigSi-3. (g) FTIR curves. (h) Schematic illustration showing the fire-retardant mechanism of the self-formed dual-barrier. (i) Photograph of the hydrophobicity of the LigSi-3 to different liquid stains. (j) Static contact angle of the different liquid on the surface of LigSi-3. (k) Laser optical 3D surface image and depth profile of the LigSi-3. (l) Photographs showing the intrinsic superhydrophobicity and the static contact angles of the different surfaces by mechanical cutting. (m) Photographs of liquid repellency to impinging water droplet. (n) Photos of self-cleaning performance.

m kg⁻¹) as compared with previously reported state-of-the-art hybrid aerogels (Figure 3g and Table S4). The outstanding mechanical stability of the LigSi provided a good foundation for insulation applications. Due to the aromatic structure of lignin and their uniform organic–inorganic hybrid composition, the LigSi materials exhibited excellent thermal stability. As shown in Figure 3h, the elastic modulus of the LigSi materials hardly changes over the operating temperature range

of –20 to 100 °C, which will eliminate the safety hazards caused by temperature-induced deformation of the materials during use. Given that LigSi-3 aerogel has the optimal mechanical strength, abundant micro-nanostructure, and high degree of silicification, the LigSi-3 was selected as a typical sample in this work to complete the subsequent characterization of functional properties.

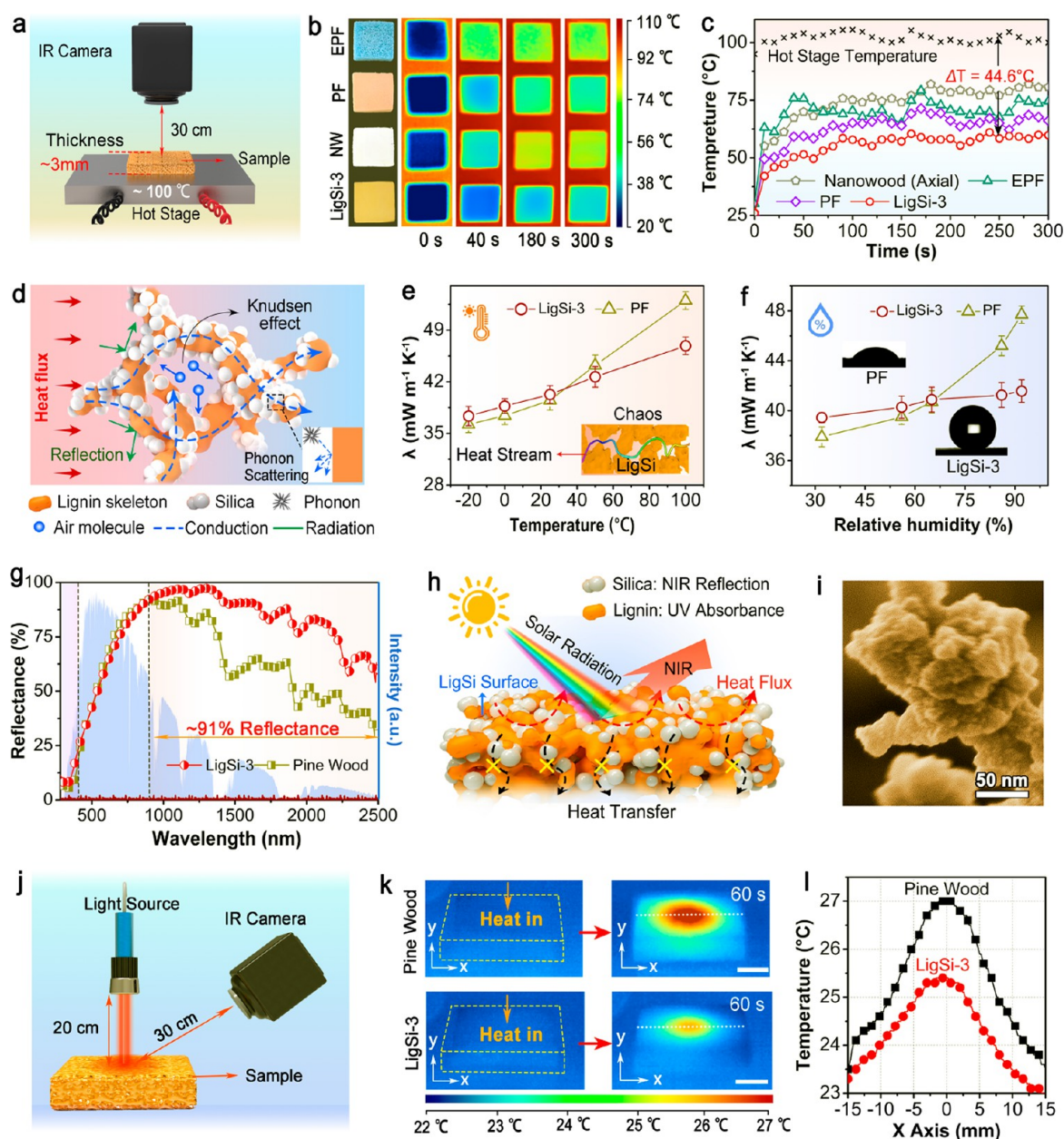


Figure 5. Thermal insulation and optical properties. (a) Setup for evaluating the thermal insulation property of samples. (b) Picture and IR images of LigSi-3, NW, PF, and EPF on a 100 °C hot stage, and (c) TST-time curves of the samples. (d) Schematic illustration of the heat transfer process of the LigSi-3. (e) Thermal conductivity of LigSi-3 and commercial PF as a function of temperature at constant absolute humidity. (f) Thermal conductivity of LigSi-3 and commercial PF as a function of RH at 25 °C. (g) Reflectance of the LigSi-3 and nature pine wood covering the solar radiation spectrum. (h) Schematic illustration showing the low photothermal conversion. (i) SEM image illustrates the multilevel microstructure of the LigSi-3. (j) Setup for evaluating the photothermal conversion of samples. (k) IR images of the LigSi-3 and the pine wood illuminated by a NIR light (1350–1600 nm). Scale bars are 1 cm. (l) Temperature profiles for the samples in part k.

Exceptional Fire Retardancy. The fire resistance of heat-insulating materials is crucial for energy-efficient buildings, as it allows sufficient time for evacuation before the building collapse. The high-temperature flame resistance of LigSi-3 was investigated using the flame of a propane/butane blowtorch (~1200 °C) (Figure 4a). As a result, the LigSi-3 exhibits outstanding fire retardancy and self-extinguishes immediately when removed from igniting the propane/butane flame (Movie S1). However, the control sample was readily ignited upon exposure to the burner, indicative of a high ignitability (Figure S14). What's more, after a high-temperature heating

test, LigSi-3 preserved its morphological integrity and the nonexposed backside of the material was still pristine (Figure 4a). The high silica content (38.9%) and high charring capability of the LigSi-3 is the main reason for the exceptional fire-shielding effect (Figure 4b).

The flame retardancy behavior of LigSi-3 under a forced fire scenario was further evaluated by cone calorimetry. Some critical fire parameters, such as heat release rate (HRR), total heat release (THR), smoke release rate (SRR), and total smoke release (TSR) as a function of time, were recorded. As presented in Figure 4c and Figure S15a, the LigSi-3 exhibits a

clearly shorter self-extinguishment after burning of 127 s, leading to ultralow peak values of HRR of 158.2 kW/m² and a SRR of 0.027 m²/s, ~59% and 49% lower than those of the control sample, respectively. In addition, both TSR and THR values of the LigSi-3 were significantly reduced by 37.8% and 56.5% compared to the control sample (Figure 4d and Figure S15b). These results further clearly demonstrated the high fire retardancy efficiency of as-designed silica mineralized lignin aerogel.

Generally, the flame retardant effect comes from either the gas or the condensed phase or in both phases. In theory, the condensed phase plays a dominant role in the flame retardant behavior of the LigSi-3 because of its high pyrolysis residue yield above 54 wt % (Figure 4b). To further shed light on the flame retardant mechanism of the LigSi-3 in the condensed phase, the LigSi-3 was subjected to the alcohol lamp flame, which simulated fire with an unrestricted oxygen supply, for an extended 30 min and recorded by thermal images (Figure S16). The morphologies and structures of char residues for the LigSi-3 are examined. The carbonized organic domain and the silica shell at the front edge were firmly integrated. As shown in Figure 4e, the char residue of the LigSi-3 appears to have a compact structure with few pores. In comparison, the white residue of the silica shell at the front edge of the carbonized LigSi-3 shows a loose nanoscale porous network structure (Figure 4f), which served as a flame-retardant and thermal insulation layer. The FTIR spectrum of the char residue for the LigSi-3 (Figure 4g) shows several characteristic peaks at 1599 cm⁻¹ (benzene ring), 1100–1000 cm⁻¹ (ν [Si–O–Si]), 800 cm⁻¹ (δ [Si–O]), and 450 cm⁻¹ (ρ [Si–O]) indicating the formation of a hybrid char/SiO₂ layer. In comparison, the white residue at the front edge of the carbonized LigSi-3 demonstrates the disappearance of the characteristic peaks at 1599 cm⁻¹ (benzene ring), which further indicates the dual condensed-phase action of the organic–inorganic hybrid LigSi-3.

Given the above analysis, it is reasonable to conclude that the self-formed dual char/SiO₂ barriers provide an effective lockdown of the heat transfer and oxygen permeation. By this mechanism, we further propose a schematic illustration for the combustion process for the LigSi-3 (Figure 4h). The high carbon content (about 45%)⁵⁵ of lignin promoted the formation of the first protective char layer, which limited the heat and mass transport of pyrolyzed LigSi. Upon extending the pyrolysis time, the carbon layer was gradually removed because of oxidative pyrolysis in air. Afterward, a continuous network of inorganic silica aerogel formed in situ and covered the surface of the pyrolyzed LigSi as the second barrier, which protected the material against further thermal decomposition.

Intrinsic Superhydrophobic and Self-Cleaning Performance. Water can roll on the superhydrophobic surface to remove adsorbed contaminants, viruses, and bacteria,⁵⁶ which endows the material a fascinating self-cleaning function. LigSi aerogels exhibit satisfactory hydrophobicity after annealing, and the average static water contact angle (WCA) fluctuates from 148° to 160° with different methylated silica contents (Figure S17). When the LigSi-3 was immersed in water by an external force, the existence of an air cushion between the water and the aerogel leads to reflectivity or a large number of microbubbles on the aerogel surface (Figure 4i). This phenomenon indicates that the water was in the Cassie–Baxter state, and the interaction between the water and LigSi was very weak. The WCA of LigSi-3 was approximately 158°,

which is indicative of superhydrophobicity (Movie S2). When different aqueous solutions, such as milk, orange juice, dye solution, coffee, and tea, were dropped on the surface of LigSi-3, the droplets stood steadily on the aerogel in nearly spherical shapes, indicating broad-spectrum antipollution performance (Figure 4i). The CAs of these contaminant solutions clearly indicate the excellent hydrophobicity of the surface, as shown in Figure 4j. The water repellency of the LigSi materials can be ascribed to the following aspects: (1) the cooperation of the hydrophobic aromatic skeleton structure of lignin and the hydrolytically stable methyl group of the MTES leads to very low interfacial energies of the aerogel; (2) the multilevel micronano-structure of the LigSi builds a rough surface (Figure 4k and Figure S18).

To demonstrate its hydrophobic reliability and mechanical stability, the WCA of the surface produced by a mechanical subtraction process was measured (Figure 4l). The WCAs of several cutting surfaces remained above 155° (Figure 4l), indicating that their intrinsic superhydrophobicity can resist mechanical damage. LigSi-3 also exhibits an excellent self-cleaning effect. As shown in Figure 4m, water droplets on the surface of LigSi-3 bounced off (Movie S3), and the artificial rain test confirms the good self-cleaning performance (Figure 4n). The water droplets rolled on the hydrophobic surface, simultaneously removing adsorbed pigment and dust (Movie S4). If the obtained LigSi aerogel with self-cleaning function is used as a building envelope material and exposed to the outdoor environment, the droplets of rainwater will roll on the superhydrophobic surface to ensure that the surface remains clean.

Excellent Thermal Insulation. Thermal insulation property is another crucial index for practical applications of aerogel materials in energy-efficient buildings. In order to demonstrate the application potential of the LigSi as a thermal insulator, the real thermal insulation performances of LigSi-3 were compared with those of other common thermal insulation materials through an intentionally designed setup (Figure 5a), which was used to detect the top surface temperature (TST) of the samples on 100 and 50 °C hot stages with a thermal IR imager. The samples thickness of EPF, PF, axial nanowood (NW, as previously reported),^{19,57} and LigSi-3 were all ~3 mm. As shown in Figure 5b and Figure S19a, LigSi-3 exhibited better thermal insulation properties than EPF, PF, and NW whether the temperatures of the hot stage were 100 or 50 °C. The difference between LigSi-3 and other insulation materials is evident from the TST-time curves (Figure 5c and Figure S19b). The TST of LigSi-3 on the hot stage slowly increases from room temperature (25 °C) to ~57.4 °C in 150 s, an increase of 32.4 °C, and then reaches a steady TST (Figure 5c). The temperature difference (ΔT) between the hot stage and the TST of LigSi-3 in the steady state is around 44.6 °C, suggesting its excellent thermal insulation capacity. In comparison, the TSTs of EPF, PF, and NW samples increased quickly in the first 50 s. It is worth noting that EPF, PF, and NW samples show a higher steady TST (above 60 °C). Comparison of the thermal insulation was also performed on a 50 °C hot stage (Figure S19b). The results also clearly indicate that the LigSi-3 has better thermal insulation performances than the commercial thermal insulation materials and recently reported nanowood thermal insulating material (axial).

The thermal conductivity of samples was further explored. Theoretically, the thermal conductivity (λ_{total}) of an aerogel in the air can be expressed as follows:⁵⁸

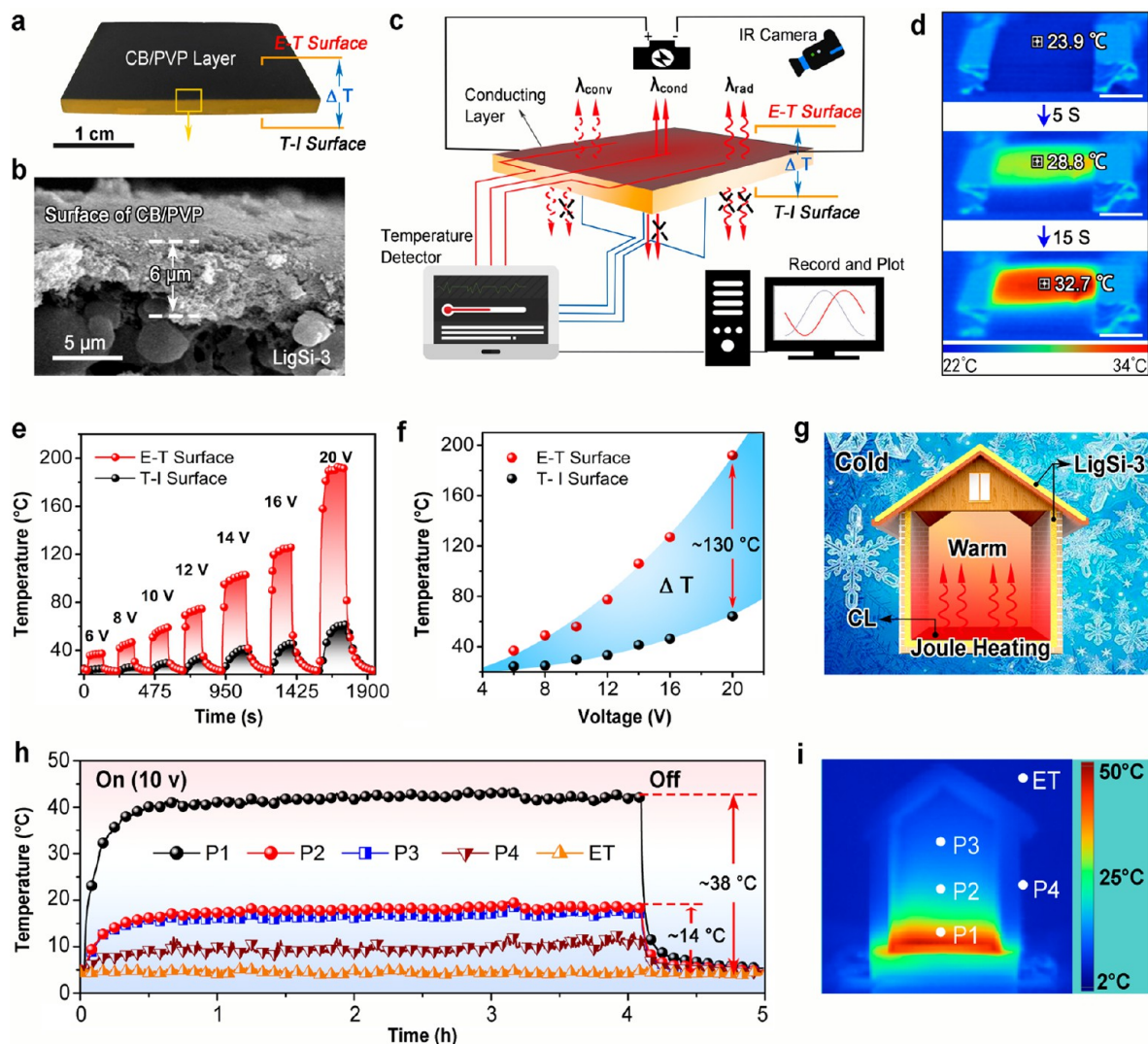


Figure 6. Dual-mode thermal device. (a) Bilayer structure of the dual-mode thermal device. (b) SEM images of the cross-section of the device material. (c) Illustrations of experimental setup for detecting the E-T and T-I behaviors of dual-mode thermal device. (d) IR images of thermal device when power applied (5 V). Scale bars are 8 mm. (e) Temperature profiles of device surface at different applied voltages. (f) Variations of absolute ΔT between E-T and T-I surfaces for given voltages. (g) Illustrations of LigSi-3 used for roofing, external siding, and floor insulation material of the energy-efficient building, which combined passive heating trapping with active heating. CL, Conducting Layer. (h) 5-hour continuous measurement of the spatial temperature distribution of the model energy-efficient building. (i) IR images of the model energy-efficient building when power applied (10 V).

$$\lambda_{\text{total}} = \lambda_{\text{conv}} + \lambda_{\text{solid}} + \lambda_{\text{air}} + \lambda_{\text{rad}} \quad (1)$$

where λ_{conv} represents thermal convection; λ_{solid} and λ_{air} are the thermal conductivities of the solid and gas phases, respectively; and λ_{rad} is the contribution of thermal radiation. The λ_{conv} should be insignificant, given that the micro/nanopore sizes are well below the onset size (1 mm) of natural convection.⁵⁹ The λ_{rad} is also neglected since silica is an efficient infrared reflector.⁶⁰ The reduction in the λ_{solid} conduction is usually achieved by lowering the bulk-density of the aerogel. The bulk-density of the LigSi-3 in the present study was approximately 0.19 g cm^{-3} , which was higher than those of flexible biobased polymer aerogels ($0.02\text{--}0.15 \text{ g cm}^{-3}$).^{7,61} As shown in Figure S20, the thermal conductivity of LigSi-3 at room temperature is about $40 \text{ mW m}^{-1} \text{ K}^{-1}$, which is relatively low for a high-bulk-density material. This was likely because the rich multilevel micro-nanostructure and the introduction of amorphous silica as an excellent phonon barrier substantially

reduces the λ_{solid} conduction (Figure Sd).⁵² The existence of abundant mesoporous is another crucial reason for the low λ_{total} of the LigSi-3. The interpenetrating porous network of LigSi-3 with pore diameters of $15\text{--}70 \text{ nm}$ was close to the mean free path of air (70 nm under ambient conditions) of the major molecules (N_2 , O_2) in the atmosphere.⁶² Thus, the collisions of gas molecules within the pores of the composite aerogels were suppressed, known as the Knudsen effect (Figure Sd), leading to a low λ_{air} value. Moreover, the thermal conductivity of LigSi-3 was found to be lower than those of most other commercial thermal-insulating materials (Figure S21),^{3,57,63,64} and similar to those of expanded polystyrene (EPS), PF, and Basotect ($35\text{--}45 \text{ mW m}^{-1} \text{ K}^{-1}$).²⁴ In addition, the thermal diffusivity of LigSi was $0.11\text{--}0.16 \text{ mm}^2 \text{ s}^{-1}$ (Figure S20), which is significantly lower than those reported for PU foams ($0.4\text{--}0.5 \text{ mm}^2 \text{ s}^{-1}$).⁶⁵

The temperature dependence of the thermal conductivity of LigSi-3 was further compared with that of a commercial PF

material (Figure 5e). For the LigSi-3 aerogel, the thermal conductivity increased from 37.4 to 45.9 mW m⁻¹ K⁻¹ as the temperature increased from -20 to 100 °C. The thermal conductivity increase rate of LigSi-3 was smaller than that of the commercial PF material, especially at high temperatures. This result may be due to the disordered micro-nanostructure of LigSi-3 strongly perturbing the heat transport path (streamline) (Figure 5e).⁶⁶

Generally, the thermal insulation properties of traditional aerogels, such as SiO₂ aerogels, polysaccharide aerogels, and phenolic resin aerogels, would gradually degenerate resulting from the high moisture absorption (easy deliquescence).³ Therefore, the thermal conductivity changes of the LigSi-3 aerogel were further investigated in environments with different air relative humidities (RH) (Figure 5f). It was found that the change in thermal conductivity of LigSi-3 showed almost ignorable increasing as the RH varied from 33% to 94% (Figure 5f). This result is mainly originating from the intrinsic superhydrophobic properties of LigSi-3, which can push the water out from the surface (see Movie S5), leading to withstanding of the high RH (Figure S22). In contrast, the thermal conductivity of the commercial PF material dramatically increased from 37.9 to 47.7 mW m⁻¹ K⁻¹ at the same RH conditions, which is attributed to the relatively high hydrophilicity and the strong water vapor absorption of the PF material (Movie S5 and Figure S22). The results clearly indicate that the thermal conductivity of the obtained LigSi-3 is very stable in a humid environment.

Low Near-Infrared Absorption. The solar radiation that reaches the Earth's surface consists of a wide range of wavelengths including ultraviolet (100–400 nm, 5%), visible light (400–780 nm, 46%), and infrared (IR, >780 nm, 49%).⁶⁷ IR radiation in the region of 780–2500 nm is classified as near-infrared (NIR) radiation and is the main portion of solar energy that heats the Earth's surface.⁸ It has been demonstrated that the development of thermal insulating materials with high NIR reflectance can minimize the heat gain from sunlight.¹⁹

A UV–vis–NIR test of a 7 mm-thick sample was carried out to evaluate the reflectance of the solar irradiation spectrum (Figure S23). The LigSi-3 exhibited an average of ~91% reflectance in the NIR spectrum (Figure 5g). The absorptivity of NIR radiation of the LigSi-3 in the solar spectrum was calculated to be ~9%, which is even lower than a previous report on the NIR absorption of NW.^{8,19} Wood is a widely used building material in wall panels and roofs that are typically exposed to direct solar irradiation. In contrast, natural pine wood (*Pseudotsuga menziesii* (Mirb.) Franco) absorbed averages of ~25% of the NIR in the solar irradiation spectrum (Figure 5g), which is much higher than that of LigSi-3. The results clearly indicate that the LigSi has an excellent ability to effectively reflect the thermal energy from the solar radiation (Newport Standard Solar Simulator).

The LigSi exhibited a high omnidirectional NIR reflectance and exceptional ultraviolet absorption attributed to the cooperative effect of multilevel micro-nanostructures and hybrid chemical composition of lignin/silica (Figure 5h).^{19,68} The porous structure with a wide size distribution of the LigSi aerogel enhanced the reflectance of the solar spectrum due to strong Mie scattering.⁶⁹ Generally, the microstructures are decorated with nanobumps with a typical feature size of ~200 nm and nanopores with a size of ~50 nm (Figure 5i and Figure 2e), which can effectively scatter solar light for improved solar

reflection.⁷⁰ In addition, the Si–O molecular structure of the LigSi allows for a small amount of absorption in the solar spectra,⁶⁰ thereby avoiding extra heat gain. Moreover, lignin is often used as a UV absorber to endow polymer materials with good weather resistance originating from its abundant phenolic structure. In order to further verify that the prepared material has a low photothermal conversion. A light source with a spot size of 5 mm (input power 0.55 W mm⁻²) generated by the 1350–1600 nm filter was incident perpendicular to the surface of the LigSi-3 and natural pine wood samples for 60 s (Figure 5j), respectively. As shown in Figure 5k, the maximum temperature on the surface of LigSi-3 was 25.3 °C, which is lower than the 27.1 °C of the natural pine wood (Figure S1), due to the lower NIR absorption of LigSi-3. The NIR reflection of the proposed material can reduce the buildup of heat in living spaces, thereby reducing the energy consumption load of air-conditioning systems.

Dual-Mode Thermal Device Applied in Cold Environments. In addition to passive heat-trapping, active heating is also necessary for modern energy-efficient building materials, especially in harsh cold environments. As shown in Figure 6a, a dual-mode thermal device was obtained by depositing a thin conductive carbon black/polyvinylpyrrolidone (CB/PVP) layer on one side of LigSi-3 using a spray-drying method (Figure S24). As a result, dual electrical-thermal (E-T) and thermal-insulation (T-I) functions were integrated into one material. From the cross-sectional SEM image of the device (Figure 6b), it was found that a CB/PVP layer with a thickness of ~6 μm was deposited on the LigSi-3 surface. Given the excellent Joule heating performance of carbon-based materials,^{13,71} the E-T and T-I behaviors of the thermal device were further investigated. As illustrated in Figure 6c, the dynamic temperature variations of the E-T and T-I surfaces were recorded and plotted by a temperature detection system. The IR imaging results revealed that the temperature of the E-T surface increased rapidly when it was used and worked at low voltages (Figure 6d and Movie S6). The temperature of the E-T surface of the device (thickness, 5 mm) increased quickly to 38 °C as a heating voltage of 6 V was applied, whereas the T-I surface maintained a temperature close to room temperature (~25 °C) with an absolute temperature difference (ΔT) of 13 °C (Figure S25). As shown in Figure 6e, the temperatures of both E-T and T-I surfaces can be precisely controlled by applying a set voltage. Figure 6f shows that a vast ΔT from 10 to 130 °C was achieved at a low-level working voltage within the safety limits (20 V). This significant ΔT value is much higher than those of previously reported aerogels,^{13,72} because the LigSi-3 has excellent thermal insulation and ultralow thermal diffusivity to delay heat flow propagation.

The potential use of the dual-mode LigSi-3 thermal device as a multifunctional energy-efficient building material is promising for the improvement of the comfort of living spaces, even in extreme weather (Figure 6g). As a proof of concept, the LigSi-3 was used for the roofing, siding, and floor insulation materials of a building model (Figure S26), and the thermal performance of the dual-mode LigSi-3 was demonstrated over 5-h continuous thermal measurements (Figure 6h). The building model was placed in a low environmental temperature (ET) of about 4 °C. When a 10-V working voltage was applied, the floor temperature (P1) and space temperature (P2, P3) increased to ~41 °C and ~16 °C, respectively, within 25 min. However, the surface temperature (P4) of the exterior siding increased only to ~9 °C. The indoor temperature remained

nearly constant until the working voltage was turned off (Figure 6h). The temperature distribution is also exhibited in the thermal IR imaging results (Figure 6i and Figure S27). As a result, the final indoor temperature after the process of E-T and T-I was found to meet the human body's demand for a comfortable environmental temperature (18–25 °C). The dual-mode thermal device exhibits favorable properties required for a biobased thermal insulating aerogel material that combines thermal management, outstanding mechanical properties, fireproofing, water resistance, and low photo-thermal conversion.

CONCLUSIONS

In summary, based on bioinspired ethylene glycol-stabilized lignin/siloxane colloid, plant polyphenol nanocomposite aerogels (LigSi) with tunable multilevel micro/nanostructures and arbitrary machinability were rationally designed and fabricated by a unusual strategy of water-induced self-assembly and *in situ* mineralization. The LigSi obtained after drying and annealing exhibits an ultrahigh specific compression modulus (376.32 kN m kg⁻¹) and specific compression strength (75.79 kN m kg⁻¹), which was attributed to the synergistic effects of hydrophobic self-assembly and *in situ* mineralization leading to the strong thick-necked micro/nanostructures. Additionally, the aerogel displays a combination of outstanding properties, including superior and durable thermal insulation under wide RH range from 33% to 94%, excellent fire resistance withstanding a ~1200 °C flame without disintegration, ultralow NIR absorption (~9%), and intrinsic self-cleaning/superhydrophobic performance (~158° WCA). The low and humidity-tolerant thermal conductivity is benefited from the multilevel nanoporous structure and intrinsic superhydrophobicity. The excellent fire resistance are attributed to the self-formed dual char/SiO₂ barriers. The cooperation of the multiscale micronanostructure and superimposed chemical nature of lignin/silica enables the material with excellent optical and self-cleaning performance. These integrated multifunctionality ensure the nanocomposite aerogel as a promising biobased thermal insulation material for safe and reliable applications in extreme environments. As a proof of concept, a dual-mode thermal device based on LigSi was designed to generate supplemental heating for the interiors of the building model in cold environments. Design and fabrication of LigSi provide substantial motivation for the development of other high-performance lignin-based nanocomposite aerogels (such as lignin/TiO₂ and lignin/Fe₃O₄, etc.) for application in the field of seawater evaporators, catalytic degradation, and energy storage.

EXPERIMENTAL SECTION

Preparation of the Silica-Mineralized Lignin Nanocomposite Aerogel (LigSi). The synthesis process is shown in Figure 1b. In detail, 2 g of EHL was dissolved in ethylene glycol (EG, 26.2 mL) to form a 6.5 wt % EHL solution. Then, 17 mmol of EGDE was added to the solution and stirred at 80 °C for 1 h to form cross-linked lignin under catalysis by triethylamine (2 mmol). Then, a small amount of water (2.4 mL) was added to the EG solution of EHL. To reach an equilibrium distribution of H₂O, the solution was allowed to stir at 25 °C for 1 h. Afterward, 55 mmol of MTES and 11.5 mmol of AEAPTES were introduced. The solution was stirred for 20 min to promote siloxane hydrolysis and dissolution in the solution. Then, a homogeneous sol was transferred to a polystyrene container, and the sealed container was stored at room temperature for 1 day to complete the co-gel process. The gel was taken out and immersed in

deionized water for 24 h at ambient temperature to simultaneously complete the process of the solvent exchange, hydrophobic self-assembly, and mineralization. The resulting silica-mineralized lignin gel was dried for 48 h in a freeze-dryer (−55 °C, 1 Pa). Finally, the lyophilized product was annealed at 180 °C for 12 h to convert into the desired mineralized lignin aerogel, and the product was named LigSi-3 aerogel. Additional samples were prepared by varying the MTES and AEAPTES concentrations. The concentration of the precursor (a mixture of lignin, MTES, EGDE, and AEAPTES), denoted by the ratio of the precursor's weight to the sol's weight, remained constant. The as-prepared silica-mineralized lignin aerogels were named LigSi-*x* (*x* = 1, 2, 3, 4, where *n* represents the amount trend of silane used, including MTES and AEAPTES). The specific formula is summarized in Table S1.

Morphology Characterization. SEM was performed with a field emission scanning electron microanalyzer (FE-SEM Hitachi S4800) at an accelerating voltage of 10 kV and a working distance of 5 mm. All samples were affixed on a sample holder using a carbon pad, followed by coating with ~10 nm of platinum. Laser scanning images of 1–2 mm thick aerogel samples mounted on SEM stubs were taken with a Keyence confocal laser scanning microscope VK-x100 at 5, 10, and 20-times magnifications, while the surface and depth profiles of the samples were measured via Keyence MultiFile Analyzer software. TEM and EDS elemental mappings were performed on an FEI Talos F200. The samples were ground and dispersed in ethanol. The solution was then dropped onto a thin carbon film (~3 nm) on a Cu TEM grid. The samples were treated with O₂/Ar₂ plasma for 1 min before TEM characterization. The high-resolution TEM (HRTEM) and energy-filtered TEM (EF-TEM) images were recorded with a JEOL-2200FS microscope operated at an accelerating voltage of 200 kV. The internal morphology of the composite aerogel was studied by a 3D X-ray micro-CT (Bruker microCT SkyScan 1272, spatial resolution, 500 nm). The phase distributions inside the composite aerogels were visualized at the subpixel scale.

More detailed experimental materials and methods are presented in the Supporting Information.

ASSOCIATED CONTENT

Supporting Information

The Supporting Information is available free of charge at <https://pubs.acs.org/doi/10.1021/acsnano.2c00755>.

Experimental procedure detailing the raw materials, preparation of thermal device, calculations, characterizations; Figures S1–S27, preparation process of LigSi, molecular dynamics simulations of the dissolution behavior, digital photos of solubilities comparison, NCI analysis, TGA curves, mechanically subtractive process, reconstructed 3D micro-CT images, HRTEM, XRD curves, nitrogen adsorption–desorption isotherms, mercury porosimetry testing curves, pore size distributions, FTIR, ²⁹Si NMR, ¹³C NMR, XPS curves, the fire test of control samples under a propane/butane blowtorch, smoke release rate (SRR) curves, total heat release (THR) curves, alcohol lamp flame test of LigSi-3, contour images of WCA profile of LigSi, laser optical surface profilometry and depth profile of LigSi, IR images and TST-time curves of samples on a 50 °C platform, thermal conductivity (λ) and thermal diffusivity (κ) of LigSi, comparison of thermal conductivity, reflectance measurement setup and reflectance curves of LigSi, temperature profiles of E-T and T-I surface at a voltage of 6 V, measurement setup of the spatial temperature distribution of energy-saving building model; Tables S1–S4, formulas of LigSi and their density, specific surface area (S_{BET}), pore volume (V_{pore}), average pores diameter, mechanical strength

values, and comparison of specific Young's modulus versus specific ultimate strength (PDF)

Movie S1, fire retardancy of the LigSi-3 under a propane/butane blowtorch flame (MP4)

Movie S2, water contact angle test of the LigSi-3 (MP4)

Movie S3, water droplets impact the LigSi-3 surface (MP4)

Movie S4, artificial rain test for the LigSi-3 (MP4)

Movie S5, comparative test of water repellency (MP4)

Movie S6, performance of E-T and T-I of dual-mode thermal devices under a 6 V voltage (MP4)

AUTHOR INFORMATION

Corresponding Authors

Rongxian Ou – Institute of Biomass Engineering and Key Laboratory for Biobased Materials and Energy of Ministry of Education, College of Materials and Energy, South China Agricultural University, Guangzhou 510642, China; Guangdong Provincial Laboratory of Lingnan Modern Agricultural Science and Technology, Guangzhou 510642, China; orcid.org/0000-0002-1675-8866; Email: rongxian_ou@scau.edu.cn

Qingwen Wang – Institute of Biomass Engineering and Key Laboratory for Biobased Materials and Energy of Ministry of Education, College of Materials and Energy, South China Agricultural University, Guangzhou 510642, China; Guangdong Provincial Laboratory of Lingnan Modern Agricultural Science and Technology, Guangzhou 510642, China; orcid.org/0000-0001-5988-9922; Email: qwwang@scau.edu.cn

Authors

Qi Fan – Institute of Biomass Engineering and Key Laboratory for Biobased Materials and Energy of Ministry of Education, College of Materials and Energy, South China Agricultural University, Guangzhou 510642, China; Guangdong Provincial Laboratory of Lingnan Modern Agricultural Science and Technology, Guangzhou 510642, China

Xiaolong Hao – Institute of Biomass Engineering and Key Laboratory for Biobased Materials and Energy of Ministry of Education, College of Materials and Energy, South China Agricultural University, Guangzhou 510642, China; Guangdong Provincial Laboratory of Lingnan Modern Agricultural Science and Technology, Guangzhou 510642, China

Qianyun Deng – Key Laboratory for Biobased Materials and Energy of Ministry of Education, College of Materials and Energy, South China Agricultural University, Guangzhou 510642, China

Zhenzhen Liu – Institute of Biomass Engineering and Key Laboratory for Biobased Materials and Energy of Ministry of Education, College of Materials and Energy, South China Agricultural University, Guangzhou 510642, China; Guangdong Provincial Laboratory of Lingnan Modern Agricultural Science and Technology, Guangzhou 510642, China; orcid.org/0000-0002-8651-1682

Lichao Sun – Key Laboratory for Biobased Materials and Energy of Ministry of Education, College of Materials and Energy, South China Agricultural University, Guangzhou 510642, China; Guangdong Provincial Laboratory of Lingnan Modern Agricultural Science and Technology, Guangzhou 510642, China

Chaoqun Zhang – Key Laboratory for Biobased Materials and Energy of Ministry of Education, College of Materials and Energy, South China Agricultural University, Guangzhou 510642, China; Guangdong Provincial Laboratory of Lingnan Modern Agricultural Science and Technology, Guangzhou 510642, China; orcid.org/0000-0001-5754-8729

Chuigen Guo – Institute of Biomass Engineering and Key Laboratory for Biobased Materials and Energy of Ministry of Education, College of Materials and Energy, South China Agricultural University, Guangzhou 510642, China; Guangdong Provincial Laboratory of Lingnan Modern Agricultural Science and Technology, Guangzhou 510642, China; orcid.org/0000-0002-8387-3012

Xiaojing Bai – School of Materials Science and Engineering, Anyang Institute of Technology, Anyang 455000, China

Complete contact information is available at:

<https://pubs.acs.org/10.1021/acsnano.2c00755>

Author Contributions

Q.W. conceived the concept of the study. Q.F., R.O., and Q.W. designed the experiments. Q.F. performed all the experiments. All the authors analyzed the data. Q.F. and R.O. mainly wrote the manuscript with contributions from all the authors. All authors have given approval to the final version of the manuscript.

Notes

The authors declare no competing financial interest.

ACKNOWLEDGMENTS

This work was financially supported by the Research and Development Program in Key Areas of Guangdong Province (Grant No. 2020B0202010008), the National Key R & D Program of China (Grant Nos. 2019YFD1101203 and 2018YFE0107100), the National Natural Science Foundation of China (Grant Nos. 32071698 and 31870547), the Project of Guangzhou Municipal Key Laboratory of Woody Biomass Functional New Materials (Grant No. 201905010005), and the Project of Key Disciplines of Forestry Engineering of Bureau of Education of Guangzhou Municipality.

REFERENCES

- (1) Fernández, J. E. Materials for Aesthetic, Energy-Efficient, and Self-Diagnostic Buildings. *Science* **2007**, *315* (5820), 1807–1810.
- (2) Apostolopoulou-Kalkavoura, V.; Munier, P.; Bergstrom, L. Thermally Insulating Nanocellulose-Based Materials. *Adv. Mater.* **2021**, *33*, No. 2001839.
- (3) Jelle, B. P. Traditional, state-of-the-art and future thermal building insulation materials and solutions—Properties, requirements and possibilities. *Energy Buildings* **2011**, *43* (10), 2549–2563.
- (4) Jiang, S.; Agarwal, S.; Greiner, A. Low-Density Open Cellular Sponges as Functional Materials. *Angew. Chem., Int. Ed.* **2017**, *56* (49), 15520–15538.
- (5) Sakuma, W.; Yamasaki, S.; Fujisawa, S.; Kodama, T.; Shiomi, J.; Kanamori, K.; Saito, T. Mechanically Strong, Scalable, Mesoporous Xerogels of Nanocellulose Featuring Light Permeability, Thermal Insulation, and Flame Self-Extinction. *ACS Nano* **2021**, *15* (1), 1436–1444.
- (6) Liu, C.; Luan, P. C.; Li, Q.; Cheng, Z.; Xiang, P. Y.; Liu, D. T.; Hou, Y.; Yang, Y.; Zhu, H. L. Biopolymers Derived from Trees as Sustainable Multifunctional Materials: A Review. *Adv. Mater.* **2021**, *33*, No. 2001654.
- (7) Smalyukh, I. I. Thermal Management by Engineering the Alignment of Nanocellulose. *Adv. Mater.* **2021**, *33*, No. 2001228.















- (8) Li, T.; Zhai, Y.; He, S.; Gan, W.; Wei, Z.; Heidarinejad, M.; Dalgo, D.; Mi, R.; Zhao, X.; Song, J.; Dai, J.; Chen, C.; Aili, A.; Vellore, A.; Martini, A.; Yang, R.; Srebric, J.; Yin, X.; Hu, L. A radiative cooling structural material. *Science* **2019**, *364* (6442), 760–763.
- (9) Zhao, S.; Malfait, W. J.; Guerrero-Alburquerque, N.; Koebel, M. M.; Nystrom, G. Biopolymer Aerogels and Foams: Chemistry, Properties, and Applications. *Angew. Chem., Int. Ed.* **2018**, *57* (26), 7580–7608.
- (10) He, S.; Chen, C.; Li, T.; Song, J.; Zhao, X.; Kuang, Y.; Liu, Y.; Pei, Y.; Hitz, E.; Kong, W.; Gan, W.; Yang, B.; Yang, R.; Hu, L. An Energy-Efficient, Wood-Derived Structural Material Enabled by Pore Structure Engineering towards Building Efficiency. *Small Methods* **2020**, *4* (1), 1900747.
- (11) Shchipunov, Y.; Postnova, I. Cellulose Mineralization as a Route for Novel Functional Materials. *Adv. Funct. Mater.* **2018**, *28* (27), 1705042.
- (12) Zhang, X.; Wu, B.; Sun, S.; Wu, P. Hybrid Materials from Ultrahigh-Inorganic-Content Mineral Plastic Hydrogels: Arbitrarily Shapeable, Strong, and Tough. *Adv. Funct. Mater.* **2020**, *30* (19), 1910425.
- (13) Zhang, J.; Cheng, Y.; Tebyetekerwa, M.; Meng, S.; Zhu, M.; Lu, Y. Stiff–Soft Binary Synergistic Aerogels with Superflexibility and High Thermal Insulation Performance. *Adv. Funct. Mater.* **2019**, *29* (15), 1806407.
- (14) Zhang, Z.; Sèbe, G.; Rentsch, D.; Zimmermann, T.; Tingaut, P. Ultralightweight and Flexible Silylated Nanocellulose Sponges for the Selective Removal of Oil from Water. *Chem. Mater.* **2014**, *26* (8), 2659–2668.
- (15) Cai, J.; Liu, S.; Feng, J.; Kimura, S.; Wada, M.; Kuga, S.; Zhang, L. Cellulose-Silica Nanocomposite Aerogels by In Situ Formation of Silica in Cellulose Gel. *Angew. Chem., Int. Ed.* **2012**, *51* (9), 2076–2079.
- (16) Zhao, S.; Zhang, Z.; Sèbe, G.; Wu, R.; Rivera Virtudazo, R. V.; Tingaut, P.; Koebel, M. M. Multiscale Assembly of Superinsulating Silica Aerogels Within Silylated Nanocellulosic Scaffolds: Improved Mechanical Properties Promoted by Nanoscale Chemical Compatibility. *Adv. Funct. Mater.* **2015**, *25* (15), 2326–2334.
- (17) Zhao, S.; Malfait, W. J.; Demilecamps, A.; Zhang, Y.; Brunner, S.; Huber, L.; Tingaut, P.; Rigacci, A.; Budtova, T.; Koebel, M. M. Strong, Thermally Superinsulating Biopolymer-Silica Aerogel Hybrids by Cogelation of Silicic Acid with Pectin. *Angew. Chem., Int. Ed.* **2015**, *54* (48), 14282–6.
- (18) Zhu, J.; Xiong, R.; Zhao, F.; Peng, T.; Hu, J.; Xie, L.; Xie, H.; Wang, K.; Jiang, C. Lightweight, High-Strength, and Anisotropic Structure Composite Aerogel Based on Hydroxyapatite Nanocrystal and Chitosan with Thermal Insulation and Flame Retardant Properties. *ACS Sustainable Chem. Eng.* **2020**, *8* (1), 71–83.
- (19) Li, T.; Song, J.; Zhao, X.; Yang, Z.; Pastel, G.; Xu, S.; Jia, C.; Dai, J.; Chen, C.; Gong, A.; Jiang, F.; Yao, Y.; Fan, T.; Yang, B.; Wagberg, L.; Yang, R.; Hu, L. Anisotropic, lightweight, strong, and super thermally insulating nanowood with naturally aligned nanocellulose. *Sci. Adv.* **2018**, *4* (3), No. aar3724.
- (20) Lavoine, N.; Bergström, L. Nanocellulose-based foams and aerogels: processing, properties, and applications. *J. Mater. Chem. A* **2017**, *5* (31), 16105–16117.
- (21) Pirzada, T.; Ashrafi, Z.; Xie, W.; Khan, S. A. Cellulose Silica Hybrid Nanofiber Aerogels: From Sol–Gel Electrospun Nanofibers to Multifunctional Aerogels. *Adv. Funct. Mater.* **2020**, *30* (5), 1907359.
- (22) Zhang, J.; Cheng, Y.; Xu, C.; Gao, M.; Zhu, M.; Jiang, L. Hierarchical Interface Engineering for Advanced Nanocellulosic Hybrid Aerogels with High Compressibility and Multifunctionality. *Adv. Funct. Mater.* **2021**, *31* (19), 2009349.
- (23) Farooq, M.; Sipponen, M. H.; Seppälä, A.; Österberg, M. Eco-friendly Flame-Retardant Cellulose Nanofibril Aerogels by Incorporating Sodium Bicarbonate. *ACS Appl. Mater. Interfaces* **2018**, *10* (32), 27407–27415.
- (24) Wicklein, B.; Kocjan, A.; Salazar-Alvarez, G.; Carosio, F.; Camino, G.; Antonietti, M.; Bergström, L. Thermally insulating and fire-retardant lightweight anisotropic foams based on nanocellulose and graphene oxide. *Nat. Nanotechnol.* **2015**, *10* (3), 277–83.
- (25) Ragauskas, A. J.; Beckham, G. T.; Biddy, M. J.; Chandra, R.; Chen, F.; Davis, M. F.; Davison, B. H.; Dixon, R. A.; Gilna, P.; Keller, M.; Langan, P.; Naskar, A. K.; Saddler, J. N.; Tschaplinski, T. J.; Tuskan, G. A.; Wyman, C. E. Lignin valorization: improving lignin processing in the biorefinery. *Science* **2014**, *344* (6185), 1246843.
- (26) Yang, Y.; Deng, Y.; Tong, Z.; Wang, C. Renewable Lignin-Based Xerogels with Self-Cleaning Properties and Superhydrophobicity. *ACS Sustainable Chem. Eng.* **2014**, *2* (7), 1729–1733.
- (27) Wang, J.; Zhang, D.; Chu, F. Wood-Derived Functional Polymeric Materials. *Adv. Mater.* **2021**, *33*, No. 2001135.
- (28) Jiang, B.; Yao, Y.; Liang, Z.; Gao, J.; Chen, G.; Xia, Q.; Mi, R.; Jiao, M.; Wang, X.; Hu, L. Lignin-Based Direct Ink Printed Structural Scaffolds. *Small* **2020**, *16* (31), No. 1907212.
- (29) Jiang, B.; Chen, C.; Liang, Z.; He, S.; Kuang, Y.; Song, J.; Mi, R.; Chen, G.; Jiao, M.; Hu, L. Lignin as a Wood-Inspired Binder Enabled Strong, Water Stable, and Biodegradable Paper for Plastic Replacement. *Adv. Funct. Mater.* **2020**, *30* (4), 1906307.
- (30) Zhao, B.; Borghei, M.; Zou, T.; Wang, L.; Johansson, L.-S.; Majoinen, J.; Sipponen, M. H.; Österberg, M.; Mattos, B. D.; Rojas, O. J. Lignin-Based Porous Supraparticles for Carbon Capture. *ACS Nano* **2021**, *15* (4), 6774–6786.
- (31) Zou, T.; Sipponen, M. H.; Henn, A.; Österberg, M. Solvent-Resistant Lignin-Epoxy Hybrid Nanoparticles for Covalent Surface Modification and High-Strength Particulate Adhesives. *ACS Nano* **2021**, *15* (3), 4811–4823.
- (32) Österberg, M.; Sipponen, M. H.; Mattos, B. D.; Rojas, O. J. Spherical lignin particles: a review on their sustainability and applications. *Green Chem.* **2020**, *22* (9), 2712–2733.
- (33) You, X.; Wang, X.; Zhang, H. J.; Cui, K.; Zhang, A.; Wang, L.; Yadav, C.; Li, X. Supertough Lignin Hydrogels with Multienergy Dissipative Structures and Ultrahigh Antioxidative Activities. *ACS Appl. Mater. Interfaces* **2020**, *12* (35), 39892–39901.
- (34) Zhang, X.; Liu, W.; Yang, D.; Qiu, X. Biomimetic Supertough and Strong Biodegradable Polymeric Materials with Improved Thermal Properties and Excellent UV-Blocking Performance. *Adv. Funct. Mater.* **2019**, *29* (4), 1806912.
- (35) Laine, R. M.; Blohowiak, K. Y.; Robinson, T. R.; Hoppe, M. L.; Nardi, P.; Kampf, J.; Uhm, J. Synthesis of pentacoordinate silicon complexes from SiO₂. *Nature* **1991**, *353* (6345), 642–644.
- (36) Brovko, O.; Palamarchuk, I.; Bogdanovich, N.; Ivakhnov, A.; Chukhchin, D.; Belousova, M.; Arkhilin, M.; Gorshkova, N. Composite aerogel materials based on lignosulfonates and silica: Synthesis, structure, properties. *Mater. Chem. Phys.* **2021**, *269*, 124768.
- (37) Perez-Cantu, L.; Liebner, F.; Smirnova, I. Preparation of aerogels from wheat straw lignin by cross-linking with oligo(alkylene glycol)- α,ω -diglycidyl ethers. *Micropor. Mesopor. Mater.* **2014**, *195*, 303–310.
- (38) Zeng, Z.; Ma, X. Y. D.; Zhang, Y.; Wang, Z.; Ng, B. F.; Wan, M. P.; Lu, X. Robust Lignin-Based Aerogel Filters: High-Efficiency Capture of Ultrafine Airborne Particulates and the Mechanism. *ACS Sustainable Chem. Eng.* **2019**, *7* (7), 6959–6968.
- (39) Fan, Q.; Liu, T.; Zhang, C.; Liu, Z.; Zheng, W.; Ou, R.; Wang, Q. Extraordinary solution-processability of lignin in phenol–maleic anhydride and dielectric films with controllable properties. *J. Mater. Chem. A* **2019**, *7* (40), 23162–23172.
- (40) Xiong, W.; Qiu, X.; Yang, D.; Zhong, R.; Qian, Y.; Li, Y.; Wang, H. A simple one-pot method to prepare UV-absorbent lignin/silica hybrids based on alkali lignin from pulping black liquor and sodium metasilicate. *Chem. Eng. J.* **2017**, *326*, 803–810.
- (41) Fang, J.-y.; Ma, X.-l. In vitro simulation studies of silica deposition induced by lignin from rice. *J. Zhejiang Univ.-SC. B* **2006**, *7* (4), 267–271.
- (42) Sumper, M.; Brunner, E. Learning from Diatoms: Nature's Tools for the Production of Nanostructured Silica. *Adv. Funct. Mater.* **2006**, *16* (1), 17–26.

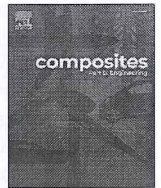
- (43) Wallace, A. K.; Chanut, N.; Voigt, C. A. Silica Nanostructures Produced Using Diatom Peptides with Designed Post-Translational Modifications. *Adv. Funct. Mater.* **2020**, *30* (30), 2000849.
- (44) Spinde, K.; Pachis, K.; Antonakaki, I.; Paasch, S.; Brunner, E.; Demadis, K. D. Influence of Polyamines and Related Macromolecules on Silicic Acid Polycondensation: Relevance to "Soluble Silicon Pools"? *Chem. Mater.* **2011**, *23* (21), 4676–4687.
- (45) Demadis, K. D.; Stathouloupoulou, A. Solubility Enhancement of Silicate with Polyamine/Polyammonium Cationic Macromolecules: Relevance to Silica-Laden Process Waters. *Ind. Eng. Chem. Res.* **2006**, *45* (12), 4436–4440.
- (46) Demadis, K. D.; Brückner, S. I.; Brunner, E.; Paasch, S.; Antonakaki, I.; Casolaro, M. The Intimate Role of Imidazole in the Stabilization of Silicic Acid by a pH-Responsive, Histidine-Grafted Polyampholyte. *Chem. Mater.* **2015**, *27* (19), 6827–6836.
- (47) Preari, M.; Spinde, K.; Lazic, J.; Brunner, E.; Demadis, K. D. Bioinspired Insights into Silicic Acid Stabilization Mechanisms: The Dominant Role of Polyethylene Glycol-Induced Hydrogen Bonding. *J. Am. Chem. Soc.* **2014**, *136* (11), 4236–4244.
- (48) Linhares, T.; Pessoa de Amorim, M. T.; Durães, L. Silica aerogel composites with embedded fibres: a review on their preparation, properties and applications. *J. Mater. Chem. A* **2019**, *7* (40), 22768–22802.
- (49) Sun, J.; Dutta, T.; Parthasarathi, R.; Kim, K. H.; Tolic, N.; Chu, R. K.; Isern, N. G.; Cort, J. R.; Simmons, B. A.; Singh, S. Rapid room temperature solubilization and depolymerization of polymeric lignin at high loadings. *Green Chem.* **2016**, *18* (22), 6012–6020.
- (50) Zhao, S.; Malfait, W. J.; Jeong, E.; Fischer, B.; Zhang, Y.; Xu, H.; Angelica, E.; Risen, W. M.; Suggs, J. W.; Koebel, M. M. Facile One-Pot Synthesis of Mechanically Robust Biopolymer-Silica Nanocomposite Aerogel by Cogelation of Silicic Acid with Chitosan in Aqueous Media. *ACS Sustainable Chem. Eng.* **2016**, *4* (10), 5674–5683.
- (51) Yu, Z. L.; Yang, N.; Apostolopoulou-Kalkavoura, V.; Qin, B.; Ma, Z. Y.; Xing, W. Y.; Qiao, C.; Bergstrom, L.; Antonietti, M.; Yu, S. H. Fire-Retardant and Thermally Insulating Phenolic-Silica Aerogels. *Angew. Chem., Int. Ed.* **2018**, *57* (17), 4538–4542.
- (52) Su, L.; Wang, H.; Niu, M.; Dai, S.; Cai, Z.; Yang, B.; Huan, H.; Pan, X. Anisotropic and hierarchical SiC@SiO₂ nanowire aerogel with exceptional stiffness and stability for thermal superinsulation. *Sci. Adv.* **2020**, *6* (26), No. eaay6689.
- (53) Yun, S.; Luo, H.; Gao, Y. Ambient-pressure drying synthesis of large resorcinol–formaldehyde-reinforced silica aerogels with enhanced mechanical strength and superhydrophobicity. *J. Mater. Chem. A* **2014**, *2* (35), 14542.
- (54) Hu, Y.; Chen, Z.; Zhuo, H.; Zhong, L.; Peng, X.; Sun, R. C. Advanced Compressible and Elastic 3D Monoliths beyond Hydrogels. *Adv. Funct. Mater.* **2019**, *29* (44), 1904472.
- (55) Li, C.; Zhao, X.; Wang, A.; Huber, G. W.; Zhang, T. Catalytic Transformation of Lignin for the Production of Chemicals and Fuels. *Chem. Rev.* **2015**, *115* (21), 11559–624.
- (56) Lu, Y.; Sathasivam, S.; Song, J.; Crick, C. R.; Carmalt, C. J.; Parkin, I. P. Robust self-cleaning surfaces that function when exposed to either air or oil. *Science* **2015**, *347* (6226), 1132–5.
- (57) Song, J.; Chen, C.; Yang, Z.; Kuang, Y.; Li, T.; Li, Y.; Huang, H.; Kierzewski, I.; Liu, B.; He, S.; Gao, T.; Yurker, S. U.; Gong, A.; Yang, B.; Hu, L. Highly Compressible, Anisotropic Aerogel with Aligned Cellulose Nanofibers. *ACS Nano* **2018**, *12* (1), 140–147.
- (58) Lu, X.; Arduini-Schuster, M.; Kuhn, J.; Nilsson, O.; Fricke, J.; Pekala, R. W. Thermal Conductivity of Monolithic Organic Aerogels. *Science* **1992**, *255* (5047), 971–972.
- (59) Glucksman, L. R. *Low Density Cellular Plastics*. Springer: Dordrecht, 1994.
- (60) Jaramillo-Fernandez, J.; Whitworth, G. L.; Pariente, J. A.; Blanco, A.; Garcia, P. D.; Lopez, C.; Sotomayor-Torres, C. M. A Self-Assembled 2D Thermofunctional Material for Radiative Cooling. *Small* **2019**, *15* (52), No. 1905290.
- (61) Hu, Z.; Yan, S.; Li, X.; You, R.; Zhang, Q.; Kaplan, D. L. Natural Silk Nanofibril Aerogels with Distinctive Filtration Capacity and Heat-Retention Performance. *ACS Nano* **2021**, *15* (5), 8171–8183.
- (62) Du, A.; Wang, H.; Zhou, B.; Zhang, C.; Wu, X.; Ge, Y.; Niu, T.; Ji, X.; Zhang, T.; Zhang, Z.; Wu, G.; Shen, J. Multifunctional Silica Nanotube Aerogels Inspired by Polar Bear Hair for Light Management and Thermal Insulation. *Chem. Mater.* **2018**, *30* (19), 6849–6857.
- (63) Williams, J. C.; Nguyen, B. N.; McCorkle, L.; Scheiman, D.; Griffin, J. S.; Steiner, S. A., 3rd; Meador, M. A. Highly Porous, Rigid-Rod Polyamide Aerogels with Superior Mechanical Properties and Unusually High Thermal Conductivity. *ACS Appl. Mater. Interfaces* **2017**, *9* (2), 1801–1809.
- (64) Takeshita, S.; Yoda, S. Chitosan Aerogels: Transparent, Flexible Thermal Insulators. *Chem. Mater.* **2015**, *27* (22), 7569–7572.
- (65) Prociak, A.; Pielichowski, J.; Sterzyński, T. Thermal diffusivity of polyurethane foams measured by the modified ångström method. *Polym. Eng. Sci.* **1999**, *39* (9), 1689–1695.
- (66) Nutz, F. A.; Philipp, A.; Kopera, B. A. F.; Dulle, M.; Retsch, M. Low Thermal Conductivity through Dense Particle Packings with Optimum Disorder. *Adv. Mater.* **2018**, *30* (14), No. 1704910.
- (67) Pakdel, E.; Naebe, M.; Sun, L.; Wang, X. Advanced Functional Fibrous Materials for Enhanced Thermoregulating Performance. *ACS Appl. Mater. Interfaces* **2019**, *11* (14), 13039–13057.
- (68) Wang, X.; Liu, X.; Li, Z.; Zhang, H.; Yang, Z.; Zhou, H.; Fan, T. Scalable Flexible Hybrid Membranes with Photonic Structures for Daytime Radiative Cooling. *Adv. Funct. Mater.* **2020**, *30* (5), 1907562.
- (69) Mandal, J.; Fu, Y.; Overvig, A. C.; Jia, M.; Sun, K.; Shi, N. N.; Zhou, H.; Xiao, X.; Yu, N.; Yang, Y. Hierarchically porous polymer coatings for highly efficient passive daytime radiative cooling. *Science* **2018**, *362* (6412), 315–319.
- (70) Zhong, H.; Li, Y.; Zhang, P.; Gao, S.; Liu, B.; Wang, Y.; Meng, T.; Zhou, Y.; Hou, H.; Xue, C.; Zhao, Y.; Wang, Z. Hierarchically Hollow Microfibers as a Scalable and Effective Thermal Insulating Cooler for Buildings. *ACS Nano* **2021**, *15* (6), 10076–10083.
- (71) Ge, J.; Shi, L. A.; Wang, Y. C.; Zhao, H. Y.; Yao, H. B.; Zhu, Y. B.; Zhang, Y.; Zhu, H. W.; Wu, H. A.; Yu, S. H. Joule-heated graphene-wrapped sponge enables fast clean-up of viscous crude-oil spill. *Nat. Nanotechnol.* **2017**, *12* (5), 434–440.
- (72) Cui, Y.; Gong, H.; Wang, Y.; Li, D.; Bai, H. A Thermally Insulating Textile Inspired by Polar Bear Hair. *Adv. Mater.* **2018**, *30* (14), No. 1706807.



composites

Part B: Engineering

Publish 	Order journal 	Search in this journal 	Guide for authors
	<input type="checkbox"/> Research article  Full text access	<p>Biomimetic dually cross-linked injectable poly(L-glutamic acid) based nanofiber composite hydrogels with self-healing, osteogenic and angiogenic properties for bone regeneration</p> <p>Bo Wang, Jia Liu, Chao Guo, Xiaogang Bao, ... Shifeng Yan Article 111492</p> <p> View PDF Article preview </p>	
	<input type="checkbox"/> Research article  Full text access	<p>Biomimetic versatile wood hybrids with gradient structure towards lightweight, high strength, fire-retardant, and deterioration-resistant materials</p> <p>Qi Fan, Xing Zhang, Chuanfu Chen, Xiaolong Hao, ... Qingwen Wang Article 111483</p> <p> View PDF Article preview </p>	
	<input type="checkbox"/> Research article  Full text access	<p>3D Printed Architected silicone composites containing a UV-curable rheological modifier with tailorable structural collapse</p> <p>Chengzhen Geng, Zhicheng Ding, Wen Qian, Yu Su, ... Ai Lu Article 111490</p> <p> View PDF Article preview </p>	
	<input type="checkbox"/> Research article  Full text access		



Biomimetic versatile wood hybrids with gradient structure towards lightweight, high strength, fire-retardant, and deterioration-resistant materials

Qi Fan ^{a,b,1}, Xing Zhang ^{a,1}, Chuanfu Chen ^a, Xiaolong Hao ^{a,b}, Zhenzhen Liu ^{a,b},
Rongxian Ou ^{a,b,*}, Qingwen Wang ^{a,b}

^a Institute of Biomass Engineering, Key Laboratory of Energy Plants Resource and Utilization, Ministry of Agriculture and Rural Affairs, South China Agricultural University, Guangzhou, 510642, China

^b Key Laboratory for Biobased Materials and Energy of Ministry of Education, College of Materials and Energy, South China Agricultural University, Guangzhou, 510642, China

ARTICLE INFO

Handling Editor: Dr Hao Wang

Keywords:

Biomimetic gradient structures
Wood-based hybrid materials
High strength
Fire resistance
Deterioration resistance

ABSTRACT

The development of versatile wood-based biomaterials with integrated low density, high surface hardness, high strength, fire-resistance, anti-decay, and termite-resistance is highly desirable, yet challenging to skillfully fabricate. Inspired by the ubiquity of gradient biostructures in nature, we achieve biomimetic gradient densification structures by controlling the distribution of thermal-moisture fields within the wood, and combine this with in-situ curing of polyacrylic acid/borate supramolecular resins within the wood cells to transform bulk natural wood into lightweight, high strength, and multifunctional materials. The optimally gradient-densified hybrid wood, with a slight increase in density, demonstrates markedly improved mechanical properties ($\approx 2.4 \times$ increase in surface hardness, $\approx 52\%$ increase in flexural strength), excellent dimensional stability, and leaching resistance. In addition, the collaboration of the gradient-densified structure and the in-situ cured acrylic resin/borate supramolecular network provides the biomimetic wood hybrids with excellent fire resistance (V-0 rating in fire retardant grade, 74 % reduction in total smoke release, $\approx 2.5 \times$ increase in fire performance index), decay and mildew resistance (mass loss of less than 10 %), as well as termite resistance (100 % protection efficiency and termite kill rate) properties. It is the first report to combine gradient densification with in-situ curing of supramolecular resins in the structural design and functionalization of wood-based composites. This new design principle provides guidance for fabricating advanced all-in-one wood materials with applications in lightweight, strong, fire-resistant, deterioration-resistant, and scalable building and furniture materials.

1. Introduction

Lightweight, high-strength, and multifunctional materials are gaining rising attention in the fields of building materials [1,2], vehicle-based applications [3], as well as home furnishings [4]. However, the vast majority of structural materials currently in widespread use are synthetic or petroleum-based materials that have heavy weights [5]. In order to reduce the weight of structural materials, elaborate structural designs and complex manufacturing processes such as welding [6], riveting [7], and 3D printing [8,9] are often required. In

addition, synthetic materials, such as steels, alloys, and polymers, are adverse environmental impact, high cost, and energy-intensive [9–11]. Natural wood, especially fast-growing wood, has been used in building and furniture construction for thousands of years because it is low-density, renewable, abundant, and low-cost [12]. However, the mechanical properties (strength and surface hardness), flammability, and susceptibility to biodegradation of fast-growing wood are not ideal for many advanced engineering structures and applications [13].

In order to overcome the above mentioned disadvantages, various wood modification methods including chemical modification [14,15],

* Corresponding author. Institute of Biomass Engineering, Key Laboratory of Energy Plants Resource and Utilization, Ministry of Agriculture and Rural Affairs, South China Agricultural University, Guangzhou, 510642, China.

E-mail address: rongxian_ou@scau.edu.cn (R. Ou).

¹ Dr. Qi Fan and Xing Zhang equally contributed to this work and were listed as co-first authors.



thermo-hydro [16], and thermo-hydro-mechanical modification [17] have been proposed. Among these, thermo-hydro-mechanical bulk densification has been identified as a promising eco-friendly method to enhance the mechanical performance of natural wood [18,19]. This method involves complete densification of wood in the compression direction, resulting in a uniform increase in density along that direction [20]. Furthermore, the densification method can significantly enhance the flame retardant properties of wood materials [21]. This is because the process removes spaces between cell walls, resulting in a highly compact laminated structure that can prevent oxygen infiltration [21]. This structure also allows for the generation of a dense insulating char layer that impedes the transfer of heat and the diffusion of oxygen during the combustion process [22]. However, prior to bulk densification, the natural wood is typically required to be pretreated with steam, heat, ammonia, cold rolling, and even delignification [23], which greatly increases energy consumption, reduces manufacturing efficiency, and compromises environmental friendliness. Moreover, bulk densification results in a dramatic reduction in thickness of the natural wood (typically by 50–80 %) [24,25], which means a significant decrease in the volume utilization of wood and an exponential increase in the density of the material [26].

Over millions of years, organisms have evolved fascinating bio-structured materials with delicate structural features [5], providing us with a rich source of inspiration for the design of lightweight and high-strength materials [27]. Gradient structure, as one representative strategy implemented in nature [28], consisting of hard out-layer, tough internal layer, and gradient interlayer is widely present in bamboo, bone, and shells [29,30]. Structural gradients are increasingly being introduced into various synthetic materials, such as hydrogels [31], polymer composites [32,33], and alloys [34], providing them with enhanced strength, hardness, and fatigue resistance through deformation mechanisms [35,36]. Natural wood has a uniform pore distribution and density along the tangential and radial directions [37]. Specifically, under the influence of a preset thermo-hydraulic chelating field, the cell walls of natural wood (contain amorphous hemicellulose and lignin with glass transition temperatures) can transition from rigid state to a thermoplastic state [17]. As a result, the wood cells will collapse further to become denser under specific loads [38]. Therefore, it is possible to achieve biomimetic gradient densification of wood by controlling different temperature between top and bottom press platens to manipulate the distribution of the thermal-hydraulic field along the tangential or radial direction of the wood and pressing to a certain thickness. The gradient densified wood is a type of non-bulk compressed wood that offers advantages such as shorter processing time and less loss of wood volume [39,40]. However, almost all densified woods usually lack dimensional stability including spring-back and deformation when exposed to high humidity or directly soaked in water [19,26].

Impregnation modification provides a possible technology platform for creating wood composites with improved dimensional stability and versatility [41,42]. Traditional melamine-formaldehyde and phenol-formaldehyde resins have been applied in the field of impregnation modification of wood for more than half a century [43,44]. Due to the environmental and health hazards they produce and their lack of functional features [45,46], there is an urgent necessity to find alternatives. Low-viscosity waterborne acrylic resins that can be thermally initiated cross-linked provide an ideal alternative for various advanced wood composites applications [47]. These resins are easily modified and readily penetrate the wood cells [26,48]. In addition, a great deal of effort has been employed in recent years to impregnate wood cells with functional reagents to prepare wood-based functional materials with features such as fire retardancy [49], decay resistance [50], and anti-termite [14]. However, it is rarely reported that multifunctional wood can be obtained by employing a single low-cost and low-toxicity reagent. Disodium octaborate tetrahydrate (DOT) is a new type of highly soluble borate containing up to 21 % boron content [51], which has excellent fire-retardant, antibacterial, anti-mold, and anti-termite

functions [52,53]. However, its susceptibility to loss during use significantly limits its applicability in wood preservation [54]. The borate anion exhibits substantial affinity towards polar groups, including hydroxyl, carboxyl, and amine groups [55,56]. This highlights the potential of the boron-oxygenating anion in DOT to construct supramolecular structures with polar polymers, ultimately addressing the issue of leaching tendency.

Herein, a versatile wood material with a biomimetic gradient structure was successfully fabricated via a simple and scalable approach (Fig. 1a and b). It involves an asymmetric hot-pressing process to achieve a controlled distribution of heat and moisture within the wood (Fig. 1b), combined with in situ cross-linking curing of acrylic resin/borate supramolecular networks. The mechanical strength, dimensional stability, surface properties, fire retardancy, anti-mold, against decay, and anti-termites were systematically investigated. In addition, it was demonstrated by micro-morphological analysis that asymmetric hot pressing resulted in gradient densification of the wood rather than “surface densification” as popularly believed. To our knowledge, this is the first report of the successful preparation of all-in-one wood material with high mechanical performance, fire resistance, and anti-deterioration, while maintaining its initial low-density properties. Comparing with the bulk densified wood, the result gradient densified wood material has superior comprehensive performance (Fig. 1c), as well as being environmentally friendly, energy-efficient, and non-hazardous at the fabrication process.

2. Experimental section

2.1. Materials

The fast-growing poplar wood (*Populus euramevicana* cv. ‘1-214’) used in this study originates from Luohe, Henan Province, China. Disodium octaborate tetrahydrate ($\text{Na}_2\text{B}_8\text{O}_{13}\cdot 4\text{H}_2\text{O}$, >98 %) were purchased from Sigma-Aldrich. Waterborne acrylic resin (WAR, Acrodur® DS 3530) with a density, solid content, viscosity range, and pH value of 1.06 g cm^{-3} , 50 %, 150–300 mPa s, and 3.5, respectively, originates from BASF China Co., Ltd., Shanghai, China. The WAR resin is a modified polyacrylic acid, which can be thermally cured at a temperature above 130°C in the presence of a polyalcohol (crosslinking agent) creating a polyester thermoset material [48] (Fig. S1).

2.2. Methods

2.2.1. Preparation of acrylic acid/borate supramolecular resins

Following exploratory tests, a sequence of acrylic resin/DOT solutions with an 18 % weight concentration (w/w) were prepared through dilution with deionized water. Different acrylic resin/DOT ratios (1:0, 9:1, 5.67:1, 4:1, 3:1 and 0:1) were successfully prepared (Table S1), and were used for subsequent impregnation.

2.2.2. Impregnation

The aqueous solution of polyacrylic acid/DOT supramolecular resins prepared separately according to the formula was poured into a stainless-steel container, and then the wood samples were completely submerged in the solution using a weight of 100 g. Subsequently, the containers were placed in a vacuum/high-pressure impregnation tank at room temperature, maintaining a vacuum of -0.08 MPa for 20 min, and then pressurized to 0.6 MPa for 1 h. The pressure was then reduced to atmospheric pressure and the impregnated wood samples were removed from the vacuum/pressurized impregnation tank. Afterward, the excess resin solution was wiped off the surface of the samples. The impregnated wood samples were air-dried for 12 h and then vacuum-dried at 60°C for 48 h at a vacuum level of approximately -0.08 MPa . Prior to unilateral gradient densification, all samples were conditioned at 25°C and 65 % relative humidity (RH) until equilibrium moisture content (EMC) was reached.

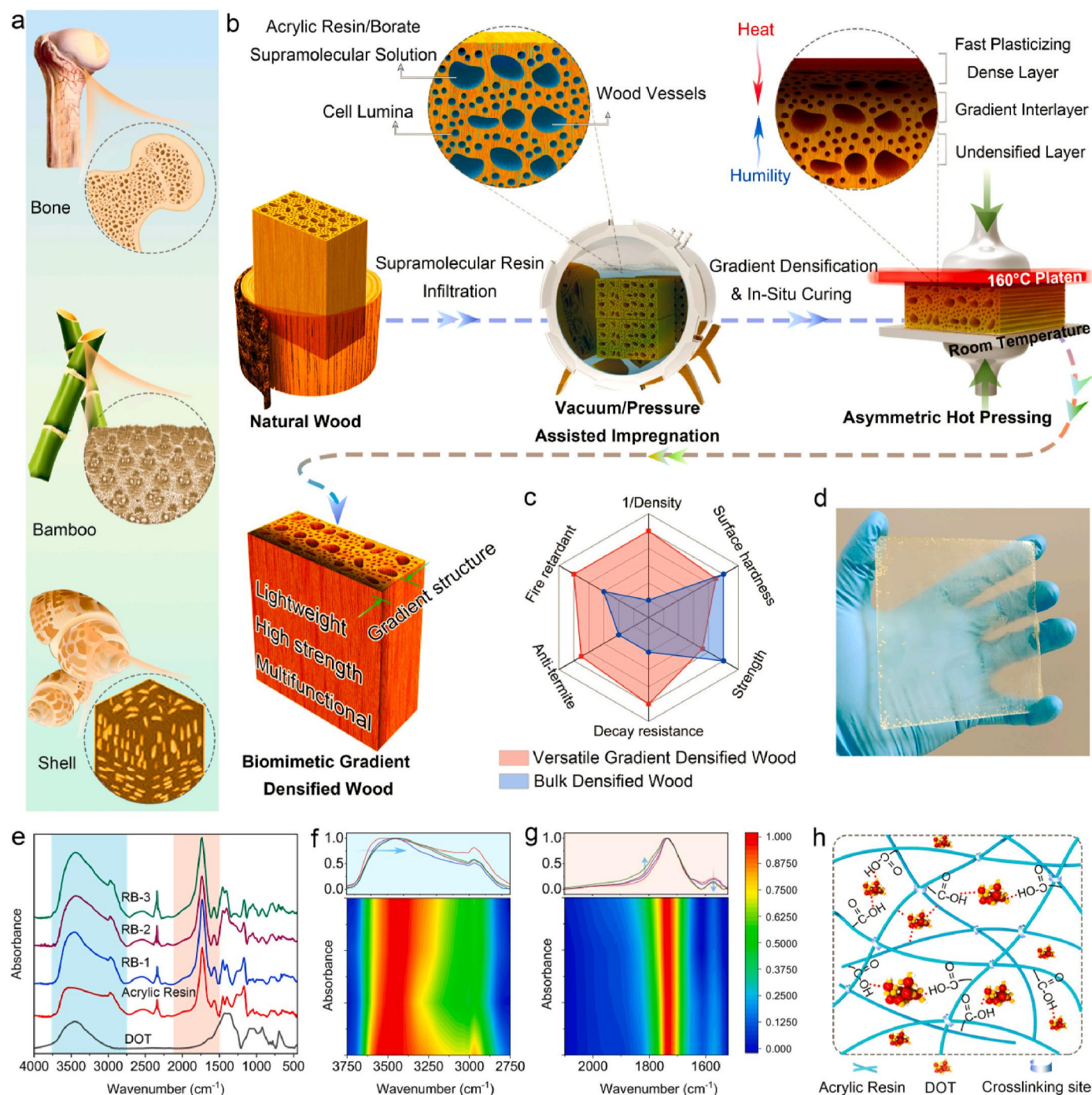


Fig. 1. Design and strategy of versatile wood hybrids with biomimetic gradient structure. (a) Schematic images of representative bones, bamboo and shells with gradient structures in nature. (b) Schematic demonstrating the top-down approach of gradient densification assisted with aqueous acrylate/borate supramolecular resin impregnation to transforming bulk natural wood directly into multifunctional unilateral gradient densified wood. (c) Radar chart qualitatively comparing the properties of multifunctional gradient densified wood with those of bulk densified wood, showing multifunctional gradient densified wood has lower density, high mechanical strength and surface hardness, excellent fire retardancy and anti-biodegradation features. (d) Digital image of the acrylic acid/DOT (with a ratio of 16.2:1.8) supramolecular resin after curing. (e) FTIR spectra and 2D contour maps (f and g) of the acrylic acid/DOT supramolecular resins with different ratios of DOT. (h) Schematic showing the non-covalent interactions to immobilizing disodium octaborate tetrahydrate (DOT) molecules in the acrylic resin networks.

2.2.3. Unilateral gradient densification

The wood samples were subjected to unilateral gradient densification according to the temperature-pressure-time process shown in Fig. S2, using a hot press machine with a maximum pressure of 100 metric tons. The temperatures of the upper and lower plates were set at 160 °C and room temperature, respectively. When the upper plate reached the set temperature, the wood samples were placed into the hot

press machine for unilateral densification. The pressure was gradually increased to 6 MPa and the wood samples were hot pressed under the above conditions for 10 min while ensuring that the acrylic resin within the wood was fully cured. The temperature of the upper plate was then quickly reduced to room temperature and pressed for 15 min while maintaining the 6 MPa pressure. Two metal stops were used to ensure that the wood samples were compressed to a target thickness of 10 mm

with a compression rate of 23 %. The unilateral gradient densified wood samples were conditioned at 20 °C and 65 % relative humidity (RH) until they reached EMC before further testing.

The gradient densified wood samples assisted with impregnation polyacrylic acid/DOT supramolecular resins were denoted as UGD-RB, based on increasing DOT ratio, these samples were labeled as UGD-RB- x ($x = 1, 2, 3, 4$) (Table S1). The untreated control wood was recorded as C-W, and wood treated only with unilateral gradient densification was recorded as UGD-W. The densified wood samples impregnated only with an aqueous solution of 18 wt% acrylic resin or DOT were labeled UGD-R and UGD-B, respectively.

Details of the material characterization are presented in the Supplementary Information.

3. Results and discussion

3.1. Fabrication, morphology, and vertical density profiles

Our approach involves a two-step process that directly converts the natural bulk wood into a versatile, unilaterally gradient densified wood, rather than a highly contaminated partial removal of lignin from the natural wood. Aqueous solutions of polyacrylic acid/DOT supramolecular resins were prepared with varying amounts of DOT and denoted RB- x (Table S1), where x increases as the ratio of DOT to polyacrylic acid increases. The cured composite of RB-1, presented in Fig. 1d, appears transparent with a yellowish tint. As shown in Fig. 1e–g, FTIR analysis of polyacrylic acid/DOT supramolecular resins with varying ratios revealed significant peak shifts in the hydroxyl (Fig. 1f) and carbonyl (Fig. 1g) features as the DOT ratio increased, demonstrating that the polyacrylic acid molecules had strong non-covalent interactions with

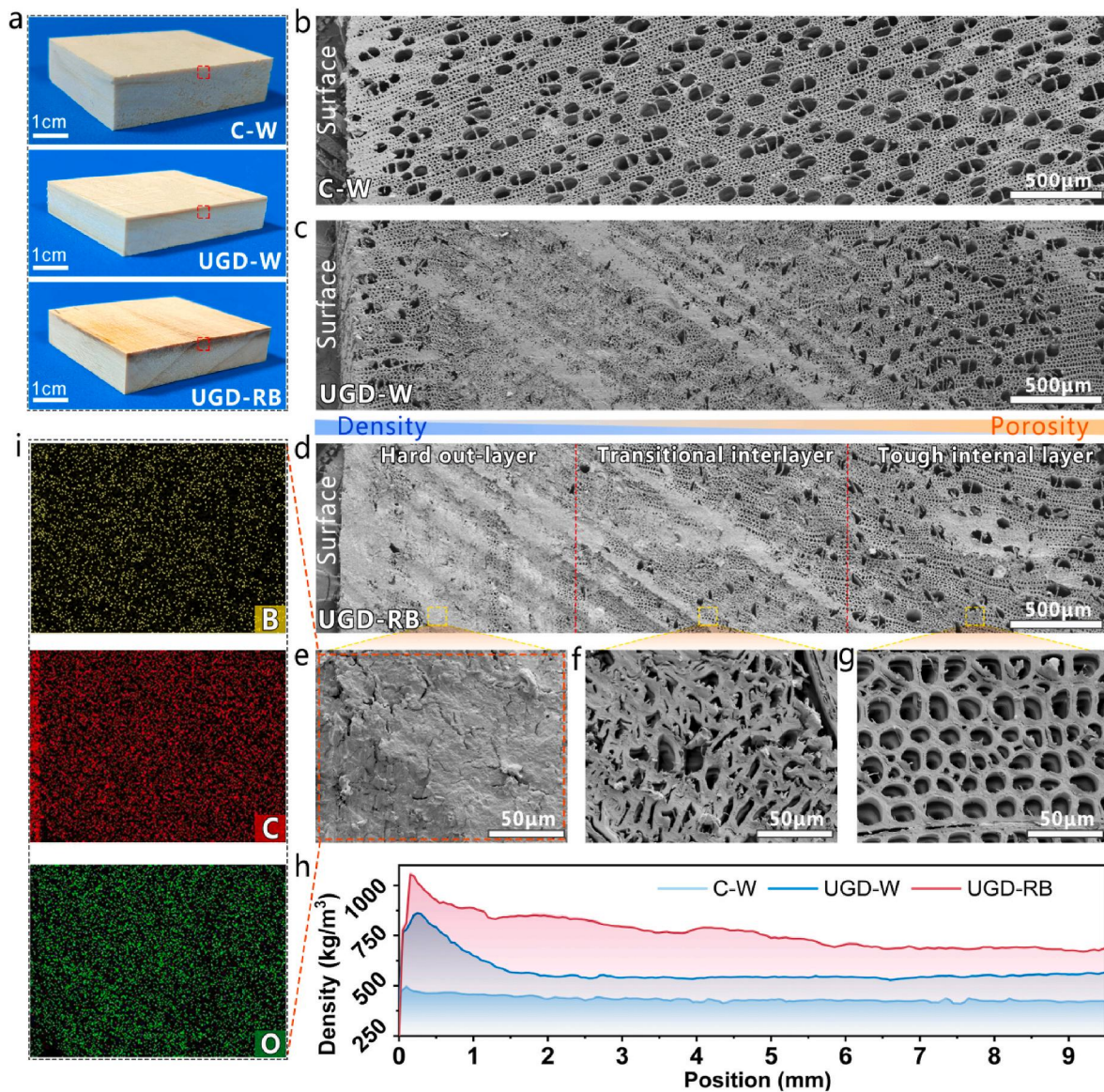


Fig. 2. Morphology, structure, and vertical density profiles (VDPs) of natural wood (C-W) and unilateral gradient densified wood with (UGD-RB) and without (UGD-W) impregnating acrylic acid/DOT supramolecular resin. (a) Photographs of the UGD-RB, UGD-W, and C-W. (b) Cross-sectional high-magnification SEM image of natural poplar wood, demonstrating its uniform pore distribution. (c and d) Cross-sectional high-magnification SEM image of UGD-W and UGD-RB, demonstrating the gradient distribution of their pores. (e–g) SEM images of the pore characteristics in the different regions in (d), indicating the gradient densified characterization. (h) The vertical density profiles of UGD-RB, UGD-W, and C-W. (i) The EDX spectra of cross sections of UGD-RB, exhibiting the presence of boron element due to the impregnation of acrylic acid/borate supramolecular resin.

the borate anions and sodium ions of DOT (Fig. 1h). Bulk wood was first subjected to vacuum/pressure-assisted impregnation with an aqueous solution of acrylic acid/DOT supramolecular resins, followed by asymmetric hot pressing to control the location and diffusion rate of the heat and moisture fields, resulting in rapid obtaining of the material in tens of minutes. The main reason for gradient densification is that when the surface of the wood comes into contact with a hot platen, heat is transferred to the interior of the wood, while the moisture within the wood is transferred to the heated surface layer. This results in a rapid gradient thermal softening of the wood cell walls from the surface to the interior. Furthermore, during asymmetric hot pressing supramolecular resins undergo thermally initiated cross-linking within the multilevel structure of wood.

As shown in Fig. 2a, both the unilateral gradient densification treatment alone (UGD-W) and the unilateral gradient densification assisted with acrylic acid/DOT supramolecular resin impregnation

modification treatment (UGD-RB) resulted in a reduction of approximately 23 % in the thickness of the wood pieces compared to natural wood (C-W). The color of the obtained UGD-W and UGD-RB samples did not change significantly. UGD-W and UGD-RB wood exhibit unique gradient-variable microstructures, as shown in Fig. 2b–d. Fig. 2e–g displays high-magnification SEM images of the densified, transitional, and undensified regions of UGD-RB wood, respectively, indicating gradient-variable pore size distributions. Completely collapsed wood cell walls are observed in the densified region of UGD-RB tightly interwoven along the cross-section (Fig. 2e). In contrast, the densified region of UGD-W left many gaps between the collapsed cell walls (Fig. S3). This indicates that the impregnated acrylic resin has good filling, softening, and bonding effects on the gaps in the cell walls, implying that UGD-RB exhibits better surface hardness and mechanical strength.

The vertical density profiles (VDPs) of UGD-RB, UGD-W, and C-W are presented in Fig. 2h and Fig. S4. The results indicate that the

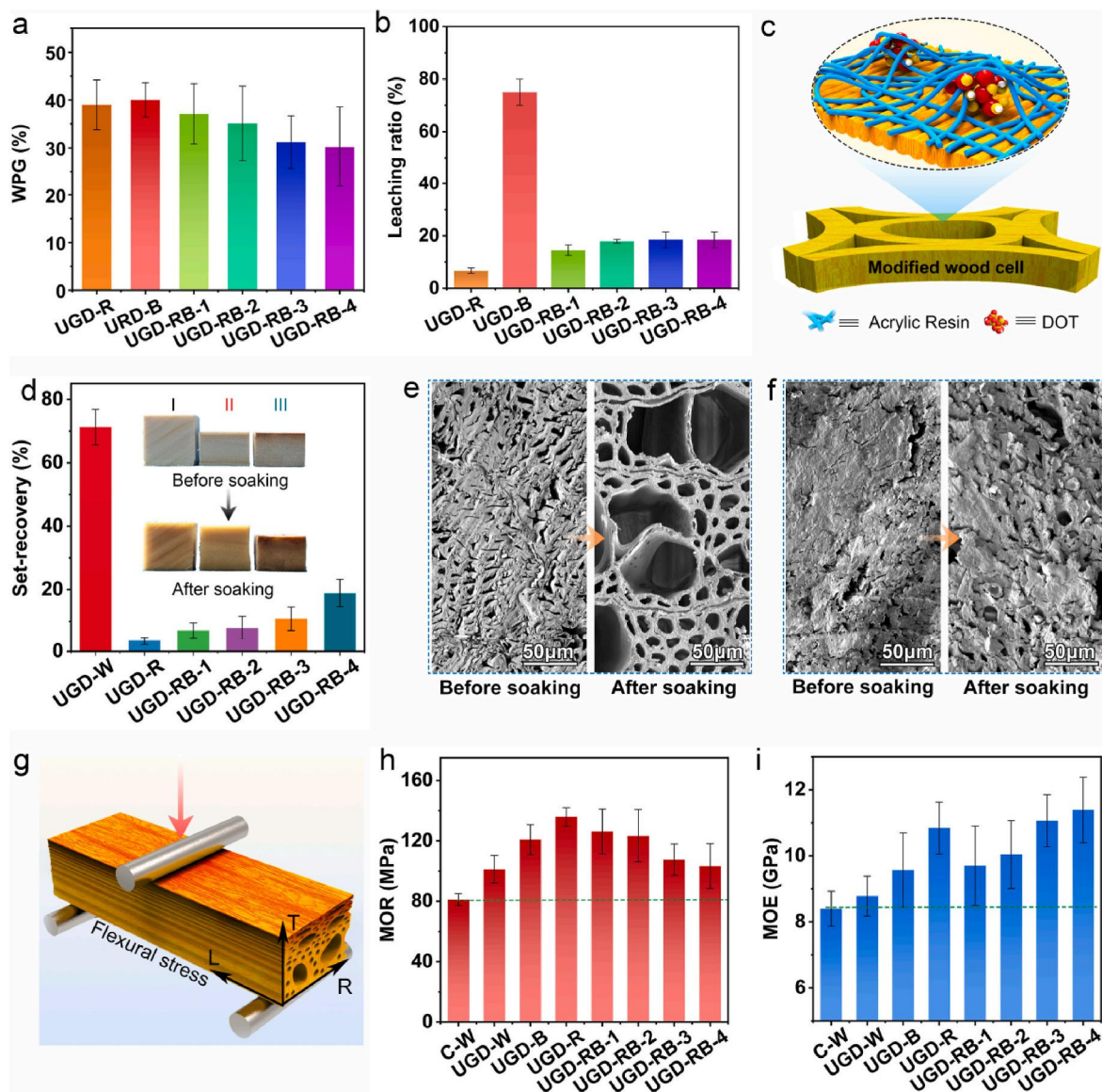


Fig. 3. Weight percent gain (WPG), leaching ratio, set-recovery, and mechanical performance. (a) WPG of the unilateral gradient densified wood impregnate with different ratios of acrylic resin/DOT solution. (b) Leaching ratio of samples. (c) Schematic illustration of the cured crosslinked network of waterborne acrylic resin immobilizing DOT in wood cells. (d) Set-recovery of different wood samples soaked in water at 40 °C for 24 h. Inset: I for natural wood, II for UGD-W wood, III for UGD-RB-4 wood. (e) SEM images of densified layer of UGD-RB-4 wood before and after soaking in water at 40 °C for 24 h. (f) SEM images of densified layer of UGD-W wood before and after soaking in water at 40 °C for 24 h. (g) Schematic diagram of bending strength tests. (h and i) Modulus of rupture (MOR) and modulus of elasticity (MOE) of the samples.

gradient densified wood (UGD-W and UGD-RB) exhibits an asymmetric structure. The densified side of UGD-RB has a density of up to 1200 kg/m³, while the other side has a density close to that of the natural wood (approximately 500 kg/m³). As shown in Fig. 2i, the EDX mapping reveals the distribution of elemental boron in the cell walls of the cross-section of the dense layer of UGD-RB wood (Fig. 2e), indicating that acrylic acid/DOT supramolecular resin has penetrated into the interior of the wood.

3.2. Basic physical properties and mechanical performance

The weight percent gain (WPG) of UGD-RB impregnated with acrylic acid/DOT supramolecular resin solution at a concentration of 18 % varied with different ratios of acrylic resin and DOT. As shown in Fig. 3a, the WPG tended to decrease with the increase of DOT. This may be due to the high percentage of DOT, which increases the interaction between acrylic molecules and borate, thereby increasing the viscosity of acrylic resin/DOT and resulting in a slight decrease in WPG. Nonetheless, the WPG of all samples exceeded 25 %. The leaching ratio is used to measure the stability of treatment agent fixation in wood. We tested the leaching rate of the various modified wood, as depicted in Fig. 3b. The leaching rate of UGD-RB treated with the acrylic resin/DOT solution decreased to less than 18 %, which can be attributed to the effective encapsulation and non-covalent bonding attraction of the cured cross-linking network of the acrylic resin in the wood (Fig. 3c).

Fig. 3d illustrates the set-recovery value of the densified layer as a function of the acrylic resin/DOT ratio. After undergoing a single soak-dry treatment, the densified layer of the UGD-W samples exhibited a significant set-recovery of approximately 72 %. This nearly complete recovery of the densified layer can be attributed to the release of elastic strain energy stored in the cell wall [57]. The highly magnified SEM images in Fig. 3e demonstrate the microscopic morphology of the dense layer of the UGD-W wood sample before and after being immersed in water at 40 °C for 24 h. It is evident that the dense layer of the UGD-W exhibits a near-complete recovering to its initial multi-luminal cellular structure following water absorption. The set-recovery value, however, exhibits a significant decrease when the cell wall is anchored by the cured resin. Rapid heat-induced cross-linking of polycarboxylic acids with multifunctional alcohols results in strong adhesion between wood and resin [58], which prevents water penetration and resilience of highly intertwined cell walls. The lowest set-recovery value of 3.5 % was obtained for the UGD-R sample. Due to the hydrophilic nature of DOT, the set-recovery value of UGD-RB increased with increasing DOT content. Nevertheless, even the UGD-RB-4 sample with the highest DOT content still exhibited a significantly lower set-recovery value compared to UGD-W, at approximately 18 %. As shown in Fig. 3f, the dense layer of UGD-RB-4 before and after water treatment maintained an almost completely densified structure. The results further indicated that the prepared UGD-RB wood exhibited excellent dimensional stability at macroscopic level even after water immersion treatment.

The samples were further tested for bending mechanical properties (Fig. 3g), and the results of their statistical analysis are presented in Table S2. The MOE and MOR of C-W were 8.4 GPa and 81.1 MPa, respectively (Fig. 3h and i). The MOE and MOR of UGD-W were 8.78 GPa and 101.2 MPa, which were about 4.5 % and 24.7 % higher, respectively, than those of untreated C-W. The above results indicated that unilateral gradient densification alone can improve the mechanical properties of wood. The MOE and MOR of UGD-B impregnated with DOT only further increased to 9.57 GPa and 120.8 MPa, respectively. The results suggest that DOT cross-links or interacts with wood cell walls during the hot pressing. The MOE and MOR values of UGD-R (impregnated with acrylic resin only) respectively reached 10.84 GPa and 135.9 MPa, which are 23.5 % and 34.3 % higher than those of UGD-W, respectively. The result demonstrates that the rapid thermal curing of the acrylic resin during the hot pressing process contributes to the enhancement of mechanical properties of wood by forming a robust

cross-linked structure.

As the acrylic resin/DOT ratio decreases, the MOR of UGD-RB gradually decreases resulting from the decrease in the ratio of resin, but remains higher than that of UGD-W. For example, the MOR of UGD-RB-2 was 21.9 % and 52.2 % higher than that of UGD-W and natural wood, respectively. Among the UGD-RB samples, UGD-RB-4 had the highest MOE value, which increased as the ratio of acrylic resin/DOT decreased (Fig. 3i). The average MOE of UGD-RB ranged from 9.7 to 11.39 GPa, slightly higher than that of UGD-B and UGD-R. The MOE of UGD-RB was 15.5%–35.6 % than that of natural wood and 10.5%–29.7 % higher than that of UGD-W.

In conclusion, the mechanical properties of UGD-RB were significantly improved compared to UGD-W and natural wood, suggesting that unilateral gradient densification combined with acrylic acid/DOT supramolecular resins impregnation modification holds great potential for transforming fast-growing wood into engineered or structural wood materials with high strength and low density as well as multifunctionality.

3.3. Surface properties

The surface hardness of densified wood increased significantly due to gradient densification and in situ curing of the functional resin. As seen in Fig. 4a, the surface hardness of UGD-W increased by 56 % compared to C-W. The surface hardness values of UGD-RB further increased to 5.85–6.15 kN, which was about 1.5-fold higher than that of UGD-W. Fig. 4b illustrated a comparison of the surface hardness versus density of gradient densified wood with some other common woods. The results demonstrate that there is a near linear relationship between the surface hardness of the nature woods and their density. However, UGD-RB wood has a more prominent surface hardness/density ratio than other common nature woods. The density of UGD-RB is strongly related to its thickness in theory. It is hypothesized that if the thickness of UGD-RB is increased, then its apparent density will decrease. This result demonstrates that UGD-RB wood can be used as an alternative to expensive high-density wood for flooring, slabs, and walls to reduce building weight and minimize costs.

Fig. 4c–f shows the laser optical 3D surface images and depth profiles of C-W, UGD-W, and UGD-RB. The results demonstrate that the control sample C-W has the highest surface roughness (Ra) value (3.65 μm), which was attributed to the presence of open cell lumens. The Ra value of the UGD-W wood decreased to 2.88 μm, because gradient densification reduces the dimples on the surface of the wood. The Ra values of the UGD-RB further decreased, e.g., the Ra value of the UGD-RB-4 was 1.18 μm, which was caused by the surface cell lumen filling by cured resin. The surface depth profile of Fig. 4f further visually confirmed the flat and smooth surface of the prepared multifunctional wood through the strategy of gradient densification combined with in-situ curing of functional resin. Thus, UGD-RB wood can be directly used in furniture and architectural components to provide tactile smoothness.

The wettability of the liquid on wood surface affected the dimensional stability and stain resistance of the wood. Fig. 4g and h shows the curves of water contact angle (WCA) and diiodomethane contact angle (DIICA) versus time for untreated C-W, UGD-W, UGD-R, and UGD-RB-4 surfaces, respectively. Due to the inherent hydrophilicity of the wood cell wall, C-W was easily wetted and the WCA of C-W dropped below 10° within 1 min (Fig. 4g). The dense structure of UGD-W delayed water uptake, and it took 2 min for the WCA to fall below 10°. However, the hydrophobicity of UGD-R was significantly higher, and it took 8 min for the WCA to decrease to about 10°, which was attributed to the cross-linked network of acrylic resin cured in situ in the cell wall that prevented water penetration. The slightly lower hydrophobicity of UGD-RB than that of UGD-R was attributed to the introduction of DOT. Nevertheless, the water repellency of the surface of the experimental group in which UGD-RB-4 containing the most DOT was still close to that of UGD-R. This further demonstrates that the hydrophilic DOT was effectively

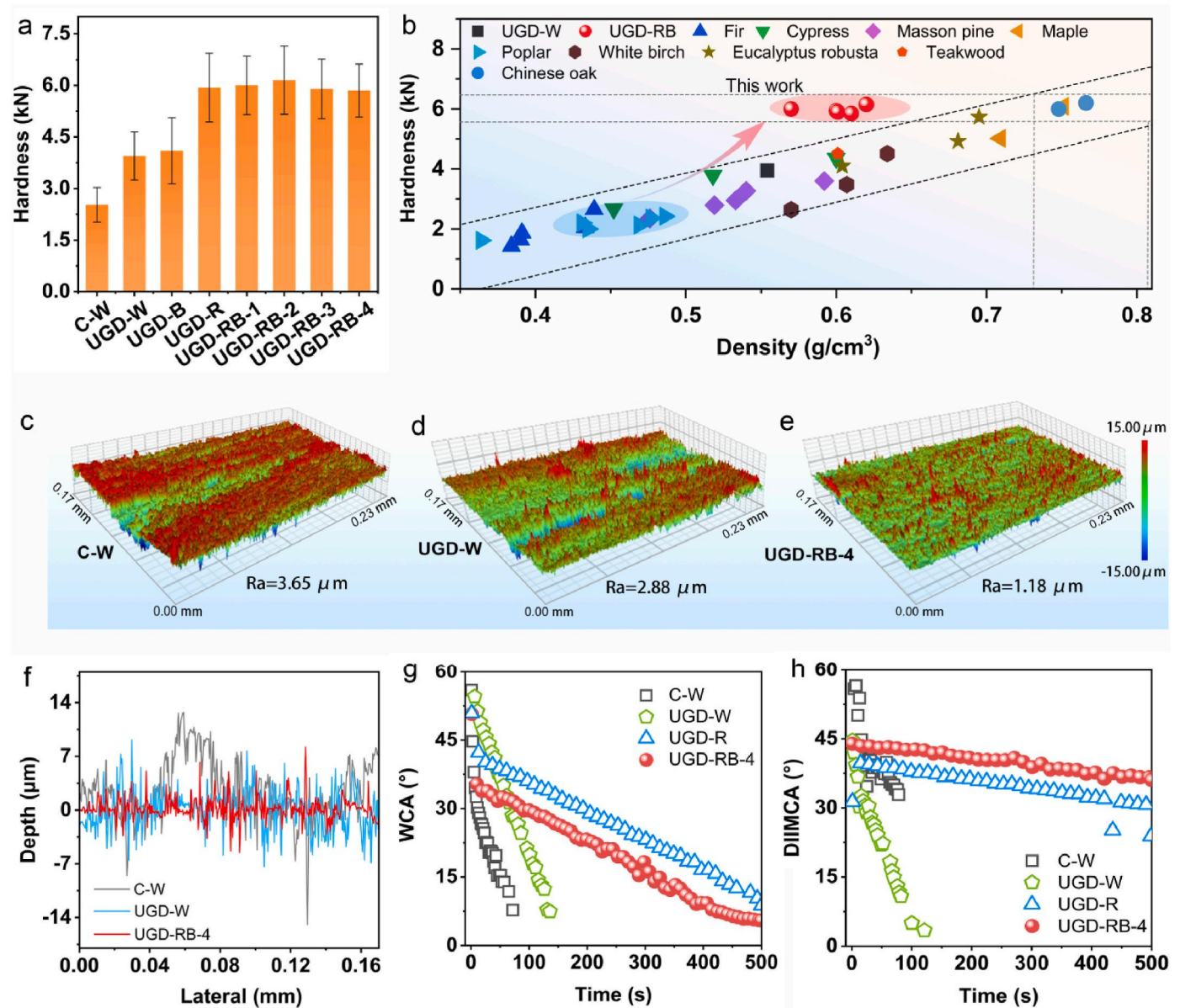


Fig. 4. Evaluation of surface properties. (a) Surface hardness of the UGD-W, UGD-RB samples and natural wood, the thickness of the test samples was 4 cm. (b) Comparison of surface hardness versus density of UGD-W and UGD-RB wood with some other nature wood species, refer to Table S3 (c-f) Laser optical 3D surface images and depth profiles of C-W, UGD-W, and UGD-RB. (g and h) Variation of water contact angle (WCA) and diiodomethane contact angle (DIICA) with time for different wood surfaces.

encapsulated. Diiodomethane is often used to characterize the oleophobic properties of material surfaces. As shown in Fig. 4h, C-W and UGD-W were easily wetted by diiodomethane, and DIICA dropped below 10° within 2 min. However, the surfaces of UGD-R and UGD-RB-4 repelled diiodomethane significantly, and DIICA remained almost stable at $\sim 40^\circ$ within 8 min. This is due to the reduced porosity of the UGD-R and UGD-RB-4 surfaces as well as the highly cross-linked network structure of the acrylic resin. Interestingly, DIICA of UGD-RB-4 was higher than that of UGD-R, indicating that the cured acrylic resin modified by DOT has better anti-oil capacity.

3.4. Fire-retardant performance and thermal stability

The fire retardancy of the UGD-RB samples was evaluated using classic UL-94 vertical burning and limiting oxygen index (LOI) tests. A visual illustration of the fire retardancy of the different samples is provided in Fig. 5a-f and Fig. S5. The C-W and UGD-W samples burned out

quickly upon contact with the flame, whereas the UGD-RB samples were able to undergo a second ignition test. The results demonstrate that the C-W, UGD-W, and UGD-RB-1 samples failed to achieve a V-0 rating in UL-94 vertical burning testing, with LOI values of 22 %, 23 %, and 37 % (Fig. 5g), respectively. In contrast, UGD-RB-2, UGD-RB-3, and UGD-RB-4 achieved a V-0 rating in UL-94 testing with LOI values of 43 %, 50 %, and 54 % (Fig. 5g), respectively, demonstrating a high level of fire safety.

The above results demonstrate that the addition of a small amount of DOT can significantly improve the fire-retardant properties of fast-growing poplar wood. This improvement can be attributed to the fact that the UGD-RB samples generate a vitreous fire-retardant layer of borate on wood surface during the burning process, which blocks the fire source and prevents heat and oxygen transmission into the interior of the wood. In addition, the crystalline water contained in DOT absorbs heat during thermal decomposition, lowering the combustion temperature and slowing down the burning speed and fire propagation in wood.

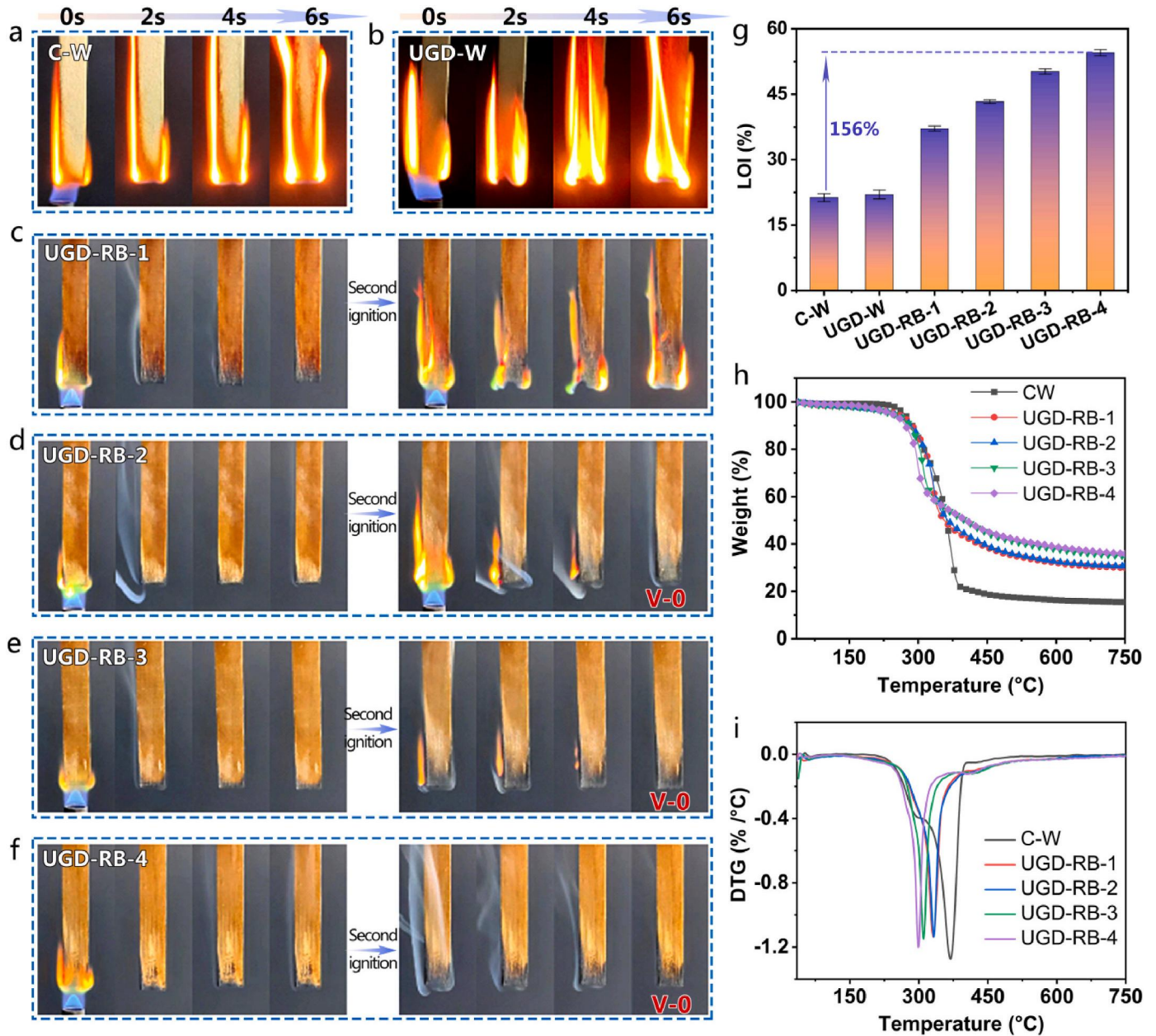


Fig. 5. Vertical burning properties, limiting oxygen index (LOI), and thermal stability. (a–f) Photo images of natural wood (C–W) and different UGD wood during vertical burning test. (g) LOI of C–W, UGD–W, and UGD–RB wood. (h) Thermogravimetric (TG) analysis curves of C–W and UGD–RB. (i) Derivative thermogravimetric (DTG) curves of C–W and UGD–RB.

The optimized UGD–RB wood exhibits superior fire retardancy compared to most of the previously reported fire retardant modified woods [59].

The TGA and DTG curves for various samples under nitrogen are presented in Fig. 5h and i, respectively. The TG curve of natural wood in Fig. 5h exhibits the typical thermal degradation characteristics of wood, while the DTG curve displays two decomposition peaks at 367.6 °C and 315.2 °C (Fig. 5i), which can be attributed to the decomposition of cellulose and hemicellulose, respectively. In contrast, the thermal degradation behavior of the UGD–RB samples changed significantly. As shown in Fig. 5h, the UGD–RB samples still exhibited higher weight loss at 410–750 °C compared to the CW samples, which may be related to the self-pyrolysis and catalytic charring of the acrylic resin/DOT. In addition, the T_{d10} (the temperature at 10 % weight loss) and T_{peak} (temperature corresponding to maximum degradation rate) values of UGD–RB samples decreased with increasing DOT content (Table S4),

indicating the accelerated thermal decomposition of the matrix and enhanced char residue formation. The char residue of UGD–RB samples significantly increased with DOT content, demonstrating that DOT improved the char-forming ability of gradient densified wood samples. At 750 °C, UGD–RB-4 exhibited a char residue of 35.4 %, which was approximately twofold higher compared to C–W (Table S4). This result suggests that the introduction of DOT greatly contributed to the catalytic charring ability of wood.

3.5. Fire-retardant evaluation based on cone calorimetry

The cone calorimeter is a bench-scale instrument for the simulation and evaluation of the fire-resistant behavior of materials in practical fire scenarios, providing crucial flammability parameters such as heat release rate (HRR), total heat release (THR), smoke production rate (SPR), and total smoke production (TSP). We evaluated the flammability

of the wood samples by cone calorimetry under a heat flux of 50 kW/m^2 in the horizontal position.

The variation of HRR, THR, SPR, and TSP as a function of combustion time for C-W, UGD-W, and UGD-RB is shown in Fig. 6, and the relevant parameters are summarized in Table S5. HRR demonstrates an

important characterization of the intensity and spread of the burning flame during the actual combustion process. The HRR curves of the wood exhibit two principal peaks (Fig. 6a). The initial peak originating from char formation, which as a protective layer prevents the rapid release of combustible gases produced from wood pyrolysis, resulting in

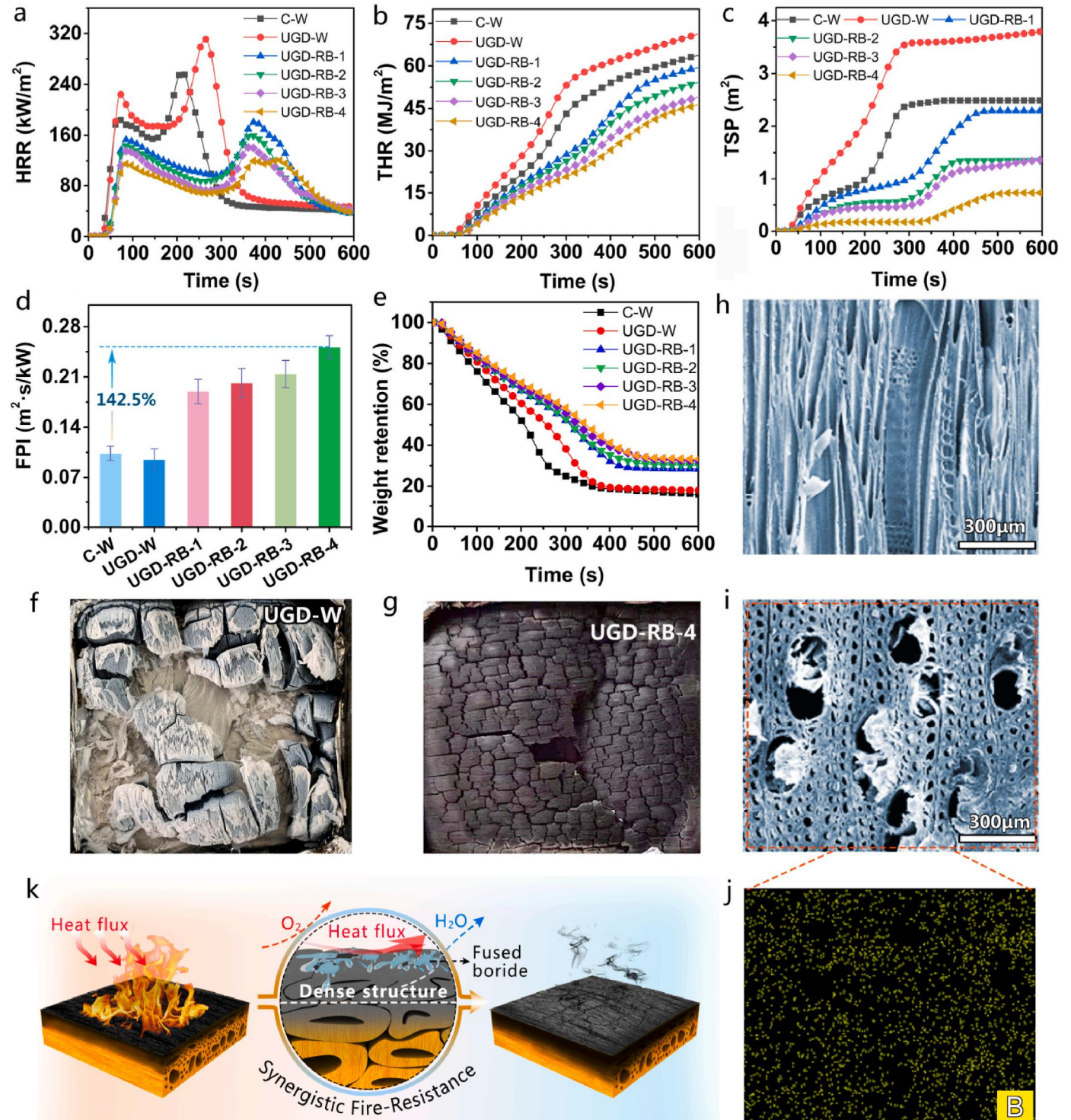


Fig. 6. Evaluation of fire-retardant properties and mechanisms based on cone calorimeter testing. (a) Average heat release rate (HRR). (b) Total heat release (THR). (c) Total smoke production (TSP). (d) Fire performance index (FPI). (e) Mass retention. (f and g) Photographs of macroscopic morphology of residual char of UGD-W and UGD-RB-4 after cone tests, showing that the acrylic acid/DOT supramolecular resins had good catalytic properties for wood char formation. (h) Cross-sectional and (i) tangent-sectional SEM images of the residual char of UGD-RB-4 after 600 s cone tests, demonstrating that the residual char retains the intact wood microstructure. (j) Cross-sectional element mapping of the residual char of UGD-RB-4. (k) Schematic diagram of the combustion behavior of the UGD-RB wood demonstrating the synergistic effect of gradient densification and acrylic acid/DOT supramolecular resins for protecting materials from fire.

a lower peak HRR in the first stage. As burning continues, the protective char layer continues to thermally degrade and crack, resulting in an increase in the HRR, causing a second stage of peak heat release rate (PHRR).

Compared to the control group of C-W, UGD-W exhibited a prolonged ignition time from 11 s to 17 s, despite having higher PHRR and THR values (Fig. 6a and b). This is attributed to the increase in mass per unit volume caused by densification, the bulk density of the gradient-densified wood increases, resulting in higher PHRR and THR values. The reduction in surface layer pores due to gradient densification caused a delay in both ignition time and the second PHRR appearance. The introduction of DOT into the UGD-RB samples decreased the PHRR and THR values. The THR of UGD-RB samples gradually decreased with the increase of DOT content. For example, the THR of UGD-RB-4 was 22 % lower than that of UGD-RB-1, from 59.46 MJ/m² to 46.28 MJ/m². This is attributed to the promotion of thermal degradation of wood components by DOT, leading to the rapid formation of a protective char layer, which in turn significantly reduces PHRR and THR values. These diminished heat release parameters indicated that UGD-RB wood exhibited a low fire hazard.

The TSP curves are shown in Fig. 6c, and the TSP values of UGD-RB-4 were also significantly reduced by 70.7 % and 80.8 % compared with C-W and UGD-W, respectively. It is noteworthy that the smoke suppression effect was the addition of a certain amount of DOT significantly reduced the SPR and improved the smoke suppression effect (Fig. S6). This effect is attributed to the generation of a structurally stable boron-containing carbon layer, as well as the fact that DOT can generate a glassy covering at high temperatures, thus blocking the smoke. In addition, DOT can release crystallized water molecules at high temperatures, which also contributes to smoke suppression.

The fire performance index (FPI) is a crucial criterion for assessing fire hazard and is calculated as the ratio of the time of ignition to the first peak of the HRR. Compared with the C-W, the FPI of UGD-RB was significantly higher, with a maximum increase of 142.5 % (Fig. 6d), indicating a significant reduction in fire hazard. Fig. 6e illustrates the residual mass change curves of the wood samples in the cone combustion test. The results indicate that the residual yield of the UGD-RB samples is more than twofold compared to C-W and UGD-W, implying a catalytic char-forming effect. As shown in Fig. 6f and Fig. S7, the results of the cone tests demonstrate that both C-W and UGD-W were left with only ash and fragmented char after the test. In contrast, the UGD-RB samples all formed a more complete charcoal layer after burning (Fig. 6g and Fig. S7), thus further confirming the char-forming flame retardation.

The residual char of UGD-RB-4 after the cone test was observed using SEM. As shown in Fig. 6h and i, the internal structure of the residual char of the UGD-RB-4 sample maintained a complete fibrous tracheid and vessel structure, indicating that acrylic resin/DOT has an excellent fire-retardant protective effect on the wood substrates. The presence of boron (Fig. 6j) was further confirmed by the elemental distribution of the char layer, which was derived from the acrylic acid/DOT supramolecular resin, demonstrating the formation of a thermally stable boron-containing hybrid char layer. As a result, the char residue of UGD-RB was significantly higher than that of the control sample.

Based on the above analysis, the flame retardant behavior of UGD-RB is illustrated in Fig. 6k. When exposed to a flame, the dense structure of the surface layer hinders the entry of oxygen, which delays the ignition time and the appearance time of HRR peak. Meanwhile, DOT catalyzes the charring of the wood and produces a large amount of borides, such as B₂O₃, and water vapor through a dehydration reaction. The water vapor not only dilutes the flammable gases but also inhibits the HRR of UGD-RB, thus exerting a gas-phase flame retardant effect. In addition, molten boride adheres to the char surface, thus enhancing the thermal oxidative stability of the char layer. With the synergistic effect of gradient densification and acrylic/DOT supramolecular resin, UGD-RB can quickly form a dense char layer on the surface during combustion, thus

preventing the invasion of external oxygen and heat. Exposure of UGD-RB to flame generates multiple flame retardant mechanisms, which can be classified into catalytic charring and condensed/gas-phase functions. Therefore, UGD-RB exhibits excellent flame retardancy.

3.6. White rot fungi and mildew resistance

Given that the UGD-RB-1 sample failed to pass the V-0 rating of UL-94, we did not further investigate its biodegradation resistance. The anti-mold tests were conducted in accordance with the Chinese National Standard GB/T 13942.1–2009. The detailed procedure was previously reported in study [60]. Fig. 7 illustrates photographs of unmodified and modified poplar wood samples following a three-month decay test with white-rot fungus. The C-W samples displayed heavy mycelia coverage, indicating high susceptibility to white-rot fungus infection. In contrast, the UGD-R sample had a reduced mycelium presence on its surface, suggesting some anti-decay activity. The UGD-RB samples were notably mycelium-free, indicating a significant reduction of white-rot fungus infection compared with other samples. These results provide evidence that the combined treatment with acrylic resin/DOT significantly improved the decay resistance of poplar wood.

Furthermore, the mass loss of the wood samples was measured. As shown in Fig. 7b and c, C-W samples were heavily infested with white rot fungi, with mass losses as high as 66 %, indicating a low resistance to decay (IV). The mass loss of UGD-R samples impregnated only with acrylic resin was 49 %, which was 26 % less relative to C-W. The weight loss of UGD-RB-2, UGD-RB-3, and UGD-RB-4 samples under the action of white-rot fungi was only 9 %, 8.4 %, and 7.7 %, respectively, suggesting that they have high resistance to decay (I). This may be attributed to the combined effect of DOT and acrylic resin in improving the decay resistance of wood. The acrylic resin fills the gaps in the internal dense layer of the wood during hot pressing and improves the water resistance. DOT is an inorganic compound widely used in wood preservation to inhibit the growth of fungi, insects and bacteria [51]. This combination creates a composite preservative system that makes modified wood more resistant to decay and water, resulting in a longer service life.

The resistance of the modified wood to mold growth was further investigated by inoculating the mixed mold spores onto different wood samples and incubating them for 4 weeks. After incubation, the infection values were determined by observing the infection area on the sample surfaces and then ranked on a scale of 0–4 (see Methods). Fig. 7d shows the appearance of the different samples after the mold test, and it is evident that the surfaces of C-W and UGD-R wood were heavily infected by molds with an average infection value of 4 (Table 1). In contrast, the UGD-RB-2, UGD-RB-3, and UGD-RB-4 samples all exhibited superior mold resistance, with an average infection value of 0 and an average protection efficiency of 100 % against the mixture of molds (Table 1). The superior mold resistance of the UGD-RB samples was attributed to the fact that DOT destroys molds by hindering cell wall synthesis, inhibiting metabolism by binding to enzymes, and disrupting cell membrane [61].

3.7. Anti-termite attack

The resistance of the samples against Formosan subterranean termites (*C. formosanus* Shiraki) was assessed in accordance with the Chinese National Standard GB/T 18,260–2015 under laboratory conditions. The detailed procedure was described in a previous study [62]. A 4-week indoor termite resistance test was conducted on natural wood, UGD-R and UGD-RB samples to assess their termite resistance ratings. The results demonstrated that C-W was heavily attacked by termites, with an average mass loss of 51.6 %, an average termite resistance rating of 4.6 (Fig. 8b–d and Table S6), and an average termite survival rate of 65.3 % (Fig. 8d).

Compared with C-W, UGD-R exhibited greater termite resistance (Fig. 8a), with an average mass loss rate of 22.1 %, an average termite

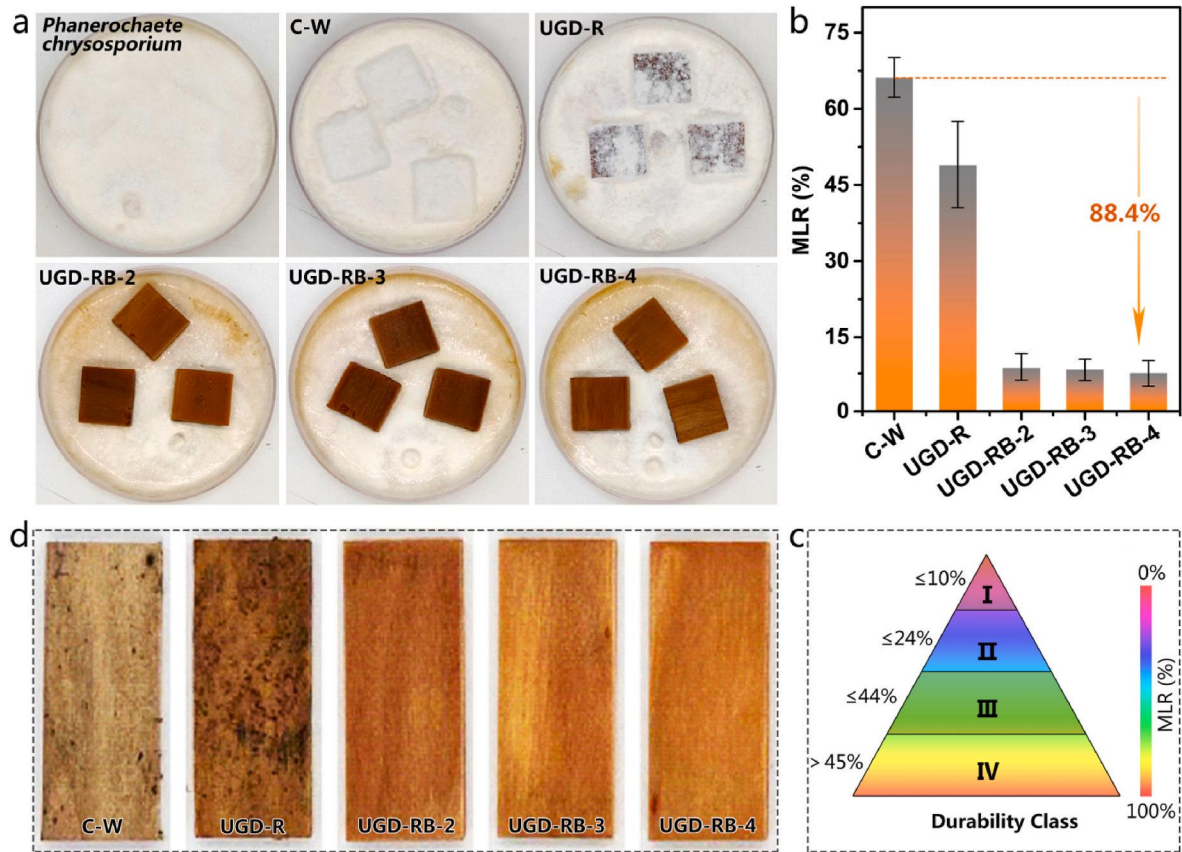


Fig. 7. Anti-decay and mildew resistance of natural wood (C-W) and unilateral gradient densified wood. (a) Appearance of natural wood and unilateral gradient densified wood after white-rot decay test. (b) Mass loss of natural wood and unilateral gradient densified wood after white-rot decay test. (c) Durability class of decay resistance. (d) Appearance of natural wood and unilateral densified wood after anti-mildew tests (after 4 weeks of mold incubation).

Table 1
The resistance of the natural wood and modified wood to mixed mildew.

Samples	Index	Evaluation result
C-W	Infection value	4
	Protective efficiency (%)	/
UGD-R	Infection value	4
	Protective efficiency (%)	/
UGD-RB-2	Infection value	0
	Protective efficiency (%)	100 %
UGD-RB-3	Infection value	0
	Protective efficiency (%)	100 %
UGD-RB-4	Infection value	0
	Protective efficiency (%)	100 %

resistance rating of 8, and an average termite survival rate of 33.5 % (Fig. 8b–d and Table S7). This was attributed to the fact that the acrylate resin cured in the cell cavities of poplar wood could resist termite attack to some extent. At the end of the experiment, the survival rate of termites in the test bottles containing UGD-R samples was more than 30 %. This suggests that the termite resistance of the UGD-R samples was not achieved by killing the termites through toxicity, but rather by altering the properties of the wood itself to make it less attractive to termites.

UGD-RB-2, UGD-RB-3 and UGD-RB-4 showed extremely superior termite resistance ability (Fig. 8b–d and Table S7), with average mass loss of 14.6 %, 12.2 %, and 8.3 %, and average termite resistance ratings of 9.1, 9.3, and 9, respectively, and termite survival rates of 0 %. The reason for this is that DOT contained in UGD-RB wood can produce gastric toxicity to termites after being ingested by termites [63]. Specifically, DOT can kill the protozoa that secrete cellulase to digest lignocellulose in the gut of the termite, thereby inhibiting cellulase

secretion, leading to termite death from starvation [64]. The aforementioned effect is passed to other termites via trophallaxis [50], killing the termite population and protecting wood from termite attack.

4. Conclusion

In summary, we proposed a simple and skillful approach to fabricate a biomimetic gradient densified wood material (UGD-RB) with integrated lightweight, high-strength, fire-retardant, and deterioration-resistant properties. Compared to unmodified natural wood, optimized UGD-RB has a slight increase in density, but demonstrates ≈ 2.4 -fold higher surface hardness, ≈ 52 % higher flexural strength, and ≈ 23 % higher flexural modulus. The in-situ crosslinking of the acrylic resin/DOT supramolecular network immobilizes the collapsed cell walls, resulting in excellent dimensional stability of the material and good leaching resistance. In addition, UGD-RB has attractive integrated versatility. The synergistic effect of the gradient densification and the polyacrylic acid/DOT supramolecular network gives UGD-RB excellent fire retardancy, including fire retardant ratings up to V-0, LOI of 54 %, and significant reductions in THR (27 %) and TSP (74 %). UGD-RB also exhibits outstanding resistance to decay, mildew, and termites due to the presence of the acrylic acid/DOT supramolecular resin in the wood cells. Compared to the bulk densified wood preparation, which involves low volume utilization and heavy environmental pollution of lignin removal process, the proposed simple and efficient method is more promising for large-scale application of building and furniture materials. Although acrylic resins are more expensive than typical formaldehyde-based resins for impregnation, waterborne acrylic resins offer definitive advantages in terms of environmental benefits and improvements in mechanical properties. Furthermore, acrylic resins, with their highly

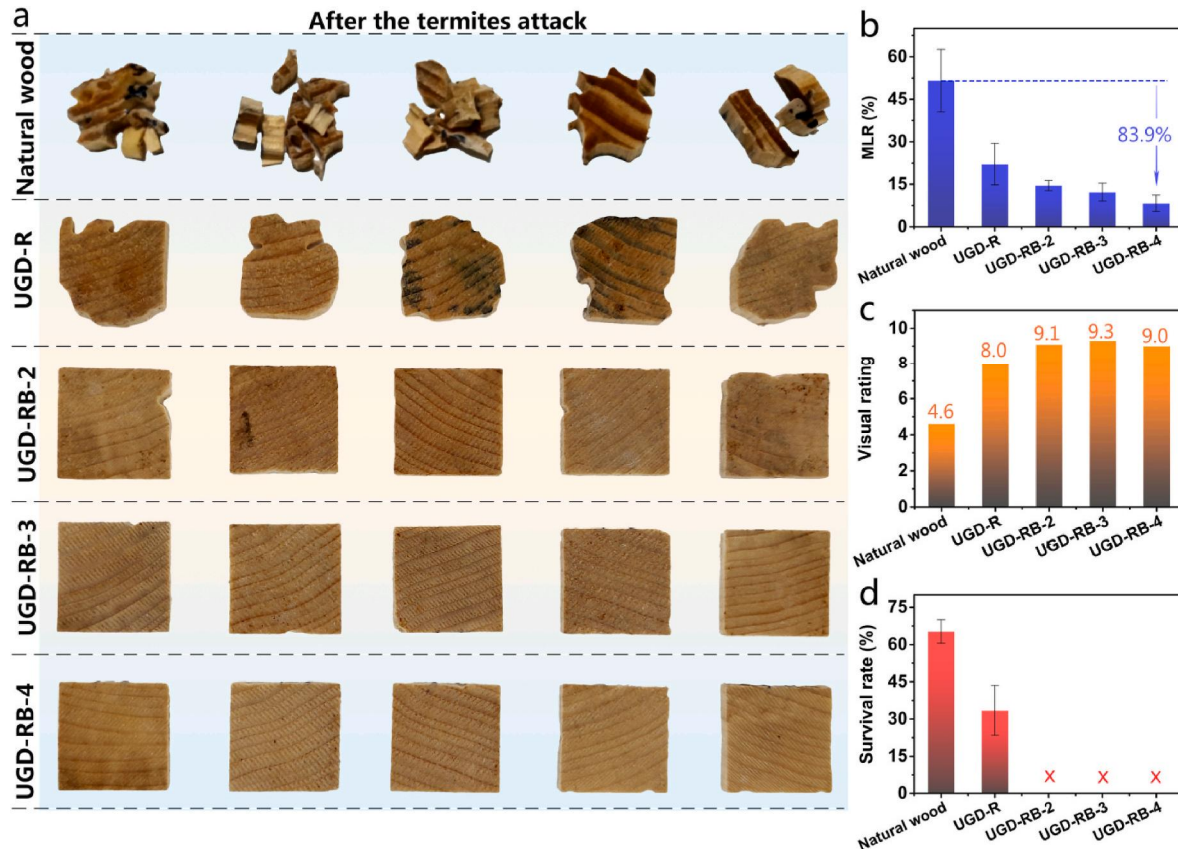


Fig. 8. Evaluation of anti-termite properties of natural wood and modified wood. (a) Appearance of the different wood samples after termite attack. (b) Mass loss of natural wood and modified wood after termite attack test. (c) Visual rating of anti-termite properties for the different wood samples. (d) Average termite survival rate after termite attack test.

adjustable solids content, exhibit excellent compatibility with a wide range of functionalized modifiers. This compatibility facilitates the development of functional woods that possess flame retardant, anti-decay, and even conductive properties. In summary, the proposed manufacturing strategy for high-performance and multifunctional fast-growing wood with a biomimetic gradient structure presents an economically attractive option for high-value utilization of fast-growing wood.

CRedit authorship contribution statement

Qi Fan: Writing – review & editing, Investigation, Funding acquisition, Formal analysis. **Xing Zhang:** Methodology, Investigation, Formal analysis, Writing – original draft. **Chuanfu Chen:** Formal analysis, Investigation. **Xiaolong Hao:** Formal analysis. **Zhenzhen Liu:** Formal analysis. **Rongxian Ou:** Conceptualization, Funding acquisition, Investigation, Supervision, Writing – review & editing. **Qingwen Wang:** Funding acquisition, Supervision.

Declaration of competing interest

The authors declare that they have no known competing financial interests or personal relationships that could have appeared to influence the work reported in this paper.

Data availability

Data will be made available on request.

Acknowledgements

This work was financially supported by the Research and Development Program in Key Areas of Guangdong Province, China (2020B0202010008), the National Natural Science Foundation of China (32071698 and 52103110), the China Postdoctoral Science Foundation (2021M701258) and the Project of Key Disciplines of Forestry Engineering of Bureau of Education of Guangzhou Municipality, China.

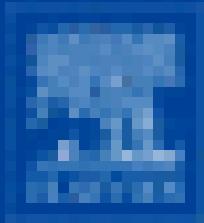
Appendix A. Supplementary data

Supplementary data to this article can be found online at <https://doi.org/10.1016/j.compositesb.2024.111483>.

References

- [1] Li T, Zhai Y, He S, Gan W, Wei Z, Heidarinejad M, et al. A radiative cooling structural material. *Science* 2019;364(6442):760–3.
- [2] Ding Y, Pang Z, Lan K, Yao Y, Panzarasa G, Xu L, et al. Emerging engineered wood for building applications. *Chem Rev* 2022;123(5):1843–88.
- [3] Lee H, Jang J-u, Kim J, Sang Kim Y, Cho J, Na Kim M, et al. True self-reinforced composites enabled by tuning of molecular structure for lightweight structural materials in future mobility. *Chem Eng J* 2023;465:142996.
- [4] Zhi L, Zhang C, Liu Z, Liu T, Dou X, Chen Y, et al. Flexible decorative wood veneer with high strength, wearability and moisture penetrability enabled by infiltrating castor oil-based waterborne polyurethanes. *Compos B Eng* 2022;230:109502.
- [5] Wegst UGK, Bai H, Saiz E, Tomsia AP, Ritchie RO. Bioinspired structural materials. *Nat Mater* 2014;14(1):23–36.
- [6] Lionetto F, Mele C, Leo P, D'Ostuni S, Balle F, Maffezzoli A. Ultrasonic spot welding of carbon fiber reinforced epoxy composites to aluminum: mechanical and electrochemical characterization. *Compos B Eng* 2018;144:134–42.
- [7] Bester F, Kruger J, Zijl Gv. Rivet reinforcement for concrete printing. *Addit Manuf* 2023;67:103490.
- [8] Jiang J, Oguzlu H, Jiang F. 3D printing of lightweight, super-strong yet flexible all-cellulose structure. *Chem Eng J* 2021;405:126668.

- [9] Zou X, Jiang MY, Chen K, Chen BX, Reddy KM, Zhang SY, et al. Mechanism of defect formation during friction spot joining of 3D-printed TC4 alloy and ultra-high molecular weight polyethylene. *Mater Des* 2020;195:108989.
- [10] Xu Z, Munyaneza NE, Zhang Q, Sun M, Posada C, Venturo P, et al. Chemical upcycling of polyethylene, polypropylene, and mixtures to high-value surfactants. *Science* 2023;381(6658):666–71.
- [11] Wang Z, Lu W, Zhao H, Liebscher CH, He J, Ponge D, et al. Ultrastrong lightweight compositionally complex steels via dual-nanoprecipitation. *Sci Adv* 2020;6(46): eaba9543.
- [12] Li Z, Chu S, Zhang Y, Lin L, Liu X. Transforming interface properties of wood laminate composites functionalized by adhesive penetration. *Compos B Eng* 2023; 263:110859.
- [13] Guo D, Guo N, Fu F, Yang S, Li G, Chu F. Preparation and mechanical failure analysis of wood-epoxy polymer composites with excellent mechanical performances. *Compos B Eng* 2022;235:109748.
- [14] Zhou H, Wen D, Hao X, Chen C, Zhao N, Ou R, et al. Nanostructured multifunctional wood hybrids fabricated via in situ mineralization of zinc borate in hierarchical wood structures. *Chem Eng J* 2023;451:138308.
- [15] Lin X, Qiu C, Wang K, Zhang Y, Wan C, Fan M, et al. Biomimetic bone tissue structure: an ultrastrong thermal energy storage wood. *Chem Eng J* 2023;457: 141351.
- [16] Liang Y, Zheng G, Xia C, Zuo S, Ge S, Yang R, et al. Synthesis of ultra-high strength structured material from steam-modified delignification of wood. *J Clean Prod* 2022;351:131531.
- [17] Huang Y, Lin Q, Fu F, Lin L, Yu W. Scalable high-performance wood-based composites prepared by hydro-mechanical treatment. *Compos B Eng* 2023;267: 111041.
- [18] Chen Y, Dang B, Wang C, Wang Y, Yang Y, Liu M, et al. Intelligent designs from nature: biomimetic applications in wood technology. *Prog Mater Sci* 2023;139: 101164.
- [19] Song J, Chen C, Zhu S, Zhu M, Dai J, Ray U, et al. Processing bulk natural wood into a high-performance structural material. *Nature* 2018;554(7691):224–8.
- [20] Luan Y, Fang C-H, Ma Y-F, Fei B-H. Wood mechanical densification: a review on processing. *Mater Manuf Process* 2021;37(4):359–71.
- [21] Gan W, Chen C, Wang Z, Song J, Kuang Y, He S, et al. Dense, self-formed char layer enables a fire-retardant wood structural material. *Adv Funct Mater* 2019;29(14): 1807444.
- [22] Tang Q, Zou M, Gao K, Chang L, Gao L, Guo W. Laminating delignified wood veneers toward high-strength, flame-retardant composites for structural applications. *ACS Sustainable Chem Eng* 2021;9(32):10717–26.
- [23] Luan Y, Fang C-H, Ma Y-F, Fei B-H. Wood mechanical densification: a review on processing. *Mater Manuf Process* 2022;37(4):359–71.
- [24] Chen G, Chen C, Pei Y, He S, Liu Y, Jiang B, et al. A strong, flame-retardant, and thermally insulating wood laminate. *Chem Eng J* 2020;383:123109.
- [25] Fan Z, Sun H, Zhang L, Zhao X, Hu Y. Lightweight, high-strength wood prepared by deep eutectic solvent treatment as a green structural material. *ACS Sustainable Chem Eng* 2022;10(29):9600–11.
- [26] Wu J, Fan Q, Wang Q, Guo Q, Tu D, Chen C, et al. Improved performance of poplar wood by an environmentally-friendly process combining surface impregnation of a reactive waterborne acrylic resin and unilateral surface densification. *J Clean Prod* 2020;261:121022.
- [27] Ruiz-Hitzky E, Darder M, Aranda P, Ariga K. Advances in biomimetic and nanostructured biohybrid materials. *Adv Mater* 2010;22(3):323–36.
- [28] Fan W, Shan C, Guo H, Sang J, Wang R, Zheng R, et al. Dual-gradient enabled ultrafast biomimetic snapping of hydrogel materials. *Sci Adv* 2019;5(4):eaav7174.
- [29] Koyama M, Zhang Z, Wang M, Ponge D, Raabe D, Tsuzaki K, et al. Bone-like crack resistance in hierarchical metastable nanolaminated steels. *Science* 2017;355(6329): 1055–7.
- [30] Jiang SJ, Wang MH, Wang ZY, Gao HL, Chen SM, Cong YH, et al. Radially porous nanocomposite scaffolds with enhanced capability for guiding bone regeneration in vivo. *Adv Funct Mater* 2022;32(18):2110931.
- [31] Zhu W, Wang J, Sun W, Zhou S, He M. Preparation of gradient hydrogel for pressure sensing by combining freezing and directional diffusion processes. *Chem Eng J* 2023;451:138335.
- [32] Kokkinis D, Bouville F, Studart AR. 3D printing of materials with tunable failure via bioinspired mechanical gradients. *Adv Mater* 2018;30(19):1705808.
- [33] Guo J, Li C, Ling S, Huang W, Chen Y, Kaplan DL. Multiscale design and synthesis of biomimetic gradient protein/biosilica composites for interfacial tissue engineering. *Biomaterials* 2017;145:44–55.
- [34] Pan Q, Zhang L, Feng R, Lu Q, An K, Chuang AC, et al. Gradient cell-structured high-entropy alloy with exceptional strength and ductility. *Science* 2021;374 (6570):984–9.
- [35] Wen SM, Chen SM, Gao W, Zheng Z, Bao JZ, Cui C, et al. Biomimetic gradient bouligand structure enhances impact resistance of ceramic-polymer composites. *Adv Mater* 2023;35(21).
- [36] Zhang ZB, Gao HL, Wen SM, Pang J, Zhang SC, Cui C, et al. Scalable manufacturing of mechanical robust bioinspired ceramic-resin composites with locally tunable heterogeneous structures. *Adv Mater* 2023;35(14).
- [37] Wang K, Zhang T, Li C, Xiao X, Tang Y, Fang X, et al. Shape-reconfigurable transparent wood based on solid-state plasticity of polythiourethane for smart building materials with tunable light guiding, energy saving, and fire alarm actuating functions. *Compos B Eng* 2022;246:110260.
- [38] Ge S, Shi Y, Chen X, Zhou Y, Naushad M, Verma M, et al. Sustainable upcycling of plastic waste and wood fibers into high-performance laminated wood-polymer composite via one-step cell collapse and chemical bonding approach. *Adv Compos Hybrid Mater* 2023;6(4).
- [39] Chen C, Tu D, Zhou Q, Zhou J, Wang X, Cherdchim B, et al. Development and evaluation of a surface-densified wood composite with an asymmetric structure. *Construct Build Mater* 2020;242:118007.
- [40] Zhang X, Fan Q, Chen C, Hao X, Liu Z, Ou R, et al. Enhanced mechanical performance and fire resistance of poplar wood: unilateral surface densification assisted with N/P doped acrylic resin impregnation. *Construct Build Mater* 2023; 398:132470.
- [41] Chen G, Wu Z, Shen Z, Li H-Y, Li J, Lü B, et al. Scalable, strong and water-stable wood-derived bioplastic. *Chem Eng J* 2022;439:135680.
- [42] Fu Q, Ansari F, Zhou Q, Berglund LA. Wood nanotechnology for strong, mesoporous, and hydrophobic biocomposites for selective separation of oil/water mixtures. *ACS Nano* 2018;12(3):2222–30.
- [43] Samanta P, Samanta A, Montanari C, Li Y, Maddalena L, Carosio F, et al. Fire-retardant and transparent wood biocomposite based on commercial thermoset. *Compos Appl Sci Manuf* 2022;156:106863.
- [44] Altgen M, Awais M, Altgen D, Klüppel A, Mäkelä M, Rautkari L. Distribution and curing reactions of melamine formaldehyde resin in cells of impregnation-modified wood. *Sci Rep* 2020;10(1).
- [45] Gibier M, Sadeghisadeghabad M, Girods P, Zoulalian A, Rogaume Y. Furniture wood waste depollution through hydrolysis under pressurized water steam: experimental work and kinetic modeling. *J Hazard Mater* 2022;436:129126.
- [46] Zhang B, Chang Z, Li J, Li X, Kan Y, Gao Z. Effect of kaolin content on the performances of kaolin-hybridized soybean meal-based adhesives for wood composites. *Compos B Eng* 2019;173:106919.
- [47] Tamrakar S, Kiziltas A, Mielewski D, Zander R. Characterization of kenaf and glass fiber reinforced hybrid composites for underbody shield applications. *Compos B Eng* 2021;216:108805.
- [48] Salim MS, Ariawan D, Ahmad Rasyid MF, Ahmad Thirmizir MZ, Mat Taib R, Mohd Ishak ZA. Effect of fibre surface treatment on interfacial and mechanical properties of non-woven kenaf fibre reinforced acrylic based polyester composites. *Polym Compos* 2017;40(S1).
- [49] Fu Q, Medina L, Li Y, Carosio F, Hajian A, Berglund LA. Nanostructured wood hybrids for fire-retardancy prepared by clay impregnation into the cell wall. *ACS Appl Mater Interfaces* 2017;9(41):36154–63.
- [50] Šimůnková K, Reinprecht L, Nábelková J, Hýšek Š, Kindl J, Borůvka V, et al. Caffeine – perspective natural biocide for wood protection against decaying fungi and termites. *J Clean Prod* 2021;304:127110.
- [51] Alade AA, Naghizadeh Z, Wessels CB, Stolze H, Militz H. Characterizing surface adhesion-related chemical properties of copper azole and disodium octaborate tetrahydrate-impregnated *Eucalyptus grandis* wood. *J Adhes Sci Technol* 2023;37 (15):2261–84.
- [52] Codina R, Lockey RF, Diwadkar R, Mobly LL, Godfrey S. Disodium octaborate tetrahydrate (DOT) application and vacuum cleaning, a combined strategy to control house dust mites. *Allergy* 2003;58(4):318–24.
- [53] Iyigundogdu Z, Basar B, Couvreur R, Tamrakar S, Yoon J, Ersoy OG, et al. Thermoplastic elastomers containing antimicrobial and antiviral additives for mobility applications. *Compos B Eng* 2022;242:110060.
- [54] Mohareb A, Thévenon MF, Wozniak E, Gérardin P. Effects of polyvinyl alcohol on leachability and efficacy of boron wood preservatives against fungal decay and termite attack. *Wood Sci Technol* 2011;45(3):407–17.
- [55] Zhou Z, Liu T, Tan Y, Zhou W, Wang Y, Shi SQ, et al. A high-performance, full-degradable bioinspired newspaper-based composite enhanced by borate ester bonds. *Compos Sci Technol* 2023;241:110130.
- [56] Lv J, Li X, Yin H, Wang L, Pei Y, Lv X. Controlled release of vancomycin hydrochloride from a composite structure of polymeric films and porous fibers on implants. *Chem Eng J* 2017;325:601–10.
- [57] Zhang D, Yang K, Zhang T, Luo M, Li M, Li Z, et al. A facile “thick to thin” strategy for integrating high volumetric energy density and excellent flexibility into MXene/wood free-standing electrode for supercapacitors. *Chem Eng J* 2023;460: 141733.
- [58] Li X, Wang Z, Li W, Sun J. Superstrong water-based supramolecular adhesives derived from poly(vinyl alcohol)/Poly(acrylic acid) complexes. *ACS Mater Lett* 2021;3(6):875–82.
- [59] Militz H. Fire retardant treatment of wood—state of the art and future perspectives. In: *Wood & fire safety: proceedings of the 9th international conference on wood & fire safety* 2020. Springer Nature; 2020. p. 97.
- [60] Peng Y, Fan Q, Ou R, Hao X, Guo C, Liu Z, et al. Modification of poplar wood cells using 1,3-dihydroxymethyl-4,5-dihydroxyethylideneurea/alkaline lignin for enhanced mechanical properties and decay resistance. *Construct Build Mater* 2023; 368:130354.
- [61] Iyigundogdu Z, Saribas I. The effect of various boron compounds on the antimicrobial activity of hardened mortars. *Construct Build Mater* 2022;351: 128958.
- [62] Dong Y, Liu X, Liu J, Yan Y, Liu X, Wang K, et al. Evaluation of anti-mold, termite resistance and physical-mechanical properties of bamboo cross-linking modified by polycarboxylic acids. *Construct Build Mater* 2021;272:121953.
- [63] Kartal SN, Hwang W-J, Yamamoto A, Tanaka M, Matsumura K, Imamura Y. Wood modification with a commercial silicon emulsion: effects on boron release and decay and termite resistance. *Int Biodeterior Biodegrad* 2007;60(3):189–96.
- [64] Kose Demirel G, Temiz A, Palanti S, Terziev N. Decay, insect, and termite resistance of wood modified with epoxidized vegetable oils. *Holzforschung* 2021;75(3): 281–7.



ISSN 0950-4230

Construction and Building **MATERIALS**

*An International Journal
Dedicated to the Investigation
and Innovative Use of
Materials in Construction
and Repair*

CONSTRUCTION & BUILDING MATERIALS
ELSEVIER

Actions for selected articles

Select all / Deselect all



Download PDFs



Export citations



Show all article previews



View PDF

Article preview



Research article • Full text access

Def-related expansion in concrete samples and blocks with nano-sio₂

Mariana O.G.P. Bragança, Nicole P. Hasparyk, Kleber F. Portella, Bruna Gomes Dias, ... Selmo C. Kuperman
Article 131009



View PDF

Article preview



Research article • Full text access

Fast realization of high-strength, repeatable, damp-heat resistant bamboo-strip scarf bonding joints via hot-melt adhesives

Ruijian Chen, Qi Fan, Rongxian Ou, Xiaolong Hao, Qingwen Wang
Article 131331



View PDF

Article preview



Research article • Full text access

Experimental study on dynamic mechanical properties and damage characteristics of coral reef limestone

Hui Zhang, Huiqi Ren, Chaomin Mu, Xiangyun Wu, ... Fei Wang
Article 131007



View PDF

Article preview

Contents

77

Review Articles

Research Articles

Erratum





Fast realization of high-strength, repeatable, damp-heat resistant bamboo-strip scarf bonding joints via hot-melt adhesives

Ruijian Chen^{a,1}, Qi Fan^{a,b,1}, Rongxian Ou^{a,b,*}, Xiaolong Hao^{a,b}, Qingwen Wang^{a,b,*}

^a Institute of Biomass Engineering, Key Laboratory of Energy Plants Resource and Utilization (Ministry of Agriculture and Rural Affairs), South China Agricultural University, Guangzhou 510642, China

^b Key Laboratory for Biobased Materials and Energy of Ministry of Education, College of Materials and Energy, South China Agricultural University, 483 Wushan Road, Guangzhou 510642, China

ARTICLE INFO

Keywords:

Bamboo strip
Hot-melt adhesives
Scarf jointing
Damp-heat aging
Tensile strength

ABSTRACT

Bamboo, which has excellent mechanical strength, is an ideal raw material for manufacturing high-performance bio-composites. However, due to a lack of fast, high-strength lengthening technology for bamboo units, the large-scale, mechanized, continuous production of bamboo woven materials has not been fully developed. In this work, bamboo strips (BS) with 0.5 mm thickness were used as a basic unit to prepare lengthened bamboo strips with the scarf jointing method. The effects of scarf jointed angles and hot-melt adhesive type on the scarf bonding performance were systematically investigated. The tensile strength of BS scarf joints appears to increase as the scarf joint angle decrease. Scarf joints prepared with low-cost thermoplastic polyurethane (TPU) film outperform those prepared with reactive polyurethane (PUR) or ethylene vinyl acetate copolymer (EVA) hot-melt adhesives in terms of maximum tensile strength (197.9 MPa), secondary repeated bonding performance, and damp-heat aging resistance, where tensile strength of 136 MPa was retained after a 120 h cycle aging test. Specimens bonded with PUR adhesive are resistant to damp-heat aging, but show unsatisfactory secondary repeated bonding performance. The tensile strength and damp-heat aging resistance of EVA bonded specimens are unacceptable due to an unreliable bonding interface. We developed a facile solution for high-strength BS lengthening with repeated bonding and damp-heat resistant characteristics, which may provide technical support for the large-scale, mechanized manufacturing of bamboo-based composites.

1. Introduction

Bamboo is a renewable natural resource that is highly ecologically, economically, and culturally valuable [1–3]. Compared with trees, bamboo has the advantages of fast growth, early harvest, and high yield [4–6], making it an ideal potential replacement for wood [7]. The special tissular structure of bamboo provides it excellent physical and mechanical properties [8,9], including strength, toughness, and hardness [10–13]. Bamboo strip/fiber, known as “natural glass fiber”, can be used to replace glass fiber or carbon fiber to manufacture lightweight high-strength bio-composites [14,15]. Vigorous development across the bamboo industry would benefit the natural environment, revitalize rural economies, and assist in satisfying “double carbon” goals [16].

The length of commercial bamboo is generally not more than 3.2 m [17]. In the continuous mechanical manufacturing of large-scale

bamboo weaving or bamboo winding materials, unit materials in the form of strips, skins, or bundles must be lengthened [18]. Bamboo unit materials are generally lengthened by finger joint, lap joint, scarf joint, or buckle joint methods, all of which require adhesives [18–21]. Finger and snap joints are commonly used to lengthen thick bamboo unit materials, but the resulting joints cannot tolerate strong tensile stress or large bending load, making the materials vulnerable to failure and damage [20,22].

Overlap and scarf joints are commonly used to lengthen thin bamboo unit materials; these forms provide a large bonding area, uniform stress distribution, and resistance to tensile and bending stresses [23–26]. However, the concave and convex parts of overlap joints make the strip surfaces uneven, which easily creates defects [27]. Scarf joints have no uneven parts, however, and prevent the concentration of shear stress by reducing the secondary bending moment and peel stress [28,29]. Thus,

* Corresponding authors.

E-mail addresses: rongxian_ou@scau.edu.cn (R. Ou), qwqiang@scau.edu.cn (Q. Wang).

¹ Ruijian Chen and Dr. Qi Fan equally contributed to this work and were listed as co-first authors.

the scarf joint is the ideal form to lengthen bamboo strip (BS).

Existing bonding and lengthening methods for bamboo unit materials are usually based on thermosetting adhesives such as phenolic resin, urea formaldehyde resin, and epoxy resin [20,22,30]. These adhesives need to be cured by hot (cold) pressure for long periods of time, which drives down production efficiency. Moreover, phenolic resin and urea formaldehyde resin release free formaldehyde into the natural environment [31] and the joints they form are brittle, low in strength, not damp-heat resistant, and incapable of repeated bonding [32,33].

Hot-melt adhesive is a plastic adhesive that can change its physical state as temperature changes within a certain range [34]. It is popular as it is green, strong, and bonds quickly [35]. Existing commercial hot-melt adhesives mainly include thermoplastic polyurethane (TPU), reactive polyurethane hot-melt adhesive (PUR), and ethylene vinyl acetate copolymer (EVA) [36]. Among them, TPU is formed by the copolymerization of diisocyanate molecules with polyols including macromolecular polyols and low molecular polyols (chain extenders) [37]. TPU film has high bonding strength and aging resistance [38]. The main component of PUR is isocyanate terminated polyurethane prepolymer, which has excellent bonding strength, temperature resistance, chemical corrosion resistance, and aging resistance [39]. EVA hot-melt adhesive cures quickly, adheres strongly, and is somewhat flexible [37].

TPU adhesive film, PUR, and EVA were utilized in this study to fabricate fast, high-strength, repeatable, and damp-heat resistant BS scarf bonding joints. The effects of different BS scarf joint slopes on the bonding strength of the three hot-melt adhesives were evaluated accordingly, as well as the damp-heat aging resistance and secondary repeated bonding of the joints. Our goal is to develop a high strength, fast lengthening technology for BS that allows for continuous mechanical braiding or winding.

2. Materials and methods

2.1. Materials

Four-year-old Moso bamboo (*Phyllostachys pubescens* Mazel) without stress, biological degradation, or structural defects was collected from

Anxi County, Fujian Province, China. As shown in Fig. 1a, bamboo culms were cut from 4-m-long units at a height of 50 cm above ground. Internode bamboo strips measuring 50 mm × 10 mm × 0.5 mm (L × T × R) were prepared from the first layer outside after removal of the bamboo green. All BS were conditioned in a climate room at 20 °C and 65 % relative humidity (RH) until equilibrium moisture content (EMC) was reached before further processing. Nine types of TPU adhesive films with various melting points and thicknesses were purchased from Tianhai Hot Melt Adhesive Technology Co., Ltd., China. PUR (TECH-NOMELT 270/7S) and EVA (TECHNOMELT KS3561) hot-melt adhesives were supplied by Henkel (China) Investment Co., Ltd. The detailed technical parameters of the adhesives are listed in Table 1.

2.2. Methods

The scarf jointed surfaces were manually sanded using 240-mesh sanding belt. Scarf angles of 1.79, 2.05, 2.39, and 2.86 were selected corresponding to slopes of 1:32, 1:28, 1:24, and 1:20, respectively. The

Table 1
Melting point and scarf jointed processing parameters of the hot-melt adhesives.

Type	Melting point (°C)	Set temperature (°C)	Cold pressing time (s)	Cold pressing pressure (bar)
TPU-1 ^a	75~80	90 ± 2	8	1.5
TPU-2 ^b	90 ~ 95	110 ± 2	8	1.5
TPU-3 ^b	95 ~ 105	115 ± 2	8	1.5
TPU-4 ^b	115 ~ 120	130 ± 2	8	1.5
TPU-5 ^b	120 ~ 125	135 ± 2	8	1.5
PUR	120 ~ 140	130 ± 2	8	1.5
EVA	92 ~ 102	110 ± 2	8	1.5

^a nominal thickness of 0.03 mm, 0.06 mm, 0.10 mm, 0.13 mm, 0.16 mm;

^b nominal thickness of 0.10 mm.

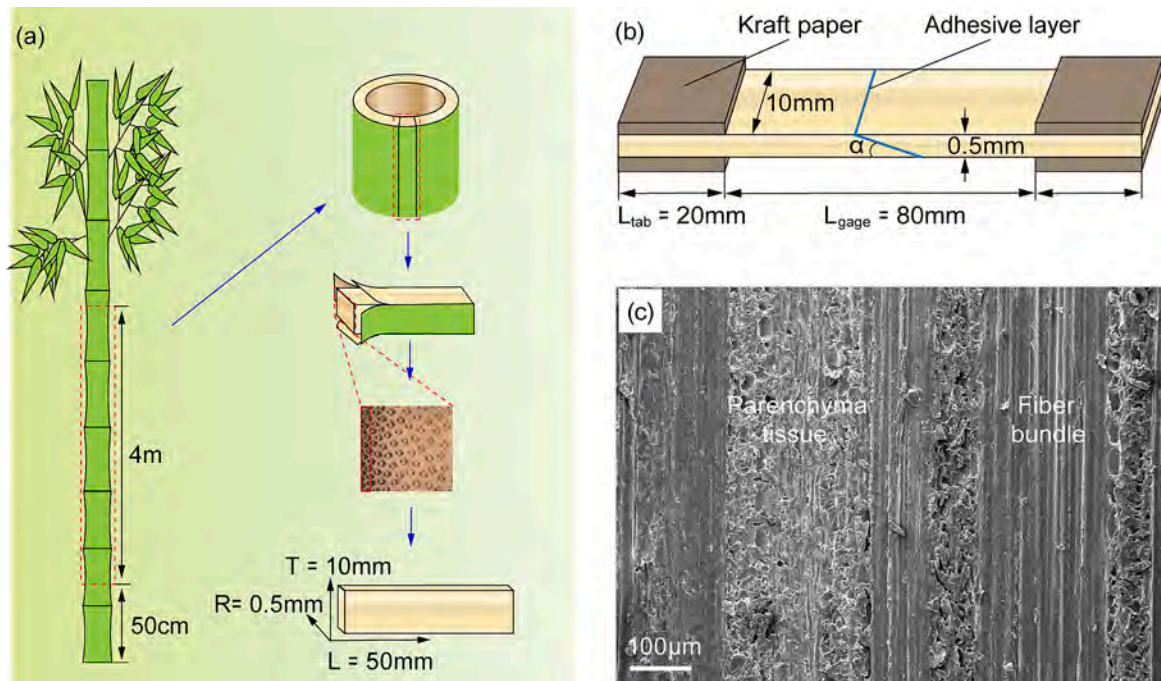


Fig. 1. (a) Schematic illustration of the preparation of bamboo strips. (b) A schematic of the scarf jointed specimens and (c) The SEM micrograph of the scarf sanded surface.

hot-melt adhesives were pre-melted to reach set temperatures (Table 1) and applied to the scarf sanded surfaces. The gummed scarf sanded surfaces were immediately docked with each other, then the jointed surfaces were cold-pressed at room temperature for 8 s under 1.5 bar. The scarf jointed bamboo strip specimens (Fig. 1b) were conditioned at 20 °C and 65 % RH until EMC was reached prior to testing.

2.2.1. Uniaxial tensile tests

Kraft papers measuring $20 \times 10 \times 1$ mm were bonded to the grip areas of the specimens to enable uniform load distribution and reduce the likelihood of failure (Fig. 2). Uniaxial tensile loading was applied to the scarf jointed specimens according to ASTM D3039 by a universal testing instrument (MDW-20 J, Tianchen Testing Machine Manufacturing Co., Ltd., Jinan, China) at a crosshead speed of 5 mm min^{-1} . The tensile strength of the scarf joints was reported here is the average value of five replicates.

2.2.2. Damp-heat (DH) aging

The scarf jointed specimens were subjected to alternate DH aging for ten 24-h cycles according to GB/T 2573–2008: (1) 25 °C–60 °C within 2 h under 95 % RH, (2) 60 °C for 10 h under (93 ± 3)% RH, (3)

60 °C–25 °C within 2 h under 95 % RH, (4) 25 °C for 10 h under 95 % RH. Specimens aged for 24 h, 72 h, 120 h, 168 h, and 240 h were collected for uniaxial tensile tests. The fractured 240 h-aged specimens after tensile tests were rebounded before retesting the tensile strength of the scarf joints. Five replicates were used for each specimen.

2.2.3. Scanning electron microscopy (SEM)

The bonding layer of the scarf jointed specimens before uniaxial tensile tests and the scarf jointed surfaces after uniaxial tensile tests were observed using an EVO18 scanning electron microscope (Carl Zeiss, Oberkochen, Germany) at 10 kV.

3. Results and discussion

3.1. Scarf bonding performance of TPU adhesive film

3.1.1. Scarf bonding joints with different slopes

For the scarf jointed bamboo strips prepared with different slopes, the hot-melt adhesive film was pre-heated and then quickly cold-pressed into the designated shape. The adhesive layer was evenly distributed on the scarf surface to be glued with no (or very little) overflow at the joint edge.

The tensile strength, stress–strain curves, and typical failure forms of BS scarf bonding joints prepared with TPU-1 adhesive film are shown in Fig. 2. As shown in Fig. 2a, the tensile strength of the BS scarf joints increases 70.94 % (from 109.6 MPa to 187.4 MPa) with decrease in slope. As shown in Fig. 2b, under tensile loading, the strain at failure and maximum tensile strength increase with as the slope decreases. When the scarf jointed specimen is subjected to a tensile load, the tensile stress of the adhesive joint has a normal stress perpendicular to the bonding interface and a shear stress parallel to the bonding interface [40]. The bonding interface of the specimen is destroyed under the combined action of the two stresses. Since the applied tensile load is parallel to the central direction of the specimen, there is no torsion and the stress distribution along the bonding interface is uniform. As shown in Fig. 2c, the main failure form is in the adhesive layer accompanied by a small amount of interface failure, while the BS remains undamaged.

To sum up, within the range set in the experiment, the scarf jointed BS prepared with a slope of 1/32 show the best tensile strength. A decrease in the slope of the bonding surface increases the bonding area and thus the bonding strength. We used a slope of 1/32 in subsequent tests accordingly.

3.1.2. Scarf bonding performance of TPU with different melting points

Scarf jointed BS with a scarf slope of 1/32 were prepared using TPU adhesive films with thickness of 0.1 mm and five different melting points. The tensile strength, stress–strain curves, and tensile failure modes are shown in Fig. 3. The melting point of TPU adhesive film significantly influences the tensile strength of the scarf jointed BS: It decreases first and then increases as the melting point increases. The maximum tensile strength is 187.4 MPa when the melting point is 75 °C ~ 80 °C and the lowest tensile strength is 79.8 MPa when the melting point is 95–105 °C. This is because TPU is a linear polymer with a large number of intermolecular hydrogen bonds. Its relatively low melting point indicates small molecular weight and low melt viscosity, which are conducive to the infiltration in bamboo fibers. These properties altogether give TPU a thick bonding transition layer resulting in high bonding strength, particularly as the melting point continues to increase.

As shown in Fig. 3b, under tensile loading, the stress and strain of the scarf jointed specimen prepared with TPU decrease first and then increase as the melting point of the adhesive film increases. The stress and strain of the scarf bonding joints prepared with TPU-1 adhesive film is the largest. As shown in Fig. 3c, the main failure mode of the joint is cohesive failure of the adhesive layer. Moreover, there was no damage to the BS in this case. TPU-1 adhesive film shows the lowest melting point

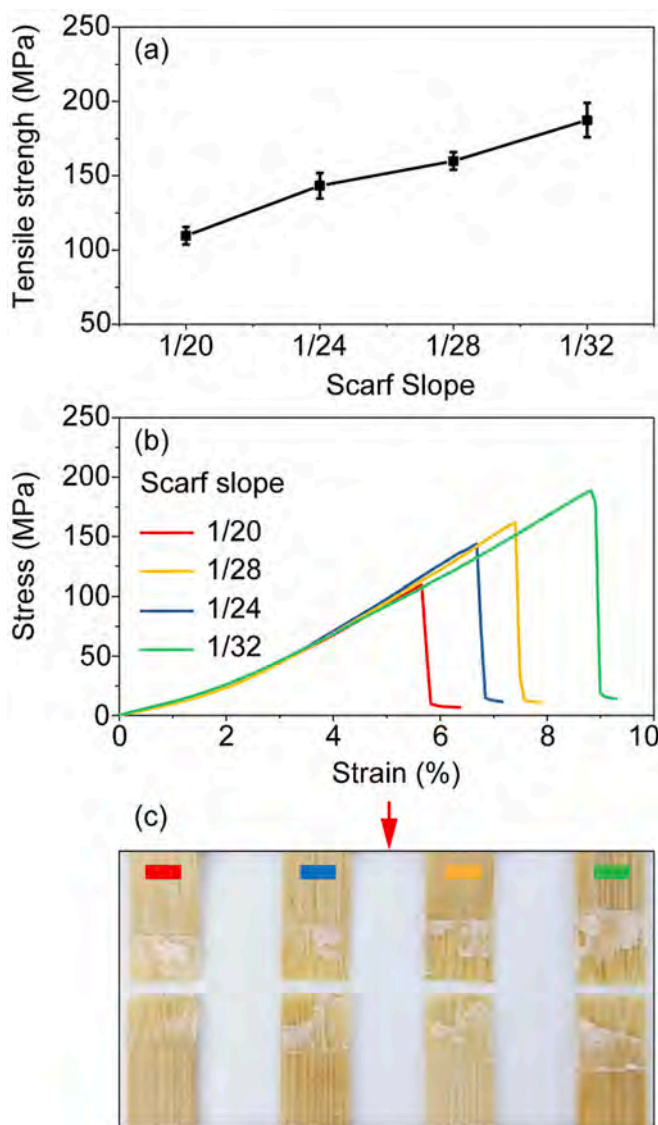


Fig. 2. Tensile performance of lengthening bamboo strips using TPU-1 films by different slopes of scarf bonding. (a) Tensile strength, (b) stress–strain curves, and (c) photos of failure forms.

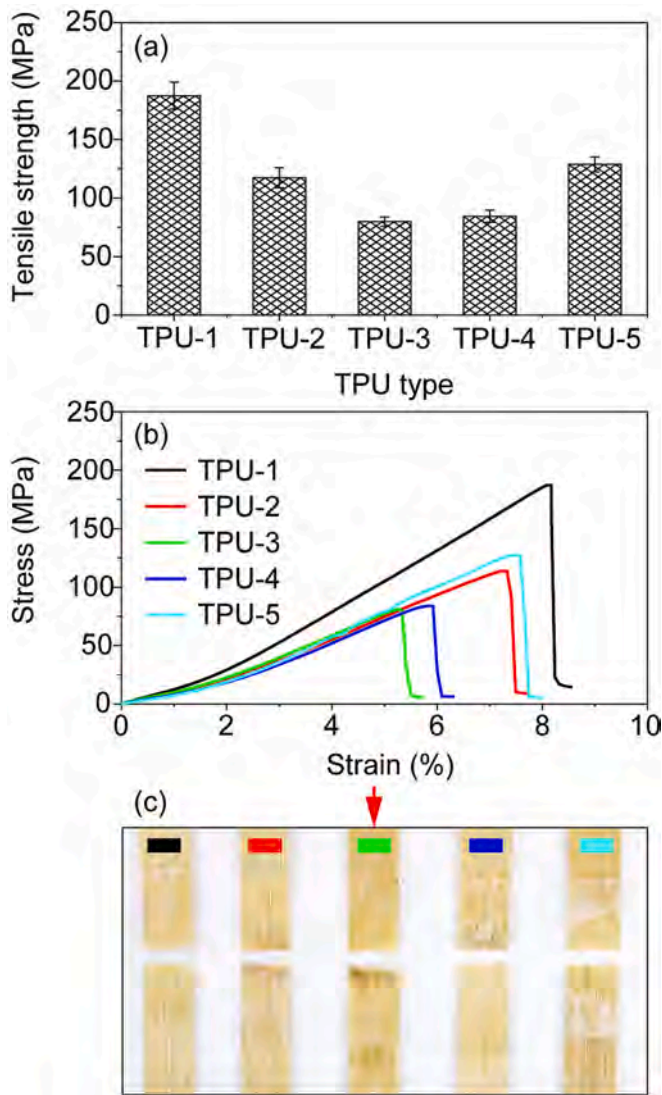


Fig. 3. Tensile performance of scarf jointed specimens prepared by TPU adhesive films with five different melting points. (a) Tensile strength, (b) stress-strain curves, and (c) photos of failure forms.

and yields scarf jointed specimens with optimal tensile properties. Thus, we used TPU-1 adhesive film in all subsequent tests.

3.1.3. Scarf bonding performance of TPU adhesive film with different thickness

TPU-1 adhesive films with thickness of 0.03 mm, 0.06 mm, 0.10 mm, 0.13 mm, and 0.16 mm were used to produce scarf jointed samples with a slope of 1/32. The resulting tensile strength, stress-strain curve, and typical tensile failure form are shown in Fig. 4. The tensile strength of the scarf jointed specimen increases first and then decreases as the film thickness increases, but there is no significant difference in strength. The tensile strength is highest with a 0.06 mm thick adhesive film at 197.9 MPa, which exceeds the average tensile strength of bamboo knots [41]. The minimum tensile strength appears with 0.16 mm thick adhesive film, at 170.8 MPa.

As shown in Fig. 4b, the stress and strain values firstly increase and then decrease with the increase of TPU film thickness. This is because thicker adhesive layers are more prone to shear failure and the damage forms of adhesive layer failure and interface failure are more obvious. Considering cost as well as bonding performance, TPU-1 adhesive film with 0.06 mm thickness is the best choice for preparing high-strength scarf jointed BS.

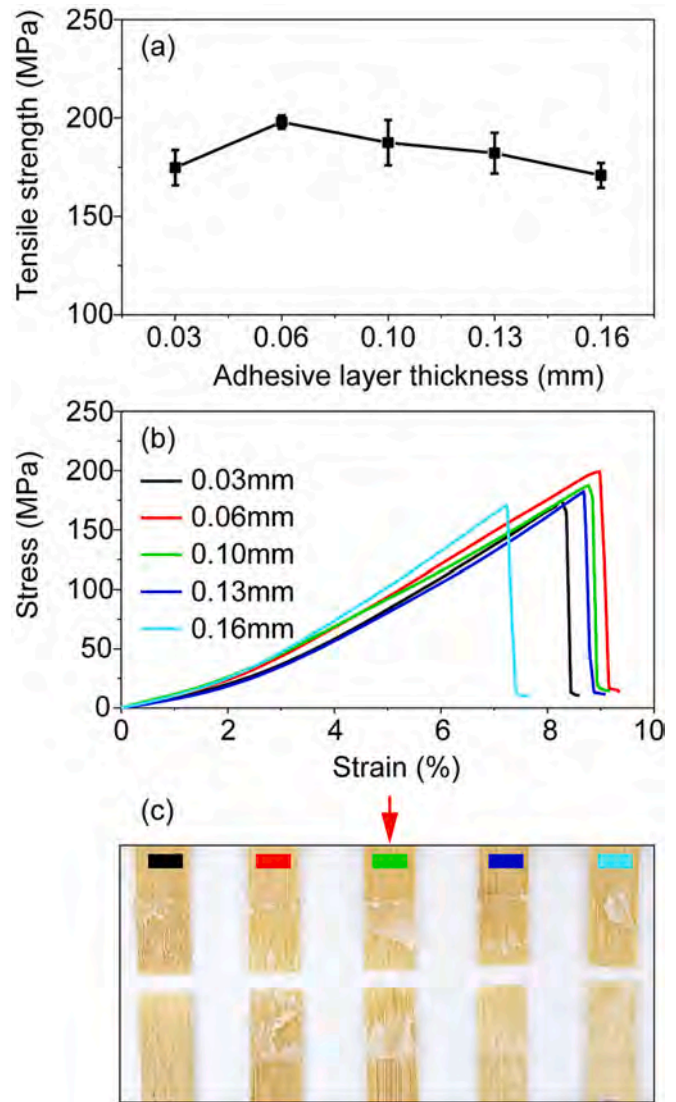


Fig. 4. Tensile performance of scarf jointed specimens prepared by TPU adhesive films with five different thicknesses. (a) Tensile strength, (b) stress-strain curves, and (c) photos of failure forms.

3.2. Comparison of scarf joint performance among TPU, PUR, and EVA

We next prepared scarf jointed BS with a slope of 1/32 with TPU-1 adhesive film (0.06 mm thickness), PUR, and EVA hot-melt adhesive to test the respective effects of the adhesives on the tensile strength, stress-strain curves, and tensile failure mode of the strips. As shown in Fig. 5a, the tensile strength of the PUR scarf jointed specimen is 180.0 MPa while the adhesive properties of EVA are relatively poor at only 89.3 MPa, which is only 45 % of TPU-1. As shown in Fig. 5b, the maximum load strains of scarf jointed BS specimens prepared with TPU-1 and EVA are 9 % and 8 %, respectively, while the maximum load strain of the PUR specimen is 14 %. Comparing with very few existing relevant studies (Table 2)[42–44], we have not only realized a faster (within 8 s) lengthening technique of bamboo-strips, but also the lengthened bamboo-strips have the optimal tensile strength (198 MPa).

In addition, because EVA has good resilience, the tensile stress strain curve of EVA bonded scarf joints differs from those of TPU-1 and PUR (Fig. 5b). When the EVA scarf jointed test piece was damaged by the maximum tensile load, the adhesive layer showed cohesive failure but was not completely broken. We found a certain amount of elongated filiform adhesive layer bonded to the scarf jointed surface, which makes

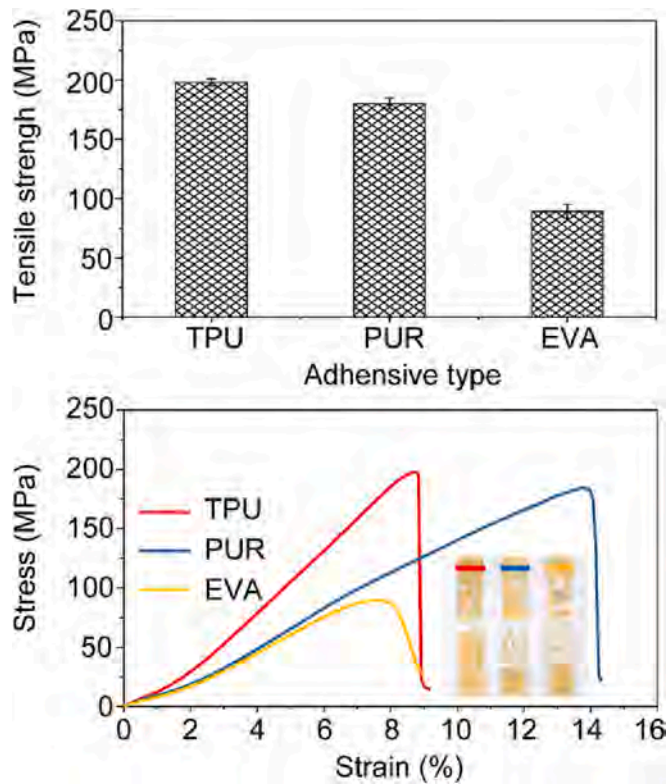


Fig. 5. Tensile performance of scarf jointed specimens prepared with different hot melt adhesives. (a) Tensile strength and (b) stress-strain curves and photos of failure forms.

Table 2
Comparison of other relevant researches on the scarf joint technology.

Material	Adhesive type	Processing technology	Pressing technology Time/ s	Pressure/ MPa	Tensile strength /MPa
6.5 mm Bamboo strip [42]	polyurethane	Cold pressing	10,800	1.0	106.26 ± 7.00
6.5 mm Bamboo strip [42]	polyurethane	Cold pressing	10,800	1.2	122.85 ± 20.56
6.5 mm Bamboo strip [42]	polyurethane	Cold pressing	10,800	1.5	67.30 ± 16.28
2.0 mm Poplar veneer [43]	urea formaldehyde resin	120 °C Hot pressing	360	0.65	38.74 ± 7.25
5.0 mm Birch veneer [44]	polyvinyl acetate	Cold pressing	86,400	0.5	84.28 ± 10.37
This work	TPU-1	Cold pressing	8	0.15	197.91 ± 3.39
This work	PUR	Cold pressing	8	0.15	180.07 ± 4.59
This work	EVA	Cold pressing	8	0.15	89.32 ± 5.87

the stress strain curve drop slowly though the damaged test piece retains some residual strength.

The maximum tensile strength of the TPU-1 scarf jointed specimen is mainly attributable to the uniform, thin adhesive layer at the joint

interface creating a tight seal at the surface (Fig. 6a). These joints were subjected to uniform, longitudinal shear stress. PUR and EVA are too viscous to be coated into such a layer on the inclined grinding surface of BS.

The adhesive layer thickness of PUR and EVA is about 0.089 mm and 0.081 mm respectively, which are thicker than TPU-1. As shown in Fig. 6a, the uneven thicknesses of the adhesive layers give the BS specimens inconsistent bonding tightness. There are air holes in the adhesive layers of PUR and EVA as well (Fig. 6a), which ultimately create uneven longitudinal shear stress and reduce bonding strength. As shown in Fig. 6b, the fracture mode of the adhesive layer of the TPU bonded joint is dominated by brittle fracture behavior. By contrast, the silver texture of the residual adhesive layer surface of EVA bonded joints indicates ductile fracture. PUR bonded joints demonstrate a quasi-brittle fracture behavior. This result is consistent with the stress-strain curves (Fig. 5b).

In conclusion, the smaller molecular weight and uniformity of the TPU-1 adhesive film with low melt viscosity yields wetting and permeability in BS fabrication, resulting in excellent bonding strength. The reactive PUR adhesive contains chemically active polar groups that can react with moisture in the air; moisture and active hydroxyl (–OH) groups on the BS surface cause crosslinking in PUR. This irreversible, strong, non-covalent interaction yields high bonding strength. EVA hot-melt adhesive has certain flexibility but relatively low strength, allowing only physical adhesion with the inclined grinding surface of BS and resulting in poor tensile properties.

3.3. Damp-heat aging property of scarf bonding joints

The damp-heat aging properties of BS scarf jointed with the three hot-melt adhesives were tested via 10 240-h damp-heat aging cycles. As shown in Fig. 7a, the tensile strength of the TPU-1 scarf jointed specimen decreases gradually after the treatment. At 240 h, the tensile strength of the specimen decreases to 88.7 MPa, which is 55 % lower than the initial value. The TPU-1 adhesive film with uniform thickness created tight bonding in the joint between the two BS. Nevertheless, the adhesive layer of TPU-1 adhesive gradually stripped and damaged under the dual action of humidity and temperature field (Fig. 7b). This may be due to mechanical interlocking and non-covalent interaction as the main bonding mechanisms of TPU adhesive.

After damp-heat aging treatment, the tensile strength of PUR scarf jointed BS gradually decreased from 180 MPa to 155 MPa in the first three cycles, then increased slightly. The tensile strength of the specimen aged for 240 h (10 cycles) is 156.6 MPa, only 13 % lower than the initial value. This is mainly because after a long period of damp-heat cycling treatment with high and low temperatures, the –NCO of the PUR fully reacted with the ambient moisture and surface –OH of BS to form a tightly cross-linked network. However, the thermal expansion and cold contraction of the adhesive layer and BS caused a certain degree of failure of the crosslinked network and physical adhesive nails, which reduced the overall tensile property though high tensile strength was retained.

After the damp-heat aging treatment, the tensile strength of scarf bonding joints prepared with EVA hot-melt adhesive decreased sharply from the initial value 89.3 MPa to 20.5 MPa in the first cycle with only 3.5 MPa remaining after 240 h. On the one hand, the bonding strength of EVA hot melt adhesive and BS is low, which easily leads to the destruction of adhesive layer during the damp-heat aging treatment. On the other hand, the molecular structure of EVA hot melt adhesive is dominated by non-polar structure, which does not form covalent crosslinking with BS, resulting in the failure of bonding under the action of heat and humidity.

3.4. Secondary repeated bonding performance

After 240 h of damp-heat aging treatment, the broken scarf bonding

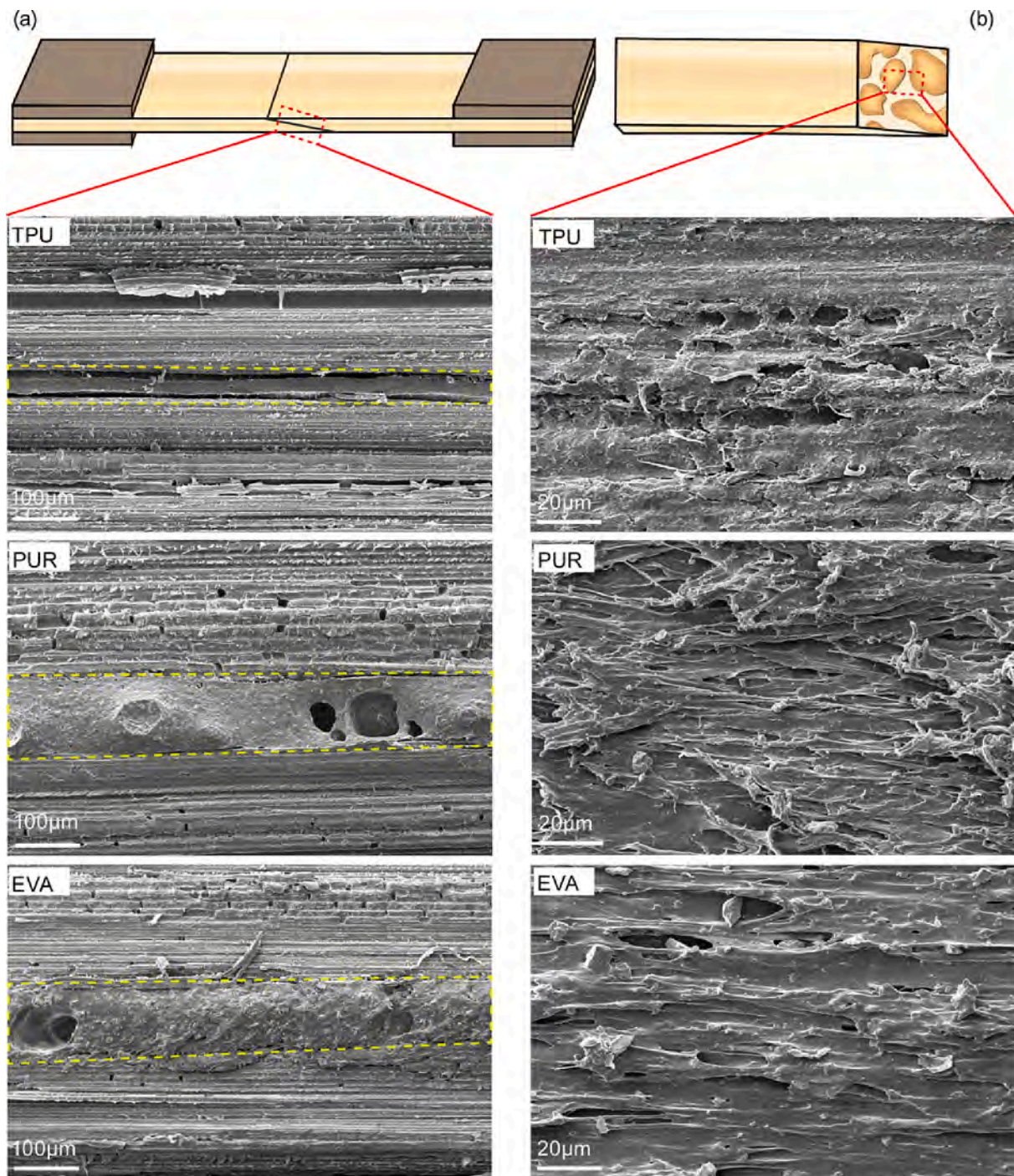


Fig. 6. SEM micrographs of scarf bonding joints. (a) Longitudinal sections of bonding interface and (b) the surfaces of residual adhesive layers after tensile failure.

joints of BS were remade by heating and melting the residual adhesive layer and cold-pressing. After this secondary repeated bonding, the tensile strength of scarf bonding joint specimens with TPU-1 and EVA increased by 13 % and 36 % of the initial values, respectively, to 223.8 MPa and 121.6 MPa (Fig. 8). This is mainly because TPU and EVA hot-melt adhesives have the thermal plasticity of linear polymer materials, resulting in excellent repeated bonding performance. In addition, the pores of the BS become larger after damp-heat aging, which increases the permeability of the adhesive layer during secondary repeated (repair) bonding under pressure. Therefore, the secondary bonding strength of TPU and EVA is higher than the primary bonding strength. However, the tensile strength of PUR scarf jointed specimens after 240 h

damp-heat aging and twice-repeated bonding decreases by 16 %, mainly because the melting point of reactive PUR adhesive increases and the active group decreases after the first melting, which drives down the bonding properties and tensile strength of the specimen.

4. Conclusion

We realized the rapid (within 8 s) and high-strength (198 MPa) lengthening of scarf jointed BS with repeatable bonding and damp-heat resistant characteristics in this study. The results may provide technical support for the mechanized, continuous weaving of bamboo units into high-strength reinforcement materials, as well as the continuous

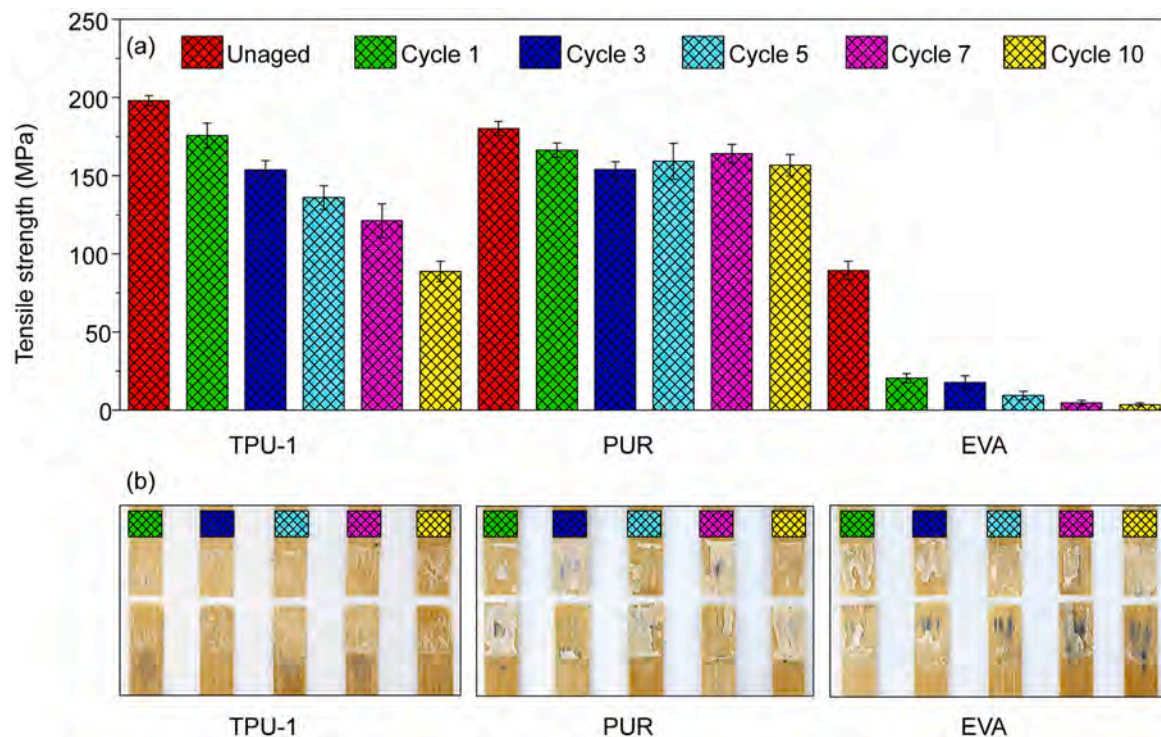


Fig. 7. Comparison of tensile performance of specimens with different hot melt adhesive by damp-heat aging treatment. (a) Tensile strength and (b) photos of failure forms.

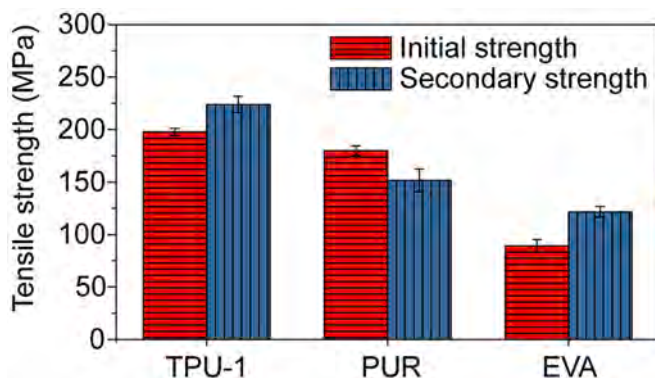


Fig. 8. Comparison of tensile strength of specimens with different hot melt adhesive by first and secondary repeated bonding.

manufacturing of large-area bamboo matrix composites.

(1) The scarf jointed BS prepared with TPU adhesive film at a slope of 1/32 and 0.06 mm thickness shows a maximum tensile strength of 198 MPa, which exceeds the average tensile strength of BS with nodes. The scarf jointed slope, melting point, and thickness of adhesive film significantly affect the tensile properties of the resulting jointed strips. A smaller slope indicates a larger bonding area. A thinner adhesive layer and a lower melting point of adhesive film enhanced the bonding properties and tensile strength.

(2) Comparing with TPU adhesive film, scarf jointed BS prepared with wet reactive PUR and EVA hot-melt adhesives show poor adhesive layer uniformity and require excessive amounts of adhesive that are likely to overflow at the edge. Therefore, the tensile properties of the specimens were found to be lower than those with the TPU film as well. Due to the moisture curing property of PUR, its scarf jointed specimens show excellent damp-heat aging resistance but poor secondary repeated bonding performance. In contrast, the thermoplastic TPU adhesive film has the highest bonding strength, its scarf jointed specimens have the

best comprehensive performance of damp-heat aging resistance and secondary repeated bonding properties.

Declaration of Competing Interest

The authors declare that they have no known competing financial interests or personal relationships that could have appeared to influence the work reported in this paper.

Data availability

Data will be made available on request.

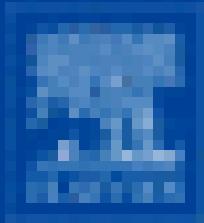
Acknowledgments

This work was financially supported by the Research and Development Program in Key Areas of Guangdong Province (2020B0202010008), the National Natural Science Foundation of China (32071698, 52103110), the China Postdoctoral Science Foundation (2021 M701258) and the Project of Key Disciplines of Forestry Engineering of Bureau of Education of Guangzhou Municipality.

References

- [1] M. Daba, Industrial, Carbon Sequestration and Climate Change Mitigation Potentials of Bamboo, *Journal of Scientific Research and Reports*. 12 (4) (2016) 1–8.
- [2] Y. Lou, Y. Li, K. Buckingham, G. Henley, G. Zhou, Bamboo and Climate Change Mitigation, *International Network for Bamboo & Rattan*, 2010. Technical Report.
- [3] Y.C. Tripathi, K. Kar, N.K. Vasu, Bamboo-A Renewable Resource of Incessant Possibilities, *Conservation and Management of Bamboo*, Resources (2009).
- [4] S. Yongjun, L. Enbin, Z. Guomo, S. Zhenming, Y. Shuhong, Bamboo Shoot Growth Model Based on the Stochastic Process and Its Application, *Scientia Silvae Sinicae*. 49 (9) (2013) 89–93.
- [5] L.I. Nianping, D. Zeng, Q. Wang, J. Long, Experimental Study on the Heat-transfer Characteristics of New Bamboo Structure Building, *Science & Technology Review*. 28 (20) (2010) 87–90.
- [6] Y. Zhang, J. Wang, Z. Ma, H. Zhou, Y. Yang, W. Zhang, S.O. Engineering, Effects of torrefaction temperature on composition and characteristics of gas-solid-liquid

- three-phase products in bamboo torrefaction process, Transactions of the Chinese Society of Agricultural Engineering. 34 (18) (2018) 242–251.
- [7] J. Zhou, W. Fu, Y. Qing, W. Han, Z. Zhao, B. Zhang, Fabrication and Performance of a Glue-Pressed Engineered Honeycomb Bamboo (GPEHB) Structure with Finger-jointed Ends as a Potential Substitute for Wood Lumber, *Bioresources*. 10 (2) (2015) 3302–3313.
 - [8] W. Liese, Research on bamboo, *Wood Science & Technology*. 21 (3) (1987) 189–209.
 - [9] M. Chen, L. Ye, H. Li, G. Wang, B. Fei, Flexural strength and ductility of moso bamboo, *Construction and Building Material*. 246 (2020), 118418.
 - [10] I.M. Low, Z.Y. Che, B.A. Latella, Mapping the structure, composition and mechanical properties of bamboo, *Journal of Materials Research*. 21 (8) (2006) 1969–1976.
 - [11] L. Zou, H. Jin, W.Y. Lu, X. Li, Nanoscale structural and mechanical characterization of the cell wall of bamboo fibers, *Materials science & engineering C*. 29 (4) (2009) 1375–1379.
 - [12] H. Li, S. Shen, The mechanical properties of bamboo and vascular bundles, *Journal of Materials Research*. 26 (21) (2011) 2749–2756.
 - [13] T. Tan, N. Rahbar, S.M. Allameh, S. Kwofie, W.O. Soboyejo, Mechanical properties of functionally graded hierarchical bamboo structures, *Acta Biomater*. 7 (10) (2011) 3796–3803.
 - [14] X. Zhou, G. Su, L. Chen, Heat-treated bamboo powder improves anti-mold performance of bamboo powder/polypropylene composites, Transactions of the Chinese Society of Agricultural Engineering. 33 (24) (2017) 308–314.
 - [15] C.R. Deo, Polymer Matrix Composite using Natural Fiber Lantana-Camara (2010).
 - [16] Z. Zhang, W. Li, L. Li, C. Zha, Green Industry Path of Rural Revitalization-Based on Jingxian County of Anhui Province, *Agricultural Outlook*. 15 (06) (2019) 100–103.
 - [17] Y.X. Huang, Q.Q. Lin, Y.H. Zhang, X.D. Li, Effect of Joint Type of bamboo Strips on Bending Properties of Bamboo Laminates under Lateral Pressing, *CHINA WOOD INDUSTRY*. 33 (3) (2019) 53–56.
 - [18] M.C. Yeh, Y.L. Lin, Finger joint performance of structural laminated bamboo member, *Journal of Wood Science*. 58 (2) (2012) 120–127.
 - [19] W. Zhu, X. Cui, W.F. Liu, The Influence of Connecting and Laminating on the Performance of Flattened Bamboo Board, *Journal of Bamboo Research*. 37 (3) (2018) 58–63.
 - [20] Q. Lin, Y. Huang, X. Li, A. Zhu, W. Yu, Effects of shape, location and quantity of the joint on bending properties of laminated bamboo lumber, *Construction and Building Materials*. 230 (2019), 117023.
 - [21] Q. Lin, Y. Huang, X. Li, A. Zhu, W. Yu, Directional Bamboo Laminated Lumber: A New Material with Infinite Lengthening, *WORLD BAMBOO AND RATTAN*. 17 (2) (2019) 18–21.
 - [22] R. Anokye, E.S. Bakar, J. Ratnasingam, A.C.C. Yong, N.N. Bakar, The effects of nodes and resin on the mechanical properties of laminated bamboo timber produced from *Gigantochloa scortechinii*, *Construction and Building Materials*. 105 (2016) 285–290.
 - [23] S. Nassar, K. Sakai, Effect of Cyclic Heat, Humidity, and Joining Method on the Static and Dynamic Performance of Lightweight Multimaterial Single-Lap Joints, *Journal of Manufacturing Science & Engineering Transactions of the ASME* (2015).
 - [24] Y. Boutar, S. Naimi, S. Mezlini, L.F.M.D. Silva, M. Hamdaoui, M.B.S. Ali, Effect of adhesive thickness and surface roughness on the shear strength of aluminium one-component polyurethane adhesive single-lap joints for automotive applications, *Journal of Adhesion Science & Technology*. 30 (17) (2016) 1–17.
 - [25] R.A. Chaudhuri, S. Chiu, Three-dimensional asymptotic stress field in the vicinity of an adhesively bonded scarf joint interface, *Composite Structures*. 89 (3) (2009) 475–483.
 - [26] D.L. Alves, R. Campilho, R. Moreira, F. Silva, L. Silva, Experimental and numerical analysis of hybrid adhesively-bonded scarf joints, *International Journal of Adhesion & Adhesives*. 17 (2018) 705–712.
 - [27] J.J. Bikerman, The science of adhesive joints, *The science of adhesive joints*, 1961.
 - [28] D.M. Gleich, M.J. Van Tooren, Shear and peel stress analysis of an adhesively bonded scarf joint, *Journal of Adhesion Science & Technology*. 14 (6) (2000) 879–893.
 - [29] S. Haraga, N. Okazaki, K. Oda, N. Tsutsumi, Evaluation of adhesive scarf joint strength by using singular stress field of small interface crack, *IOP Conference Series Materials Science and Engineering*. 372 (1) (2018) 12015.
 - [30] P. Hass, F.K. Wittel, P. Niemz, Generic failure mechanisms in adhesive bonds, *Holzforschung*. 67 (2) (2013) 207–215.
 - [31] J. Wu, C. Chen, H. Zhang, L. Xia, T. Zhang, Eco-friendly fiberboard production without binder using poplar wood shavings bio-pretreated by white rot fungi *Coriolus versicolor*, *Construction and Building Materials*. 236 (10) (2020), 117620.
 - [32] A.J. Kinloch, S.G.M. Little, J.F. Watts, The role of the interphase in the environmental failure of adhesive joints, *Acta Materialia*. 48 (18–19) (2000) 4543–4553.
 - [33] G. Doyle, R.A. Pethrick, Environmental effects on the ageing of epoxy adhesive joints, *International Journal of Adhesion & Adhesive*. 29 (1) (2009) 77–90.
 - [34] Z. Zhang, D.J. Macquarrie, J.H. Clark, A.S. Matharu, Chemical modification of starch and the application of expanded starch and its esters in hot melt adhesive, *RSC Advances*. 4 (79) (2014) 41947–41955.
 - [35] H.H. Shih, G.R. Hamed, Peel adhesion and viscoelasticity of poly(ethylene-co-vinyl acetate)-based hot melt adhesives. I. The effect of tackifier compatibility, *Journal of Applied Polymer Science*. 63 (3) (1997) 323–331.
 - [36] Y.J. Park, H.J. Kim, Hot-melt adhesive properties of EVA/aromatic hydrocarbon resin blend, *International Journal of Adhesion & Adhesives*. 23 (5) (2003) 383–392.
 - [37] H.D. Kim, T.U. Lee, J.O. Huh, D.I. Lee, Preparation and properties of segmented thermoplastic polyurethane elastomers with two different soft segments, *Journal of Applied Polymer Science*. 73 (3) (1999) 345–352.
 - [38] A. Kultys, M. Rogulska, H. Gluchowska, The effect of soft-segment structure on the properties of novel thermoplastic polyurethane elastomers based on an unconventional chain extender, *Polymer International*. 60 (4) (2011) 652–659.
 - [39] P. Liu, Research progress of moisture curing PUR hot melt adhesive, *China Adhesives*. 28 (08) (2019) 56–61.
 - [40] H. Jrad, H. Mallek, A. Bouhamed, Stress distribution in adhesively bonded scarf joint under thermo-mechanical loads, *The Journal of Adhesion*. 212017–218464 (2017).
 - [41] Z. Wang, H. Li, D. Yang, Z. Xiong, U. Sayed, R. Lorenzo, I. Corbi, O. Corbi, C. Hong, Bamboo node effect on the tensile properties of side press-laminated bamboo lumber, *Wood Science and Technology*. 55 (1) (2021) 195–214.
 - [42] X.J. Wang, S.J. Shen, S.P. Zhao, T.T. Jin, C. Qiu, Bamboo scarf mechanical properties of jointed samples, *China Wood Industry*. 29 (5) (2015) 14–16.
 - [43] Z.R. Tang, S.Y. Zhou, S.Y. Hu, Y.L. Wen, Study on slip joint for poplar veneer, *China Wood Industry*. 20 (6) (2006) 23–25.
 - [44] W. Lu, Mechanical properties research of wood glue joints, *Northeast Forestry University*, 2013.



Construction and Building **MATERIALS**

*An International Journal
Dedicated to the Investigation
and Innovative Use of
Materials in Construction
and Repair*

CONSTRUCTION & BUILDING MATERIALS
www.elsevier.com/locate/conbuildmat

Actions for selected articles

Select all / Deselect all



Download PDFs



Export citations

Show all article previews



Research article • Full text access

Effects of sulfate and freeze–thaw cycles on the bond behavior of CFRP–concrete interface

Jiawei Zhang, Hang Li, Shengwei Liu, Lin Sun, ... Rongling Zhang
Article 130368



View PDF

Article preview



Research article • Full text access

Modification of poplar wood cells using 1,3-dihydroxymethyl-4,5-dihydroxyethylideneurea/alkaline lignin for enhanced mechanical properties and decay resistance

Yuxin Peng, Qi Fan, Rongxian Ou, Xiaolong Hao, ... Qingwen Wang
Article 130354



View PDF

Article preview



Research article • Full text access

Temperature regulation and rheological properties assessment of asphalt binders modified with paraffin/ SiO₂ micro-encapsulated phase change materials

Xueting Wang, Huaxin Chen, Dongliang Kuang, Siyu Wu
Article 130377



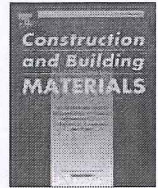
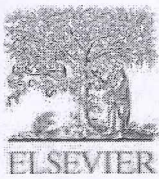
View PDF

Article preview



Research article • Full text access





Modification of poplar wood cells using 1,3-dihydroxymethyl-4,5-dihydroxyethylideneurea/alkaline lignin for enhanced mechanical properties and decay resistance

Yuxin Peng^{a,1}, Qi Fan^{a,c,d,1}, Rongxian Ou^{a,c,d}, Xiaolong Hao^{a,c,d}, Chuigen Guo^{a,c,d},
Zhenzhen Liu^{a,c,d}, Tao Liu^{b,d,*}, Lichao Sun^{a,d,*}, Qingwen Wang^{a,c,d}

^a Key Laboratory for Biobased Materials and Energy of Ministry of Education, College of Materials and Energy, South China Agricultural University, Guangzhou 510642, China

^b College of Food Science, South China Agricultural University, Guangzhou 510642, China

^c Institute of Biomass Engineering, Key Laboratory of Energy Plants Resource and Utilization, Ministry of Agriculture and Rural Affairs, South China Agricultural University, Guangzhou 510642, China

^d Guangdong Laboratory for Lingnan Modern Agricultural Science and Technology, 483 Wushan Road, Guangzhou 510642, China

ARTICLE INFO

Keywords:

Wood modification
Alkaline lignin
1,3-dihydroxymethyl-4,5-dihydroxyethylideneurea
Mechanical properties
Decay resistance

ABSTRACT

Fast-growing poplar wood was modified by using 1,3-dihydroxymethyl-4,5-dihydroxyethylideneurea (DM) and alkaline lignin (AL) to improve its mechanical properties and decay resistance. AL was first used in combination with DM for wood impregnation modification. The weight percent gain, dimensional stability, mechanical properties, decay resistance and microcosmic changes of all wood samples were evaluated systematically. The results indicated that the maximum weight percent gain and anti-swelling efficiency of poplar wood after modification with DM-AL reached 46.2 % and 52 %, respectively. Compared with the unmodified samples, the bending strength, modulus of elasticity and hardness of the wood samples modified with DM-AL increased by 40 % – 60 %. Notably, the impact strength of samples modified with DM-AL was 18–26 % higher than that of samples modified with DM only, which may be due to the fact that the AL macromolecules slowed down the infiltration of DM-AL into the wood cell walls. The decay resistance of optimal modified samples against the decay fungus was improved by ~80 % compared with unmodified sample. Furthermore, scanning electron microscopy-energy dispersive spectroscopy (SEM-EDS) confirmed that DM-AL modifiers impregnated into wood cell lumens. Fourier transform infrared spectroscopy (FTIR) demonstrated that the DM resin crosslinked with wood cell walls and AL macromolecules. In general, this study provides a facile, low-cost and green method to improve the comprehensive performance of fast-growing poplar, including mechanical properties and decay resistance.

1. Introduction

Because of its advantages of beautiful appearance, easy processing, high strength ratio, wood is one of the most important natural renewable materials and has been widely used in construction, furniture and decoration[1,2]. However, the existing natural forest resources cannot meet the growing demand for wood utilization, and large-scale logging of natural forests can also cause harm to the ecological environment. Artificial fast-growing forests have the advantages of fast-growth rate,

large yield, and short harvesting period, and are an important substitute for natural forest resources[3,4]. The utilization of fast-growing wood can meet the increasing needs of wood and is a meaningful way to protect natural resources, which has attracted great attention[5,6].

Chemical modification is an effective method to improve the mechanical properties, dimensional stability, flame retardancy, decay and mildew resistance, and aging resistance of fast-growing wood[7]. Among the chemical modification techniques, resin impregnation is a high-efficiency, low cost and simple way to increase the multifaceted

* Corresponding authors at: College of Food Science, South China Agricultural University, Guangzhou 510642, China (T. Liu); Key Laboratory for Biobased Materials and Energy of Ministry of Education, College of Materials and Energy, South China Agricultural University, Guangzhou 510642, China (L. Sun).

E-mail addresses: liutao@scau.edu.cn (T. Liu), sunlichao@scau.edu.cn (L. Sun).

¹ Equally contributed to this work and were listed as co-first authors.



Table 1
Experimental formulation of impregnated resin.

Samples	Alkaline lignin (wt.%)	DM resins (wt.%)	MgCl ₂ (wt.%)
Ctrl	/	/	/
MgCl ₂	/	/	1.5
12 %AL	12	/	1.5
30 %DM	/	30	1.5
8 %AL + 30 %DM	8	30	1.5
12 %AL + 30 %DM	12	30	1.5
16 %AL + 30 %DM	16	30	1.5

properties of wood[8,9]. The most common methods of chemical modification are thermosetting resin treatment[10], acetylation treatment[11], furfurylation treatment[12], nano compound treatment[13], nitrogen hydroxymethyl compound treatment[14], etc. Recently, researchers have explored a method to improve the dimensional stability by using Glycerol-maleic anhydride (GMA)-thermal treatment[15]. Also, Resa[16] et al. found that furfurylation treatment had a significant improvement in dimensional stability and durability of short rotation teak wood. The most commonly used in nitrogen hydroxymethyl compound treatment is 1,3-dihydroxymethyl-4,5-dihydroxyethylideneurea (DM), which can enter into the cell walls and polymerize under acidic catalysts at elevated temperatures, is a promising resin for wood modification[17]. The DM modified wood shows excellent properties for dimensional stability, decay resistance, aging resistance[18]. Mariusz[19] studied the physical and mechanical performance of DM modified oil palm (*Elaeis guineensis* Jacq.) and found that the density of the modified wood increased by 45 %, while the water absorption and thickness swelling reduced, and the bending strength and modulus of elasticity were significantly improved. Furthermore, Emmerich[20] found that the anti-fungal efficacy and biological durability of wood were considerably improved by DM modification. However, DM modified wood suffers from part of poor mechanical properties. Bollmus[21] and Xie[22] reported that the DM modification could reduce the bending strength and impact strength of modified wood. Therefore, it is necessary to develop a new method to simultaneously improve the mechanical and anti-decay properties of DM modified wood.

Lignin, as a natural binder, keeps the cellulose fibers tightly linked to each other in wood cells. Previous studies have found that lignin can not only increases the impact resistance, compressive strength and bending strength of wood, but also prevent the wood cell from some photo-aging or biological reactions[23–25]. Herein, based on the natural wood bionic principle and inspired by the role of lignin in wood structure, a combined treatment using DM resins and alkaline lignin (AL), were impregnated into wood along with catalyst MgCl₂. After modification, the dimensional stability, mechanical properties and decay resistance of fast-growing poplar were systematically evaluated and analyzed. The improvement of mechanical and anti-decay properties of modified wood was attributed to the modification of cell wall and filling of cell cavity by DM-AL modifiers, as well as the partial chemical cross-linking of DM resins and AL. The purpose of this research is to build up a non-hazardous and inexpensive modification technology throughout the process, and to provide new ideas for wood modification and utilization of lignin biomass resources.

2. Experiment

2.1. Materials

Poplar was bought from Aozhuo Wood Co., Ltd. in Dongguan City, Guangdong Province, wooden size 2 m × 170 mm × 20 mm (L × T × R), the density of wood used for impregnation was about 0.45 g/cm³, stored in a cool dry place for ventilation until the moisture content is about 12 %. Prior to impregnation, the wood was cut into 20 mm × 20 mm × 20 mm for physical properties tests, 180 mm × 10 mm × 10 mm for bending strength and modulus of elasticity (MOE) tests, 50 mm × 50

mm × 20 mm for hardness test, 300 mm × 20 mm × 20 mm for impact strength test and 30 mm × 20 mm × 20 mm (L × T × R) for compression strength test, respectively, and then oven dried at 103 °C, weighed and noted mass. DMDHEU (DM) resins with the boiling point of 621.4 °C, the molecular weight of 178, and solid content of 55 %, respectively, was obtained from Lanxiang Resin Co., Ltd. in Zhongshan City, Guangdong Province. Alkaline lignin (AL) contained sulfonate groups, soluble in water, black powder, the molecular weight of about Mn:1595, PD:1.03, analytical grade, was supplied by TCI Co., Ltd. MgCl₂·6H₂O of analytical grade, purity of 98 %, was purchased from Zeshen Co., Ltd. in Anhui Province.

2.2. Impregnation of wood

According to previous literatures, MgCl₂ was used as catalyst for DM resin.[17,19,20,26]. Considering the wood weight gain effect results of the pre-experiment, DM resins concentration and catalyst MgCl₂ concentration were chosen to be 30 wt%, 1.5 wt%, respectively. In condition, the concentrations of sulfonate alkaline lignin were 8, 12, 16 wt% in this study. The specific impregnation formula was presented in Table1.

To avoid the acidic MgCl₂ influence the penetration of AL into the wood, a two-step impregnation was adopted to prepare the AL and DM treated wood samples. The aqueous DM-AL solutions of impregnation with different AL concentrations were prepared by the addition of AL and deionized water into the DM resins solutions (Table 1). The wood samples were impregnated fully in a vacuum of −0.01 MPa for 30 min and then held by 0.5 MPa of pressure for 2 h. After the samples were full of impregnation solutions to the saturated state, air-dry them in a cool and ventilated condition for 24 h, and then heat wood samples in an oven at 103 °C until completely dry. In the second treatment, the impregnated wood was immersed by 1.5 % MgCl₂ solutions, following the same condition of the first impregnation, then put into an oven to accomplish polymerization at the environment temperature of 60 °C for 2 h, and 103 °C for 12 h (Scheme 1). In order to ensure the accuracy of the experiment, all the treated wood samples in this paper were washed with water to remove the physically adsorbed AL and DM resin from the surface after the curing of DM resin. The samples were measured to gain the dimensional and mechanical data after cooling to room temperature.

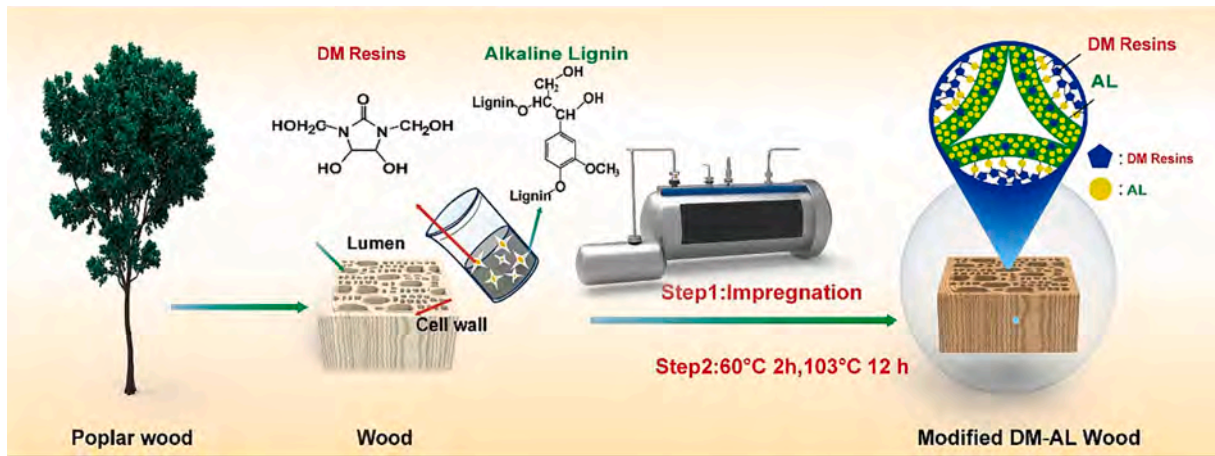
2.3. Characterization

2.3.1. Viscosity of the impregnating solution

The viscosity of the impregnating solutions was determined by modular smart advanced rheometer (MCR502 Shanghai Anton Paar Co., Ltd). The viscosity of the impregnating solutions was measured using the rheometer, where the shear rate ranged from 0.1 to 100 s^{−1} in increments of 10 s^{−1}. The test was repeated three times for each sample of the same mass and the average value was obtained.

2.3.2. Physical properties

The physical properties of all impregnated samples were tested according to the national standards of GB/T 1927.2–2021[27] and GB/T 1927.5–2021[28]. The weight percent gain (WPG) was calculated by equation (1). The oven-dry density of the wood samples tested for physical properties had been controlled around at 0.4 g/cm³ (Green density:0.45 g/cm³) before the impregnation. The oven-dry density of all modified samples was tested after the impregnation. The dimensional stability of wood samples was characterized by the anti-swelling efficiency (ASE). The leaching ratio (LR) was measured by submerging the modified and unmodified wood with deionized water in beaker and pressed with a heavy object to ensure complete submersion, which were changed water daily for 10 days, weighted the mass and recorded the size after oven-drying and under water absorption maximum. The measured samples were 20 mm × 20 mm × 20 mm (L × T × R) provided with 12 parallel replicates in each group. ASE and LR were calculated



Scheme 1. The schematic diagram of DM-AL impregnation modified wood.

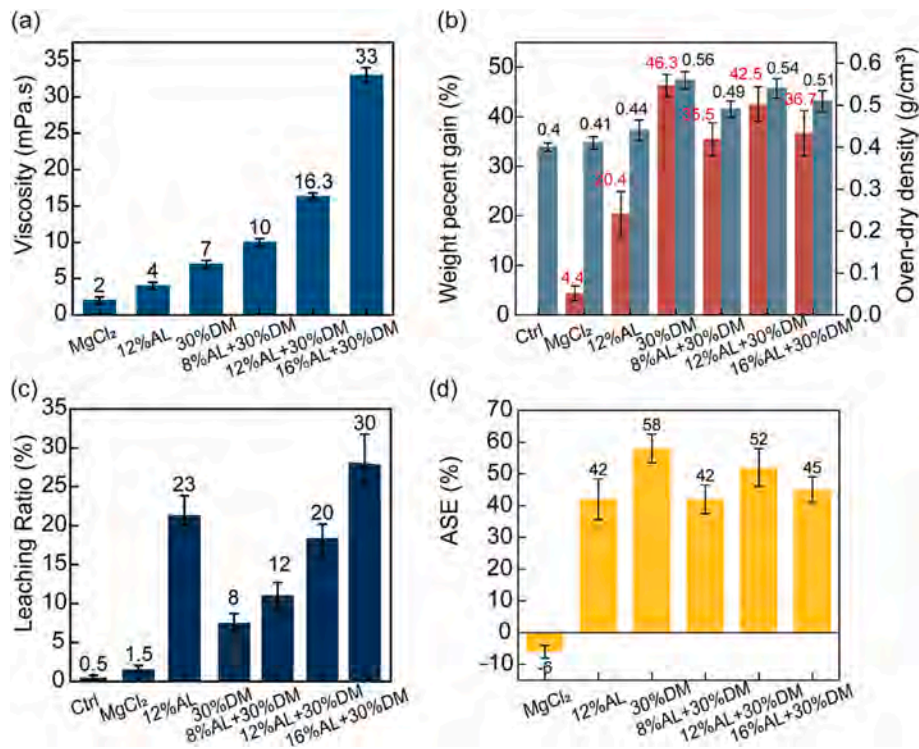


Fig. 1. The viscosity of impregnating solutions (a); the oven-dry density and WPG (b); LR (c) and ASE (d) of wood samples modified with chemicals at different concentrations.

according to equation (2) and (3).

$$WPG(\%) = \frac{W_2 - W_1}{W_1} \times 100 \quad (1)$$

Where W_1 is the oven-dry mass before impregnation and W_2 is the oven-dry mass after impregnation.

$$ASE(\%) = \frac{S_c - S_t}{S_c} \quad (2)$$

Where S_c is the swelling expansion of unmodified wood and S_t is the volume swelling of modified wood.

$$LR(\%) = \frac{W_2 - W_3}{W_2} \times 100 \quad (3)$$

Where W_2 is the oven-dry mass after impregnation and W_3 is the oven-dry mass after leaching.

2.3.3. Morphological analyses

The distribution of modification chemicals and elemental analysis in wood were observed by scanning electron microscopy-Energy dispersive spectroscopy (ZEISS EVO18 Beijing Presix Instrument Co., Ltd.). The cross section and radial section of the surfaces of the test samples were sliced with a SEM slicing knife. The sliced samples were stick to aluminum stubs and then oven-dry at 60 °C overnight. Prior to SEM-EDS analysis, the samples were sputter coated with a layer of gold. Unmodified samples and samples modified with 12 %AL, 30 %DM, and 12 %AL + 30 %DM were analyzed.

2.3.4. Mechanical properties

Bending strength and Modulus of elasticity (MOE) of modification wood were tested by CMT-1000 universal mechanical testing machine. The sawn wood was 180 mm × 10 mm × 10 mm (L × T × R), tested in a

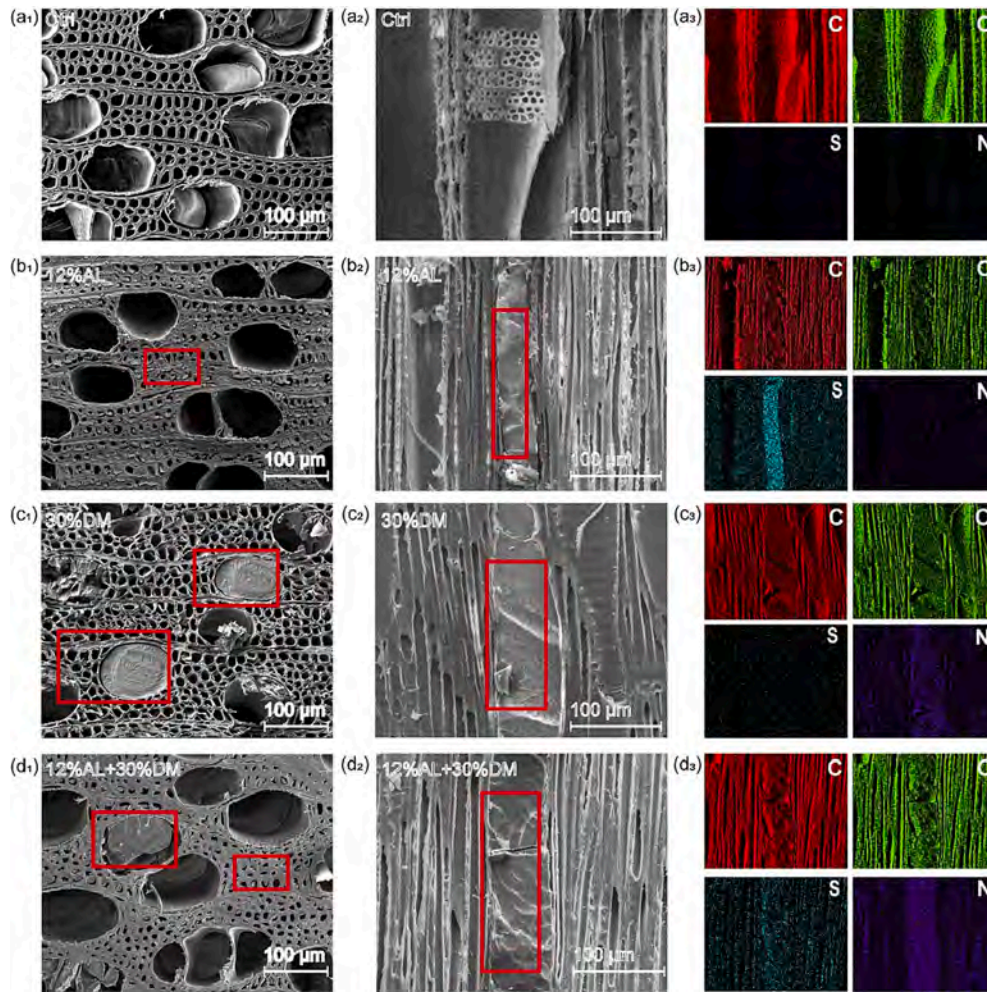


Fig. 2. The micrographs of the cross sections of the unmodified wood samples (a₁) and the impregnated modified wood samples (b₁, c₁, d₁), the micrographs and EDS of radical section of the unmodified (a₂, a₃) and the impregnated modified wood samples (b₂, b₃, c₂, c₃, d₂, d₃).

three-point bending model with a span of 150 mm, and the loading speed was 6 mm/min. Compression strength was determined in accordance with the standard GB/T 1927.12–2021[29]. The sample dimensions were 30 mm × 20 mm × 20 mm (L × T × R). The loading speed was 2 mm/min. Hardness was measured in accordance with the standard GB/T 1927.19–2021[30]. Impact strength was measured using pendulum type wood impact testing machine (MJB-100, Jinan, China) according to the standard GB/T 1927.17–2021[31], and the sample dimensions were 300 mm × 20 mm × 20 mm (L × T × R). All samples to be tested were subjected to leaching treatment and conditioned to constant weight at a relative humidity of 65 % ± 5 % and temperature of 20 °C ± 2 °C. Each set of formulations for each mechanical experiment contained 15 replicate specimens.

2.3.5. Fourier-transform infrared test

The Fourier-transform infrared (FTIR) spectra of unmodified samples and samples modified with 12 %AL + 30 %DM wood powder (100–120 mesh), ingredient of AL and DM resins, and cured DM with AL, were recorded in KBr pellets at a resolution of 4 cm⁻¹ with 32 scans and a scanning range of 400–4000 cm⁻¹ (PerkinElmer Spectrum 100 INFRARED spectrometer).

2.3.6. Decay test

The wood decay resistance test was revised and conducted according to the national standards of GB/T 13942.1–2009[32], using white-rot fungus, *Phanerochaete chrysosporium* and brown-rot fungus, *Monilinia*

laxa (Aderh. & Ruhland) Honey, which were purchased from Beijing Beina Biotechnology Co., ltd. Fresh colonies of the two fungi were grown in PDA (potato dextrose agar) solid medium in a growing chamber at 25

± 2 °C and 65 ± 5 % relative humidity for 10 days. The testing wood samples were sawn 10 mm × 10 mm × 5 mm, and the unfixed resins on the surface was washed off before the anti-fungal test experiment. Then wood samples were measured oven-dry mass and autoclaved (121 °C, 30 min). The wood samples (the unmodified samples and modified samples with 30 %DM, 12 %AL, 8 %AL + 30 %DM, 12 %AL + 30 %DM, and 16 %AL + 30 %DM) were placed on the surface of the petri dishes full of mycelium under the aseptic condition then incubated at 25 °C for 30 days. 36 replicates were arranged of one formula for each decay fungus. After 30 days of decay experiments, the surface of the wood samples was scraped clean of mycelium and oven-dried at 103 °C, recording the mass of decay tested wood. The extent of the fungus attack was measured based on the percentage of mass loss. The mass loss rate (Eq. (4)) is as follows:

$$\text{Massloss}(\%) := \frac{W_4 - W_5}{W_4} \times 100 \quad (4)$$

Where W_4 is the oven-dry mass after impregnation and W_5 is the oven-dry mass after 30 days of decay experiment.

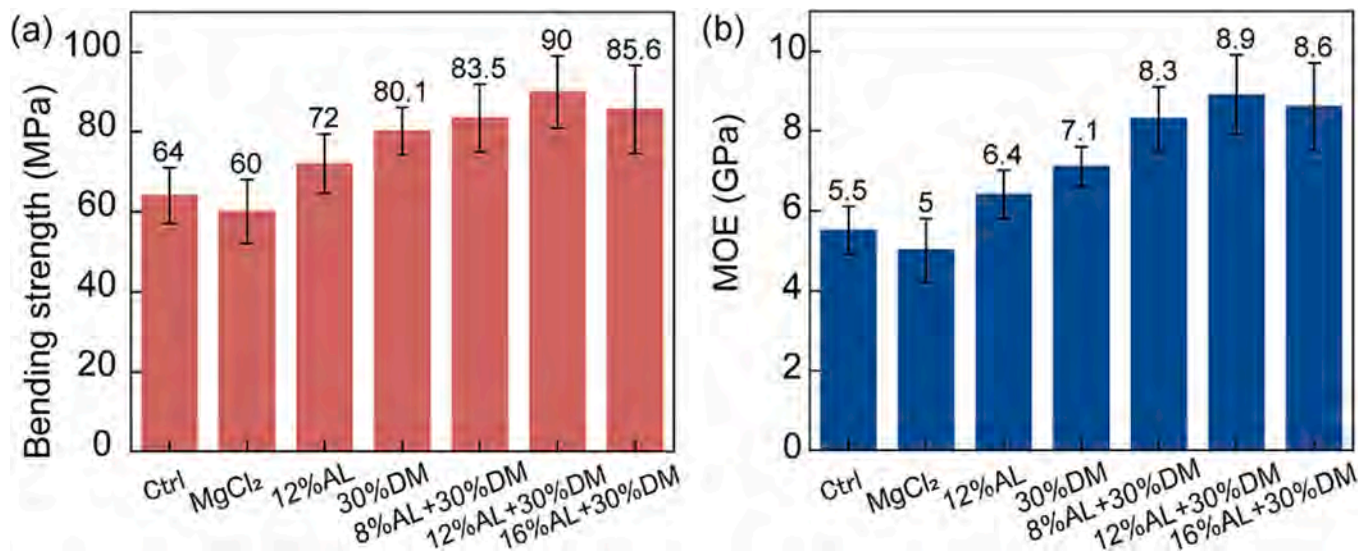


Fig. 3. Bending strength (a) and MOE (b) of the unmodified and the impregnated modified wood samples.

3. Results and discussion

3.1. Physical properties

The viscosity of impregnating solutions is given in Fig. 1a. The viscosity of both AL and DM solutions alone was quite low. And the viscosity was gradually increased with the increase of AL content in the mixed AL + DM impregnating solution, the viscosity of 16 %AL + 30 %DM was 33 mPa s, which was still a high fluidity liquid. The WPG and density of treated wood are shown in Fig. 1b, it was found that the higher the WPG of the treated wood, the higher the density. The WPG of wood samples impregnated with 12 %AL was 20.4 %, while the wood samples with 30 %DM resins reached 46.3 %, indicating both the AL and DM resins can be impregnated into wood effectively. The lower WPG of 12 %AL than that of 30 %DM should be ascribed to the larger molecular weight, the more heterogeneous and complicated structure of AL (Mn:1595, PD:1.03) compared with DM resins[33]. Compared with AL, the molecular weight of DM resins was only 178, which could diffuse into the wood and deposit in the wood cell cavities and interstices more easily, and some DM resins can immerse into the wood cell and react with the hydroxyl groups on the wood cell walls[34,35]. For the samples with both AL and DM resin, the WPG of wood samples increased with the AL concentration increasing from 8 % to 12 %, indicating that AL could enter into the wood in the presence of DM resin, and the WPG of 12 %AL + 30 %DM was slightly lower than that of 30 %DM treatment alone. Moreover, the reduction in WPG of 16 %AL + 30 %DM should be attributed to the higher content of AL being more likely to pre-polymerize with DM resin, resulting in an increase in molecular weight, which further leads to a higher viscosity of the impregnating solution, making it more difficult to penetrate into the wood and ultimately resulting in a lower WPG than the group treated with DM resin alone[36,37].

As shown in Fig. 1c, the LR of modified wood samples was in the range of 12–30 %, and the LR of 12 %AL + 30 %DM was slightly lower than 12 %AL individual treatment, suggesting that DM resins could improve the retention rate of AL. Moreover, the dimensional stability of wood samples was characterized by the ASE. As shown in Fig. 1d, the ASE of only MgCl₂ modified wood samples was less than 0, indicating that MgCl₂ had a negative effect on the dimensional stability of the wood due to its acidity. In contrast, higher ASE of the modified wood were obtained after DM, AL and DM-AL treatment, demonstrated that both AL and DM resins had a positive influence on the dimension stability of wood, causing better water resistance of modified wood. As some AL

physically bulking the cell lumens of the wood, the absorption of external water was reduced thereby enhancing the dimensional stability of the wood. The ASE of 30 %DM was higher than the other samples, which might be ascribed to the better filling effect of DM in the pores of wood cell walls due to its smaller molecular weight, and the chemical cross-linking of DM with the cell wall to form permanent cell wall swelling and reduce the accessibility of water molecules to the adsorption sites[38]. Moreover, with the increase of AL content in the impregnating solution, the ASE value of 12 %AL + 30 %DM was most pronounced in the modified samples, reaching 52 %. The reason might account for the result that some AL cross-linked with DM resins to form a network and was fixed in the wood, which increased the swelling degree of the wood and blocks the moisture channel of the wood[39,40]. Therefore, the AL solution compounded with DM resins can effectively improve the dimensional stability of modified wood.

3.2. Morphological analyses

Fig. 2 shows the SEM-EDS comparison between unmodified wood and optimal impregnated modified wood 12 %AL + 30 %DM. As seen in Fig. 2a1 and b1, the pits in the wood vessels and the gaps between the cell lumens in 12 %AL were covered by AL compared to control samples, and the conduit fillers of 12 %AL contained the characteristic sulfur element without the nitrogen element, the sulfur element was belonged to the residual sulfonic acid groups on 12 %AL (Fig. 2b3). It demonstrated that AL molecules was able to enter the cell lumens of the wood. From Fig. 2c1, DM resins cured into macromolecules filled with large vessels in the wood while AL was mainly physically filled. Hence, the characteristic nitrogen element of DM resins was distributed in and around the wood vessels in 30 %DM (Fig. 2c3). In Fig. 2d1, it can be observed that DM resin and AL of 12 %AL + 30 %DM forming polymer deposited wood vessels compared to 12 %AL. Combined with the WPG of 30 %DM above 40 % in Fig. 1b, it was confirmed that DM resins had good compatibility and cross-linking within the wood structure, and the introduction of DM resins helped to fix AL in wood better. From the radical section of the wood (Fig. 2b2), the AL molecules were physically filled in the wood conduits. As seen in Fig. 2d2, DM resins cross-linked with AL to form a macromolecular polymer, which was densely filled in the wood vessels and did not shrink after curing. It can be further demonstrated that DM and AL were deposited throughout the wood vessels and cell interstices, and the sulfur element was more uniformly distributed in the 12 %AL + 30 %DM compared to the 12 %AL (Fig. 2d3). Therefore, the modification of wood with both DM resin and AL

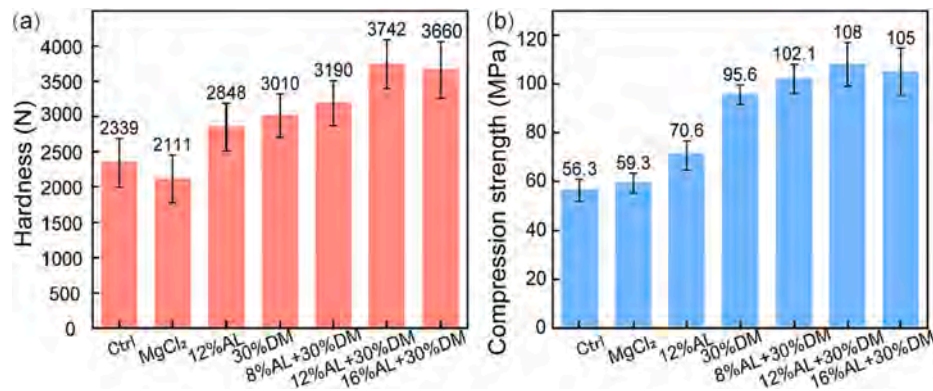


Fig. 4. Hardness (a) and compression strength (b) of the unmodified and the impregnated modified wood samples.

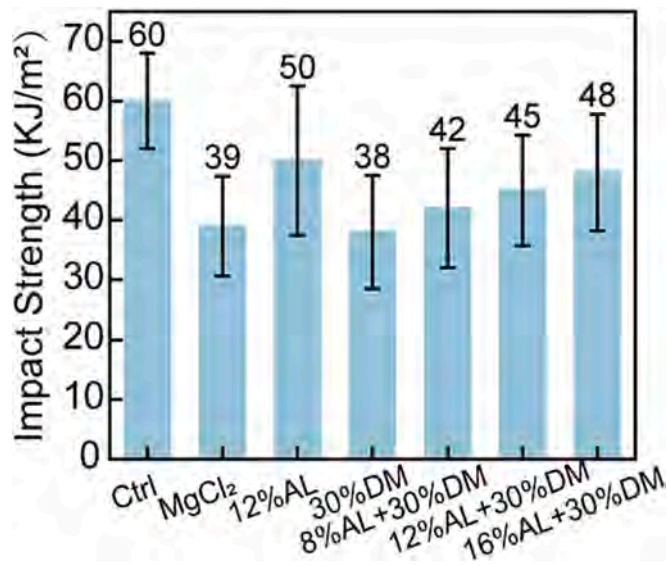


Fig. 5. Impact strength of the unmodified wood and the impregnated modified wood samples.

contributed to the thickening of the wood cell wall, which could hinder the entry of water molecules into cell walls and improve the dimensional stability of wood[41].

3.3. Bending strength and MOE of modified wood

From Fig. 3a can be found that the bending strength of wood

significantly improved with DM-AL modification compared with unmodified wood samples, which differed from the results of previous studies on the reduction of bending degree of wood impregnated with DM resins and catalyst $MgCl_2$ [7,35]. The bending strength of modified wood increased to 72 MPa after 12 %AL individual impregnation and 80.1 MPa for DM resins alone modified wood. When the 12 %AL + 30 %DM were used, the maximum of bending strength obtained was 90 MPa. This should be attributed to that the AL could crosslink with DM to form a rigid network structure, which solidifies in the cell wall lumbers and making wood stiff reinforcement, resulting in a high WPG of wood samples and an increase in bending strength[37,42,43]. Moreover, Fig. 3b shows that the MOE of DM modified wood increased from 5.5 to 7.1 GPa compared with that of control. For samples modified with AL combined DM, the MOE of modified wood increased first and then decreased with the increase of AL concentration, and the 12 %AL + 30 %DM displayed the highest MOE at 8.9 GPa. Because AL could be physically attached to the wood cell wall, it played the role of dispersing and transmitting stress to the wood cell, reducing the deformation under the action of external force and improving the MOE[43,44]. Meanwhile, the DM resins could be formed a self-condensation reaction, and the DM was cross-linked with the microfibrils in the wood, which hindered the free movement of the microfibrils and improved the stiffness of the wood cell wall[45].

3.4. Hardness and compression strength

As shown in Fig. 4a, the hardness of DM-AL modified wood samples were significantly improved. The hardness of DM-AL wood modified was increased to 3190 N (8 %AL + 30 %DM), 3742 N (12 %AL + 30 %DM), and 3660 N (16 %AL + 30 %DM), increased by 36 %, 60 %, and 56 %, respectively. The compression strength of modified wood after DM-AL

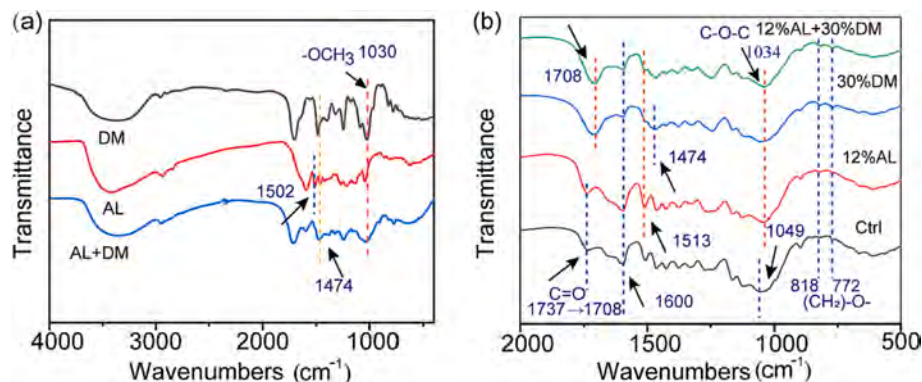


Fig. 6. FTIR spectra of the raw material of DM resins, AL and mixtures of 12 %AL + 30 %DM cured by $MgCl_2$, respectively (a); unmodified wood, wood modified with 12 %AL + 30 %DM, 30 %DM, and 12 %AL, respectively (b).

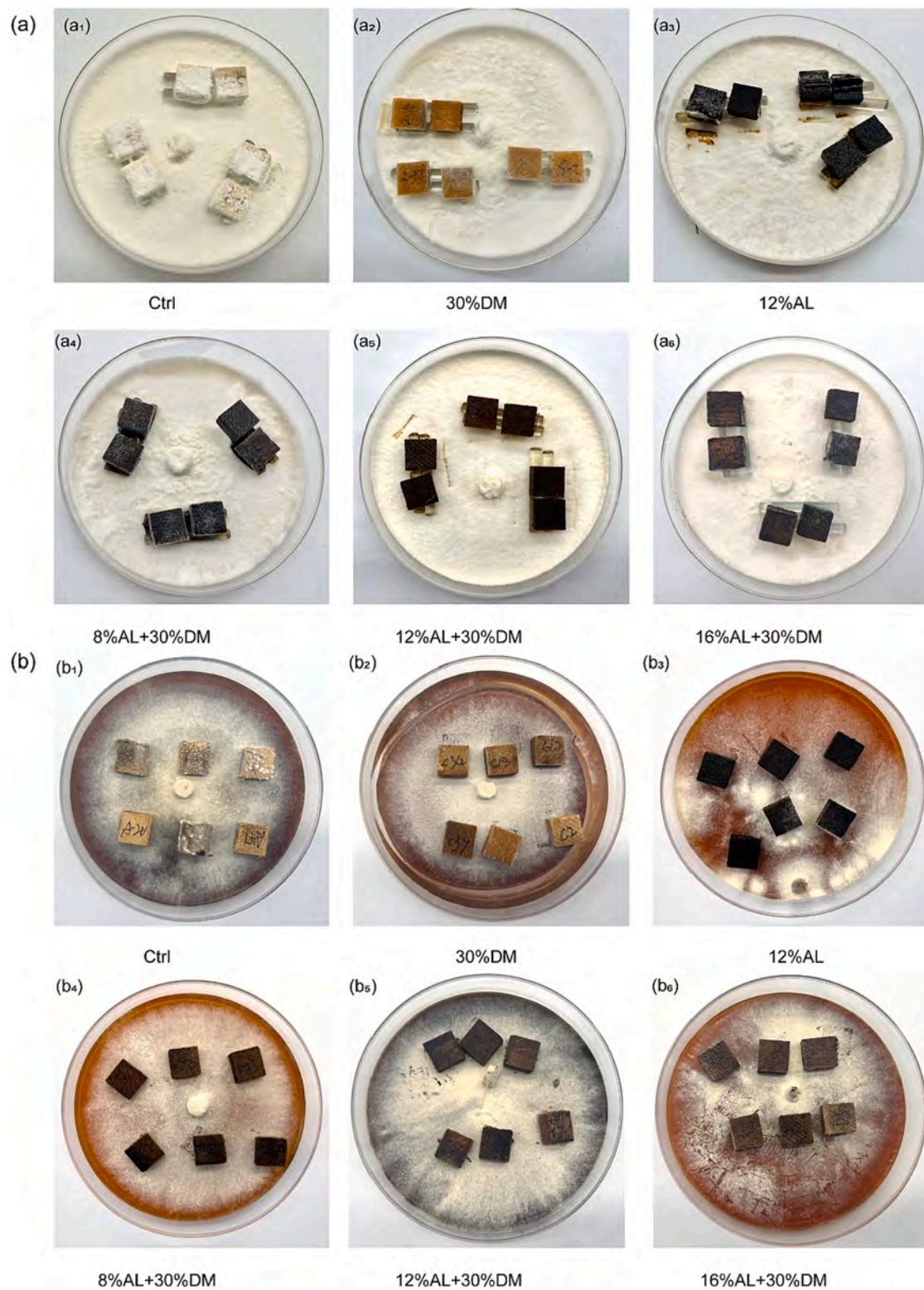


Fig. 7. The wood photographs after white-rot and brown-rot decay experiments of wood samples (a), (b).

treatment was significantly improved. Among all modified wood samples, the compression strength of 12 %AL + 30 %DM reached the highest 108 MPa. However, the compression strength decreased when AL concentration exceeded 12 %, which was consistent with the WPG. It can be explained that the DM-AL modifiers penetrated into the wood vessels, wood cell lumen, wood cell wall micropores and intercellular interlayer spaces, and deposited in the porous structure of wood cells after curing.

Thus, the deformation of wood cell space became smaller when under pressure, which reduced the relative freedom of microfibril, and finally increased the compression strength of wood [35]. It was further demonstrated that DM-AL bound to the cell wall physically or chemically, thus improving the cell wall strength, and finally increased the compressive strength of wood.

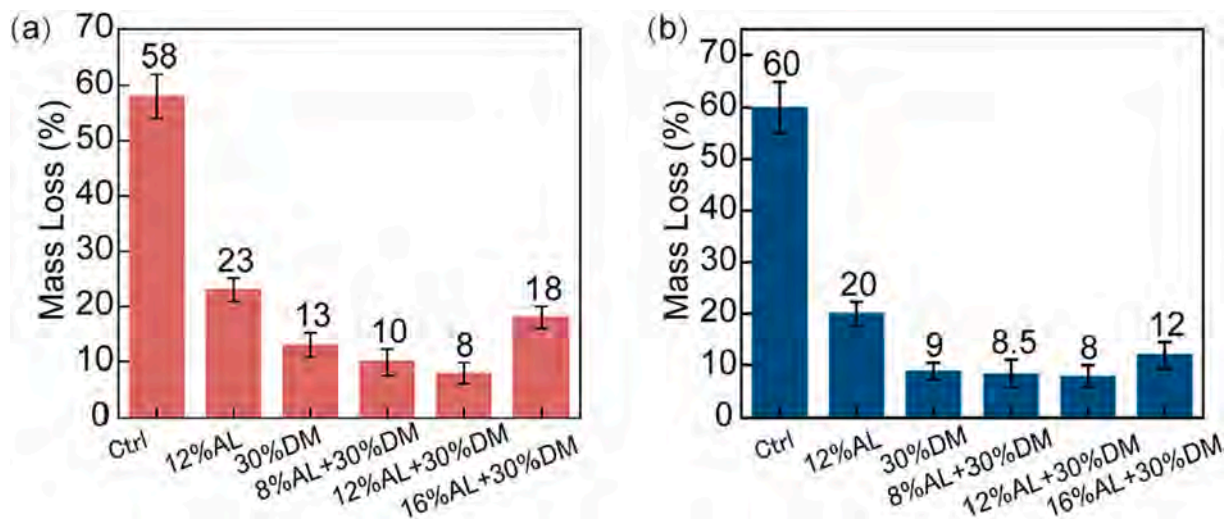


Fig. 8. Mass loss of unmodified wood samples and wood samples with DM-AL at different concentrations after white-rot (a) and brown-rot decay test (b).

3.5. Impact strength

Fig. 5 shows that the impact performance of DM modified wood samples was dramatically decreased compared those of the control samples. The reduction in impact strength was mainly attributed to the cross-linking of the wood cell wall components with the DM hydroxyl groups to form a rigid three-dimensional network[36]. Thus, the relative slip between cellulose molecular chains was correspondingly reduced, because the three-dimensional network molecular did not move easily when wood was subjected to transient impact loading[46]. In addition, the presence of catalyst $MgCl_2$ was likely to have polysaccharides of wood cell wall hydrolyzed, resulting in the decline of impact strength. As compared with DM modified wood, with the introduction of AL, the impact strength of 12 %AL + 30 %DM was increased to 45 KJ/m^2 , 16 %AL + 30 %DM reached 48 KJ/m^2 , which may be due to the fact that the crosslinking of AL and DM reduced the crosslinking between DM and cells, preserving the relative slip of the molecular fiber chain[47]. The above results confirmed that AL had a positive effect on the impact strength loss of fast-growing wood caused by DM modification.

3.6. Fourier transform infrared spectroscopy

Fig. 6a presents FTIR spectra of the of DM resins, AL and AL + DM cured with $MgCl_2$. It can be observed that in the spectrum of DM + AL, when compared with the spectra of AL, the original absorption band of lignin at 1502 cm^{-1} was disappeared, and the characteristic band at 1474 cm^{-1} was significantly enhanced, which was caused by the reaction between DM and AL, the influence of nitrogen hydroxyl methyl group and the introduction of amide group[37,48]. The absorption band of methoxy group ($-OCH_3$) at 1003 cm^{-1} also widened with the increase of methoxy content in AL. As shown in Fig. 6b, the band intensity at 1600 cm^{-1} was the characteristic absorption band of lignin. The vibration absorption band of 12 %AL was stronger than that of control samples, indicating that lignin content in wood increases[44]. However, the band intensity of 12 %AL + 30 %DM sample was weakened due to the reaction between DM and AL or lignin in wood [22,49]. Similarly, the absorption band on the spectrum of the 12 %AL were 1513 cm^{-1} , which was covered and shifted to 1467 cm^{-1} after treatment with DM. Moreover, compared with unmodified wood, the C—O absorption band of 12 %AL + 30 %DM was enhanced and shifted from 1731 cm^{-1} to 1708 cm^{-1} , because the O=CN bond shifted after impregnating wood with DM resins[42]. Furthermore, the characteristic absorption band of C—O—C shifted from 1049 cm^{-1} to 1034 cm^{-1} , indicating that wood cells cross-linked with DM resins or DM resins self-polymerized to form

an ether bond[37]. More importantly, the methylene characteristic bands of 12 %AL + 30 %DM were found at 772 cm^{-1} and 818 cm^{-1} , suggesting the AL, DM and wood cells were cross-linked with each other [50,51]. Therefore, the above results further prove that the successful chemical crosslinking reaction occurs between DM, AL and some functional groups in wood which can effectively fix DM and AL in wood cells and improve the physical and mechanical properties of modified wood.

3.7. Decay resistance

Fig. 7 shows the images of unmodified wood and modified wood samples after 30 days of decay test by white-rot fungus and brown-rot fungus, respectively. As shown in Fig. 7a1, the ctrl sample was clearly seen to be covered with a large number of mycelia, which suggested that the ctrl was susceptible to infection by white-rot fungus. In comparison, it was clearly observed that there was less mycelium on the surfaces of 30 %DM and 12 %AL, displaying a certain anti-decay activity (Fig. 7a2 and a3). The mycelia on the 12 %AL + 30 %DM was almost invisible, which was notably decreased than that of other samples. It was indicated that the decay resistance of poplar wood was significantly improved after the 12 %AL + 30 %DM combined treatment (Fig. 7a5).

As shown in Fig. 7b1, the obvious typical brown-rot can be found on the surface of ctrl sample with browning discoloration and mycelium. It was illustrated that brown-rot fungus attacked the interior structure of wood seriously, combined with the mass loss rate of the control group. Additionally, it was observed after 30 %DM or 12%AL treatment appeared as a small amount of mycelium and browning of the wood surface. (Fig. 7b2 and b3). Although the DM-AL modified wood had a certain mass loss when exposed to brown-rot, it still maintained its appearance, and no obvious mycelium was observed by naked eye (Fig. 7b4 – b6). Further determination of the anti-decay effect should be combined with the mass loss rate and scanning electron microscopy.

Moreover, the mass loss of wood samples were calculated according to GB/T 1349.2[32]. It was observed that the unmodified wood samples severely attacked by decay white-rot fungus and brown-rot fungus with the large mass loss 58 % and 60 % (Fig. 8), respectively, which belonged to the non-decay resistant grade. Wood samples impregnated with AL revealed a slight mass loss of 23 % and 20 % (white-rot fungus and brown-rot fungus), respectively, while DM resins modified samples showed a lower loss rate of 13 % and 9 %, respectively. For the samples modified by AL combined with DM resin, 12 %AL + 30 %DM displayed the lowest mass loss to white-rot fungus and brown-rot fungus at 8 %, which should be attributed to its high WPG and well crosslinking. Generally speaking, all modified wood samples achieved decay-resistant

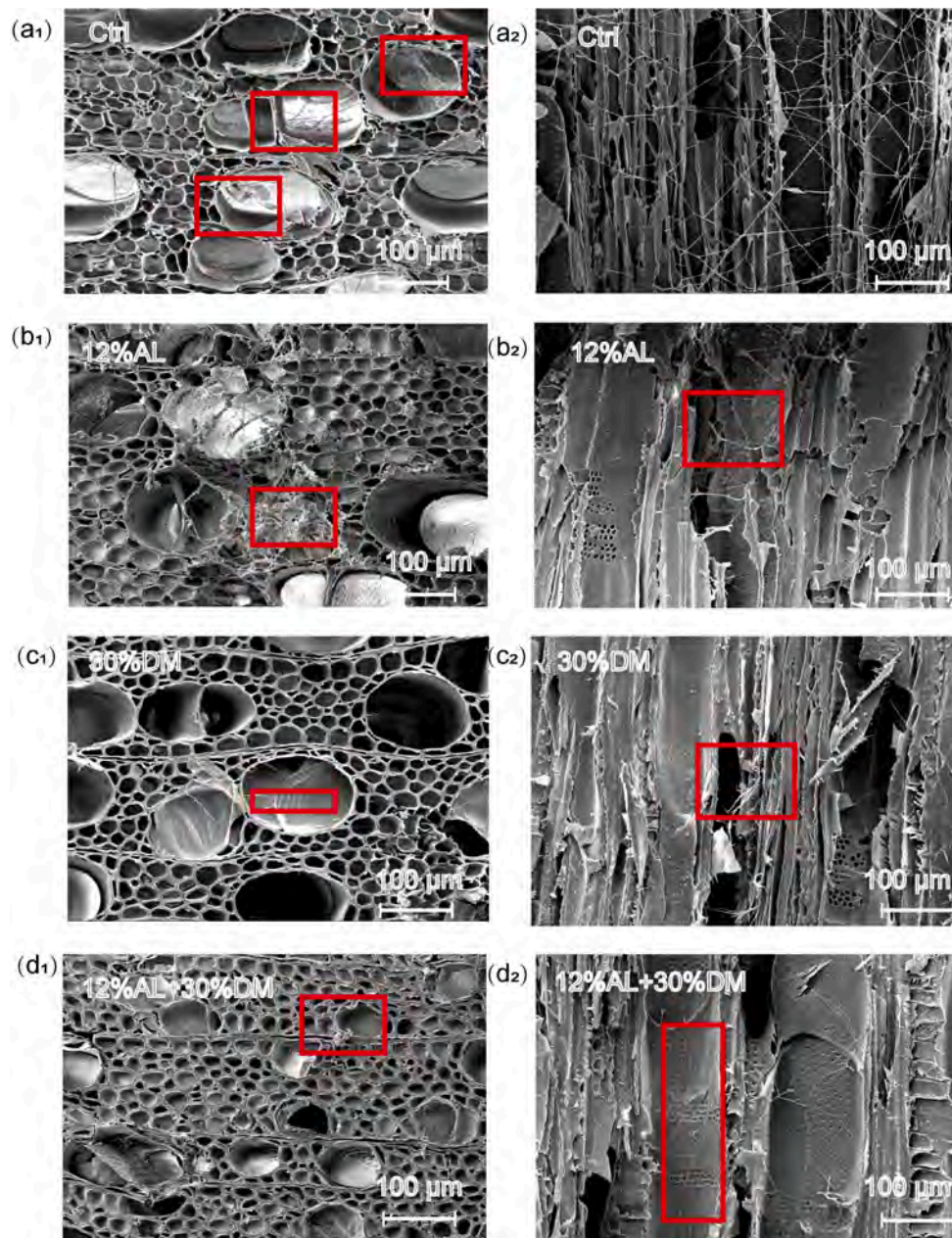


Fig. 9. The micrographs of the cross sections of the unmodified wood samples (a₁) and the impregnated modified wood samples (b₁, c₁, d₁), radial section of the unmodified (a₂) and the impregnated modified wood samples (b₂, c₂, d₂) after white-rot decay.

degrees and above, and the anti-fungal effect of this experimental treatment scheme against brown-rot was more evident than that against white-rot from the mass-loss rate. Therefore, the above results confirmed that the anti-fungal properties of poplar against white-rot and brown-rot were greatly improved by the modification of DM-AL, which provided good protection for wood against fungal attack.

Fig. 9 and Fig. 10a₁, a₂ shows the morphologies of the untreated wood samples after white-rot and brown-rot decay. The wood cell wall matrixes of untreated wood samples were badly destroyed by fungus and wood cell vessels were covered with mycelium. Fig. 9b₁ and b₂ shows a few mycelia left on the wall and wood matrix slightly destroyed, indicating that the 12 %AL had better decay resistance than the unmodified wood for white-rot decay. It can be observed that the damages and compression in wood cell walls due to brown-rot infestation (Fig. 9b₁), indicating the AL itself may have insufficient decay resistance to act as a sole preservative. However, while for 30 %DM, there were fewest

mycelia left of cell wall and the structures were still intact (Figs. 9 and 10c₁ and c₂). Hence, the DM modification effectively achieved the good decay resistance for wood. The most effective treatment (12 %AL + 30 %DM), which cannot observe visible mycelium in the cross section of the wood samples and those cell wall structures retained their overall shape. Therefore, DM-AL endowed the modified wood with excellent decay resistance, attributed to synergistic effect of DM and AL. Consequently, the DM-AL modification possessed the more excellent decay resistance of wood against both the white-rot fungus and brown-rot fungus than other samples, further proving that modification was more effective against fungus.

4. Conclusion

The fast-growing poplar wood was modified by the combination of DM resins and alkaline lignin (AL), with the MgCl₂ as the catalyst. A two-

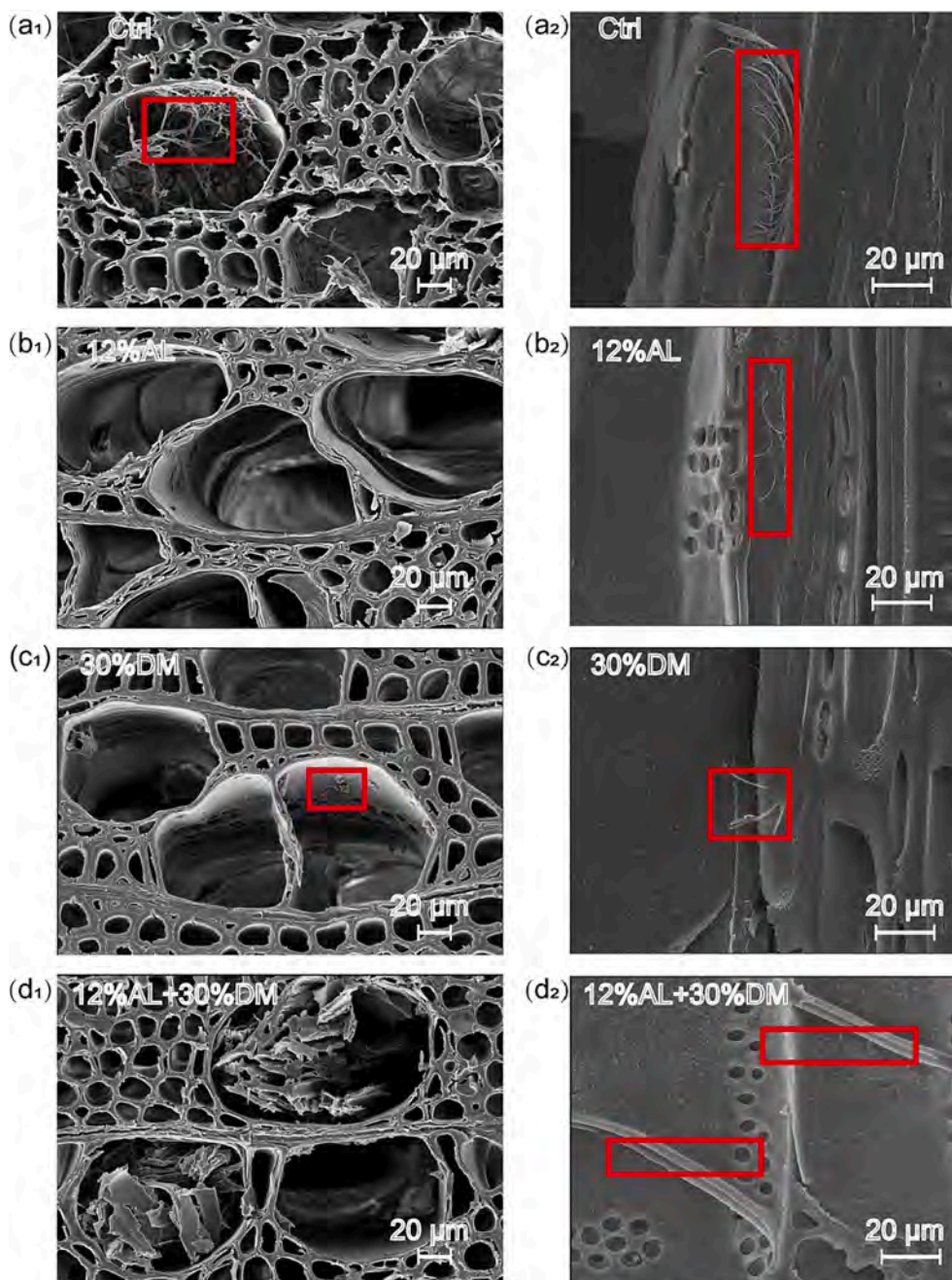


Fig. 10. The micrographs of the cross sections of the unmodified wood samples (a₁) and the impregnated modified wood samples (b₁, c₁, d₁), radial section of the unmodified (a₂) and the impregnated modified wood samples (b₂, c₂, d₂) after brown-rot decay.

step impregnation was adopted to avoid the acidic $MgCl_2$ influence the penetration of AL into the wood, and the physicochemical properties of the fast-growing poplar wood was systemically studied. After the modification by vacuum pressure impregnation and chemical cross-linking of AL and DM resins, the overall properties of combined treated wood are substantially improved compared to the control groups, including the wood treated by AL and DM resins alone. Among them, the optimal group 12 %AL + 30 %DM displayed high WPG of 42 % and high ASE of 52 %, showing good dimensional stability. The mechanical properties of the wood treated by 12 %AL + 30 %DM were also significantly improved compared to the untreated wood, including 40 % increase in bending strength, 60 % increase in MOE, 60 % increase in hardness, 90 % increase in compressive resistance. Meanwhile, the AL macromolecules can effectively reduce the impact strength reduction caused by DM resin treatment alone. Especially, the decay resistance of

DM-AL combined modified wood has also been greatly improved, which was attributed to the synergistic effect of DM and AL. This work provides a simple, low-cost, green approach to poplar wood modification and efficient utilization of lignin.

CRediT authorship contribution statement

Yuxin Peng: Writing – review & editing. **Qi Fan:** Writing – review & editing. **Rongxian Ou:** . **Xiaolong Hao:** . **Chuigen Guo:** . **Zhenzhen Liu:** . **Tao Liu:** . **Lichao Sun:** . **Qingwen Wang:** .

Declaration of Competing Interest

The authors declare that they have no known competing financial interests or personal relationships that could have appeared to influence

the work reported in this paper.

Data availability

Data will be made available on request.

Acknowledgments

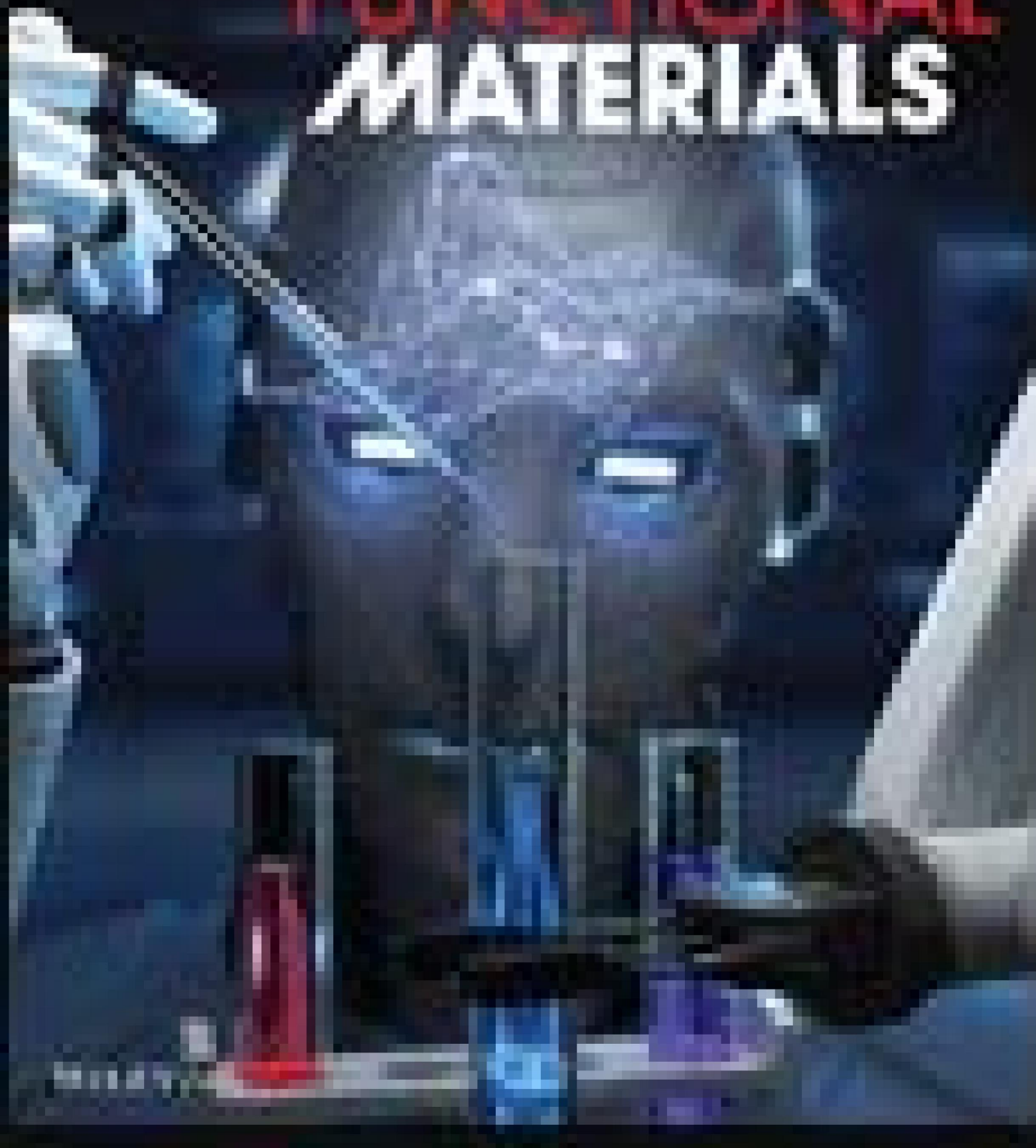
This work was financially supported by the Research and Development Program in Key Areas of Guangdong Province (2020B0202010008), the Guangdong Basic and Applied Basic Research Foundation (2021A1515011014), the National Natural Science Foundation of China (32001264, 52103110), the China Postdoctoral Science Foundation (2021M701258) and the Project of Key Disciplines of Forestry Engineering of Bureau of Education of Guangzhou Municipality.

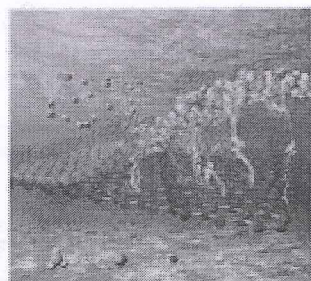
References

- [1] Y. Dong, Y. Yan, Y. Zhang, S. Zhang, J. Li, Combined treatment for conversion of fast-growing poplar wood to magnetic wood with high dimensional stability[J], *Wood Science and Technology* 50 (3) (2016) 503–517.
- [2] Y. Qin, Y. Dong, J. Li, Effect of Modification with Melamine–Urea–Formaldehyde Resin on the Properties of Eucalyptus and Poplar[J], *Journal of Wood Chemistry and Technology* 39 (5) (2019) 360–371.
- [3] H. Yang, M. Gao, J. Wang, H. Mu, D. Qi, Fast Preparation of High-Performance Wood Materials Assisted by Ultrasonic and Vacuum Impregnation[J], *Forests* 12 (5) (2021) 567.
- [4] J. Wang, Y. Yao, Y. Huang, Y. Ma, J. Xi, X. Wang, H. Li, Z. Yang, Effects of the combination of compression and impregnation with phenolic resin on the dimensional stability in the multiscale wood structure of Chinese fir[J], *Construction and Building Materials* 327 (2022) 126960.
- [5] J. Li, A. Zhang, S. Zhang, et al., High-performance imitation precious wood from low-cost poplar wood via high-rate permeability of phenolic resins[J], *Journal of Vinyl and Additive Technology* 39 (7) (2018) 2431–2440.
- [6] F. Jiang, T. Li, Y. Li, Y. Zhang, A. Gong, J. Dai, E. Hitz, W. Luo, L. Hu, Wood-Based Nanotechnologies toward Sustainability[J], *Advanced Materials* 30 (1) (2018) 1703453.
- [7] Y. Xie, Q. Fu, Q. Wang, Z. Xiao, H. Militz, Effects of chemical modification on the mechanical properties of wood[J] Einfluss chemischer Modifikation auf die mechanischen Eigenschaften von Holz, *European Journal of Wood and Wood Products* 71 (4) (2013) 401–416.
- [8] B. Xu, K. Yu, H. Wu, et al., Mechanical properties and engineering application potential of the densified poplar[J], *Wood Material Science and Engineering* 3 (2021) 1–9.
- [9] K. Yue, J. Wu, L. Xu, Z. Tang, Z. Chen, W. Liu, L. u. Wang, Use impregnation and densification to improve mechanical properties and combustion performance of Chinese fir[J], *Construction and Building Materials* 241 (2020) 118101.
- [10] C.-F. Lin, O. Karlsson, J. Martinka, P. Rantuch, E. Garskaite, G.I. Mantanis, D. Jones, D. Sandberg, Approaching Highly Leaching-Resistant Fire-Retardant Wood by In Situ Polymerization with Melamine Formaldehyde Resin[J], *ACS Omega* 6 (19) (2021) 12733–12745.
- [11] S. Rabe, P. Klack, H. Bahr, B. Scharfel, Assessing the fire behavior of woods modified by N-methylol crosslinking, thermal treatment, and acetylation[J], *Fire and Materials* 44 (4) (2020) 530–539.
- [12] M. Liu, F. Guo, H. Wang, W. Ren, M. Cao, Y. Yu, Highly Stable Wood Material with Low Resin Consumption via Vapor Phase Furfurylation in Cell Walls[J], *ACS Sustainable Chemistry & Engineering* 8 (37) (2020) 13924–13933.
- [13] F.C. Dirna, I. Rahayu, L.H. Zaini, W. Darmawan, E. Prihatini, Improvement of Fast-Growing Wood Species Characteristics by MEG and Nano SiO₂ Impregnation[J], *Journal of the Korean Wood Science and Technology* 48 (1) (2020) 41–49.
- [14] D. Wang, Q. Ling, Y. Nie, Y. Zhang, W. Zhang, H. Wang, F. Sun, In-Situ Cross-Linking of Waterborne Epoxy Resin Inside Wood for Enhancing Its Dimensional Stability, Thermal Stability, and Decay Resistance[J], *Acs Applied Polymer Materials* 3 (12) (2021) 6265–6273.
- [15] R. Martha, M. Mubarak, I. Batubara, I.S. Rahayu, L. Setiono, W. Darmawan, F. O. Akong, B. George, C. Gérardin, P. Gérardin, Effect of glycerol-maleic anhydride treatment on technological properties of short rotation teak wood[J], *Wood Science and Technology* 55 (6) (2021) 1795–1819.
- [16] R. Martha, M. Mubarak, I. Batubara, I.S. Rahayu, L. Setiono, W. Darmawan, F. O. Akong, B. George, C. Gérardin, P. Gérardin, Effect of furfurylation treatment on technological properties of short rotation teak wood [J], *Journal of Materials Research and Technology* 12 (2021) 1689–1699.
- [17] L. Emmerich, S. Bollmus, H. Militz, Wood modification with DMDHEU (1,3-dimethylol-4,5-dihydroxyethyleneurea) – State of the art, recent research activities and future perspectives[J], *Wood Material Science and Engineering* 14 (1) (2017) 3–18.
- [18] R. Kurt, E.D. Tomak, The effect of DMDHEU modification on physical and biological properties of parallel strand lumbers[J], *Construction and Building Materials* 195 (2019) 497–504.
- [19] M. Mamiński, P. Kozakiewicz, W. Jaskółowski, K.L. Chin, P.S. H'ng, R. Toczyłowska-Mamińska, Enhancement of technical value of oil palm (*Elaeis guineensis* Jacq.) waste trunk through modification with 1,3-dimethylol-4,5-dihydroxyethyleneurea (DMDHEU)[J], *European Journal of Wood and Wood Products* 74 (6) (2016) 837–844.
- [20] L. Emmerich, H. Militz, C. Brischke, Long-term performance of DMDHEU-treated wood installed in different test set-ups in ground, above ground and in the marine environment[J], *International Wood Products Journal* 11 (1) (2020) 27–37.
- [21] S. Bollmus, C. Beeretz, H. Militz, Tensile and Impact Bending Properties of Chemically Modified Scots Pine[J], *Forests* 11 (1) (2020) 84.
- [22] Y. Xie, A. Krause, H. Militz, H. Turkulin, K. Richter, C. Mai, Effect of treatments with 1,3-dimethylol-4,5-dihydroxy-ethyleneurea (DMDHEU) on the tensile properties of wood[J], *Holzforchung* 61 (1) (2007) 43–50.
- [23] L. Blaschek, A. Champagne, C. Dimotakis, Nuoendagula, R. Decou, S. Hishiyama, S. Kratzer, S. Kajita, E. Pesquet, Cellular and Genetic Regulation of Coniferaldehyde Incorporation in Lignin of Herbaceous and Woody Plants by Quantitative Wiesner Staining[J], *Front Plant Sci* 11 (2020).
- [24] H. Luo, M.M. Abu-Omar, Chemicals From Lignin[J], *Encyclopedia of Sustainable Technologies* (2017) 573–585.
- [25] W. Willems, P. Gerardin, H. Militz, The average carbon oxidation state of thermally modified wood as a marker for its decay resistance against Basidiomycetes[J], *Polymer Degradation and Stability* 98 (11) (2013) 2140–2145.
- [26] L. Emmerich, M. Bleckmann, S. Strobusch, C. Brischke, S. Bollmus, H. Militz, Growth behavior of wood-destroying fungi in chemically modified wood: wood degradation and translocation of nitrogen compounds[J], *Holzforchung* 75 (9) (2021) 786–797.
- [27] GB/T 1927.2-2021 standard. Test methods for physical and mechanical properties of small clear wood specimens—Part 2: Sampling methods and general requirements, 2021.
- [28] GB/T 1927.5-2021 standard. Test methods for physical and mechanical properties of small clear wood specimens—Part 5: Determination of density, 2021.
- [29] GB/T 1927.12-2021 standard. Test methods for physical and mechanical properties of small clear wood specimens—Part 12: Determination of strength in compression perpendicular to grain, 2021.
- [30] GB/T 1927.19-2021 standard. Test methods for physical and mechanical properties of small clear wood specimens—Part 19: Determination of static hardness, 2021.
- [31] GB/T 1927.17-2021 standard. Test methods for physical and mechanical properties of small clear wood specimens—Part 17: Determination of impact bending strength, 2021.
- [32] GB/T 13942.1-2009 standard. Durability of wood - Part 1: Method for laboratory test of natural decay resistance, 2009.
- [33] C. Zhao, S. Li, H. Zhang, F. Yue, F. Lu, Structural insights into the alkali lignins involving the formation and transformation of arylglycerols and enol ethers[J], *International Journal of Biological Macromolecules* 152 (2020) 411–417.
- [34] A. Dieste, A. Krause, C. Mai, G. Sèbe, S. Grelier, H. Militz, Modification of Fagus sylvatica L. with 1,3-dimethylol-4,5-dihydroxy ethylene urea (DMDHEU). Part 2: Pore size distribution determined by differential scanning calorimetry[J], *Holzforchung* 63 (1) (2009) 89–93.
- [35] L. Emmerich, M. Altgen, L. Rautkari, H. Militz, Sorption behavior and hydroxyl accessibility of wood treated with different cyclic N-methylol compounds[J], *Journal of Materials Science* 55 (35) (2020) 16561–16575.
- [36] T. Jiang, H. Gao, J. Sun, Y. Xie, X. Li, Impact of DMDHEU Resin Treatment on the Mechanical Properties of Poplar[J], *Polymers and Polymer Composites* 22 (8) (2014) 669–674.
- [37] J. Yuan, Y. Hu, L. Li, et al., The Mechanical Strength Change of Wood Modified with DMDHEU[J], *Bioresources* 8 (2013) 1076–1088.
- [38] W. Li, L. Chen, Y. Li, X. Li, Bamboo modification with 1,3-dimethylol-4,5-dihydroxyethyleneurea (DMDHEU) catalyzed by maleic anhydride[J], *Journal of Wood Chemistry and Technology* 40 (2) (2020) 126–135.
- [39] A. Dieste, A. Krause, S. Bollmus, H. Militz, Physical and mechanical properties of plywood produced with 1,3-dimethylol-4,5-dihydroxyethyleneurea (DMDHEU)-modified veneers of Betula sp. and Fagus sylvatica[J] Physikalische und mechanische Eigenschaften von Sperrholz aus mit 1,3-Dimethylol-4,5-Dihydroxyethyleneurea (DMDHEU) modifizierten Birken- und Buchenfurnieren, *Holz als Roh- und Werkstoff* 66 (4) (2008) 281–287.
- [40] Krause A, Jones D, Zee M, et al. Interlace treatment-wood modification with N-methylol compounds[J]. *Proceedings of the First European Conference Modification*, 2003, 1(1): 317–327.
- [41] Y. Dong, K. Wang, J. Li, S. Zhang, S.Q. Shi, Environmentally Benign Wood Modifications: A Review[J], *ACS Sustainable Chemistry & Engineering* 8 (9) (2020) 3532–3540.
- [42] M. Cai, Z. Fu, Y. Cai, Z. Li, C. Xu, C. Xu, S. Li, Effect of Impregnation with Maltodextrin and 1,3-Dimethylol-4,5-Dihydroxyethyleneurea on Poplar Wood[J], *Forests* 9 (11) (2018) 676.
- [43] M. Liu, Q. Yi, J. Li, E. Ma, R. u. Liu, Synergistic effect of montmorillonite/lignin on improvement of water resistance and dimensional stability of Populus cathayana [J], *Industrial Crops and Products* 141 (2019) 111747.
- [44] H. Zhou, J. Li, E.J.P. Ma, et al., Multiscale Modification of Populus cathayana by Alkali Lignin Combined with Heat Treatment[J], *Polymers* 10 (11) (2018) 1240.
- [45] Y. Xie, A. Krause, H. Militz, C. Mai, Weathering of uncoated and coated wood treated with methylated 1,3-dimethylol-4,5-dihydroxyethyleneurea (mDMDHEU) [J] Bewitterung von unbeschichtetem und beschichtetem Holz behandelt mit methyliertem 1,3-Dimethylol-4,5-dihydroxyethyleneurea (mDMDHEU), *Holz als Roh- und Werkstoff* 66 (6) (2008) 455–464.

- [46] R. Yasuda, K. Minat, M. Norimoto, Chemical modification of wood by non-formaldehyde cross-linking reagents[J], *Wood Science and Technology* 29 (4) (1995) 243–251.
- [47] L. Emmerich, C. Brischke, S. Bollmus, H. Militz, Dynamic strength properties and structural integrity of wood modified with cyclic N-methylol and N-methyl compounds[J], *Holzforschung* 75 (10) (2021) 932–944.
- [48] H. Ren, L. Zhu, Comparison of the structural characterization of lignophenols and alkaline lignins before and after methylation[J], *Wood Science and Technology* 52 (4) (2018) 1133–1151.
- [49] X. Bi, Y. Zhang, P. Li, Y. Wu, G. Yuan, Y. Zuo, Building bridging structures and crystallization reinforcement in sodium silicate-modified poplar by dimethylol dihydroxyethylene urea[J], *Wood Science and Technology* 56 (5) (2022) 1487–1508.
- [50] A.-D. Muna, Nathir,, et al., Green Approach to Corrosion Inhibition of Mild Steel by Lignin Sulfonate in Acidic Media[J], *Journal of Iron and Steel Research International* 23 (7) (2016) 11.
- [51] M.A. Nada A-a, M. El-Sakhawy, S.M. Kamel, Infra-red spectroscopic study of lignins [J], *Polymer Degradation and Stability* 60 (2) (1998) 247–251.

ADVANCED FUNCTIONAL MATERIALS





The boron-doped carbon felt is rich in electron-deficient sites and defects, which improve the adsorption of negatively charged Zn(OH)_4^{2-} . The robust Zn nucleation sites lead to low Zn nucleation and deposition overpotentials, addressing

critical issues with zinc metal anodes such as dendrite formation and side reactions (HER).

Abstract | **Full text** | **PDF** | **References**
| **Request permissions**

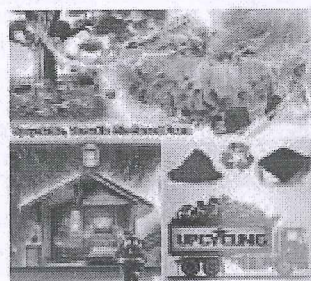
Full Access

Ultrastrong and Thermo-Remoldable Lignin-Based Polyurethane Foam Insulation with Active-Passive Fire Resistance

Lichao Sun, Yujia Guo, Rongxian Ou, Jingwen Xu, Fei Gao, Qingzhi Meng, Sili Chen, Chuigen Guo, Qi Fan, Qingwen Wang

2405424 | Version of Record online: 19 June 2024

<https://doi.org/10.1002/adfm.202405424>



Ultrastrong and thermo-remoldable bio-based composite foams with non-flammability, humidity-tolerant thermal insulation, and superb water vapor barrier are created via an economically attractive one-pot strategy. Based on

unique "expansion-conductivity" behavior, the as-prepared foams can be constructed as a sensitive fire alarm system with an ultra-long alarm time (>1800 s). Post-consumer foams can be quickly upcycled into bulk composites toward recycling economy.

Abstract | **Full text** | **PDF** | **References**
| **Request permissions**

Full Access

A Safe Ether Electrolyte Enabling High-Rate Lithium Metal Batteries

Tao Yang, Liang Li, Jiahang Zou, Yiqing Yao, Qingan Zhang, Zhipeng Jiang, Yongtao Li

2404945 | Version of Record online: 19 June 2024

<https://doi.org/10.1002/adfm.202404945>

A safe ether electrolyte (SEE) is designed using 1,2-dimethoxyethane as the primary solvent, ensuring rapid Li^+ transport and high compatibility toward the lithium metal



RESEARCH ARTICLE

Ultrastrong and Thermo-Remoldable Lignin-Based Polyurethane Foam Insulation with Active-Passive Fire Resistance

Lichao Sun, Yujia Guo, Rongxian Ou, Jingwen Xu, Fei Gao, Qingzhi Meng, Sili Chen, Chuigen Guo, Qi Fan,* and Qingwen Wang

Foam thermal insulators are indispensable for prevailing energy-saving engineering, however their widespread use brings intractability such as unsustainability, “white pollution”, and fire hazards. The emergence of bio-based foams is highly appreciated, but the fabrication approaches are economically unattractive and/or the product properties are inferior, making their large-scale implementation unviable. Herein, a versatile, thermally remoldable phosphate-containing polyurethane composite foam (LPU-G) is constructed from natural lignin and expanded graphite flakes via an atmospheric pressure and scalable one-pot strategy. The optimal LPU-G exhibits exceptional mechanical strength, capable of supporting over 6000 times its weight without significant deformation. Moreover, the LPU-G demonstrates the desired multifunctionality in handling extreme circumstances, including humidity-tolerant thermal insulation, superb water vapor barrier, and withstanding $\approx 1200^\circ\text{C}$ flame without ignition. Based on the “expansion-conductivity” micro-mechanism, LPU-G is the first foam material to be constructed as a sensitive fire alarm system with an ultra-long alarm time ($>1800\text{ s}$). Surprisingly, LPU-G can be rapidly upcycled into recyclable bulk composites for a second life through simple thermo-molding processes rooted in the multi-dynamic behavior of the phosphate, carbamate, and hydrogen bonds. The easy-to-scale LPU-G represents a new generation of thermal insulators that address concerns regarding unsustainability, high cost, fire risk, and inferior mechanical properties.

1. Introduction

Maintaining comfortable temperatures inside buildings consumes $\approx 32\%$ of the world's energy annually,^[1] making insulation materials such as polymer foams highly coveted for improving the energy efficiency of buildings.^[2] Polyurethane (PU) foam, with a global annual production of ≈ 400 million cubic meters, stands out for its exceptional adaptability to a wide range of practical scenarios.^[3] However, the intractability of PU foams has become a growing concern.^[2a,4] Currently, almost all PU foam materials are disposed of in landfills or incinerated after their intended use, resulting in an unacceptable ecological impact.^[5] Additionally, fire safety concerns arise from the highly combustible nature of conventional petroleum-based PU foams.^[6] Henceforth, there is an urgent need to develop a novel renewable and/or recyclable non-flammable PU foam materials that possess intelligent fire alarm response capabilities to promote sustainability on a large scale.

To enhance the sustainability of the polymer foam industry, it is imperative to develop naturally sourced components as alternatives to petroleum-based ones.

Numerous bio-based polyols derived from vegetable oils, carbohydrates, proteins or lignin have been partially substituted for petrochemical polyols in conjunction with fossil-based polyisocyanates for the development of PU foam materials.^[7] In particular, lignin as the most abundant natural polyphenolic polymer on Earth possesses a multitude of captivating characteristics such as high stiffness, elevated carbon content, and excellent water resistance.^[8] These properties serve to counterbalance the weak mechanical properties, flammability, and moisture susceptibility limitations associated with PU foams.^[6,9] However, the conventional approach to synthesizing lignin-based polyols typically involves high-pressure catalytic depolymerization, limited lignin loading levels, and time-consuming modification steps, which significantly impedes the advancement of lignin-derived PU foams.^[9,10] Therefore, there is a strong demand for a facile one-pot process to generate high-performance

L. Sun, Y. Guo, R. Ou, J. Xu, F. Gao, Q. Meng, S. Chen, C. Guo, Q. Fan, Q. Wang
Key Laboratory for Biobased Materials and Energy of Ministry of Education
College of Materials and Energy
South China Agricultural University
Guangzhou 510642, China
E-mail: fanqi2021@scau.edu.cn

R. Ou, F. Gao, C. Guo, Q. Fan, Q. Wang
Institute of Biomass Engineering
Key Laboratory of Energy Plants Resource and Utilization
Ministry of Agriculture and Rural Affairs
South China Agricultural University
Guangzhou 510642, China

The ORCID identification number(s) for the author(s) of this article can be found under <https://doi.org/10.1002/adfm.202405424>

DOI: 10.1002/adfm.202405424

lignin-based polyols. Additionally, the extensive utilization of fossil-based polyisocyanates inevitably contributes to the substantial carbon footprint associated with the final PU foams.

Upcycling the post-consumer polymer into higher value products presents an additional sustainable solution to mitigate the carbon footprint.^[11] The economic and environmental appeal of thermomechanical remodeling for upcycling surpasses that of chemical upcycling.^[12] However, the presence of permanently crosslinked networks in thermosetting PU foams significantly hampers their practical recyclability through melting processes.^[4,13] The incorporation of covalent adaptable networks (CANs) represents a promising strategy for creating malleable thermosets that can be reconfigured, reprocessed, or reshaped via exchange reaction-induced network topology rearrangement under external stimuli like heat, pH, or UV light.^[14] Several CANs types for PU have been reported in recent literature, including urea bonds,^[15] thiourethane bonds,^[16] hydroxyl-carbamate exchange reactions,^[17] and disulfide bonds.^[18] Nevertheless, scant evidence regarding CANs for PU foams or bio-based PU foams can be found in previous reports despite more than two-thirds of commercial PU products being manufactured as foams.

Polymeric networks containing phosphate triesters allow enable topological rearrangement through dynamic transesterification, a well-recognized process for ribonucleic acid modification and cleavage.^[19] Moreover, phosphate esters polyols have the potential to serve as environmentally friendly flame retardants.^[20] Therefore, designing a one-pot strategy for the preparation of lignin-based phosphonate polyols holds great promise for the production of cost-effective, upcyclable, and flame-retardant lignin-derived PU foams. However, achieving complete non-flammability in PU foams by relying solely on the intrinsic flame-retardant structures poses a significant challenge due to their inherent high porosity.^[21]

Constructing foam materials with early fire alarm response is another promising approach to prevent fire disasters by allowing more time for evacuation before the fire becomes uncontrollable.^[22] Recently, various fire alarm systems (FAS) have emerged based on different alarming mechanisms, such as resistance transition,^[22b,23] thermal-electric conversion,^[24] and shape/phase change.^[25] Among these, the resistance transition strategy is favored for its reliability and ease of implementation. Nevertheless, the currently prevalent fire-warning materials have numerous limitations, like inadequate alarm duration and lack of fire-resistant feature.^[22a,26] Additionally, developing highly sensitive, long-term fire-warning and fire-resistant FAS based on foam materials through resistance transition strategy presents two formidable challenges: i) achieving a rapid decrease in electrical resistance when exposed to flames is hindered by the intricate porous network structure of foams;^[22a,26] and ii) incorporating high amounts of flame-retardant fillers disrupts the foam's porous network structure and significantly compromises its mechanical properties.^[6]

To address the aforementioned predicament, we proposed a cost-effective and scalable one-pot approach for fabricating mechanically robust, non-flammable, and thermally remoldable lignin phosphate-based polyurethane/expanded graphite (LPU-G) foams, which represent a new generation of thermally insulating materials providing exceptional active-passive fireproofing performance for energy-efficient engineering. The present

work demonstrates a significant departure from the conventional lignin-based polyol, as we successfully prepared lignin-phosphonate polyols (LPOHs) employing a highly efficient dissolution system of lignin/ethylene glycol under atmospheric pressure conditions (Figure 1a). The novel LPU-G foam can be fabricated via a straightforward room temperature foaming process, eliminating the need for extra petro-polyols. Compared to commercially available petroleum-based PU foams, the obtained LPU-G foam exhibits exceptional mechanical properties, favorable humidity-tolerant thermal insulation, as well as superb water vapor barrier. Owing to its dynamic dual-phase flame retardant behavior, the LPU-G foam demonstrates non-flammable properties even when exposed to a fire attack at $\approx 1200^\circ\text{C}$. In addition, based on the unique “expansion-conduction” behavior of LPU-G foam, we have successfully constructed a highly sensitive foam-based FAS with an unprecedented long fire warning time (>1800 s). Particularly, the thermally induced multi-dynamic behavior consisting of the phosphate and carbamate, along with the rearrangement of hydrogen bonds, facilitate the rapid upcycling of LPU-G foams into recyclable bulk composites through a simple thermo-molding process.

2. Results and Discussion

2.1. Fabrication Principles of LPU-G Foams

The LPU-G foam was obtained by the proposed cost-effective and easily scalable one-pot process under atmospheric pressure (Figure 1a), which eliminates the low-sustainability problems of high-pressure catalytic depolymerization and time-consuming multi-step modifications associated with the traditional lignin-based PU foam synthesis. Initially, a high lignin loading was achieved by exploiting ethylene glycol which has high solubility for lignin, as demonstrated in our previous work.^[8a] Subsequently, the lignin/ethylene glycol solution system was directly employed to synthesize LPOHs through phosphorus pentoxide incorporation. Low viscosity and economically attractive ethylene glycol has a high boiling point and can dissolve more than 35 wt.% of lignin, allowing for atmospheric pressure synthesis and highly tunable rheological properties of LPOHs (Figure S1, Supporting Information). Following that, melamine was introduced as a salt-forming reagent in order to neutralize the generated protons, thereby enhancing the system's reactivity toward isocyanate and improving the mechanical properties of the prepared foams. Moreover, incorporating expanded graphite (EG) flakes derived from natural graphite not only enhances flame retardancy but also addresses the challenge posed by porous foams' limited electrical resistance transition rate by exploiting the remarkable thermal expansion feature, thus facilitating smart FAS construction. Additionally, owing to the high surface polarity of EG, it can be uniformly dispersed within the LPOH. The LPOH containing EG flakes is mechanically mixed with the isocyanate to initiate an exothermic nucleophilic addition reaction that promotes room temperature foaming and curing of the prepolymer, resulting in LPU-G foams formation without requiring additional commercial polyols. A series of $\text{L}_x\text{PU-G}_y$ foams was developed, where x and y represent the varying amounts of lignin and EG flakes used, respectively. The specific formulation is presented in Tables S1–S3 (Supporting Information).

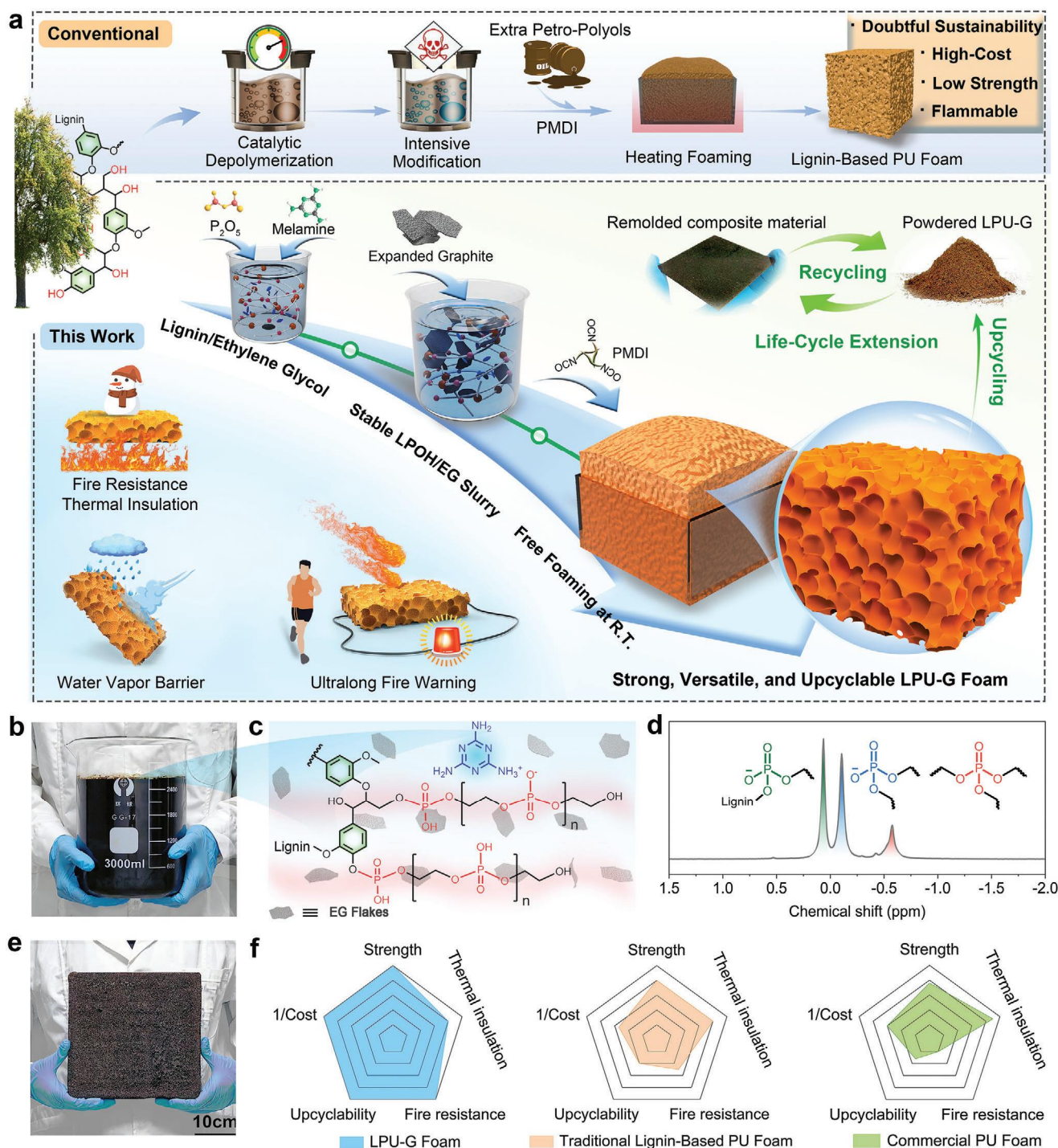


Figure 1. Conceptual design, scale-up fabrication, and structure of the high performance and multifunctional LPU-G foam. a) Schematic comparison of conventional and current preparation strategies, demonstrating that the LPU-G foam produced using a highly sustainable one-pot strategy has exceptional mechanical strength, upcyclability, fire-resistance, waterproofing, and ultra-long fire alarm capability. b) Photograph and c) structure diagram of large-scale preparation of LPOHs. d) ^{31}P NMR of LPOH dissolved in DMSO- d_6 . e) Photograph of large-scale LPU-G foam. f) Radar plots comparing the performance of LPU-G foam, traditional lignin-based PU foam, and commercial PU foam, in which the results are normalized by the maximum value of each characteristic.

The preparation of LPOHs on a large scale can be easily achieved (Figure 1b), indicating their economic attractiveness. Typical structures of LPOH/expanded graphite flakes are shown schematically in Figure 1c. To our satisfaction, the ^{31}P NMR spectra of LPOH dissolved in $\text{DMSO}-d_6$ exhibit several distinct peaks with moderate line widths (Figure 1d), providing conclusive evidence for the formation of triphosphate cross-links.^[19b] The presence of a peak at -0.6 ppm in the ^{31}P NMR spectra confirms the existence of triphosphate species, while the occurrence of two peaks near 0 ppm can be attributed to the generation of dialkyl phosphate monoanions resulting from salt-forming reactions.^[27] In addition, FTIR spectra confirmed the presence of several P–O–C characteristic peaks in LPOH (Figure S2, Supporting Information). The hydroxyl values (Figure S3, Supporting Information) and molecular weights (Table S4, Supporting Information) of LPOHs were also characterized. The LPU–G possesses the potential for large-scale manufacturing (Figure 1e) and demonstrates robust mechanical properties, non-combustibility, favorable humidity-tolerant thermal insulation, as well as excellent reprocessing/upcycling. Moreover, it can be effectively employed in constructing FASs with outstanding performance. Therefore, LPU–G foams have the potential to be a sustainable, versatile, and practical alternatives to traditional lignin-based PU foams and commercially available PU foams (Figure 1f).

2.2. Morphology and Structure

To achieve a uniform and closed-cell foam structure, it is crucial to meticulously balance the curing and foaming rates of the prepolymer in order to regulate nucleation and cell growth rates (Figure 2a). The initial rheological properties of the polyol are crucial for this process. Fortunately, lignin can be easily incorporated to tailor the viscosity of LPOH within a broad range (0.05 – 5000 Pa·s) (Figure S1, Supporting Information). Moreover, when compared to polyols containing lower levels of lignin, both LPOH_3 and LPOH_4 demonstrated typical shear-thinning behavior beyond the critical shear rate due to an increased concentration of aromatic lignin that amplifies their non-Newtonian characteristics. The incorporation of EG flakes into LPOH_3 resulted in a lower critical shear rate compared to pure LPOH_3 (Figure 2b), as it disrupted intermolecular interactions and rapidly relaxed the molecular networks within the polyol. The surface of L_0PU foams exhibits vesicles with diverse sizes at macroscopic level (Figure 2c), whereas the microscopic morphology reveals irregular and immature cells (Figure 2d). This may be caused by the low viscosity and inadequate function degree of LPOH_0 . With an increasing lignin loading in LPOH, the surfaces of L_1PU and L_2PU foams exhibit a uniformly porous structure on a macroscopic scale, while the microscopic morphology displays more regular cells with a wide normal distribution but predominantly open-cell states (Figure S4, Supporting Information). In contrast, L_3PU foams prepared from LPOH_3 demonstrate a more uniform closed-cell structure with smaller average pore size (Figure 2e,g), indicating that lignin loading plays a crucial role in regulating the viscosity and function degree of LPOH for preparing foams with homogeneous cell sizes closed-cell structures. However, in comparison to L_3PU foam samples, the L_4PU foam exhibited a higher prevalence of open-cells and a narrower distribution of cell sizes

(Figure S4, Supporting Information). This phenomenon can be attributed to the elevated viscosity of LPOH_4 (Figure S1, Supporting Information), which effectively impedes the growth rate of foam cells.

The incorporation of EG flakes had a limited impact on the alteration in cell diameter of the foams and only marginally increased the thickness of the cell wall (Figure 2f). In comparison to other L_3PU –G samples, excessive loading of EG flakes in L_3PU – G_4 resulted in more breaks and defects within its cellular structure (Figure S3, Supporting Information), indicating an influence on both nucleation and growth during the foaming process, thereby compromising the integrity of the cellular structure. Conversely, L_3PU – G_3 foam exhibited an homogeneous cellular structure similar to that of L_3PU , with significantly smaller sizes and narrower distributions compared to those observed for L_0PU (Figure 2g).

EDX spectroscopy of the L_3PU – G_3 foam reveals a homogeneous distribution of the elements phosphorus, nitrogen, carbon, and oxygen (Figure 2h). The structures of LPU, L_3PU , and L_3PU – G_3 foams were examined using FTIR spectroscopy (Figure 2i). The broader and overlapping peaks observed at 3200 – 3670 cm^{-1} were attributed to the asymmetric stretching vibration of $-\text{NH}$ from the urethane bond and the stretching vibration of $-\text{OH}$, which is essential for the transesterification on the trialkyl phosphate cross-link,^[19b,27] thus translating to viscous flow of the material. The absence of $-\text{N}=\text{C}=\text{O}$ peaks at 2280 cm^{-1} indicated that the isocyanate was completely consumed. Moreover, the presence of urethane and urea groups was confirmed by observing peaks at 1700 cm^{-1} corresponding to $\text{C}=\text{O}$ stretching vibrations. Additionally, absorption peaks at 1295 cm^{-1} ($\text{P}=\text{O}$) and 1055 cm^{-1} ($\text{P}-\text{O}-\text{C}$) provided evidence for the existence of phosphate ester groups within the foams.^[28] Furthermore, absorption bands observed at 3310 , 3169 , and 803 cm^{-1} corresponded to $-\text{NH}_2$, $-\text{NH}_4^+$, and triazine ring in melamine, respectively, suggesting electrostatic interactions between melamine molecules with phosphate group. These results collectively demonstrated successful preparation of LPU foam. The full XPS spectra of L_0PU , L_3PU , and L_3PU – G_3 foams are shown in Figure 2j, revealing the presence of P 2p peaks at 133 eV, C 1s peaks at 284 eV, N 1s peaks at 399 eV, and O 1s peaks at 532 eV. In Figure 2k, the C 1s spectra of the three samples were fitted with three characteristic polyurethane peaks located at 284.8 eV ($\text{C}-\text{C}$), 286.3 eV ($\text{C}-\text{N}$), and 289.3 eV ($\text{C}-\text{O}$ and $\text{C}=\text{O}$). Furthermore, high-resolution XPS spectra of P 2p exhibited three distinct peaks at 133.3 , 134.3 , and 135.0 eV indicating the presence phosphonate, phosphate, and polyphosphate groups (Figure 2l).^[29] This result provides additional validation to the previous ^{31}P NMR and FTIR results.

2.3. Mechanical Properties

The mechanical properties of foams are crucial for ensuring the reliability of their practical application in energy-saving projects. The compression curves of LPU foams with different lignin loadings revealed three distinct regions corresponding to all stress–strain curves (Figure S5, Supporting Information): the linear Hookean region at low-pressure strains (I), the plateau region representing elastic buckling (II), and the densification region (III). In contrast to many commercially

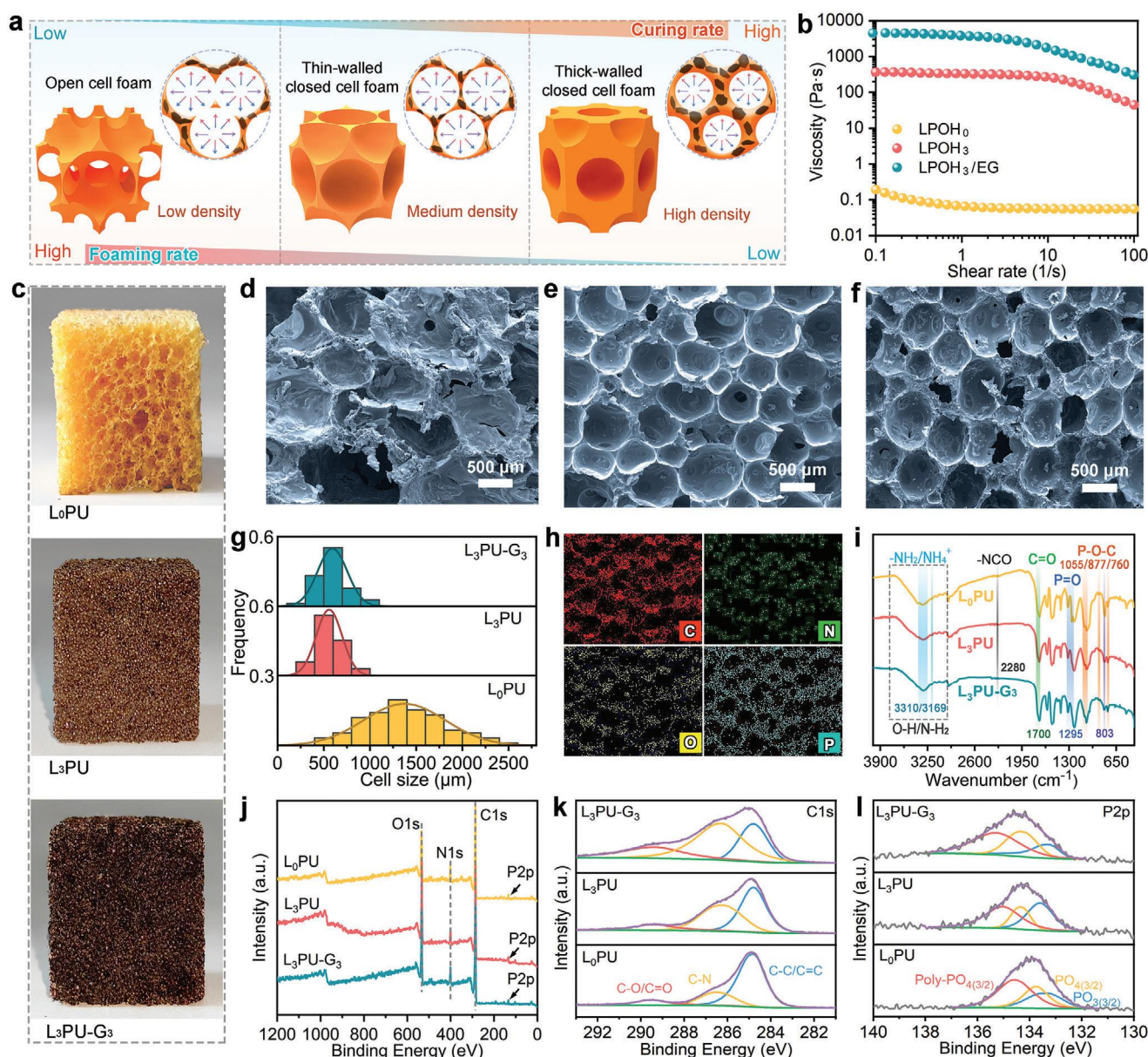


Figure 2. Morphology and chemical structure of the resulting foams. a) Schematic illustration of the co-regulation of the curing and foaming rates on the morphology of the foams. b) Viscosity curves of the different polyols versus shear rate. c) Photographs of the typical 3D foams. d–f) High-magnification SEM images of L₀PU, L₃PU, and L₃PU-G₃ foams. g) Cell size distributions of the different foams with Gaussian fitting curves. h) EDX spectroscopy of the L₃PU-G₃ foam, showing the uniform distribution of phosphorus, nitrogen, carbon, and oxygen. i) FTIR and j–l) XPS results of the L₀PU, L₃PU, and L₃PU-G₃ foams.

available rigid polyurethane foams, the prepared LPU foams exhibited remarkable toughness and stiffness properties by being able to withstand compression up to 80% or higher without catastrophic fragmentation (Figure S5, Supporting Information). Among them, the lignin-free L₀PU foam showed the lowest compressive strength and compressive modulus, measuring only 45.9 kPa and 0.71 MPa, respectively, with obvious fluctuations in its stress–strain curves indicating brittle fracture of the skeleton structure. Upon reaching a lignin content of 30 wt.%, both compressive strength and modulus of L₃PU foam significantly increased to 394.5 kPa and 11.81 MPa, respectively – rep-

resenting an ≈ 7.6 -fold and 15.6-fold increase compared to those values obtained for L₀PU foam. The above results underscore the pivotal role of lignin addition in enhancing the mechanical properties of LPU foams, primarily due to its ability to augment the crosslink density of the foam.

However, the stress–strain curves of L₄PU exhibited fluctuations within the range of 4% to 50%, indicating its inherent brittleness, which can be attributed to incomplete cross-linking between isocyanate and excessive aromatic lignin introduced into the system. Among LPU samples, L₃PU demonstrated the highest specific strength value of 3.3 kN·m kg⁻¹ (Figure S5,

Supporting Information), reaffirming its superior mechanical properties. Considering its intact cell structure, high lignin loading, and optimal mechanical performance, L₃PU foam was selected as a representative sample for further investigation on the impact of EG flakes on foam properties. The stress–strain curves of L₃PU-G foams also exhibited the typical three regions (Figure 3a). The apparent density of L₃PU-G foams slightly increased with increasing EG loading (Table S5, Supporting Information), which can be attributed to the higher density of the EG flakes themselves. The introduction of a small amount of EG flakes significantly decreased the compressive properties of the foam due to their disruption of the nucleation process, thereby affecting the integrity of its multicellular compartmentalized structure. However, further increase in EG flakes resulted in an improvement in compressive strength for L₃PU-G foam (Figure 3b), probably due to the improved rheological properties of the prepolymer by the EG flakes and thus a more homogeneous foam structure. Nevertheless, L₃PU-G₃ foam demonstrated satisfactory strength (318.8 MPa) and modulus (5.78 MPa), which were 6.9 and 8.1 times higher than those of L₀PU, respectively. The exceptional load-bearing capacity and lightweight properties of L₃PU-G₃ are demonstrated by its ability to support an object 6000 times larger than its own weight without any obvious deformation, as depicted in Figure 3c. A comparison with other rigid lignin-based polyurethane foams reported in recent years reveals that L₃PU-G₃ exhibits superior compressive strength and Young's modulus (Figure 3d). Additionally, L₃PU-G₃ demonstrated comparable compressive strength and superior compressive modulus to commercially available PU foams with similar densities (Figure S6, Supporting Information), fully satisfying the mechanical requirements for commercial exterior wall insulation materials.

In addition, cyclic compression of L₃PU-G₃ over a 5% strain range (Figure 3e), showed that the hysteresis loop was found to be much smaller in the second cycle after the first cycle, similar to the Mullins effect encountered in most flexible materials.^[30] This phenomenon can be attributed to insufficient time and suitable conditions for network rebuilding, resulting in inefficient energy dissipation by the fractured network. Remarkably, even after undergoing 40 compression cycles, L₃PU-G₃ retained over 70% of their compressive strength, indicating its mechanical robustness rather than brittleness (Figure 3e). Finite element simulations of the L₃PU-G₃ honeycomb structure further suggest that wall flexure dominated by buckling, rather than brittle cracking, occurs during compression (Figure 3f). Consequently, we consider L₃PU-G₃ to possess superior mechanical properties overall, making it better suited for practical applications. Therefore, we select L₃PU-G₃ for the subsequent investigation of functionality.

2.4. Heat and Water Vapor Barrier

Addressing the vulnerability of intrinsically hydrophilic PU foams to external environmental moisture (e.g., deterioration-prone thermal insulation) is critical to their practical use in energy-efficient engineering. The hydrophobic nature of L₃PU-G₃ foam is evidenced by the presence of numerous microbubbles on its surface when immersed in water under external force (Figure S7, Supporting Information). L₀PU foam exhibits a wa-

ter contact angle (WCA) of 105° and has the shortest retention time of 120 s, indicating its high surface energy and large pores that hinder stable droplet adhesion on the surface (Figure 3g). In contrast, LPU-G foams demonstrate enhanced hydrophobicity with sustained retention times exceeding 300 s for WCAs ranging from 115° to 138°, which can be attributed to two factors: 1) the hydrophobic aromatic backbone structure of lignin reduces the foams' surface energy; 2) incorporation of EG flakes enhances the foams' surface roughness.

To demonstrate the actual performance of L₃PU-G₃ as a thermal insulation material, a setup was designed (Figure 3h). Specifically, an infrared camera was used to record the top surface temperature (TST) profiles at three points (Sp1, Sp2, and Sp3) of the L₃PU-G₃ foam on 100 °C hot stage over a 60-min period. The TST of L₃PU-G₃ increased from room temperature (27 °C) to ≈38 °C within the first 10 min, which was only an increase of 11 °C, and then remained stable until the end of the test (60 min) (Figure 3i,j). The temperature difference (ΔT) between the hot plate and the average TST after stabilization was ≈61 °C, indicating that the samples have excellent thermal insulation properties. Similarly, L₃PU-G₃ showed excellent low temperature insulation, with a ΔT of ≈78 °C between the stabilized TST and the −60 °C cold plate, and a drop in TST of only 7 °C by the end of the test (Figure S8, Supporting Information). This can be attributed to the low thermal conductivity of L₃PU-G₃, which is only ≈50 mW m^{−1} K^{−1} (Figure 3k), resulting from the abundant closed-cell structure that impedes heat flow transfer (Figure 3l). Additionally, L₃PU-G₃ was compared to commercially available phenolic foam (PF), melamine formaldehyde foam (MF), and extruded polystyrene foam (EPF) in terms of thermal insulation performance (Figure S9, Supporting Information). The results demonstrated that L₃PU-G₃ exhibits comparable or even superior thermal insulation performance with PF and EPF. The thermal conductivity of the prepared foams, while not being as efficient as that of PU foams with an optimal thermal conductivity near 20 mW m^{−1} K^{−1},^[21b] is overshadowed by the superior mechanical strength of the former. This implies their suitability for situations requiring exceptional mechanical robustness. We further compared the thermal conductivity of L₀PU and LPU-G foams in different relative humidity (RH) environments. It was found that after 24 h of treatment in a closed humid environment at 95% relative humidity (RH), the thermal conductivity of LPU-G foam changed <5%, while that of L₀PU increased by 22.7% (Figure 3k). The results demonstrate that LPU-G has excellent humidity-tolerant thermal insulation properties, which are highly desirable for many applications, especially for energy-saving engineering such as exterior wall insulation, pipe insulation, and cold storage insulation.

Additionally, the water vapor barrier capacity of LPU and LPU-G foams was evaluated using a custom-built experimental setup (Figure 3m). The results demonstrated that L₃PU and L₃PU-G₃ exhibited superior water vapor barrier capacity. The constant rate of mass change (G) of L₀PU, as shown in Figure 3n, is significantly higher compared to the other foams. This can be attributed primarily to its open cell structure and intrinsic hydrophilic properties. Among all LPU-G foams, L₃PU-G₃ foam had the highest water vapour barrier factor (μ) (Figure S10, Supporting Information) and the lowest water vapour permeability (δ) (Figure 3o) of 3.4 ng/(Pa·m·s), which is lower than that of the commercial

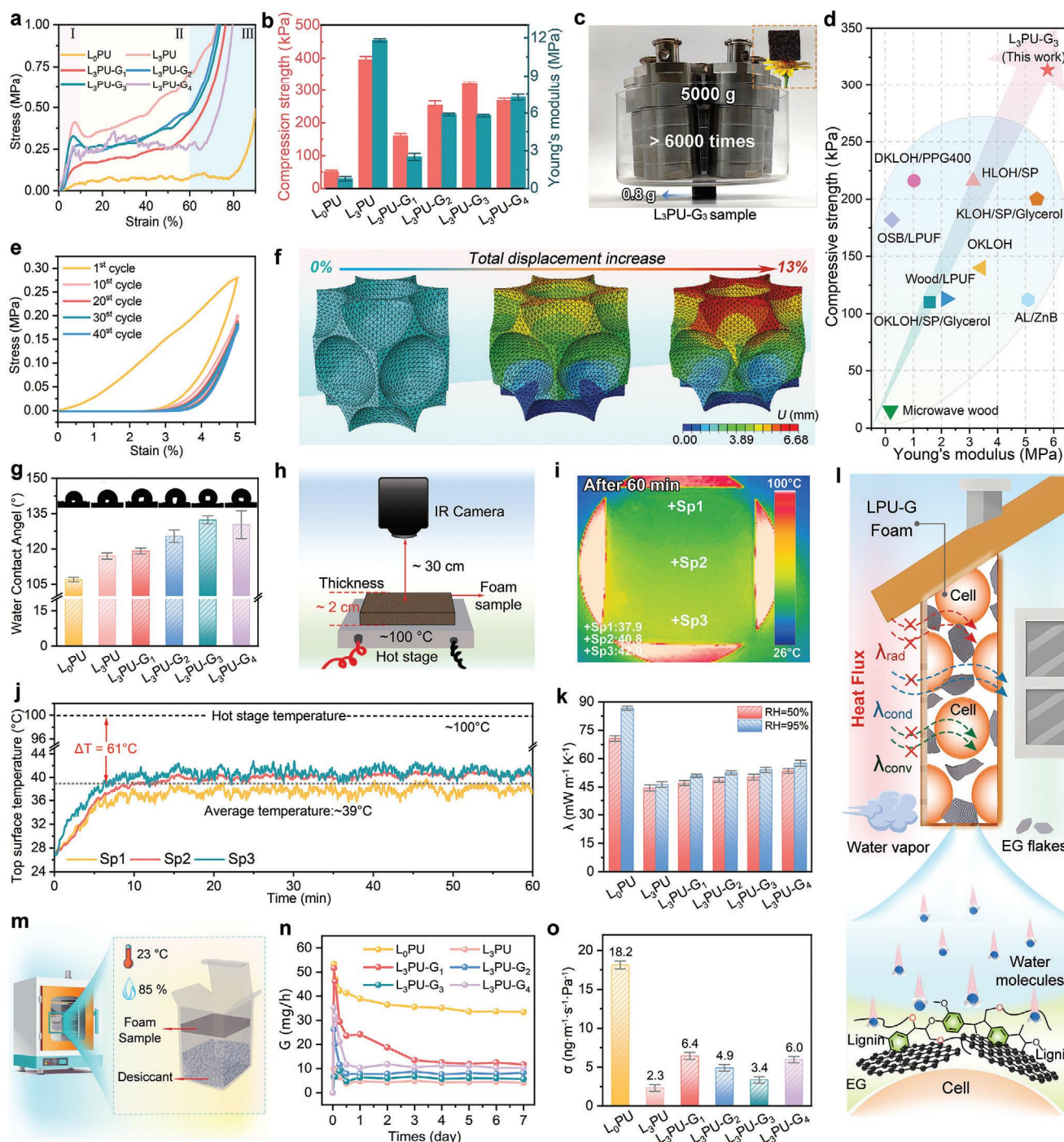


Figure 3. Mechanical, thermal insulation, and water vapor barrier properties. a) Compressive stress–strain curves of different LPU and LPU-G foams. b) Compressive strength and Young's modulus of the resulting foams. c) The low density L₃PU-G₃ foam supporting an object over 6000 times its own weight without significant deformation. d) Comparison of compressive strength versus Young's modulus of L₃PU-G₃ foam with some other lignin-based rigid foams, refer to Table S6 (Supporting Information). e) Cyclic compression curves of L₃PU-G₃ for 40 cycles at 5% strain, demonstrating mechanically robust rather than brittle materials. f) FEM simulations of honeycomb structures for the L₃PU-G₃, colored by the total displacement of element nodes, demonstrating bending-dominated wall buckling. g) Water contact angle (WCA) of the resulting foams. h) Setup for evaluating the thermal insulation properties of the foams. i) IR imaging of the top surface temperatures for L₃PU-G₃ foam on a 100 °C hot stage after 60 min. j) The temperature curves of the top surface versus time. k) Thermal conductivity of the L₀PU and L₃PU-G foams after 24 h of exposure at 20% and 95% relative humidity, respectively. l) Schematic showing the excellent barrier of L₃PU-G to heat and water vapor. m) The homemade setup for testing the water vapor permeability. n) The constant rate of mass change (G) of the foam materials as function of time. o) Water vapor permeability (δ).

polystyrene external wall insulation foam of $\approx 4.0 \text{ ng}/(\text{Pa} \cdot \text{m} \cdot \text{s})$.^[31] This may be due to the hydrophobic lignin aromatic structure and completely closed cell structure in $\text{L}_3\text{PU-G}_3$, which effectively inhibits water vapor absorption and diffusion processes (Figure 3l).

2.5. Fireproofing and Its Mechanism

The flame retardant properties of organic foam heat-insulating materials are crucial in energy-saving applications due to its porous structure is highly flammable, which pose a significant risk to human life and property. A high-temperature flame resistance evaluation setup was designed to visually compare the fire performance of L_3PU , $\text{L}_3\text{PU-G}_3$ foams and commercial flame-retardant PU foam (Figure 4a). The foam samples were exposed to a butane flame at $\approx 1200^\circ\text{C}$ (Movie S1, Supporting Information). Upon contact with the ignition source, the commercial PU foam immediately ignited and the flame rapidly spread throughout the sample (Figure S11, Supporting Information). After 30 s of exposure, the backside temperature rose to $\approx 289^\circ\text{C}$ while continuing to burn until it was burned through after 78 s. However, both L_3PU and $\text{L}_3\text{PU-G}_3$ did not ignite after being exposed for 30 s and their backside temperatures remained close to room temperature at 48 and 31°C respectively (Figure 4b), without any apparent damage or deformation. This can be primarily attributed to the significant enhancement in charring ability provided by lignin phosphonate (Figure S12, Supporting Information), while also synergistically interacting with the expanded graphite flakes.

The burning behavior of LPU and LPU-G foams was preliminarily assessed using the limiting oxygen index (LOI) and the UL-94 vertical burning test (Figure 4c). The results demonstrated that the control L_0PU foam, with an LOI of only 18.7 vol%, exhibited easy ignition. The LOI of the L_3PU foam was elevated to 24.3 vol%; although it could still ignite during the UL-94 vertical flame test, its burning rate significantly decelerated, while maintaining shape integrity even after 48 s of exposure to flames (Figure S13, Supporting Information). These results demonstrated that incorporating lignin phosphonate can effectively impede flame spread. Furthermore, $\text{L}_3\text{PU-G}_3$ exhibited an LOI value of 31.8 vol%, which was a remarkable increase by 70.1% compared to that of L_0PU . During the UL-94 flame test, $\text{L}_3\text{PU-G}_3$ achieved a V-0 rating as two consecutive 10-s flame attacks failed to ignite it (Movie S2, Supporting Information).

During cone calorimetry testing, the L_0PU foam exhibited rapid heat release upon ignition, as evidenced by the peak heat release rate (pHRR) of 475.4 kW m^{-2} achieved within 49 s, as depicted in Figure 4d and Table S7 (Supporting Information). In contrast, the L_3PU exhibited a longer time to ignition (TTI) and experienced a 40% decrease in its pHRR, indicating the effective fire retardancy of lignin incorporation into the material. Furthermore, while the TTI of $\text{L}_3\text{PU-G}_3$ foam did not show further extension, it demonstrated a remarkable decrease in pHRR to 181.3 kW m^{-2} , which is 61.9% lower than that observed for L_0PU foam. Additionally, total heat release (THR) value for $\text{L}_3\text{PU-G}_3$ was found to be the smallest at 16.28 MJ m^{-2} (Figure S14, Supporting Information). The result highlighted the substantial enhancement in flame retardancy achieved through synergistic effects between lignin phosphonate and EG flakes.

In order to gain a deeper understanding of the correlation between TTI and pHRR, the flame retardancy index (FPI) and

fire spread index (FGI) were introduced. Generally, a higher FPI value and a lower FGI value indicated reduced actual fire risk of the material.^[32] As shown in Figure 4e, the incorporation of lignin and EG flakes significantly mitigated the fire hazard associated with the foams. To demonstrate the superior flame retardant properties of the $\text{L}_3\text{PU-G}_3$ foam compared to previously reported PU foams, we compared the pHRR reduction with respect to LOI values (Figure 4f). The results indicated that $\text{L}_3\text{PU-G}_3$ exhibited higher pHRR reduction and LOI values than other bio-based flame retardant PU foams, surpassing even many fire-retardant coated PU foams in terms of excellent flame retardancy. Due to the good inherent flame retardancy of L_3PU , adding just a small amount of EG flakes ($<5 \text{ wt.}\%$) is enough to achieve a remarkable LOI value in $\text{L}_3\text{PU-G}_3$. This is different from the usual method of adding over 20 wt.% of flame retardants to achieve the desired flame retardancy,^[23,33] which can compromise the mechanical properties of the material.

The primary cause of casualties in real fire incidents is the inhalation of excessive smoke and toxic gases.^[21b] Therefore, an analysis was conducted on the smoke and CO production of the prepared foams during combustion (Figure S12, Supporting Information). Compared to L_0PU , the peak smoke produce rate (pSPR), total smoke production (TSP), and CO production of $\text{L}_3\text{PU-G}_3$ were reduced by 58.8%, 29.4%, and 70.1% (Figure 4g), respectively. This result can be attributed to the charring effect of lignin phosphate as well as the formation of a fluffy and porous worm-like char layer produced by EG flakes on the surface of the sample during combustion process. The char layer effectively isolated heat transfer and oxygen supply, thereby reducing smoke generation.

The $\text{L}_3\text{PU-G}_3$ and L_3PU samples exhibited high char residues of 30.8% and 25.1%, respectively, after cone testing, while the L_0PU sample underwent almost complete combustion (Figure 4h). The char residues of the L_3PU sample retained a portion of the foam structure (Figure 4i), indicating that the expanded char layer formed by lignin phosphates as a backbone structure provided effective protection for the internal matrix. The result of elemental mapping demonstrated a homogeneous distribution of C/N/O/P elements (Figure 4j), and XPS survey analysis revealed a reduction in nitrogen and phosphorus content within the char residue of the L_3PU samples (Figure S15, Supporting Information), suggesting a potential dual flame retardant mechanism operating in both gas phase and condensed phase during combustion processes. The char residue of $\text{L}_3\text{PU-G}_3$ was unbroken and retained its intact shape (Figure 4i). Scanning electron microscope (SEM) results showed that the porous carbon produced by the foam matrix and the large number of continuous worm-like carbon layers formed by the EG flakes (Figure 4i). The XPS survey results show that the C—C/C=C content of $\text{L}_3\text{PU-G}_3$ increased by 22.7% compared with that before combustion (Figure S15, Supporting Information), suggesting that the synergistic effect of lignin and EG can effectively improve the degree of aromatization of char residues.

In light of the aforementioned analysis, it is reasonable to conclude that the self-forming dynamic dual-phase barriers ensure excellent flame retardancy. Building upon this mechanism, we further present a schematic diagram illustrating the flame retardant process of $\text{L}_3\text{PU-G}_3$ (Figure 4k). The thermal decomposition of lignin phosphonate melamine salts into phosphorus oxygen

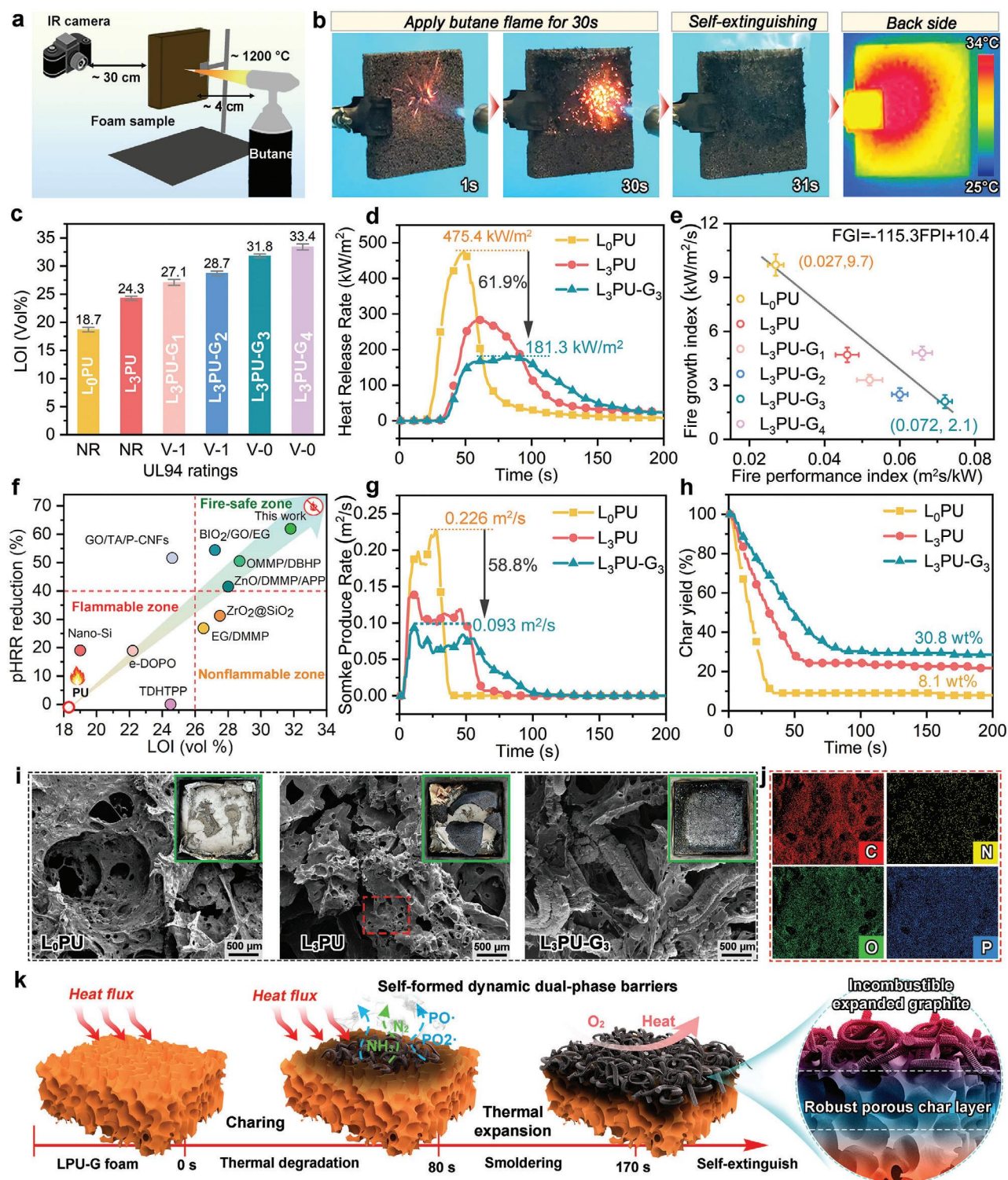


Figure 4. Evaluation of the fire-retardant properties and mechanisms. a) The setup for evaluating fire shield performance. b) Photographs illustrating the burning behavior of L₃PU-G₃ under butane flame for 30 s and the temperature of the foams' backside upon extinguishing, captured by an infrared camera. c) LOI values and UL-94 ratings for LPU and LPU-G foams. d) Average heat release rate (HRR). e) Fire performance index (FPI) versus fire growth index (FGI). f) Comparison of flame retardancy (pHRR reduction versus LOI value) of the resulting L₃PU-G₃ foam with other flame-retardant PU foams reported previously, refer to Table S8 (Supporting Information). g) Average smoke produce rate (SPR). h) Mass loss curves. i) Photographs and SEM images of the char residue from L₀PU, L₃PU, and L₃PU-G₃. j) Elemental mapping of the char residue for L₃PU. k) Schematic illustration showing the fire-retardant mechanism of the dynamic dual-phase.

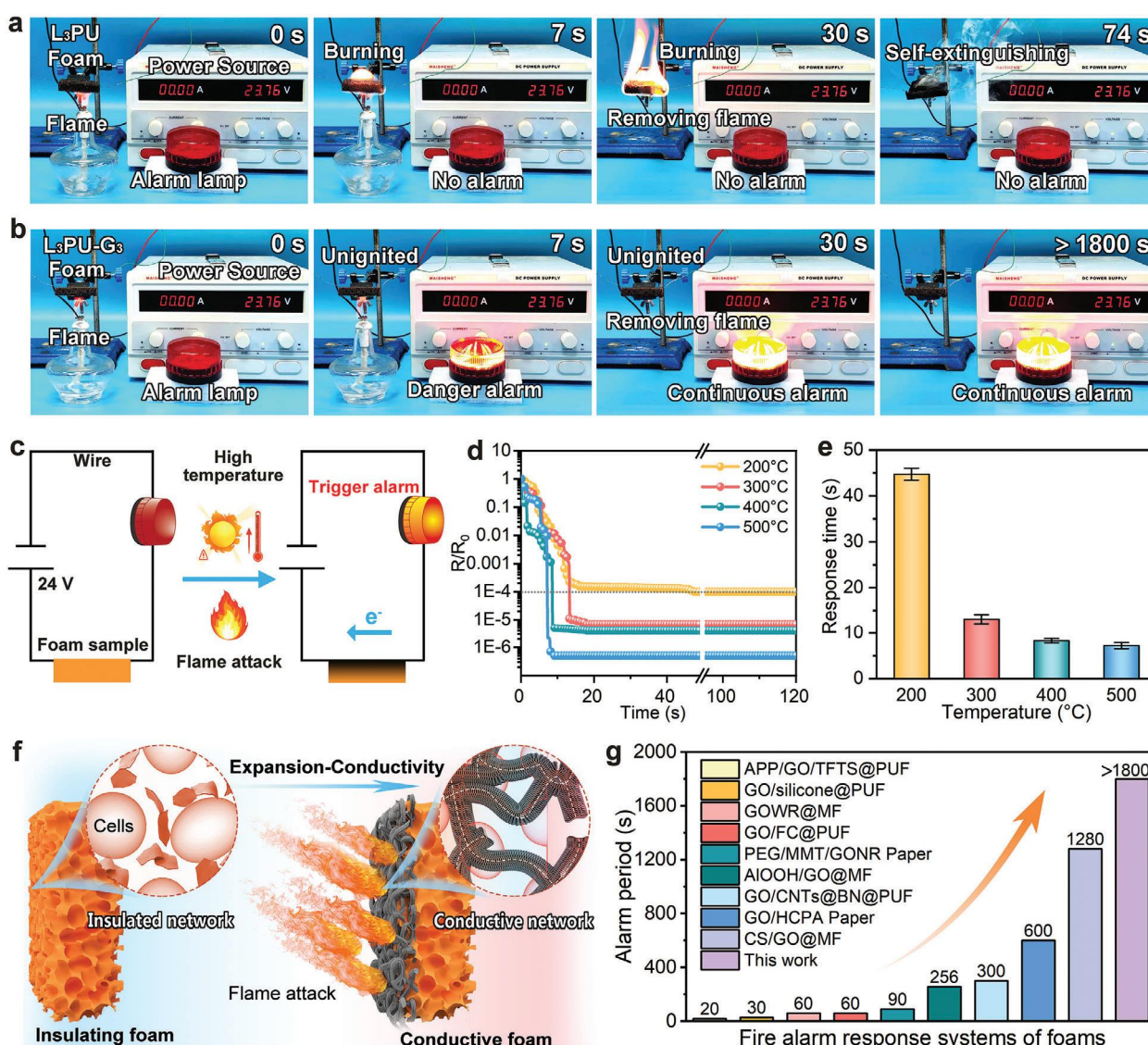


Figure 5. Flame rapid detection and early warning behaviors. Photographs of flame detection processes of a) L₃PU and b) L₃PU-G₃ foams. c) Schematic illustration of fire alarm sensor based on LPU-G foam under flame attack. d) Resistance changes of L₃PU-G₃ foam under flame attack at different temperatures, showing e) different fire warning response times. f) Schematic illustration demonstrating the proposed fire-warning mechanism of thermal expansion-connection. g) Comparison of continuous alarm time of L₃PU-G₃ foam and previously reported fire alarm sensor materials, refer to Table S9 (Supporting Information).

radicals and nitrogen-containing compounds establishes the initial layer of a dynamic gas-phase barrier, effectively inhibiting flame spread. The high carbon content of lignin ($\approx 45\%$) and the rapid formation of a worm-like fluffy carbon layer on the surface of the sample upon heating of the EG effectively prevented heat transfer and oxygen penetration, which provided the second layer of the flame retardant barrier.

2.6. “Expansion-Conductivity” Induced Intelligent Fire Warning

In addition to passive fire retardation, active fire protection features are also necessary for modern energy-efficient buildings, especially in high-rise residences. Conventional active fire protec-

tion primarily relies on smoke sensors, which are triggered only when the smoke concentration surpasses a predefined threshold value. Consequently, existing fire detectors often fail to provide timely fire warnings.^[22] Herein, we realized for the first time that high-strength, non-combustible, heat-insulating bio-based foams with excellent active fire alarm functions can be achieved by adding low-cost EG flakes in small quantities. **Figure 5c** depicts the structure and working mechanism of the fire alarm system (FAS) based on the resistive transformation of the LPU-G foam. The system is established by connecting the LPU-G foam to the alarm light and a low voltage DC power supply (≈ 24 V) via wires. LPU-G foam exhibits typical electrical insulation properties due to its porous structure and the discontinuity of low-content EG flakes. However, when LPU-G foams are exposed to

flame or high temperatures, their internal EG flakes rapidly expand into larger sizes of intercontacting worm-like structures, resulting in a 3D continuous conductive network that triggers an alarm light (Figure 5f).

In order to visually evaluate the fire warning capability of the developed L₃PU-G₃ foam, including fire response sensitivity and duration of warning time, we recorded the fire detection and alerting process of the homemade fire alarm system, as depicted in Figure 5a,b. The experiment demonstrated that L₃PU foam can be ignited by an alcohol lamp flame within a few seconds but quickly self-extinguishes due to its good flame retardancy. Notably, the fire alarm did not trigger during the experiment (Figure 5a; Movie S3, Supporting Information). In contrast, when the L₃PU-G₃ foam was exposed to alcohol lamp flame, the alarm light was triggered within 7 s, and the sample did not ignite. Even if the flame source was removed, the alarm lamp will continue to alarm steadily for more than 1800 s (Figure 5b; Movie S4, Supporting Information). Notably, to improve the accuracy of the flame response time, a precision resistor was used to monitor and record the resistance of the sample in real time. The results showed that the resistance value of the L₃PU-G₃ decreased rapidly after a flame attack, and an alarm was triggered when the resistance value changes by more than four orders of magnitude and reaches below the warning line (resistance range of $\approx 30\text{--}50\text{ k}\Omega$) (Figure 5d). Due to the irreversibility of the EG conductive network, the resistance value remains almost unchanged after removing the flame, which demonstrated the reliable fire warning capability of L₃PU-G₃ foam. Furthermore, the response speed of L₃PU-G₃ varies depending on the ambient temperature, with a shorter response time for higher flame temperatures in the fire alarm (Figure 5e). In practical application, the temperature-induced warning function is attractive for sensor materials, as it can provide people with an opportunity to timely find and remove the potential fire hazards.

Based on the above experimental results, we propose an “expansion-conductivity” working mechanism to explain the excellent intelligent fire warning function of LPU-G foam. As shown in Figure 5f, when the foam is exposed to flames, the EG flakes in the matrix is thermally expanded, transforming from dispersed EG flakes into continuous worm-like carbon layers, forming a conductive network that activates the alarm light. Thus, the challenges of developing foam sensing materials with high sensitivity, long alarm time, high strength, and low cost have been overcome.

Compared to other reported graphene oxide-based fire alarm systems (Table S9, Supporting Information), our fire alarm system constructed directly based on the low-cost LPU-G foam provides the longest stable continuous alarm time to date ($>1800\text{ s}$) (Figure 5g). Additionally, the LPU-G foam exhibits favorable heat insulation, excellent flame retardancy, and high alarm sensitivity, making it a promising material for energy-saving and intelligent fire prevention in high-rise buildings.

2.7. Upcyclable and Reprocessable Performance

The recycling of post-consumer polymers for their reutilization holds great promise; however, a major challenge lies in the expeditious upcycling of waste through streamlined, energy-efficient,

and environmentally-friendly processes. To assess the recycling potential of LPU-G foam, reprocessing tests were conducted by compression molding. The foam was first powdered and then placed in a stainless steel mold and compressed at 160 °C for 5 min at a load of 3 MPa to obtain a black bulk composite (Figure 6a). The results of dynamic mechanical analysis demonstrated that the storage modulus of L₀PU, L₃PU, and L₃PU-G₃ foams exhibits a gradual drop with increasing temperature and there is no obvious rubbery platform (Figure 6b). This implied that the prepared foams have thermo-mechanical reshaping properties. According to Maxwell's model, the relaxation time (τ^*) of the polymer is defined as the time that modulus decays to 1/e of the initial modulus.^[34] The stress relaxation curves of L₀PU, L₃PU, and L₃PU-G₃ foams at 160 °C exhibit relaxation times of 12, 19, and 15 s, respectively (Figure S16, Supporting Information). This further demonstrated the potential of the prepared foams to be molded.

The sustainability of recycled LPU-G bulk composites is greatly increased if they can be remolded at the end of their service life. Therefore, we cut and remolded the recycled L₃PU-G₃ bulk composites several times. The stress relaxation curves of the L₃PU-G₃ bulk composites after three reprocessing cycles were almost identical to those of the original bulk composites (Figure 6c). In addition, the tensile strength retention reached 76.2% (Figure 6d) after three reprocessing cycles (Figure S17, Supporting Information), indicating that the reprocessability and mechanical properties of L₃PU-G₃ were satisfactorily recovered. The reprocessed L₃PU-G₃ bulk composites exhibited a slight improvement in fracture elongation, which could be attributed to the plasticizing effect of small molecule derivatives generated through pyrolysis of a fraction of lignin during mechanical-thermal remodeling processes.

Temperature-dependent IR spectroscopy revealed thermally triggered dissociation of L₃PU-G₃ through H-bonding and dynamic chemical linkages. Upon heating from 50 to 170 °C, the P—O—C stretching vibration peak at 1050 cm⁻¹ exhibited minimal shift but gradually decreased in intensity (Figure 6e). Upon subsequent cooling, the intensity rebounded, indicating a dynamic equilibrium between dissociation and reformation of the phosphate during this process. In addition, the 3308 cm⁻¹ band of the H-bonding-related N—H groups weakened significantly with increasing temperature, while the 3380 cm⁻¹ band of the disordered N—H stretching vibrations remained almost unchanged (Figure S18, Supporting Information). This suggested that the H-bonded N—H groups undergo rapid dissociation accompanied by depletion.^[35] To further elucidate the sensitivity of carbamate bonds, we conducted temperature-dependent IR on L₃PU-G₃ in the C=O stretching region, ranging from 50 to 170 °C (Figure 6f). It is evident that thermal exposure resulting in a weakening of internal interactions, which was manifested by a redshift of the ordered H-bond-related $\nu(\text{C=O})$ at 1705 cm⁻¹ and sec-amides (I) at 1670 cm⁻¹ toward higher wavenumbers, accompanied by the emergence of free $\nu(\text{C=O})$ signals.^[35,36] The results demonstrated the occurrence of chemical exchange behavior of carbamates, particularly when organotin is utilized as a catalyst for transcarbamoylation.^[4]

The temperature-dependent IR spectra were further utilized to generate 2D correlation spectra (2DCOS) in order to extract more nuanced information regarding the sequential events

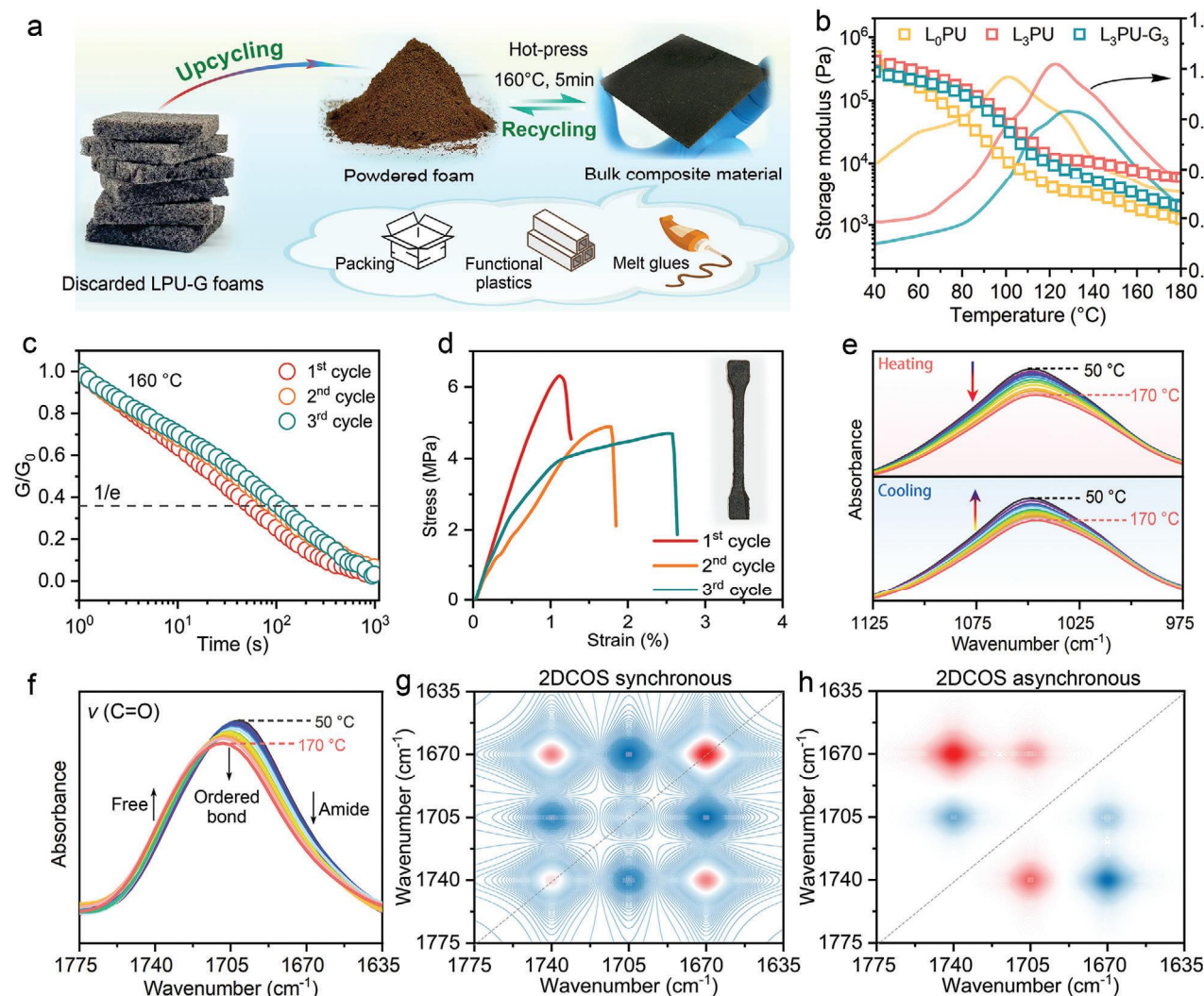


Figure 6. Upcyclable and reprocessable performance. a) The powdered foam was cyclically thermomolded by compression for 5 min at 160 °C under a 3 MPa load. b) Storage modulus and loss factor ($\tan \delta$) as a function of temperature. c) Normalized stress-relaxation curves of L₃PU-G₃ bulk composite after recycle remolding. d) Tensile strength-strain curves and sample shape of L₃PU-G₃ after recycle remolding. e) The in situ temperature-dependent FTIR spectra of L₃PU-G₃ during heating and cooling, showing reversible formation of phosphate ester. f) The in situ temperature-dependent IR spectra of L₃PU-G₃ from 50 to 170 °C in the range of 1775–1635 cm⁻¹. The 2D-COS synchronous and asynchronous spectra are shown as g) and h), respectively. The opposite variation directions of the band intensity are represented by the pink and blue colors, respectively.

during heating. In the synchronized spectra depicted in Figure 6g, three auto-peaks were observed along the diagonal, indicating a conspicuous alteration of the carbonyl stretching vibration peak with variations in temperature.^[37] There are no auto peaks on the diagonal of the asynchronous spectrum in Figure 6h. Asymmetrical positive and negative cross peaks to the diagonal are observed at (1705 and 1740 cm⁻¹), (1670 and 1740 cm⁻¹), and (1670 and 1705 cm⁻¹). According to Noda's rule,^[36,38] when the specified cross peaks of (ν_1 , ν_2) change in the same direction (positive or negative) in both synchrotron and asynchronous spectra, they are indicated by the same color. The intensity change of ν_1 occurs before ν_2 and vice versa. Thus, we can determine that the order of bands is 1705 cm⁻¹ > 1740 cm⁻¹ > 1670 cm⁻¹. This result suggested that the reorganization of H-bonds precedes the cleavage of carbamate bonds, thereby provid-

ing an explanation for the initial changes observed in internal H-bonds upon heating the foam sample.

Based on the aforementioned results, we deduced that the reprocessability demonstrated by LPU-G foams may be attributed to a combination of thermally induced dynamic behavior of phosphate and carbamate esters, as well as rearrangements in hydrogen bonding. The exceptional remoldability of LPU-G foams promises their rapid upcycling into packaging materials with electromagnetic shielding properties, conductive composites, functional hot-melt adhesives, and more.

3. Conclusion

A versatile, thermally remoldable, and high-performance composite foam (LPU-G) from plant polyphenol and expanded

graphite flakes was constructed based on a simple and highly efficient dissolution system of lignin/ethylene glycol. The proposed atmospheric pressure and scalable one-pot strategy is highly economically attractive. The optimal LPU-G, with its ultra-robust mechanical properties, meets the requirements of energy-saving materials for commercial facades. Furthermore, LPU-G demonstrates excellent humidity-tolerant thermal insulation and exceptional water vapor barrier that are attributed to its hydrophobic aromatic lignin skeleton and abundant closed-cell macrostructure. The dynamic dual-phase flame retardant behavior of LPU-G enables it to withstand flames of $\approx 1200^\circ\text{C}$ without ignition. These integrated functionalities make LPU-G highly desirable for energy-efficient engineering in extreme environments. Notably, LPU-G exhibits a unique “expansion-conductivity” property when exposed to high temperature sources. Based on this characteristic, it is the first foam material to be constructed as a sensitive FAS with an ultra-long alarm time (>1800 s). Additionally, LPU-G can be rapidly upcycled into recyclable bulk composites by simple thermo-molding processes rooted in the dynamic behavior of the phosphate and carbamate esters, as well as the rearrangement of hydrogen bonds. As a result, bio-based LPU-G can be given a second life after consumption, greatly reducing its carbon footprint. The obtained results would enable the development of cutting-edge thermal insulators, particularly within the aerospace, transportation, and energy-efficient building industries. Furthermore, the potential applications of LPU-G can be extended to emerging fields such as electromagnetic shielding and durable sensor components.

4. Experimental Section

Synthesis of LPOH: LPOH was prepared by employing an atmospheric, eco-friendly, and one-pot processing strategy. Typically, 75 g of dried EHL powder was added to a three-necked glass flask containing 150 g of ethylene glycol and mechanically stirred at 400 rpm for 1 h at 110°C under atmospheric pressure to ensure that the lignin was completely dissolved. After that, it was cooled to room temperature. Subsequently, during stirring, 13.75 g of phosphorus pentoxide was slowly added. The reaction temperature was gradually raised to 150°C for esterification polycondensation and stirred at 400 rpm for 3 h. Finally, 11.25 g of melamine was added to the above reaction solution and stirred for 1 h to accomplish salification. Then, the reaction solution was poured out, set aside to cool, and labeled as LPOH_3 . A series of LPOH_x ($x = 0, 1, 2, 3, 4$, where x represents the amount trend of lignin used) was developed by tuning the amount of added lignin, as shown in Table S1 (Supporting Information).

Fabrication of Mechanically Robust and Versatile LPU-G Foams: Initially, LPOH_3 was mixed with a certain amount of EG flakes to obtain a homogeneously dispersed slurry that could be stabilized for >6 months. Then, LPOH_3/EG slurry was stirred with the catalyst stannous octanoate, chain extender 1,4-butanediol, foam stabilizer silicone oil, and blowing agent n -pentane at 1000 rpm for 5 min. Afterward, poly((phenyl isocyanate)-co-formaldehyde) (PMDI) was added and stirring was continued for 30 s. The slurry was introduced into a polypropylene plastic mold for free-foaming at room temperature. Once the foam had finished expanding, it was removed and left to mature in an oven at 80°C for 24 h in order to obtain $\text{L}_3\text{PU-G}_y$ foam ($y = 0, 1, 2, 3, 4$, where y represents the amount trend of EG flakes used). In addition, a series of L_xPU foams (without EG flakes) were produced as a control group using different LPOHs according to the above procedure. Specific formulations of L_xPU and $\text{L}_3\text{PU-G}_y$ foams are shown in Tables S2 and S3 (Supporting Information).

Characterizations: The morphology of the foams was observed by a scanning electron microscopy (SEM, Zeiss EVO18, ZEISS, Germany) with

an accelerating voltage of 10 kV, and the foams were coated with gold before observation. The molecular weight and PDI of the samples were determined using color gel permeation chromatography (GPC, Shimadzu, Japan) with THF as the eluent at a flow rate of 1.0 mL min^{-1} . ^{31}P -NMR spectral measurements were conducted using a 400 MHz spectrometer (Bruker Avance III, Bruker, Germany) with $\text{DMSO-}d_6$ as the solvent. X-ray photoelectron spectroscopy (XPS, K-Alpha, Thermo Fisher, USA) was performed using Al K_α radiation ($h\nu = 1486.6\text{ eV}$). In situ temperature-dependent Fourier transform infrared spectrometer (In situ temperature-dependent FTIR, Nicolet IS50, Thermo Fisher, USA) was used to analyze the chemical structure of foams from 25 to 150°C at 1°C min^{-1} . The water contact angle was carried out by a contact angle meter (DSA100, KRÜSS, Germany), using a $2\text{ }\mu\text{L}$ droplet as an indicator. The LOI value was measured by an oxygen index meter (ZY66155A, ZONSKY, China) according to ASTM D2863-13. The vertical flame test was performed on an instrument (UL94-X, MOTIS, China) according to ASTM D3801-10. Samples measuring $100 \times 100 \times 10\text{ mm}$ were tested using cone calorimetry (CCT, MOTIS, China) at a heat flux of 35 kW m^{-2} in accordance with ISO 5660-1. Stress-relaxation experiments were performed on a rheometer (SPA, DHR-2, TA Instruments, USA) equipped with a lower electrical temperature module and an active upper heating system, employing a textured 25 mm plane-plane geometry.

The more detailed experimental section is available in the Supporting Information.

Supporting Information

Supporting Information is available from the Wiley Online Library or from the author.

Acknowledgements

L.S. and Y.G. equally contributed to this work and were listed as co-first authors. This work was financially supported by the Research and Development Program in Key Areas of Guangdong Province (Grant No. 2020B0202010008), the National Natural Science Foundation of China (Grant No. 52103110), the China Postdoctoral Science Foundation (Grant No. 2021M701258), and the Research and Development Program in Key Areas of Guangzhou (Grant No. 2024B03J1380).

Conflict of Interest

The authors declare no conflict of interest.

Data Availability Statement

The data that support the findings of this study are available from the corresponding author upon reasonable request.

Keywords

active/passive fireproofing, bio-based foams, multifunctionality, one-pot strategy, reprocessing

Received: March 28, 2024

Revised: June 11, 2024

Published online:

[1] X. Cao, X. Dai, J. Liu, *Energy Buildings* **2016**, 128, 198.

[2] a) Z. Liu, Z. Fang, N. Zheng, K. Yang, Z. Sun, S. Li, W. Li, J. Wu, T. Xie, *Nat. Chem.* **2023**, 15, 1773; b) A. Mouren, L. Avérous, *Chem. Soc. Rev.* **2023**, 52, 277.

- [3] F. Monie, B. Grignard, J. M. Thomassin, R. Mereau, T. Tassaing, C. Jerome, C. Detrembleur, *Angew. Chem., Int. Ed.* **2020**, *59*, 17033.
- [4] D. T. Sheppard, K. Jin, L. S. Hamachi, W. Dean, D. J. Fortman, C. J. Ellison, W. R. Dichtel, *ACS Central Sci.* **2020**, *6*, 921.
- [5] a) T. M. Nguyen-Ha, T. B. Nguyen, T. A. Nguyen, L. H. Pham, D. H. Nguyen, D. M. Nguyen, D. Hoang, E. Oh, J. Suhr, *Chem. Eng. J.* **2023**, *474*, 145585; b) Y. Deng, R. Dewil, L. Appels, R. Ansart, J. Baeyens, Q. Kang, *J. Environm. Managem.* **2021**, *278*, 111527.
- [6] A. Yadav, F. M. de Souza, T. Dawsey, R. K. Gupta, *Industr. Eng. Chem. Res.* **2022**, *61*, 15046.
- [7] a) X. Ma, C. Zhang, P. Gnanasekar, P. Xiao, Q. Luo, S. Li, D. Qin, T. Chen, J. Chen, J. Zhu, N. Yan, *Chem. Eng. J.* **2021**, *415*, 128956; b) M. Stanzione, M. Oliviero, M. Cocca, M. E. Errico, G. Gentile, M. Avella, M. Lavorgna, G. G. Buonocore, L. Verdolotti, *Carbohydr. Polym.* **2020**, *231*, 115772; c) J. Peyrton, C. Chambaretaud, A. Sarbu, L. Avérus, *ACS Sustain. Chem. Eng.* **2020**, *8*, 12187; d) X. Chen, J. Li, H. Essawy, A. Pizzi, E. Fredon, C. Gerardin, G. Du, X. Zhou, *Construct. Build. Mater.* **2022**, *315*, 125711.
- [8] a) Q. Fan, R. Ou, X. Hao, Q. Deng, Z. Liu, L. Sun, C. Zhang, C. Guo, X. Bai, Q. Wang, *ACS Nano* **2022**, *16*, 9062; b) Q. Fan, T. Liu, C. Zhang, Z. Liu, W. Zheng, R. Ou, Q. Wang, *J. Mater. Chem. A* **2019**, *7*, 23162.
- [9] H. Haridevan, D. A. C. Evans, A. J. Ragauskas, D. J. Martin, P. K. Annamalai, *Green Chem.* **2021**, *23*, 8725.
- [10] N. Mahmood, Z. Yuan, J. Schmidt, M. Tymchyshyn, C. Xu, *Green Chem.* **2016**, *18*, 2385.
- [11] a) J. Sternberg, S. Pilla, *Nat. Sustainabil.* **2023**, *6*, 316; b) O. Guselnikova, O. Semyonov, E. Sviridova, R. Gulyaev, A. Gorbunova, D. Kogolev, A. Trelin, Y. Yamauchi, R. Boukherroub, P. Postnikov, *Chem. Soc. Rev.* **2023**, *52*, 4755.
- [12] X. Zhao, B. Boruah, K. F. Chin, M. Đokić, J. M. Modak, H. S. Soo, *Adv. Mater.* **2021**, *34*, 2100843.
- [13] X.-Z. Wang, M.-S. Lu, J.-B. Zeng, Y. Weng, Y.-D. Li, *Green Chem.* **2021**, *23*, 307.
- [14] a) N. Zheng, J. Hou, Y. Xu, Z. Fang, W. Zou, Q. Zhao, T. Xie, *ACS Macro Lett.* **2017**, *6*, 326; b) M. Podgórski, B. D. Fairbanks, B. E. Kirkpatrick, M. McBride, A. Martinez, A. Dobson, N. J. Bongiardina, C. N. Bowman, *Adv. Mater.* **2020**, *32*, 1906876; c) W. Zou, B. Jin, Y. Wu, H. Song, Y. Luo, F. Huang, J. Qian, Q. Zhao, T. Xie, *Sci. Adv.* **2020**, *6*, eaaz2362.
- [15] R. Guo, Q. Zhang, Y. Wu, H. Chen, Y. Liu, J. Wang, X. Duan, Q. Chen, Z. Ge, Y. Zhang, *Adv. Mater.* **2023**, *35*, 2212130.
- [16] X. Lopez de Pariza, P. Fanlo, L. Polo Fonseca, A. Ruiz de Luzuriaga, H. Sardon, *Progr. Polym. Sci.* **2023**, *145*, 101735.
- [17] C. Bakkali-Hassani, D. Berne, V. Ladmiral, S. Caillol, *Macromolecules* **2022**, *55*, 7974.
- [18] Y. Eom, S.-M. Kim, M. Lee, H. Jeon, J. Park, E. S. Lee, S. Y. Hwang, J. Park, D. X. Oh, *Nat. Commun.* **2021**, *12*, 621.
- [19] a) X. Feng, G. Li, *ACS Appl. Mater. Interfaces* **2020**, *12*, 57486; b) S. Majumdar, H. Zhang, M. Soleimani, R. A. T. M. van Benthem, J. P. A. Heuts, R. P. Sijbesma, *ACS Macro Lett.* **2020**, *9*, 1753.
- [20] H. Yang, B. Yu, X. Xu, S. Bourbigot, H. Wang, P. Song, *Green Chem.* **2020**, *22*, 2129.
- [21] a) S. Wang, X. Wang, X. Wang, H. Li, J. Sun, W. Sun, Y. Yao, X. Gu, S. Zhang, *Chem. Eng. J.* **2020**, *385*, 123755; b) Z. Ma, X. Liu, X. Xu, L. Liu, B. Yu, C. Maluk, G. Huang, H. Wang, P. Song, *ACS Nano* **2021**, *15*, 11667.
- [22] a) L.-Y. Lv, C.-F. Cao, Y.-X. Qu, G.-D. Zhang, L. Zhao, K. Cao, P. Song, L.-C. Tang, *Mater. Sci. Eng.: R: Rep.* **2022**, *150*, 100690; b) C.-F. Cao, B. Yu, J. Huang, X.-L. Feng, L.-Y. Lv, F.-N. Sun, L.-C. Tang, J. Feng, P. Song, H. Wang, *ACS Nano* **2022**, *16*, 20865.
- [23] C.-F. Cao, B. Yu, B.-F. Guo, W.-J. Hu, F.-N. Sun, Z.-H. Zhang, S.-N. Li, W. Wu, L.-C. Tang, P. Song, H. Wang, *Chem. Eng. J.* **2022**, *439*, 134516.
- [24] a) B. Wang, X. Lai, H. Li, C. Jiang, J. Gao, X. Zeng, *ACS Appl. Mater. Interfaces* **2021**, *13*, 23020; b) H. Xie, X. Lai, H. Li, J. Gao, X. Zeng, *J. Coll. Interface Sci.* **2021**, *602*, 756.
- [25] a) J. Jia, N. Gao, R. Li, S. Liao, S. Lyu, Y. Wang, *Chem. Eng. J.* **2022**, *437*, 133285; b) X. Zhao, L.-M. Peng, Y. Chen, X.-J. Zha, W.-D. Li, L. Bai, K. Ke, R.-Y. Bao, M.-B. Yang, W. Yang, *Mater. Horiz.* **2021**, *8*, 1230.
- [26] L. Liu, J. Feng, Y. Xue, V. Chevali, Y. Zhang, Y. Shi, L. C. Tang, P. Song, *Adv. Funct. Mater.* **2022**, *33*, 2212124.
- [27] S. Penczek, J. Pretula, P. Kubisa, K. Kaluzynski, R. Szymanski, *Progr. Polym. Sci.* **2015**, *45*, 44.
- [28] H. Zhu, Z. Peng, Y. Chen, G. Li, L. Wang, Y. Tang, R. Pang, Z. U. H. Khan, P. Wan, *RSC Adv.* **2014**, *4*, 55271.
- [29] K. S. Siow, L. Britcher, S. Kumar, H. J. Griesser, *Plasma Proc. Polym.* **2014**, *11*, 133.
- [30] Y. Huang, L. Xiao, J. Zhou, T. Liu, Y. Yan, S. Long, X. Li, *Adv. Funct. Mater.* **2021**, *31*, 2103917.
- [31] C. Lafond, P. Blanchet, *Buildings* **2020**, *10*, 81.
- [32] Z. Ma, J. Zhang, C. Maluk, Y. Yu, S. M. Seraji, B. Yu, H. Wang, P. Song, *Matter* **2022**, *5*, 911.
- [33] S.-X. Wang, H.-B. Zhao, W.-H. Rao, S.-C. Huang, T. Wang, W. Liao, Y.-Z. Wang, *Polymer* **2018**, *153*, 616.
- [34] T. Debsharma, V. Amfilochiou, A. A. Wróblewska, I. De Baere, W. Van Paepegem, F. E. Du Prez, *J. Am. Chem. Soc.* **2022**, *144*, 12280.
- [35] R. Liang, H. Zhang, Y. Wang, J. Ye, L. Guo, L. He, X. Li, T. Qiu, X. Tuo, *Chem. Eng. J.* **2022**, *442*, 136204.
- [36] Y. Shi, B. Wu, S. Sun, P. Wu, *Advanced Materials* **2023**, *36*, 2310576.
- [37] Q. Quan, C. Fan, N. Pan, M. Zhu, T. Zhang, Z. Wang, Y. Dong, Y. Wu, M. Tang, X. Zhou, M. Chen, *Adv. Funct. Mater.* **2023**, *33*, 2303381.
- [38] a) I. Noda, *Appl. Spectrosc.* **1993**, *47*, 1329; b) I. Noda, A. E. Dowrey, C. Marcott, G. M. Story, Y. Ozaki, *Appl. Spectrosc.* **2000**, *54*, 236A.

INDUSTRIAL CROPS AND PRODUCTS

(FORMERLY BIOMASS TECHNOLOGY JOURNAL)



Research article • Full text access

Identification of high carnosic acid rosemary (*Salvia rosmarinus* Spenn.) genotypes through genetic diversity exploitation, chemical profiling, and transcriptomic approaches

Symela Ntoanidou, Aikaterini Kaplani, Charikleia Paloukopoulou, Christos Bazakos, ... Angelos K. Kanellis
Article 118562

View PDF Article preview

Research article • Full text access

Handling-friendly, waterproof, and mildew-resistant all-bio-based soybean protein adhesives with high-bonding performance via bio-inspired hydrophobic-enhanced crosslinking network

Sili Chen, Tao Liu, Yujia Guo, Xiaolong Hao, ... Rongxian Ou
Article 118583

View PDF Article preview

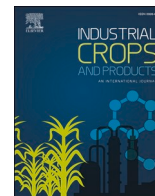
Research article • Full text access

Ensemble model-based analysis of the effects of environmental factors on the distribution and chemical composition of *Asparagus cochinchinensis* (Lour.) Merr.

Tingting Zhang, Ya Yuan, Ying Han, Wanqing Feng, ... Lili Zhou
Article 118584

View PDF Article preview





Handling-friendly, waterproof, and mildew-resistant all-bio-based soybean protein adhesives with high-bonding performance via bio-inspired hydrophobic-enhanced crosslinking network

Sili Chen^{a,b}, Tao Liu^{c,*}, Yujia Guo^b, Xiaolong Hao^{a,b}, Lichao Sun^b, Chuigen Guo^{a,b},
Qi Fan^{a,b,**}, Rongxian Ou^{a,b}

^a Institute of Biomass Engineering, Key Laboratory of Energy Plants Resource and Utilization, Ministry of Agriculture and Rural Affairs, South China Agricultural University, Guangzhou 510642, China

^b Key Laboratory for Biobased Materials and Energy of Ministry of Education, College of Materials and Energy, South China Agricultural University, Guangzhou 510642, China

^c College of Food Science, South China Agricultural University, Guangzhou 510642, China

ARTICLE INFO

Keywords:

All-bio-based adhesives
Biomimetic bonding
Multiple cross-linked networks
Mildew-resistance
Waterproofing

ABSTRACT

Eco-friendly and formaldehyde-free soybean protein adhesives are highly attractive to the wood-based panel industry but typically suffer from low water-resistant bonding strength, high viscosity, and susceptibility to mildew. Inspired by adaptive hydrophobic and hydrophilic interactions of mussel foot proteins, herein, a high-performance and versatile all-bio-based adhesive (STF) was synthesized through employing bio-derived furfural and natural tannic acid to assist soybean protein in developing a biomimetic physical/chemical cross-linking network. The collaboration of the hydrophobic furan ring and the hydrophilic catecholic moiety endowed the as-prepared STF adhesives with exceptional water-resistant bonding strength, easy-coating performance, and mildew resistance. Compared to the original soybean protein, the optimal STF demonstrated dry and wet shear strengths of up to 2.52 MPa and 1.71 MPa, respectively, representing an increase of 65.8 % and 263.8 %. Notably, the aged bonding strength of STF surpassed that of previously reported soybean protein-based adhesives with a value as high as 1.19 MPa. The viscosity of the STF decreased by ≈ 98.1 % compared to the unmodified adhesive. Additionally, the STF exhibited excellent mildew resistance (no mildew for 7 days) and storage stability (> 72 h). Combined with life cycle assessment, the biomimetic STF adhesive holds great potential for large-scale production of environment-friendly wood panels.

1. Introduction

Currently, the global annual consumption of adhesives for wood-based panels is around 50 million tons, of which formaldehyde-based adhesives account for approximately 90 % (Hussin et al., 2022; Yang et al., 2023). Alarming, the formaldehyde-based resin adhesives cause the release of carcinogenic formaldehyde from wood-based panels into the production workplace and living environment, seriously endangering human health (Westerman et al., 2023). In addition, given the rapid depletion of global non-renewable petroleum resources, formaldehyde-based resin adhesives for the wood industry contradict

the current societal push toward sustainable development (Kan et al., 2022). Therefore, the development of high-performance adhesives that are formaldehyde-free, renewable, and capable of large-scale production is of great fascination to the contemporary society (Chang et al., 2023; Zhao et al., 2022).

As a by-product of the soybean oil industry, soybean protein is inexpensive, easy to modify, and rich in reactive functional groups, including carboxy ($-\text{COOH}$), hydroxyl ($-\text{OH}$), and amino ($-\text{NH}_2$) groups (Zhang et al., 2022b), making it a potential alternative to formaldehyde-based resin adhesives in the production of wood-based panels (Mi et al., 2022; Zhang et al., 2022a). Nonetheless, as a natural

* Corresponding author.

** Corresponding author at: Institute of Biomass Engineering, Key Laboratory of Energy Plants Resource and Utilization, Ministry of Agriculture and Rural Affairs, South China Agricultural University, Guangzhou 510642, China.

E-mail addresses: liutao@scau.edu.cn (T. Liu), fanqi2021@scau.edu.cn (Q. Fan).

<https://doi.org/10.1016/j.indcrop.2024.118583>

Received 24 February 2024; Received in revised form 30 March 2024; Accepted 16 April 2024

Available online 22 April 2024

0926-6690/© 2024 Elsevier B.V. All rights reserved.

polymer, soybean protein presents noteworthy drawbacks when utilized in adhesives due to its intricate four-level protein structure and numerous hydrophilic groups, which results in poor water-resistant bonding strength (wet shear strength of pure soybean protein-based adhesives < 0.47 MPa) (Liang et al., 2023). In addition, the strong intermolecular interactions, such as hydrogen and disulfide bonds, lead to high viscosity, poor fluidity, and inadequate brushability of soybean protein adhesives (Liu et al., 2022b). These factors contribute to a reduction in bonding strength and increased challenges in adhesive processing (Sun et al., 2023). Moreover, soybean protein functions as a nutrient easily susceptible to microbial attack, decreasing its storage stability and promoting early deterioration (Kan et al., 2023). These factors negatively impact the wide-scale application of soybean protein adhesives.

To reverse these dilemmas, various chemical and physical methods have been utilized to improve the performances of the soybean protein-based wood adhesives. These methods involve physical modifications (Yue et al., 2020), chemical cross-linking (Li et al., 2023a; Yan et al., 2022), biomimetic adjustments (Li et al., 2023b), inorganic nano-materials reinforcement (Xu et al., 2022a), and toughening with hyper-branched polymers (Liu et al., 2022a), etc. Among them, chemical cross-linking of soybean protein is commonly considered the most effective strategy to enhance the bonding strength and waterproof property of soybean protein-based adhesives. Prevalent chemical cross-linkers, such as isocyanates (Yin et al., 2021), acrylates (Fapeng et al., 2017), anhydrides (Qi et al., 2013), metal hydroxides (Li et al., 2023d), and siloxane coupling agents (Xu et al., 2022b), provide benefits for the soybean protein-based adhesives. All of these modifiers enhance

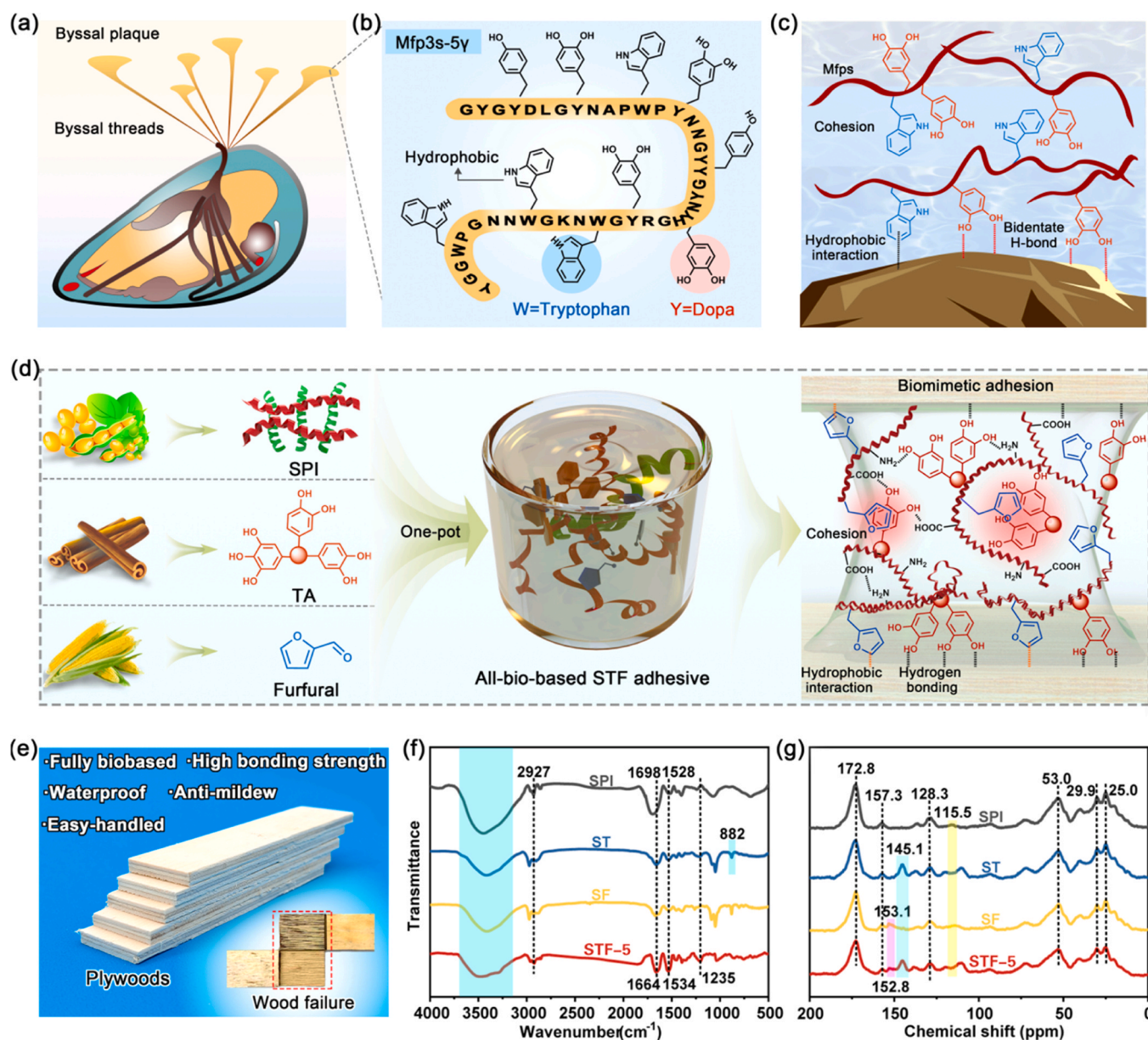


Fig. 1. Bioinspired design and preparation strategy of the all-bio-based STF adhesive. a) Schematic of byssal plaques of mussel. b) Sequences of mussel foot protein (Mfp) 3-5γ, hydrophobic tryptophan moiety and catechol moiety of Dopa are highlighted in light blue and pink, respectively. c) Schematic illustration of underwater adhesion of Mfps to rocks, demonstrating that hydrophobic interaction enhances Dopa-mediated adhesion. d) Schematic illustration of the preparation of all-bio-based STF adhesive and its biomimetic adhesion mechanism to wood veneer. e) Schematic illustration of three-layer plywood specimens bonded with easy-handled, water-resistant, and anti-mildew all-bio-based STF adhesives and wood failure of the specimen after a wet strength test (inset). f) FT-IR spectra and g) solid-state ^{13}C NMR of SPI, ST, SF, and STF adhesives before curing.

adhesive performance by reacting with soybean protein molecules through their functional groups, which leads to a boost in the cross-linking density and hydrophobicity of the curing adhesives. However, chemical cross-linked soybean protein-based adhesives exhibit high initial viscosity, which diminishes production efficiency and negatively impacts the quality of wood-based panels (Huang et al., 2022a). In addition, these modifiers are almost sourced from non-renewable petrochemical resources and fail to address the underlying issue of the downgrade renewability of soybean protein adhesives. Furthermore, to our knowledge, no research has been found to report a cost-effective and straightforward method for achieving the desired combination of high bonding strength, ease of coating, and mildew resistance in an all-bio-based soybean protein adhesive.

The investigation of marine sessile organisms has yielded novel insights for developing high-performance adhesives. For instance, marine mussels appear especially interesting to scientists due to the pivotal function of their post-translationally modified amino acids such as 3,4-dihydroxyphenylalanine (DOPA) and phosphorylated serine in their underwater adhesion (Pang et al., 2022; Qi et al., 2023). Relatively simple polymers that contain catechol have the ability to mimic a few of the features of mussel proteins and generate an adhesive with a degree of bonding strength (Li et al., 2023c; Wei et al., 2012a). Tannic acid (TA), an inexpensive polyphenol compound that exists abundantly in plants, is considered a DOPA analog for adhesive modification (Liu et al., 2021). Based on phenol-amine chemistry, complexation processing of soybean protein with TA in solution provides a convenient method for preparing an adhesive with tunable composition, bonding properties, and mildew resistance (Li et al., 2022; Zhang et al., 2020). Nevertheless, soybean protein/TA adhesives do not meet the rigorous water resistance standards required for wood-based panels intended for outdoor use that must withstand prolonged exposure to boiling water (Ghahri et al., 2022).

Actually, strong wet adhesion in mussel foot proteins is a complex process of adaptive hydrophobic and hydrophilic interactions that goes beyond a straightforward DOPA-mediated formulation (Wei et al., 2012b; Yu et al., 2013). Researches have revealed that the existence of pendant hydrophobic aromatic tryptophan, nested with DOPA in the sequence of mussel foot proteins (Figs. 1a and 1b) (Wei et al., 2012b), significantly enhances adhesion at a neutral pH and contributes to cohesive interactions between adhesive proteins (Fig. 1c) (Yu et al., 2013). Therefore, following the design principle of hydrophobic modification of soybean protein molecules followed by their complexation with TA is expected to yield high performance bio-based adhesives with excellent water-resistant bonding properties.

Herein, inspired by adaptive hydrophobic and hydrophilic interactions of mussel foot proteins, we demonstrated a facile, one-pot, and scale-up approach for the fabrication of an all-bio-based adhesive, STF, through modifying a complex of soy isolate protein (SPI) and TA with bio-derived furfural (Fig. 1d). The STF exhibits high bonding strength, excellent water resistance, ease of coating, and good mildew resistance. It holds great promise for the development of environmentally friendly and sustainable wood-based panels (Fig. 1e). In this system, the polyphenolic structure of TA and SPI molecules can generate strong non-covalent interactions, which shield the weak intermolecular interactions of the proteins, thereby reducing viscosity and improving bonding strength. Furfural, as a bio-based cross-linking agent, enhances the hydrophobicity of the adhesives matrix by reacting with protein amino groups. It can further improve water resistance of STF through cross-linking and co-polymerization with TA and SPI. Moreover, the synergistic effect of TA and furfural substantially improves the adhesive's mildew resistance. Formulation, brushability, bonding performance, water resistance, antimicrobial resistance, and life cycle assessment (LCA) of the STF were systematically investigated.

2. Materials and methods

2.1. Materials

Soybean protein isolate (SPI, 90% protein content) was bought from Dulai Biotechnology Co., Ltd. (Nanjing, China). Tannic acid (TA, 98%) and furfural (CP) were bought from Adamas-beta Co., Ltd. (Shanghai, China). Sodium hydroxide (NaOH, AR) and hydrochloric acid (HCl, AR) were purchased from Guangzhou Chemical Reagent Factory Co., Ltd. (Guangzhou, China). Poplar veneers with a moisture content of 10–12% and measuring $400 \times 400 \times 1.5 \text{ mm}^3$ (length, width, and thickness) were acquired from Linyi Jieya Trading Co., Ltd. (Linyi, China). All raw materials are not further purified.

2.2. Preparation of adhesives

STF adhesives were synthesized by a facile method. The formulations of adhesives are summarized in Table 1 and Table 2. Briefly, 20 g of SPI and 80 g of distilled water were mixed well in a three-necked vial, and 1.7 g of 40 wt% NaOH solution was added to adjust the pH of the slurry to 10. Homogeneous slurry was obtained by stirring at 400 rpm for 1 h at 65 °C. Subsequently, an amount of TA was added to the slurry and stirred at the same temperature for 1 h. The pH of the slurry was adjusted to 5 with hydrochloric acid solution (19 wt%), a certain amount of furfural was added and stirred at 65 °C for 30 min to obtain the STF adhesive. Control adhesives, labeled as SPI, were synthesized without TA and furfural. Adhesives with added TA or furfural were named ST and SF, respectively. Synthesis conditions are the same as for STF adhesives. Uncured adhesive powder was obtained through facile lyophilization process, while cured adhesives were acquired by treating them at a temperature of 170 °C for 2 h. The powders of both uncured and cured adhesives were collected for further structural characterization.

2.3. Evaluation of the bonding strength

The resultant plywood panels were sawed into $100 \text{ mm} \times 25 \text{ mm}$ specimens. The dry, wet, and aged bonding strength were evaluated according to the China National standard GB/T 17657–2013 and GB/T 9846–2015. Briefly, the shear strength of the plywood specimens acquired without soaking is the dry bonding strength. The wet bonding strength is determined by measuring the shear strength of plywood specimens that have been soaked in water at $63 \pm 3 \text{ °C}$ for 3 h and subsequently cooled to room temperature.

The plywood samples were boiled for 4 h, then air-dried using a blower oven at 60 °C for 16–20 h, followed by another 4-hour boiling cycle. The samples were later immersed in cold water with a temperature lower than 30 °C for at least 1 h. The resulting shear strength is referred to as the aging bond strength. The shear strength of plywood specimens was tested on a universal testing machine (AI-7000 M-GD, Goodtechwill, Taiwan, China) and calculated according to Eq. (1):

Table 1
Design and results of orthogonal experiment.

Sample	A pH	B TA /wt %	C Furfural /wt%	D Temperature /°C	Dry shear strength /MPa	Wet shear strength /MPa
STF-1	4	20	20	160	2.22±0.19	1.27±0.13
STF-2	4	15	25	170	2.48±0.16	1.25±0.07
STF-3	4	25	15	180	2.26±0.21	1.54±0.17
STF-4	5	25	25	160	2.09±0.07	1.57±0.19
STF-5	5	20	15	170	2.52±0.09	1.71±0.05
STF-6	5	15	20	180	2.34±0.17	1.59±0.12
STF-7	6	15	15	160	1.64±0.11	0.91±0.17
STF-8	6	25	20	170	2.26±0.14	1.15±0.16
STF-9	6	20	25	180	1.89±0.08	1.28±0.18

Table 2

The formulations of SPI, ST, SF, and STF-5 adhesives.

Samples	SPI/g	Water/mL	TA/wt%	Furfural/wt%	pH
SPI	20	80	0	0	7
ST	20	80	20	0	5
SF	20	80	0	15	5
STF-5	20	80	20	15	5

$$\text{Shear strength (MPa)} = \frac{\text{Tension Force (N)}}{\text{Bonding Area (mm}^2\text{)}} \quad (1)$$

2.4. Mildew resistance test

The open Petri dishes with fresh adhesive samples were placed in an oven that maintained a constant temperature of 30 ± 2 °C and a relative humidity of 95 ± 2 %. The mildew growth of the samples was recorded with a digital camera every 24 h. Pixel values of the mildew area p_1 and the total area of the adhesive p_0 were counted by Image J2x software, and the mildew growth rate was calculated according to Eq. (2):

$$\text{Mildew growth rate (\%)} = \frac{p_1}{p_0} \times 100\% \quad (2)$$

2.5. Life cycle assessment

The weight of each sample was scaled up to 1000 times the actual amount used and then modelled and evaluated for environmental impact using Simapro 9 software. The formula for calculating power consumption was calculated using according to Eq. (3):

$$\text{Power consumption (kW/h)} = \text{Rated power} \times \text{Experimental time} \times \frac{\text{Real work}}{\text{Rated work}} \quad (3)$$

More detailed experimental materials and methods are presented in the [Supplementary Information](#).

3. Results and discussion

3.1. Fabrication and structural characteristics of adhesives

As shown in Fig. 1a-d, inspired by the hydrophobic enhancement of Dopa-mediated adhesion in mussel foot protein, we demonstrated a facile, one-pot, and scale-up approach for the fabrication of an all-bio-based STF adhesive through modifying a complex of SPI/TA with bio-derived furfural. Notably, SPI, TA, and furfural are currently manufactured at train car scales, resulting in 100% sustainable and renewable properties of STF adhesive. The chemical structures and intermolecular interactions of STF adhesive were analyzed by FT-IR and ^{13}C NMR.

The FT-IR spectra of the uncured adhesive samples were shown in Fig. 1f, and their formulations were presented in Table 2. The characteristic hydroxyl peaks of ST in the range of $3700\text{--}3200\text{ cm}^{-1}$ were significantly shifted to lower wave numbers compared to the untreated SPI adhesive. This result demonstrated that the phenolic hydroxyl groups of TA may be involved in the adhesive system through hydrogen bonding interactions (Wang et al., 2017). The hydroxyl characteristic peaks of SF were significantly lower. In addition, the C--N-- characteristic peak of SF at 1235 cm^{-1} was blue-shifted in the spectrum of SF comparing with the untreated SPI adhesive. All these results suggested that the aldehyde group of furfural may have reacted with the amino group of SPI. After the introduction of TA and furfural, the C=O and C--H bending vibrations at 1698 and 1528 cm^{-1} were shifted to 1664 and 1534 cm^{-1} , respectively, compared to the untreated SPI adhesive, which could potentially be attributed to the amide bond formed between the

furfural-grafted molecules of SPI. The C--H bending vibration at 1528 cm^{-1} was shifted to 1534 cm^{-1} , which may be originated from the non-covalent interactions among SPI, TA and furfural. In addition, the characteristic benzene ring peak of 882 cm^{-1} for TA and the characteristic C=C stretching peak of 1640 cm^{-1} for furfural were weakened in the STF, which may be due to various factors, such as the co-condensation reaction between TA and furfural, the intricate interaction between furfural and protein molecules, and the self-condensation reaction of furfural, among other possibilities (Faggio et al., 2023; Huang et al., 2022b).

The ^{13}C NMR was used to further investigate the structure of the STF adhesive before curing (Fig. 1g). The peaks with chemical shifts of 172.8, 128.3, 53.0, 29.9, and 25.0 ppm for the untreated SPI adhesive may be ascribed to the resonance of carbonyl group, aromatic, α -carbon, β -carbon, and γ -carbon, respectively (Jin et al., 2020). A resonance peak at 145.1 ppm was observed for the phenolic C--OH carbon of TA's catechol structure in both ST and STF adhesives, providing evidence of the presence of TA. The addition of furfural resulted in a new signal peak at 152.8 ppm in SF and STF adhesives, primarily associated with C--N-- vibrations. Meanwhile, the signal peaks of the amino and aldehyde groups displayed a concomitant decrease at 157.3 and 115.5 ppm (Chen et al., 2023a), respectively. The above results indicated that there may be intricate chemical and physical cross-linking interactions between TA, furfural, and SPI molecules. These interactions may involve hydrophobic interactions and hydrogen bonding between TA and the furan ring, weak interactions between TA and SPI, chemical cross-linking among TA, SPI, and furfural, and Diels-Alder reaction between furan nuclei and its derived structure obtained by furan ring opening (Chen et al., 2023b).

3.2. Evaluation of wood veneers bonded with adhesives

The bonding strength is a critical property of adhesives. In this study, the bonding strength was evaluated by testing the shear strength of three-layer plywood bonded with adhesives synthesized by different processes (Fig. 2a and b). For this purpose, orthogonal experiments were performed to investigate the effect of various factors that affect the dry and wet shear strength of adhesives (Table 1). These factors included the pH of the final adhesives (A), the content of TA (B) and furfural (C), and the hot-pressing temperature (D) at which the plywood was prepared (Li et al., 2018). It can be found that pH had the greatest impact on the dry and wet shear strength of adhesives. As shown in Fig. 2c and Table 1, the wet shear strength of the plywood was the highest when the pH was 5. The hot-pressing temperature also had a certain impact on the performance of adhesives. Lower temperatures, like 160 °C, result in the lowest wet shear strength. As the temperature increased, both the dry and wet shear strength of the adhesives increased. The preliminary results indicated that the optimal formula which was $\text{A}_2\text{B}_2\text{C}_1\text{D}_2$ (STF-5: pH 5, TA 20%, furfural 15 %, hot-pressing temperature 170 °C), represented the optimal formulation (Table S1), exhibiting the highest dry and wet shear strengths of 2.5 MPa and 1.71 MPa, respectively. In addition, the factors were ranked in the following order of influence: $\text{A} > \text{D} > \text{B} > \text{C}$.

The wet shear strength of the unmodified SPI adhesive was only 0.47 MPa (Fig. 2d and Table S2), which was attributed to the abundant hydrophilic groups in SPI that reduced the water resistance. The connection between SPI molecules is mainly established by hydrogen bonding, and the wood-based panels prepared by SPI could fail in a humid environment, which ultimately cannot meet the minimum bonding strength of 0.7 MPa as required by the Chinese national standard for indoor-type plywood (GB/T 9846–2015). Modified with TA and furfural, the wet shear strength of the STF adhesive reached up to 1.71 MPa. This was mainly due to the formation of multiple covalent cross-linked networks within the adhesive, which improved the shear strength of the adhesive matrix as well as the adhesion to the wood veneer surface.

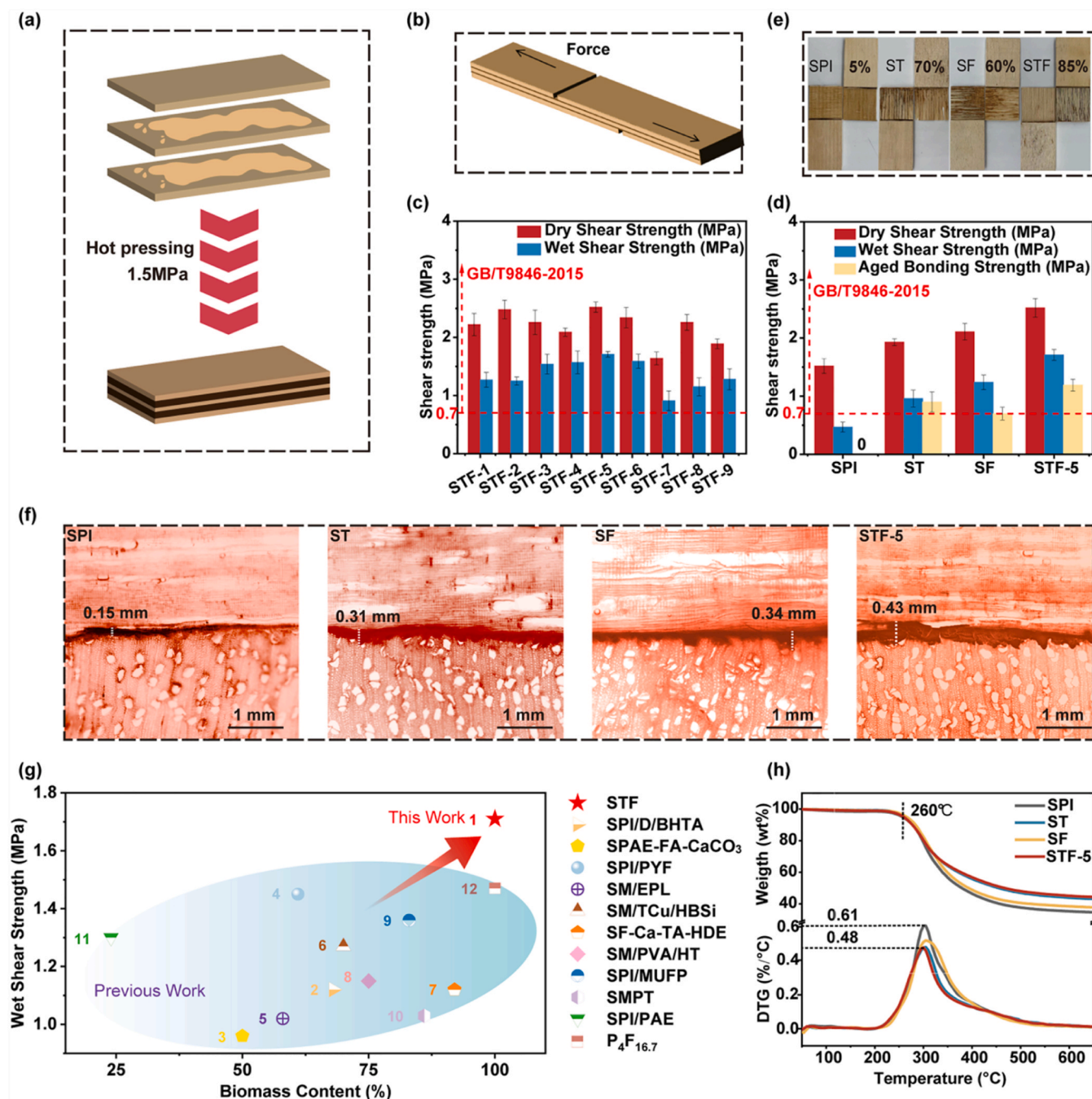


Fig. 2. Evaluation of wood veneers bonded with STF adhesives. a) Schematic illustration of preparation of three-layer plywood specimens. b) Schematic diagram of the three-layer plywood for testing shear strength. c) Dry and wet shear strengths of the plywood bonded with different STF adhesives obtained from orthogonal experimental design. d) Dry, wet, and aged bonding strengths of the plywood bonded with STF-5 adhesive and three other control adhesives. e) Photographs and wood failure rates of representative plywood bonded with SPI, ST, SF, STF-5 adhesives after testing for wet shear strength. f) Optical microscopy images of the cross-section of adhesive layers in the plywood samples. g) Comparison of biomass content versus wet shear strength of STF-5 with other previously reported soy protein-based adhesives. Details are included in [Supplementary Table S3](#). h) Thermogravimetry and derivative thermogravimetry (DTG) curves of the different adhesives.

To further elucidate the effects of TA and furfural on the bonding properties of STF adhesives, control groups modified only with TA or furfural, labeled ST and SF, respectively, were established (Table 2). The various shear strengths of unmodified SPI, ST, SF, and the optimal group STF-5 were tested and compared. The results demonstrated that the dry and wet shear strengths and aged bonding strengths of ST and SF were lower than those of STF-5, proving that the multiple crosslinking in STF-5 significantly improved the bonding performance of the adhesives. The aged bonding strength of STF-5 reached 1.19 MPa, which exceeded the 0.9 MPa of ST and the 0.7 MPa of SF, and met the Chinese national

standard for the bonding strength of outdoor Type I plywood. This excellent aged bonding strength has not been previously reported for soybean protein-based adhesives. These results highlighted the excellent hydro-thermal resistance of STF adhesives. Comparing the wood failure percentages of the samples after shear testing (Fig. 2e), the STF-5-bonded samples had the highest wood failure percentage of 85% compared to SPI, ST, and SF, demonstrating that the interaction between the adhesive and the wood was stronger than the wood itself.

The penetration depth of the adhesives can indirectly reflect the bonding strength of the plywood. As shown in Fig. 2f, STF-5 has a

penetration depth nearly three times that of SPI. Based on the subsequent discussion of adhesive viscosity, STF-5 has the lowest apparent viscosity and better fluidity, which enabled it to be evenly applied and penetrated the interior of the wood veneer to form adhesive nails. This effectively promoted mechanical interlocking with the wood and improved the bonding strength.

Fig. 2g and Table S3 compared the wet shear strengths and biomass contents of STF-5 with other previously reported bio-based adhesives. The STF-5 adhesives not only have a high biomass content of 100% but also exhibit better wet shear strength than other reported bio-based adhesives. Given that STF-5 exhibits superior bonding strength, the subsequent exploration of material properties will be represented by STF-5.

The thermal stability of the adhesives was further studied using the thermal gravimetric analysis (TGA) technique through an N_2 atmosphere, as presented in Fig. 2h. The degradation of adhesives was mainly divided into two stages. The first stage (before $260^\circ C$) was primarily related to the volatilization of some small molecules and the instability of chemical bonds in SPI. The second stage occurred after $260^\circ C$, which was due to the degradation of the soybean protein backbone. Comparing the mass residue rates of ST (43.2 wt%) and SPI (34.7 wt%), it can be

inferred that TA was the primary reason for improving the char formation in STF. The char residue rate of STF-5 increased to 44.2 %, possibly due to the better thermal stability of the crosslinked structure formed by SPI with TA and furfural. As shown in Fig. 2h, the derivative thermogravimetry curves illustrated that the peak of decomposition rate of SPI and STF-5 exhibited a marked difference. This indicated that the structure constructed by introducing TA and furfural effectively slowed down the thermal degradation of the soybean protein backbone structure. The above results further demonstrated that STF-5 possessed a compact and dense structure.

3.3. Viscosity, coating, and storage stability of adhesives

The adhesive's coating performance is determined by its appropriate viscosity and good initial adhesion, both of which directly impact the adhesive's application in the wood industry (Xu et al., 2020a). Viscosity, determined by intermolecular forces, has a direct effect on the adhesive's fluidity. Adhesives with better fluidity are more likely to have uniformly distributed adhesive. Thus, viscosity and coating performance must be considered. As shown in Fig. 3a, the apparent viscosity of unmodified SPI was as high as 44230 mPa·s due to significant

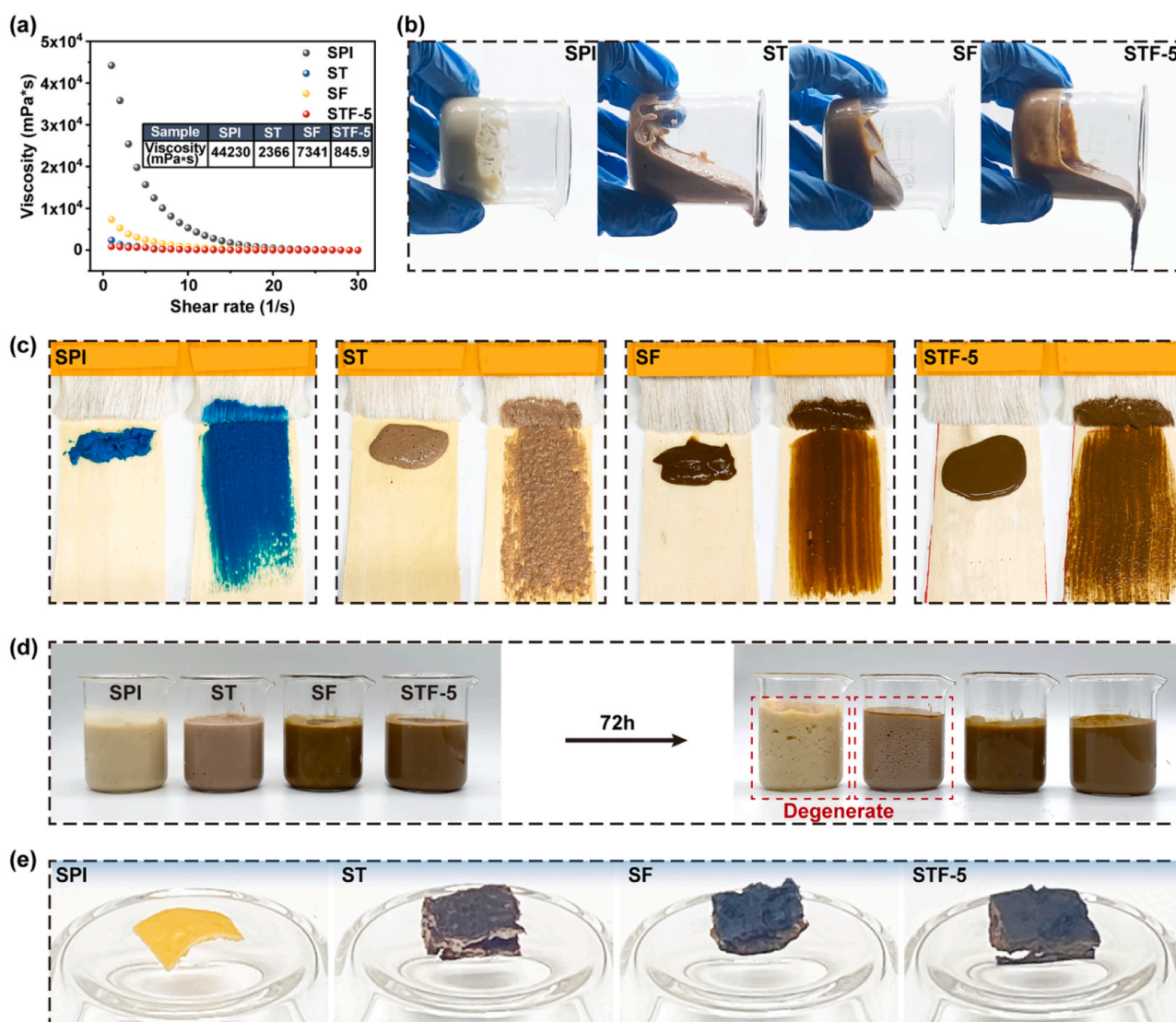


Fig. 3. Performance of adhesives in terms of viscosity, coating, and storage stability. a) Steady shear rheology curves. b) Photographs of fluidity for the different adhesives. c) Photographs of coating performance of the adhesives on the wood veneers. d) Photographs of the adhesives of freshly-prepared and after 72 h storage at room temperature. e) Macroscopic morphology of the curing adhesives.

intramolecular and intermolecular forces, which was poor in fluidity (Fig. 3b) and reduced the penetration of the adhesive into the wood veneer, thus negatively affected the bonding strength. However, after the introduction of TA and furfural, the apparent viscosity of the adhesive was reduced to 2366 mPa·s and 7341 mPa·s, respectively. In addition, the viscosity of the optimized STF-5 was only 845.9 mPa·s representing a significant enhancement in its flowability. The improved flowability mainly attributed to the physical and chemical interactions of TA and furfural with the SPI molecules reducing the entanglement of the soybean protein molecules, thus greatly improving the processability of the adhesive (Xu et al., 2020b).

During the coating process, the underdeveloped flowability of the adhesive can lead to uneven application and reduced penetration, leading to weakened plywood strength. As shown in Fig. 3c, the high viscosity of SPI can cause sticking and uneven application when applied by brush. The coating properties of the modified adhesives were all improved, especially STF-5, which had the most uniform and non-heavy coating surface. However, the ST coating surface could see the accumulation of slag, which might be due to the complex precipitation produced by the combination of protein and tannin.

The stability of the modified adhesive was also improved. The SPI

and ST groups showed significant changes after 72 h (Fig. 3d), with many bubbles and delamination occurring within the adhesive (Wang et al., 2019). While SF and STF showed no significant changes, which was probably attributed to the furfural modification of the amino groups of proteins, which reduced the destabilization of the colloid due to agglomeration, and on the other hand, may be related to the improvement of mildew resistance of the adhesives. Fig. 3e and Table S4 demonstrated the film morphology of the same weight adhesives after curing and the solid content of different adhesives. It can be observed that the SPI has a monolithic shape, whereas the volume of the film of all the modified adhesives has increased, signaling an increase in solid content.

3.4. Bonding mechanism of adhesive

Excellent bonding properties of adhesives usually require that the adhesive layer has a strong cohesive force and is tightly bound to the interface between the wood veneers. To investigate the bonding mechanism of STF adhesive, the cured adhesives were evaluated using FT-IR spectroscopy, XRD and XPS techniques. The FT-IR spectra of the three raw materials, the control groups (SPI, ST, and SF) and STF-5 were

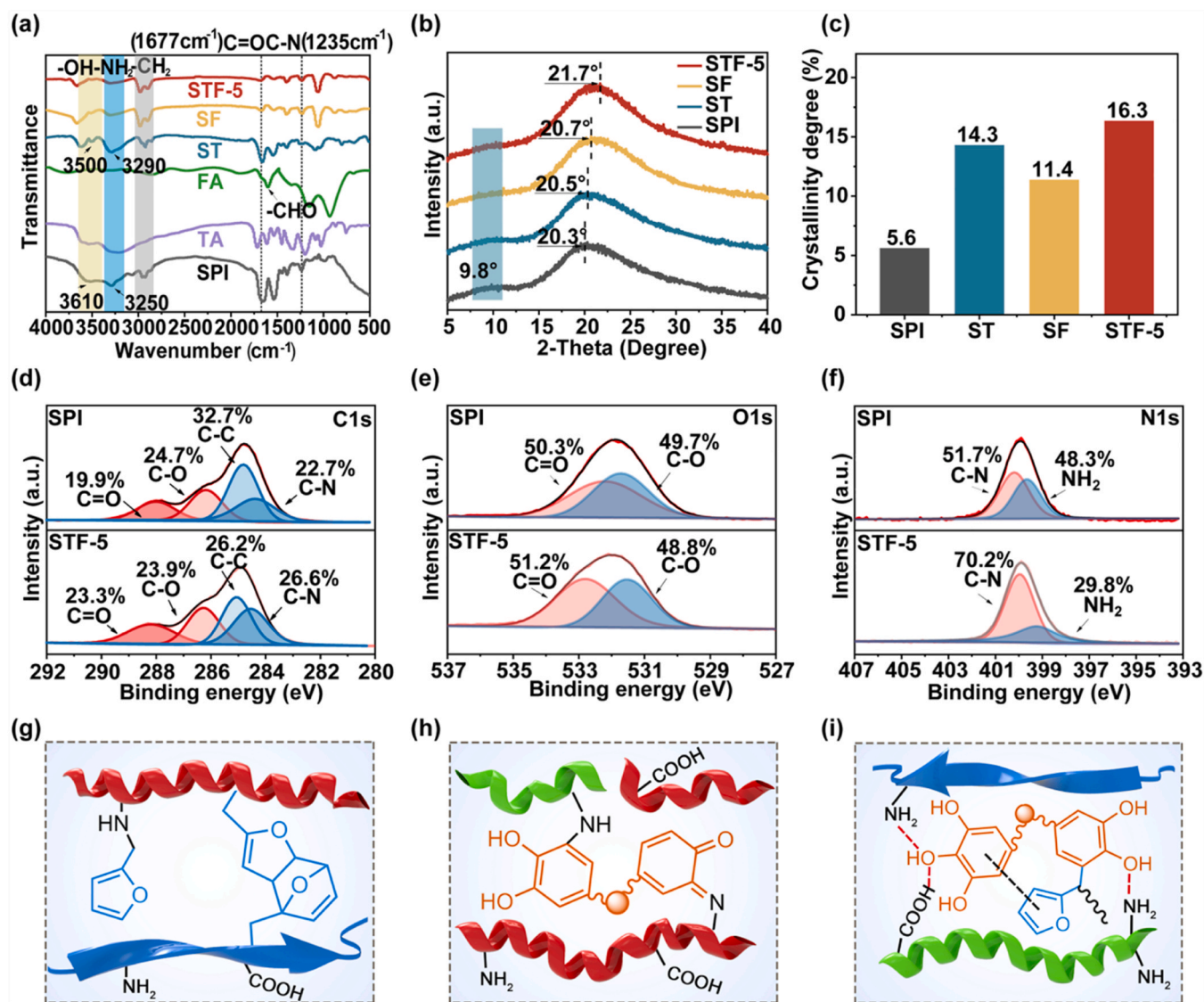


Fig. 4. Characterization of curing mechanism. a) FT-IR spectra of SPI, TA, furfural, ST, SF, and STF-5. b) XRD spectra and c) crystallinity degree of SPI, ST, SF, and STF-5. d-f) XPS fitting curves of high-resolution C1s, O1s, and N1s spectra of SPI and STF-5. g-i) Schematic of the proposed curing mechanism of the SFT adhesive.

shown in Fig. 4a. The broad bands in the range of $3600\text{--}3200\text{ cm}^{-1}$ for SPI were attributed to the freely bound --OH and --NH_2 . Upon introduction of TA, --OH and --NH_2 of ST shifted from $3610, 3250\text{ cm}^{-1}$ to $3500, 3290\text{ cm}^{-1}$, respectively, indicating the existence of complex weak interactions between SPI and TA, such as hydrogen bonding (Jin et al., 2020). In addition, the stretching vibration of C=O in amide II at 1677 cm^{-1} weakened. TA contains a considerable amount of active phenolic hydroxyl, which has high reactivity and can form hydrogen bonding and hydrophobic interactions with SPI (Jin et al., 2020). This reduced the hydrophilicity brought about by hydroxyl, amino and carboxyl groups, improved the hydrophobicity of the adhesive, and enhanced its internal cohesive structure. The disappearance of the aldehyde characteristic peaked at 1640 cm^{-1} of furfural in SF, and the weakened --NH_2 feature peaked in SF compared to SPI. Furthermore, the characteristic peaks of --OH and --NH_2 feature peaked in STF decreased, indicated that there may be a chemical reaction between TA, furfural

and SPI. Besides, the --C=N-- bond in STF at 1677 cm^{-1} was stronger than that of ST and SF. The aldehyde group in furfural reacted with the amino group of SPI to form --C=N-- , which was converted to the more stable --C=N-- after high-temperature hot press curing due to the unstable dynamic covalent bond of --C=N-- (Xu et al., 2021).

Furthermore, X-ray diffraction (XRD) was utilized to analyze variations in the crystalline structure among the different adhesives. It was observed that the α -helix and β -sheet peaks of SPI were present in the XRD spectrum (Fig. 4b) at 9.8° and 20.3° , respectively (Chen et al., 2023a). The peak area of the characteristic α -helix region in each sample showed a flattening trend due to the interaction between the modified agents and peptide bonds in the protein molecule that built new cross-linking structures and weakened the original crystalline structure. Meanwhile, the characteristic peak of SPI at 20.3° (β -sheet) broadened and shifted to 21.7° after the introduction of TA and furfural into STF-5. This could potentially lead to a partial collapse of the crystalline

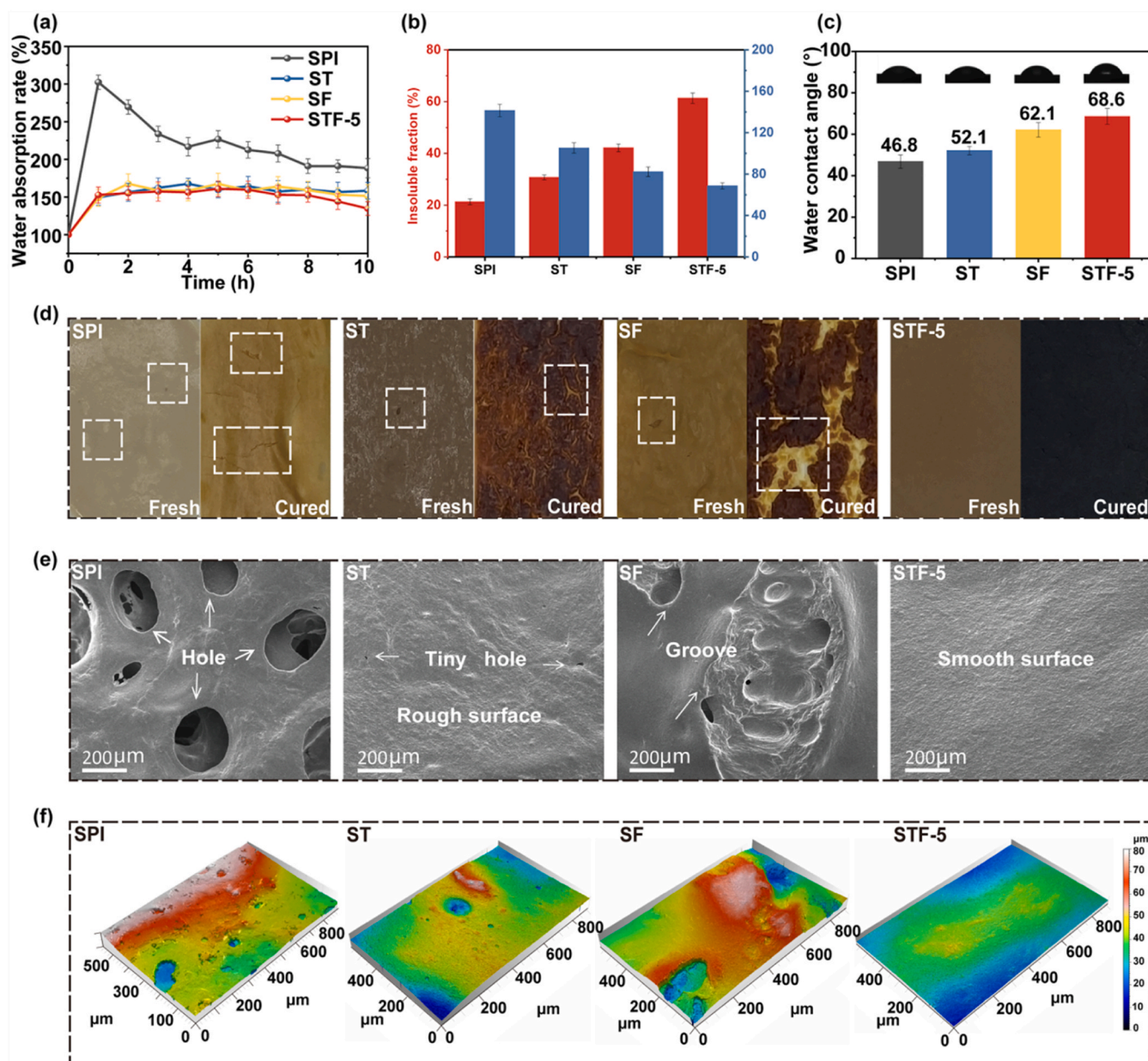


Fig. 5. Water resistance and surface morphology of curing adhesives. a) Water absorption rate of the curing adhesives. b) Insoluble fraction and swelling rate of the curing adhesives. c) Water contact angles of the curing adhesives. d) Visual examination of the surface morphology of fresh adhesives versus curing adhesives. e) SEM images of the curing adhesive surfaces. f) Laser optical 3D surface images of the curing adhesive films.

structure of the protein molecule as a result of the synergistic action of physical and chemical effects. The crystallinity of different adhesives was calculated based on the XRD results (Fig. 4c), and it was found that the addition of TA and furfural increased the crystallinity from 5.58 % to 16.32 %. The new covalent bonds and hydrogen bonds produced by the combination of TA and furfural with SPI might alter and enhance the crystalline structure of SPI to form a more compact structure (Kan et al., 2023).

To better understand the compositional change in the structure of the adhesives, XPS spectra of different adhesives were obtained (Fig. 4d-f and Fig. S1). The C1s deconvolution peaks for SPI and STF-5 adhesives were shown in Fig. 4d. The decrease in the peak areas of C-C and C-O and the increase in the peak areas of C=O and C-N in STF-5 as compared to SPI may be attributed to the formation of amide bonds between the aldehyde group of furfural and the amino group of SPI (Zeng et al., 2023). In the O1s spectra of SPI and STF-5, it can be found that the peak area changes of SPI and STF-5 were basically consistent with the C1s spectra (Fig. 4e). In addition, the N1s spectra of SPI were separated into two sub-peaks (Fig. 4f), which corresponded to the nitrogen-containing groups of $-NH_2$ and C-N (Xu et al., 2021). In the N1s spectra of STF-5, a decrease in the peak area of $-NH_2$ was observed, which implied that the number of amino groups in the protein molecule involved in the reaction was reduced to produce C=N and C-N. Nevertheless, the conversion to C=N took place subsequent to the curing process, owing to the instability of C=N, thereby leading to a notable enhancement in the peak area of the C-N (Peng et al., 2023). Fig. 4g-i illustrated the diverse covalent and non-covalent crosslinks that could exist among SPI, TA, and furfural in the STF adhesive matrix following thermal curing.

3.5. Water resistance and microstructure of curing adhesives

The water resistance of the adhesives is a key factor affecting their mechanical properties and actual application life under humid conditions. As shown in Fig. 5a, the SPI sample demonstrated the lowest water resistance, as its mass rose by 210% after being submerged in water for 10 h. Abundant hydrophilic groups and porous structure of soybean protein facilitate significant water absorption and consequent swelling. After being soaked for 2 h, the mass of SPI samples decreased mainly due to the disintegration of soybean protein's internal structure and the dissolution of small molecule peptides. However, the addition of TA and furfural significantly mitigated the upward trend of water absorption exhibited by ST and SF, especially with extended soaking periods. This indicated that the water resistance of the soybean protein adhesives modified by the TA and furfural was significantly improved.

The gel test can be used to determine the degree of cross-linking and water absorption of the cured adhesives (Bai et al., 2021). As shown in Fig. 5b, the results obtained by measuring the insoluble fraction (21.25%) and the swelling rate (141.35%) of the untreated SPI adhesive demonstrated that the adhesive was significantly hydrophilic. Incorporating TA and furfural led to the maximum insoluble fraction (61.34%) and minimum swelling rate (68.72%), which can be attributed to the successful non-covalent weak interaction and chemical reaction among the phenolic hydroxyl group of TA, the aldehyde group of furfural, and soybean protein molecules. As a result, STF-5 exhibited a physical and chemical intertwined network, leading to improved water resistance. The improved water contact angle (WCA) of modified SF, ST and STF-5 compared to SPI (Fig. 5c) may be the result of the interaction of TA and furfural with SPI, which significantly improved the hydrophobicity of STF-5.

As shown in Fig. 5d, the fresh SPI adhesive showcased a bubbly surface, while the cured sample displayed cracks and an uneven surface. Upon adding TA, the surface pores of the fresh adhesive declined, and the viscosity decreased while flowability improved. However, the cured sample still exhibited a host of tiny cracks. Compared to the untreated SPI, the SF demonstrated improvement on the surface morphology of the fresh adhesive, but a patch of visible cracks was found in the cured

sample (Fig. 5d). In contrast, the fresh adhesive surface of STF-5 was flat and bubble-free, with the lowest viscosity and smooth surface of the cured samples. The surface morphology of the cured adhesive was analyzed using SEM (Fig. 5e). On the unmodified SPI adhesive surface, there were multiple pores resulting from voids produced during water evaporation at high temperatures. Consequently, moisture could permeate into the interior through these channels, resulting in the low water resistance and strength of the unmodified SPI adhesive. The addition of TA significantly improved the surface of the adhesives by eliminating large pores and creating a more complex network structure through its interaction with proteins. The addition of furfural produced a smooth surface and formed grooves and textures not previously present. The aldehydic group of furfural reacted with the hydroxyl, thiol, and amino groups in protein, bridging the dispersed peptide chains to form new robust materials. However, the brittleness of the furfural cross-linking products resulted in shrinkage and cracking of the SF adhesive film surface (Swain et al., 2004). The smooth and elastic surface of STF-5 without cracks was attributed to the multiple cross-linking of TA and furfural with protein molecules, and the strong intermolecular forces resulted in a more homogeneous and compact structure of the adhesive. Furthermore, Fig. 5f showed the three-dimensional surface profile of the adhesives, which was in general agreement with the above analysis.

3.6. Mildew resistance of adhesives

Since soybean protein is a nutrient-rich natural substance for microorganisms, it is easily deteriorated by mildew, which is a major impediment to the wider commercial applications of soybean protein adhesives. Fig. 6a illustrated the anti-mildew test photos of the various adhesives prepared. It was evident from the results that the untreated SPI adhesive's surface color became darker over time, mildew colonies gradually spread, and an unpleasant odor was detected. On the seventh day of monitoring, the surface of the SPI adhesive was wholly covered with mildew colonies. However, in ST and SF adhesives, mildew growth was efficiently suppressed during the first three days of testing (Fig. 6b and Table S5). However, after the seventh day, mildew growth exceeded 95% of the adhesive's surface area. The results demonstrated that the addition of TA or furfural alone improved the mildew resistance of the adhesive in the short term. Notably, STF-5 adhesive demonstrated exceptional mildew resistance (Fig. 6a and b), as only microscopic colonies appeared on the surface after seven days of monitoring, accounting for only 0.15% of the adhesive's surface (Table S5). The interaction of TA, furfural, and soybean protein creates multiple complex networks that may cause protein denaturation. The active groups' synergistic interaction of TA (e.g. active phenolic structure can effectively scavenge oxygen-free radicals and inhibit lipid peroxidation) and furfural attacks the mildew cell wall (Fig. 6c) (Pizzi and Scharfetter, 2003; Zeng et al., 2024). Furthermore, they inactivate enzymes and active proteins present on the mildew cells' surface, reducing their reproduction rate, thus enhancing the anti-mildew properties of the adhesive.

3.7. Life cycle assessment

Life cycle assessment (LCA) refers to the potential impacts on the environment from the acquisition of raw materials, production and consumption to the disposal of the product after use (Harrison et al., 2023). The demand for adhesives for wood-based panels is increasing, driven by a focus on improving people's quality of life. However, the production and disposal of adhesives for wood-based panels may emit harmful gases that pose a significant risk to the surrounding environment, including the air, water, and soil. Air, water, and soil pollution damages the ecological environment, directly endangering human health and the safety of ecosystems. Thus, LCA is an important approach for the development of new materials to evaluate their sustainability and impacts on the environment and the human health. LCA analysis results

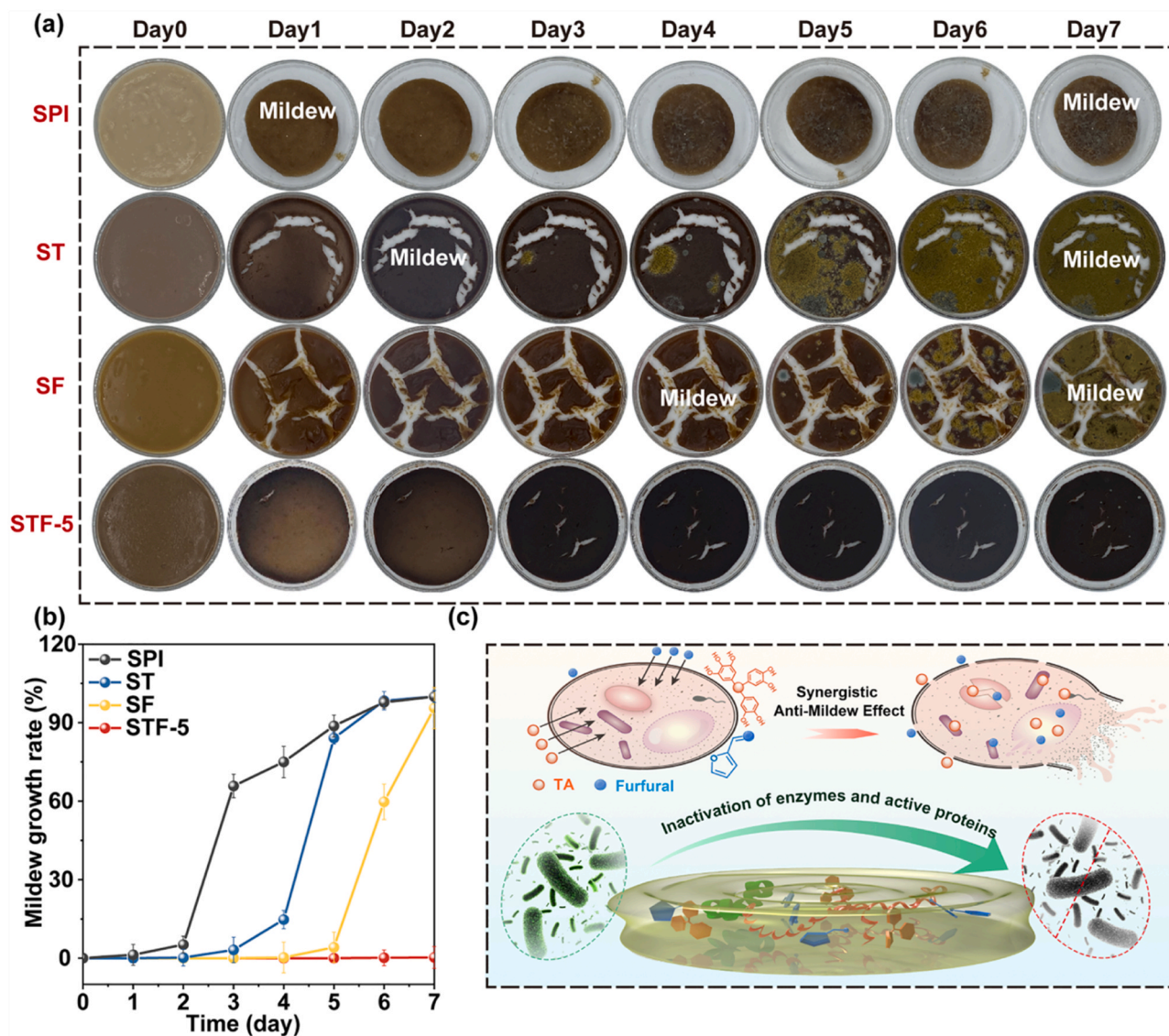


Fig. 6. Mildew resistant performance of the adhesives. a) Photographs of anti-mildew tests conducted at different periods. b) Mildew growth rate on the surface of different adhesives. c) Schematic illustration of the proposed mildew resistance mechanism for STF adhesive.

demonstrated that the human health and ecological impact of STF-5 was significantly lower than that of conventional urea formaldehyde resin (UF) and phenol formaldehyde resin (PF) adhesives (Fig. 7), making the development of fully bio-based and formaldehyde-free STF-5 adhesives highly promising.

4. Conclusions

In this work, an easy-handled, water-resistant, and anti-mildew all-bio-based STF adhesive with high-bonding performance was developed inspired by the adaptive hydrophobic and hydrophilic interactions of mussel foot proteins. Furfural, acting as a bio-derived cross-linking agent, can enhance the hydrophobicity and co-adhesion of soybean protein molecules by modifying the furan ring to the soy protein molecules. In addition, TA was utilized to create intricate non-covalent interactions with soybean protein molecules, diminishing the entanglement of molecular chains and lowering the adhesive viscosity while boosting bonding strength. The three-component fully bio-based adhesive can be produced with a facile one-pot strategy and exhibits the desired high performance for use in the wood-based panel industry. Compared with unmodified SPI adhesive, using the STF adhesive to

prepare plywood increased the dry shear strength by 65.8 % and the wet shear strength by 263.8%. Notably, the aging bonding strength of plywood with the STF adhesive reached 1.19 MPa, which exceeds that of previously reported soybean protein-based adhesives. In addition, STF features excellent mildew resistance and fluidity (brushability) as well as superior thermal stability. LCA results demonstrated that the development of fully bio-based and formaldehyde-free STF adhesives is highly promising. Therefore, this work is conducive to the sustainable development of the wood adhesive industry and meets the demand for green development in modern society.

CRediT authorship contribution statement

Tao Liu: Writing – review & editing, Investigation, Formal analysis, Conceptualization. **Sili Chen:** Writing – original draft, Methodology, Investigation, Formal analysis. **Xiaolong Hao:** Formal analysis. **Yujia Guo:** Investigation, Formal analysis. **Chuiqin Guo:** Formal analysis. **Lichao Sun:** Formal analysis. **Rongxian Ou:** Writing – review & editing, Supervision, Investigation, Funding acquisition, Conceptualization. **Qi Fan:** Writing – review & editing, Investigation, Funding acquisition, Formal analysis, Conceptualization.

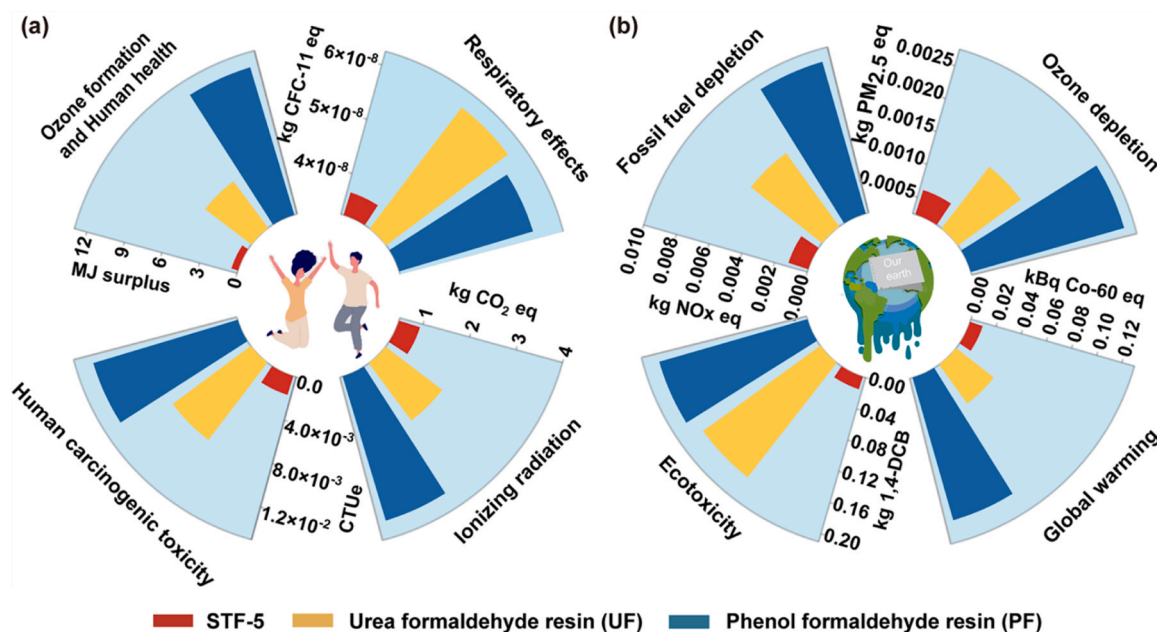


Fig. 7. Life cycle assessment of STF-5, urea formaldehyde resin (UF), and phenol formaldehyde resin (PF). a) Indicators related to human health, including ozone formation and human health, respiratory effects, ionizing radiation, and human carcinogenic toxicity. b) Indicators related to ecosystem, including fossil fuel depletion, ozone depletion, global warming, and ecotoxicity.

Declaration of Competing Interest

The authors declare that they have no known competing financial interests or personal relationships that could have appeared to influence the work reported in this paper.

Data Availability

Data will be made available on request.

Acknowledgements

This work was financially supported by the Research and Development Program in Key Areas of Guangdong Province (2020B0202010008), the National Natural Science Foundation of China (32071698 and 52103110), the China Postdoctoral Science Foundation (2021M701258), and the Research and Development Program in Key Areas of Guangzhou (2024B03J1380).

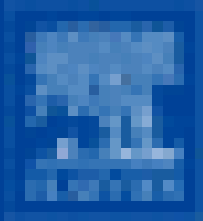
Appendix A. Supporting information

Supplementary data associated with this article can be found in the online version at [doi:10.1016/j.indcrop.2024.118583](https://doi.org/10.1016/j.indcrop.2024.118583).

References

- Bai, M., Cao, J., Li, J., Li, C., 2021. Development of soybeans starch based tough, water resistant and mildew-proof adhesives through multiple cross linking cooperation strategy. *J. Clean. Prod.* 321, 129001 <https://doi.org/10.1016/j.jclepro.2021.129001>.
- Chang, Z., Shen, Y., Xue, J., Sun, Y., Zhang, S., 2023. Fabrication of strong and tough multifunctional soy protein adhesives via constructing catechol-iron ion fiber-reinforced hierarchical structure inspired by mussel byssus. *Ind. Crops Prod.* 202 <https://doi.org/10.1016/j.indcrop.2023.116992>.
- Chen, S., Aladejana, J.T., Li, X., Bai, M., Shi, S.Q., Kang, H., Cao, J., Li, J., 2023a. A strong, antimildew, and fully bio-based adhesive fabricated by soybean meal and dialdehyde chitosan. *Ind. Crops Prod.* 194, 116277 <https://doi.org/10.1016/j.indcrop.2023.116277>.
- Chen, X., Yang, Z., Yang, F., Zhang, J., Pizzi, A., Essawy, H., Du, G., Zhou, X., 2023b. Development of easy-handled, formaldehyde-free, high-bonding performance bio-sourced wood adhesives by co-reaction of furfuryl alcohol and wheat gluten protein. *Chem. Eng. J.* 462, 142161 <https://doi.org/10.1016/j.cej.2023.142161>.
- Faggio, N., Marotta, A., Ambrogio, V., Cerruti, P., Gentile, G., 2023. Fully bio-based furan/ maleic anhydride epoxy resin with enhanced adhesive properties. *J. Mater. Sci.* 58, 7195–7208. <https://doi.org/10.1007/s10853-023-08458-8>.
- Fapeng, W., Jifu, W., Chunpeng, W., Fuxiang, C., Xiaohuan, L., Jiuyin, P., 2017. Fabrication of soybean protein-acrylate composite mini-emulsion toward wood adhesive. *Eur. J. Wood Wood Prod.* 76, 305–313. <https://doi.org/10.1007/s00107-017-1190-y>.
- Ghahri, S., Pizzi, A., Hajiassani, R., 2022. A study of concept to prepare totally biosourced wood adhesives from only soy protein and tannin. *Polymers* 14, 1150. <https://doi.org/10.3390/polym14061150>.
- Harrison, T.R., Gupta, V.K., Alam, P., Perriman, A.W., Scarpa, F., Thakur, V.K., 2023. From trash to treasure: sourcing high-value, sustainable cellulosic materials from living bioreactor waste streams. *Int. J. Biol. Macromol.* 233 <https://doi.org/10.1016/j.ijbiomac.2023.123511>.
- Huang, X., Chen, Y., Li, J., Li, J., Gao, Q., Zhan, X., 2022a. Improving the coating and prepressing properties of soybean meal adhesive by constructing a biomimetic topological structure. *MATER. Des.* 223, 111163–111174. <https://doi.org/10.1016/j.matdes.2022.111163>.
- Huang, X., Ji, Y., Guo, L., Xu, Q., Jin, L., Fu, Y., Wang, Y., 2022b. Incorporating tannin onto regenerated cellulose film towards sustainable active packaging. *Ind. Crops Prod.* 180 <https://doi.org/10.1016/j.indcrop.2022.114710>.
- Hussain, M.H., Abd Latif, N.H., Hamidon, T.S., Idris, N.N., Hashim, R., Appaturi, J.N., Brosse, N., Ziegler-Devlin, I., Chrusiel, L., Fatriasari, W., Syamani, F.A., Iswanto, A. H., Hua, L.S., Al Edrus, S.S.A.O., Lum, W.C., Antov, P., Savov, V., Rahandi Lubis, M. A., Kristak, L., Reh, R., Sedliacik, J., 2022. Latest advancements in high-performance bio-based wood adhesives: A critical review. *J. Mater. Res. Technol.* 21, 3909–3946. <https://doi.org/10.1016/j.jmrt.2022.10.156>.
- Jin, S., Li, K., Gao, Q., Zhang, W., Chen, H., Li, J., Shi, S.Q., 2020. Multiple crosslinking strategy to achieve high bonding strength and antibacterial properties of double-network soy adhesive. *J. Clean. Prod.* 254, 120143 <https://doi.org/10.1016/j.jclepro.2020.120143>.
- Kan, Y., Sun, B., Bai, Y., Gao, Z., 2022. Double-network strategy for a cost-effective soybean meal-based adhesive with required and stable water resistance for structural use. *Compos. Part B-Eng.* 235, 109744 <https://doi.org/10.1016/j.compositesb.2022.109744>.
- Kan, Y., Kan, H., Bai, Y., Zhang, S., Gao, Z., 2023. Effective and environmentally safe self-antimildew strategy to simultaneously improve the mildew and water resistances of soybean flour-based adhesives. *J. Clean. Prod.* 392, 136319 <https://doi.org/10.1016/j.jclepro.2023.136319>.
- Li, F., Gu, W., Gong, S., Zhou, W., Shi, S.Q., Gao, Q., Fang, Z., Li, J., 2023a. Design of amphiphilic-function-aiding biopolymer adhesives for strong and durable underwater adhesion via a simple solvent-exchange approach. *Chem. Eng. J.* 469, 143793 <https://doi.org/10.1016/j.cej.2023.143793>.
- Li, H., Fan, R., Zhang, F., Cui, Z., Li, J., Cai, Y., Kang, L., Zhan, X., Li, J., Tian, D., 2023b. A spider-silk-inspired soybean protein adhesive with high-strength and mildew-resistant via synergistic effect of MXene nanosheets and chitosan. *Ind. Crops Prod.* 193, 116252 <https://doi.org/10.1016/j.indcrop.2023.116252>.
- Li, K., Jin, S., Zeng, G., Zhou, Y., Zhang, F., Li, J., Shi, S.Q., Li, J., 2022. Biomimetic development of a strong, mildew-resistant soy protein adhesive via mineral-organic

- system and phenol-amine synergy. *Ind. Crops Prod.* 187 <https://doi.org/10.1016/j.indcrop.2022.115412>.
- Li, K., Xu, Z., Liu, X., He, Y., Tian, X., Xu, X., Bo, G., Yuan, S., Xu, L., Yang, M., Yan, J., Zhang, H., Yan, Y., 2023c. Mussel foot inspired bionic adhesive material enhanced by a reconstructed in vitro system for interfacial adhesion. *Chem. Eng. J.* 452, 139580 <https://doi.org/10.1016/j.cej.2022.139580>.
- Li, Y., Xiao, H., Pan, Y., Wang, L., 2018. Novel composite adsorbent consisting of dissolved cellulose fiber/microfibrillated cellulose for dye removal from aqueous solution. *ACS Sustain. Chem. Eng.* 6, 6994–7002. <https://doi.org/10.1021/acssuschemeng.8b00829>.
- Li, Y., Cai, L., Zhang, X., Chen, Y., Cui, Z., Luo, J., Li, J., Li, J., Shi, S.Q., Gao, Q., 2023d. Development of a strong and multifunctional soy protein-based adhesive with excellent coating and prepressing in wet state by constructing a radical polymerization and organic-inorganic mineralization bionic structure. *J. Clean. Prod.* 400, 136730 <https://doi.org/10.1016/j.jclepro.2023.136730>.
- Liang, Y., Luo, Y., Wang, Y., Fei, T., Dai, L., Zhang, D., Ma, H., Cai, L., Xia, C., 2023. Effects of lysine on the interfacial bonding of epoxy resin cross-linked soy-based wood adhesive. *Molecules* 28 (3), 1391. <https://doi.org/10.3390/molecules28031391>.
- Liu, J., Wang, H., Ou, R., Yi, X., Liu, T., Liu, Z., Wang, Q., 2021. Anti-bacterial silk-based hydrogels for multifunctional electrical skin with mechanical-thermal dual sensitive integration. *Chem. Eng. J.* 426, 130722 <https://doi.org/10.1016/j.cej.2021.130722>.
- Liu, Z., Liu, T., Gu, W., Zhang, X., Li, J., Shi, S.Q., Gao, Q., 2022a. Hyperbranched catechol biomineralization for preparing super antibacterial and fire-resistant soybean protein adhesives with long-term adhesion. *Chem. Eng. J.* 449 <https://doi.org/10.1016/j.cej.2022.137822>.
- Liu, Z., Liu, T., Li, Y., Zhang, X., Xu, Y., Li, J., Gao, Q., 2022b. Performance of soybean protein adhesive cross-linked by lignin and cuprum. *J. Clean. Prod.* 366 <https://doi.org/10.1016/j.jclepro.2022.132906>.
- Mi, Y., Bai, Y., Gao, D., Gao, Z., Gu, H., Yang, W., 2022. Controllable crosslinking system of soy protein-based adhesives via soybean polysaccharide for wood composites. *J. Appl. Polym. Sci.* 139, 1–9. <https://doi.org/10.1002/app.53161>.
- Pang, H., Ma, C., Zhang, S., 2022. Conversion of soybean oil extraction wastes into high-performance wood adhesives based on mussel-inspired cation- π interactions. *Int. J. Biol. Macromol.* 209, 83–92. <https://doi.org/10.1016/j.ijbiomac.2022.03.152>.
- Peng, H., Li, H., Zhang, X., Tang, J., Liang, Y., Qiao, L., Zhu, Y., Hou, M., Wei, S., Zhang, Z., Liu, C., Li, X., Liang, B., Song, B., Guo, B., Zhang, J., 2023. 3D-exosomes laden multifunctional hydrogel enhances diabetic wound healing via accelerated angiogenesis. *Chem. Eng. J.* 475 <https://doi.org/10.1016/j.cej.2023.146238>.
- Pizzi, A., Scharfetter, H.O., 2003. The chemistry and development of tannin-based adhesives for exterior plywood. *J. Appl. Polym. Sci.* 22, 1745–1761. <https://doi.org/10.1002/app.1978.070220623>.
- Qi, G., Li, N., Wang, D., Sun, X.S., 2013. Physicochemical properties of soy protein adhesives modified by 2-octen-1-ylsuccinic anhydride. *Ind. Crops Prod.* 46, 165–172. <https://doi.org/10.1016/j.indcrop.2013.01.024>.
- Qi, Z., Yang, C., Li, D., Zhang, J., Xie, P., Xue, X., Yang, G., Wang, C., 2023. A green mussel-bioinspired strategy for grafting 3-ene urushiol and AgNPs into soy protein isolate and fabricating a high-strength antimicrobial bioplastic film. *Int. J. Biol. Macromol.* 241, 124670 <https://doi.org/10.1016/j.ijbiomac.2023.124670>.
- Sun, Y., Li, Z., Yan, Q., Zhang, S., Shi, X., Li, S., Chen, S., 2023. Complex coacervation behavior between cationic polyamides and anionic epoxy resins endowed improved cold-pressing performance of soy protein adhesive. *Constr. Build. Mater.* 387, 131532–131542. <https://doi.org/10.1016/j.conbuildmat.2023.131532>.
- Swain, S.N., Rao, K.K., Nayak, P.L., 2004. Biodegradable polymers. III. Spectral, thermal, mechanical, and morphological properties of cross-linked furfural-soy protein concentrate. *J. Appl. Polym. Sci.* 93, 2590–2596. <https://doi.org/10.1002/app.20729>.
- Wang, Z., Zhao, S., Song, R., Zhang, W., Zhang, S., Li, J., 2017. The synergy between natural polyphenol-inspired catechol moieties and plant protein-derived bio-adhesive enhances the wet bonding strength. *Sci. Rep.* 7, 9664. <https://doi.org/10.1038/s41598-017-10007-8>.
- Wang, Z., Wen, Y., Zhao, S., Zhang, W., Ji, Y., Zhang, S., Li, J., 2019. Soy protein as a sustainable surfactant to functionalize boron nitride nanosheets and its application for preparing thermally conductive biobased composites. *Ind. Crops Prod.* 137, 239–247. <https://doi.org/10.1016/j.indcrop.2019.04.054>.
- Wei, W., Yu, J., Broomell, C., Israelachvili, J.N., Waite, J.H., 2012a. Hydrophobic enhancement of dopa-mediated adhesion in a mussel foot protein. *J. Am. Chem. Soc.* 135, 377–383. <https://doi.org/10.1021/ja309590f>.
- Wei, W., Yu, J., Broomell, C., Israelachvili, J.N., Waite, J.H., 2012b. Hydrophobic enhancement of dopa-mediated adhesion in a mussel foot protein. *J. Am. Chem. Soc.* 135, 377–383. <https://doi.org/10.1021/ja309590f>.
- Westerman, C.R., McGill, B.C., Wilker, J.J., 2023. Sustainably sourced components to generate high-strength adhesives. *Nature* 621, 306–311. <https://doi.org/10.1038/s41586-023-06335-7>.
- Xu, C., Xu, Y., Chen, M., Zhang, Y., Li, J., Gao, Q., Shi, S.Q., 2020a. Soy protein adhesive with bio-based epoxidized daidzein for high strength and mildew resistance. *Chem. Eng. J.* 390 <https://doi.org/10.1016/j.cej.2020.124622>.
- Xu, Y., Han, Y., Shi, S.Q., Gao, Q., Li, J., 2020b. Preparation of a moderate viscosity, high performance and adequately-stabilized soy protein-based adhesive via recombination of protein molecules. *J. Clean. Prod.* 255, 120303 <https://doi.org/10.1016/j.jclepro.2020.120303>.
- Xu, Y., Han, Y., Li, Y., Li, J., Li, J., Gao, Q., 2022a. Preparation of a strong, mildew-resistant, and flame-retardant biomimetic multifunctional soy protein adhesive via the construction of an organic-inorganic hybrid multiple-bonding structure. *Chem. Eng. J.* 437, 135437 <https://doi.org/10.1016/j.cej.2022.135437>.
- Xu, Y., Huang, X., Zhang, Y., Liu, Z., Luo, J., Li, J., Li, J., Gao, Q., 2021. A high bonding performance and antibacterial soybean meal adhesive with Maillard reaction based cross-linked structure. *Compos. B. Eng.* 227, 109403 <https://doi.org/10.1016/j.compositesb.2021.109403>.
- Xu, Y., Zhang, X., Liu, Z., Zhang, X., Luo, J., Li, J., Shi, S.Q., Li, J., Gao, Q., 2022b. Constructing SiO₂ nanohybrid to develop a strong soy protein adhesive with excellent flame-retardant and coating ability. *Chem. Eng. J.* 446, 137065 <https://doi.org/10.1016/j.cej.2022.137065>.
- Yan, Q., Ma, C., Liang, Z., Zhang, S., 2022. High-temperature soybean meal adhesive based on disulfide bond rearrangement and multiple crosslinking: water resistance and prepressing adhesion. *J. Clean. Prod.* 373, 133709 <https://doi.org/10.1016/j.jclepro.2022.133709>.
- Yang, G., Gong, Z., Luo, X., Chen, L., Shuai, L., 2023. Bonding wood with uncondensed lignins as adhesives. *Nature* 621, 511–515. <https://doi.org/10.1038/s41586-023-06507-5>.
- Yin, H., Zhang, E., Zhu, Z., Han, L., Zheng, P., Zeng, H., Chen, N., 2021. Soy-based adhesives functionalized with pressure-responsive crosslinker microcapsules for enhanced wet adhesion. *ACS Appl. Polym. Mater.* 3, 1032–1041. <https://doi.org/10.1021/acsaapm.0c01295>.
- Yu, J., Kan, Y., Rapp, M., Danner, E., Wei, W., Das, S., Miller, D.R., Chen, Y., Waite, J.H., Israelachvili, J.N., 2013. Adaptive hydrophobic and hydrophilic interactions of mussel foot proteins with organic thin films. *Proc. Natl. Acad. Sci.* 110, 15680–15685. <https://doi.org/10.1073/pnas.1315015110>.
- Yue, L., Shi, R., Yi, Z., Shi, S.Q., Gao, Q., Li, J., 2020. A high-performance soybean meal-based plywood adhesive prepared via an ultrasonic process and using significantly lower amounts of chemical additives. *J. Clean. Prod.* 274, 123017 <https://doi.org/10.1016/j.jclepro.2020.123017>.
- Zeng, G., Zhou, Y., Wang, T., Li, K., Dong, Y., Li, J., Li, J., Fang, Z., 2023. A bio-based adhesive reinforced with functionalized nanomaterials to build multiple strong and weak cross-linked networks with high strength and excellent mold resistance. *Chem. Eng. J.* 453, 139761 <https://doi.org/10.1016/j.cej.2022.139761>.
- Zeng, G., Dong, Y., Luo, J., Zhou, Y., Li, C., Li, K., Li, X., Li, J., 2024. Desirable strong and tough adhesive inspired by dragonfly wings and plant cell walls. *ACS Nano*. <https://doi.org/10.1021/acsnano.3c11160>.
- Zhang, J., Long, C., Zhang, X., Liu, Z., Zhang, X., Liu, T., Li, J., Gao, Q., 2022a. An easy-coating, versatile, and strong soy flour adhesive via a biomineralized structure combined with a biomimetic brush-like polymer. *Chem. Eng. J.* 450, 138387 <https://doi.org/10.1016/j.cej.2022.138387>.
- Zhang, W., Wang, R., Sun, Z., Zhu, X., Zhao, Q., Zhang, T., Cholewinski, A., Yang, F., Zhao, B., Pinnaratip, R., Forooshani, P.K., Lee, B.P., 2020. Catechol-functionalized hydrogels: biomimetic design, adhesion mechanism, and biomedical applications. *Chem. Soc. Rev.* 49, 433–464. <https://doi.org/10.1039/c9cs00285e>.
- Zhang, X., Xu, C., Liu, Z., Shi, S.Q., Li, J., Luo, J., Gao, Q., 2022b. A water-resistant and mildewproof soy protein adhesive enhanced by epoxidized xylitol. *Ind. Crops Prod.* 180, 114794 <https://doi.org/10.1016/j.indcrop.2022.114794>.
- Zhao, Z., Liu, T., Ou, R., Hao, X., Fan, Q., Guo, C., Sun, L., Liu, Z., Wang, Q., 2022. Fully biobased soy protein adhesives with integrated high-strength, waterproof, mildew-resistant, and flame-retardant properties. *ACS Sustain. Chem. Eng.* 10, 6675–6686. <https://doi.org/10.1021/acssuschemeng.2c00742>.



ISSN 0950-2688

Construction and Building **MATERIALS**

*An International Journal
Dedicated to the Investigation
and Innovative Use of
Materials in Construction
and Repair*

CONSTRUCTION & BUILDING MATERIALS
www.elsevier.com/locate/conbuildmat

Articles & Issues ▾

About ▾

Publish ▾



Search in this journal

Guide for authors

Actions for selected articles

Select all / Deselect all



Download PDFs



Export citations



Show all article previews

☐ Research article ● Open access

Grading of recovered Norway spruce (*Picea abies*) timber for structural purposes

Daniel F. Llana, Guillermo Íñiguez-González, Mitja Plos, Goran Turk
Article 132440



View PDF

Article preview ▾

☐ Research article ● Full text access

Contents

Enhanced mechanical performance and fire resistance of poplar wood: Unilateral surface densification assisted with N/P doped acrylic resin impregnation

Review Articles

Xing Zhang, Qi Fan, Chuanfu Chen, Xiaolong Hao, ... Qingwen Wang
Article 132470



View PDF

Article preview ▾

Research Articles

Short Communications

☐ Research article ● Full text access

Effect of zinc oxide on corrosion resistance of magnesium ammonium phosphate cement-based coating

Yong Zhi, Qing Wu, Hongli Ma, Yadi Wu, ... Ning Yang
Article 132473

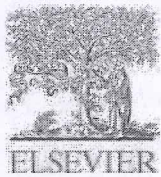
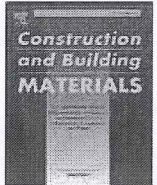


View PDF

Article preview ▾

☐ Research article ● Full text access





Enhanced mechanical performance and fire resistance of poplar wood: Unilateral surface densification assisted with N/P doped acrylic resin impregnation

Xing Zhang^a, Qi Fan^{a,b,*}, Chuanfu Chen^a, Xiaolong Hao^{a,b}, Zhenzhen Liu^{a,b}, Rongxian Ou^{a,b}, Qingwen Wang^{a,b}

^a Institute of Biomass Engineering, Key Laboratory of Energy Plants Resource and Utilization, Ministry of Agriculture and Rural Affairs, South China Agricultural University, Guangzhou 510642, China

^b Key Laboratory for Biobased Materials and Energy of Ministry of Education, College of Materials and Energy, South China Agricultural University, Guangzhou 510642, China

ARTICLE INFO

Keywords:

Fast-growing poplar
Waterborne acrylic resin
Impregnation
Surface densification
Fire retardant
Mechanical properties

ABSTRACT

It is difficult to significantly improve the mechanical performance and fire-resistance of fast-growing wood without increasing its density. In this study, a modified poplar wood (USD-RA-W) with low-density, high dimensional stability, high mechanical strength, and fire resistance was successfully prepared by unilateral surface densification assisted with the impregnation of waterborne acrylic resin (WAR)/ammonium phytate (APA). The flexural and impact strength values of USD-RA-W increased by 52% and 48%, respectively, compared to the control samples (C-W). The surface hardness and wear resistance of USD-RA-W were also significantly improved, with a 132% increase in hardness and a 22% reduction in weight loss relative to C-W. The improvement in mechanical properties is attributed to the synergistic effects of surface densification and impregnation modification of APA-doped acrylic resin. The *in-situ*-cured resin network provides excellent dimensional stability by fixing the spring-back of the densified surface of the material. USD-RA-W shows significantly improved fire retardancy due to the introduction of bio-based APA. UL-94 analysis results show that the fire-retardant grade of the USD-RA-W passed V-0 and the limited oxygen index reached 50%. Cone calorimeter test results indicate that the total heat release rate and smoke release rate of the experimental group decreased by 32% and 77%, respectively, while the char residue reached 41%. A simple and green physicochemical method for the preparation of high-performance USD-RA-W was established in this study. The proposed treated wood may be applicable in structural building materials and interior decoration fields.

1. Introduction

Fast-growing poplar is a commercial wood species favored for its fast growth, early harvest time, and a short rotation period [1,2]. However, its loose texture and poor mechanical properties make it unsuitable as a structural building or high-grade interior decoration material [3,4]. The inflammability of untreated wood also poses a serious threat to the safety of human lives and property [5], which is, naturally, a serious concern [6,7]. It is necessary to modify fast-growing poplar wood to improve its mechanical properties and fire retardance before it will satisfy the requirements for practical application [8,9].

It is very challenging to simultaneously improve the mechanical properties and fire retardance of fast-growing poplar wood without sacrificing its inherently low density. Among existing physical modification methods, the bulk thermo-mechanical densification process has been shown to effectively improve the mechanical and physical properties of fast-growing wood species [10,11]. However, bulk densification process requires compressing the wood throughout its entire thickness [12], resulting in volume loss and wasted energy.

Compared with bulk densification, surface densification (SD) offers several distinct advantages. In terms of material efficiency, SD allows for the maximum utilization of wood without sacrificing its physical

* Corresponding authors at: Institute of Biomass Engineering, Key Laboratory of Energy Plants Resource and Utilization, Ministry of Agriculture and Rural Affairs, South China Agricultural University, Guangzhou 510642, China.

E-mail addresses: fanqscience@126.com (Q. Fan), rongxian_ou@scau.edu.cn (R. Ou).

<https://doi.org/10.1016/j.conbuildmat.2023.132470>

Received 4 March 2023; Received in revised form 28 June 2023; Accepted 9 July 2023

Available online 14 July 2023

0950-0618/© 2023 Elsevier Ltd. All rights reserved.

performance [13]. Unilateral surface densification (USD) is even more cost-effective and energy-efficient, allowing the production of value-added wood products with minimal volume loss [14]. However, USD creates disadvantages such as spring-back of the densified layers and poor dimensional stability [15].

Impregnation modification, one of the most commonly used chemical modification methods [16,17], has been extensively researched as it can significantly improve the dimensional stability of fast-growing wood [18,19]. Amino-formaldehyde resins and phenolic resins are often impregnated to fast-growing wood to enhance its mechanical and physical properties [20]. Impregnation modification combined with bulk densification can reduce the deformation recovery of modified wood by the fixed action amino-formaldehyde resin or phenolic resin crosslinking networks [21]. However, overuse of formaldehyde- and phenol-containing resins creates potential environmental issues and health threats. There is demand for an innovative, green, low-molecular-weight, fast-curing impregnation resin precursor.

Acrodur® is a water-based, formaldehyde-free reactive acrylic resin developed by BASF for use as an adhesive for natural fibers [22]. It is an alternative to formaldehyde-containing phenolic resins or other solvent-based thermosetting adhesives [23,24]. Below its curing temperature (135 °C), Acrodur® is a storage-stable aqueous resin. Above its curing temperature, Acrodur® can be cured rapidly by thermal-induced free radical polymerization and cross-linking of acrylic resin precursors with functional alcohols [25]. The cured resin material has thermosetting properties such as abrasion resistance as well as excellent thermal, mechanical, and chemical stability [26].

In a previous study [27], we surface-impregnated poplar wood with a reactive waterborne acrylic resin of Acrodur® followed by USD; the treated wood exhibited high dimensional stability, excellent surface hardness, and strong bending properties. To this effect, we assert that Acrodur® resin is ideal for improving the overall properties of unilateral surface-densified wood products [28]. Unfortunately, Acrodur® resins and wood are both flammable; they are unsuitable for use in areas with strict fire-resistance requirements. It may be possible, however, to improve the flame retardancy of Acrodur® resins to expand its practical applicability.

Introducing fire retardancy into the matrix is a direct, effective approach to improving the fire-resistance of polymer resin. Impregnating wood with fire-retardant resin can protect the wood itself from fire, while also strengthening the wood matrix [29,30]. The cured crosslinking network of the resin fixates doped fire-retardant components to reduce the loss, migration, and moisture absorption of the fire retardant [31]. Fire retardants containing halogens release harmful gases and smoke when burning, however, so many countries strictly regulate their application [32].

By contrast, phosphorus and nitrogen fire retardants have attracted a great deal of research attention due to their compatibility, low smoke

production, and low toxicity. Phosphorous fire retardants can produce phosphoric acid during combustion to promote the dehydration of the polymer matrix into carbon, creating a condensed-phase fire retardant effect [33,34]. Recently, Song et al. synthesized a bio-based fire-retardant curing agent of ammonium hydrogen phytate by controlling the reaction between phytate and urea. Modified wood coated with the mixture of melamine-urea formaldehyde resin and ammonium phytate (APA) showed an LOI value as high as 39.1% and an excellent fire retardant rating of V-0 [35].

In this work, modified poplar wood (USD-RA-W) with low density, high mechanical performance, and fire resistance was successfully prepared via a combination of environmentally friendly physico-chemical modifications. The poplar wood was impregnated with a composite precursor resin consisting of waterborne acrylic resin (WAR) and APA, then further treated with USD (Fig. 1). The effects of different WAR/APA ratios on the fire resistance and physico-mechanical properties of the unilateral densified wood were investigated. The fire-retardant mechanism was also determined. The proposed high-performance USD-RA-W can be used to create fire-safe, green, high-quality, and low-cost building materials, furniture, and interior decorative items.

2. Experimental section

2.1. Materials

The fast-growing poplar wood (*Populus euramevicana* cv. T-214') used in this study originates from Luohe, Henan Province, China. Phytic acid aqueous solution (70%) was purchased from Guolunmei Biotechnology Co., Ltd., Guangzhou, China. Urea was supplied by Jinhua Chemical Reagent Co., Ltd., Guangzhou, China. Water-based acrylic resin (Acrodur® DS 3530) with a density, solid content, viscosity range, and pH value of 1.06 g cm⁻³, 50%, 150–300 mPa s, and 3.5, respectively, originates from BASF China Co., Ltd., Shanghai, China. The main active ingredients are a mixture of polycarboxylic acids with multi-functional alcohol.

2.2. Preparation of USD-RA-W materials

2.2.1. Preparation of N/P doped acrylic resin

The preparation of APA was based on previous reports [36,37]. In detail, phytic acid (PA) and urea with fixed proportions were added to a flask and refluxed in a closed environment. Each mole of phytic acid corresponds to 5 mol of urea. The APA synthesis route is shown in Fig. 2. A light-yellow liquid was obtained after stirring and heating for 4 h at 120 °C. The liquid frozen in a freeze dryer and purified, then the resulting salt solids were denoted as APA. Based on exploratory tests, a series of WAR/APA solution with 18 wt% (w/w) concentration was prepared by dilution with deionized water. Different WAR/APA ratios

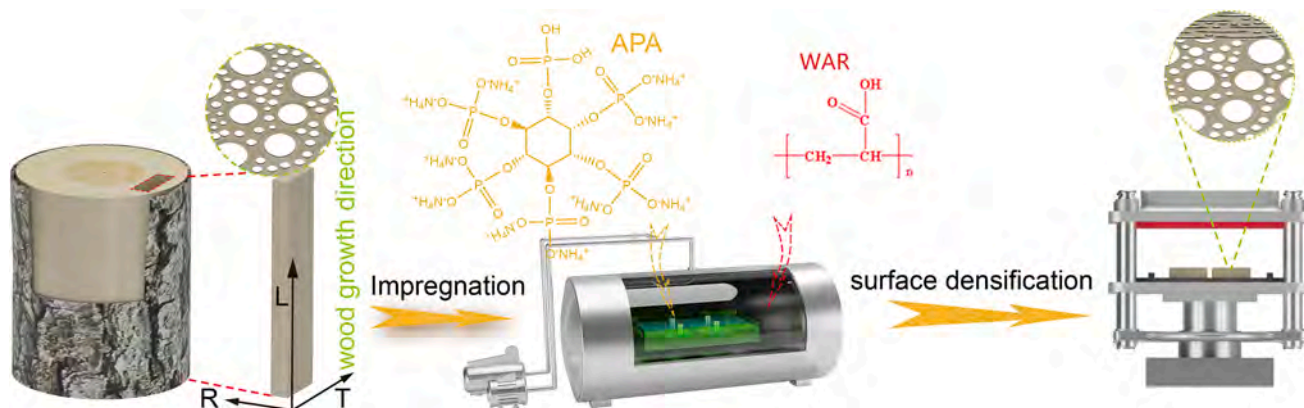


Fig. 1. Schematic demonstrating the wood modification process of unilateral surface densification assisted with impregnation of an N/P doped acrylic resin.

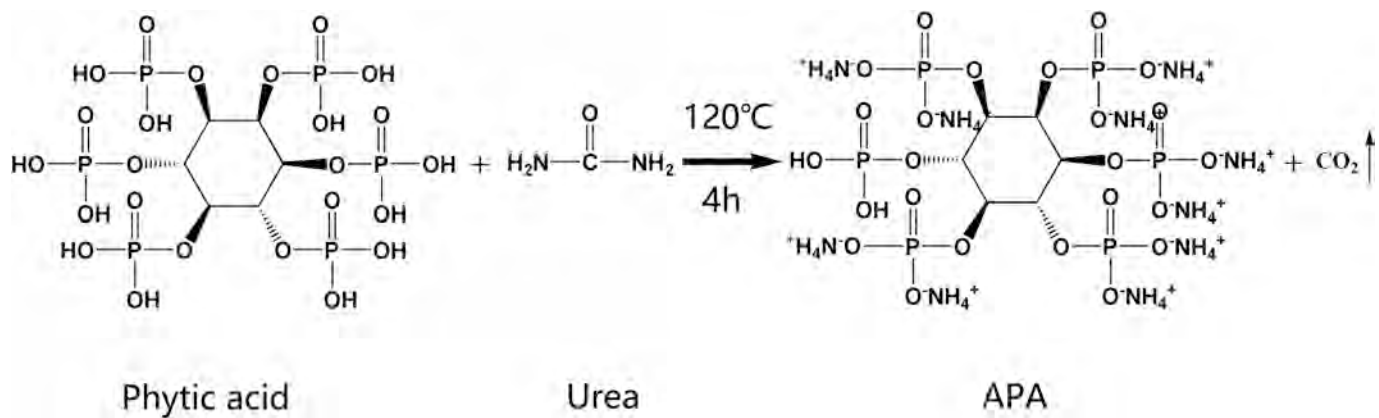


Fig. 2. Synthetic route of APA via the reaction between phytic acid and urea.

(1:0, 4:1, 3:1, 2:1, 4:3, 1:1 and 0:1) were successfully prepared, and were used for subsequent impregnation (Table 1).

2.2.2. Impregnation

The wood samples with dimensions of $170 \times 100 \times 13$ mm (L \times T \times R) were placed into a stainless-steel container and pressed with 100 g weights. Different mass ratios of N/P doped acrylic resin were poured into containers and submerged into the wood samples in the radial direction (Table 1). The containers were loaded into a vacuum high-pressure impregnation tank at room temperature. The tank was pumped down to about -0.08 MPa and held for 20 min, then the vacuum was released to ambient pressure as the solution initially entered the wood. The air pressure inside the tank was increased to 0.6 MPa and held for 1 h to allow the solution enter the wood more fully (Fig. 3a). Finally, the impregnated samples were removed from the vacuum tank and the any excess resin solution was wiped away from the surface.

The samples were left for 12 h to air dry indoors, then loaded into a vacuum oven at 60°C for 48 h. The vacuum was pumped down to about -0.08 MPa to complete the process. All samples were conditioned at 20°C and 65% relative humidity (RH) until equilibrium moisture content (EMC) was attained prior to densification.

2.2.3. Unilateral surface densification

The SD process for treating wood samples (Table 2) was carried out according to the steps shown in Fig. 3b using a hydraulic press machine (Qingdao Go World Rubber Machine Co., Ltd., Qingdao, China) with 100 metric ton capacity. The pressing tray dimensions were 60×60 cm. The upper platen was set to 160°C and the lower platen to room temperature. After the upper platen reached the designated 160°C , the samples were placed in direct contact on the lower platen and the press was closed immediately. When the pressure reached 6 MPa, the wood

samples were held under compression for 10 min to ensure curing of the impregnated acrylic resin. The samples were with a thickness of 13 mm compressed in the radial direction to a target thickness of 10 mm using two metal gauges at a nominal compression ratio of 23% (Fig. 1) after the sample was cooled to room temperature. Finally, all densified samples were conditioned at 20°C and 65% RH until EMC prior to further testing.

The fully impregnated and unilaterally surface-densified wood samples after equilibration were labeled as USD-RA-W. Five groups of USD-RA-W were marked as USD-RA-W1, USD-RA-W2, USD-RA-W3, USD-RA-W4, and USD-RA-W5 as WAR/APA ratio decreased from 4:1 to 1:1. The untreated control wood was labeled as C-W. The only surface-densified wood was labeled as USD-W, the wood only impregnated with 18 wt% WAR aqueous solution was labeled as USD-R-W, and the wood only impregnated with 18 wt% APA aqueous solution was labeled as USD-A-W.

2.3. Characterization

2.3.1. Micromorphology and energy dispersive spectrometry

Scanning electron microscopy (SEM) was conducted using an EVO 18 (Carl Zeiss, Germany) microscope at an accelerating voltage of 18 kV to observe the morphologies of the treated wood samples. Transverse sections of the densified layer were hand-cut using a razor blade. The samples for were painted with a conductive gold layer to prepare them for SEM imaging.

The sectional microstructure and contents of carbon, nitrogen, oxygen, and phosphorus in the char layers were examined with a ZEISS EVO18 SEM device (Germany) and an energy dispersive spectrometer (EDS) (EVO MA15, Germany) after cone testing.

2.3.2. Weight percent gain and leaching ratio measurements

The weight of the impregnated wood sample (m_2) was measured and the weight percent gain (WPG) induced by impregnation was calculated as follows:

$$WPG(\%) = \frac{m_2 - m_1}{m_1} \times 100\% \quad (1)$$

where m_1 and m_2 are oven-dry masses of the sample before and after impregnation, respectively (g).

The modified wood samples with dimensions of $20 \times 20 \times 10$ mm (L \times T \times R) were immersed in deionized water at 40°C for 24 h. The leaching ratio of the resin was calculated as follows:

$$Leachingratio(\%) = \frac{m_2 - m_x}{m_2 - m_1} \times 100\% \quad (2)$$

Where, m_x is oven-dry masses after 24 h immersion, m_1 and m_2 as in equation (1).

Table 1

The resin formulations used to impregnate different wood samples.

Wood samples	WAR/APA resin		Concentration of WAR/APA resin (wt.%)
	Acrylic resin (Phr.)	APA (Phr.)	
C-W ^a	0	0	0
USD-W ^b	0	0	0
USD-R-W	18	0	18
USD-A-W	0	18	18
USD-RA-W1	14.4	3.6	18
USD-RA-W2	13.5	4.5	18
USD-RA-W3	12	6	18
USD-RA-W4	10.3	7.7	18
USD-RA-W5	9	9	18

a: Deionized water impregnation treatment as the control group.

b: Deionized water impregnation treatment followed by unilateral densification.

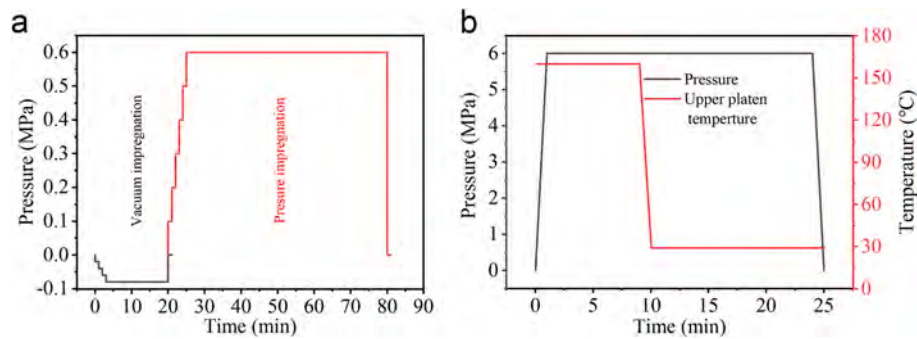


Fig. 3. Schematic development of process parameters during (a) vacuum impregnation and (b) unilateral surface densification.

Table 2

Basic physical properties of the un-densified control and unilaterally surface-densified wood.

Sample	T (°C)	Density ^a (kg m ⁻³)	Density ^b (kg m ⁻³)	EMC(%)	Density ^c (kg m ⁻³)	t ₁ (mm)	t ₂ (mm)
C-W	160	465	–	11.2	–	–	–
USD-W	160	484	554	9.12	882	0.21	0.83
USD-R-W	160	488	624	9.27	1184	0.61	2.13
USD-A-W	160	485	601	9.35	1124	0.54	2.04
USD-RA-W1	160	477	609	9.31	1173	0.42	1.92
USD-RA-W2	160	486	617	9.29	1109	0.3	1.75
USD-RA-W3	160	475	605	9.5	1053	0.35	1.22
USD-RA-W4	160	477	609	9.31	1143	0.42	1.22
USD-RA-W5	160	475	612	9.37	1013	0.3	1.21

T (°C): temperature of the upper platen during unilaterally surface densification.

Density^a (kg m⁻³) and Density^b (kg m⁻³): average density of the wood samples before and after unilaterally surface densification, respectively.

Density^c (kg m⁻³): the peak density of the densified layer.

t₁ (mm): thickness between surface and peak.

t₂ (mm): thickness of the effective dense layer with a density greater than 750 kg m⁻³.

2.3.3. Vertical density profile (VDP) measurements

An X-ray densitometer (DPX-300Lt, IMAL, Italy) was used to measure the VDP of the specimens after WCA measurements at intervals of 0.05 mm through the specimen thickness (radial direction).

2.3.4. Abrasion resistance

The abrasion resistance of each 100 × 100 × 10 mm (L × T × R) sample was measured according to ISO 7784e2:2006 on a Taber abrasion tester (Shanghai Pushen Chemical Machinery Co., Ltd., Shanghai, China). The mass losses were calculated after 500 revolutions with two wheels at a load of 1000 g and a rotation speed of 60 rpm. Three replicates were measured for each sample and the mean value was calculated as the final result.

2.3.5. Surface roughness measurements

Surface roughness measurements of 100 × 100 × 10 mm (L × T × R) specimens were conducted according to ISO 4287:1997 on a contact stylus profilometer (Hommel-Etamic W5, Jenoptik, Germany). Average roughness (R_a) was used to characterize the surface characteristics. The final value of R_a was calculated by averaging nine different positions on each sample.

2.3.6. Static hardness measurements

Static hardness testing of the specimens was carried out according to ISO 13061e12:2017 on a universal testing machine (AI-7000 M–GD, Goodtechwill, Taiwan, China) (Standardization, 2017) after VDP measurements. The machine was equipped with an 11.28 mm diameter indenter, which was placed on the surface of the densified layer and compressed at a rate of 4 mm min⁻¹ until a displacement of 2.82 mm was reached. The maximum load was recorded and the surface hardness H_W (N) was calculated as follows.

$$H_W = K \times F \quad (3)$$

where H_W is the surface hardness at moisture content (W, N); F is the maximum load, (N); K = 4/3 for 2.82 mm displacement.

2.3.7. Contact angle measurements

A drop shape analyzer (DSA100 HP, Krüss GmbH, Hamburg, Germany) was used to measure the water contact angles (WCA) of the specimens after surface roughness measurements with a 2 μL deionized water droplet. Each average WCA value was obtained from at least three parallel measurements on different areas of the same surface.

2.3.8. Set recovery measurements

The specimens measuring 20 × 20 × 3 mm (L × T × R) were cut from the densified layer wood samples. The specimens were soaked in deionized water at 40 °C for 24 h. Set recovery (SR) was determined by measuring the oven-dried (103 °C, 6 h) specimen thickness before and after soaking. A screw micrometer with an accuracy of 0.001 mm was used to measure thickness of the four different points from each specimen. SR was calculated as:

$$SR = \left[\frac{(T_s - T_d)}{(T_0 - T_d)} \right] \times 100\% \quad (4)$$

where T₀, T_d, and T_s are the thicknesses of the oven-dried undensified, densified, and recovered specimens in the radial direction, respectively.

2.3.9. Thermogravimetric analysis

The thermal decomposition of the modified wood was determined by thermogravimetric analysis (TGA) (TG 209 F1Libra TM analyzer, Netzsch, Germany). Specimens of approximately 8 mg were heated under N₂ atmosphere with 20 ml min⁻¹ from 35 to 800 °C at 10 °C min⁻¹.

2.3.10. Limited oxygen index (LOI)

Specimens with dimensions of $130 \times 6.5 \times 3$ mm ($L \times T \times R$) were cut from the densified layer of the unimpregnated and impregnated samples were used to measure the limited oxygen index (LOI) (HC-2 oxygen index meter, Jiangning Analysis Instrument Company, China) based on ASTM D2836. Fifteen replicates were measured for each sample.

2.3.11. UL-94 vertical burning testing

Pure and densified layered samples with dimensions of $130 \times 13 \times 3$ mm ($L \times T \times R$) were test in accordance with ASTM D6413 on a UL-94-X type vertical burning tester (Kunshan Modislike Combustion Technical Instrument Co., LTD., China). Ten replicates were tested for each sample.

2.3.12. Cone calorimetric analysis (Cone)

A cone calorimeter (CCT, MOTIS Combustion Technology, China) was used to evaluate the flammability of the pure and modified wood samples with dimensions of $100 \times 100 \times 10$ mm ($L \times T \times R$) based on ISO 5660-1:2016 at a heat flux of 50 kW m^{-2} . A standard metal frame and aluminum foil were used to protect the modified wood sample edges. Each treatment was conducted in triplicate.

2.3.13. Bending property measurements

The modulus of elasticity (MOE) and modulus of rupture (MOR) of specimens $175 \times 15 \times 10$ mm ($L \times T \times R$) in size were measured according to ISO 13061-3:2014 and ISO1361-4:2014, respectively, on a universal testing machine (AG-I, Shimadzu Corporation, Kyoto, Japan) under three-point bending. The densified surface was placed upward and touched the loading head during testing. Eight replicates were tested for each sample.

2.3.14. Impact bending strength measurement

The impact bending strength of the samples was determined according to GB/T1927.17-2021. Eight replicates were used for each sample. The width and thickness of each test samples were 15 mm and 10 mm, respectively, the length was 120 mm, and the span length was 70 mm. An Amsler pendulum impact test machine was used to measure impact bending strength. The weight of the pendulum hammer was 7.5 kg.

Impact bending strength was calculated as:

$$a = \frac{1000W}{A} \quad (5)$$

where a is the impact bending strength (kJ/m^2), W is the energy absorbed by the sample (J), and A is the cross-sectional area of the specimen (mm^2).

3. Results and discussion

3.1. Weight percent gain and leaching

Fig. 4a shows where the weight percent gain (WPG) of the modified wood samples varied with different WAR/APA ratios when the concentration of WAR/APA solution was 18 wt%. The WPG of the wood samples decreased as APA increased. This is due to the hydrophilicity of APA, which reduces WPG.

Fig. 4b shows that the leaching ratio of USD-A-W (with only APA impregnated) was 92.2 wt%. After mixing with acrylic resin, the leaching ratio of USD-RA-W1 decreased to 10.9 wt%; thus, the acrylic resin effectively encapsulated the APA. The leaching ratio of the mixture of WAR/APA gradually increased as acrylic resin decreased, which suggests that an increase in acrylic resin accounts for the more effective fixation of APA.

3.2. VDPs and cell morphology of wood samples

The vertical density profiles (VDPs) of unilaterally surface-densified wood and the un-densified control sample are shown in Fig. 5a. The density of the hardwood normally used for solid wood flooring is $650\text{--}800 \text{ kg m}^{-3}$, so the thickness of an effectively dense layer was defined here as a density greater than 750 kg m^{-3} . In the thermo-hydro-mechanical process, the cell wall of wood (a complex consisting of cellulose, hemicellulose, and amorphous lignin) is deformed, changing from glassy to rubbery under heat-wet conditions.

As shown in Fig. 5a, the VDP shape of USD-W samples is narrow and sharp. This profile originates from the limited heat transfer to the inner layer of wood. The peak density, thickness between the surface and peak (t_1), and thickness of the effective dense layer (t_2) of the only unilaterally surface-densified wood (USD-W) samples were 882 kg m^{-3} , 0.21 mm, and 0.83 mm, respectively. Increasing the ratio of acrylic resin increased the peak density, t_1 , and t_2 (Fig. 5a). The peak density, t_1 , and t_2 of USD-RA-W5 (unilaterally surface-densified wood assisted with impregnating WAR/APA) all increased compared to USD-W (Table 2).

It is worth noting that the t_2 value of USD-RA-W5 were more than twice those of USD-W. Acrylic resin has plasticizing effect on wood cell walls at high temperatures; the presence of thermoplastic acrylic resin in the cell lumens also increases the thermal conductivity of the wood, resulting in more heat being radiated to the inner layers. for these reasons, the thickness of the effectively dense layer and peak density of USD-RA-W5 were much higher than those of wood samples without resin impregnation. Unlike C-W, USD-W and USD-RA-W5 have a clearly observable dense layer (Fig. 5b).

SEM analysis revealed the microstructures of un-densified control wood and the densified layers of USD-W and USD-RA-W5 (Fig. 5c-e). The wood cell walls were deformed in the direction of densification and the volume of the cell lumen was significantly reduced after treatment.

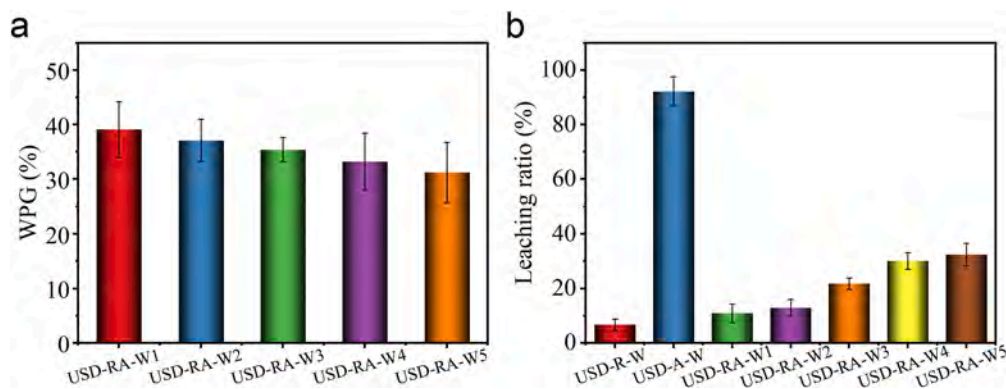


Fig. 4. (a) Weight percent gain (WPG) of the densified wood samples after impregnation with different WAR/APA ratios and (b) the leaching ratio of samples.

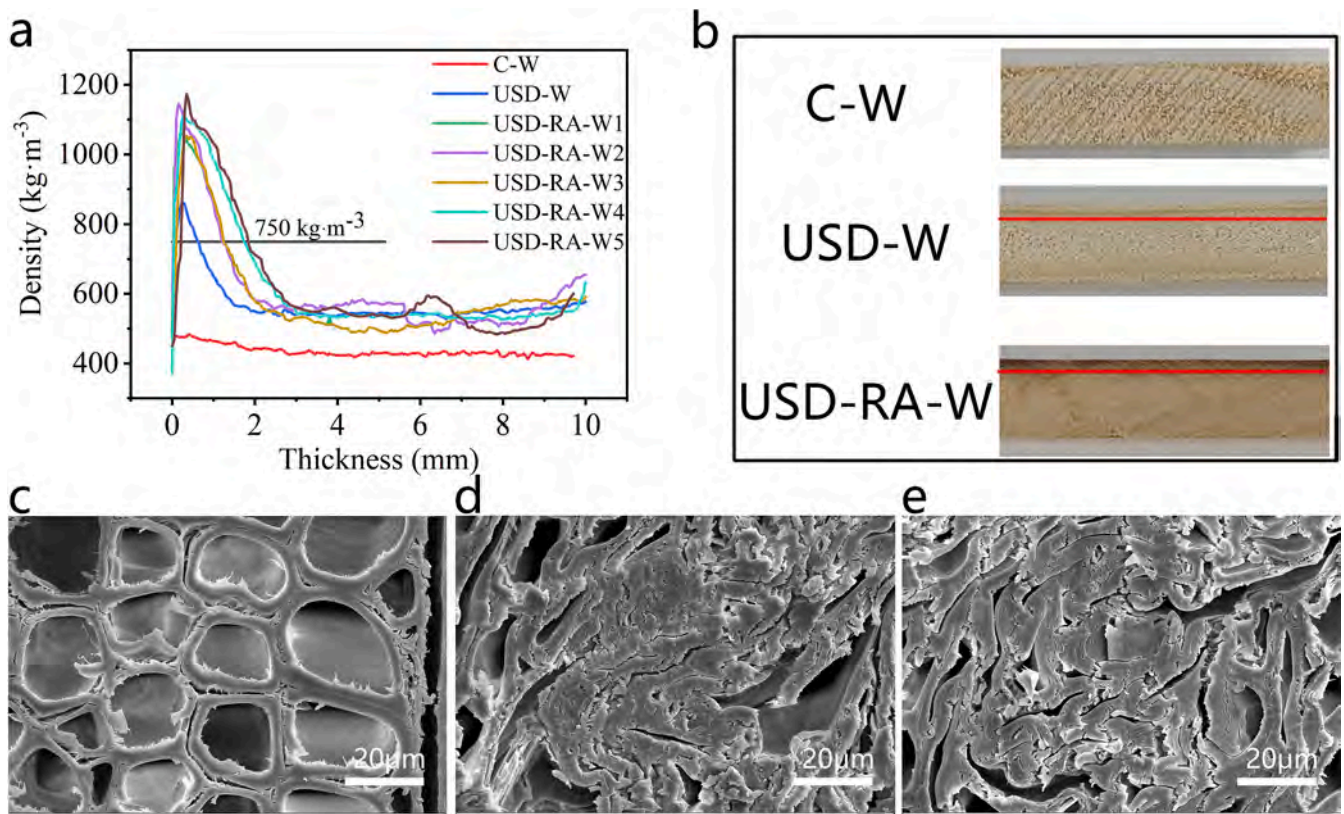


Fig. 5. (a) Density profiles of un-densified control (C-W), only unilaterally surface-densified wood (USD-W), and unilaterally surface-densified wood samples impregnated with different WAR/APA ratios (USD-RA-W). (b) Digital photos of C-W, USD-W, and USD-RA-W5. Scanning electron micrographs of (c) C-W, (d) USD-W, and (e) USD-RA-W5.

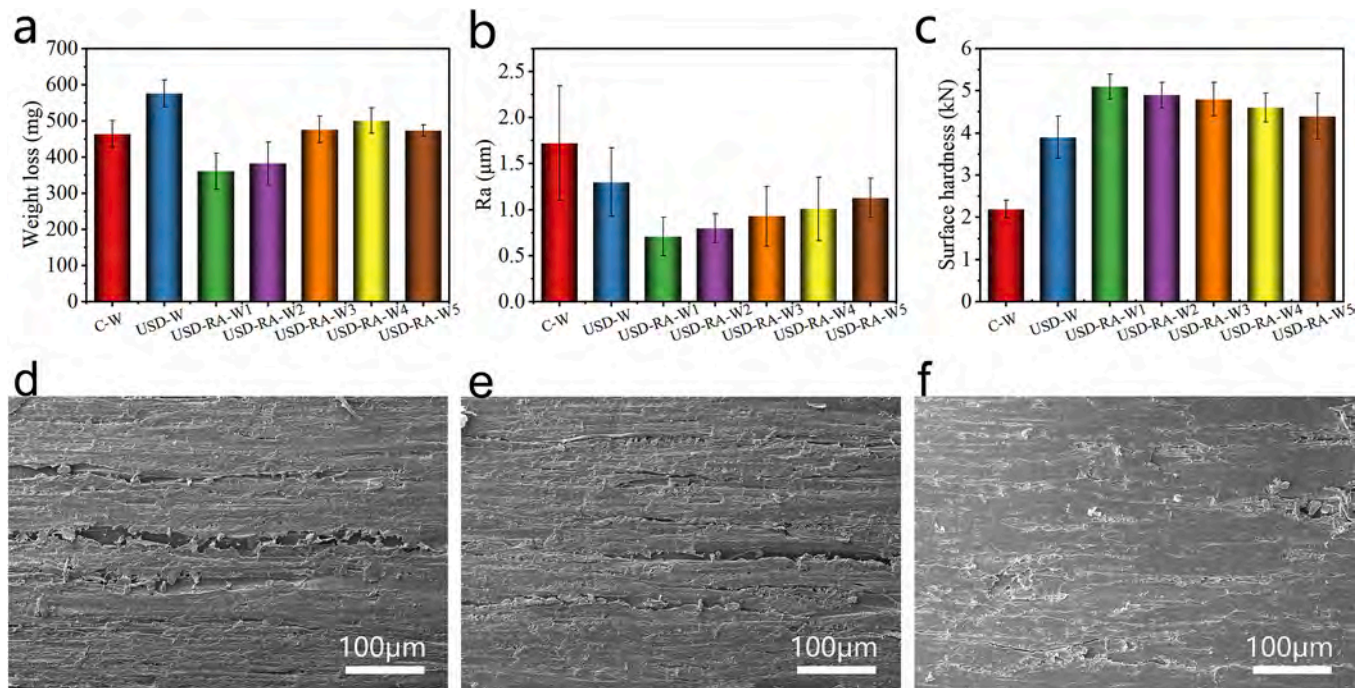


Fig. 6. (a) Weight loss of the un-densified control (C-W), only unilaterally surface-densified wood (USD-W), and unilaterally surface-densified wood samples impregnated with different WAR/APA ratios (USD-RA-W) after 500 revolutions (b) average roughness (R_a) of the wood samples (c) the hardness of the wood samples; SEM micrographs of the surface morphology of (d) C-W, (e) USD-W, and (f) USD-RA-W5.

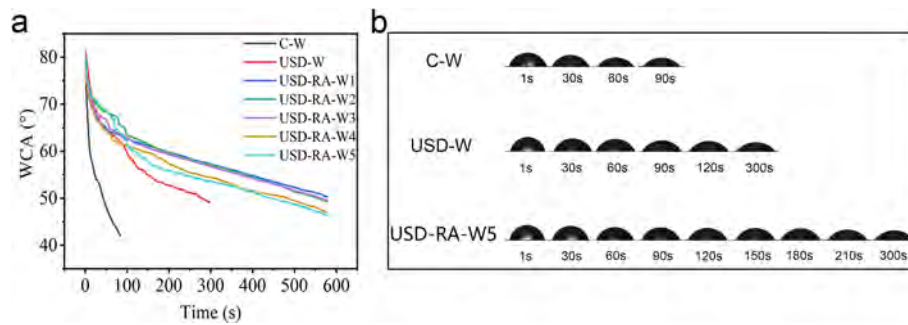


Fig. 7. (a) Changes of water contact angle (WCA) against time on different samples, (b) photographs of water droplets on the surface of different samples with the contact time.

The wood did not deform uniformly between tissue types and instead was dependent on cell wall thickness, cell shape, and lumen diameter.

Due to compression, the deformation of cell lumens is wavy and serrated. These deformation phenomena were mainly caused by the elastic yielding of cell walls (Fig. 5d, 5e). The USD process has a sufficient plasticizing effect on the wood cell walls, so cell wall fracture was not observed. The structural integrity of the wood ensured that the mechanical properties were improved after treatment. For the resin-impregnated samples (Fig. 5e), cell lumens (fibers and vessels) were filled with APA doped acrylic resin and the cells were less compressed. The cured APA doped resin contributed to high surface density and hardness.

3.3. Abrasion resistance, surface roughness, and hardness

Abrasion resistance is an important indicator of flooring, desktop, and panels material effectiveness. The weight loss values of the undensified control wood after 500 revolutions were 464.5 mg (Fig. 6a). Generally, abrasive wear varies with structural rigidity, hardness, and toughness. The weight loss of the USD-W increased compared to the undensified controls. This may have resulted from the brittle densified surface, which was more easily removed by abrasive particles. After impregnation of APA doped acrylic resin, the abrasion resistance increased further on account of the reduction in weight loss. This phenomenon may be attributed to the dense cross-linked structure of the cured APA doped acrylic resin and the strong interfacial interaction between the cell walls and the resin. In addition, the impregnated resin contained a higher percentage of acrylic materials which enhanced the wearability of USD-RA-W.

Fig. 6b shows the average roughness (R_a) values of samples. The undensified control had the largest R_a (1.7 μm). As shown in Fig. 6d, we attributed this to the presence of open cell lumens. After densification, the R_a values of USD-W wood decreased to 1.3 μm . However, open cell lumens were still observed on the surface (Fig. 6e). The R_a value decreased after impregnating the APA doped acrylic resin. USD-RA-W1 had the smoothest surface characteristics with R_a values of 0.9 μm . All impregnated samples had smaller roughness values than the only-densified wood, because the cell lumens on the surface were filled with cured resin (Fig. 6f).

The hardness values of C-W, USD-W, and USD-RA-W samples are shown in Fig. 6c. As expected, the hardness of the USD-W sample significantly increased due to the effects of the densification treatment. USD-RA-W surface hardness ranged from 4510 to 5103 N, which is twice as high as that of the un-densified control. The impregnated acrylic resin increased the hardness (Fig. 6c). We also found hardness to be directly related to the peak density, t_1 , and t_2 . The densified layer beneath the effectively dense layer also influenced overall hardness. The USD-RA-W1 shows the highest ratio of hardness/density amongst all wood samples, indicating that it would be suitable for manufacturing flooring, desktops, and tabletops.

3.4. WCA of wood samples

Fig. 7b shows images of water droplets on the surfaces of the undensified control, USD-W, and USD-RA-W samples. Due to the hydrophilic nature of the wood cell walls, the un-densified control was easily wetted. The WCA of the un-densified control dropped to less than 50° within 1 min (Fig. 7a). The wettability of USD-W samples changed significantly. The densified structure of USD-W delayed the absorption of water; it took 6 min to decrease WCA below 50°. The hydrophobicity of the USD-RA-W5 sample was ever further improved (Fig. 7a, 7b). The WCA of the USD-RA-W5 sample decreased slowly and was higher than 45° after 10 min. USD-RA-W1 exhibits optimal hydrophobicity among the treated samples likely because it contains the maximum amount of acrylic resin, which forms dense crosslinking networks of covalent and hydrogen bonds with the hydroxyl groups of cell walls to prevent water penetration [38].

3.5. Set-recovery

Fig. 8 shows the set-recovery values of densified layers as a function of WAR/APA ratio. The compressive deformation of the densified layer of USD-W samples recovered to about 72% after one soaking-drying cycle. The high set-recovery values of the USD-W samples is attributable to the release of the elastic strain energy stored in cell walls [39]. The set-recovery value dramatically decreased when the deformation was fixed by cured resin. The rapid thermal cross-linking of polycarboxylic acids with multi-functional alcohol formed strong wood-resin-adhesion [40], which prevents the penetration of water and spring-back of the buckled cell wall. Only WAR impregnated (18 wt%) wood showed the lowest set-recovery value (Fig. 8). The set-recovery

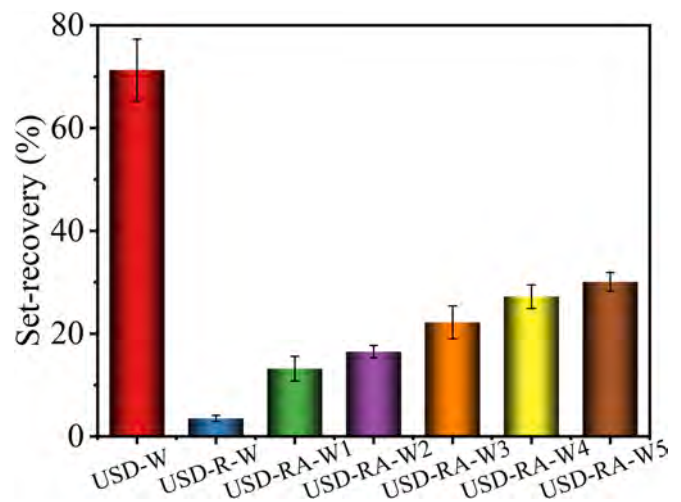


Fig. 8. Set-recovery of the wood samples.

values of USD-RA-W increased with APA content because APA is hydrophilic. Despite this, USD-RA-W5 samples with the highest APA contents still showed a much lower set-recovery than USD-W.

3.6. Thermal stability

The thermal stability of the wood samples was characterized by TGA and derivative thermogravimetric (DTG) analysis as shown in Fig. 9 and Table 3. As shown in Fig. 9a, the TG curves indicate a one-stage thermal degradation of the wood samples. The large, sharp decomposition peak at 367.6 °C can be attributed to the thermal decomposition of cellulose. The thermal degradation behavior of the wood samples impregnated with WAR/APA changed (Fig. 9). The thermogravimetric curves of USD-RA-W samples show weight loss around 410 °C associated with the thermal degradation of acrylic resin, including dehydration of the resin and the formation of residual char.

As shown in Table 3, the $T_{d10\%}$ (temperature at 10% weight loss) and T_{peak} (temperature corresponding to maximum degradation rate) values of USD-RA-W samples shifted to a lower temperature as APA content increased. APA accelerated the thermal decomposition of the matrix and promoted char residue formation. The char residue of USD-RA-W samples increased significantly with APA content, which further indicates that APA enhanced the char-forming ability of densified wood samples. The char residue of USD-RA-W5 reached 40.74% at 800 °C, compared to the 15.37% char residue of C-W (Table 3). The introduction of APA may have contributed substantially to the fire retardancy of unilaterally surface-densified wood.

3.7. LOI and vertical burning test

The fire retardancy of the USD-RA-W sample was estimated by classic LOI and UL-94 vertical burning tests. The results are shown in Fig. 10 and Table 4. As shown in Fig. 10, C-W, USD-W, and USD-RA-W1 failed to pass the UL-94 vertical burning test with low LOI values of 22%, 23%, 30.5%, respectively. In comparison, the USD-RA-W2 successfully passed the V-1 rating in the UL-94 test; its LOI value reached 36%, indicating a high level of fire safety.

Notably, USD-RA-W3, USD-RA-W4, and USD-RA-W5 samples all achieved a V-0 rating (Fig. 10). The LOI value of USD-RA-W gradually increased with APA content. A relatively small addition of fire retardant APA appears to markedly improve the fire retardancy of the unilaterally surface-densified poplar wood. Small APA additions also have little effect on the resin curing process. This satisfactory fire-retardant behavior in unilaterally surface-densified wood impregnated with WAR/APA is superior to the fire-retardant modified poplar wood that has been previously reported [41].

Table 3

TGA analysis data of C-W and USD-RA-W.

Sample	$T_{d10\%}$ (°C)	T_{peak} (°C)	R_{800} (wt.%)
C-W	241.21	367.60	15.37
USD-RA-W1	213.42	297.21	27.60
USD-RA-W2	185.61	285.65	34.52
USD-RA-W3	182.52	284.51	35.21
USD-RA-W4	179.56	282.25	38.35
USD-RA-W5	178.41	281.30	40.74

3.8. Cone calorimeter test

The cone calorimeter is a bench-scale instrument for evaluating the fire-resistant behavior of polymers. It provides several key flammability parameters such as heat release rate (HRR), total heat release (THR), smoke produce rate (SPR), and total smoke rate (TSP).

The HRR and THR as a function of burning time for the C-W and the modified wood, including USD-W and USD-RA-W5, are shown in Fig. 11; the relevant data are summarized in Table 5.

As shown in Fig. 11, USD-W showed the highest peak heat release rate (PHRR) and THR. Compared with USD-W, the introduction of APA reduced PHRR and THR values in USD-RA-W. The THR of USD-RA-W decreased gradually as APA addition increased. USD-RA-W5 had a 45% lower THR than USD-W, from 71.3 MJ m⁻² to 39 MJ m⁻². The low heat release parameters demonstrate low fire hazards.

The TSP values of the USD-RA-W5 sample decreased by 77% and 86% compared to those of C-W and USD-W, respectively. We mainly attribute this smoke suppression action to the ability of USD-RA-W to form denser and larger protective char barrier layers during combustion. The smoke suppression of the samples significantly improved once the amount of added APA reached a certain value. USD-RA-W shows a significant decrease in THR and TSP compared to USD-W, indicating that the plastic compounding process inhibited wood combustion and fire spreading. After the wood cells were compressed, voids and spaces inside the dense layer of the wood were greatly reduced; this reduced the amount of oxygen to support combustion thus increasing fire retardancy. The volatility of USD-RA-W also decreased compared to other samples, which indicates a potential vapor-phase mechanism. In effect, the proposed poplar wood modification yields efficient fire retardancy.

Fig. 12 shows that only some ashes and disintegrated charcoal fragments were left in the C-W and USD-W after the cone test. The high char yield of USD-RA-W implies a catalytic char-forming effect as well. The residual char layers of the C-W and USD-W showed an extensive range of collapse, while those of USD-RA-W were discontinuous and broken (Fig. 12). As shown in Fig. 12, we observed an intumescent char layer that formed for USD-RA-W during combustion, which played an important role in improving fire retardancy.

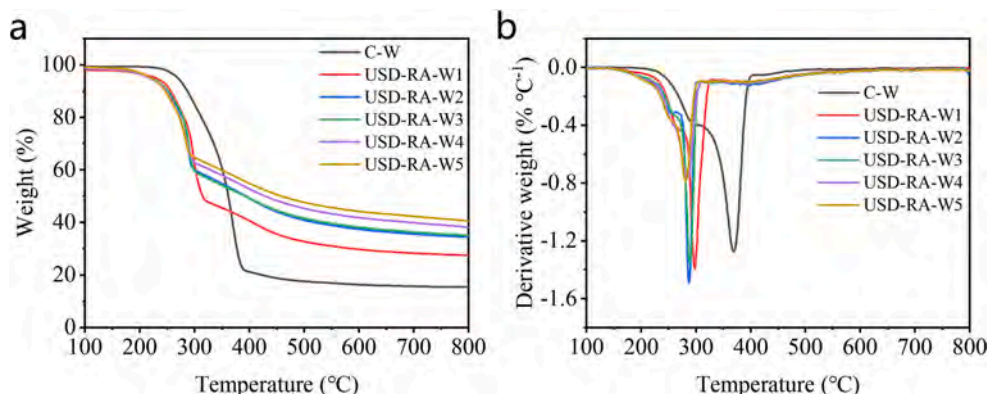


Fig. 9. (a) TG and (b) DTG curves of C-W and USD-RA-W.



Fig. 10. Digital photos of C-W, USD-W, and USD-RA-W during UL-94 test.

Table 4

LOI values and UL-94 rating of C-W, USD-W, and USD-RA-W.

Sample	UL-94	LOI (%)
C-W	Failed	22
USD-W	Failed	23
USD-RA-W1	Failed	30.5
USD-RA-W2	V-1	36
USD-RA-W3	V-0	39
USD-RA-W4	V-0	43.5
USD-RA-W5	V-0	50

3.9. Fire-retardant mechanism

We observed the morphology of USD-RA-W5 after the cone tests by SEM to further explore the fire retardancy mechanism. As shown in Fig. 13a and 13b, the interior structure of the burned USD-RA-W5 maintained a complete fibrous tracheid and vessel structure of in the wood, indicating that impregnation with WAR/APA created excellent protection ability for the wood substrate.

The elemental distribution of the char layer is shown in (Fig. 13c, 13d). Phosphorus and nitrogen elements (Fig. 13d) were detected in the

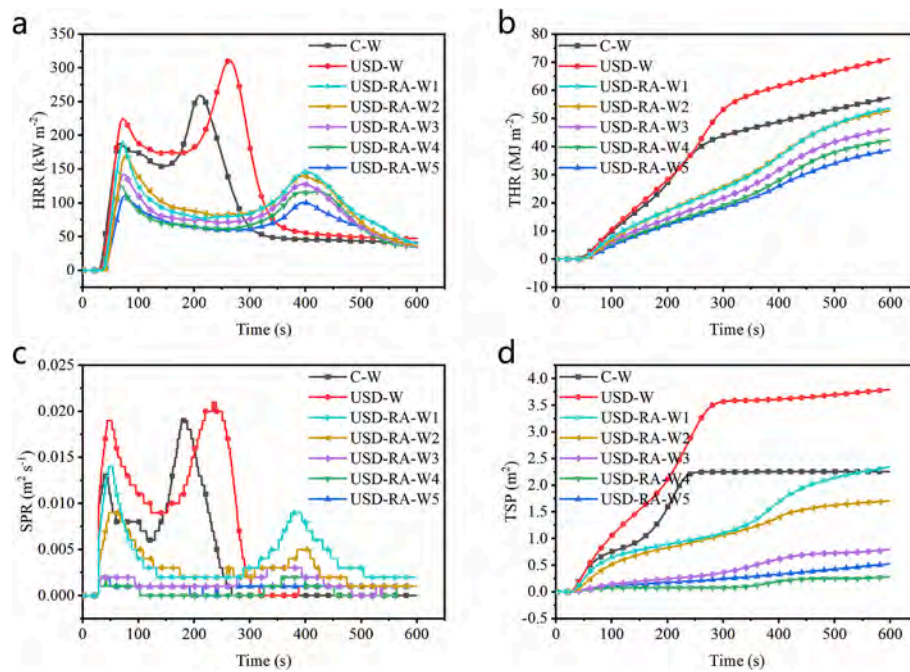


Fig. 11. The HRR (a), THR (b), SPR (c), and TSP (d) curves of C-W, USD-W, and USD-RA-W.

Table 5

Cone calorimeter data of C-W, USD-W, and USD-RA-W.

Group	PHRR (kW m ⁻²)	THR (MJ m ⁻²)	SPR (m ² s ⁻¹)	TSP(m ²)
C-W	258.80	57.4	0.018	2.256
USD-W	311.45	71.31	0.022	3.794
USD-RA-W1	145.78	53.68	0.009	2.347
USD-RA-W2	139.81	52.74	0.005	1.707
USD-RA-W3	127.70	46.29	0.003	0.796
USD-RA-W4	116.80	42.31	0.002	0.281
USD-RA-W5	100.48	38.75	0.002	0.523

char layer of USD-RA-W5, which promoted the formation of a thermal stable P/N/C-containing hybrid char layer that improved the char yield over other samples. This type of char layer can suppress the transmission of heat and volatiles effectively and prevent further degradation of wood substrates. The remarkable fire retardancy of wood treated by the proposed method is thus attributable to the typical synergistic fire retardancy of nitrogen and phosphorus.

3.10. Mechanical properties

As USD-RA-W1 failed to pass UL-94 fire retardant test, we did not further analyze its mechanical properties and instead focused on other samples. As shown in Fig. 14a, the average modulus of elasticity (MOE) and modulus of rupture (MOR) of untreated control were 8.4 GPa and 81.1 MPa, respectively. The MOE and MOR of USD-W were 8.78 GPa and 101.2 MPa, respectively, which are higher than those of the control by about 4.5% and 24.7%. SD thus improved the mechanical properties of the wood. The MOE and MOR of USD-A-W samples only impregnated with APA were 9.57 GPa and 124.8 MPa. The MOE and MOR of USD-R-W samples only impregnated with WAR (18 wt%) were 10.84 GPa and 135.9 MPa, respectively, which were further increased about 13.3% and 8.1% higher than those of USD-A-W samples. The acrylic resin filled in the cell lumens of USD-R-W enhance the adhesion between wood fibers and improve the mechanical strength of the wood matrix.

For the USD-RA-W samples impregnated with APA-doped acrylic resin, MOE values were 11.17–12.68 GPa, which are higher than those of the only-unilaterally surface-densified wood and 32.9–50.9% higher than those of the control group. Among them, the USD-RA-W3 sample showed the highest MOR and MOE. Hence, the introduction of a proper amount of APA into the pure impregnating resin can significantly improve the fire resistance of wood without damaging its mechanical strength.

As shown in Fig. 14b, the impact strength (99.3 kJ m⁻²) of USD-W was about one-fold higher than that of untreated wood (47.6 kJ m⁻²). This is due to the composite reinforcement effect of the dense layer leading high strength and toughness in the wood matrix, thus significantly increasing its impact strength. The impact strength (62.5–75.1 kJ m⁻²) of USD-RA-W samples was smaller than that of USD-W. This is due to the thermal crosslinking reaction between acrylic resin and wood cell walls having formed a rigid network structure. When subjected to impact load, the fibers in this structure did not easily slip, resulting in lower impact strength. However, the impact strength of USD-RA-W was still 37%–57.8% higher than that of the control group, which is a surprising result that chemical modification of wood generally results in decreased impact strength compared to natural wood [42].

4. Conclusion

We developed an environmentally friendly and energy-efficient process in this study to fabricate modified poplar wood (USD-RA-W) with high performance (including low density, high fire resistance, high dimensional stability, and high mechanical strength) by combining the impregnation of N/P doped acrylic resin and unilateral surface densification. The influence of WAR/APA ratios on fire retardancy, basic physical properties, and mechanical properties were systematically discussed.

The introduction of bio-based fire retardant APA greatly improved the fire retardancy of USD-RA-W. The *in-situ* cured WAR effectively fixed APA molecules and reduced loss from USD-RA-W. The surface properties of USD-RA-W, such as roughness and wear resistance, were dependent

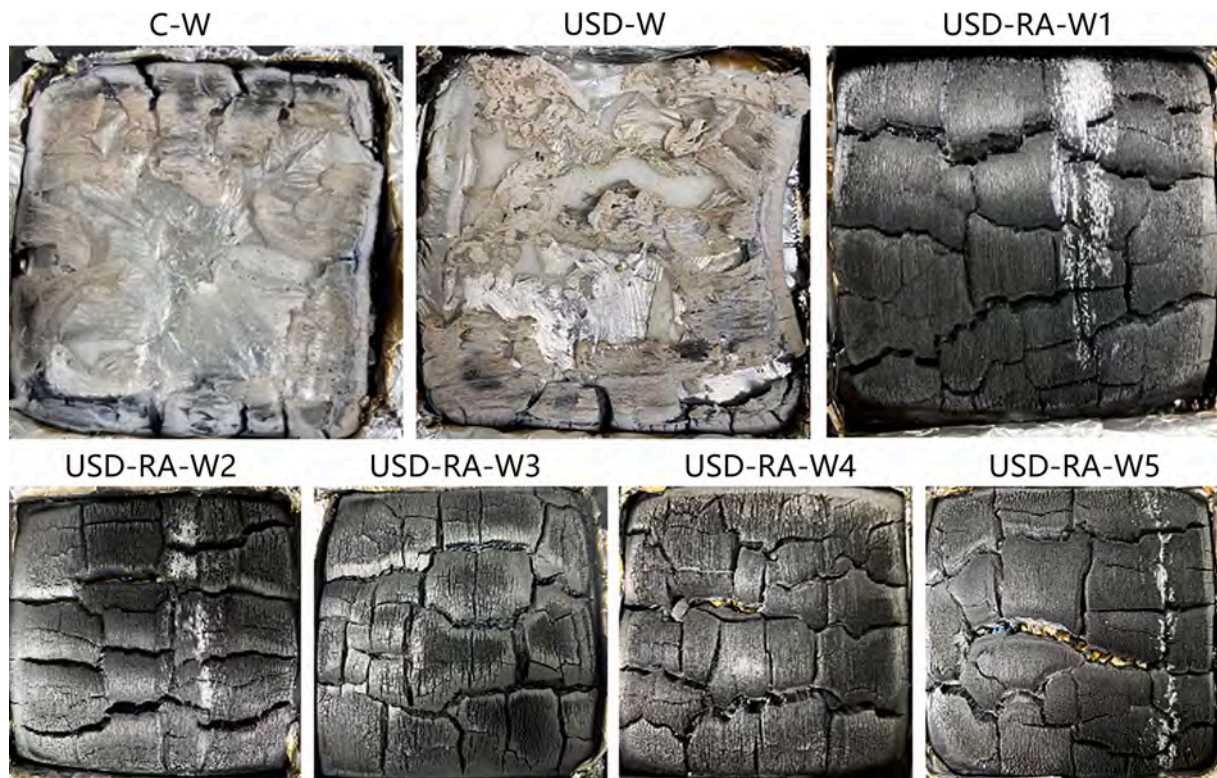


Fig. 12. The morphologies of wood samples after cone tests.

on the ratio of WAR/APA. The surface hardness values of the USD-RA-W samples were almost twice as high as those of the control group. Due to the fixed action of the cross-linked network of WAR, the USD-RA-W samples exhibited excellent dimensional stability. The MOE and MOR of USD-RA-W were much higher than those of the only-unilaterally-surface-densified wood. The impact strength of USD-RA-W was also

much higher than those of the untreated wood resulting from the composite reinforcement effect of the densified layer.

Compared with conventional formaldehyde-based resins, although acrylic resins are more costly, they offer significant improvements in environmental benefit as well as in mechanical properties and dimensional stability of fast-growing wood. In addition, acrylic resins have

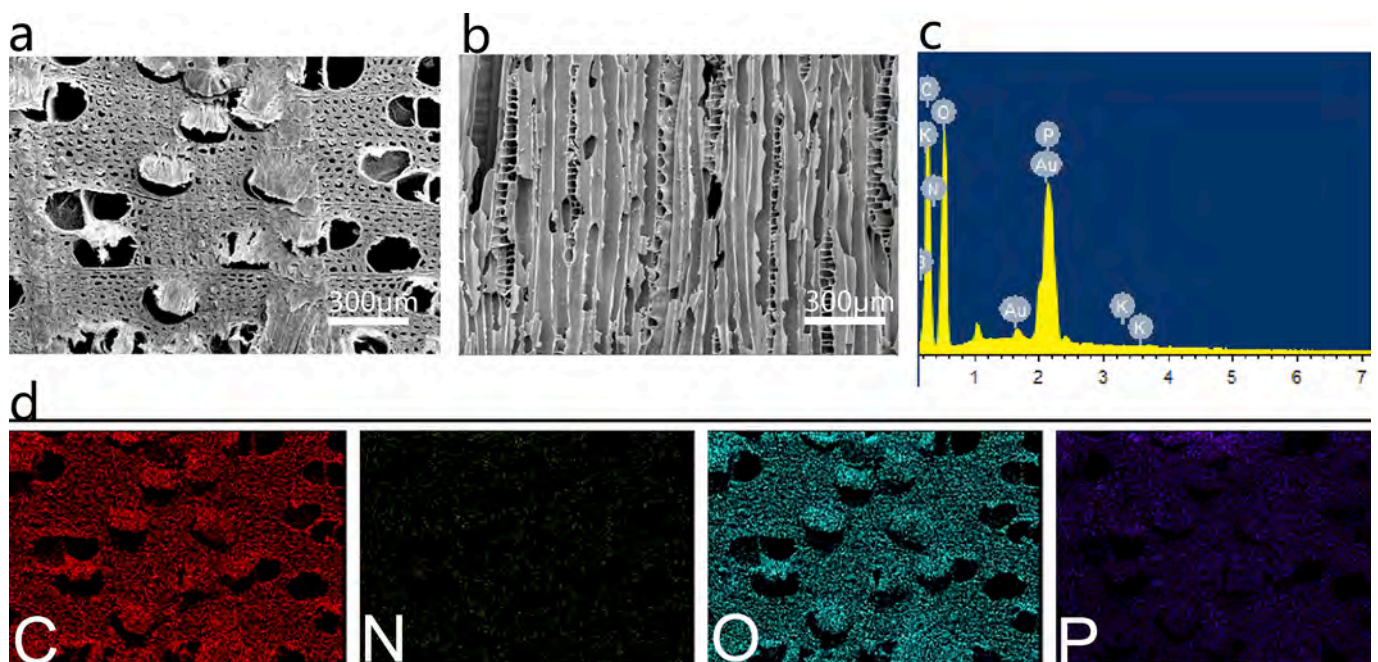


Fig. 13. Microstructure EDS mapping of the char residue for USD-RA-W5 after 500 s cone tests: (a) cross section, (b) tangential section, (c) EDS spectra, and (d) element mapping.

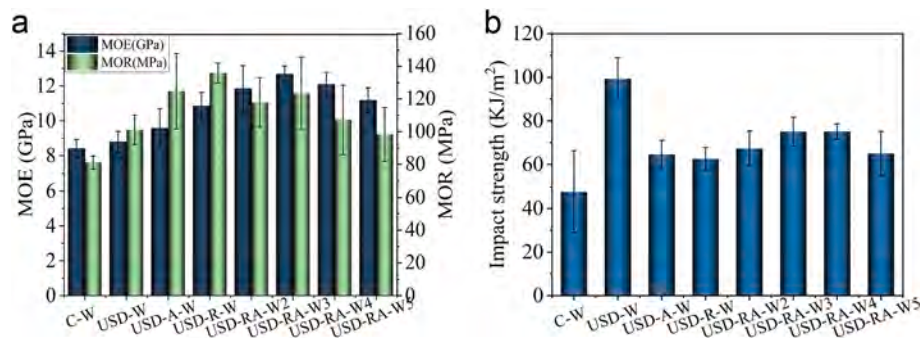


Fig. 14. (a) Modulus of elasticity (MOE) and modulus of rupture (MOR) of the wood samples (b) the impact strength of the wood samples.

good compatibility with most fire retardants and can easily achieve enhancement in both mechanical properties and fire retardancy. These advantages make acrylic resins a promising option for improving the overall performance of fast-growing wood in the future. In conclusion, the fast-growing wood treated with the proposed unilateral surface densification combined with functional resin modification will be suitable for home improvement, construction and other engineering applications.

CRediT authorship contribution statement

Xing Zhang: Methodology, Investigation, Writing – review & editing, Formal analysis, Writing – original draft. **Qi Fan:** Investigation, Writing – review & editing, Funding acquisition, Formal analysis. **Chuanfu Chen:** Investigation, Formal analysis. **Xiaolong Hao:** Formal analysis. **Zhenzhen Liu:** Formal analysis. **Rongxian Ou:** Conceptualization, Writing – review & editing, Funding acquisition, Supervision. **Qingwen Wang:** Funding acquisition, Supervision.

Declaration of Competing Interest

The authors declare that they have no known competing financial interests or personal relationships that could have appeared to influence the work reported in this paper.

Data availability

Data will be made available on request.

Acknowledgements

This work was financially supported by the Research and Development Program in Key Areas of Guangdong Province (2020B0202010008), the National Natural Science Foundation of China (32071698 and 52103110), the China Postdoctoral Science Foundation (2021M701258) and the Project of Key Disciplines of Forestry Engineering of Bureau of Education of Guangzhou Municipality.

References

- [1] X.H. Hao, M.L. Li, Y.S. Huang, Y.H. Sun, K.X. Zhang, C.G. Guo, High-Strength, Dimensionally Stable, and Flame-Retardant Fast-Growing Poplar Prepared by Ammonium Polyphosphate-Waterborne Epoxy Impregnation, *ACS Appl. Polym. Mater.* 4 (2) (2022) 1305–1313.
- [2] X.W. Cheng, D. Lu, K. Yue, W.D. Lu, Z.F. Zhang, Fire Resistance Improvement of Fast-Growing Poplar Wood Based on Combined Modification Using Resin Impregnation and Compression, *Polymers* 14 (17) (2022) 3574.
- [3] Y.X. Peng, Q. Fan, R.X. Ou, X.L. Hao, C.G. Guo, Z.Z. Liu, T. Liu, L.C. Sun, Q. W. Wang, Modification of poplar wood cells using 1,3-dihydroxymethyl-4,5-dihydroxyethylideneurea/alkaline lignin for enhanced mechanical properties and decay resistance, *Constr. Build. Mater.* 368 (2023), 130354.
- [4] C.F. Chen, D.Y. Tu, Q.F. Zhou, J.H. Zhou, X.J. Wang, B. Cherdchim, R.X. Ou, Development and evaluation of a surface-densified wood composite with an asymmetric structure, *Constr. Build. Mater.* 242 (2020), 118007.
- [5] J.H. Lu, P. Jiang, Z.L. Chen, L.M. Li, Y.X. Huang, Flame retardancy, thermal stability, and hygroscopicity of wood materials modified with melamine and amino trimethylene phosphonic acid, *Constr. Build. Mater.* 267 (2021), 121042.
- [6] T.T. Ma, L.P. Li, Q.W. Wang, C.G. Guo, Targeted synthesis of Zn-based porous aromatic framework for enhancing fire safety and anti-corrosion performance of wood substrate, *Compos. B Eng.* 183 (2020), 107697.
- [7] W.T. Gan, C.J. Chen, Z.Y. Wang, J.W. Song, Y.D. Kuang, S.M. He, R.Y. Mi, P. B. Sunderland, L.B. Hu, Dense, self-formed char layer enables a fire-retardant wood structural material, *Adv. Funct. Mater.* 29 (14) (2019) 1807444.
- [8] Q.L. Fu, L. Medina, Y.Y. Li, F. Carosio, A. Hajian, L.A. Berglund, Nanostructured wood hybrids for fire-retardancy prepared by clay impregnation into the cell wall, *ACS Appl. Mater. Inter.* 9 (41) (2017) 36154–36163.
- [9] H.Z. Guo, M. Özparpucu, E. Windeisen-Holzhauser, C.M. Schlepütz, E. Quadranti, S. Gaan, C. Dreimol, I. Burgert, Engineering, Struvite mineralized wood as sustainable building material: mechanical and combustion behavior, *ACS Sustain. Chem. Eng.* 8 (28) (2020) 10402–10412.
- [10] X. Yan-jun, L. Yi-xing, S. Yao-xing, Heat-treated wood and its development in Europe, *J. Forestry Res.* 13 (3) (2002) 224–230.
- [11] C.R. Welzbacher, J. Wehsener, A.O. Rapp, P. Haller, Thermo-mechanical densification combined with thermal modification of Norway spruce (*Picea abies* Karst) in industrial scale-Dimensional stability and durability aspectsThermo-mechanische Verdichtung und thermische Modifikation von Fichtenholz (*Picea abies* Karst) im industriellen Maßstab – Betrachtung der Dimensionsstabilität und Dauerhaftigkeit, *Eur. J. Wood Wood Prod.* 66 (1) (2008) 39–49.
- [12] X.J. Wang, D.Y. Tu, C.F. Chen, Q.F. Zhou, H.X. Huang, Z.H. Zheng, Z.P. Zhu, A thermal modification technique combining bulk densification and heat treatment for poplar wood with low moisture content, *Constr. Build. Mater.* 291 (2021), 123395.
- [13] L. Rautkari, K. Laine, N. Laffin, M. Hughes, Surface modification of Scots pine: the effect of process parameters on the through thickness density profile, *J. Mater. Sci.* 46 (2011) 4780–4786.
- [14] T. Belt, L. Rautkari, K. Laine, C.A.S. Hill, Cupping behaviour of surface densified Scots pine wood: The effect of process parameters and correlation with density profile characteristics, *J. Mater. Sci.* 48 (2013) 6426–6430.
- [15] Z.H. Zheng, C.F. Chen, Y.S. Huang, R.X. Ou, C.S. Hu, X.J. Wang, Q.F. Zhou, D. Y. Tu, Developing a Unilaterally Surface-Densified Wood Composite with Excellent Performance through Surface Impregnation of Furfuryl Alcohol Resin, *ACS Appl. Polym. Mater.* 4 (8) (2022) 5308–5318.
- [16] H.Y. Zhou, D.X. Wen, X.L. Hao, C.F. Chen, N.H. Zhao, R.X. Ou, Q.W. Wang, Nanostructured multifunctional wood hybrids fabricated via in situ mineralization of zinc borate in hierarchical wood structures, *Chem. Eng. J.* 451 (2023), 138308.
- [17] B.B. Kuai, Z.H. Wang, J.S. Gao, J.W. Tong, T.Y. Zhan, Y.L. Zhang, J.X. Lu, L.P. Cai, Development of densified wood with high strength and excellent dimensional stability by impregnating delignified poplar by sodium silicate, *Constr. Build. Mater.* 344 (2022), 128282.
- [18] J.F. Wang, Y. Yao, Y.Q. Huang, Y.J. Ma, J.Y. Xi, X.Z. Wang, H.G. Li, Z.Q. Yang, Effects of the combination of compression and impregnation with phenolic resin on the dimensional stability in the multiscale wood structure of Chinese fir, *Constr. Build. Mater.* 327 (2022), 126960.
- [19] P. Li, Y. Zhang, Y.F. Zuo, J.X. Lu, G.M. Yuan, Y.Q. Wu, Preparation and characterization of sodium silicate impregnated Chinese fir wood with high strength, water resistance, flame retardant and smoke suppression, *J. Mater. Res. Technol.* 9 (1) (2020) 1043–1053.
- [20] M. Altgen, D. Altgen, A. Klüppel, L. Rautkari, Effect of curing conditions on the water vapor sorption behavior of melamine formaldehyde resin and resin-modified wood, *J. Mater. Sci.* 55 (25) (2020) 11253–11266.
- [21] Z.H. Li, X.M. Zhang, S.S. Song, K. Xu, J.X. Lyu, X.J. Li, Curing characteristics of low molecular weight melamine-urea-formaldehyde (MUF) resin-impregnated poplar wood, *Constr. Build. Mater.* 325 (2022), 126814.
- [22] E.G.M. Romão, M.P. Oliveira, L.M. Guerrini, Evaluation of the oligomeric epoxy silane as coupling agent on thermal and mechanical properties of water-based acrylate adhesives, *Polym. Eng. Sci.* 62 (10) (2022) 3310–3322.
- [23] S. Ummartyotin, M. Sain, Preparation of a cellulose and water-based resin composite, *Mater. Lett.* 123 (2014) 70–74.
- [24] M.S. Salim, D. Ariawan, M.F.A. Rasyid, M.Z.A. Thirmizir, R.M. Taib, Z.M. Ishak, Effect of fibre surface treatment on interfacial and mechanical properties of non-

- woven kenaf fibre reinforced acrylic based polyester composites, *Polym. Compos.* 40 (S1) (2019) E214–E226.
- [25] R. Dong, L.L. Liu, Preparation and properties of acrylic resin coating modified by functional graphene oxide, *Appl. Surf. Sci.* 368 (2016) 378–387.
- [26] X. Gao, Y. Liu, Y. Qi, R. Gong, F. Yao, J. Luo, Y. Zhao, Y. Dai, J. Wang, C. Lian, X. Dong, Y. Li, Acrylic Resin Filling Cell Lumen Enabled Laminated Poplar Veneer Lumber as Structural Building Material, *Polymers* 14 (23) (2022) 5277.
- [27] J.W. Wu, Q. Fan, Q.W. Wang, Q. Guo, D.Y. Tu, C.F. Chen, Y.Y. Xiao, R.X. Ou, Improved performance of poplar wood by an environmentally-friendly process combining surface impregnation of a reactive waterborne acrylic resin and unilateral surface densification, *J. Clean. Prod.* 261 (2020), 121022.
- [28] O. Ozgenc, U.C. Yildiz, Weathering resistance of oriental spruce wood treated with different protection processes, *J. Mater. Civil. Eng.* 28 (8) (2016) 04016054.
- [29] J.H. Zou, H.J. Duan, Y.S. Chen, S. Ji, J.F. Cao, H.R. Ma, AP/N/S-containing high-efficiency flame retardant endowing epoxy resin with excellent flame retardance, mechanical properties and heat resistance, *Compos. B Eng.* 199 (2020), 108228.
- [30] C.Y. Jiao, L. Sun, Q. Shao, J.Y. Song, Q. Hu, N. Naik, Z.H. Guo, Advances in waterborne acrylic resins: synthesis principle, modification strategies, and their applications, *ACS Omega* 6 (4) (2021) 2443–2449.
- [31] T.P. Ye, S.F. Liao, Y. Zhang, M.J. Chen, Y. Xiao, X.Y. Liu, Z.G. Liu, D.Y. Wang, Cu (0) and Cu (II) decorated graphene hybrid on improving fireproof efficiency of intumescent flame-retardant epoxy resins, *Compos. B Eng.* 175 (2019), 107189.
- [32] H. Wang, S. Li, Z.M. Zhu, X.Z. Yin, L.X. Wang, Y.X. Weng, X.Y. Wang, Stability, A novel DOPO-based flame retardant containing benzimidazolone structure with high charring ability towards low flammability and smoke epoxy resins, *Polym. Degrad. Stabil.* 183 (2021), 109426.
- [33] T. Liu, L.C. Sun, R.X. Ou, Q. Fan, L.P. Li, C.G. Guo, Z.Z. Liu, Q.W. Wang, Flame retardant eugenol-based thiol-ene polymer networks with high mechanical strength and transparency, *Chem. Eng. J.* 368 (2019) 359–368.
- [34] F.C. Xu, H.Y. Zhang, J.G. Wu, Synergistic catalytic flame retardant effect of zirconium phosphate on the poplar plywood, *Constr. Build. Mater.* 290 (2021), 123208.
- [35] H. An, Z. Gu, L.P. Zhou, S.Y. Liu, C. Li, M. Zhang, Y.X. Xu, P.X. Zhang, Y.Q. Wen, Janus Mucosal Dressing with a Tough and Adhesive Hydrogel based on Synergistic Effects of Gelatin, Polydopamine, and Nano-clay, *Acta Biomater.* 149 (2022) 126–138.
- [36] Q.Q. Guo, Y.F. Yang, L. Li, J. Sun, W. Liu, X.Y. Gu, H.F. Li, S. Zhang, Construction of bio-safety flame retardant coatings on polyethylene terephthalate fabric with ammonium phytate and cyclodextrin, *Polym. Advan. Technol.* 32 (11) (2021) 4440–4449.
- [37] Y.J. Feng, Y. Zhou, D.K. Li, S. He, F.X. Zhang, G.X. Zhang, A plant-based reactive ammonium phytate for use as a flame-retardant for cotton fabric, *Carbohydr. Polym.* 175 (2017) 636–644.
- [38] M. Khalfallah, B. Abbès, F. Abbès, Y.Q. Guo, V. Marcel, A. Duval, F. Vanfleteren, F. Rousseau, Innovative flax tapes reinforced Acrodur biocomposites: A new alternative for automotive applications, *Mater. Des.* 64 (2014) 116–126.
- [39] R.X. Ou, Y.J. Xie, Q.W. Wang, S.J. Sui, M.P. Wolcott, Thermoplastic deformation of poplar wood plasticized by ionic liquids measured by a nonisothermal compression technique, *Holzforschung* 68 (5) (2014) 555–566.
- [40] L. Medina, R. Schledjewski, A.K. Schlarb, Process related mechanical properties of press molded natural fiber reinforced polymers, *Compos. Sci. Technol.* 69 (9) (2009) 1404–1411.
- [41] J.X. Jiang, J.Z. Li, Q. Gao, Effect of flame retardant treatment on dimensional stability and thermal degradation of wood, *Constr. Build. Mater.* 75 (2015) 74–81.
- [42] X.H. Feng, Z.F. Xiao, S.J. Sui, Q.W. Wang, Y.J. Xie, Esterification of wood with citric acid: The catalytic effects of sodium hypophosphite (SHP), *Holzforschung* 68 (4) (2014) 427–433.

第41卷 第9期 Vol.41 No.9

ISSN 1000-3851

CN 11-1801/TB

复合材料学报

Acta Materiae Compositae Sinica

2024.9

北京航空航天大学 主办
中国复合材料学会

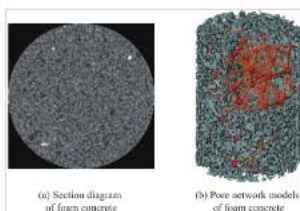
-专刊-

Stretched Aramid Honeycomb Cell Structure

pp. 4752-4764

 [摘要](289)  [HTML全文] (198)

 [PDF 7478KB](19)  [长摘要]  [创新点]



考虑异形孔的泡沫混凝土单轴压缩离散元模拟

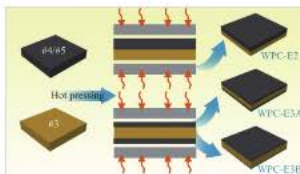
周程涛, 陈波, 高志涵, 陈家林, 陈锴

2024, 41(7): 3727-3737. doi: [10.13801/j.cnki.fhclxb.20231127.001](https://doi.org/10.13801/j.cnki.fhclxb.20231127.001)

 [摘要](370)  [HTML全文] (186)

 [PDF 6834KB](17)  [长摘要]

生物纳米复合材料



多层夹芯结构木塑复合材料阻燃与力学性能

郭雨佳, 徐靖雯, 陈文礼, 樊奇, 孙理超, 王清文

2024, 41(7): 3738-3746. doi: [10.13801/j.cnki.fhclxb.20231106.003](https://doi.org/10.13801/j.cnki.fhclxb.20231106.003)

 [摘要](370)  [HTML全文] (212)

 [PDF 4801KB](20)  [长摘要]  [创新点]



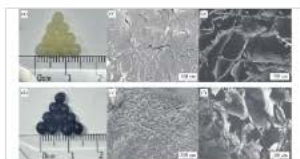
面向抗肿瘤的可协同光热/化疗纳米体系的构建及其药物控释行为

黄润, 吴刘军, 施鸿棋, 顾英剑, 潘育松

2024, 41(7): 3747-3756. doi: [10.13801/j.cnki.fhclxb.20231120.001](https://doi.org/10.13801/j.cnki.fhclxb.20231120.001)

 [摘要](331)  [HTML全文] (273)

 [PDF 4067KB](20)  [创新点]



聚吡咯/壳聚糖-海藻酸钠复合微球的制备及其药物缓释性能

李莎, 张新浩, 贾睿, 罗钰, 邢建宇

2024, 41(7): 3757-3764. doi: [10.13801/j.cnki.fhclxb.20231123.001](https://doi.org/10.13801/j.cnki.fhclxb.20231123.001)

 [摘要](443)  [HTML全文] (191)

 [PDF 3963KB](32)  [创新点]

金属基和陶瓷基复合材料

DOI: 10.13801/j.cnki.fhclxb.20231106.003

多层夹芯结构木塑复合材料阻燃与力学性能



分享本文

郭雨佳¹, 徐靖雯¹, 陈文礼¹, 樊奇^{*1}, 孙理超^{*1,2}, 王清文^{1,2}

(1. 华南农业大学 生物基材料与能源教育部重点实验室, 广州 510642; 2. 岭南现代农业科学与技术广东省实验室, 广州 510642)

摘要: 针对传统膨胀石墨阻燃木塑复合材料 (WPCs) 阻燃剂添加量高、力学性能变差的问题, 本研究以杨木木粉 (WF)、高密度聚乙烯 (HDPE)、膨胀石墨 (EG) 与纳米二氧化硅 (n-SiO₂) 为主要原料, 通过层积热压工艺和结构优化设计制备了具有多层夹芯结构的阻燃增强木塑复合材料。采用锥形量热仪、垂直燃烧测试仪、极限氧指数 (LOI) 仪和万能力学试验机分别探究了单层、双层和三层夹芯结构对木塑复合材料阻燃和力学性能的影响。结果表明, 相比于对照组 (WPC-0), 阻燃层中 EG 和增强层中 n-SiO₂ 的含量分别为 10% 和 5% 时, 双层和三层夹芯结构木塑复合材料的热释放速率和总热释放、烟释放速率和总烟释放均有显著降低, 残余物质量明显提升。其中三层夹芯结构木塑复合材料 (WPC-E3B) 的 LOI 值由 20.8% 提高至 30.6%, UL-94 达到 V-0 级。此外, 相较于 WPC-0, WPC-E3B 的冲击强度提升了 61.9%, 拉伸与弯曲强度分别提高了 16.2% 和 13.4%。
关键词: 木塑复合材料; 可膨胀石墨; 纳米二氧化硅; 夹芯结构; 阻燃性能; 力学性能

中图分类号: TB332 文献标志码: A 文章编号: 1000-3851(2024)07-3741-09

Flame retardant and mechanical properties of wood-plastic composites
with multi-layer sandwich structures

GUO Yujia¹, XU Jingwen¹, CHEN Wenli¹, FAN Qi^{*1}, SUN Lichao^{*1,2}, WANG Qingwen^{1,2}

(1. Key Laboratory for Biobased Materials and Energy of Ministry of Education, South China Agricultural University, Guangzhou 510642, China; 2. Guangdong Laboratory of Lingnan Modern Agriculture, Guangzhou 510642, China)

Abstract: In order to solve the problems of high flame-retardant addition and deterioration of mechanical properties in the modification of wood-plastic composites (WPCs) by traditional expandable graphite, flame-retardant reinforced wood-plastic composites with a multilayered sandwich structure were prepared by laminated hot pressing process and structure optimization design using poplar wood flour (WF), high-density polyethylene (HDPE), expandable graphite (EG) and nano-silicon dioxide (n-SiO₂) as the main raw materials. And the appropriate characterization and equipment such as cone calorimeter, vertical burner, limiting oxygen index (LOI) tester and mechanical testing machine were used to investigate the effects of single layer, double layer and triple layer sandwich structures on the flame retardant and mechanical properties of wood-plastic composites, respectively. The experimental results show that compared with the control wood-plastic composite (WPC-0), the multilayer structure wood-plastic composites exhibit significant reduction of heat release rate, total heat release, smoke production rate and total smoke production, and remarkable improvement of residue yield in the cone test when the contents of EG in the flame-retardant layer and n-SiO₂ in the reinforcement layer are 10% and 5%, respectively. Among all the multilayer wood-plastic composites, WPC-E3B with a triple layer sandwich structure improves its LOI from 20.8% to 30.6% and passes the UL-94 test with a V-0 rating. Moreover, it also shows better mechanical proper-

收稿日期: 2023-09-04; 修回日期: 2023-10-08; 录用日期: 2023-10-21; 网络首发时间: 2023-11-06 17:06:48
网络首发地址: <https://doi.org/10.13801/j.cnki.fhclxb.20231106.003>
基金项目: 广东省基础与应用基础研究基金 (2021A1515011014); 广东省重点领域研发计划项目 (2020B0202010008) Guangdong Basic and Applied Basic Research Foundation (2021A1515011014); Research and Development Program in Key Areas of Guangdong Province (2020B0202010008)
通信作者: 樊奇, 博士, 讲师, 研究方向为生物基复合材料。 E-mail: fanqi2021@scau.edu.cn;
孙理超, 博士, 副教授, 硕士生导师, 研究方向为生物质复合材料。 E-mail: sunlichao@scau.edu.cn
引用格式: 郭雨佳, 徐靖雯, 陈文礼, 等. 多层夹芯结构木塑复合材料阻燃与力学性能 [J]. 复合材料学报, 2024, 41(7): 3741-3749.
GUO Yujia, XU Jingwen, CHEN Wenli, et al. Flame retardant and mechanical properties of wood-plastic composites with multi-layer sandwich structures[J]. Acta Materiae Compositae Sinica, 2024, 41(7): 3741-3749(in Chinese).

ties compared with WPC-0, such as a 61.9% increase in impact strength and 16.2% and 13.4% increases in tensile and flexural strength, respectively.

Keywords: wood-plastic composites; expandable graphite; nano-silica; sandwich structure; flame retardancy; mechanical properties

近年来,木材工业已逐渐发展成为能源消耗少、环境污染小的绿色低碳产业,在推进碳达峰、碳中和的过程中发挥着重要作用。然而,由于森林资源的匮乏加之国家天然林保护工程政策,我国木材的供需矛盾日渐突出,木材对外依存度已超过 50%^[1-4],开发制备高性能功能化的木塑复合材料(WPC)对于缓解木材资源紧张具有重要意义。WPC是由木质纤维和热塑性塑料熔融共混挤出、热压或注塑成型而制得的一类环境友好型复合材料。它既继承了木材的天然亲和感、质轻高强和易于加工的优点,又克服了木材尺寸稳定性差、不耐腐蚀、各向异性等缺陷,能够作为一种高经济性复合材料并广泛应用于园林景观、包装物流、家装及建筑等众多领域^[5-7]。

然而,以木质纤维、聚乙烯/聚丙烯为主要组分制备的木塑复合材料极易燃烧,在实际使用中必须进行阻燃处理。膨胀型阻燃剂(IFR)体系通常由酸源、炭源和气源组成,且已被证实可以显著提高WPC的阻燃性能^[8-11]。当IFR被加热或受到高温燃烧时,炭源在酸源的催化作用下脱水成炭,碳化物在气源分解的气体作用下生成一种包裹在材料表面的较厚多孔膨胀炭层,用于隔绝热传导和可燃性气体的扩散,从而抑制WPC燃烧^[12]。可膨胀石墨(EG)作为IFR中的代表,价格低廉,无毒低烟,且膨胀倍率高,具有优异的阻燃效果。Schartel等^[13]制备了以EG为阻燃剂的亚麻纤维/聚丙烯复合材料,发现当EG添加量为25%时,WPC通过UL94 V-1级。王迪^[14]采用EG/聚磷酸铵(APP)协效阻燃EPS基木塑复合材料,结果表明,当EG与APP配比为1:1时,复合材料阻燃性能最好;当协同阻燃体系添加量在10份以上时,WPC可达UL94 V-0级。由此可见,EG可作为一种理想的添加型IFR用于WPC的阻燃处理。

但是,与大多数添加型阻燃剂一样,高含量EG的引入通常会使得WPC的力学性能严重下降^[15-17]。因此,研究人员尝试从各种途径来改善复合材料力学性能,尽可能将阻燃剂所带来的影响程度降到最低。Huang等^[18]通过自组装聚乙烯亚胺(PEI)/纤维素纳米晶体(CNC)/APP设计了一种支化交联

网络聚电解质复合物(PEC),证实PEC提供氢键间的相互作用能够有效增强塑料基体与木质纤维、阻燃剂之间的界面相容性,从而改善复合材料整体的力学性能。申辉^[19]采用硬脂酸钠对氢氧化镁进行表面改性处理,并与EG复配共同制备阻燃聚乙烯材料。结果表明,相较于未改性材料体系,改性氢氧化镁与聚乙烯颗粒之间的相容性提高,增强了加工过程中阻燃剂与基体材料之间的结合性能。周海洋^[20]探究了SiO₂对WPC力学性能的影响,结果表明,在粒子均匀分散的前提下,0.5wt%~9wt%的SiO₂能够将复合材料的力学性能提升15%~30%;Buddi等^[21]探究了不同含量的纳米二氧化硅(n-SiO₂)对高密度聚乙烯(HDPE)基木塑复合材料力学性能的影响,结果表明,n-SiO₂用量为5wt%时,对复合材料的增强效果最佳;Sun等^[22]对比研究了EG/APP在WPC中分散分布和分层分布对材料阻燃性能和力学性能的影响,结果表明,分层分布的阻燃WPC能够更好地提升材料的阻燃性能和弯曲强度。

基于上述研究结论,本文以EG为阻燃剂,n-SiO₂为增强剂,制备了表层阻燃、芯层增强的多层夹芯结构木塑复合材料,并探究不同的结构设计对复合材料阻燃和力学性能的影响,研究结果对开发高性能、功能型木塑复合材料,拓展木塑复合材料的应用领域具有重要的现实意义。

1 实验材料及方法

1.1 原材料

杨木纤维(WF,约40目),购于东莞鱼珠木材市场;HDPE,型号5000S,密度为0.95 g/cm³,熔融指数0.09 g/10 min (190℃,2.16 kg),购于中国石化扬子石油化工有限公司;马来酸酐接枝聚乙烯(MAPE),接枝率约为1%,熔融指数0.17 g/10 min (190℃,2.16 kg),购于广州市合诚化学有限公司;润滑剂530D,主要成分为硬脂酸钠,购于广州市合诚化学有限公司;n-SiO₂,粒径15~20 nm,购于巨利金属材料有限公司;EG,80目,纯度99%,购于青岛腾盛达碳素机械有限公司。

1.2 单层木塑复合材料的制备

取杨木木粉置于105℃的电热鼓风干燥箱

(9140AS, 嘉兴市中兴医疗仪器有限公司) 中干燥 24 h 以除去水分, 与其他各组分按照原料配比 (表 1) 添加至高速搅拌机 (HRS-10 L, 东莞市环鑫机械有限公司) 中, 在转速 100 r/min、温度 80℃ 的条件下搅拌 10 min 充分混合。将混合好的物料加至锥形双螺杆挤出机 (65/132, 南京赛旺科技发展有限公司) 进行熔融复合, 机筒各区温度控制在 160~175℃, 机头温度控制在 160℃ 左右, 螺杆转速 100 r/min。挤出的物料经冷却粉碎后均匀平

铺于模具中, 在平板硫化机 (6170-A-30T, 东莞市优特尔仪器科技有限公司) 中热压成型, 具体工艺参数为预压温度 165℃, 压力 2 MPa, 时间 3 min; 热压温度 165℃, 压力 6 MPa, 热压时间 5 min。热压后进行冷压定型。制备得到的#0、#1、#2 和#3 分别作为单层木塑复合材料 WPC-0、WPC-E1、WPC-EG 和 WPC-Si 直接参与后续相关性性能表征。同时, #3 作为芯层材料、#4 和#5 作为表层材料, 可进一步层积热压得到多层夹芯木塑复合材料。

表 1 单层木塑复合材料 (WPCs) 各组分配方

Table 1 Formulation for the preparation of single-layer wood-plastic composites (WPCs)

Sample	HDPE/wt%	WF/wt%	EG/wt%	n-SiO ₂ /wt%	MAPE/wt%	530D/wt%	Role in multilayer WPCs
#0	45	50	0	0	3	2	—
#1	45	35	10	5	3	2	—
#2	45	40	10	0	3	2	—
#3	45	45	0	5	3	2	Core layer
#4	45	30	20	0	3	2	Surface layer
#5	45	10	40	0	3	2	Surface layer

Notes: HDPE—High-density polyethylene; WF—Wood flour; EG—Expandable graphite; n-SiO₂—Nano-silicon dioxide; MAPE—; 530D—;

1.3 多层夹芯结构木塑复合材料的制备

多层夹芯结构木塑复合材料的具体制备过程如图 1 所示。将 1.2 节得到单板#3、#4、#5 按照表 2 的复合方式堆叠, 放入平板硫化机中二次热压以制备多层夹芯结构木塑复合材料。所有样品的热压条件一致: 预压温度 165℃, 压力 2 MPa, 时间 3 min; 热压温度 165℃, 压力 6 MPa, 热压时间 5 min。热压后冷却至室温, 得到的多层夹芯木塑复合材料的厚度均为 4 mm。

表 2 多层夹芯木塑复合材料的组成

Table 2 Composition of multilayer sandwich WPCs

Sample	Core-layered	Surface-layered
WPC-E2	#3 (2 mm)*1	#4 (2 mm)*1
WPC-E3A	#3 (2 mm)*1	#4 (1 mm)*2
WPC-E3B	#3 (3 mm)*1	#5 (0.5 mm)*2

Note: The type, thickness and quantity of boards required for multilayer wood-plastic composites are shown in the table. For example, #5 (0.5 mm)*2 represents two samples of #5 with a thickness of 0.5 mm.

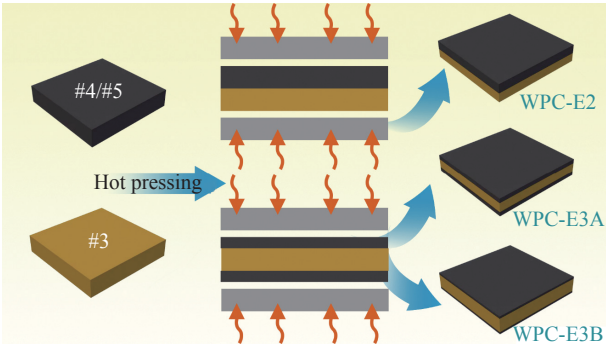


图 1 多层夹芯木塑复合材料的制备流程图

Fig. 1 Preparation process of multilayer sandwich WPCs

1.4 性能测试方法

使用氧指数仪 (ZY6155A, 东莞市中诺质检仪器设备有限公司) 按照 GB/T 2406.1—2008 标准 [23] 测定复合材料样品的极限氧指数 (LOI)。试样尺寸为 80 mm×10 mm×4 mm。

使用水平垂直燃烧仪 (UL94-X, 昆山莫帝斯科燃烧技术仪器有限公司) 按照 GB/T 2408—2021 标准 [24] 中的垂直燃烧试验进行复合材料样品阻燃等级的评定。试样尺寸为 130 mm×10 mm×4 mm。

使用锥形量热仪 (CONE, 型号 CCT, 昆山莫帝斯科燃烧技术仪器有限公司) 按照 ISO 5660-1 标准 [25] 进行燃烧测试, 测试样品的平均热释放速率、总热释放量、总产烟量与质量保留率等参数。试样尺寸为 100 mm×100 mm×4 mm, 热流辐射 50 kW/m²。

CONE 燃烧后的炭层样品经喷金处理, 采用扫描电子显微镜 (EVO18, 德国 Carl Zeiss 公司) 观察试样的炭层微观形貌, 加速电压为 10 kV。

采用高低温万能试验机 (AL-7000-MUT 20KN, 高特威尔检测仪器 (青岛) 有限公司), 参照 ASTM D638—22 标准 [26] 进行拉伸测试。每组至少测试 6

个试样，试样尺寸为 165 mm×13 mm×4 mm。

使用高低温万能试验机，参考 ASTM D790—17 标准^[27] 进行三点弯曲测试。每组至少测试 6 个试样，试样尺寸为 80 mm×12.7 mm×4 mm。

使用电子悬臂梁冲击试验机 (XJ-50G, 承德市金建检测仪器有限公司), 参考 ASTM D256—23 标准^[28] 进行冲击强度测试。每组至少测试 6 个试样，试样尺寸为 80 mm×12.7 mm×4 mm。

2 结果与讨论

2.1 木塑复合材料的燃烧性能

不同结构的木塑复合材料锥形量热仪曲线与燃烧数据分别如表 3 与图 2 所示。从表 3 和图 2(a) 能够看出，与 WPC-0 相比，WPC-Si 的点燃时间 (TTI)、总热释放量 (THR) 与总产烟量 (TSP) 均无明显改善，因此本文暂不讨论 n-SiO₂ 协效阻燃的情况。在体系中加入膨胀石墨后，所有样品均表现出 10 s 以上的点火延迟，且两个热释放速率峰

值 (PHRR1、PHRR2) 均有所下降，证明 EG 对延缓木塑复合材料明火的产生和燃烧强度均有积极作用。相较于单层阻燃 WPC，双层和三层夹芯阻燃样品对材料热释放的抑制能力更强。值得注意的是，WPC-E3B 对第一热释放速率峰值有明显抑制作用，PHRR1 较对照组样品下降了 85.3%；而 WPC-E2 对第二热释放速率峰值的抑制效果更显著，PHRR2 较对照组样品下降了 61.5%。这是由于 WPC-E3B 的表层结构中阻燃剂浓度更高，在接触火源时能够更加迅速地形成膨胀炭层，在复合材料燃烧前期保护芯层材料继续受热，并一定程度隔绝氧气，短时间内控制火焰的燃烧及向复合材料内部的传递。而 WPC-E2 的阻燃剂分布空间更广，能够持续地产生新的膨胀炭层，从而长时间的抑制材料的燃烧强度。由图 2(b) 可知，二者 600 s 内总热释放量比较接近，相较于 WPC-0 分别下降了 39.8% 和 40.1%。

表 3 不同结构的木塑复合材料在锥形量热仪 (CONE) 试验所得燃烧数据

Table 3 Combustion data of wood-plastic composites with different structures in the cone calorimeter (CONE)

Sample	TTI/s	PHRR1/(kW·m ⁻²)	PHRR2/(kW·m ⁻²)	THR/(MJ·m ⁻²)	TSP/m ²	MR/%
WPC-0	15	510.3	553.8	129.8	11.3	15.2
WPC-Si	16	419.6	415.3	119.1	11.9	23.5
WPC-E1	25	361.2	488.1	107.1	11.0	35.6
WPC-E2	26	161.1	213.0	77.7	6.5	53.0
WPC-E3A	26	154.1	485.3	92.0	7.4	44.7
WPC-E3B	27	74.8	338.7	78.1	7.1	52.5

Notes: TTI—Time to ignition; PHRR1—Peak first heat release rate; PHRR2—Peak second heat release rate; THR—Total heat release; TSP—Total smoke production; MR—Mass of residue.

如图 2(c) 与图 2(d) 所示，相较于 EG 直接分散在 WPC 中，分层结构阻燃的木塑复合材料能够更好地发挥膨胀炭层吸附烟雾、隔绝可燃性气体的凝聚相阻燃机制^[22]。经阻燃处理后的 4 组样品中，除单层阻燃样品 WPC-E1，其余样品的产烟量明显降低。双层和三层 WPC 的总产烟量分别为 6.5 m²、7.4 m² 和 7.1 m²，相较于 WPC-0 分别降低了 42.5%、34.5% 和 37.2%。同时，复合材料燃烧后的残余物质质量大幅提高，相较于未处理 WPC 的增幅分别为 248.7%、194.1.% 和 245.4%。进一步证明多层结构具有更明显的抑烟和成炭优势。当木塑复合材料接触到火源时，含有 EG 的表层材料能够迅速膨胀生成连续、致密的炭层，附着在芯层材料表面，同时进一步促进木塑复合材料本身炭化，最大化发挥炭层吸附和屏蔽作用。

2.2 木塑复合材料的氧指数与垂直燃烧性能

为进一步探究木塑复合材料的阻燃性能，对 5 组样品进行了垂直燃烧 (UL-94) 与极限氧指数 (LOI) 测试，测试结果如表 4 所示。在 UL-94 测试中，所有样品均未发生熔滴现象，对照组样品 WPC-0 与单层阻燃样品 WPC-E1 的余焰时间均大于 30 s，无法达到等级要求。而多层木塑复合材料表现出明显优越性，WPC-E2 达到 V-1 级，具有三层夹芯结构的样品 WPC-E3A 与 WPC-E3B 均达到 UL-94 的 V-0 级。

由表 4 可知，当在木塑复合材料中加入阻燃剂后，所有样品的 LOI 值均得到不同程度的提高。相较于 WPC-E1，多层结构木塑复合材料提升为难燃材料，这与 UL-94 的测试结果是一致的。值得注意的是，三层阻燃样品相较于双层阻燃样品

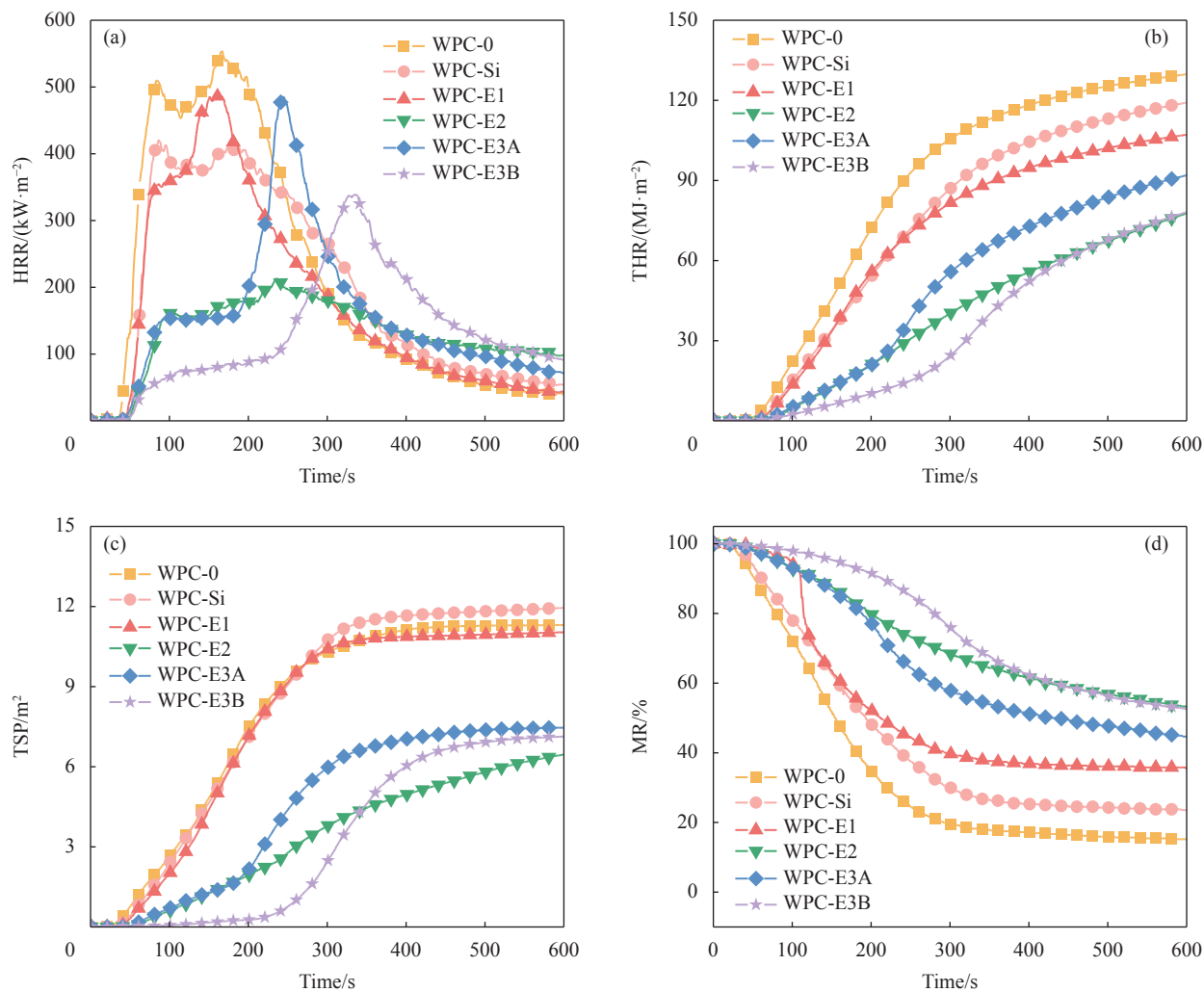


图2 不同结构的WPCs在CONE试验600 s内燃烧参数曲线
Fig. 2 Combustion data curves of WPCs with different structures in the CONE within 600 s

的极限氧指数进一步提高，其中WPC-E3B具有最高的LOI值，相较于对照组样品提升了47.1%，在极限氧指数测试中表现出最佳的阻燃效果。

表4 不同结构的WPCs的极限氧指数(LOI)与垂直燃烧等级
Table 4 Limiting oxygen index (LOI) and UL-94 rating of WPCs with different structures

Sample	Vertical flame test	LOI/%
WPC-0	N-R	20.8
WPC-E1	N-R	25.7
WPC-E2	V-1	27.3
WPC-E3A	V-0	29.1
WPC-E3B	V-0	30.6

然而，由于测试方法的不同，UL-94和LOI测试数据结果与CONE略有差异，主要原因是垂直燃烧与LOI测试均为垂直的引燃方式，即火焰与样品的断面接触，这使三层夹芯结构可以发挥

更大的阻燃优势，由于上、下表层受热后同时膨胀成炭，抑制火焰向内蔓延，为芯层材料提供全面的保护作用，避免了单侧火源引燃整个样品的可能^[29]。在两组三层夹芯结构阻燃WPC中，WPC-E3B由于单位面积内EG含量更高，能在接触火源的瞬间形成更厚的膨胀炭层，更好地发挥屏蔽热量与可燃气体的作用，进一步提高了夹芯结构的阻燃效率。

2.3 木塑复合材料的残炭形貌

微观结构的不同通常会决定材料的物理性能，如力学性能、热稳定性和燃烧性能等^[30]。因此，燃烧后的微观形貌在很大程度上能够反映材料的燃烧机制。不同结构的木塑复合材料在CONE试验后的数码照片与SEM图像如图3所示。由图3(a)可见，对照组样品经CONE测试后仅剩少量碎片状残炭，这是木粉和HDPE在高温下加热

产生的焦炭残渣^[31]。此时燃烧残余物质量最低，SEM 图像中表现出光滑、疏松的残炭骨架结构和多处孔洞，在燃烧过程中为热量、烟尘和氧气的输送提供通道，因此表现出最高的释热量和产烟量。而在图 3(b)~3(d) 中，加入 EG 的 3 组样品均能观察到堆叠而成的“蠕虫状”膨胀炭层，大大提高了样品的燃烧残余物质量。当含有 EG 的木塑复合材料暴露于热源或燃烧时，石墨片层中硫化物与碳原子发生氧化还原反应，释放出大量 CO₂、SO₂ 与水蒸气，促进 WPC 脱水成炭^[32]。这些气体不仅能够稀释体系及周围环境中的可燃性气体浓度，还有助于石墨薄片迅速膨胀为原体积

的数百倍，从而在 WPC 的表层形成具有良好绝热、隔氧作用的连续多孔炭层。由炭层的微观形貌可以看出，EG 经热解膨化，生成的膨胀石墨体积大，层状结构明显，链状结构清晰，表面裂纹少，具有良好的密实性。包覆在 WPC 表面时，能够有效抑制热源和氧气向内传播，从而延缓内部基材的进一步燃烧和热降解。相较于 WPC-E2 和 WPC-E3A，WPC-E3B 的数码照片中显示出应有的 EG 膨胀高度，没有出现炭层塌陷崩溃的现象。放大至 500 倍时能够看到相互堆积的连续残炭结构，说明炭层的致密性优于其他两组样品，对 WPC 的内部结构起到了更好的保护作用。

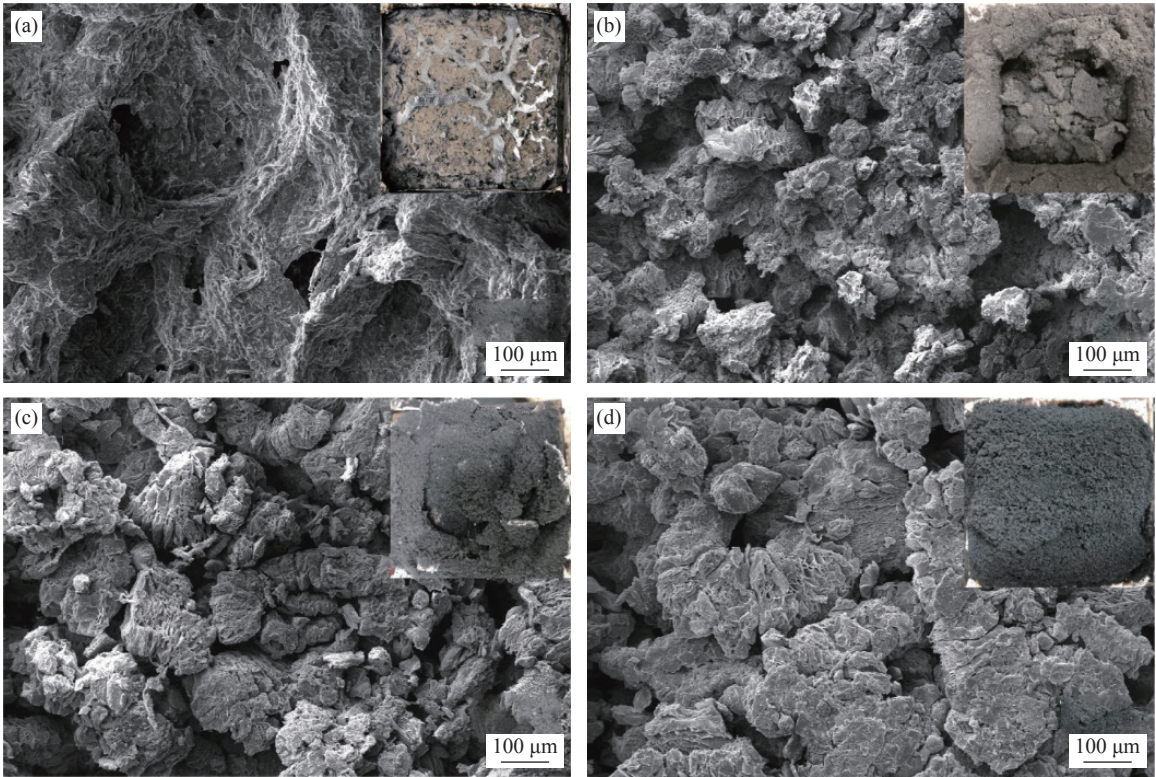


图 3 不同结构的 WPCs 在 CONE 试验后的宏观照片与 SEM 图像: (a) WPC-0; (b) WPC-E1; (c) WPC-E2; (d) WPC-E3B

Fig. 3 Macrophotographs and SEM images of WPCs with different structures after CONE test: (a) WPC-0; (b) WPC-E1; (c) WPC-E2; (d) WPC-E3B

2.4 木塑复合材料的力学性能

图 4 为不同结构的木塑复合材料的力学性能。由图 4(a) 可知，与 WPC-0 相比，所有木塑复合材料的冲击强度均有不同程度的提高，其中多层结构木塑复合材料的提升最为明显。这一方面是由于分散在基体内部的刚性粒子和石墨薄片能够在材料受到外力冲击、发生断裂时部分吸收能量；另一方面是由于多层木塑复合材料不同性质的层间能量耗散作用。其中，三层夹芯木塑复合材料

WPC-E3B 的冲击强度达 6.8 kJ/m²，相较于对照组提升 61.9%。

如图 4(b)、图 4(c) 所示，WPC-Si 的拉伸和弯曲性能均有明显提升，说明 n-SiO₂ 的加入可以有效增强 WPCs 的力学性能，这也是木塑复合材料经 EG 和 n-SiO₂ 复配处理后抗拉性能和抗弯性能得以保持的原因：① n-SiO₂ 作为一种无机刚性粒子，木质纤维和 HDPE 共混复合后，可以增大复合体系的刚性，导致 WPCs 整体模量增大^[33]；②

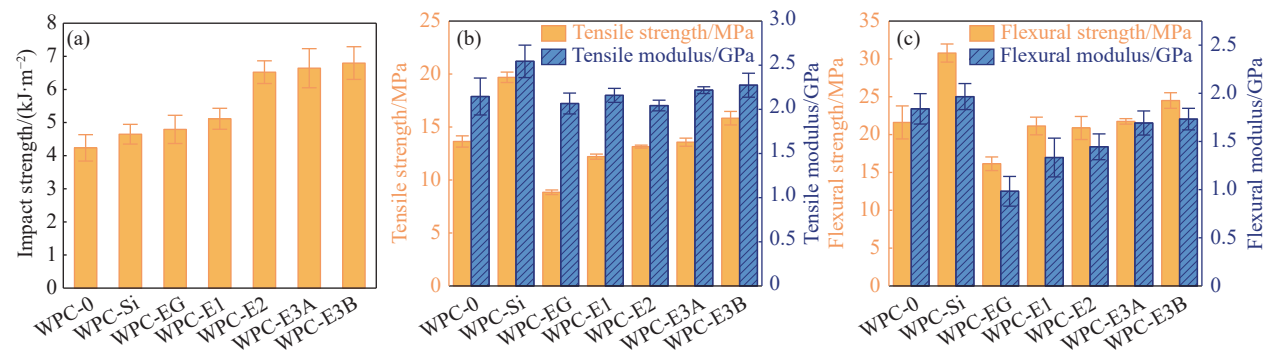


图 4 不同结构的 WPCs 的力学性能: (a) 冲击强度; (b) 拉伸强度与模量; (c) 弯曲强度与模量

Fig. 4 Mechanical properties of WPCs with different structures: (a) Impact strength; (b) Tensile strength and modulus; (c) Flexural strength and modulus

由于纳米粒子粒径小, 比表面积大, 能够有效填补在木质纤维与 HDPE 的间隙中, 并与 HDPE 分子链充分吸附、键合, 从而提高塑料基体承受载荷的能力, 对 WPCs 产生增强作用^[34]。三层夹芯木塑复合材料 WPC-E3B 的拉伸强度和弯曲强度分别到达 15.8 MPa 和 24.5 MPa, 相较于对照组分别提高 16.2% 和 13.4%。这是由于 WPC-E3B 的芯层厚度最大, 上下表层厚度最小, 最大程度上保留了 n-SiO₂ 对芯层材料的增强作用, 从而提升复合材料整体的力学性能。

2.5 三层夹芯 WPC 的阻燃增强机制

图 5 展示了三层夹芯木塑复合材料的阻燃增强机制:①相较于单层和双层阻燃 WPC, 三层夹芯 WPC 能够更好地发挥凝聚相阻燃机制: 上下表层中的膨胀石墨薄片在接触到热源的瞬间迅速膨胀为原体积的数百倍, 在 WPC 基材表面生成密实、连续的多孔炭层, 有效抑制烟尘和毒气释放的同时, 隔绝热量和可燃性气体的进入, 给予内部芯材更全面的保护作用。与同样具有三层夹芯结构的 WPC-E3A 相比, WPC-E3B 表层中 EG 含浓度更高, 能够在更短的时间内膨胀成炭, 进一步缩短了基材持续受热和燃烧的时间, 提高了表层阻燃的效率。②与单层 WPC 不同, 三层夹芯结构给予木塑复合材料更高抵御外界作用的能力, 使其表现出更好的力学性能。以冲击外力作用为例, 当入射力冲击 WPC-E3B 时, 相对柔韧的上表层会吸收部分作用力^[35], 穿过上表层的剩余作用力由于界面结合作用在刚性的芯层材料中被进一步分散, 加载方向上仅有少部分作用力能够传递至下表层, 无法引起复合材料的完全断裂, 从而对 WPC 提供了有效的保护作用。因此, 这种三层夹芯结构能够在大幅提高 WPCs 阻燃性能的同时,

最大程度上保证其力学强度, 是一种提升复合材料综合性能的有效方法。

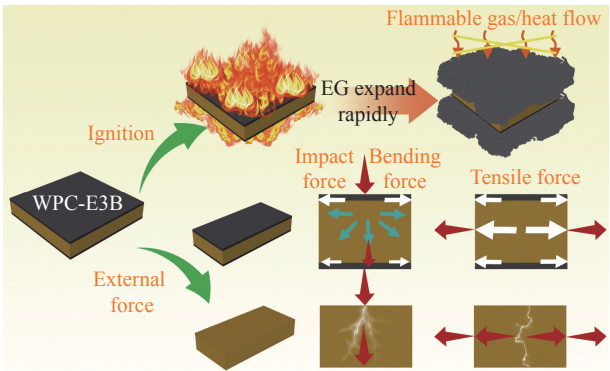


图 5 三层夹芯 WPCs 的阻燃增强机制

Fig. 5 Flame retardant enhancement mechanism of WPCs with a triple layer sandwich structure

3 结论

本文以膨胀石墨 (EG) 和纳米二氧化硅 (n-SiO₂) 为阻燃剂和增强剂分别制备了单层、双层、三层夹芯结构的木塑复合材料 (WPCs), 并探究了不同结构设计以及配方对木塑复合材料阻燃和力学性能的影响, 证明多层夹芯结构对提升木塑复合材料阻燃和力学性能均有明显效果, 为高性能功能化木塑复合材料的开发提供了重要的参考依据。

(1) 阻燃性能方面, 加入 EG 后木塑复合材料的燃烧强度和燃烧能力明显降低, 阻燃性能显著提升。其中, 以 EG 阻燃木塑复合材料为表层, n-SiO₂ 增强木塑复合材料为芯层的木塑复合材料具有比单层木塑复合材料更好的阻燃表现, 在锥形量热仪测试中表现出更低的热释放速率峰值、总热释放和总烟释放。在垂直燃烧 (UL-94) 和极限氧指数 (LOI) 测试中, 三层夹芯 WPC-E3B 表现出最高等级, UL-94 达到 V-0 级, LOI 值达 30.6%。

(2) 燃烧后的宏观照片与扫描电镜结果显示, 三层夹芯结构表现出较单层、双层结构更加连续、致密的炭层结构。这是由于三层夹芯结构能够更好地发挥膨胀石墨的凝聚相阻燃机制, 上下表层中的 EG 在接触热源后迅速膨胀成炭, 在 WPC 四周形成具有良好绝热作用的致密炭层, 防止内部芯层进一步燃烧。

(3) 力学性能方面, 以 EG 阻燃木塑复合材料为表层, n-SiO₂ 增强木塑复合材料为芯层的木塑复合材料力学性能均有明显提升, 是由于 n-SiO₂ 的增强作用以及多层复合的合理结构设计有效弥补了阻燃剂对复合材料力学性能的负面影响。其中, 三层夹芯结构 WPC-E3B 的冲击强度、拉伸强度和弯曲强度分别为 6.8 kJ/m²、15.8 MPa 和 24.8 MPa, 较未阻燃增强处理的 WPC 分别提升 61.9%、16.2% 和 13.4%, 证实了三层夹芯结构的优越性。

参考文献:

- [1] 郭辰星, 朱震锋, 刘嘉琦. 新时期中国木材资源供需: 现状、问题及方略 [J]. 中国林业经济, 2019(5): 66-69.
GUO Chenxing, ZHU Zhenfeng, LIU Jiaqi. Supply and demand of timber resources in China in the new era: Current situation, problems and strategies [J]. China Forestry Economics, 2019(5): 66-69(in Chinese).
- [2] BALLA V K, KATE K H, SATYAVOULU J, et al. Additive manufacturing of natural fiber reinforced polymer composites: Processing and prospects [J]. Composites Part B: Engineering, 2019, 174: 106956.
- [3] MOHANTY A K, VIVEKANANDAN S, PIN J M, et al. Composites from renewable and sustainable resources: Challenges and innovations [J]. Science, 2018, 362(6414): 536-542.
- [4] 劳万里, 段新芳, 吕斌. 木材工业助力“双碳”目标大有可为 [EB/OL]. 2022-01-07. <https://www.forestry.gov.cn/main/586/20220107/090254715222376.html>
LAO Wanli, DUAN Xinfang, LYU Bin. Wood industry has great potential to contribute to the "double carbon" target [EB/OL]. 2022-01-07. <https://www.forestry.gov.cn/main/586/20220107/090254715222376.html> (in Chinese).
- [5] 王清文, 易欣, 沈静. 木塑复合材料在家具制造领域的发展机遇 [J]. 林业工程学报, 2016, 1(3): 1-8.
WANG Qingwen, YI Xin, SHEN Jing. Tailoring wood-plastic composites for furniture production: Possibilities and opportunities [J]. Journal of Forestry Engineering, 2016, 1(3): 1-8(in Chinese).
- [6] 徐俊杰, 郝笑龙, 周海洋, 等. 超高填充聚丙烯基木塑复合材料高低温性能 [J]. 复合材料学报, 2021, 38(12): 4106-4122.
XU Junjie, HAO Xiaolong, ZHOU Haiyang, et al. High- and low-temperature performance of ultra-highly filled polypropylene-based wood plastic composite [J]. Acta Materialiae Compositae Sinica, 2021, 38(12): 4106-4122(in Chinese).
- [7] 苍琼, 朱一丞, 张鑫, 等. 高性能木塑复合材料的制备 [J]. 工业技术与职业教育, 2022, 20(5): 7-10.
CANG Qiong, ZHU Yicheng, ZHANG Xin, et al. Preparation of high performance wood-plastic composites [J]. Industrial Technology & Vocational Education, 2022, 20(5): 7-10(in Chinese).
- [8] SHAO Z B, DENG C, TAN Y, et al. An efficient mono-component polymeric intumescent flame retardant for polypropylene: Preparation and application [J]. ACS Applied Materials & Interfaces, 2014, 6(10): 7363-7370.
- [9] 张爱丽, 林梅. 阻燃型室内用木塑复合材料制备与性能 [J]. 工程塑料应用, 2021, 49(10): 148-152.
ZHANG Aili, LIN Mei. Preparation and performance of flame-retardant indoor wood-plastic composite materials [J]. Engineering Plastics Applications, 2021, 49(10): 148-152(in Chinese).
- [10] 梁兵. 利用膨胀型阻燃剂制备无卤阻燃木塑复合材料及其制备方法 [D]. 沈阳: 沈阳化工大学, 2012.
LIANG Bing. Preparation of halogen-free flame-retardant wood-plastic composites using intumescent flame retardant and its preparation method [D]. Shenyang: Shenyang University of Chemical Technology, 2012(in Chinese).
- [11] 郭垂根, 陈永祥, 白钢, 等. 改性炭黑/膨胀石墨/聚磷酸铵阻燃木塑复合材料的性能研究 [J]. 材料导报, 2015, 29(8): 68-73.
GUO Chuigen, CHEN Yongxiang, BAI Gang, et al. Study on performance of flame retarded wood plastic composites with modified carbon black (M-CB)/expandable graphite (EG)/ammonium polyphosphate (APP) [J]. Materials Reports, 2015, 29(8): 68-73(in Chinese).
- [12] HU X C, ZHU X J, SUN Z Q. Fireproof performance of the intumescent fire retardant coatings with layered double hydroxides additives [J]. Construction and Building Materials, 2020, 256: 119445.
- [13] SCHARTEL B, BRANU U, SCHWARZ U, et al. Fire retardancy of polypropylene/flax blends [J]. Polymer, 2003, 44(20): 6241-6250.
- [14] 王迪. 可膨胀聚苯乙烯基木塑复合材料的阻燃性能研究 [D]. 北京: 北京化工大学, 2020.
WANG Di. Study on flame retardant properties of expandable polystyrene wood-plastic composites [D]. Beijing: Beijing University of Chemical Technology, 2020(in Chinese).
- [15] ZHENG J Q, LI B, GUO C G, et al. Flame-retardant properties of acrylonitrile butadiene styrene/wood flour composites filled with expandable graphite and ammonium polyphosphate [J]. Journal of Applied Polymer Science, 2014, 131: 40281.

- [16] TURKU I, KARKI T. The influence of carbon-based fillers on the flammability of polypropylene-based co-extruded wood-plastic composite[J]. *Fire and Materials*, 2016, 40: 498-506.
- [17] MOKHENA T C, SADIKU E R, MOCAHANE M J, et al. Mechanical properties of fire retardant wood-plastic composites: A review[J]. *Express Polymer Letters*, 2021, 15(8): 744-780.
- [18] HUANG Y P, ZHANG S, CHEN H, et al. A branched polyelectrolyte complex enables efficient flame retardant and excellent robustness for wood/polymer composites[J]. *Polymers*, 2020, 12(11): 2438.
- [19] 申辉. 改性氢氧化镁/可膨胀石墨复配阻燃研究[D]. 成都: 成都理工大学, 2013.
- SHEN Hui. The research on multiplexing of modified magnesium hydroxide/expandable graphite[D]. Chengdu: Chengdu University of Technology, 2013(in Chinese).
- [20] 周海洋. 无机纳米粒子网络结构功能化木粉-HDPE 复合材料[D]. 哈尔滨: 东北林业大学, 2019.
- ZHUO Haiyang. Inorganic nano-particle network structure functionalized wood flour-HDPE composites[D]. Harbin: Northeast Forestry University, 2019(in Chinese).
- [21] BUDDI T, RAO B N, SINGH S K, et al. Development and analysis of high density poly ethylene (HDPE) nano SiO₂ and wood powder reinforced polymer matrix hybrid nano composites[J]. *Journal of Experimental Nanoscience*, 2018, 13: S24-S30.
- [22] SUN L C, XIE Y J, OU R X, et al. The influence of double-layered distribution of fire retardants on the fire retardancy and mechanical properties of wood fiber polypropylene composites[J]. *Construction and Building Materials*, 2020, 242: 118047.
- [23] 中国国家标准化管理委员会. 塑料用氧指数测定燃烧行为 第1部分: GB/T 2406.1—2008[S]. 北京: 中国标准出版社, 2008.
- Standardization Administration of the People's Republic of China. Plastics—Determination of combustion behaviour by oxygen index—Part 1: GB/T 2406.1—2008[S]. Beijing: China Standards Press, 2008(in Chinese).
- [24] 中国国家标准化管理委员会. 塑料 燃烧性能的测定 水平法和垂直法: GB/T 2408—2021[S]. 北京: 中国标准出版社, 2021.
- Standardization Administration of the People's Republic of China. Determination of combustion properties of plastics—Horizontal method and vertical method: GB/T 2408—2021[S]. Beijing: China Standards Press, 2021(in Chinese).
- [25] International Organization for Standardization. Reaction-to-fire tests—Heat release, smoke production and mass loss rate—Part 1: Heat release rate (cone calorimeter method) and smoke production rate (dynamic measurement): ISO 5660-1: 2015[S]. England: International Organization for Standardization, 2015.
- [26] American Society of Testing Materials. Standard test method for tensile properties of plastics: ASTM D638—22[S]. West Conshohocken: American Society of Testing Materials, 2022.
- [27] American Society of Testing Materials. Standard test methods for flexural properties of unreinforced and reinforced plastics and electrical insulating materials: ASTM D790—17[S]. West Conshohocken: American Society of Testing Materials, 2017.
- [28] American Society of Testing Materials. Standard test methods for determining the izod pendulum impact resistance of plastics: ASTM D256—23[S]. West Conshohocken: American Society of Testing Materials, 2023.
- [29] 霍玉娜, 魏童, 周雪莲, 等. 以石塑为表层的 WF/HDPE 夹层结构复合材料的性能[J]. 林业工程学报, 2023, 8(4): 27-34.
- HUO Yuna, WEI Tong, ZHOU Xuelian, et al. Performance of sandwiched WF/HDPE composites with stone-flour/HDPE surface layer[J]. *Journal of Forest Engineering*, 2023, 8(4): 27-34(in Chinese).
- [30] CHEN B, MONTANARI C, POPOV S, et al. A distortion-map-based method for morphology generation in multi-phase materials-application to wood[J]. *Composites Science and Technology*, 2023, 224: 110262.
- [31] OSVALDOVA L M, KOSUTOVA K, LEE S H, et al. Ignition and burning of selected tree species from tropical and northern temperate zones[J]. *Advanced Industrial and Engineering Polymer Research*, 2023, 6(2): 195-202.
- [32] 郑建强. EG/APP 膨胀阻燃 ABS 基木塑复合材料的制备与性能研究[D]. 哈尔滨: 东北林业大学, 2013.
- ZHENG Jianqiang. Study on preparation and performance of EG/APP IFR flame retardant ABS-based WPC[D]. Harbin: Northeast Forestry University, 2013(in Chinese).
- [33] 董倩倩, 李凯夫, 蔡奇龙, 等. 3D 打印用聚乳酸/松木粉/纳米二氧化硅木塑复合材料性能研究[J]. 塑料科技, 2019, 47(1): 85-89.
- DONG Qianqian, LI Kaifu, CAI Qilong, et al. Properties of PLA/PWF/nano-SiO₂ wood-plastic composites for 3D printing[J]. *Plastics Science and Technology*, 2019, 47(1): 85-89(in Chinese).
- [34] 周松, 王静怡, 张再昌, 等. 纳米 SiO₂/竹纤维/环氧树脂复合材料性能研究[J]. 塑料助剂, 2009(2): 47-50.
- ZHOU Song, WANG Jingyi, ZHANG Zaichang, et al. Study on properties of nano-SiO₂/bamboo fiber/epoxy resin ternary composites[J]. *Plastic Additives*, 2009(2): 47-50(in Chinese).
- [35] KIM B J, YAO F, HAN G P, et al. Mechanical and physical properties of core-shell structured wood plastic composites: Effect of shells with hybrid mineral and wood fillers[J]. *Composites Part B: Engineering*, 2013, 45(1): 1040-1048.

BIOPOLYMERS AND COMPOSITES

PROCESSING AND CHARACTERIZATION

*Edited by Samy A. Madbouly
and Chaoqun Zhang*

Contents

List of contributing authors — XI

Paul Gregory, Souvik Banerjee, Chuanshen Du and Martin Thuo

1 Introduction: biopolymers and biocomposites — 1

- 1.1 Introduction — 1
 - 1.1.1 Classification of biopolymers — 2
 - 1.1.2 Biocomposites — 4
 - 1.1.3 Biomimetic composites — 9
 - 1.1.4 Processing of Bio-polymers — 11
 - 1.1.5 Neoteric processing and applications — 15
 - 1.1.6 Conclusion — 22
 - References — 22

Fan Qi, Zhang Chaoqun, Yang Weijun, Wang Qingwen and Ou Rongxian

2 Lignin-based polymers — 27

- 2.1 Introduction — 27
- 2.2 Lignin recovery — 30
 - 2.2.1 Kraft pulping — 30
 - 2.2.2 Sulfite pulping — 30
 - 2.2.3 Soda pulping — 31
 - 2.2.4 Organosolv — 31
 - 2.2.5 Acidolysis — 32
 - 2.2.6 Enzymatic liberation — 32
- 2.3 Lignin derived polymers — 32
 - 2.3.1 Lignin as a macromonomer — 32
 - 2.3.2 Lignin-derived phenolic compounds as monomers — 43
- 2.4 Lignin-based polymer composites — 49
 - 2.4.1 Lignin-based thermoplastic polymer composites — 49
 - 2.4.2 Lignin-based rubber composites — 52
 - 2.4.3 Lignin-based thermosetting polymer composites — 55
- 2.5 Conclusions and outlooks — 56
- References — 57

Xing Zhou, Yaya Hao, Xin Zhang, Xinyu He and Chaoqun Zhang

3 Cellulose-based polymers — 65

- 3.1 Introduction — 65
- 3.2 The categories of cellulose polymers in different forms — 67
 - 3.2.1 Cellulose fibers — 67
 - 3.2.2 Cellulose membrane — 69
 - 3.2.3 Cellulose gel — 71

3.2.4	Cellulose bioplastics —	72
3.2.5	Nanocrystalline cellulose —	73
3.2.6	Bacterial cellulose —	78
3.3	The structure and properties of cellulose —	80
3.3.1	Chemical structure —	80
3.3.2	Aggregation structure —	82
3.4	Swelling and dissolution of cellulose —	83
3.4.1	Solvents and principles of cellulose dissolution —	83
3.4.2	Nonderivatizing solvents —	83
3.4.3	Derivatization solvent —	89
3.4.4	Preparation and characterization of cellulose derivates —	89
3.4.5	Grafting copolymerization of cellulose —	100
3.5	Concluding remarks and future trends —	102
	References —	103

Guoqiang Zhu, Chengguo Liu and Chaoqun Zhang

4	Plant oil-based polymers —	113
4.1	Introduction —	113
4.2	Structure and modification of plant oils —	114
4.2.1	Structure of plant oils —	114
4.2.2	Modification of oils and their derivatives —	115
4.3	Oil-based thermosetting polymers —	119
4.3.1	Direct-polymerized polymers —	119
4.3.2	Alkyd resins —	121
4.3.3	Unsaturated polyester resins —	121
4.3.4	Epoxy resins —	124
4.3.5	Polyurethane resins —	127
4.3.6	Other thermosetting polymers —	140
4.4	Oil-based thermoplastic polymers —	141
4.4.1	Polyamides —	141
4.4.2	Polyesters —	143
4.4.3	Other thermoplastic polymers —	145
4.5	Conclusions —	146
	References —	147

Xing Zhou, Xin Zhang, Pu Mengyuan, Xinyu He, and Chaoqun Zhang

5	Bio-based polyurethane aqueous dispersions —	155
5.1	Introduction —	155
5.2	WPU synthesized from biomass resources —	157
5.2.1	Properties of polymer dispersion —	157
5.2.2	Vegetable oil-based polyols —	158

5.2.3	Vegetable oil based isocyanates —	166
5.2.4	Lignin based polyols —	167
5.2.5	Cashew nut shell liquid based polyols —	168
5.2.6	Plant straw based polyols —	168
5.2.7	Terpene based polyols —	169
5.2.8	Rosin based polyols —	170
5.3	WPU modified by biomass resources —	171
5.3.1	Cellulose —	171
5.3.2	Starch —	172
5.3.3	Chitosan —	174
5.3.4	Lignin —	174
5.3.5	Sodium alginate —	175
5.3.6	Natural phenolic acid —	175
5.4	Application —	176
5.5	Conclusion and outlook —	178
	References —	179

Samy Madbouly, Sean Edlis and Nicolas Ionadi

6	Soybean-based polymers and composites —	189
6.1	Introduction —	189
6.2	Production of DSF, SPC, and SPI —	192
6.3	Recent advancements —	194
6.4	Conclusion —	205
	References —	206

James Goodsel and Samy Madbouly

7	Biodegradable polylactic acid (PLA) —	209
7.1	Introduction —	209
7.2	Polymer composites —	210
7.2.1	Nanocellulose —	210
7.2.2	Nanoclays —	211
7.2.3	Carbon nanotubes —	212
7.2.4	Graphene —	212
7.2.5	Other functional nanofillers —	212
7.3	Polymer blends —	217
7.4	Applications —	224
7.5	Conclusion —	231
	References —	232

Samy A. Madbouly

8	Bio-based polyhydroxyalkanoates blends and composites —	235
8.1	Introduction —	235
8.2	Synthesis of PHAs —	237

8.3	Chemical modification of PHA —	239
8.4	PHAs blends and composites —	240
8.5	Conclusion —	249
	References —	250

Emily Archer, Marissa Torretti and Samy Madbouly

9 Biodegradable polycaprolactone (PCL) based polymer and composites — 255

9.1	Introduction —	255
9.2	Synthesis of poly(α -hydroxy acid)s —	258
9.2.1	Initiators/catalysts for the synthesis of poly(α -hydroxy acid)s —	259
9.3	Biodegradability of PCL —	259
9.3.1	Other microorganisms that degrade PCL —	261
9.4	Characterization behavior of PCL —	266
9.5	Development of a biodegradable PCL film —	268
9.6	Biomedical applications of PCL —	273
9.7	Conclusion —	274
	References —	275

Ty Burford, William Rieg and Samy Madbouly

10 Biodegradable poly(butylene adipate-co-terephthalate) (PBAT) — 279

10.1	Introduction —	279
10.2	Biodegradation —	281
10.3	Mechanical, thermal, and rheological properties of PBAT —	283
10.4	PBAT thermal degradation —	287
10.4.1	PBAT blends (PLA) —	291
10.4.2	PBAT blends (corn stovers) —	298
10.4.3	PBAT/TPS blends —	302
10.5	Processing of PBAT/wollastonite biocomposites used in medical applications —	306
10.6	Conclusion —	306
	References —	307

Medhat S. Farahat Khedr

11 Bio-based polyamide — 309

11.1	Introduction —	309
11.1.1	Global warming potential GWP (kg CO ₂ equivalent) —	310
11.2	Polyamides and nylon: background —	310
11.3	Biobased aliphatic bio-PAs —	313
11.4	Mechanical characteristics and applications of common aliphatic PAs —	318

11.5	PA6 and PA6.6 —	318
11.6	PA11, PA12 and PA12.12 —	319
11.7	PA4.6 and PA4.10 —	322
11.8	PA6.10, PA6.12, PA5.10, PA10.10, PA10.12, PA10.12 and PA13.6 —	323
11.9	Fully aromatic (aramids) and semi-aromatic (polyphthalamides) PPAs —	325
11.10	Market analysis and insights: global bio-PAs market —	326
	References —	327

Tanner Alauzen, Shaelyn Ross and Samy Madbouly

12	Biodegradable shape-memory polymers and composites —	331
12.1	Introduction —	331
12.2	Classification of shape memory polymers —	332
12.2.1	Composition and structure —	333
12.2.2	Shape memory polymers with net points —	334
12.2.3	Stimulus method —	336
12.2.4	Shape memory function —	337
12.3	Shape-memory polymer composites —	339
12.4	Applications —	344
12.5	Conclusion —	348
	References —	348

Israd H. Jaafar, Sabrina S. Jedlicka and John P. Coulter

13	Poly(glycerol sebacate) – a revolutionary biopolymer —	353
13.1	Introduction —	353
13.2	Synthesis and material characterization —	356
13.2.1	Thermal analysis —	357
13.2.2	ATR-FTIR —	358
13.2.3	Mechanical properties —	360
13.3	Microfabrication —	361
13.4	Human mesenchymal stem cell culture on PGS —	363
13.4.1	Cell proliferation —	363
13.4.2	Phase contrast microscopy —	365
13.4.3	Scanning electron microscopy images —	365
13.4.4	Immunocytochemistry (ICC) and cytoskeletal examination —	368
13.5	Degradation —	369
13.6	Summary —	371
	References —	371

Index —	375
----------------	------------

Fan Qi, Zhang Chaoqun, Yang Weijun, Wang Qingwen and
Ou Rongxian*

Lignin-based polymers

Abstract: On the basis of the world's continuing consumption of raw materials, there was an urgent need to seek sustainable resources. Lignin, the second naturally abundant biomass, accounts for 15–35% of the cell walls of terrestrial plants and is considered waste for low-cost applications such as thermal and electricity generation. The impressive characteristics of lignin, such as its high abundance, low density, biodegradability, antioxidation, antibacterial capability, and its CO₂ neutrality and enhancement, render it an ideal candidate for developing new polymer/composite materials. In past decades, considerable works have been conducted to effectively utilize waste lignin as a component in polymer matrices for the production of high-performance lignin-based polymers. This chapter is intended to provide an overview of the recent advances and challenges involving lignin-based polymers utilizing lignin macromonomer and its derived monolignols. These lignin-based polymers include phenol resins, polyurethane resins, polyester resins, epoxy resins, etc. The structural characteristics and functions of lignin-based polymers are discussed in each section. In addition, we also try to divide various lignin reinforced polymer composites into different polymer matrices, which can be separated into thermoplastics, rubber, and thermosets composites. This chapter is expected to increase the interest of researchers worldwide in lignin-based polymers and develop new ideas in this field.

Keywords: epoxy resins; lignin-based polymers; lignin reinforced polymer composites; phenol resins; polyester resins; polyurethane resins.

1 Introduction

Lignin is the only renewable source of aromatic chemistry. It consists of three basic structural units: *p*-coumaryl alcohol, coniferyl alcohol, and sinapyl alcohol [1, 2], as shown in Figure 1. These basic units are connected by ether and carbon-carbon bonds [3].

***Corresponding author: Rongxian Ou**, Key Laboratory for Biobased Materials and Energy of Ministry of Education, College of Materials and Energy, South China Agricultural University, Guangzhou, 510642, P. R. China; and Guangdong Provincial Laboratory of Lingnan Modern Agricultural Science and Technology, Guangzhou, P. R. China, E-mail: rongxian_ou@scau.edu.cn

Fan Qi, Zhang Chaoqun and Wang Qingwen, Key Laboratory for Biobased Materials and Energy of Ministry of Education, College of Materials and Energy, South China Agricultural University, Guangzhou, 510642, P. R. China; and Guangdong Provincial Laboratory of Lingnan Modern Agricultural Science and Technology, Guangzhou, P. R. China

Yang Weijun, The Key Laboratory of Synthetic and Biological Colloids, Ministry of Education, Jiangnan University, 214122 Wuxi, P. R. China



Lignin is low-cost and has many fascinating properties such as biodegradability, antioxidant activity, high thermal stability, and favorable stiffness, or high elastic modulus [4–6]. These advantages drive the development of lignin as a versatile product. However, the low reactivity and brittleness of lignin and its incompatibility with other polymer systems make it virtually unsuccessful in the manufacture of lignin-based high-performance materials [7, 8]. It is hoped that these shortcomings can be overcome by the chemical or physical modification of lignin and the synthesis of lignin-derived polymers [7, 9].

Lignin vascular plants were formed by chemical controlled random phenol free-radical coupling polymerization. However, the lignification theory is still under discussion, because enzyme pathways, called “dirigent” proteins, have been proposed. The composition, molecular weight, and content of lignin vary between plant species. The abundance of lignin usually decreases in the order of softwood > hardwood > grass. Schematic diagrams of hardwood and softwood lignin structures are shown in Figures 2 and 3, respectively. The structure is just a figure and does not indicate a specific order. The components derived from coniferyl, sinapyl, and *p*-coumaryl alcohol are shown in color, and some examples are given to illustrate the linkages among these components. The linkages include β -O-4, 4-O-5, β -5, β -1, 5–5, dibenzodioxocin, and β - β linkages, of which the β -O-4 linkage is dominant, consisting of >40% of the linkage structures.

Lignin is more sustainable than some other renewable polymer feedstocks, such as scarce mint or quercetin, and edible sugars and starch, as it is neither rare nor a source of food. So far, various studies have reported on different lignin valorization methods for modifying lignin and synthesizing lignin-based polymers [12, 13]. Some critical review articles have emphasized the problem of lignin being converted into functional materials. The mechanical and thermal characteristics of lignin-based copolymers, composites, and blends are discussed by Argyropoulos and coworkers [13]. The recent advances in lignin applications in developing green polymer composites and hydrogels are reviewed by Thakur and coworkers [14, 15]. The existing methods and strategies for preparing functional carbon materials from lignin by the thermochemical conversion are described by Liu and coworkers [16]. Kai and Zhao et al. summed up the

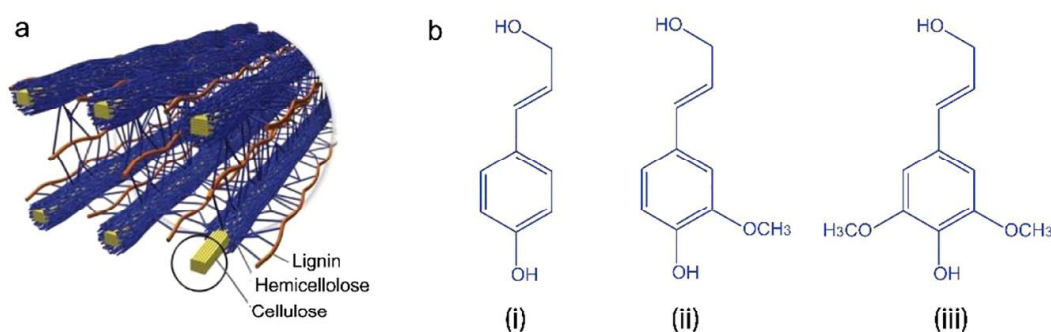


Figure 1: (a) The positional relationship between cellulose, lignin, and hemifibers in lignocellulose [10]. (b) Monolignol monomer, (i) *p*-coumaryl alcohol (4-hydroxyl phenyl, H), (ii) coniferyl alcohol (guaiacyl, G), (iii) sinapyl alcohol (syringyl, S).



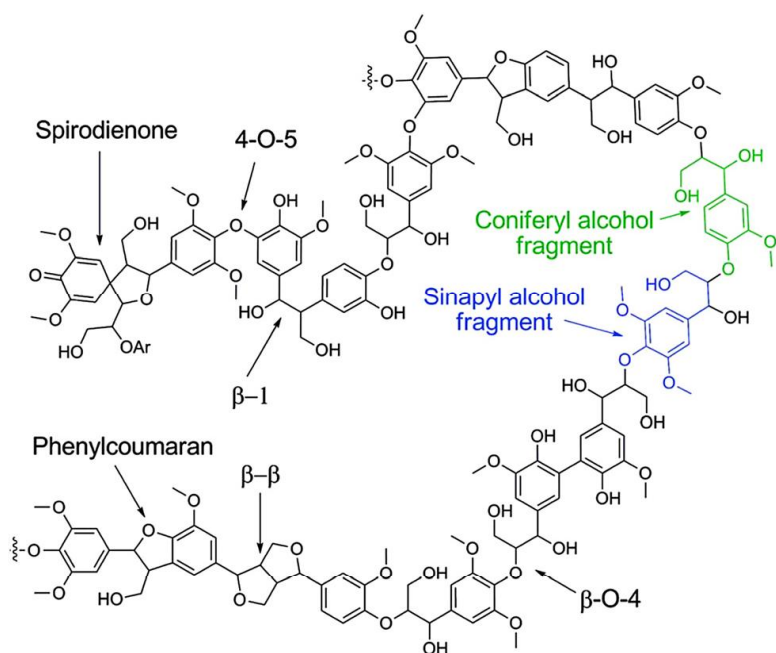


Figure 2: Schematic diagram of a hardwood lignin structure and some main linkages [11].

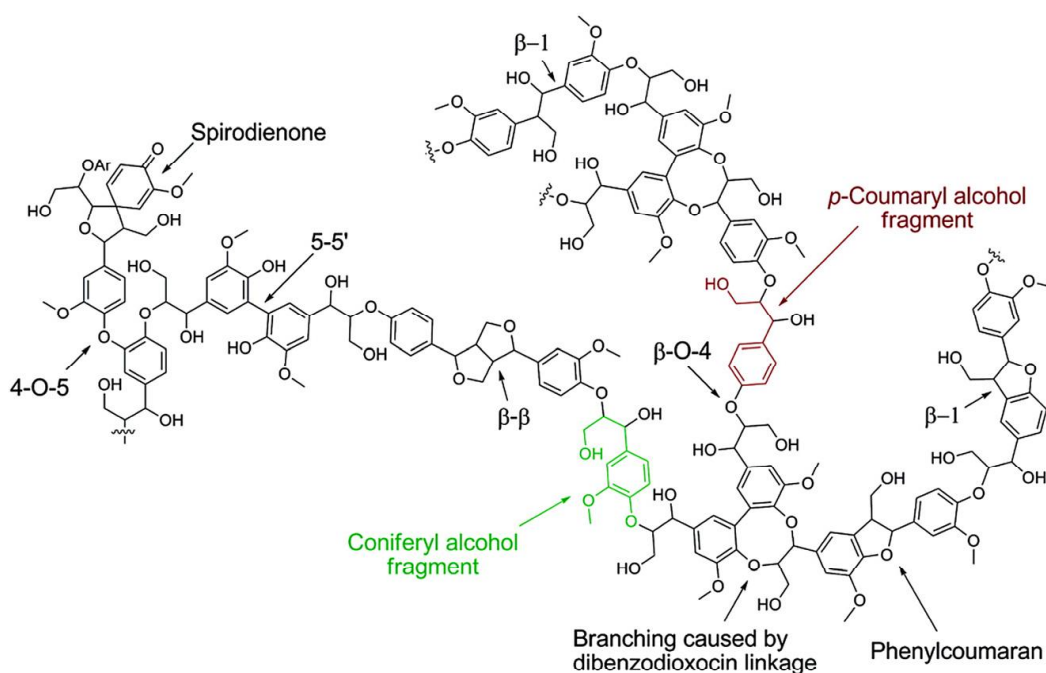


Figure 3: Schematic diagram of a softwood lignin structure and some main linkages [11].

recent advances in lignin from the perspective of different approaches to the synthesis of oligomeric copolymers, the resulting features, the various design methods to engineer lignin-based polymers and the potential applications of lignin-based functional materials [7, 17]. Vishtal et al. [18] summarized different methods of extracting lignin



and pointed out the challenge of how to convert and utilize it in industrial applications. Lawoko et al. [19] reviewed the direct usage of lignin and its chemical modifications toward micro- and nanostructured materials. Sternberg and coworkers recently summarized the literature on lignin-derived polymers in the past 20 years, and focused on a comprehensive assessment of the greenness and sustainability of the latest technology for lignin-derived polymers [20].

2 Lignin recovery

At present, traditional pulp mills are the main suppliers of technical lignins. Most of the commercially available technical lignin types are fabricated from Kraft or sulfite pulping processes [21]. In addition to these two processes, there are other processes through which lignin can be recovered, such as soda pulping, steam explosion, acid decomposition, biological treatment, organic solvent recovery and others [22]. This section briefly discusses possible processes for recovering lignin.

2.1 Kraft pulping

Kraft pulping is the main source of industrial lignin [23]. In pulping, cellulose fibers are obtained from lignocellulosics by treating it with sodium sulfide and sodium hydroxide at high temperature and high pH [24]. Hemicellulose and some cellulose are degraded to isosaccharic acid. Thus, Kraft paper pulping liquid is composed of lignin (47%), hydroxy acids (28%, such as isosaccharic acid), inorganic substances and small amounts of other organic substances [25]. Lignin can be extracted from these waste pulping liquors as a precipitate by acidification. Almost all Kraft lignin is burned for energy recovery, but the United States, for example, produces about 35,000 tons per year for many chemical by-products [23].

2.2 Sulfite pulping

Sulfite pulping is a general term used to define many sulfate chemical wood pulp processes that are carried out at different levels of pH [26]. In the acid sulfite pulping process, wood is treated at low pH, high temperature and high pressure with sodium, ammonium, magnesium or calcium sulfite/bisulfite solution [27]. Through this process, lignin, hemicellulose and extracts are broken down and the fiber's cellulose is left behind. Hemicellulose is hydrolyzed critically to release water-soluble monosaccharides in spent sulfite liquor. Depending on the pulping process, lignosulfonate can be recovered either as sodium, calcium, magnesium, or ammonium salt [28]. Currently, only about 20% of all lignosulfonates produced are used as chemicals, such as economic



binders for animal feed and road asphalt [29]. In addition, lignosulfonates can also be used as concrete or cement water-reducing agents and oil well drilling [29].

2.3 Soda pulping

Soda lignin is derived from the soda or soda-anthraquinone pulping process. Soda pulping is mainly used for annual crops such as straw, flax, bagasse and hardwood. Compared with the sulfate method, the main difference is the sulfur-free medium of the cooking liquor. Soda lignin does not contain sulfur, which means that soda lignin have a chemical composition that is closer to that of natural lignin than Kraft lignin and lignosulfonates.

2.4 Organosolv

Organosolv is a method of treating plant tissues with aqueous solutions of organic solvents (usually containing trace amounts of inorganic acids) [30]. These solvents include ethanol, methanol, butanol, phenol, acetic acid, ethyl acetate, and so on. So far, this method has not been commercially applied due to the amount of organic solvents consumed and the low quality of pulp fibers obtained [31]. The lignin molecular weight obtained by organic solvent extraction is comparatively low [32]. The data on physico-chemical characteristics of Kraft, lignosulfonate, soda, and organosolv lignin are shown in Table 1.

Table 1: Properties of technical lignins [7].

Technical lignins	Kraft	Lignosulfonate	Soda	Organosolv
Separation methods	Precipitation (pH change)	Ultrafiltration	Precipitation (pH change)	Precipitation (addition of non-solvent)
	Ultrafiltration		Ultrafiltration	Dissolved air flotation
Product status	Industrial	Industrial	Industrial	Laboratory/Pilot
Molecular weight ($\times 10^3 \text{ g mol}^{-1}$)	1.5–5 (<25)	1–50 (<150)	0.8–3 (<15)	0.5–5
Polydispersity	2.5–3.5	6–8	2.5–3.5	1.5–2.5
Sulfur (%)	1.0–3.0	3.5–8.0	0	0
Nitrogen (%)	0.05	0.02	0.2–1.0	0–0.3
Acid soluble lignin (%)	1–5	/	1–11	~2
Solubility	Alkali, some organic solvents (pyridine, DMF, and DMSO)	Water	Alkali	Wide range of organic solvents
T_g (°C)	140–150	130	140	90–110
T_d (°C)	340–370	250–260	360–370	390–400

T_g : Glass transition temperature; T_d : thermal decomposition temperature.



2.5 Acidolysis

During acid decomposition, plant material is saccharified by inorganic acids such as hydrochloric acid or sulfuric acid, and lignin is extracted and recovered as insoluble residues [33]. In the past, this process was used in Europe; In the Western Hemisphere, however, it was not considered as commercially important [34].

2.6 Enzymatic liberation

In the process of enzymatic hydrolysis, residues rich in lignin obtained by treating plant material with hemicellulase, cellulase, or pectinase [35]. This kind of lignin preparation is more similar to the “native” lignin because of the moderate processing environment employed [36].

3 Lignin derived polymers

3.1 Lignin as a macromonomer

The structure of lignin can be easily modified to develop novel materials, especially phenol and aliphatic hydroxyl groups [17]. Depending on the targeted application, lignin can be used with or without chemical modification. Without chemical conversion, lignin can be added directly to the polymer matrix, thereby reducing product costs and improving performance. For instance, unmodified lignin can be applied as an antioxidant, ultraviolet stabilizer, flame retardant, and additive to improve the rheological property of final products [37]. Although lignin has potential for direct industrial application, it can only be added in small quantities due to its weak mechanical properties and poor thermal stability. Lignin, on the other hand, can be chemically modified as the starting material for polymer synthesis or transformation into chemicals and fuels. There are four different ways to chemically modify lignin [38, 39]: (1) To depolymerize or fragment, using lignin as a carbon source or to break it down into small fragments containing aromatic rings; (2) Modifying lignin by synthesizing new chemical activity sites; (3) Chemical modification of hydroxyl groups in lignin structures; and (4) production of grafted copolymers. It is worth noting that the above chemical modification methods are highly dependent on the reactivity of lignin functional groups and the structural characteristics of lignin raw materials.

Lignin is represented in its aliphatic and phenolic hydroxyl groups at the C_α and C_γ positions on the side chains. Hydroxyl modification can lead to the formation of lignin derivatives. The effects of different functional groups on the modification of lignin have been explored (Figure 4a). Moreover, the modifications include the synthesis of new macromolecular monomers, which are more efficient and responsive by changing the



nature of chemical activity sites or increasing the activity of hydroxyl groups. Therefore, lignin's chemical reactivity is enhanced, the brittleness of lignin-based polymers is decreased, and the solubility is improved, thus improving the processing of lignin. In this way, a number of new chemical sites were introduced into the lignin structure through several chemical modifications (Figure 4b), including amination, hydroxyalkylation, sulfomethylation, nitration, and sulfonation, etc.

Degradation of lignin to monolignols or phenolic monomers is an energy-consuming process, which is one of the reasons why it is currently more valuable as a fuel than a raw material [40]. Using lignin as a raw material for the synthesis of new materials without any additional degradation, it is beneficial for the environment and energy [6]. The structure of lignin varies greatly depending on its source and the process of separation from the pulping [41]. Despite these differences, all the separated lignin contained both aliphatic and phenolic hydroxyl groups [42]. These functions can be used as connectors to create lignin-based macromonomers [43]. Currently, lignin as a nature macromonomer can be used to synthesize polyurethane, polyester, epoxy, phenolic resins and other polymers, which are briefly discussed in the next subsections [44].

3.1.1 Polyurethanes

Polyurethane is synthesized from diisocyanate and polyol by the poly-addition reaction with terminal hydroxyl groups, and has polyurethane groups in the backbone

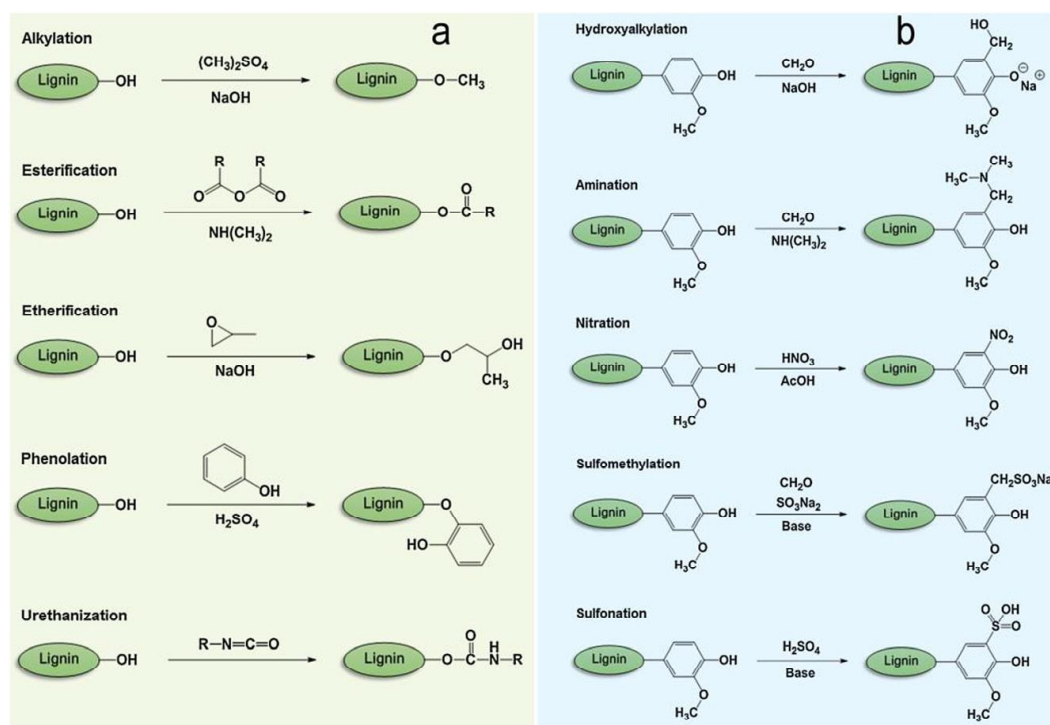


Figure 4: Schematic diagram of the chemical modifications of lignin. (a) Modification of the hydroxyl groups; (b) Generation of new chemically active sites [7].



[45]. Lignin contains abundant aliphatic and phenolic hydroxyl functions, so it can easily replace the polyol component of polyurethane [46]. Moreover, biobased polyurethanes are more degradable than those originate from petroleum-based polyols [47, 48].

By controlling reaction temperature and reaction time, Duong and his colleagues produced a high-molecular-weight polyurethane [49]. Using Kraft lignin as raw material, molecular weights of the product up to 912,000 g/mol were obtained in only 3 h [49]. Hatakayama and coworkers combined these four types of technical lignin (ligonsulfonate, Kraft, solvolysis, and alcoholysis lignin) with polypropylene glycol (PPG) or polyethylene glycol (PEG), respectively, and with a mixture produced by reaction with diphenylmethane diisocyanate [50]. Whichever the type of lignin used, authors determined that lignin loading have a greater impact on the properties of synthetic materials than any other factor, such as the ratio of isocyanate/hydroxyl group or the molecular weight of the polyols.

Seeking after materials with enhanced stiffness, Xue and his colleagues prepared a range of lignin-based rigid polyurethane foams, adding up to 39.17 wt% lignin [51]. Compared with traditional polyurethane, these biofoams have increased thermal conductivity because of their larger cell volume and lower density. Unlike rigid polyurethane foams, flexible polyurethanes consist of a flexible and hard (cross-linked) blocks. Pohjanlehto and his colleagues synthesized a sugar-based xylaric acid, polyol, and reacted them with lignin and PEG to prepare a series of polyurethanes [52]. The increase in lignin content had almost no effect on Young's modulus or T_g , but the slight improvement in thermal stability showed that the lignin acted to stabilize the final product. Compared with the typical application of lignin blends, Yiamsawas and coworkers recently reported a method of synthesizing lignin-polyurethane nanocontainers with inverse microemulsion [53]. Before reacting with toluene diisocyanate, the suspension of sodium lignosulfonate in water is mixed with the surfactant polyethylene glycol polyricol. This method produced hollow and cross-linked lignin-based polyurethane nanocontainers (diameters of 311–390 nm) with the ability to contain water-soluble cargo. The results showed that these nanocontainers remained stable in aqueous solutions for weeks and can rapidly degrade within 24 h using natural enzymes.

However, as far as we know, there are few reports on lignin-based polyurethane polymers that combine high content of lignin and high performance.

Zhang and coworkers have reported a new poly(ϵ -caprolactone) modified lignin-based polyurethane bio-plastics exhibiting high performance [54]. As shown in Figure 5, the poly(ϵ -caprolactone) as a soft segment was incorporated into the lignin under the assistance of the bridge of hexamethylene diisocyanate (HDI). In this study, HDI with long aliphatic chains was used as an activator of lignin hydroxyl groups, and the poly(ϵ -caprolactone) is added as a biodegradable soft segment to improve the flexibility of the lignin-based polyurethane [54]. The effects of lignin content, $-OH/-NCO$ molar ratio, and the molecular weight of poly(ϵ -caprolactone) on the properties of the obtained biobased polyurethane plastics were assessed [54]. The results showed



that the biobased polyurethane film still has high strength, fracture elongation and tearing strength at 19.35 MPa, 188.36% and 38.94 kN/m with the content of lignin high as 37.3%, respectively. In addition, the sample has excellent thermostability and has a good solvent-resistance. Thus, lignin modification toward the urethane chemistry is an effective approach to develop lignin-based sustainable and high-performance materials [54].

In recent years, the free radical induced thiol-ene reaction has been widely concerned by materials science and synthetic chemistry because of its low sensitivity to oxygen, easy implementation, and high yield without complicated purification methods [55, 56]. As shown in Figure 6, Cao and coworkers have reported an novel lignin-based polyurethanes coatings, which were synthesized through polymerization of lignin-based polyol with HDI without catalysts, showed excellent corrosion resistance at high lignin content [57]. In this study, the reactivity and solubility of lignin-based polyol was increased, while the phenol hydroxyl groups of enzymic hydrolysis lignin were selectively transformed into aliphatic hydroxyls via alkylation and thiol-ene reaction [57]. Due to the good dispersion and crosslinking reaction of lignin-based polyol in polyurethane network, the obtained lignin-based polyurethanes coatings have excellent mechanical properties, high thermostability, and strong corrosion-resistance. These characteristics give lignin-based polyurethanes great potential for applications in areas requiring high mechanical strength, high thermostability, and high corrosion resistance, namely, coating, adhesives and electronics. However, further optimization of the lignin-based polyurethanes coatings formulation is needed to enhance the toughness of LPU coatings and elucidate the mechanism of corrosion-resistance [57].

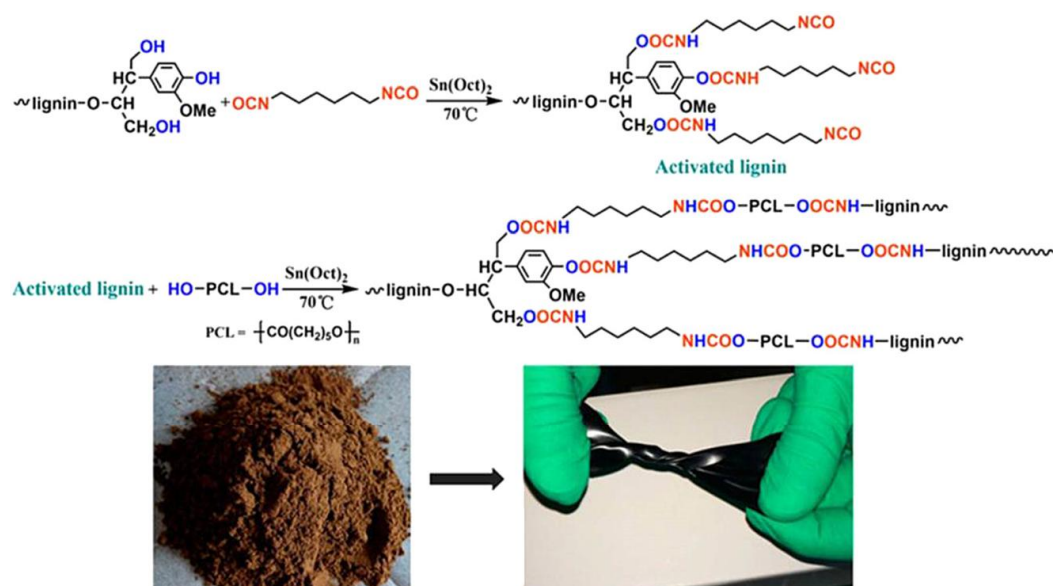


Figure 5: Synthesis route of the poly(ϵ -caprolactone) modified lignin-based polyurethane bio-plastics [54].



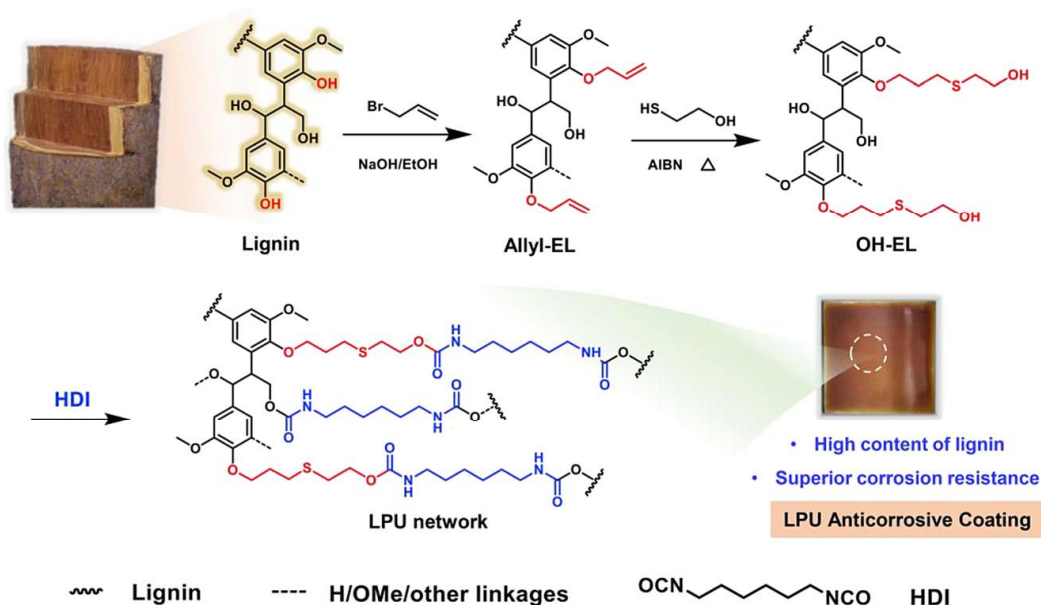


Figure 6: The synthesis route of lignin-based polyol and the schematic structure of anticorrosive coatings of thermosetting lignin-based polyurethanes [57].

Although above results support the concept of lignin incorporation, many properties require further adjustment before lignin-based polyurethanes can be used as a commercial material. In addition, batch-to-batch variation in lignin will result in batch-to-batch variation in these systems.

3.1.2 Polyesters

Polyesters are polymers containing ester bonds that can be prepared in three different ways: esterification of dicarboxylic acid with diol or dihalides, self-polyesterification of hydroxycarboxyl acids, and the ring-opening polymerizations of lactones or cyclic esters [58]. The application of lignin as macromolecular monomer of polyester synthesis usually limits the polycondensation reaction, but the ring opening reaction of lactone is also reported.

Guo and coworkers [59] prepared a series of polyesters from dicarboxylic acid chlorides, polyethylene glycol, and lignin. These polymers have been exhibited to be able to melt between 120 and 140 °C without changing smell or color, indicating a potential commercial use [60]. Bonini and coworkers [61] reacted steam-explosion lignin with dodecandioyl dichloride to produce a series of low molecular weight (1915–6382 g/mol) polymers. Using ϵ -caprolactone and carboxylic acid-functionalized lignin, Matsushita and coworkers [62] used the condensation reaction of ϵ -caprolactone and carboxylic acid-functionalized lignin to prepare polyester. Compared with poly ϵ -caprolactone, the obtained polymer has higher melting point and higher loss and storage modulus. Sivasankarapillai and his colleagues [63] created a network of highly branched



polymers by condensing lignin with a tri-branched carboxylic acid monomer, which was synthesized by the condensation of adipic acid with 1,1,1-triethanolamine.

Recent reports using another potentially biobased monomer, succinic anhydride (SAn), show the resulting materials has similar hardness and scratch resistance to petroleum-based polyester coatings [64]. Succinylated lignin dissolved in THF can be self-crosslinked by adding traditional crosslinking agents (such as diamines) (Figure 7) [64]. The resulting novel lignin-based thermosetting polyester coating systems are based on functionalization of the lignin-soluble fraction of Kraft lignin recovered by solvent extraction [64]. The synthetic polyesters were thoroughly characterized by chemical, physical and thermal properties to confirm the succinic anhydride was successfully covalent with lignin. These polyester coatings have film forming ability, thermostability, dynamic surface hardness, solvent resistance, and higher hydrophobicity than unmodified samples. The results of this study suggest that the development of lignin thermosetting polyester systems provide evidence of the potential bioderived coatings and adhesives materials [64].

The low solubility of lignin in common organic solvents limits the way of modification [65]. At present, a large number of researches show that lignin-based copolymers can play an active role in mechanical enhancement of block composites [66, 67]. However, few researches have been done on lignin-based porous materials. Lignin materials with porous structures may be more interesting than bulk materials because of their advantages of low density, high surface area, good absorbency and high permeability. Taking advantages, lignin-based porous composites have the

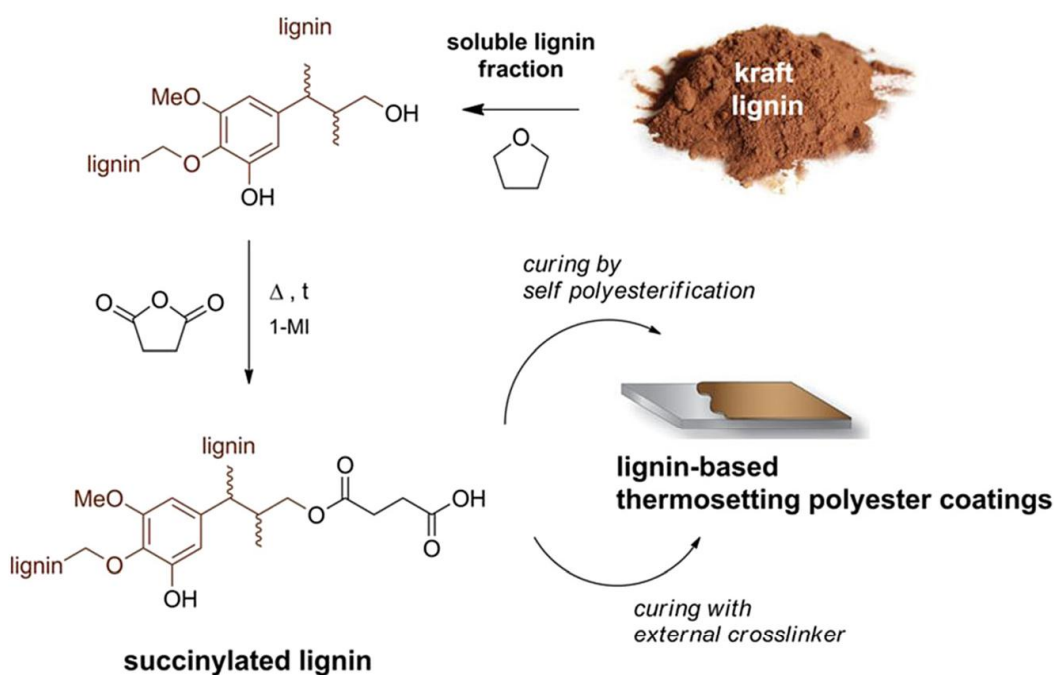


Figure 7: Synthetic scheme for the succinylated lignin for preparing crosslinked polyester coatings [64].



potential to be used in a variety of high-value applications, such as energy storage, catalysts, sensors and biomedical materials.

Recently, Kai and coworkers developed a class of novel lignin-poly (ϵ -caprolactone-co-lactide) copolymers (lignin-PCLLA) through ring-opening polymerization without solvent [68]. The obtained Lignin-PCLLA copolymers have adjustable molecular weights and glass transition temperatures [68]. It is blended with polyester by electrospinning to engineer the copolymer into ultrafine nanofibers (Figure 8). The size of the nanofibers is around 300–500 nm, and the tensile test showed that the mechanical properties of nanofibers can be improved by the mixture of lignin copolymer and polyester matrix. In addition, lignin nanofibers have good biocompatibility and antioxidant activity, demonstrating their great potential in healthcare applications [68].

3.1.3 Epoxide resins

Epoxy resin, one of the most commonly used thermoset resin materials in the fields of adhesives, coatings, composites, and electrical laminates, etc., is composed of monomers containing at least one epoxy group. Epoxy groups can be homopolymerized by cation or anion polymerization or copolymerized with comonomers, such as multifunctional amine, acids, anhydride, alcohols, and phenols [69]. The choice of epoxides and curing agents has a great influence on the mechanical, physical, and chemical properties of the products. Although lignin itself does not contain epoxy groups, the macromonomer phenolic can also be used as a curing agent/crosslinking agent for the synthesis of epoxide resins.

So far, the methods of adding bulk lignin to the thermosetting materials of epoxy resins can be summarized into three categories: the first type is the direct mixing of the

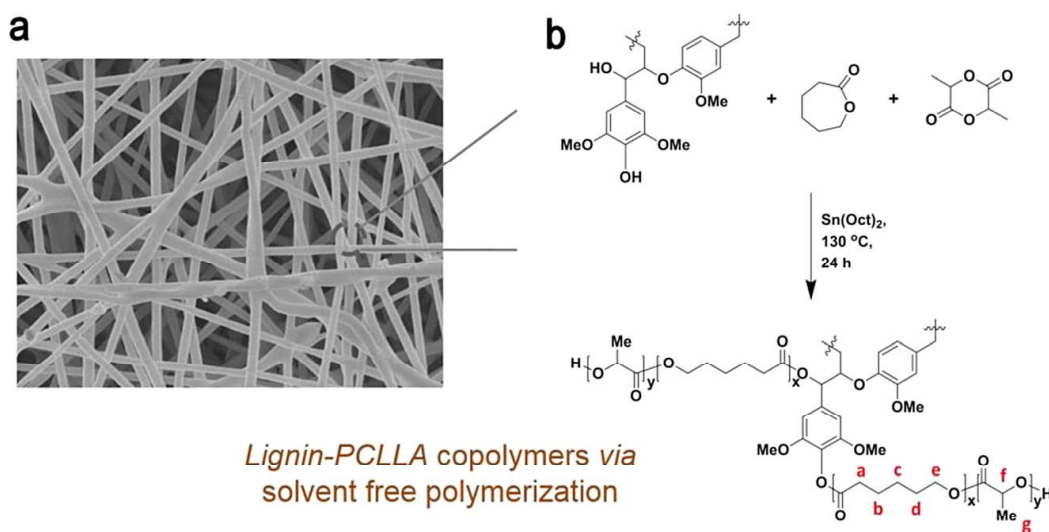


Figure 8: (a) SEM images of electrospun of lignin-PCLLA. Scale bars = 1 μ m. (b) Synthetic scheme of ring-opening copolymerization of ϵ -caprolactone, L-lactide, and lignin [68].



lignin derivatives as fillers with the ordinary epoxide resin; the second type is modifying lignin by epoxidation; and the third type is modifying lignin or its derivatives to enhance reactivity, therewith epoxidation. It is important to note that epoxy prepolymers or glycol ethers should be liquid at room temperature or elevated temperature in order to fully contact and react with the curing agent to form a homogeneous cross-linking network. Nevertheless, most reports on the epoxidation of lignin is a non-molten solid, which cannot be directly cured by curing agents [8, 70, 71].

Recently, by mixing alkaline solution of Kraft lignin with cross-linking agent of polyethylene glycol diglycidyl ether, Nonaka and his colleagues have synthesized a water-soluble variation [72]. In this system, the transition temperature of glass can be adjusted conveniently by adding alternate crosslinkers. Engelmann and his colleagues combined a low molecular weight fraction of lignin with 1,3-glycerol diglycidyl ether to produce a battery of solvent-free resins containing up to 50 wt% lignin [73]. Comparing with those control group cured by pyrogalllic acid, the higher lignin content of the lignin-based resins showed better thermostability.

Since most lignin is insoluble in organic solvents, such as enzymatic hydrolysis of lignin, and most lignin modification requires the use of organic solvents as reaction media, partial depolymerization can remarkably improve the solubility of lignin for further application [70]. Zhang and coworkers [70] have reported that Kraft lignin can be partially depolymerized through alkali catalysis in supercritical methanol to increase its solubility in organic solvents. By reacting with succinic anhydride, the partially depolymerized lignin is modified into lignin-based polycarboxylic acid (LPCA) [70]. LPCA can be applied to curing agent of epoxy resin. The results showed that LPCA could cure commercial epoxy resin at a similar temperature range. LPCA cured DER 353 resins showed a mild T_g and similar storage modulus to that of commercial anhydride cured products.

Glycidylation of lignin generally produce solid phase epoxy prepolymers, which will lead to the problem of poor compatibility with the curing agent. In order to solve this problem, Zhao and coworkers have reported a route to synthesize liquid lignin-containing epoxy prepolymers (Figure 9) [74]. In detail, lignin was phenolated by catechol (a renewable lignin derivatives), which has more phenolic hydroxyl groups than phenol [74]. The catecholized lignin was condensed with salicyl alcohol to form a novolac oligomer incorporating lignin, which was then glycidylated with epichlorohydrin to prepare a fully liquid epoxy prepolymer [74]. These lignin-based epoxy prepolymers were cross-linked by diethylenetriamine to produce homogeneous lignin-based epoxy networks (catecholized lignin content reaching 40 wt%). Compared with the solid phase counterparts, the resulting liquid lignin-based epoxy prepolymers would present wider applications.

The statistical chemical structure and poly-dispersion of lignin macromolecules limit the properties of the final materials. Therefore, in material science, extraction of lignin from mild plant extracts (such as organic solvents, enzyme hydrolysis, and partial depolymerization) is preferred. However, these lignins are not available on a



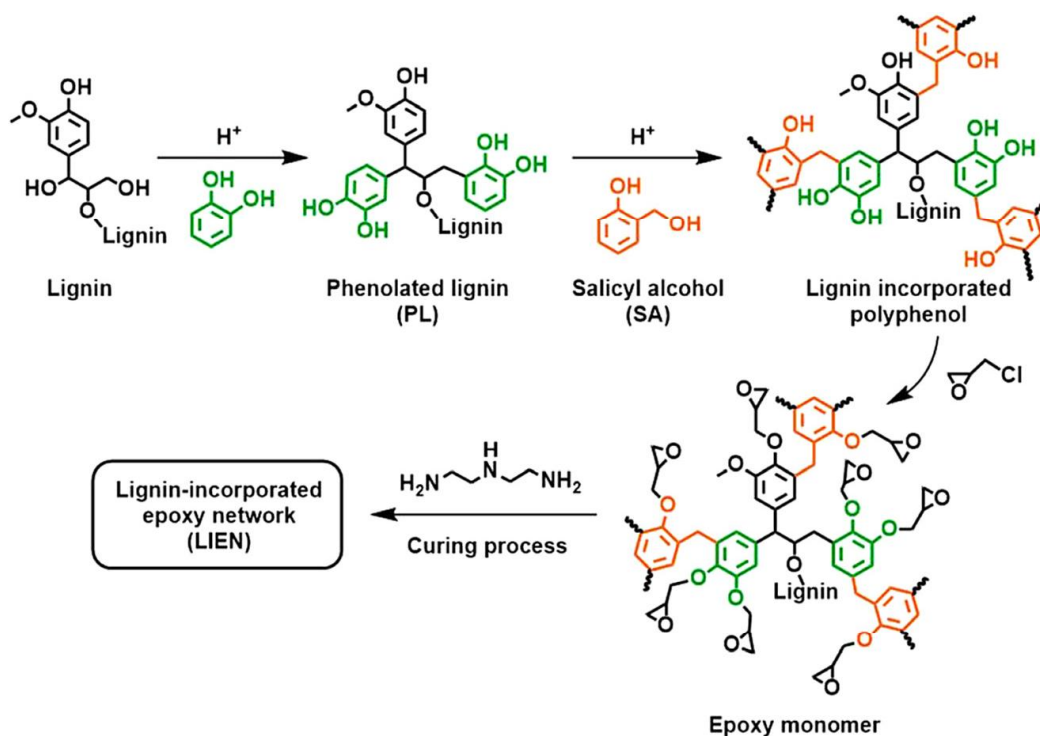


Figure 9: Synthetic scheme of catecholized lignin containing epoxy network [74].

large scale, currently, in contrast to the industrial Kraft lignin. Another way to overcome these problems is to use a purified fraction of industrial lignin.

Recently, Gioia and coworkers reported that the thermosetting epoxy resins was synthesized from high functionality and low molecular weight lignin Kraft, which was refined by solvent extraction [8]. The sequential extraction process used organic solvents such as methanol, ethanol, ethyl acetate, and acetone (Figure 10a). The extraction sequence was designed to recover the fractions with low dispersivity and gradually increasing molecular weight (Figure 10c). Then, through the reaction of epichlorohydrin with various lignin fractions, the oxirane groups were introduced by a glycidylation method (Figure 10b). The tensile strength of the resin varies from 1.2 to 5.0 MPa, increasing with the increase of molecular weight of the lignin fractions (Figure 10d). The proposed approach offers an unprecedented possibility of adjusting the network structure and performance of thermoset epoxy resins on the basis of real lignin fractions instead of lignin model compounds.

Generally, lignin imparts thermostability to the produced resins, but cannot be the sole crosslinking agent. Thus, another crosslinker must be added to obtain the desired performance. Feldman and coworkers studied a series of lignin-based epoxy resins with >40 wt% of lignin loading and other hardeners incorporated [75–77]. Addition of lignin can increase the adhesive strength of the tension, so it can reduce the cost of production of materials requiring robust adhesion [76]. In addition, the properties of the hardeners do not affect the physical performance of adhesives as much as the amount of lignin



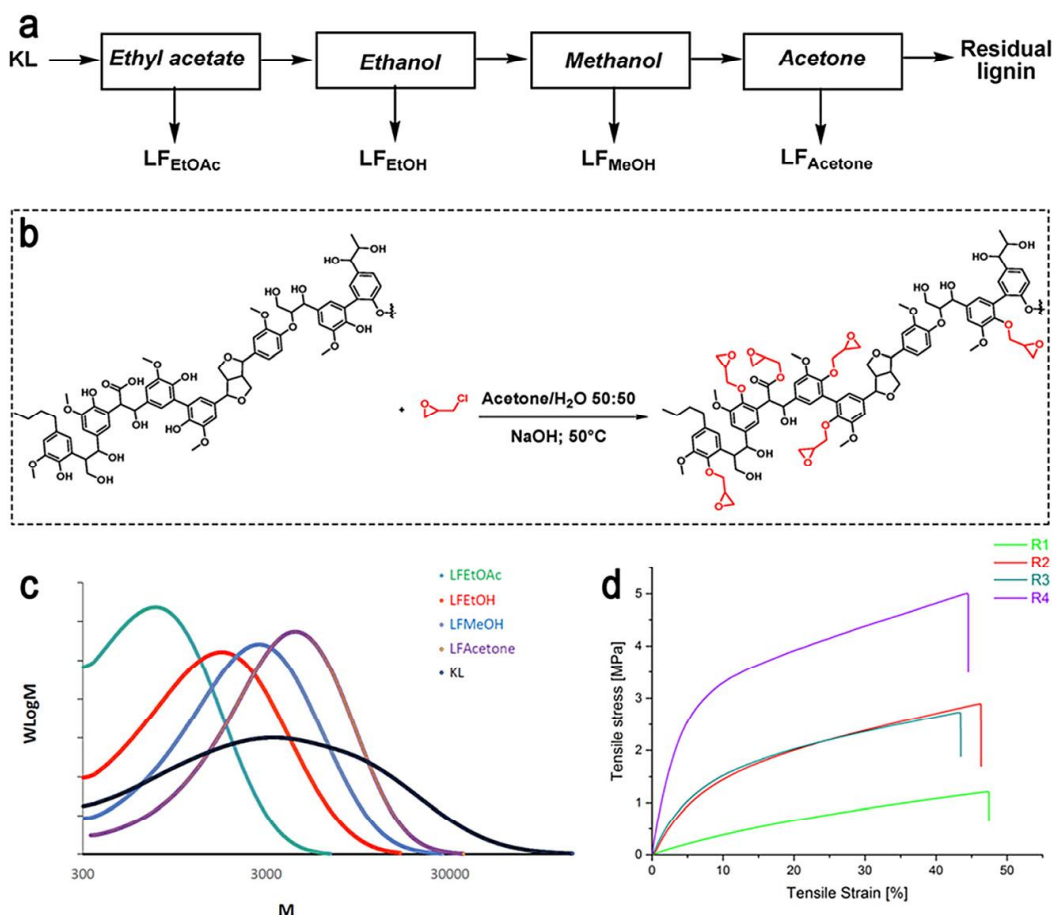


Figure 10: (a) Scheme of the sequential refining strategy; (b) Introduction of Oxirane Moieties on Lignin; (c) SEC analysis of the starting lignin compared with the obtained fractions; (d) The tensile stress–strain curves of the different lignin-based epoxy resins [8].

addition, which means that the least costly materials can be selected to reduce production costs [77].

3.1.4 Phenolic resins

Because of its unique thermal stability and flame retardancy, phenolic resin (a thermosetting rigid structure) has been widely used in the fields of petrochemical, construction, vehicles, ships, and aerospace industry [78]. The phenol/aldehyde ratio controls the cross-linking degree of the final product and determines whether the resin must be hardened by adding cross-linking agents [79]. For lignin-based phenolic resins, the phenolic chemical structure of lignin makes it a natural substitute for petroleum-based phenol in conventional synthesis schemes (Figure 11) [80]. As far as we know, there are no lignin-only phenolic resins, but there have been several attempts to replace partial phenol used with lignin to prepared lignin-based phenolic resins.

The most common type of phenolic resin is made from formaldehyde and phenol and is commonly used as adhesives. Hence, viscosity, cure rate, and the mechanical



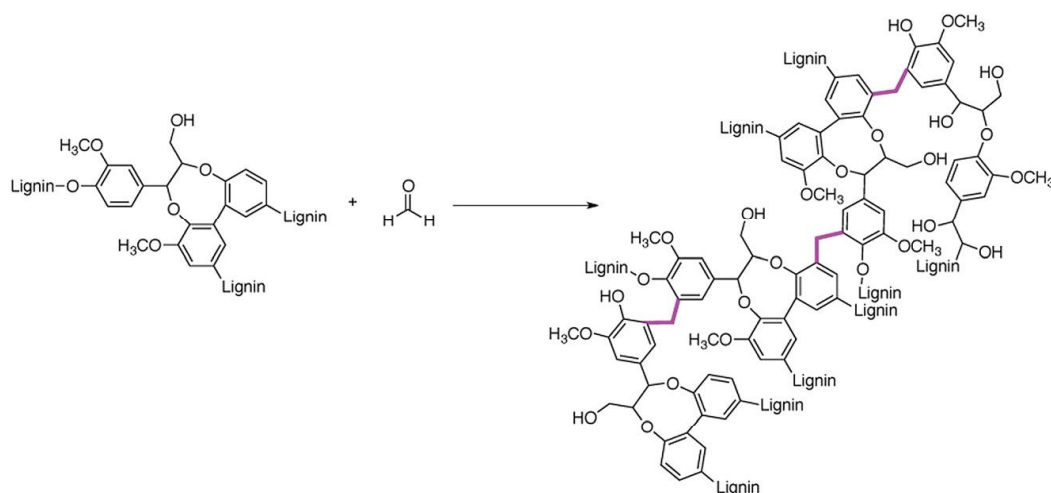


Figure 11: General scheme of phenolic resin produced by substituting phenol with lignin [4].

properties of the phenolic resin are important factors to determine their proper application. Alonso and coworkers explored the vitrification and gelation of lignin-based phenolic resins [81]. In these isometric experiments, they found that lignin-containing resins had lower activation energy than neat phenolic resin, resulting in lower curing degree at the point of gelation [81]. Vázquez and his colleagues [82] added lignin to a phenolic resin applied as an plywood adhesive. Lignin was dissolved in phenol and reacts with formaldehyde to form an adhesive that combines about 20 wt% of the lignin incorporated into the final material. Although the adhesive took longer time to cure than the traditional phenolic resin, the strength of the plywood was the similar as that produced using the conventional method. Danielson and his colleagues also developed lignin-based phenolic resins as plywood adhesives, and further evaluate its potential commercial applications [83, 84]. The resins with different proportions of lignin were prepared. The results showed that boards adhered with lignin-based phenolic resin adding 20 and 60 wt% lignin had shear strength at the superior to that of standard phenol-formaldehyde resins. Due to the brittleness of lignin, the strength of adhesives was significantly reduced by adding 80 wt%. Additionally, Dennison et al. [83] found that 50 wt% lignin addition is the ideal biobased phenolic resin to maintain resin viscosity, adhesion, and storage stability.

In fact, lignin is usually less reactive than phenol because it reacts with formaldehyde in fewer locations, consequently, it is relatively difficult to obtain highly reactive resins acceptable for foaming. Thus, many methods, such as phenol [85], depolymerization [86], and liquefaction [87], have been used to modify lignin to improve its reactivity.

Recently, Gao and coworkers [88] presented an effective method to depolymerize, demethylate and phenolize lignin catalyzed by HBr in phenol solvents under microwave radiation with moderate temperature at 90 °C (Figure 12). The reaction mixture was directly used to developed phenolic foam without further separation and purification.



Compared with the control samples, the compressive strength and thermal insulation of processing lignin-based foams were increased by 150 and 26%, respectively [88]. The results of this study provide a high value-added application of lignin in the preparation of thermal insulation materials.

3.2 Lignin-derived phenolic compounds as monomers

Current studies have shown that there are three monolignols exists in plants: coniferyl alcohol, *p*-coumaryl alcohol, and sinapyl alcohol. Monolignols are functional phenolic substances that can be used in aromatic polymer systems such as lignin [4]. A variety of phenolic monomers similar in structure to monolignols, including vanillin, cresols, guaiacols, and other lignin derived phenolic compounds provided by lignin pyrolysis, supports the prospect of tunable properties by simply selecting monomers to meet specific requirements [89]. With this in mind, this section will include several lignin-derived phenolic compounds (vanilline, cinnamic acid, *p*-coumaric acid, and ferulic acid) as monomers in polymer synthesis.

3.2.1 Vanilline derived polymers

Vanillin is currently the most readily available pure monoaromatic phenol produced on an industrial scale with lignin, which means that it is renewable and does not compete with food sources [90]. Approximately 20,000 t of vanillin are yielded every

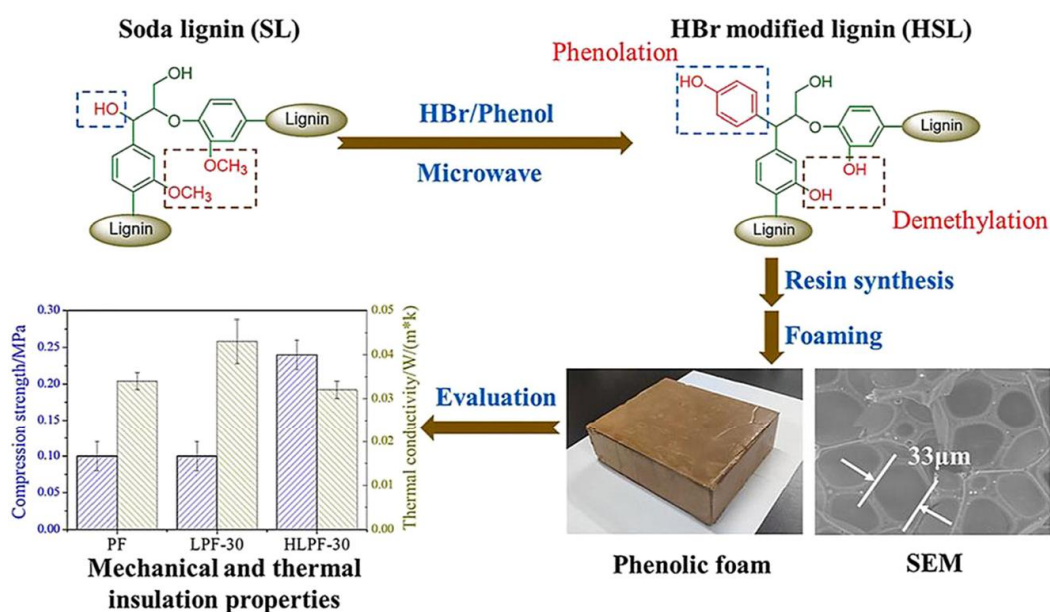


Figure 12: Schematic diagram of one-pot depolymerization, demethylation, and phenolation of lignin for phenolic foam preparation [88].



year, of which 15% comes from lignin [91]. Therefore, vanillin has the potential to become a key renewable aromatic building block.

Vanillin has many advantages. For example, it is a safe aromatic compound with two reactive functions that can be chemically modified. Therefore, vanillin can be regarded as a bifunctional compound, which is promising in the preparation of thermoplastic polymers.

In recent, Holmberg and coworkers [92] reported a general scheme for the synthesis of renewable homopolymers and block copolymers by the functionality of vanillin and reversible addition-fragmentation chain transfer polymerization.

The vanillin-based homopolymers showed glass conversion temperatures of 120 °C and degradation temperature over 300 °C, suggesting that these and similar polymers could be suitable substitutes for petroleum materials. In addition, using controlled techniques of polymerization, a vanillin-based homopolymer was chain-extended with lauryl methacrylate to prepare nanostructured block copolymers (Figure 13). The results showed that these elastomer copolymers can self-assemble in a poly(lauryl methacrylate) matrix with the form of a body-centered cubic array of vanillin-based nanospheres [92]. This work described a blueprint for controlling the polymerization of vanillin and its subsequent chain extension with a variety of comonomers, enabling the redesign and generation of novel modulated block copolymers.

Vanillin manufactures a variety of polymers, especially high-performance thermosetting materials such as epoxy resins [93] or polyphenoxylamines [94]. However, these studies mainly focus on the renewable nature of the resources and rarely address thermosets issues such as recycle trouble and flammability, etc.

Wang and coworkers prepared a novel Schiff base precursor from a rich and lignin derivative, vanillin, and produce malleable thermosetting materials combining high-performance, ultra-fast reprocessing, excellent monomer recovery, arbitrary permanent shape changes and excellent fire resistance (Figure 14) [95]. The Schiff base covalent adaptable networks showed high glass transition temperatures of about 178 °C, tensile strength of about 69 MPa, tensile modulus of about 1925 MPa. Meanwhile, the low activation energy of the bond exchange of 49–81 kJ mol⁻¹ (reprocessed in 2–10 min at

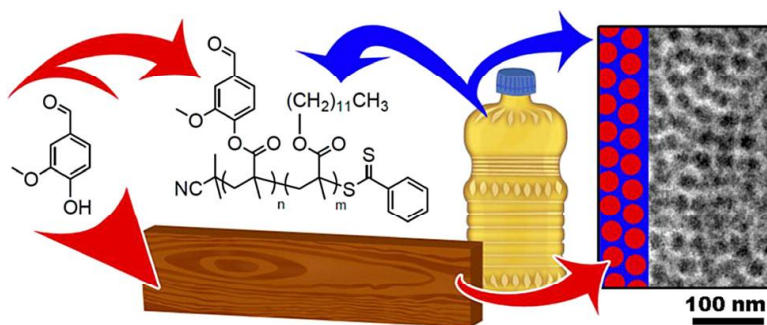


Figure 13: Schematic diagram of renewable homopolymers and block copolymers through the RAFT polymerization of vanillin [92].



180 °C) resulted in high malleability. These Schiff base covalent adaptive networks provide a good example for promoting the development of thermosetting polymer materials for nature biomass resources [95].

In addition, Zhang et al. [96] reported a novel biobased triepoxy (TEP) was synthesized based on vanillin and guaiacol as raw materials and cured with an anhydride as curing agent.

The cured TEP has the similar modulus, tensile strength, and thermal stability as bisphenol A epoxy resin. Moreover, under the catalytic action of Zn^{2+} , the cured TEP possessed dynamic trans-esterification reaction, which brought the sample stress relaxation and permitted reparability to the samples [96].

3.2.2 Cinnamic acid derived polymers

Resins made from compounds with more robust structures such as aromatic rings are more thermostable and preferable than more flexible compounds (like aliphatic chains) [4]. Lignin is used in many resin formulations, but its limited solubility is often a problem in the development and processing of new materials [97, 98]. Monolignols or lignin-derived phenolic compounds precursors contain the same desirable aromatic structure, and there is no problem of solubility of lignin macromolecule [4].

Kim and coworkers reacted cinnamic acid with a series of epoxy resins to produce a biobased cross-linked resin [99]. Then, the functional epoxy resin is cured with photo curing to make it have better thermostability and optical properties. Xin and coworkers

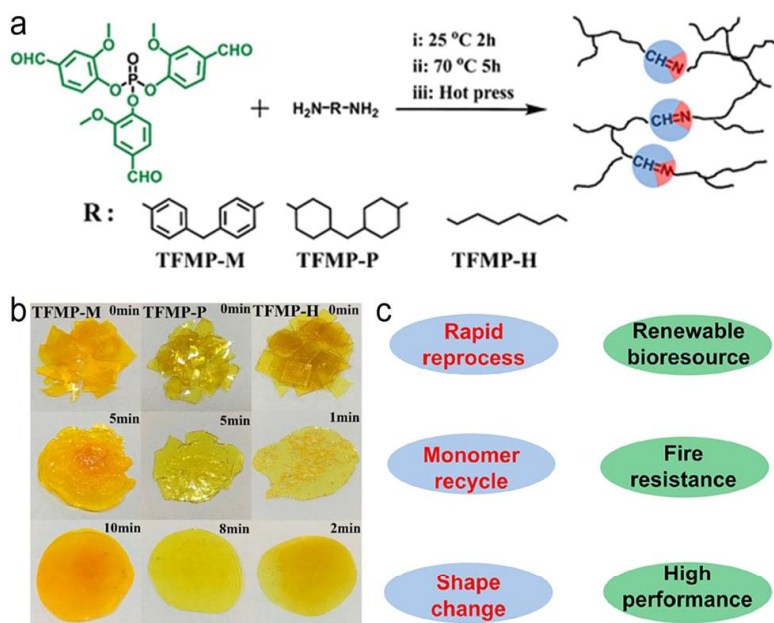


Figure 14: (a) Preparation scheme of the malleable Schiff base covalent adaptable networks; (b) Reprocess of Schiff base covalent adaptable networks at different times at 180 °C under 15 MPa pressure; (c) Outstanding qualities of the malleable thermosets based on lignin derivative vanillin [95].



[100] functionalized cinnamic acid by two synthetic steps (allylation then epoxidation) to form a double functional epoxide monomer. Then, this epoxy monomer was cross-linked with maleic anhydride derivatives as curing agents to produce a series of resins (Figure 15). The curing behaviors of the resins were alike to those of petroleum-based resins. Fache and coworkers [91] prepared epoxide resins from aromatic monomers mixture generated from the degradation process of lignin to vanillin. The mixtures (vanillin, *p*-hydroxybenzaldehyde, syringic acid, and syringaldehyde) suffered from Dakin oxidation to produced di-phenolic compounds. The obtained compound then reacts with epichlorohydrin to form the relevant epoxy compound [91].

3.2.3 *p*-coumaric acid derived polymers

Modified monolignols or precursors are more widely used in the literature because they produce monomer with good thermal stability.

Kaneko and his colleagues synthesized a biopolymer made by melt condensation of *p*-coumaric acid with sodium acetate and acetic acid. This is the first example of a liquid crystal polymer made from a single natural monomer, as shown in Figure 16 [101]. The polymer was prepared by photoinitiated cycloaddition in a liquid crystalline state and proved to have excellent cell compatibility [101]. Kaneko subsequently produced a biodegradable hyper-branched copolymer from the polymerization of 3,4-dihydrocinic cinnamate and *p*-coumaric acid [102]. The resulting material has a sufficiently high T_g to be processed, photoreactivity in liquid crystalline state, and readily degrades by hydrolysis. Matsusaki et al. copolymerized *p*-coumaric acid with lactic acid with and without solvent [103]. Although the content of *p*-coumaric acid in copolymers is much

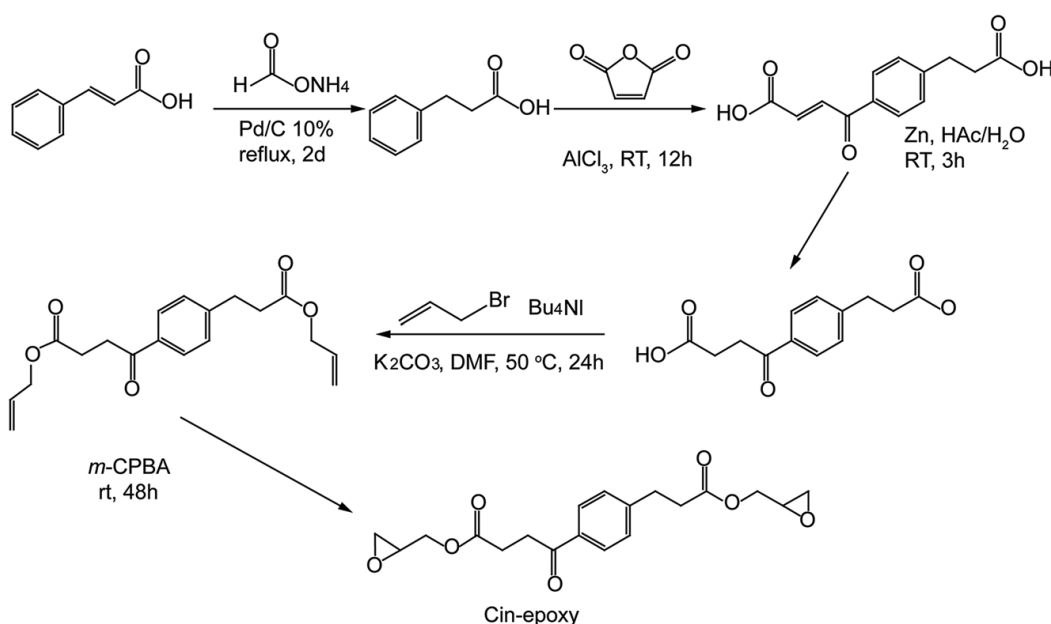


Figure 15: Synthesis scheme of cinnamic acid-derived epoxy [100].



lower than that of lactic acid, the obtained copolymers have good photoreactivity, high solubility, and biodegradability. Spiliopoulos and coworkers synthesized copolymer from *p*-hydroxy benzaldehyde and *p*-coumaric acid with thionyl chloride as catalyst under the condition of alkali [104]. The results showed that although copolymers are amorphous, once crosslinked, T_g of the resultant polyesters showed a significant increase.

The brittleness of the resulting *p*-coumaric acid derived polyester materials can be reduced by introducing other functionalities. Thi and his colleagues [105] reported a way to synthesize a macromonomer by coupling 3,4-diacetoxycinnamoyl chloride with low molecular weight poly(L-lactic acid). The macro-monomer was polymerized with sodium acetate without solvents to form branched, polydispersion, and high-molecular-weight polyester [106]. The mechanical and thermal characteristics of polymers were superior than those of poly(L-lactic acid), and the degradation rate is accelerated with the addition of acetylated coumaric acid. Nagata and coworkers [107] prepared a macromonomer through capping both adipoyl dichloride with hydroxyl functionalized *p*-coumaric acid to generate a novel dichloride macro-monomer, as shown in Figure 17. The macro-monomer was further condensed with 1,6-hexanediol to prepare a high molecular weight copolyester resin.

3.2.4 Ferulic acid derived polymers

Ferulic acid can be achieved through hydrolysis of lignin based on alkalis or enzymes [108]. With an annual output of ~318 tons, it is one of the available phenolic molecular compound from lignin, second only to vanillin [109].

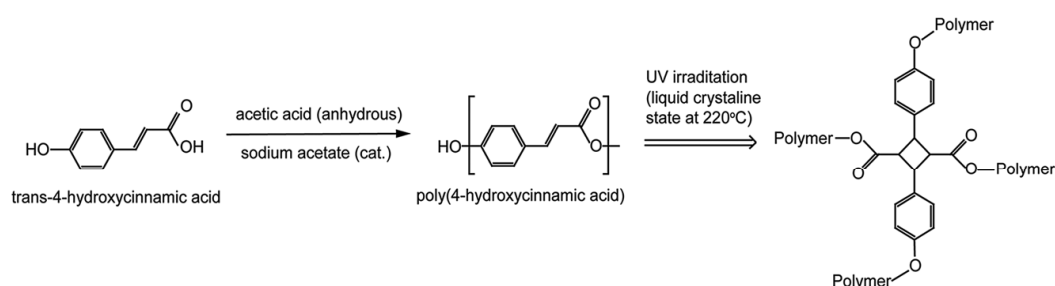


Figure 16: Projected cycloaddition of poly(*p*-coumaric acid) in a liquid crystalline state (220 °C) [101].

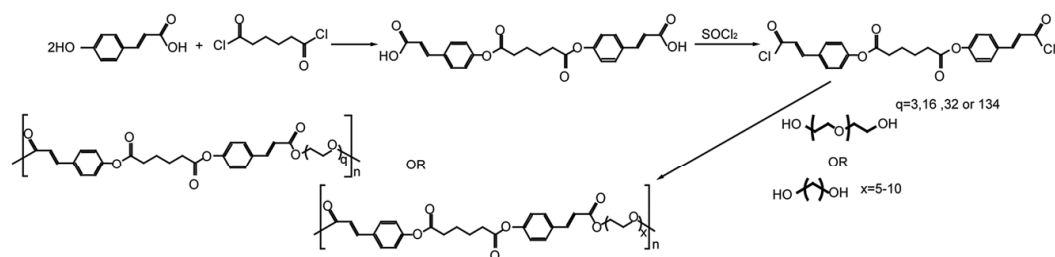


Figure 17: Scheme of *p*-coumaric acid dimer-based polyester from either aliphatic diols or polyethylene glycol [107].



Oulame and coworkers [110] prepared ferulic acid-based dimers via polycondensation of aliphatic diols with ferulic acid of different chain lengths or isosorbide. Then, the obtained diol was polymerized with 1,6-hexamethylene diisocyanate or 1,4-tolulene diisocyanate to produce a series of polyurethanes (Figure 18). These polyurethanes can be prepared with or without solvents, and showed high thermostability and controllable T_g . Although the molecular weight of these products is generally low, they support the concept of polyurethane material being synthesized from monolignol or its precursors. Chen and coworkers [111] recently synthesized polyurethane based on a dimeric cresol-based monomer. After dimerization, cresol reacts with epichlorohydrin to form a double epoxide, and then with CO_2 to produce a corresponding bis(cyclic carbonate) monomer. Then, the double functional monomer was reacted with hexamethylenediamine or isophoronediamine to generate polyurethane with excellent thermostability.

Polyphenoxyamine is a special phenolic resin, in which hexane heterocycles are synthesized via condensation of a phenol and an amine in the presence of formaldehyde [112]. The curing temperature and the physical properties of the polymer can be controlled according to the substitution of amine or phenol. Comí and his colleagues [113] synthesized a series of benzoxazines via the condensation of carboxylic acid (ferulic and coumaric acid) with formaldehyde and 1,3,5-triphenylhexahydro-1,3,5-triazine. These monomers require a curing temperature higher than their thermostable temperature, leading to decomposition instead of polymerization. Therefore, adding boron trifluoride as a ring opening catalyst can reduce curing temperature and form a variety of polymeric products, as shown in Figure 19. These products have proven to be thermostable and comparable to petroleum-based products [4].

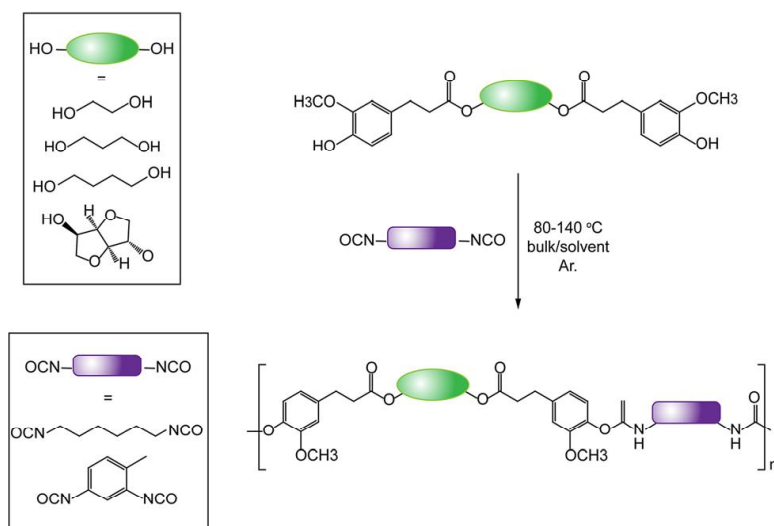


Figure 18: Scheme of the eight poly(ester-urethane) from ferulic acid-based diols [110].



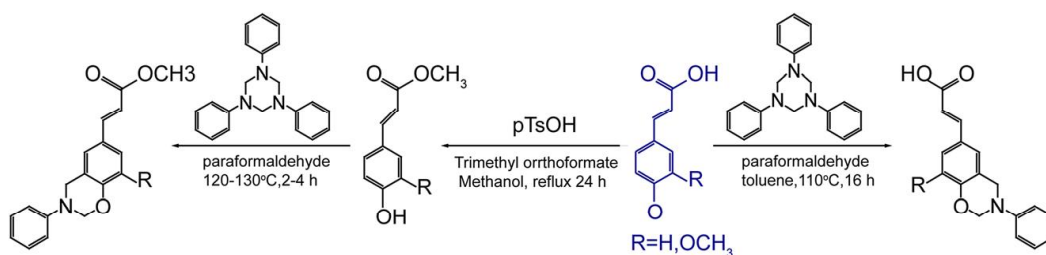


Figure 19: Synthetic scheme of *p*-coumaric acid and ferulic acid-based benzoxazines [113].

4 Lignin-based polymer composites

Polymer composites are materials achieved through strengthening polymer matrix with appropriate fibers/particle materials and can be defined in different ways [114–117]. The properties of the matrix vary from a synthetic to natural polymer depending on the application [118]. In most applications, matrices are obtained from synthetic polymers, more recently, biopolymers have been used as matrix materials [116]. Generally speaking, reinforcement materials are fibers or synthetic inlays, such as carbon, glass, and so on, or natural hemp, flax, coconut trees, bagasse, and so on. In recent years, the lignin-based polymer composites have drawn much attention in the research field at home and abroad [119, 120]. Lignin is being vigorously used as a low-cost, ecofriendly reinforcement material for the fabrication of high-performance composite materials [121, 122]. In the next section, the study of lignin-based polymer composites is described.

4.1 Lignin-based thermoplastic polymer composites

The ongoing lignin valorization studies, if successful, could make sustainable bio-manufacturing initiatives a reality. Thermoplastic plastics from lignin can be either lignin polymer alloys or functional (modified) lignin, or lignin copolymers.

Some researchers have developed lignin-enhanced thermoplastic composites. For example, a single screw extruder was used to prepare poly(ethylene terephthalate) (PET) composites reinforced with lignin [123]. The effects of lignin concentration on melting behavior and thermal stability were explored in detail by thermogravimetric analysis [123]. The results show that the content of lignin in the composites has great influence on the thermal stability. Experiments in the air show that adding lignin to the polymer composites is beneficial to forming protective surface shields, which has been found to reduce the diffusion of oxygen to the polymer body. Compared with pure PET, lignin in the composites also has a strong influence on the melt behavior of annealed specimens, which promotes the crystallization process [123]. Barzegar [124] have reported on the rheological behaviors and mechanical properties of lignin-reinforced polystyrene composites. Different polystyrene/lignin composites were developed by adding or not adding a linear triblock copolymer of styrene ethylbutylene styrene



(SEBS). The results indicated that the additive amount of lignin in the composites has significant impacts on the mechanical properties of the research system [124]. For instance, the bending and torsion modulus increase with the increase of the lignin load while its tensile properties decrease. The compatibilizer can remarkably improve the bending and tensile modulus of lignin/PS composites in this study. The increase in modulus is due to the improvement of interfacial adhesion between lignin and PS [124].

Both biomass and polymer industries are interested in developing low-cost lignin/polymer composites with excellent mechanical properties. Nevertheless, because lignin tends to accumulate in polymer matrix, macroscopical phase separation at micron scale is usually obtained. The resulting lignin/polymer composites usually exhibit significantly less strength and toughness than the neat polymers [125]. In order to solve this problem, researchers have conducted works from different perspectives.

Among the synthetic biodegradable polymers, the poly(butylene adipate-co-terephthalate) (PBAT) is an aliphatic-aromatic polyester with outstanding flexibility, mechanical properties and biocompatibility, and is an ideal choice in the fields of packaging film, agriculture, and medical devices [126]. However, the high cost and low photostability of PBAT limit its widespread commercial use. Modified lignin derivatives can improve the UV-blocking, mechanical properties, and thermostability of the composites with PBAT as matrix [127]. Recently, Wang and coworkers have reported on a novel biodegradable lignin- (30–50 wt%)based composites with excellent properties, which are prepared by adding lignin into the PBAT matrix [127]. In order to improve the compatibility of lignin and PBAT, lignin was modified by a green esterification method under microwave assistance and without solvent [127] (Figure 20a and b). The characteristic of modified lignin has fewer inter-unit linkages, higher molecular weight, lower T_g and improved hydrophobicity. In addition, the mechanical properties of the lignin/PBAT composites have been enhanced controllably by adding maleic anhydride (MAH) [127] (Figure 20c). The obtained lignin/PBAT composites have excellent UV resistance and fracture elongation, even at 40% of lignin loading, improved by 500% compared with that of unmodified specimens [127].

Generally, lignin does not form a compatible mixture with acrylonitrile butadiene styrene (ABS) thermoplastic matrix without being modified or with the assistance of the compatibility agent. Instead of using chemical modification with high cost and high energy consumption, Naskar and coworkers [126] have devised a simpler solution that improves the ductility and strength of the material through self-assembly of lignin with poly(ethylene oxide) (PEO) in ABS substrates induced by a hydrogen bonded interaction (Figure 21). In this study, a thermoplastic ABS polymer with ~30 wt% lignin was prepared through adding 10 wt% PEO, which has similar properties to pure resin. The ABS/lignin compositions containing PEO showed enhanced interface bonding of lignin with the thermoplastic ABS matrix. And even further, the formula was reinforced with short carbon fiber without pretreatment, exhibited outstanding mechanical properties and is suitable for automotive use [126].



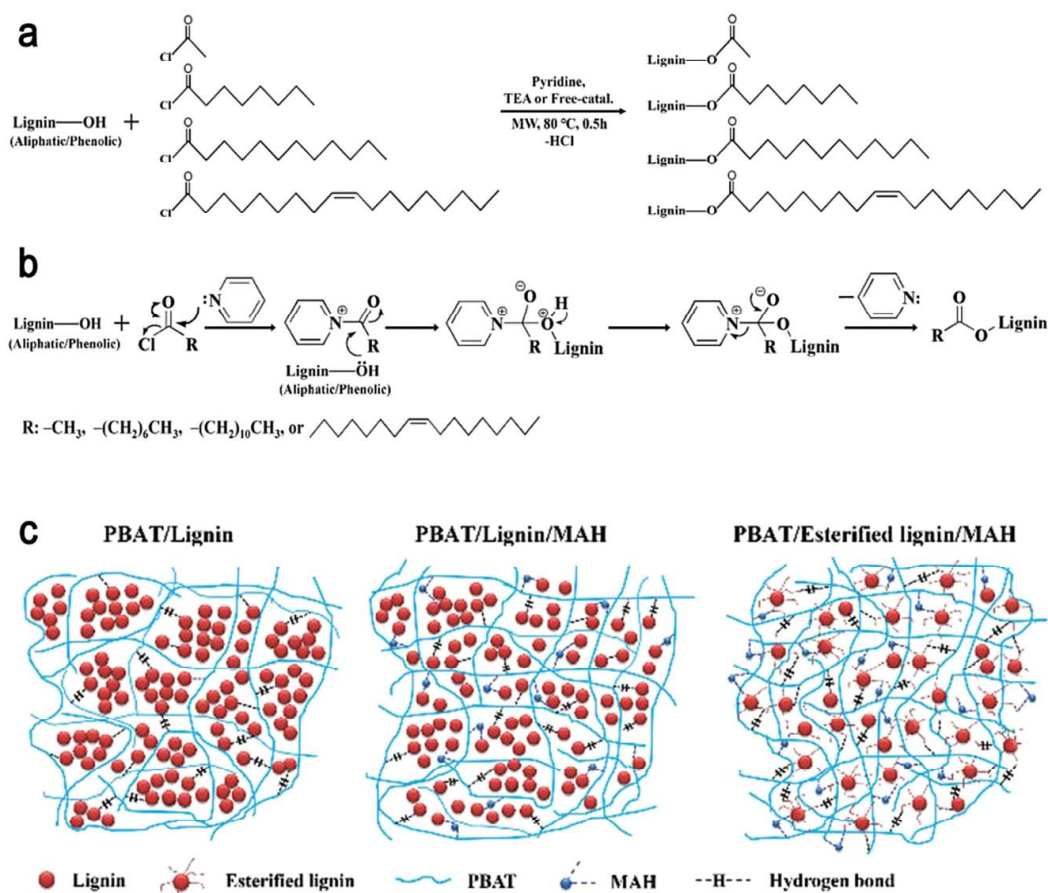


Figure 20: (a) schematic diagram of esterification of the phenolic/aliphatic hydroxyl groups of lignin with C_2 – C_{18} acyl chlorides (TEA: triethylamine, MW: microwave); (b) the process of pyridine catalyzed lignin esterification with acyl chlorides; (c) schematic diagram of lignin/PBAT composites with esterified lignin (MAH as a compatibilizer) and unmodified lignin [127].

The issue of the easy agglomeration of lignin in a polymer matrix can also be improved recently by lignin nanoparticles (LNPs). Qiu et al. [128] have reported a simple method for preparing nanostructured biomimetic polymer materials by incorporating lignosulfonic acid (LA) into a biodegradable poly(vinyl alcohol) (PVA) matrix in the form of interspersed nanoparticles. Amphiphilic LA was prepared from sodium ligninsulfonate (LS) and then dispersed in water to form uniform nanoparticles. By mixing PVA with lignin solution, a biomimetic nanoparticle-separation structure and a strong intermolecular sacrificial hydrogen bond were obtained. As shown in Figure 22, this LNPs/PVA composite showed a maximum toughness of $(172 \pm 5) \text{ J/g}$, as well as a strong tensile strength of 98.2 MPa and a large fracture strain of 282%, which are much better than most engineering plastics. LA, which measures several hundred nanometers in size, was thought to be secondary spherical particles composed of loosely aggregated primary LA (several nanometers). The fragmentation of the secondary spherical particles and the scattering of primary nanoparticles in the PVA matrix lead to the dynamic fracture and reconstruction of the sacrificial



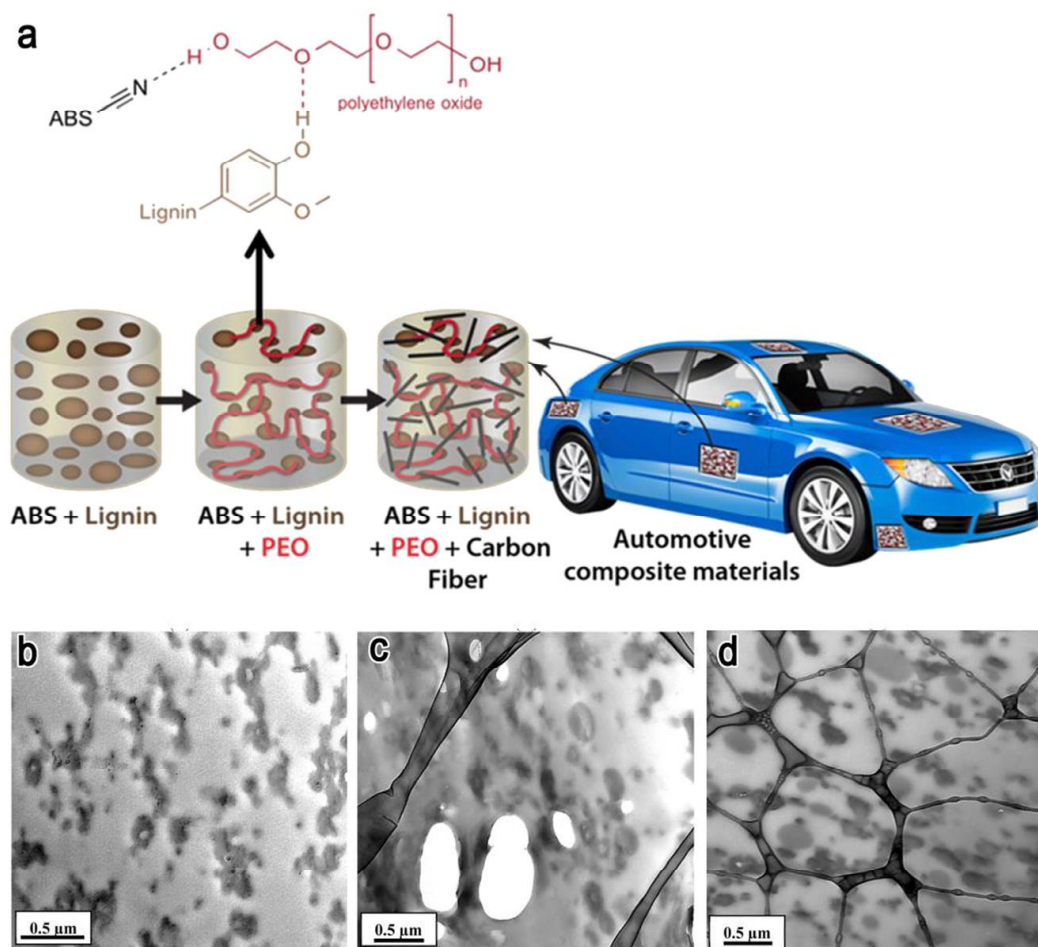


Figure 21: (a) Schematic diagram of lignin-based ABS polymer composites and short carbon fiber reinforced composites prepared from a blend improved with PEO; TEM micrographs of (b) neat ABS, (c) ABS/lignin (70/30), and (d) ABS/lignin/PEO (70/27/3) blends [126].

hydrogen bonds that were densely confined in the interphase between LA granules and PVA (Figure 23) [128]. This work is of great significance in the field of lignin-based composites and nanolignin applications [125].

4.2 Lignin-based rubber composites

A variety of polymer composites were developed with rubber as matrix and lignin as reinforcing agent or hard segment phase. Xiao and coworkers [129] have developed lignin enhanced styrene-butadiene rubber (SBR)/lignin-LDH (layered double hydroxide) composites using a melt blending method. In this research, layered dihydroxyl compounds (lignin-LDH) were synthesized by *in situ* synthesis method. The results showed that the mechanical properties of lignin-LDH/SBR were enhanced compared with the LDH/SBR composite samples [129]. Jiang and coworkers [130] have prepared nanocomposites by means of coprecipitation of lignin cationic polyelectrolyte



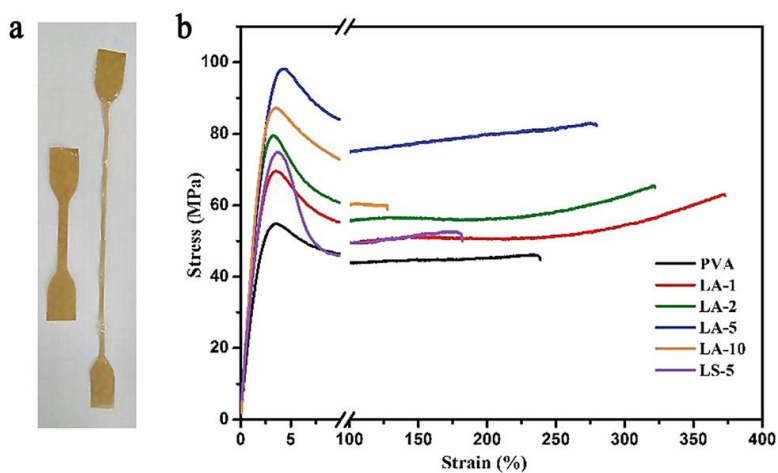


Figure 22: (a) Photo of the LA-5 film before and after extension. (b) Stress–strain curves of PVA/LA nanocomposites [128].

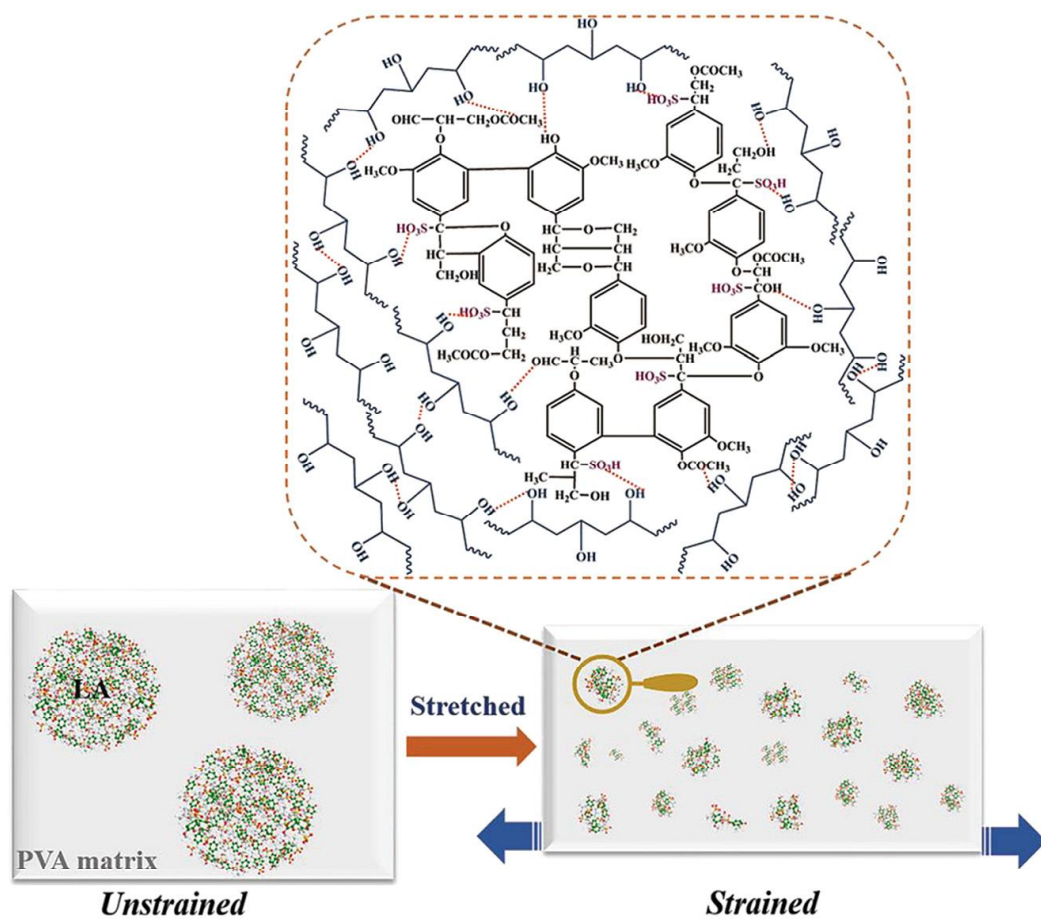


Figure 23: Enhancement mechanism of LA in PVA film [128].



complex and colloidal rubber latex. In this research, colloidal lignin-poly(diallyldimethylammonium chloride) (PDADMAC) complexes (LPCs) was prepared by self-assembly strategy. The homogenous distribution of LPCs in natural colloidal rubber latex was determined by SEM and dynamic mechanical analysis (DMA) analysis. The obtained nanocomposites showed improved thermal and mechanical properties [130].

In above cases, however, lignin was simply used as an reinforcing filler and no attempt is made to build advantageous interfacial interactions between the lignin and the rubber matrix.

Recently, Brook and coworkers [131] have developed a strategy to efficiently modify or disintegrate lignin with hydrosilanes of the Piers-Rubinsztajn (PR) reaction, which was catalyzed by $B(C_6F_5)_3$ (BCF, tris(pentafluorophenyl)borane). This process results in the conversion of phenol, aryl methoxy, and other ethers into silyl ethers or alkyl groups (Figure 24a and b). As a result, the lignin surface becomes silicified, making it more compatible with hydrophobic polymers. As a result, the lignin surfaces become silicified, rendering it more compatible with hydrophobic polymers [131]. This makes the raw softwood lignin as an enhanced filler or crosslinking additive for silicone rubber in a one-pot process. The resulting lignin-silicone elastomer has remarkable mechanical properties, even when filled with up to 40 wt% lignin. In addition, the research has presented a summary of the chemistry used in blowing foams and the ability to control the foam structures through changing treatment conditions and formulations (Figure 24c). This preparation strategy of lignin-based composites provides a new opportunities for better utilization of lignin involving silicone rubber [131, 132].

Recently, Naskar et al. [133] introduced a new method for synthesizing a novel class of high-performance renewable thermoplastic elastomers from acrylonitrile butadiene rubber (NBR) by introducing nanoscale dispersed lignin. The internal morphology and properties of this material can be regulated by a temperature-controlled mixture. The strategy is to replace the polystyrene fragments with lignin, similar to that found in soft matrices, as shown in Figure 25a and b. To further regulated lignin domain sizes, researchers selected NBR with 33, 41 and 51% acrylonitrile contents (namely NBR-41 and NBR-51, respectively) with Kraft softwood lignin (methanol extracted low-molecular-weight fractions) at ratio of 50/50 (w/w). Transmission electron microscopy (TEM) images of lignin/NBR-33 blends show the size of 0.2–2 μm domains (Figure 25c). The stress–strain curves of this mixture showed a typical behavior of reinforcement elastomers (Figure 25d). The tensile strength of the blend increases to above 30 MPa. This strain hardening is usually observed only in natural rubber because of the crystallization induced by strain (it's not common in nitrile rubber matrix). This new class of elastomers has great potential for sustainable products in the biomass industry [133].



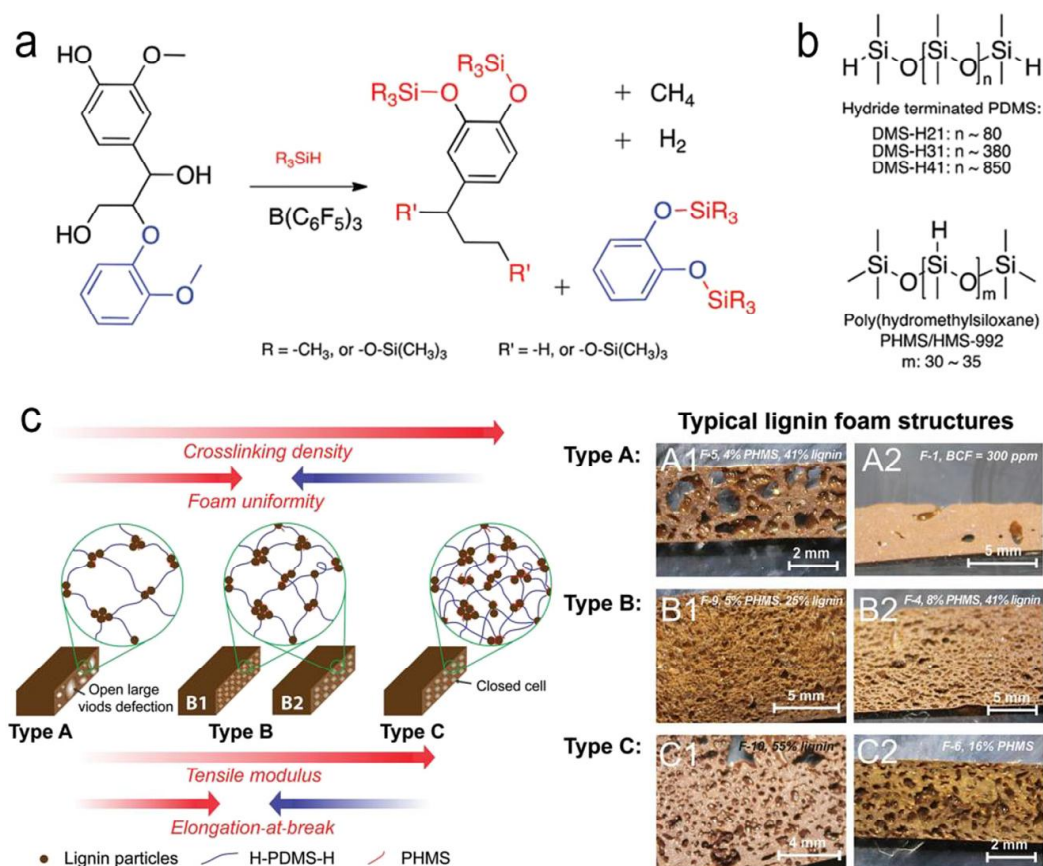


Figure 24: (a) Typical Piers–Rubinsztajn reactions at phenolic linkages of lignin; (b) The chemical structures of terminated PDMS and poly-(hydromethylsiloxane); (c) schematic diagram of lignin-silicone foam structure, and the mechanical properties they created: The tensile modulus increases with the increase of crosslinking density, and the elongation of fracture depends on the intersecting density and uniformity of foam [131].

4.3 Lignin-based thermosetting polymer composites

Developing thermosetting polymer composites using lignin as an additive is also reported. For example, Khalil and coworkers [134] have prepared epoxy matrix-based composites with empty fruit bunches as the reinforcement phase. In this study, lignin extracted from the black liquor was used as the curing agent in different ratios 15, 20, 25, and 30%, respectively. The results showed that the polymer composites with 25% lignin as the curing agent showed better mechanical properties than the composite materials prepared with commercial curing agent [134]. Doherty and coworkers [135] have developed lignin reinforced phenol-formaldehyde (PF) composites and applied them as coating with bagasse fibers as another reinforcement phase. The wetting properties showed that lignin and lignin-PF resin membranes are effective water-barrier coatings. Nevertheless, the contact angles of the lignin-PF resin membranes were found to be obviously smaller than that of commercial wax film. Lignin-based bio-oil was developed by Stanzone and his colleagues [136] for the preparation of biobased vinyl ester resin. In



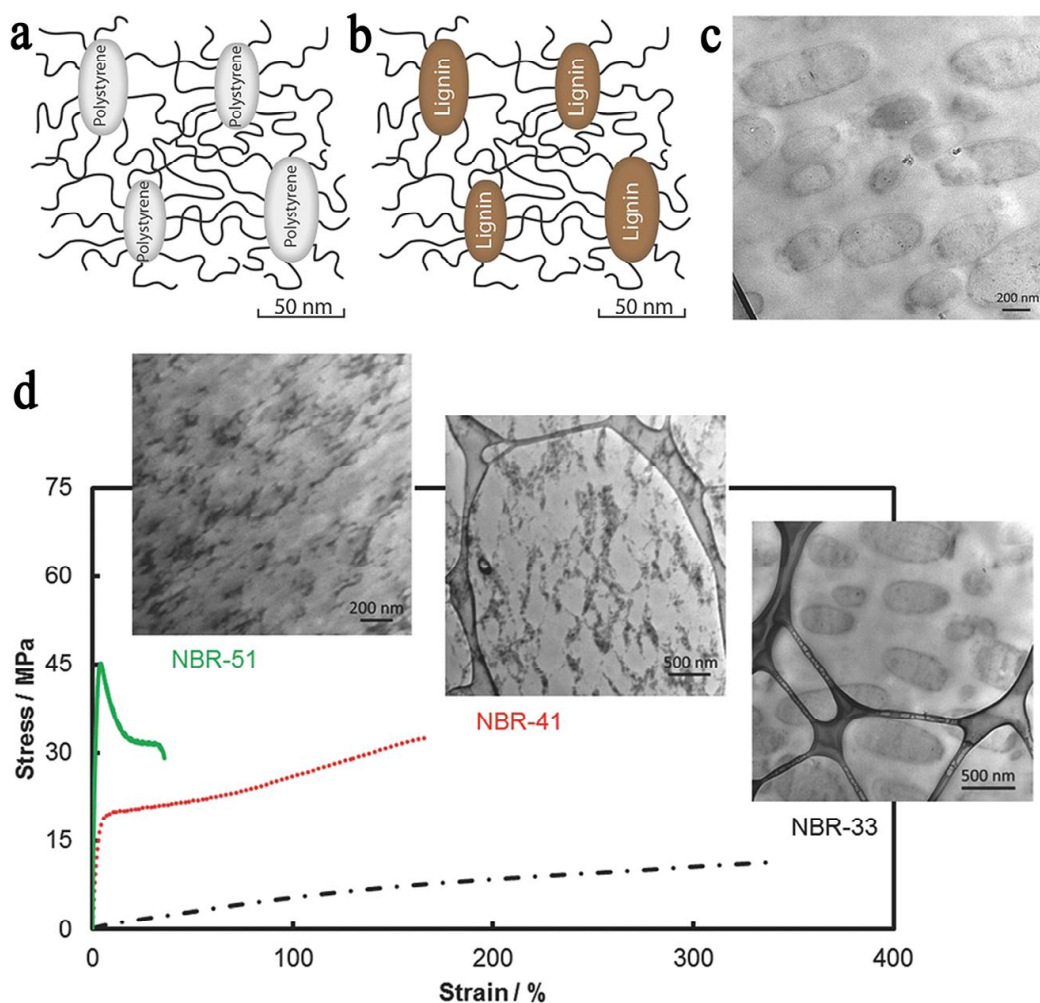


Figure 25: (a) Morphologic diagram of styrene-butadiene-styrene block copolymer. (b) Schematic diagram of lignin-based multiphase polymer in soft matrix. (c) TEM image of NBR-33/Kraft lignin composite (50/50). (d) Stress-strain curves of tensile mechanical strength of reactive composites of methanol extracted fraction of Kraft lignin and their corresponding TEM images [133].

this research, a lignin-based bio-oil mimic was prepared from methyl methacrylate and applied as a low viscosity vinyl ester resin. The thermal mechanical properties and thermostability of this thermoset were competitive with the commercially available petroleum-based and vinyl ester-based thermoset polymers [136].

5 Conclusions and outlooks

In the past 10 years, the field of lignin-based polymeric materials and composites has made great progress, and there is still room for innovation. In addition, it is important to recognize the technology of chemically modified lignin into products with integrated value without the use of expensive reagents or complex synthesis pathways. Indeed, because of their benefits, lignin-based polymers are a new class of ecofriendly and



low-cost material. Despite the many advantages of lignin, the great differences and complexity of its structure have hampered the expansion from laboratory to industrial use. In order to overcome this limitation, a great deal of research should be undertaken to better understand the physics and chemistry of natural lignin. Advanced extraction methods or pretreatment processes should also be developed for lignin purification. Based on the current literature, compared with the traditional synthetic fiber reinforced polymer composites, the application of nano- or micro-sized lignin reinforced polymers still remain highly conceivable. As discussed in this chapter, in addition to the development of polymeric composites, the mechanical, physical and physicochemical properties of lignin and various polymer substrates can be utilized toward the commercialization of low-cost and ecofriendly lignin-based materials for a variety of applications.

Author contributions: All the authors have accepted responsibility for the entire content of this submitted manuscript and approved submission.

Research funding: None declared.

Conflict of interest statement: The authors declare no conflicts of interest regarding this article.

References

1. Ragauskas AJ, Beckham GT, Biddy MJ, Chandra R, Chen F, Davis MF, et al. Lignin valorization: improving lignin processing in the biorefinery. *Science* 2014;344:1246843.
2. Luterbacher JS, Azarpira A, Motagamwala AH, Lu F, Ralph J, Dumesic JA. Lignin monomer production integrated into the γ -valerolactone sugar platform. *Energy Environ Sci* 2015;8: 2657–63.
3. Shuai L, Amiri MT, Questell-Santiago YM, Heroguel F, Li YD, Kim H, et al. Formaldehyde stabilization facilitates lignin monomer production during biomass depolymerization. *Science* 2016;354:329–33.
4. Upton BM, Kasko AM. Strategies for the conversion of lignin to high-value polymeric materials: review and perspective. *Chem Rev* 2016;116:2275–306.
5. Li C, Zhao X, Wang A, Huber GW, Zhang T. Catalytic transformation of lignin for the production of chemicals and fuels. *Chem Rev* 2015;115:11559–624.
6. Sun Z, Fridrich B, de Santi A, Elangovan S, Barta K. Bright side of lignin depolymerization: toward new platform chemicals. *Chem Rev* 2018;118:614–78.
7. Kai D, Tan MJ, Chee PL, Chua YK, Yap YL, Loh XJ. Towards lignin-based functional materials in a sustainable world. *Green Chem* 2016;18:1175–200.
8. Gioia C, Lo Re G, Lawoko M, Berglund L. Tunable thermosetting epoxies based on fractionated and well-characterized lignins. *J Am Chem Soc* 2018;140:4054–61.
9. Liu H, Chung H. Lignin-based polymers via graft copolymerization. *J Polym Sci Polym Chem* 2017; 55:3515–28.
10. Doherty WO, Mousavioun P, Fellows CM. Value-adding to cellulosic ethanol: lignin polymers. *Ind Crop Prod* 2011;33:259–76.



11. Zakzeski J, Bruijninx PCA, Jongerius AL, Weckhuysen BM. The catalytic valorization of lignin for the production of renewable chemicals. *Chem Rev* 2010;110:3552–99.
12. Gordobil O, Robles E, Egüés I, Labidi J. Lignin-ester derivatives as novel thermoplastic materials. *RSC Adv* 2016;6:86909–17.
13. Sen S, Patil S, Argyropoulos DS. Thermal properties of lignin in copolymers, blends, and composites: a review. *Green Chem* 2015;17:4862–87.
14. Thakur VK, Thakur MK, Raghavan P, Kessler MR. Progress in green polymer composites from lignin for multifunctional applications: a review. *ACS Sustain Chem Eng* 2014;2:1072–92.
15. Thakur VK, Thakur MK. Recent advances in green hydrogels from lignin: a review. *Int J Biol Macromol* 2015;72:834–47.
16. Liu W-J, Jiang H, Yu H-Q. Thermochemical conversion of lignin to functional materials: a review and future directions. *Green Chem* 2015;17:4888–907.
17. Zhao S, Abu-Omar MM. Materials based on technical bulk lignin. *ACS Sustain Chem Eng* 2021;9: 1477–93.
18. Vishtal AG, Kraslawski A. Challenges in industrial applications of technical lignins. *BioResources* 2011;6:3547–68.
19. Duval A, Lawoko M. A review on lignin-based polymeric, micro-and nano-structured materials. *React Funct Polym* 2014;85:78–96.
20. Sternberg J, Sequerth O, Pilla S. Green chemistry design in polymers derived from lignin: review and perspective. *Prog Polym Sci* 2021;113:101344.
21. Balakshin MY, Capanema EA, Sulaeva I, Schlee P, Huang Z, Feng M, et al. New opportunities in the valorization of technical lignins. *ChemSusChem* 2021;14:1016–36.
22. Calvo-Flores FG, Dobado JA. Lignin as renewable raw material. *ChemSusChem* 2010;3:1227–35.
23. Hu J, Zhang Q, Lee D-J. Kraft lignin biorefinery: a perspective. *Bioresour Technol* 2018;247:1181–3.
24. Gellerstedt G. Softwood Kraft lignin: raw material for the future. *Ind Crop Prod* 2015;77:845–54.
25. Crestini C, Lange H, Sette M, Argyropoulos DS. On the structure of softwood Kraft lignin. *Green Chem* 2017;19:4104–21.
26. Gratzl JS, Chen C-L. Chemistry of pulping: lignin reactions. Washington, DC, USA: ACS Publications; 2000.
27. Deshpande R, Giummarella N, Henriksson G, Germgård U, Sundvall L, Grundberg H, et al. The reactivity of lignin carbohydrate complex (LCC) during manufacture of dissolving sulfite pulp from softwood. *Ind Crop Prod* 2018;115:315–22.
28. Aro T, Fatehi P. Production and application of lignosulfonates and sulfonated lignin. *ChemSusChem* 2017;10:1861–77.
29. Fatehi P, Chen J. Extraction of technical lignins from pulping spent liquors, challenges and opportunities, Production of biofuels and chemicals from lignin. Heidelberg, Germany: Springer; 2016:35–54 pp.
30. El Hage R, Brosse N, Sannigrahi P, Ragauskas A. Effects of process severity on the chemical structure of Miscanthus ethanol organosolv lignin. *Polym Degrad Stabil* 2010;95:997–1003.
31. Konnerth H, Zhang J, Ma D, Prechtel MH, Yan N. Base promoted hydrogenolysis of lignin model compounds and organosolv lignin over metal catalysts in water. *Chem Eng Sci* 2015;123:155–63.
32. El Hage R, Brosse N, Chrusciel L, Sanchez C, Sannigrahi P, Ragauskas A. Characterization of milled wood lignin and ethanol organosolv lignin from miscanthus. *Polym Degrad Stabil* 2009;94: 1632–8.
33. Lou R, Wu S-B. Products properties from fast pyrolysis of enzymatic/mild acidolysis lignin. *Appl Energy* 2011;88:316–22.
34. Lei M, Wu S, Liang J, Liu C. Comprehensive understanding the chemical structure evolution and crucial intermediate radical in situ observation in enzymatic hydrolysis/mild acidolysis lignin pyrolysis. *J Anal Appl Pyrol* 2019;138:249–60.



35. Schubert WJ, Nord F. Investigations on lignin and lignification. II. The characterization of enzymatically liberated lignin. *J Am Chem Soc* 1950;72:3835–8.
36. Schubert W, Passannante A, Stevens GD, Bier M, Nord F. Investigations on lignin and lignification. XIII. Electrophoresis of native and enzymatically liberated Lignins 1. *J Am Chem Soc* 1953;75:1869–73.
37. Jiang B, Yao Y, Liang Z, Gao J, Chen G, Xia Q, et al. Lignin-based direct ink printed structural scaffolds. *Small* 2020;16:e1907212.
38. Ren T, Qi W, Su R, He Z. Promising techniques for depolymerization of lignin into value-added chemicals. *ChemCatChem* 2019;11:639–54.
39. Laurichesse S, Avérous L. Chemical modification of lignins: towards biobased polymers. *Prog Polym Sci* 2014;39:1266–90.
40. del Río JC, Rencoret J, Gutiérrez A, Elder T, Kim H, Ralph J. Lignin monomers from beyond the canonical monolignol biosynthetic pathway: another brick in the wall. *ACS Sustain Chem Eng* 2020;8:4997–5012.
41. Thornburg NE, Pecha MB, Brandner DG, Reed ML, Vermaas JV, Michener WE, et al. Mesoscale reaction–diffusion phenomena governing lignin-first biomass fractionation. *ChemSusChem* 2020;13:4495–509.
42. Liu X, Bouxin FP, Fan J, Budarin VL, Hu C, Clark JH. Recent advances in the catalytic depolymerization of lignin towards phenolic chemicals: a review. *ChemSusChem* 2020;13:4296.
43. Da Cunha C, Deffieux A, Fontanille M. Synthesis and polymerization of lignin-based macromonomers. III. Radical copolymerization of lignin-based macromonomers with methyl methacrylate. *J Appl Polym Sci* 1993;48:819–31.
44. Azhar SS, Ahn DJ. Purification of monomers leads to high-quality lignin macromonomers. Bristol, England: IOP Conference Series: Materials Science and Engineering, IOP Publishing; 2019:012021 p.
45. Petrović ZS. Polyurethanes from vegetable oils. *Polym Rev* 2008;48:109–55.
46. Sen S, Martin JD, Argyropoulos DS. Review of cellulose non-derivatizing solvent interactions with emphasis on activity in inorganic molten salt hydrates. *ACS Sustain Chem Eng* 2013;1:858–70.
47. Aniceto JP, Portugal I, Silva CM. Biomass-based polyols through oxypropylation reaction. *ChemSusChem* 2012;5:1358–68.
48. Lin S, Huang J, Chang PR, Wei S, Xu Y, Zhang Q. Structure and mechanical properties of new biomass-based nanocomposite: castor oil-based polyurethane reinforced with acetylated cellulose nanocrystal. *Carbohydr Polym* 2013;95:91–9.
49. Nam G-Y, Oh J-S, Park I-K, Luong ND, Yoon H-K, Lee S-H, et al. High molecular-weight thermoplastic polymerization of Kraft lignin macromers with diisocyanate. *BioResources* 2014;9:2359–71.
50. Hu TQ. Chemical modification, properties, and usage of lignin. New York, USA: Springer; 2002.
51. Xue B-L, Wen J-L, Sun R-C. Lignin-based rigid polyurethane foam reinforced with pulp fiber: synthesis and characterization. *ACS Sustain Chem Eng* 2014;2:1474–80.
52. Pohjanlehto H, Setälä HM, Kiely DE, McDonald AG. Lignin-xylaric acid-polyurethane-based polymer network systems: preparation and characterization. *J Appl Polym Sci* 2014;131:1–7.
53. Yiamsawas D, Baier G, Thines E, Landfester K, Wurm FR. Biodegradable lignin nanocontainers. *RSC Adv* 2014;4:11661–3.
54. Zhang Y, Liao J, Fang X, Bai F, Qiao K, Wang L. Renewable high-performance polyurethane bioplastics derived from lignin–poly(ϵ -caprolactone). *ACS Sustain Chem Eng* 2017;5:4276–84.
55. Mavila S, Sinha J, Hu Y, Podgórski M, Shah PK, Bowman CN. High refractive index photopolymers by Thiol–Yne “click” polymerization. *ACS Appl Mater Interfaces* 2021;13:15647–58.
56. Yilmaz G, Yagci Y. Light-induced step-growth polymerization. *Prog Polym Sci* 2020;100:101178.
57. Cao Y, Liu Z, Zheng B, Ou R, Fan Q, Li L, et al. Synthesis of lignin-based polyols via thiol-ene chemistry for high-performance polyurethane anticorrosive coating. *Compos B Eng* 2020;200:108295.



58. Braun E, Levin BC. Polyesters: a review of the literature on products of combustion and toxicity. *Fire Mater* 1986;10:107–23.
59. Guo Z-X, Gandini A. Polyesters from lignin—2. The copolyesterification of Kraft lignin and polyethylene glycols with dicarboxylic acid chlorides. *Eur Polym J* 1991;27:1177–80.
60. Thanh Binh NT, Luong ND, Kim DO, Lee SH, Kim BJ, Lee YS, et al. Synthesis of lignin-based thermoplastic copolyester using Kraft lignin as a macromonomer. *Compos Interface* 2009;16: 923–35.
61. Bonini C, D'Auria M, Emanuele L, Ferri R, Pucciariello R, Sabia AR. Polyurethanes and polyesters from lignin. *J Appl Polym Sci* 2005;98:1451–6.
62. Malkappa K, Jana T. Simultaneous improvement of tensile strength and elongation: an unprecedented observation in the case of hydroxyl terminated polybutadiene polyurethanes. *Ind Eng Chem Res* 2013;52:12887–96.
63. Sivasankarapillai G, McDonald AG. Synthesis and properties of lignin-highly branched poly (ester-amine) polymeric systems, *Biomass Bioenergy* 2011;35:919–31.
64. Scarica C, Suriano R, Levi M, Turri S, Griffini G. Lignin functionalized with succinic anhydride as building block for biobased thermosetting polyester coatings. *ACS Sustain Chem Eng* 2018;6: 3392–401.
65. Fan Q, Liu T, Zhang C, Liu Z, Zheng W, Ou R, et al. Extraordinary solution-processability of lignin in phenol–maleic anhydride and dielectric films with controllable properties. *J Mater Chem A* 2019;7: 23162–72.
66. Jiang B, Chen C, Liang Z, He S, Kuang Y, Song J, et al. Lignin as a wood-inspired binder enabled strong, water stable, and biodegradable paper for plastic replacement. *Adv Funct Mater* 2019;30: 1906307.
67. Cao D, Zhang Q, Hafez AM, Jiao Y, Ma Y, Li H, et al. Lignin-derived holey, layered, and thermally conductive 3D scaffold for lithium dendrite suppression. *Small Methods* 2019;3:1800539.
68. Kai D, Zhang K, Jiang L, Wong HZ, Li Z, Zhang Z, et al. Sustainable and antioxidant lignin–polyester copolymers and nanofibers for potential healthcare applications. *ACS Sustain Chem Eng* 2017;5: 6016–25.
69. Auvergne R, Caillol S, David G, Boutevin B, Pascault J-P. Biobased thermosetting epoxy: present and future. *Chem Rev* 2014;114:1082–115.
70. Qin J, Wolcott M, Zhang J. Use of polycarboxylic acid derived from partially depolymerized lignin as a curing agent for epoxy application. *ACS Sustain Chem Eng* 2013;2:188–93.
71. Zhao S, Abu-Omar MM. Synthesis of renewable thermoset polymers through successive lignin modification using lignin-derived phenols. *ACS Sustain Chem Eng* 2017;5:5059–66.
72. Nonaka Y, Tomita B, Hatano Y. Synthesis of lignin/epoxy resins in aqueous systems and their properties. *Holzforschung* 1997;51:183–7.
73. Engelmann G, Ganster J. Bio-based epoxy resins with low molecular weight Kraft lignin and pyrogallol. *Holzforschung* 2014;68:435–46.
74. Zhao S, Huang X, Whelton AJ, Abu-Omar MM. Formaldehyde-free method for incorporating lignin into epoxy thermosets. *ACS Sustain Chem Eng* 2018;6:10628–36.
75. Feldman D, Banu D, Khoury M. Epoxy–lignin polyblends. III. Thermal properties and infrared analysis. *J Appl Polym Sci* 1989;37:877–87.
76. Feldman D, Banu D, Natansohn A, Wang J. Structure–properties relations of thermally cured epoxy–lignin polyblends. *J Appl Polym Sci* 1991;42:1537–50.
77. Wang J, Banu D, Feldman D. Epoxy–lignin polyblends: effects of various components on adhesive properties. *J Adhes Sci Technol* 1992;6:587–98.
78. Wang G, Liu X, Zhang J, Sui W, Jang J, Si C. One-pot lignin depolymerization and activation by solid acid catalytic phenolation for lightweight phenolic foam preparation. *Ind Crop Prod* 2018;124: 216–25.



79. Nair CR. Advances in addition-cure phenolic resins. *Prog Polym Sci* 2004;29:401–98.
80. Gardziella A, Pilato LA, Knop A. Phenolic resins: chemistry, applications, standardization, safety and ecology. Des Moines, Iowa, USA: Springer Science & Business Media; 2013.
81. Alonso M, Oliet M, Garcia J, Rodriguez F, Echeverría J. Gelation and isoconversional kinetic analysis of lignin–phenol–formaldehyde resol resins cure. *Chem Eng J* 2006;122:159–66.
82. Vazquez G, Antorrena G, González J, Mayor J. Lignin-phenol-formaldehyde adhesives for exterior grade plywoods. *Bioresour Technol* 1995;51:187–92.
83. Danielson B, Simonson R. Kraft lignin in phenol formaldehyde resin. Part 1. Partial replacement of phenol by Kraft lignin in phenol formaldehyde adhesives for plywood. *J Adhes Sci Technol* 1998; 12:923–39.
84. Danielson B, Simonson R. Kraft lignin in phenol formaldehyde resin. Part 2. Evaluation of an industrial trial. *J Adhes Sci Technol* 1998;12:941–6.
85. Podschun J, Saake B, Lehnen R. Reactivity enhancement of organosolv lignin by phenolation for improved bio-based thermosets. *Eur Polym J* 2015;67:1–11.
86. Cederholm L, Xu Y, Tagami A, Sevastyanova O, Odelius K, Hakkarainen M. Microwave processing of lignin in green solvents: a high-yield process to narrow-dispersity oligomers. *Ind Crop Prod* 2020;145:112152.
87. Zhu G, Jin D, Zhao L, Ouyang X, Chen C, Qiu X. Microwave-assisted selective cleavage of C C bond for lignin depolymerization. *Fuel Process Technol* 2017;161:155–61.
88. Gao C, Li M, Zhu C, Hu Y, Shen T, Li M, et al. One-pot depolymerization, demethylation and phenolation of lignin catalyzed by HBr under microwave irradiation for phenolic foam preparation. *Compos B Eng* 2021;205:108530.
89. Boerjan W, Ralph J, Baucher M. Lignin biosynthesis. *Annu Rev Plant Biol* 2003;54:519–46.
90. Fache M, Boutevin B, Caillol S. Vanillin production from lignin and its use as a renewable chemical. *ACS Sustain Chem Eng* 2015;4:35–46.
91. Fache M, Boutevin B, Caillol S. Epoxy thermosets from model mixtures of the lignin-to-vanillin process. *Green Chem* 2016;18:712–25.
92. Holmberg AL, Stanzione JF, Wool RP, Epps TH. A facile method for generating designer block copolymers from functionalized lignin model compounds. *ACS Sustain Chem Eng* 2014;2:569–73.
93. Wang S, Ma S, Xu C, Liu Y, Dai J, Wang Z, et al. Vanillin-derived high-performance flame retardant epoxy resins. *Facile Synth Propert Macromol* 2017;50:1892–901.
94. Van A, Chiou K, Ishida H. Use of renewable resource vanillin for the preparation of benzoxazine resin and reactive monomeric surfactant containing oxazine ring. *Polymer* 2014;55:1443–51.
95. Wang S, Ma S, Li Q, Yuan W, Wang B, Zhu J. Robust, fire-safe, monomer-recovery, highly malleable thermosets from renewable bioresources. *Macromolecules* 2018;51:8001–12.
96. Liu T, Hao C, Zhang S, Yang X, Wang L, Han J, et al. A self-healable high glass transition temperature bioepoxy material based on vitrimer chemistry. *Macromolecules* 2018;51:5577–85.
97. Mu L, Shi Y, Chen L, Ji T, Yuan R, Wang H, et al. [N-Methyl-2-pyrrolidone][C1-C4 carboxylic acid]: a novel solvent system with exceptional lignin solubility. *Chem Commun (Camb)* 2015;51:13554–7.
98. Fan Q, Liu T, Zhang C, Liu Z, Zheng W, Ou R, et al. Extraordinary solution-processability of lignin in phenol–maleic anhydride and dielectric films with controllable properties. *J Mater Chem* 2019;7: 23162–72.
99. Kim WG. Photocure properties of high-heat-resistant photoreactive polymers with cinnamate groups. *J Appl Polym Sci* 2008;107:3615–24.
100. Xin J, Zhang P, Huang K, Zhang J. Study of green epoxy resins derived from renewable cinnamic acid and dipentene: synthesis, curing and properties. *RSC Adv* 2014;4:8525–32.
101. Kaneko T, Matsusaki M, Hang TT, Akashi M. Thermotropic liquid-crystalline polymer derived from natural cinnamoyl biomonomers. *Macromol Rapid Commun* 2004;25:673–7.



102. Kaneko T, Thi TH, Shi DJ, Akashi M. Environmentally degradable, high-performance thermoplastics from phenolic phytomonomers. *Nat Mater* 2006;5:966–70.
103. Matsusaki M, Kishida A, Stainton N, Ansell CW, Akashi M. Synthesis and characterization of novel biodegradable polymers composed of hydroxycinnamic acid and d, l-lactic acid. *J Appl Polym Sci* 2001;82:2357–64.
104. Spiliopoulos IK, Mikroyannidis JA. Unsaturated polyamides and polyesters prepared from 1, 4-bis (2-carboxyvinyl) benzene and 4-hydroxycinnamic acid. *J Polym Sci Polym Chem* 1996;34: 2799–807.
105. Thi TH, Matsusaki M, Akashi M. Thermally stable and photoreactive polylactides by the terminal conjugation of bio-based caffeic acid. *Chem Commun* 2008:3918–20.
106. Thi TH, Matsusaki M, Akashi M. Development of photoreactive degradable branched polyesters with high thermal and mechanical properties. *Biomacromolecules* 2009;10:766–72.
107. Nagata M, Hizakae S. Synthesis and characterization of photocrosslinkable biodegradable polymers derived from 4-hydroxycinnamic acid. *Macromol Biosci* 2003;3:412–9.
108. Truong HT, Van Do M, Duc Huynh L, Thi Nguyen L, Tuan Do A, Thanh Xuan Le T, et al. Ultrasound-Assisted, base-catalyzed, homogeneous reaction for ferulic acid production from γ -oryzanol. *J Chem* 2018;2018:1–9.
109. Huang Y-C, Chen Y-F, Chen C-Y, Chen W-L, Ciou Y-P, Liu W-H, et al. Production of ferulic acid from lignocellulolytic agricultural biomass by *Thermobifida fusca* thermostable esterase produced in *Yarrowia lipolytica* transformant. *Bioresour Technol* 2011;102:8117–22.
110. Oulame MZ, Pion F, Allauddin S, Raju KV, Ducrot P-H, Allais F. Renewable alternating aliphatic-aromatic poly (ester-urethane) s prepared from ferulic acid and bio-based diols. *Eur Polym J* 2015; 63:186–93.
111. Chen Q, Gao K, Peng C, Xie H, Zhao ZK, Bao M. Preparation of lignin/glycerol-based bis (cyclic carbonate) for the synthesis of polyurethanes. *Green Chem* 2015;17:4546–51.
112. Ghosh N, Kiskan B, Yagci Y. Polybenzoxazines—new high performance thermosetting resins: synthesis and properties. *Prog Polym Sci* 2007;32:1344–91.
113. Comí M, Lligadas G, Ronda JC, Galià M, Cádiz V. Renewable benzoxazine monomers from “lignin-like” naturally occurring phenolic derivatives. *J Polym Sci Polym Chem* 2013;51:4894–903.
114. GREGoRová A, Kosíková B, Osvald A. The study of lignin influence on properties of polypropylene composites. *Wood Res* 2005;50:41–8.
115. Košíková B, Demianova V, Kačuráková M. Sulfur-free lignins as composites of polypropylene films. *J Appl Polym Sci* 1993;47:1065–73.
116. Yue X, Chen F, Zhou X. Synthesis of lignin-g-MMA and the utilization of the copolymer in PVC/ wood composites. *J Macromol Sci B* 2012;51:242–54.
117. Baumberger S, Lapierre C, Monties B. Utilization of pine Kraft lignin in starch composites: impact of structural heterogeneity. *J Agric Food Chem* 1998;46:2234–40.
118. Kadla J, Kubo S, Venditti R, Gilbert R, Compere A, Griffith W. Lignin-based carbon fibers for composite fiber applications. *Carbon* 2002;40:2913–20.
119. Megiatto JD, Jr, Silva CG, Rosa DS, Frollini E. Sisal chemically modified with lignins: correlation between fibers and phenolic composites properties. *Polym Degrad Stabil* 2008;93:1109–21.
120. Nenková SK. Study of sorption properties of lignin-derivatized fibrous composites for the remediation of oil polluted receiving waters. *BioResources* 2007;2:408–18.
121. Morandim-Giannetti AA, Agnelli JAM, Lanças BZ, Magnabosco R, Casarin SA, Bettini SH. Lignin as additive in polypropylene/coir composites: thermal, mechanical and morphological properties. *Carbohydr Polym* 2012;87:2563–8.
122. Pupure L, Varna J, Joffe R, Pupurs A. An analysis of the nonlinear behavior of lignin-based flax composites. *Mech Compos Mater* 2013;49:139–54.



123. Canetti M, Bertini F. Influence of the lignin on thermal degradation and melting behaviour of poly (ethylene terephthalate) based composites. *E-Polymers* 2009;9:1–10.
124. Reza Barzegari M, Alemdar A, Zhang Y, Rodrigue D. Mechanical and rheological behavior of highly filled polystyrene with lignin. *Polym Compos* 2012;33:353–61.
125. Sun R. Across the board: runcang sun on lignin nanoparticles. *ChemSusChem* 2020;13:4768–70.
126. Akato K, Tran CD, Chen J, Naskar AK. Poly(ethylene oxide)-assisted macromolecular self-assembly of lignin in ABS matrix for sustainable composite applications. *ACS Sustain Chem Eng* 2015;3: 3070–6.
127. Wang H-M, Wang B, Yuan T-Q, Zheng L, Shi Q, Wang S-F, et al. Tunable, UV-shielding and biodegradable composites based on well-characterized lignins and poly(butylene adipate-co-terephthalate). *Green Chem* 2020;22:8623–32.
128. Zhang X, Liu W, Yang D, Qiu X. Biomimetic supertough and strong biodegradable. polymeric materials with improved thermal properties and excellent UV-blocking performance. *Adv Funct Mater* 2019;29:1806912.
129. Xiao S, Feng J, Zhu J, Wang X, Yi C, Su S. Preparation and characterization of lignin-layered double hydroxide/styrene-butadiene rubber composites. *J Appl Polym Sci* 2013;130:1308–12.
130. Jiang C, He H, Jiang H, Ma L, Jia D. Nano-lignin filled natural rubber composites: preparation and characterization. *Express Polym Lett* 2013;7:480–93.
131. Zhang J, Fleury E, Brook MA. Foamed lignin–silicone bio-composites by extrusion and then compression molding. *Green Chem* 2015;17:4647–56.
132. Zhang J, Chen Y, Sewell P, Brook MA. Utilization of softwood lignin as both crosslinker and reinforcing agent in silicone elastomers. *Green Chem* 2015;17:1811–9.
133. Tran CD, Chen J, Keum JK, Naskar AK. A new class of renewable thermoplastics with extraordinary performance from nanostructured lignin-elastomers. *Adv Funct Mater* 2016;26:2677–85.
134. Khalil HA, Marlina M, Alshammari T. Material properties of epoxy-reinforced biocomposites with lignin from empty fruit bunch as curing agent. *BioResources* 2011;6:5206–23.
135. Doherty W, Halley P, Edye L, Rogers D, Cardona F, Park Y, et al. Studies on polymers and composites from lignin and fiber derived from sugar cane. *Polym Adv Technol* 2007;18:673–8.
136. Stanzione JF, III, Giangulio PA, Sadler JM, La Scala JJ, Wool RP. Lignin-based bio-oil mimic as biobased resin for composite applications. *ACS Sustain Chem Eng* 2013;1:419–26.



证书号第 5372674 号



发 明 专 利 证 书

发 明 名 称：块状木质素-二氧化硅复合气凝胶

发 明 人：王清文;樊奇;欧荣贤;郝笑龙;刘涛;易欣;郭垂根;孙理超

专 利 号：ZL 2021 1 0828714.1

专利申请日：2021 年 07 月 22 日

专 利 权 人：华南农业大学

地 址：510642 广东省广州市天河区五山路 483 号

授权公告日：2022 年 08 月 09 日

授权公告号：CN 113526513 B

国家知识产权局依照中华人民共和国专利法进行审查，决定授予专利权，颁发发明专利证书并在专利登记簿上予以登记。专利权自授权公告之日起生效。专利权期限为二十年，自申请日起算。

专利证书记载专利权登记时的法律状况。专利权的转移、质押、无效、终止、恢复和专利权人的姓名或名称、国籍、地址变更等事项记载在专利登记簿上。



局长
申长雨

申长雨



第 1 页 (共 2 页)

其他事项参见续页

证书号 第 5372674 号

专利权人应当依照专利法及其实施细则规定缴纳年费。本专利的年费应当在每年 07 月 22 日前缴纳。未按照规定缴纳年费的，专利权自应当缴纳年费期满之日起终止。

申请日时本专利记载的申请人、发明人信息如下：

申请人：

华南农业大学

发明人：

王清文；樊奇；欧荣贤；郝笑龙；刘涛；易欣；郭垂根；孙理超

证书号第6534728号



发明专利证书

发 明 名 称：一种含有三维网络结构天然纤维复合材料的制造方法

发 明 人：王清文;郝笑龙;欧荣贤;周海洋;孙理超;唐伟;刘珍珍
李文娟;樊奇;刘涛

专 利 号：ZL 2022 1 0352315.7

专 利 申 请 日：2022年04月05日

专 利 权 人：华南农业大学

地 址：510642 广东省广州市天河区五山路483号

授权公告日：2023年12月05日

授权公告号：CN 114656658 B

国家知识产权局依照中华人民共和国专利法进行审查，决定授予专利权，颁发发明专利证书并在专利登记簿上予以登记。专利权自授权公告之日起生效。专利权期限为二十年，自申请日起算。

专利证书记载专利权登记时的法律状况。专利权的转移、质押、无效、终止、恢复和专利权人的姓名或名称、国籍、地址变更等事项记载在专利登记簿上。



局长
申长雨

申长雨



证书号 第6534728号

专利权人应当依照专利法及其实施细则规定缴纳年费。本专利的年费应当在每年04月05日前缴纳。
未按照规定缴纳年费的，专利权自应当缴纳年费期满之日起终止。

申请日时本专利记载的申请人、发明人信息如下：

申请人：

华南农业大学

发明人：

王清文;郝笑龙;欧荣贤;周海洋;孙理超;唐伟;刘珍珍;李文娟;樊奇;刘涛



荣誉证书

张一全、刘健博、陈磊、王耀程、熊芷璇、彭佳美、廖玉申、雷春光、黄尚昆、贾凡影、
蔡晓漪琳、师铭言、卓才智：

你们的项目《竹尽其用-竹产业升级升级领导者》在中国国际大学生创新大赛（20
24）广东省分赛中荣获

银 奖

指导老师：欧荣贤、郝笑龙、廖鑫、樊奇、易欣
特颁此证，以资鼓励。

广东省教育厅
二〇二四年八月

编号：20240035H



奖状



张一全、刘健博、陈磊、王耀斌、唐伟、熊正璇、彭佳美、廖玉申、

贾凡影、黄尚昆、雷春光、蔡晚璐琳、卓才智、师铭言：

你们的作品《竹尽其用——竹产业创新升级领导者》，在2024年

华南农业大学“创客杯”大学生创新大赛中荣获

金奖

指导老师：欧荣贤、郝笑龙、钟礼韬、易欣、孙理超、张超群、樊奇
特发此证，以资鼓励。

党委学生工作部（党委研究生工作部）

2024年5月24日

